PHYSI[illegible]

VOLUME 88 [illegible] NU[illegible]

# THE PHYSICAL REVIEW

*A journal of experimental and theoretical physics established by E. L. Nichols in 1893*

Published by the American Institute of Physics for the

AMERICAN PHYSICAL SOCIETY



Officers

*President*

J. H. VAN VLECK
Harvard University
Cambridge, Massachusetts

*Vice-President*

ENRICO FERMI
Institute for Nuclear Studies
University of Chicago
Chicago 37, Illinois

*Secretary*

K. K. DARROW
Bell Telephone Laboratories
*Office:*
Columbia University
New York 27, New York

*Treasurer*

G. B. PEGRAM
Columbia University
New York 27, New York

*Local Secretary for the Pacific Coast*

J. KAPLAN
University of California at Los Angeles
Los Angeles, California

*Managing Editor*

S. A. GOUDSMIT
Brookhaven National Laboratory
Upton, Long Island
New York

BOARD OF EDITORS

*Editor*

S. A. GOUDSMIT

*Assistant Editor*

S. PASTERNACK

*Associate Editors*

MARVEY BROOKS
R. F. CHRISTY
C. L. CRITCHFIELD
M. DEUTSCH
T. H. JOHNSON
BRUNO ROSSI
M. GOLDHABER
R. HOFSTADTER
A. W. LAWSON
A. PAIS
R. SERBER
C. H. TOWNES
W. P. ALLIS
F. G. BRICKWEDDE
W. B. FRETTER
CONYERS HERRING
H. W. LEVERENZ
ARNOLD NORDSIECK


Manuscripts for publication should be submitted to S. A. Goudsmit, Brookhaven National Laboratory, Upton, Long Island, New York. The authors' institutions are requested to pay a publication charge of $15 per page, which, if honored, entitles them to 100 free reprints. Instructions will be sent with galley proofs.

Proof and all correspondence concerning papers in the process of publication should be addressed to the Publication Manager, American Institute of Physics, 57 East 55 Street, New York 22, New York.


Subscription Price

*United States and Canada*: ..... $20.00
*Elsewhere*: ..... $22.00

Back Numbers[1]

*Yearly back numbers* sold unless *complete year is available*:
Prior to 1949: $25.00
Thereafter: $33.00
*Single copies*: $3.00 each, prior to July, 1929;
$1.50 each, July, 1929–December, 1941;
$3.00 each, January, 1942–December, 1946;
$1.50 each, thereafter.
*General index, 1893–1929*: $4.00.

Subscriptions, renewals, and orders for back numbers should be addressed to the American Institute of Physics, 57 East 55 Street, New York 22, New York.

Changes of address in the case of members of the American Physical Society should be addressed to the Treasurer; in the case of other subscribers to the American Institute of Physics.


[1] See Series I Index of Physics Department, Cornell University, Ithaca, New York.


The Physical Review is published semi-monthly at Prince and Lemon Streets, Lancaster, Pennsylvania.

Entered as second-class matter March 9, 1927, at the Post Office at Lancaster, Pennsylvania, under the Act of March 3, 1879.

Acceptance for mailing at special rate of postage provided for in paragraph (d-2), section 34.40, P. L. & R., of 1948, authorized January 20, 1927.

THE
PHYSICAL REVIEW

*A journal of experimental and theoretical physics established by E. L. Nichols in 1893*

SECOND SERIES, VOL. 88, NO. 4 NOVEMBER 15, 1952

# The Beta-Spectrum of Tritium and the Mass of the Neutrino*

L. M. LANGER AND R. J. D. MOFFAT
*Department of Physics, Indiana University, Bloomington, Indiana*
(Received June 23, 1952)

A direct determination of the beta-spectrum of $H^3$ has been made in a high resolution magnetic spectrometer. The experimental data are fitted by a straight line Fermi plot from 5.5 kev to the maximum energy at 17.95±0.10 kev. An upper limit of 250 volts or 0.05 percent of the mass of the electron is obtained for the rest mass of the neutrino. New estimates are obtained for the $H^3$ comparative half-life, the neutron half-life, and the value of the Fermi universal constant of beta-decay.

## INTRODUCTION

EVER since it was first realized that tritium is radioactive, the measurement of the beta-spectrum emitted in the transition to $He^3$ has offered a fascinating challenge. Because of the exceedingly small amount of kinetic energy available for the electron, the measurement of an undistorted negatron spectrum has, until recently, been beyond the capabilities of ordinary beta-spectrometer techniques. It is, moreover, this very low energy release which adds interest to the problem, since the shape of this spectrum is expected therefore to be most sensitive to the influence of any finite rest mass for the neutrino. Furthermore, since the initial and final states of this "super allowed" or "favored" transition involve only the simplest of nuclear structures, an exact determination of the energy released in the transition is important for the detailed understanding of the beta-decay process. This is particularly so if the true law of beta-decay involves a linear combination of the scalar, tensor and pseudoscalar interactions.[1] The $H^3 \rightarrow He^3$ comparative half-life ($ft$ value) is then a measure of the relative amounts of scalar and tensor present.

There are two serious difficulties which up to now have stood in the way of a direct magnetic spectrometer determination of the tritium momentum spectrum. Because of the low energy of the electrons, it is necessary to use an extremely thin and completely uniform source in order to avoid distortions of the spectrum arising from absorption and scattering. It is also required that the support for the source be vanishingly thin, or electrons reflected with loss of energy will further distort the distribution. The second obstacle has been that of obtaining a suitable detector whose sensitivity is independent of electron energy over an appreciable part of the distribution, without requiring large empirical corrections.

Because of these difficulties previous investigations have avoided the use of the spectrometer. The other methods employed have, in turn, involved inherent poor resolution which has in most cases necessitated the application of corrections of the same order of magnitude as the effect being investigated. In addition, from the scatter of the reported values for the maximum energy, it is apparent that other perturbations have been present.

Most of the results of earlier attempts to determine the end-point energy of the spectrum are summarized in the review article by Hornyak *et al.*[2] The methods employed were magnetic field cutoff, absorption of the electrons or of bremsstrahlung, cloud chambers, and proportional counters. The end-point energies reported spread from 11±2 kev to 18.9±0.5 kev. Recently, another measurement has been reported[3] of 19.4±0.4 kev, based on work with an electrostatic integral spectrograph. This last determination as well as those made with proportional counters[4,5] attempt to set an

* This work was assisted by a grant from the Frederick Gardner Cottrell Fund of the Research Corporation and by the joint program of the ONR and AEC.

[1] E. J. Konopinski and L. M. Langer, Annual Review of Nuclear Science (to be published).

[2] Hornyak, Lauritsen, Morrison, and Fowler, Revs. Modern Phys. **22**, 291 (1950).

[3] Hamilton, Alford, and Gross, Phys. Rev. **83**, 215 (1952).

[4] G. Hanna and B. Pontecorvo, Phys. Rev. **75**, 983 (1949).

[5] Curran, Angus, and Cockroft, Phil. Mag. **50**, 53 (1949) and Phys. Rev. **76**, 853 (1949).

upper limit on the rest mass of the neutrino from the shape of the spectrum near the end point. The values obtained are lower than the 5-kev limit which was possible from the shape of the higher energy $S^{35}$ spectrum.[6] All these results are not inconsistent with a neutrino rest mass of zero, although the experiments of Curran *et al.* were interpreted as indicative of a finite neutrino mass of between zero and 1 kev.

In the present investigation, the effort has been to develop source preparation and detector techniques which would make possible a straightforward, precise spectrometer determination of the tritium beta-momentum distribution. Operating the spectrometer at 0.7-percent resolution, it has thus been possible to obtain results which, without requiring the application of any large and perhaps ambiguous corrections, are capable of yielding a more precise determination of the maximum energy of the spectrum and set a closer limit on the rest mass of the neutrino.

Estimates of the half-life of tritium have varied from $10.7\pm2$ to $31\pm8$ years.[5] The most recent and probably most accurate value is $12.46\pm0.2$ years.[7] When this value of the half-life is combined with the present energy measurement, one obtains a somewhat different value for the comparative half-life and the universal Fermi constant. An estimate of the half-life of the neutron is also obtained.

## EXPERIMENTAL PROCEDURE

### Spectrometer

The tritium beta-spectrum was studied in the high resolution, 40-cm radius of curvature, shaped magnetic field spectrometer.[8] Although this instrument was designed for general use with electrons as high as 10 Mev, many of its features, such as the freedom from scattering, were particularly applicable to this low energy problem. Because of the low energies of the tritium electrons, certain modifications and improvements were incorporated. These modifications, which are related to the important problem of keeping the source at ground potential, to detection, and to measurement of the low magnetic field strength, are discussed below.

With 0.6-cm source and detector slit widths, the momentum resolution for thin internal conversion sources is measured as 0.7 percent for the full width at half-maximum. Thus, a correction was needed, only for points recorded within 2 percent of the maximum energy. These corrections (see Fig. 4) amount to only about 0.2 percent in momentum and are small compared to the effect in spectral shape which was being studied.

### Detector

A small side window G-M counter was used as a detector. The counter consists of a cylindrical, oxidized copper cathode of 0.5-in. i.d. and 1.6-in. length, with a 0.005-in. tungsten anode mounted on the axis. The electrons enter the counter through a 2.5-cm by 0.6-cm opening along the length of the counter wall. The opening is covered by a 1.5-microgram/cm$^2$ Zapon window which is supported by a fine grid of Lektromesh.[9] This grid is 0.0005 in. thick, has 150 openings to the inch, and 56 percent transmission. Such a grid should introduce no distortion of an electron distribution below about 90 kev.

A mixture of 5 parts argon to 1 part ethylene at a total pressure of 2.5-cm Hg was used as the filling gas. With this arrangement, a plateau of about 80 volts is obtained in the neighborhood of 650 volts.

In spite of the low pressure, a small amount of the gas mixture diffuses through the extremely thin counter window, into the evacuated spectrometer chamber. A modified Cartesian manostat[10] is used to regulate the counter pressure within 0.01-cm Hg. An oil diffusion pump maintains the vacuum in the spectrometer chamber at better than $5\times10^{-6}$-mm Hg. The pulses from the GM tube were constantly monitored on a cathode-ray oscilloscope and showed complete uniformity of amplitude and constancy throughout a spectrum run.

Because of the high specific ionization by the low energy electrons, essentially 100 percent detection efficiency is obtained even with the low pressure used in the counter. Tests were made by varying the counter gas mixture from 2:1 to the more nearly conventional 5:1, and by varying the total gas pressure.

### Source

The nature of this problem requires that the source be extremely thin and uniform. Significant data on spectral shapes can be obtained only in the energy interval for which neither the source nor the support introduce energy degeneration because of inelastic scattering. The demand for a thin, uniform source suggests thermal evaporation in vacuum[11] of some suitable tritiated compound onto a thin support. The requirements on the compound are that it must be stable in high vacuum at ambient temperatures, yet must evaporate without decomposition at a temperature low enough to avoid thermal damage of the thin support. Further, the specific activity must be high. Tritiated succinic acid was the final choice. This compound is quite stable at room temperature, sublimes readily at 150°C, and, as prepared,[12] had a specific activity of 0.9 mC/$\mu$g.

[6] Cook, Langer, and Price, Phys. Rev. **73**, 1395 (1948); and Phys. Rev. **74**, 548 (1948).
[7] Jenks, Ghormley, and Sweeton, Phys. Rev. **75**, 701 (1949).
[8] L. M. Langer and C. S. Cook, Rev. Sci. Instr. **19**, 247 (1948).
[9] Langer, Motz, and Price, Phys. Rev. **77**, 798 (1950).
[10] L. M. Langer and R. D. Moffat, Phys. Rev. **80**, 651 (1950).
[11] Langer, Moffat, and Price, Phys. Rev. **76**, 1725 (1949).
[12] We are grateful to E. S. Robinson and J. G. Povelites of the Los Alamos Scientific Laboratory for their cooperation in preparing the succinic acid sources.

Several sources were prepared by evaporating a 2.5-cm by 0.6-cm rectangle of succinic acid onto a 4 $\mu g/cm^2$ Zapon support. The Zapon is held by a 1.125-in. stainless steel ring which then is mounted in the spectrometer source holder.

The deposits were invisible except for a slight contrast in reflectivity which could be detected at glancing incidence in subdued light. They were estimated to be about 0.5 $\mu g/cm^2$ thick. Counting rates obtained at the peak of the beta-spectrum were between 2000 and 10,000 counts per minute.

Autoradiographs made by exposing the sources to x-ray film, showed complete uniformity of activity and proper localization of the material in the rectangular source region.

### Grounding of the Source

Two methods were used for grounding the sources to prevent electrostatic charging. First, a thin band of copper 1 cm wide and about 2-$\mu g/cm^2$ thick was evaporated thermally in vacuum onto the reverse side of the zapon support. This band extended beyond the edge of the source so as to make contact with the stainless steel ring. Such copper deposits have been measured in this laboratory to have a resistance of the order of $10^8$ ohms. This is sufficiently low to insure good grounding. The second method consists of installing an oxide coated cathode-filament assembly (from an 879 tube) just below the source in the spectrometer. The cathode was heated to normal emission temperature so that any tendency of the source to charge positive would be neutralized by electrons attracted from the emitting cathode. The emission of the cathode was checked by measuring the current to ground when the cathode potential was lowered by 45 volts.

By varying the filament temperature, spectrum runs were obtained with the cathode emission differing by a factor of 100. These were found to give the same results.

Each grounding method alone, as well as the combination of copper backing plus emitting cathode, gave spectra with identical end points. As might be expected, the additional mass of the copper grounding layer resulted in increased scattering which caused the Fermi plot of the data to deviate from a straight line at a higher energy (10 kev) than was otherwise observed (5.5 kev). With no provision for grounding, the sources appeared to charge to about 460 volts as indicated by the lower curve of Fig. 2.

The stability of the sources was checked by measuring the bremsstrahlung in a standard geometry with a thin, mica window GM counter. In spite of repeated and prolonged exposure to high vacuum, no measureable change in activity was detected. Further, repeated spectrometer runs with a given source were found to agree without need for intensity adjustments.

### Magnetic Field

The current for the magnet is supplied by an electronically stabilized source and was monitored by periodically reading the value on a type $K$ potentiometer. The current was stable to better than 1 part in 10,000 during the time required for any point.

Special apparatus was constructed for the measurement of the magnetic field intensity. This experiment required operating in the range of 3.5–15 gauss and the usual field measuring apparatus[13] was not sufficiently sensitive. It was found satisfactory to measure the voltage generated by a coil rotating in the magnetic field. A small coil of 1-cm diameter was driven by an 1800-rpm synchronous motor. The 30-cycle pick-up voltage was brought out through a rotating primary transformer[13] and fed through a narrow band filter and a stabilized amplifier and read on a voltmeter of 0.5 percent accuracy. By appropriate settings of a precision high impedance voltage divider, readings of 10–20 volts were obtained for the region under investigation.

This system was intercalibrated with the deflections from a conventional ballistic galvanometer, flip coil, and standard mutual inductance arrangement. A slight nonlinearity of the amplifier system was overcome by interpreting the voltmeter readings in terms of the appropriate ballistic galvanometer deflection.

The magnetic field shape was carefully checked to insure that there was no variation of the gradient with field intensity. The rotating search coil was mounted so that its position between the pole faces could be varied. Measurements of the field strength relative to the value at the mean radius of 40.32 cm were made as a function of radial position for various field intensities. These measurements included the region from the inside of the beam to the point outside the beam at which the rotating coil was finally located. It was found that cycling of the magnet on the proper hysteresis curve insured reproducibility of the proper field shape. The data were all obtained by successively increasing the energizing current always in the same direction.

### Calibration

Immediately before and after each tritium run, a calibration of the spectrometer was made in terms of the "$A$" line of thorium $C''$. The momentum of this line has been obtained[14] with high accuracy as $H\rho = 533.66 \pm 0.12$. It was selected because it lies close to the end point of the tritium beta-spectrum.

Sources of ThB in equilibrium with its products were prepared by electrostatically collecting the recoil atoms from Th active deposit. The 0.6 cm wide, 0.015-g/cm² Al strip used as a collector was then employed as a grounded source of the Th "$A$" line electrons. The extrapolation of the high energy edge of this line's

[13] L. M. Langer and F. R. Scott, Rev. Sci. Instr. **21**, 522 (1950).

[14] H. Craig, Phys. Rev. **85**, 688 (1952); see also, J. Surugue, Ann. phys. **11**, 8, 484 (1937).

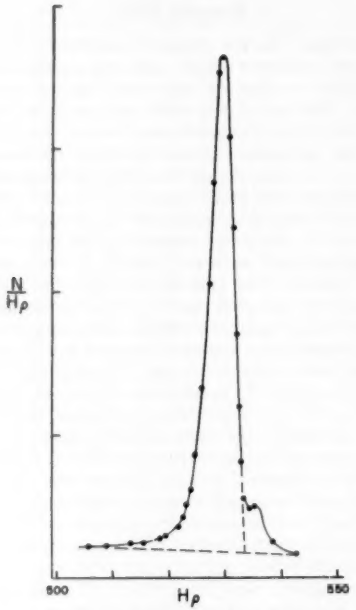


FIG. 1. Typical momentum profile obtained for the "$A$" line of ThC'' used for calibration.

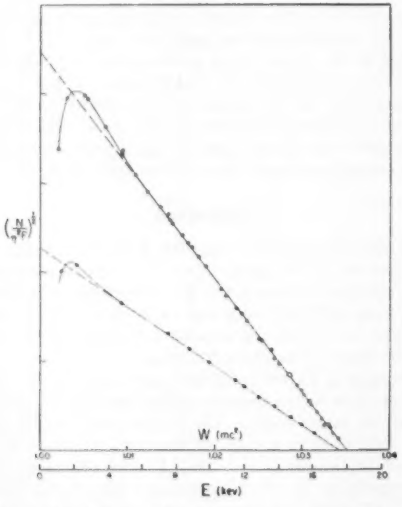


FIG. 2. Fermi plots of the tritium beta-spectrum. The upper curve is for a source grounded by an emitting cathode. The lower curve is for an ungrounded source.

profile was used as a calibration point. Figure 1 shows a typical run. The "$A$" line arises from internal conversion in the $L_I$ shell. The line resulting from the much less frequent conversion in the $L_{II}$ shell does not interfere with the calibration. Because of broadening by the thick Al backing, the line obtained with these sources had a width at half-maximum of 0.9 percent. This broadening does not affect the calibration if the high energy edge extrapolation is used. Correction was made for the fact that this edge corresponds to electrons which have traversed a trajectory with an effective radius, $\rho=\rho_0-\frac{1}{4}(S+\delta)$, where $\rho_0$ is the nominal mean radius and $S$ and $\delta$ are the source and counter slit widths, respectively.

Small corrections for finite geometrical resolution were applied to those points on the tritium spectrum which fall in the immediate neighborhood of the end point.

## RESULTS AND CONCLUSIONS

### The Beta-Spectrum and End Point

The upper curve of Fig. 2 shows a typical Fermi plot of the tritium electron spectrum. The data are fitted well by a straight line from the maximum energy down to 5.5 kev, where the effect of source and backing thickness begin to produce a noticeable excess of low energy electrons. The falling portion of the curve below 2 kev shows the result of attenuation by the thin Zapon counter window. Extrapolation of the straight line, which is the theoretical curve for zero neutrino rest mass, yields an end point of 17.95±0.10 kev. This curve was obtained with a source which was prevented from charging only with the heated cathode. The lower curve of Fig. 2 shows the effect of no provision for grounding the source. Here the whole spectrum appears to be shifted so that the maximum energy appears at 17.49 kev, or 460 volts lower than obtained with a grounded source. Figure 3 shows the result of evaporating 2 $\mu$g/cm$^2$ of copper behind the same source as used for obtaining the data of Fig. 2. As might be expected, the end point remains unchanged, since either method of grounding seems to be sufficient in itself. However, the deviation from the straight line, because of the additional mass of copper, occurs at the higher energy of 10 kev.

In another series of experiments, the sources were mounted so that the 4 $\mu$g/cm$^2$ Zapon support came between the succinic acid deposit and the detector. In general, the results of these experiments shown in Fig. 4 are the same as for those obtained for sources mounted in the normal manner, except for the fact that the curves are shifted so as to appear to give an end point about 250 volts lower. The deviations from the straight line again set in at higher energies. Curve $B$ is for the cathode-emission grounded source, curve $A$ for a copper deposit grounded source. Curve $C$ is for an ungrounded source. It is apparent from these experiments that there is no appreciable penetration of the

succinic acid into the Zapon support—the sort of thing one might expect with sources prepared by adsorption of tritium gas.

### Neutrino Rest Mass

The phenomenological definition of the neutrino and Fermi's use of it in his formulation of the theory of beta-decay make no stipulation about the rest mass of the neutrino other than that it is probably small. It has been shown[15] that if the neutrino were to have a finite rest mass, $\nu$, it would become manifest in its influence on the momentum distribution of the electrons in beta-decay. In that case, the distribution formula for electrons of momentum $\eta$ may be written as

$$Nd\eta = \text{const}F(Z, W)\eta^2K(K^2-\nu^2)^{\frac{1}{2}}(1\mp\nu/WK)d\eta,$$

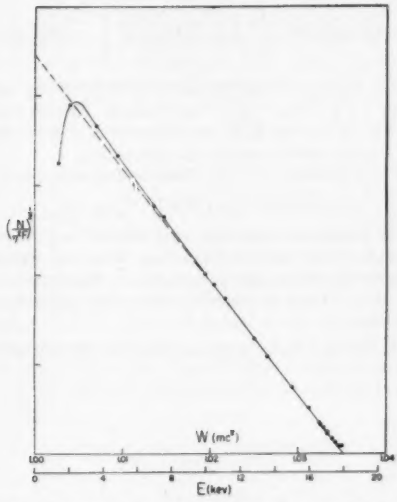


FIG. 3. Fermi plot of the tritium spectrum data obtained with a source which was grounded by a $2\mu$ g/cm² Cu deposit on the backing.

where $N$ is the number of electrons in unit momentum interval, $F$ is the Coulomb factor, $K$ is the neutrino energy and $W=(1+\eta^2)^{\frac{1}{2}}$ is the electron energy, in units of $mc^2$.[16] The negative sign applies if it is a Dirac antineutrino which accompanies negatron emission. The plus sign would apply to Fermi's original formulation of the theory in which the neutrino accompanies negatron emission. The possible validity of such a formulation was substantiated by the considerations of Yang and Tiomno.[17]

The influence of a finite neutrino mass is most pronounced near the maximum energy of the beta-spectrum. The Fermi plot then is no longer a straight line. Instead, it turns sharply towards the energy axis. The distance between the theoretical true end point and the point, defined by the usual straight line extrapolation of the negatron spectrum obtained at low energies, turns out then to be equal to $\nu/2$ or to $3\nu/2$, depending on whether it is the Dirac anti-neutrino or neutrino which is emitted in the process. If a Majorana neutrino were emitted, this distance would be equal to $\nu$. Recent theoretical considerations[18] suggest that the neutrino is a Dirac rather than a Majorana particle. In the following, the negative sign is assumed corresponding to a Dirac antineutrino going with negatron emission. A Fermi plot of the data in the region near the end point is shown in Fig. 5. Both vertical and horizontal scales have been enlarged to show greater detail. The theoretical curves for various neutrino rest energies are shown for comparison with the data. These curves have all been normalized to the observed

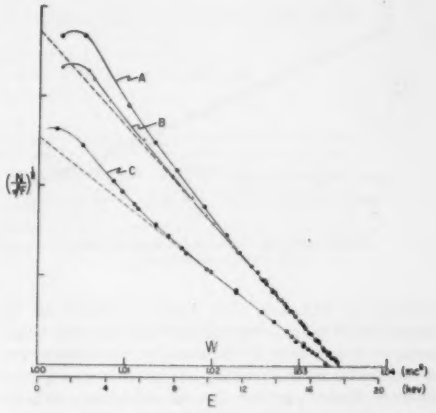


FIG. 4. Fermi plots obtained with sources reversed so that the Zapon support was between the activity and the detector.

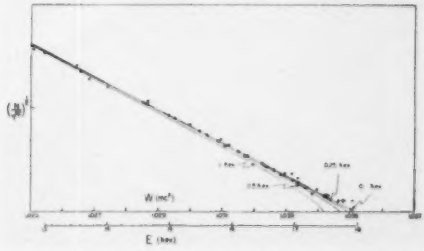

FIG. 5. Expanded Fermi plot of the tritium spectrum in the region near the end point. The curves are the theoretical plots expected for the indicated rest mass of the neutrino.

[15] O. Kofoed-Hansen, Phys. Rev. **71**, 451 (1947).
[16] J. R. Pruett, Phys. Rev. **73**, 1219 (1948); see also reference 6.
[17] C. Yang and J. Tiomno, Phys. Rev. **79**, 485 (1950).
[18] E. R. Caianiello, Phys. Rev. **86**, 564 (1952).

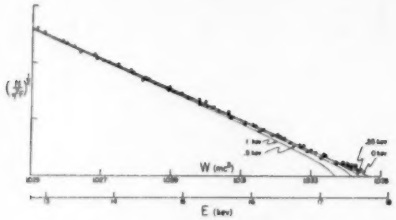


FIG. 6. Like Fig. 5, except for data obtained with the sources reversed.

intensity at 10.5 kev. The small magnitude of the resolution correction required in the immediate neighborhood of the end point is shown by the displacement of the circles to the position of the crosses. Figure 6 shows a similar plot for the data obtained with the source reversed.

The data are consistent with a Dirac neutrino rest mass of zero and set an upper limit on any finite rest mass of 250 volts or 0.05 percent of the rest mass of the electron.

## Comparative Half-Life

The value of 17.95±0.10 kev for the beta-maximum energy, together with the half-life of 12.46±0.2 years,[7] permit a more precise evaluation of the comparative half-life of the super allowed $H^3 \rightarrow He^3$ transition. The result is $ft = 1014 \pm 20$ sec or $\log ft = 3.006$.[19]

[19] The value of $f$ was calculated from Eqs. A6 and A7 given by E. Feenberg and G. Trigg, Revs. Modern Phys. **22**, 404 (1950).

## Neutron Half-Life

If one assumes that the comparative half-life for the neutron decay is the same as for that of $H^3$, one can combine the present results with the measured energy of 0.782±0.002 Mev for the neutron decay[20] to get an estimate of the neutron half-life. The value so obtained is 10.4±0.6 minutes. This value is in good agreement with the experimental value obtained by Robson of 12.8±2.5 minutes.

## Universal Fermi Constant

The $H^3$ decay is an $S_{\frac{1}{2}} \rightarrow S_{\frac{1}{2}}$ transition. If the law of beta-decay is indeed a linear combination of the Fermi and Gamow-Teller forms of interaction,[1] then the universal constant $G$ of beta-decay is given by the relation

$$ft = 5.57 \times 10^{-20} G^{-2} \left[ \left| \int \boldsymbol{\sigma} \right|^2 + K^2 \left| \int 1 \right|^2 \right]^{-1} = 1014 \text{ sec},$$

if $G$ is in units of $mc^2(\hbar/mc)^3 = 4.73 \times 10^{-38}$ erg cm³. Here, $|\int \boldsymbol{\sigma}|$ and $|\int 1|$ are matrix elements and $K = G_F/G_{G-T}$ is the ratio of the strengths of the Fermi and Gamow-Teller parts of the interaction.

If $[|\int \boldsymbol{\sigma}|^2 + K^2 |\int 1|^2]$ is normalized to unity, then

$$G = 7.41 \times 10^{-12} = 3.50 \times 10^{-49} \text{ erg cm}^3.$$

The authors are indebted to Professor E. J. Konopinski for many helpful discussions. They also wish to acknowledge the cooperation of Mr. E. Plassmann and Dr. H. C. Price in assisting with some preliminary experiments.

[20] See reference 2; also, J. Robson, Phys. Rev. **83**, 349 (1951).

# Angular and Direction-Polarization Correlation for $Co^{60}$, $Cs^{134}$, and $Sb^{124}$†

ROBERT M. KLOEPPER,* E. S. LENNOX, AND M. L. WIEDENBECK
*Randall Laboratory of Physics, University of Michigan, Ann Arbor, Michigan*
(Received June 23, 1952)

Using the experimental techniques of Metzger and Deutsch the gamma-gamma angular and direction-polarization correlations have been measured for $Co^{60}$, $Cs^{134}$ and $Sb^{124}$. The reliable results of previous investigations were confirmed for $Co^{60}$ and served to check the instrument. The direction-polarization of $Cs^{134}$ is consistent with a 4–2–0; *EQ,EQ* spin assignment. The absence of gamma-gamma angular and direction-polarization correlation in $Sb^{124}$ requires a multipole mixture for the upper transition and a 3–2–0 spin assignment to the levels involved in the gamma-gamma transitions with no parity changes. The beta-gamma angular and direction-polarization correlation in $Sb^{124}$ agrees with the 3–2–0 spin assignments for the levels of the beta-gamma transitions and with an *EQ* gamma.

WE have measured the angular correlation (between the directions of emission of one gamma-ray and of a successive gamma-ray) as well as the direction-polarization correlation (between the direction of emission of a gamma-ray and the polarization of another accompanying quantum) of successive nuclear transitions in $Co^{60}$, $Cs^{134}$, and $Sb^{124}$. In addition, we have measured the beta-gamma correlation functions for $Sb^{124}$.

The direction-polarization correlation functions, when interpreted in light of angular correlation data, allow one to assign both the multipole order of the gamma-transitions and the parity changes involved. Parity change is directly related to the electric or magnetic nature of the gamma-ray (if its multipole order is known). One may determine not only the over-all parity change from initial-to-final states but also the individual parity changes from initial-to-intermediate and intermediate-to-final states. The Compton scattering process is utilized as the polarization-sensitive process in the polarimeter.

## I. GAMMA-GAMMA CORRELATION MEASUREMENTS

### Apparatus

The experimental arrangement (Fig. 1) is essentially that of Metzger and Deutsch[1] in which plastic scintillation phosphors on 5819 photomultipliers have been used throughout. The source, mounted at the center of the white azimuth circle, is (behind the lead shield) at the intersection of the axes of rotation of the polarization-sensitive counters (2 and 3) and of the polarization-insensitive direction counter (1). The source is attached to and rotates (at its axis) with the direction counter.

Stability of mechanical alignment is extremely important and is maintained by suitable, stable mounting brackets and bearings. The scintillation counters are shielded from the effects of external magnetic fields with ¼-in. wall soft-iron tubing. Tests show that with all orientations the variation of the counting rate in each counter is $<\pm 0.5$ percent; the effect of such variation is eliminated to first order by dividing the triple coincidence rate by the single channel counting rates at the various positions. The scattering phosphor is a truncated cone, 4.0 cm long with a base diameter of 4.3 cm, attached to photomultiplier 3 which in turn is clamped at its base and not rotated. The magnetic shield for this counter and the polarimeter arms (2′ and 2″) rotate about the center-line as axis. The plastic phosphors and extensive lead shielding provide collimation for counters 1 and 3 and limit each to a solid angle of about $0.04\pi$ steradian.

Triode-connected 6AK5 cathode-followers are used at the base of all photomultipliers. The outputs of the polarimeter photomultipliers (2′ and 2″) are combined in a summing circuit and connected to a modified Atomic Instrument Company model 204-B linear amplifier. Each of the outputs from 1 and 3 is likewise amplified. The three discriminator outputs of the 204-B's are applied to a threefold crystal coincidence circuit whose output is, in turn, passed through a 204-B. Four scalers simultaneously monitor the three single channel counting rates and the triple total coincidence rate. Double coincidence rates and resolving

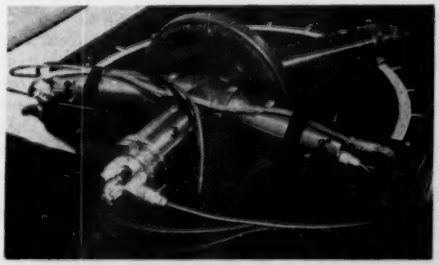

FIG. 1. Photograph showing direction-polarization correlation detector head. Counters 1 and 3 comprise the angular correlation (direction-sensing) counters and define the $\theta$-plane. Counters 2 (2′ and 2″) and 3 are the polarimeter elements and define the $\phi$ plane.

† This paper is part of a dissertation submitted in partial fulfillment of the requirements for the degree of Doctor of Philosophy in the University of Michigan by R.M.K. under the faculty supervision of M.L.W.

* Now at Los Alamos Scientific Laboratory.

[1] F. Metzger and M. Deutsch, Phys. Rev. 78, 551 (1950).

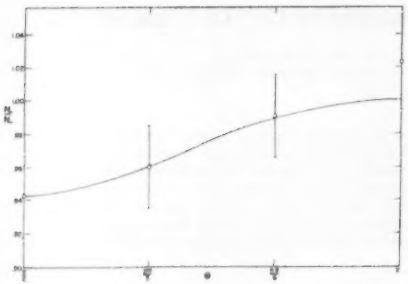

FIG. 2. Direction-polarization correlation of $Co^{60}$. Solid line is theoretical correlation function, assuming 4–2–0; *EQ,EQ* transitions and $R$ equal 1.44.

time measurements are made very frequently to provide reliable corrections for accidentals. The resolving time is maintained at $0.200\pm0.004$ μsec by slight, occasional pulse-shape adjustments, being constant to $\pm1$ percent for periods of a few days to four weeks and to $<\pm0.5$ percent during a day's operation.

The probable errors have been computed from statistical considerations, with each run weighted in accord with observed instrument stability. These probable errors agree well with the probable deviations from the mean, giving a measure of the statistical consistency. For one run approximately 2400 total triple coincidences were recorded at each setting of $\phi$ at 0, $\pi/2$, $\pi$, and $3\pi/2$. Counting rates differed, depending upon, for example, gain settings, source strength, particle energy of the source being measured, and counter efficiency. Typical single channel rates in counts/second are 5000 to 11,000 for counters 1 and 3 and 800 to 1700 for the sum of counters 2′ and 2″. The total triple coincidence rate varied from 0.45 to 1.20 counts-second, again depending upon the equipment adjustment, which was never changed during a run. Approximately seven runs comprised the data for one point. The source strength was adjusted to give a total accidental rate about equal to the triple real rate. All sources were obtained from Oak Ridge.

The $\theta$-plane is defined by the lines from the source to the scatterer (3) and from the source to the direction counter (1). The detector plane contains the lines from source to scatterer and from scatterer to polarimeter phosphors 2′ and 2″. $N_{\parallel}$ is the real triple coincidence rate with $\phi=0$, $\pi$; i.e., with the detector plane *in* the $\theta$-plane. $N_{\perp}$ is the real triple coincidence rate with $\phi=\pi/2$, $3\pi/2$. No direction-polarization correlation should be observed at $\theta=\pi$; i.e., $N_{\parallel}/N_{\perp}$ should equal 1.0. Data taken at $\theta=\pi$ serve as an additional check on the instrument. For measuring angular correlation the polarimeter counters (2′ and 2″) are inactivated and double coincidences between counters 1 and 3 are recorded as a function of $\theta$. All beta-components are shielded from the detectors by aluminum absorbers.

### Cobalt 60

Our gamma-gamma angular correlation measurement for $Co^{60}$ agrees very well with other measurements[2,3] after correction for finite solid angle and fits theoretical values calculated on the 4–2–0; $L=2$, $L=2$, assumption. A direction-polarization correlation measurement of this nuclide is in agreement with previous work[1,4] and is an indication of the reliability of the instrument. The experimental results are presented in Fig. 2. The solid line is calculated on the 4–2–0, *EQ,EQ*, scheme assuming an asymmetry ratio[1] $R$ of 1.44.

### Cesium 134

The gamma-gamma angular correlation data for $Cs^{134}$ are fit reasonably well by the 4–2–0; $L=2$, $L=2$, function in which one assumes a symmetrical component of 35 percent; i.e., $1+0.65[W(\theta)-1]$. Our $W(\pi)$ value of $1.108\pm0.010$ agrees well with that of Robinson and Madansky.[5] At $\theta=2\pi/3$ the experimental value is about 1.8 percent lower than the calculated value; the experimental error at this point is $\pm0.6$ percent. This low value at $\theta=2\pi/3$ agrees with the results of Beyster[4] and may indicate that a symmetrical (no correlation) component does not adequately explain the angular correlation of $Cs^{134}$.

Previous determinations[1,4] of the direction-polarization correlation function of $Cs^{134}$ differ. The gamma-gamma direction-polarization correlation results for $Cs^{134}$ are presented in Fig. 3 and agree with those of Metzger and Deutsch.[1] For the experimental arrangement used, a value of $R$ equal to 2.0 was calculated at 0.7 Mev, assuming that $R$ is 1.44 at 1.24 Mev ($Co^{60}$). The solid line is obtained by using the value $R=2.0$, the angular correlation coefficients as calculated above (with the symmetrical component), and an *EQ,EQ* cascade.

### Antimony 124

We have reinvestigated the gamma-gamma angular correlation and, in addition, have searched for a gamma-gamma direction-polarization correlation in $Sb^{124}$. Antimony 124 has previously been reported[6,7] to give no gamma-gamma angular correlation. Table I shows the results of our measurements, where the angular correlation function $W(\theta)$, the ratio of counting rates $N(\theta)/N(\pi/2)$, has been corrected for finite solid angle. The probable errors are calculated from statistics and the probable error of $N(\pi/2)$ is included in all $W(\theta)$. The higher value $W(\pi)$ could be due to a trace of positron contamination in our source; this possibility

[2] E. L. Brady and M. Deutsch, Phys. Rev. **78**, 558 (1950).
[3] J. R. Beyster and M. L. Wiedenbeck, Phys. Rev. **79**, 411 (1950).
[4] A. H. Williams and M. L. Wiedenbeck, Phys. Rev. **78**, 822 (1950).
[5] B. L. Robinson and L. Madansky, Phys. Rev. **84**, 604 (1951).
[6] J. R. Beyster and M. L. Wiedenbeck, Phys. Rev. **79**, 169 (1950).
[7] D. T. Stevenson and M. Deutsch, Phys. Rev. **83**, 1202 (1951).

of correlation due to annihilation radiation cannot be ruled out. All betas were shielded from the detectors with aluminum.

The complexity of the decay scheme of $Sb^{124}$ as now proposed[8] gives rise to some uncertainty as to the gamma-rays involved in a gamma-gamma correlation measurement which does not discriminate between the various gamma-ray energies. On the basis of the proposed scheme, considering the abundances, one can best assume that most of the gamma-gamma coincidences and correlation arise from the 1.7-Mev and the 0.60-Mev (lowest) gamma-rays.

The absence of gamma-gamma angular correlation and direction-polarization correlation requires that one of the transitions be mixed and further places restrictions on the angular momenta of the levels that are involved. For the ground state we take $J=0$ (even-even) and for the first excited state $J=2$ on the basis of internal conversion data.[9,10] For the transitions $[MD,EQ;EQ]$ we then have the choice for the upper level $J=3$, 2, 1. Using the calculations of Ling and Falkoff[11] and of Zinnes,[12] we find that only $J=3$ with $\beta=0.09$ (i.e., $\sim$10 percent mixture of $EQ$ with $MD$) fits the experimental results. The arbitrariness of the relative phase is only to a sign of the interference term. For this case $R/Q=0$; $S/Q=0.3$ percent for the angular correlation and $J_{\parallel}/J_{\perp}\approx 87$ percent (for $\theta=\pi/2$) for the direction-polarization correlation. This much polarization correlation could have been missed because of the inefficiency of the scattering crystal as a polarimeter. For $J_{\parallel}/J_{\perp}=0.87$ and $R$ calculated as 1.56, we compute an expected $N_{\parallel}/N_{\perp}=1.03$ at $\theta=\pi/2$, which is almost within the quoted statistical uncertainty. If the upper transition were of higher multipole order than $MD$ or $EQ$, this probably would have been detected as internal conversion in the work of Hutchinson.[9]

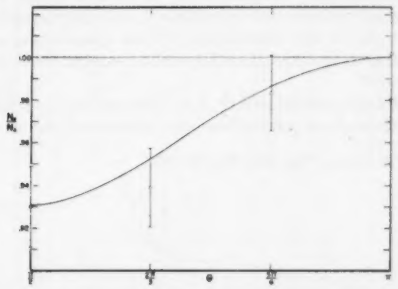

FIG. 3. Direction-polarization correlation of $Cs^{134}$. Solid line is theoretical correlation function, assuming $J$-values of 4–2–0 with $EQ,EQ$ transitions, $R$ equal 2.0, and a 35 percent symmetrical component.

[8] Kern, Zaffarano, and Mitchell, Phys. Rev. **73**, 1142 (1948).
[9] D. R. Hutchinson and M. L. Wiedenbeck, Phys. Rev. **88**, 699 (1952).
[10] F. R. Metzger, Phys. Rev. **86**, 435 (1952).
[11] D. S. Ling, Jr., and D. L. Falkoff, Phys. Rev. **76**, 1639 (1949).
[12] I. Zinnes, Phys. Rev. **80**, 386 (1950).

TABLE I. Gamma-gamma angular correlation $W(\theta)$ and direction-polarization correlation $N_{\parallel}/N_{\perp}$ for $Sb^{124}$.

| $\theta$ | $W(\theta)$ | Probable error | $N_{\parallel}/N_{\perp}$ | Probable error |
|---|---|---|---|---|
| $\pi/2$ | 1.000 | ... | 0.985 | 0.024 |
| $2\pi/3$ | 0.983 | 0.006 | ... | ... |
| $3\pi/4$ | ... | ... | 1.017 | 0.028 |
| $5\pi/6$ | 0.996 | 0.006 | ... | ... |
| $\pi$ | 1.021 | 0.007 | 0.994 | 0.019 |

## II. BETA-GAMMA CORRELATION MEASUREMENTS OF ANTIMONY 124

Accepting an integral portion of the higher energy components of the beta-spectrum of $Sb^{124}$, we have remeasured the beta-gamma angular correlation and have investigated the beta-gamma direction-polarization correlation as a function of $\theta$.

### Apparatus

The equipment of the gamma-gamma correlation work was adapted for beta-gamma correlation experiments by substituting for the plastic phosphor of the direction counter 1 an anthracene crystal 1 mm thick and 29 mm in diameter, making a beta-detector of the direction counter. The source (about 0.008 cm thick) is mounted on a cellophane backing, 0.003 cm thick, by evaporating a $SbCl_3$ solution to dryness. The backing and the source are adequately thin because the correlation is associated with the higher energy betas, which are not seriously scattered by these thicknesses of backing and source. The beta-rays were collimated by a circular aluminum slit and by the size of the beta-detector crystal. To eliminate the lower energy components from the beta-spectrum, a total absorber thickness of 217 mg/cm² was inserted between the source and the beta detector, of which 208 mg/cm² was an aluminum shield on the front of the anthracene crystal. All betas were shielded from the scatterer by 1300-mg/cm² aluminum.

### Beta-Gamma Angular Correlation

The integral beta-gamma angular correlation function, obtained with this experimental arrangement, is plotted in Fig. 4. The solid line (A) is the observed angular correlation function while the dotted line (B) is this correlation function corrected for the effect of gamma-gamma coincidences. The mean energy of emission of those betas which pass through the absorber has been calculated graphically from spectral data[9] as $1.31\pm0.2$ Mev. This calculation assumes that, within the range of energies admitted, each beta carries the same angular correlation. From the differential correlation value calculated at this energy for spins 3–2–0

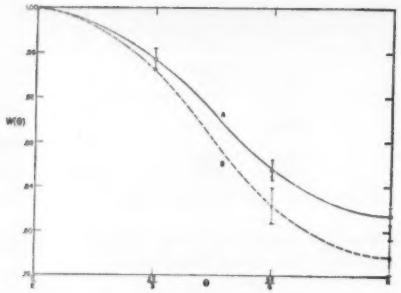

FIG. 4. (*A*) Observed beta-gamma integral angular correlation function; the average energy accepted is approximately 1.3 Mev. (*B*) Correlation function (*A*) corrected for gamma-gamma coincidences.

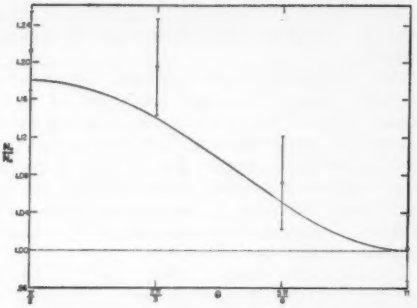

FIG. 5. Experimental beta-gamma direction-polarization correlation function for $Sb^{124}$. Solid line is calculated assuming no parity change in the gamma-transition.

with the $B_{ij}$ matrix element effective in the beta transition, one obtains $W(\pi)=0.80\pm0.03$, after accounting for finite solid angle and the symmetries of the gamma-gamma angular correlation, in good agreement with the observed $0.814\pm0.008$. For a 1–1–0 spin assignment we calculate a $W(\pi)=0.76\pm0.03$. However, it is to be pointed out that this integral angular correlation work is not as sensitive for differentiating between the 3–2–0 and the 1–1–0 assignments as are the data of differential angular correlation.[7]

### Beta-Gamma Direction-Polarization Correlation

The observed beta-gamma direction-polarization correlation values for $Sb^{124}$ are presented in Fig. 5. Lloyd[13] has given a theoretical direction-polarization correlation function which reduces in second order in the coefficients of the Legendre polynomials to

$$N_{\beta\gamma}(\theta;\phi)=1+A\{P_2(\mu)+(\rho/2\epsilon)P_2^2(\mu)\cos2\phi\},$$

where $N_{\beta\gamma}(\theta;\phi)$ is the counting rate with angle $\theta$ between counter 1, the source, and counter 3 and with the angle $\phi$ between the detector plane and the $\theta$-plane, $P_2(\mu)$ and $P_2^2(\mu)$ are the Legendre and associated Legendre polynomials, respectively, with $\mu=\cos\theta$, and $\rho/\epsilon=-(R-1)/(R+1)$. ($R$ is the asymmetry ratio of the polarimeter.) This reduction also includes an assumption that the gamma-ray is a pure multipole with no parity change ($EQ$ or $MD$).

The coefficient $A$ is determined experimentally from the beta-gamma angular correlation data. For angular correlation $\rho_k=0$ in the above function and $W(\pi)$ becomes $(1+A)/(1-A/2)$, from which one can calculate $A$. Correcting $A$ for finite solid angle and using a calculated value of $R=2.2$ for 0.60 Mev, we have determined the function shown by the solid line in Fig. 5. For a yes parity change ($ED$ or $MQ$) the reciprocal of this function results. Our experimental value of $N_{\parallel}/N_{\perp}$ at $\theta=\pi/2$ is $1.211\pm0.042$; Stump[14] finds $1.075\pm0.043$ for approximately the same absorber thickness.

The angular correlation data suggest 3–2–0 for the spins of the states involved in the beta-gamma transitions, requiring the gamma-ray to be quadrupole. The direction-polarization correlation (no parity change) is that of an $EQ$ gamma-ray. These assignments are further substantiated by internal conversion coefficient data.[9,10]

We are grateful to S. P. Lloyd for making the results of his work on polarization correlations available to us.

[13] Stuart P. Lloyd (private communication).

[14] R. Stump, Phys. Rev. **86**, 249 (1952).

# Reinvestigation of the Radioactivity of $Sb^{124}$

D. R. HUTCHINSON AND M. L. WIEDENBECK
*Randall Laboratory of Physics, University of Michigan, Ann Arbor, Michigan*

(Received June 23, 1952)

The beta-spectrum of $Sb^{124}$ was studied with a thin-lens spectrometer with particular emphasis on the internal conversion of the 0.607- and 1.7-Mev gamma-rays and the shape of the high energy beta-spectrum. The conversion coefficients of the 0.607-Mev gamma-ray were found to be $\alpha_K = 3.63 \pm 0.40 \times 10^{-3}$, $\alpha_L = 5.15 \pm 1.0 \times 10^{-4}$. Comparison of $\alpha_K$ with theoretical values indicated the transition to be electric quadrupole. An upper limit of $5 \times 10^{-4}$ has been set on the conversion coefficient of the 1.7-Mev gamma-ray. The highest energy beta-component was shown to be first-forbidden. The next highest beta-component may possibly be first forbidden also.

CONSIDERABLE work has been done on the radiations of $Sb^{124}$ whose decay is both interesting and complex.[1–4] However, in consequence of the seeming difficulty of reconciling some experimental results with theory, especially with regard to assignment of spin and parity changes, further study of this radioisotope has been undertaken. In the present investigation the beta-spectrum of $Sb^{124}$ was studied with particular interest in the internal conversion of the 0.607- and 1.7-Mev gamma-rays.

The measurements were carried out by means of a thin-lens spectrometer[5] with baffles arranged for a resolving power of 1.8 percent. The field current was supplied by a bank of storage batteries and measurements of the field were accurately determined by means of a type-K potentiometer. The instrument was calibrated on the internal conversion line of $Cs^{137}$. The abscissa ($I$) of Fig. 1 is measured in arbitrary current units in which one current unit represents $B\rho$ equal to 811.4 gauss-cm.

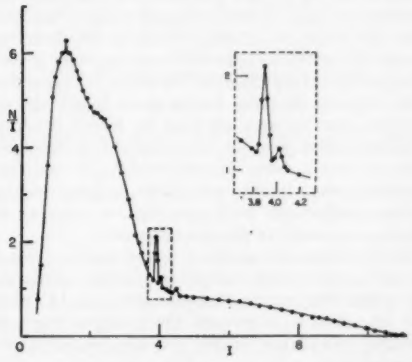


FIG. 1. Beta-spectrum of $Sb^{124}$. Inset shows the $K$- and $L$-conversion line of the 607-kev transition.

The beta-source was prepared by drying $SbCl_3$ rapidly on an aluminized Zapon film having a thickness of 0.034 mg/cm². The thin source disk, 5 mm in diameter, was covered with a 0.017 mg/cm² layer of Zapon. A Geiger counter with a Zapon window of 0.25 mg/cm² was used for detecting the beta-particles. This window had a low energy cutoff of approximately 10 kev.

The momentum spectrum of $Sb^{124}$ is shown in Fig. 1. The inset shows the region of the 607-kev internal conversion line. Careful investigation of this region showed a clear separation of the $K$ and $L$ conversion lines. Since this gamma-ray follows all beta-rays in the proposed decay scheme,[1] the $K$ and $L$ internal conversion coefficients can be determined from the ratio of the areas under each conversion line to that of the entire continuous spectrum. Likewise, of course, the $K/L$ ratio can be evaluated. The experimental values were found to be

$$\alpha_K = 0.00363 \pm 0.0004, \quad \alpha_L = 0.000515 \pm 0.0001,$$
$$K/L = 7.1.$$

If we compare the $\alpha_K$ value with the theoretical values of Rose *et al.*,[6] we find closest agreement with the value

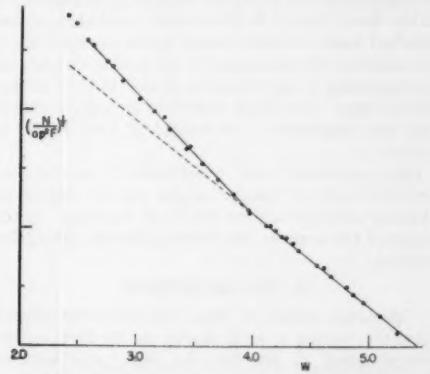


FIG. 2. Fermi plot of upper beta-spectrum of $Sb^{124}$. The upper part has been made linear by applying the $B_{ij}$ correction.

[1] Kern, Zaffarano, and Mitchell, Phys. Rev. **73**, 1142 (1948).
[2] C. S. Cook and L. M. Langer, Phys. Rev. **73**, 1149 (1948).
[3] E. T. Jurney and A. C. G. Mitchell, Phys. Rev. **73**, 1153 (1948).
[4] Langer, Moffat, and Price, Phys. Rev. **79**, 808 (1950).
[5] George A. Bradley, thesis, University of Michigan (1952) (unpublished).
[6] Rose, Goertzel, and Perry, *K-Shell Internal Conversion Coefficients; Revised Tables*, Oak Ridge National Laboratory Report ORNL-1023 (unpublished).

for electric quadrupole. This agrees with the result of Metzger[7] regarding the multipole order of the 607-kev gamma-ray. On the other hand, the present result indicates that there is no need for revising the presently accepted decay scheme.

A careful search was made for conversion electrons which might be associated with the 1.7-Mev transition. Although no excess of electrons was found, it is possible to set an upper limit of 0.0005 for the conversion coefficient. (It is assumed that 62 percent of the transitions go through this state.) The values, as given in the table of Rose, indicate that this transition cannot be as highly forbidden as electric octupole or magnetic quadrupole.

[7] F. R. Metzger, Phys. Rev. **86**, 435 (1952).

A Fermi plot of the high energy part of the beta-spectrum was made. Plotted as an allowed spectrum (not shown) the curve was not linear, but the upper portion was made linear by applying the $B_{ij}$ correction factor as shown in Fig. 2. This indicates that the highest energy component is first forbidden in agreement with the proposal of Langer.[4] The end-point energy was found to be 2.27±0.01 Mev. It is possible that the next lower energy component is likewise first forbidden, although the evidence of the Fermi plot cannot be conclusive in this regard.

A noteworthy feature of the beta-spectrum is the appearance of two distinct low energy components. These undoubtedly are the components having end-point energies of 480 and 650 kev.

PHYSICAL REVIEW VOLUME 88, NUMBER 4 NOVEMBER 15, 1952

# Angular Distributions of Protons and Tritons from Deuteron-Induced Reactions on $Be^9$†

H. W. Fulbright, J. A. Bruner, D. A. Bromley, and L. M. Goldman
*University of Rochester, Rochester, New York*

(Received July 29, 1952)

The angular distributions and absolute cross sections for the reactions $Be^9(d,p)Be^{10}$, $Be^9(d,p)Be^{10*}$ (3.37 Mev), and $Be^9(d,t)Be^8$ have been determined with 3.6-Mev deuterons. Both proton distributions have shapes characteristic of $l_n=1$ in the Butler theory. The peak cross sections found for these reactions are 3.1±0.6 and 4.5±0.9 mb/steradian, respectively. The triton distribution is peaked at 0°. Its cross section at 5° is 15.5±3 mb/steradian.

## I. INTRODUCTION

THE angular distributions of protons from the $Be^9(d,p)Be^{10}$ (ground state) and $Be^9(d,p)Be^{10*}$ (3.37 Mev excited state) reactions have been examined by El Bedewi[1] and by Black[2] and have been found to be characteristic of $p$ neutron capture ($l_n=1$) according to the Butler theory. In those experiments observations were not made at small enough angles to show clearly the existence of a maximum in the proton distribution corresponding to the formation of $Be^{10}$ in its 3.37-Mev excited state. Thus there seemed to be a slight chance that the assignment $l_n=0$ instead of $l_n=1$ might be correct.

Our experiment was undertaken to extend the previous work to smaller angles and to obtain an absolute cross section for the $(d,p)$ processes. In the course of the work we also investigated the $Be^9(d,t)Be^8$ reaction.

## II. THE EXPERIMENT

Collimated deuterons from the Rochester 26-inch cyclotron, having a mean energy of 3.6 Mev and an energy spread of less than 0.1 Mev, were directed through the scattering chamber into a Faraday cup. The current of deuterons into the cup was amplified and integrated electronically. A Be scattering foil[3] of average mass 0.48 mg/cm² was mounted in the center of the scattering chamber. An argon-filled ionization chamber having a Frisch grid and a 0.003-in. aluminum window was used to detect charged particles emerging from the target. Its position could be adjusted from outside the scattering chamber to any angle up to 160°. The pressure in the chamber was about 100 psi, sufficiently high so that the ranges of all heavy charged particles entering were less than the length of the ion chamber. Pulses from the ion chamber were amplified, then fed into a thirty-channel pulse-height analyzer.[4] An electromagnetically retractable polonium alpha-particle source was built into the ion chamber for testing and energy calibration purposes.

Observations were made at angles ranging from 4° to 160°, beam current integrator readings being used for normalizing except at angles less than 13° where the ion chamber intercepted the deuteron beam. An auxiliary scintillation counter was used for normalizing in those cases.

## III. RESULTS

A typical pulse-height distribution is shown in Fig. 1. The assignments of the three peaks to the reactions

† Work performed under the auspices of AEC.

[1] F. A. El Bedewi, Proc. Phys. Soc. (London) **65**, 64 (1952).

[2] C. F. Black, Phys. Rev. **87**, 205 (1952).

[3] Originally prepared and sent to this laboratory several years ago by Dr. Hugh Bradner.

[4] Fulbright, McCarthy, and McCutchen, Phys. Rev. **87**, 184 (1952).

indicated were made by comparison of their measured energies with the energies expected from the known $Q$ values for the respective reactions. The energies were determined by comparison of the heights of the pulses with the height of polonium $\alpha$-particle pulses from the calibrating source. The gas pressure was reduced to about two atmospheres during calibration runs because of ion recombination observed with alpha-particles at 100 psi. It was assumed that the pulse heights were proportional to the kinetic energies lost by the particles in the gas.[5] Energies calculated for various scattering angles were consistent.

Angular distributions and cross sections for the three groups of particles are shown in Figs. 2–4. The results shown are a compilation from three separate sets of

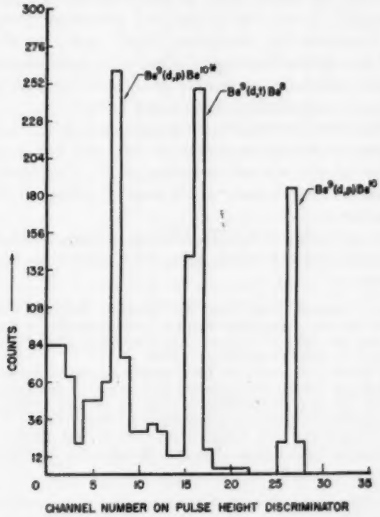


FIG. 1. Typical pulse-height distribution obtained at 26.5 degrees. The true zero pulse height is depressed 5½ channels.

data. In preparing these curves from the pulse-height distributions it was necessary to make allowances for background. Very little background was observed near the high energy proton group; however, a large background had to be subtracted from the low energy proton group, expecially at angles less than 20° where the background was comparable with the peak height.

The background is a rather broad distribution of pulses. It is probably due to a mixture of particles such as protons from $(d,p)$ reactions on target impurities, recoiling argon ions from fast neutrons, and beta particles. The impurity most likely to cause trouble is

[5] There is evidence that this should be a good enough assumption for our purpose: Jesse, Forstat, and Sadauski, Phys. Rev. **77**, 782 (1950); L. H. Gray, Proc. Cambridge Phil. Soc. **40**, 72 (1944); and U. Fano, Phys. Rev. **70**, 44 (1946).

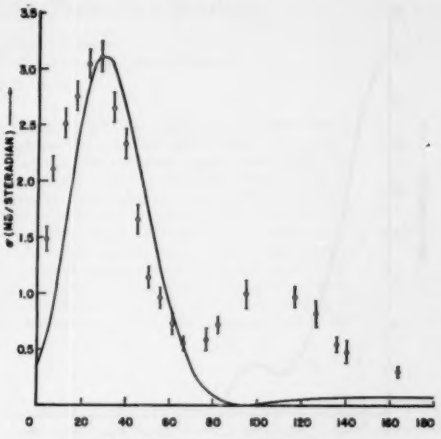


FIG. 2. Angular distribution of ground-state proton group. Curve is Butler theory prediction for 3.6-Mev deuterons, with $r_0=4.5\times10^{-13}$ cm and $Q=4.59$ Mev.

oxygen. At small angles the reaction $O^{16}(d,p)O^{17*}$ (0.87-Mev state) should give protons which are indistinguishable from the lower energy group from the

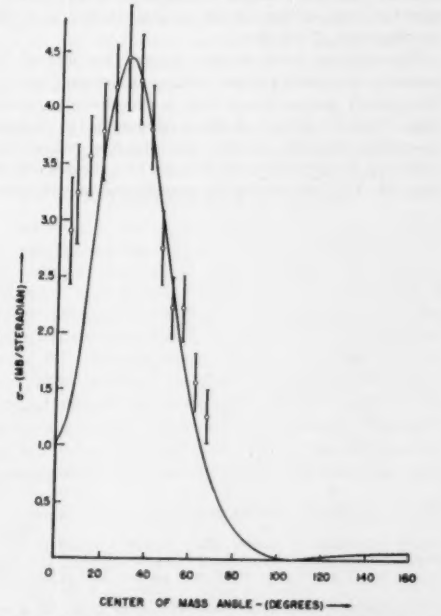


FIG. 3. Angular distribution of 3.37-Mev excited state proton group. Curve is theoretical prediction for 3.6-Mev deuterons and $r_0=4.5\times10^{-13}$ cm.

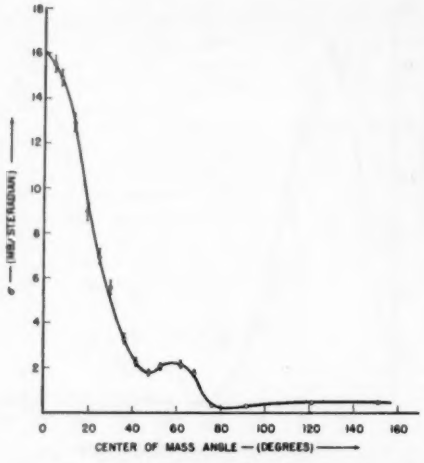


FIG. 4. Angular distribution of tritons from the reaction $Be^9(d,t)Be^8$.

beryllium reaction. The impurity group should be strongly peaked at 0°, since it is from an $l_n=0$ reaction, but its influence was found to be small, so we may conclude that our target contained little oxygen, or that the cross section for the oxygen reaction is small for deuterons of 3.6 Mev.

The absolute cross sections quoted are limited in accuracy to twenty percent because of uncertainties in the current measurements and in the effective target mass. Proton currents of about one-fourth the normal operating deuteron current are observed when the cyclotron is operated at low pressure with the deuterium shut off. They are due to the acceleration of molecular hydrogen which is stripped by the scattering foil. When the cyclotron is operated normally the proton contribution drops to one percent or less of the total beam current, presumably because the molecular ions are broken up by collisions with deuterium molecules. An auxiliary experiment carried out with a gold foil scatterer gave five percent agreement with the Coulomb scattering cross section.

## IV. DISCUSSION AND CONCLUSIONS

Both the ground state and first excited state proton groups from the $Be^9(d,p)Be^{10}$ reaction show agreement with Butler's cruves for $l_n=1$. The peak cross sections found for these reactions are $3.1\pm0.6$ and $4.5\pm0.9$ mb/steradian, respectively.[6] The secondary maximum occurring at about 105° in the high energy group apparently is not due to an $l_n=3$ admixture because the corresponding theoretical curve peaks at about 80°.[7] An explanation might be found in a more complete theory, especially one taking account of nuclear scattering, as suggested by Daitch and French.[8]

The triton distribution is strongly peaked at 0°, with a small secondary maximum at 60°, and has a cross section of $15.5\pm3$ mb/steradian at 5°. The shape is similar to that found by El Bedewi[9] using 7.7-Mev deuterons.

We are indebted to Mr. William Skillman and Mr. James Raz for the calculations of the theoretical Butler curves.

[6] A. J. Salmon, Proc. Phys. Soc. (London) **A64**, 848 (1951), reports for the ground state reaction $\sigma=0.43\pm0.09\times10^{-26}$ cm²/steradian for 301-kev deuterons and $\sigma=2.96\pm0.59\times10^{-26}$ cm²/steradian for 440-kev deuterons; $\theta=90°$.

[7] J. R. Holt, Report of the International Physics Conference at Copenhagen (1952), has suggested accounting for the secondary peak in the angular distribution observed for the $Al^{27}(d,p)Al^{28}$ (first excited state) case by a mixture of $l_n=0$ and 2.

[8] P. Daitch and J. B. French, Phys. Rev. **87**, 900 (1952).

[9] F. A. El Bedewi, Proc. Phys. Soc. (London) **64**, 947 (1951).

# Superconductivity of Indium-Thallium Solid Solutions

J. W. STOUT AND LESTER GUTTMAN
*Institute for the Study of Metals, University of Chicago, Chicago, Illinois*
(Received July 28, 1952)

Measurements are reported on the superconducting properties of indium-thallium solid solutions in the composition range from pure indium to 50 percent thallium. The magnetic induction and the electrical resistance were measured at various temperatures and magnetic field strengths. Single crystal specimens of composition 0, 5, 10, 15, and 20 atom percent thallium, and polycrystalline specimens containing 15, 20, 38, and 50 percent thallium, were investigated. In the more dilute solutions the penetration of field into the specimen at constant temperature was sharp and the restoration of resistance occurred at substantially the same field. As the concentration of thallium increased, the flux penetration occurred over a wider range of field and the resistance appeared only after practically all the flux had penetrated. For the single crystal specimens the trapped flux in zero field was less than 20 percent of that corresponding to unit permeability at the field where flux penetration begins. The breadth of transition in the polycrystalline specimens was like that of the single crystals, but the trapped flux was much larger. The critical fields for destruction of superconductivity are given for the range 0 to 20 percent thallium and the electronic heat capacities of the normal metal are calculated from them.

PREVIOUS work on the superconducting properties of alloys[1] has indicated that, in contrast to the behavior of pure metals, alloy specimens are characterized by broad transitions extending over a range of temperature in zero magnetic field and, upon the application of a magnetic field at constant temperature, by a gradual penetration of flux into the sample occurring over a wide range of field strengths. Furthermore, the magnetic field necessary to restore electrical resistance is greater, often by as much as a factor of 10, than the field at which substantially all of the flux has penetrated into the specimen. Upon the removal of a magnetic field there is a large amount of trapped flux (absence of Meissner effect). These properties have been explained[1] by assuming that in an alloy there is a "sponge" structure so that different parts of a specimen have different critical temperatures and critical field strengths.

In an alloy consisting of two or more solid phases, one would expect that the physical and chemical inhomogeneities would account for a variation in superconducting properties throughout the specimen. However, for an ordered single-phase intermetallic compound there is no evident reason for inhomogeneities and indeed Shoenberg[2] has found that a carefully prepared specimen of the compound $Au_2Bi$ exhibits superconducting properties similar to those of a pure metal. In recent experiments on the compound MgTl we have found a similar behavior. In contrast to an ordered compound, a random solid solution is disordered on an atomic scale, but would be uniform on a scale comparable to the penetration depth of a magnetic field in a superconductor. In order to investigate the properties of a superconducting solid solution we chose the system indium-thallium. This system has the advantage that the melting temperatures are convenient for growing single crystals and that the components are both ideal "soft" superconductors. Measurements of the transition temperatures of indium-thallium alloys made on polycrystalline specimens have been reported by Meissner, Franz, and Westerhoff.[3] By an x-ray investigation Guttman[4] has found that there is a continuous range of solid solutions extending from pure indium to 59 atom percent Tl. There is a transformation from a face-centered tetragonal to a face-centered cubic structure, at room temperature occurring at a composition of 22.7 atom percent thallium, but there is evidently no separation into two phases of different composition upon passing through this transition, which is probably one of second order.[5] Brief preliminary reports of our measurements on the superconductivity of indium-thallium alloys have been published.[6]

## PREPARATION OF SAMPLES

All samples used were in the form of cylinders about 6 mm in diameter and 15 cm long. Solutions of the appropriate composition were prepared by melting together pure indium (99.95 percent) and thallium (99.95 percent) with vigorous stirring under an atmosphere of nitrogen, and then casting in a cold graphite mold. The castings, which were about 19 mm in diameter, were rolled and swaged into cylinders. The single crystal samples were grown in precision bore Pyrex tubes into which the cylinders slipped easily. The inside of each tube was rinsed with a solution of 0.01 percent mineral oil in carbon tetrachloride. The thin film of oil

[1] See, e.g., K. Mendelssohn, Repts. Progr. Phys. **10**, 358 (1946); D. Shoenberg, *Superconductivity* (Cambridge University Press, Cambridge, 1938), Chap. VI.
[2] D. Shoenberg, Nature **142**, 874 (1938).
[3] Meissner, Franz, and Westerhoff, Ann. Physik [5] **13**, 505 (1932).
[4] L. Guttman, J. Metals (Trans. Am. Inst. Mining Met. Engrs. **188**, 1472 (1950)); Bowles, Barrett, and Guttman, J. Metals (Trans. Am. Inst. Mining Met. Engrs. **188**, 1478 (1950)).
[5] See J. W. Stout, Phys. Rev. **74**, 605 (1948).
[6] J. W. Stout and L. Guttman, Phys. Rev. **79**, 396 (1950); Proc. Natl. Bur. Standards Symposium on Low Temperature Physics (March, 1951) (unpublished).

TABLE I. Composition of In—Tl single crystal specimens.

| Nominal | Atom percent thallium Top | Bottom |
|---|---|---|
| 5 | 5.04 | 5.05 |
| 10 | 10.07 | 10.07 |
| 15 | 14.91 | 15.26 |
| 20 | 19.35 | 20.43 |

remaining after the evaporation of the solvent facilitated the removal of the finished crystal. After insertion of the sample, the tube was evacuated to $10^{-5}$ mm of mercury and sealed off. It was then placed in a vertical electric tube furnace controlled at such a temperature that the specimen was first entirely melted. The tube was then lowered at a rate of 13 mm per hour so that the solid grew from the bottom. The crystals could usually be removed from the tubes by gentle tapping, but in some cases, to avoid deformation, the glass was dissolved in HF solution without appreciably attacking the alloys. The samples as removed from the growing tubes were about 30 cm long. A region 15 cm long, of a single crystallographic orientation, was cut from each specimen by a glass string saw moistened with concentrated nitric acid. The saw cutting was entirely by the chemical action of the nitric acid, and the string pressure was not great enough to deform the single crystal. Etching with acetic acid and $H_2O_2$ showed that the specimens employed for the superconductivity measurements were essentially single crystals, although some had small regions where slip had occurred in handling. The 20 percent thallium specimen had transformed from cubic to tetragonal during cooling to room temperature after solidification and there were transformation markings on its surface resembling, but on a much larger scale, those described by Guttman[4] for polycrystalline samples. The sample was probably a single crystal when it solidified from the melt, but in passing through the transformation it broke down into a set of tetragonal crystals having fixed orientations (see Bowles *et al.*[4]) relative to the original cubic axes. The energy of the interfaces between these various orientations of the tetragonal crystals, as is the case with boundaries between crystallographic twins, is apparently very small compared to that of ordinary grain boundaries in a polycrystalline specimen and we observed nothing in the superconducting properties of the 20 percent single crystal which could be ascribed to these boundaries.

Samples for analysis were taken from the regions near the cut ends of the specimen. The results are listed in Table I. The 5 and 10 percent specimens are uniform within the accuracy of the analysis, but the other two are definitely richer in thallium at the bottom end. Reference to the phase diagram[4] shows that at the melting point solid of 5 and 10 percent composition is in equilibrium with liquid richer in thallium, whereas the 15 and 20 percent solid is in equilibrium with indium-rich liquid. In the growing of a long single crystal, if there is no convection in the liquid, a steady state will be obtained in which the solid crystallizing has the over-all composition. The adjacent liquid is in equilibrium with this solid and there is a concentration gradient from the solid interface to a point beyond which the liquid has substantially the over-all composition. When the liquid in equilibrium with the solid is more dense (thallium rich) the region of concentration gradient is stable against convection; however, in the case of the 15 and 20 percent specimens convection probably occurred and a steady state was not attained.

In order to compare the behavior of single and polycrystal specimens and also to extend the composition range beyond the point where single crystals can be grown from the melt, a series of polycrystal specimens was prepared. To produce large grains, a strain-anneal technique was used. The cast samples were reduced to rods slightly larger than the desired final diameter and stretched in a tensile machine so as to obtain a uniform elongation of 2 to 3 percent. They were then cut to length, the ends rounded in a lathe, and the samples annealed in $N_2$-filled tubes in an oil bath at 140–145°C for 7–16 days. For the 50 percent specimen, the temperature was 118°C, obtained by boiling *n*-butyl alcohol. During annealing the individual crystals grew to a size of about 1 to 2 mm. The samples prepared by this technique were quite uniform in composition. The results of analysis of samples cut from the top and bottom of each specimen are shown in Table II.

TABLE II. Composition of In—Tl polycrystal specimens.

| Nominal | Atom percent thallium Top | Bottom |
|---|---|---|
| 15 | 15.05 | 15.08 |
| 20 | 19.95 | 19.96 |
| 30 | 30.10 | 30.04 |
| 38 | 37.92 | 37.96 |
| 50 | 49.82 | 49.54 |

## APPARATUS

Measurements were made on all the specimens both of magnetic induction and electrical resistance at various temperatures and magnetic field strengths. A uniform magnetic field, parallel to the cylindrical axis of the samples, was provided by a solenoid mounted in the liquid nitrogen both surrounding the helium dewar. The solenoid was made of No. 16 Formex insulated copper wire wound in accurately turned grooves in four concentric Micarta tubes. The precision of the machining was such that the field for a given current could be calculated to within 0.1 percent from the dimensions of the solenoid. The magnetic field at the end of a 15-cm long specimen was 1.6 percent less than at its center and the variation over a region 4 cm long near the

center, the part which most influences the secondary coils, was only 0.1 percent.

For the induction measurements the samples were mounted in Lucite holders on each of which was wound a two-layer coil, 16 mm long, of about 300 turns of No. 40 Formex insulated copper wire. The Lucite tubes were machined to a thickness of 0.25 mm beneath the coils in order to minimize leakage flux. Slots were cut in the tubes to insure contact between the samples and the helium bath. Five specimen holders could be mounted in the Dewar, arranged symmetrically around a central tube which housed the stirrer for the bath, a Micarta screw driven by a variable speed motor. The specimen holders fitted accurately into a support which aligned the axis of the samples parallel to the field direction. The coils on the sample holders were connected through a selector switch to a ballistic galvanometer. In making a measurement the magnetic field in the solenoid was changed rapidly and the galvanometer deflection corresponding to the change in flux of induction through a coil was observed.

For the resistance measurements the samples were mounted in the Dewar in the same position relative to the solenoid as for the induction measurements. Current and potential leads were attached by means of small split copper rings held in place by brass screws kept tight with spring washers of phosphor bronze. The upper current lead was mounted rigidly on a Micarta support, but the other three leads were attached firmly only to the specimen so that no strain was produced by differential thermal contraction of the specimens and holder. There was negligible contact resistance at all temperatures between the specimens and the split rings to which the current and potential leads were soldered (with nonsuperconducting zinc-cadmium solder). No error was introduced because of possible contact resistance, since it enters into the resistance calculation only in its effect on the galvanometer sensitivity. The current (measured across a standard 0.01-ohm resistor) and the potential were read on a Wenner potentiometer with a sensitivity of about 0.01 microvolt. Because of the large size of the specimens the resistances of the samples were small, ranging at the boiling point of helium from $1.53\times10^{-6}$ ohm for the pure indium to $1.69\times10^{-4}$ ohm for the 50 percent thallium specimen. The accuracy of the resistance measurements was about 3 percent for the pure indium specimen and about 0.5 percent for the others.

The temperature of the samples was determined from the vapor pressure of the helium bath, using the table of van Dijk and Shoenberg.[7] At the higher pressures the bath pressure was held constant by a solenoid valve controlled by a mercury manometer and at the lower pressures was either controlled manually or allowed to come to equilibrium with the pump. In all measurements above the lambda-point the stirrer was operated to assist in obtaining temperature equilibrium throughout the bath. The resistance-temperature data in zero field were taken with the bath slowly cooling, since the temperature equilibrium is then assisted by convection. Warming curves gave apparent temperatures a few thousandths of a degree higher for the superconducting transitions, probably due to incomplete thermal equilibrium even in the stirred bath.

[7] H. van Dijk and D. Shoenberg, Nature **164**, 151 (1949).

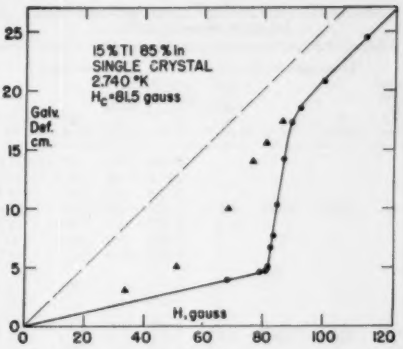


FIG. 1. Galvanometer deflection *versus* magnetic field.

## THE INDUCTION MEASUREMENTS

A typical set of data obtained in the measurement of the magnetic induction of a specimen at constant temperature and in different magnetic fields is shown in Fig. 1. In making a measurement the galvanometer deflection was observed corresponding to a sudden change of the applied magnetic field from some constant value to zero. The current in the solenoid was regulated by an electronic controller operating on the field current of the generator and could be set and held constant to better than 0.1 percent. The galvanometer deflection is proportional to the change in the flux of induction through the measuring coil surrounding the sample in going from a field equal to the solenoid field plus the earth's field to the earth's field alone. The value of the earth's field (0.4 gauss) was measured at the position of the samples, and a small correction has been made for this in the calculation of the magnetic induction in the sample. The dashed line in Fig. 1 is the curve for a sample of unit permeability, determined from measurements above the superconducting transition temperature. The points indicated by filled circles are obtained by setting the field at a constant value, approached from low fields, and then quickly switching it off. When the sample is completely superconducting, the small galvanometer deflections observed, due to the leakage flux between the sample and the coil, lie on a straight line through the origin. As the magnetic field is increased beyond a critical value, the flux penetrates into the sample with a rapid increase in galvanometer deflection.

TABLE III. Data on single crystal specimens from induction measurements.

| Nominal composition percent thallium | Parameters for Eq. (1) $H_0$ gauss | $T_s$, °K | $\gamma \times 10^4$ cal deg$^{-2}$ (g atom)$^{-1}$ | Observed data $T$, °K | $B_0$ gauss | $H_c$ gauss | $H_c$ (obs)$-H_c$ (Eq. 1) |
|---|---|---|---|---|---|---|---|
| | | | | 3.185 | 1.6 | 32.8 | 1.8 |
| | | | | 2.975 | 3.8 | 63.9 | 0.6 |
| | | | | 2.738 | 9.2 | 95.7 | −1.4 |
| 0 | 284.3 | 3.374 | 4.3 | 2.578 | 9.6 | 116.7 | −1.6 |
| | | | | 2.222 | 14.5 | 159.9 | −1.1 |
| | | | | 1.895 | 19.2 | 194.8 | 0.2 |
| | | | | 1.325 | 25.9 | 242.1 | 1.7 |
| | | | | 3.170 | 3.1 | 20.5 | 2.3 |
| | | | | 2.975 | 8.2 | 48.8 | −0.2 |
| | | | | 2.737 | 11.9 | 83.1 | −0.9 |
| 5 | 276.5 | 3.280 | 4.3 | 2.579 | 19.8 | 103.5 | −2.1 |
| | | | | 2.226 | 29.3 | 148.5 | −0.7 |
| | | | | 1.907 | 34.7 | 183.2 | 0.2 |
| | | | | 1.309 | 42.8 | 233.9 | 1.4 |
| | | | | 3.162 | 2.7 | 17.8 | 1.7 |
| | | | | 2.954 | 7.5 | 49.9 | −0.3 |
| | | | | 2.740 | 16.1 | 82.7 | −0.3 |
| 10 | 284.7 | 3.255 | 4.6 | 2.579 | 15.1 | 104.0 | −2.0 |
| | | | | 2.228 | 30.2 | 150.4 | −0.9 |
| | | | | 1.915 | 36.4 | 187.2 | 1.0 |
| | | | | 1.301 | 48.5 | 239.9 | 0.7 |
| | | | | 3.152 | 2.3 | 16.0 | −1.0 |
| | | | | 2.946 | 8.2 | 50.4 | 0.0 |
| | | | | 2.740 | 22.0 | 81.5 | 0.0 |
| 15 | 281.1 | 3.252 | 4.5 | 2.591 | 17.6 | 104.2 | 1.5 |
| | | | | 1.920 | 35.7 | 183.0 | −0.1 |
| | | | | 1.293 | 46.3 | 236.1 | −0.6 |
| | | | | 3.143 | 1.9 | 11.5 | −0.9 |
| | | | | 2.924 | 7.4 | 44.0 | −0.6 |
| | | | | 2.730 | 16.0 | 71.2 | −0.1 |
| 20 | 252.3 | 3.223 | 3.7 | 2.591 | 14.6 | 90.8 | 1.6 |
| | | | | 1.922 | 21.1 | 164.2 | 1.6 |
| | | | | 1.286 | 37.6 | 210.4 | −1.7 |

When the flux penetration into the sample is complete, ($B=H$), the galvanometer deflections lie on a straight line with slope equal to that observed for a sample of unit permeability, but displaced downwards by an amount proportional to the trapped magnetic induction, $B_0$, in zero field. Once a sample had been exposed to a field large enough to insure complete flux penetration, it was found that, at constant temperature, the value of $B_0$ remained the same. This is indicated by the fact that at high fields the points for galvanometer deflection *versus* field lie on a straight line and by the reproducibility of the measurements. It was also found that the total flux change observed in decreasing the field to zero in several steps was equal to that of a single step over the same range of field, and that the galvanometer deflection in throwing a field off was equal to that observed when the same field was thrown on. The points indicated by triangles in Fig. 1 were obtained by first throwing on a large field at which flux penetration is complete, decreasing the field to the value corresponding to the abscissa of the point, and measuring the galvanometer deflection when the latter field was reduced to zero. These points are evidence of a hysteresis in the induction in the sample according to whether a given value of field is approached from the high or low side. This type of hysteresis was found for the pure indium sample as well as the others. After some measurements had been taken on the indium single crystal with the roughly square ends left by the string saw, we removed the sample and rounded the ends by electrolytic polishing. This treatment considerably reduced the hysteresis observed on reducing the field, but did not otherwise change the curve of galvanometer deflection *versus* field. In Table III the data at 2.738 and 2.222°K are for the specimen with the ends rounded.

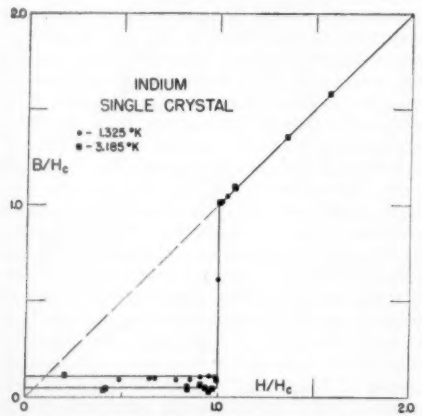


FIG. 2. Reduced magnetic induction *versus* reduced field.

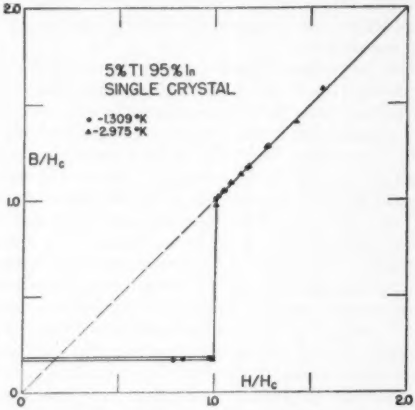


FIG. 3. Reduced magnetic induction *versus* reduced field.

Since, when the fields were approached from the low

side, the shape of the curves for the pure indium specimen and the more dilute alloys corresponded to the sharp penetration of flux at a critical field characteristic of an ideal superconductor, most of our measurements were made in this fashion. In the curves given below, the hysteresis points have been omitted and the plotted points represent the flux of induction, as approached from low fields, in samples previously conditioned by exposure to a supercritical field and then brought back to zero field. If one calls $\Delta$ the observed galvanometer deflection, $k_1$ the slope of galvanometer deflection *versus* field above the superconducting transition temperature, and $k_2$ the slope of galvanometer deflection *versus* field when the sample is completely superconducting, then the change in induction in the sample upon changing from field $H$ to zero is given by

$$B-B_0=(\Delta-k_2H)/(k_1-k_2).$$

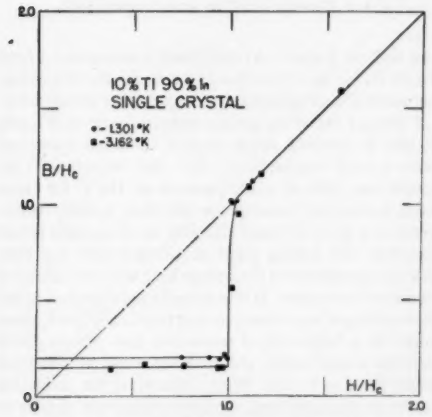


FIG. 4. Reduced magnetic induction *versus* reduced field.

The points at high fields when $B=H$ serve to determine the value of $B_0$. In the case of the single crystal specimens we found that the beginning of flux penetration occurred sharply, and although in the 15 and 20 percent specimens measurements taken very close together in field showed a slight rounding rather than an abrupt discontinuity at the start of flux penetration, it was easy to choose a critical field as the intersection, on a plot of galvanometer deflection *versus* field, of the straight line corresponding to the completely superconducting region with the rapidly rising curve corresponding to the penetration of flux. Wexler and Corak[8] have found that when flux penetration occurs over a range of field, the field corresponding to initial flux penetration corresponds most closely to the thermodynamic critical field. The values of the critical fields, $H_c$, and of the residual induction in zero field, $B_0$, are

[8] A. Wexler and W. C. Corak, Phys. Rev. **85**, 85 (1952).

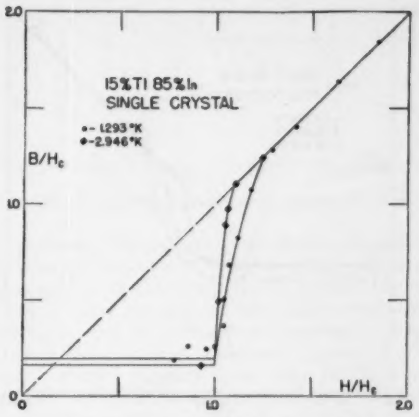


FIG. 5. Reduced magnetic induction *versus* reduced field.

given in Table III. The observed critical fields fitted fairly well the parabolic expression

$$H_c=H_0(1-T^2/T_0^2). \quad (1)$$

The values of the parameters $H_0$ and $T_0$ for each composition are listed in Table III and the deviations of the observed critical fields from those calculated by Eq. (1) are given.

In Figs. 2 to 6 are plotted the values of $B/H_c$ *versus* $H/H_c$ for the five single crystal specimens. In order to avoid a clutter of indistinguishable points, we have included for each sample only data at a relatively high and a relatively low temperature. In general, the curves at the other temperatures listed in Table III fall between those shown on the graphs. For the pure

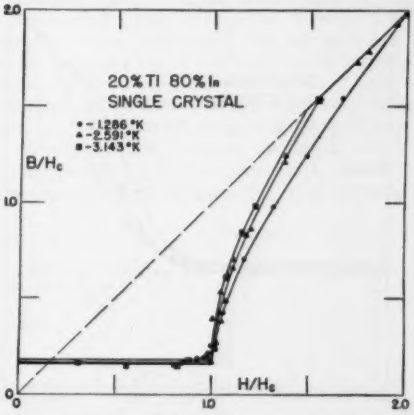


FIG. 6. Reduced magnetic induction *versus* reduced field.

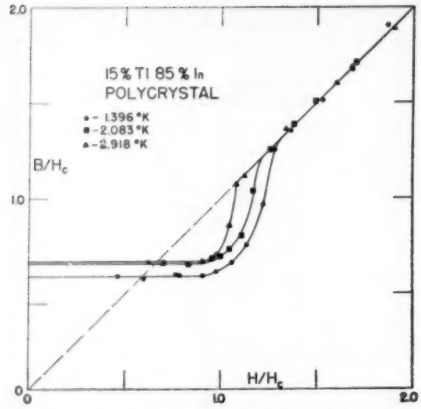


FIG. 7. Reduced magnetic induction *versus* reduced field.

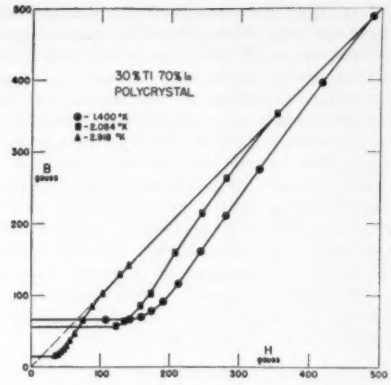


FIG. 9. Magnetic induction *versus* magnetic field.

indium and the 5 and 10 percent thallium samples the shape of the curve of $B/H_c$ *versus* $H/H_c$ was within the limits of error the same at all temperatures. The transitions are quite sharp. For the indium and the 5 percent alloy, the flux penetration was complete within less than 1 percent range of field. For the 10 percent sample the initial flux penetration was rapid, but there is some rounding at the high field side, indicating that a field about 4 percent greater than the critical field is necessary to obtain substantially complete flux penetration. The curves for various temperatures superimposed within the accuracy of the measurements. The 15 and 20 percent specimens showed an increasing range of flux penetration and for these specimens the range was broader at lower temperatures, as can be seen by reference to Figs. 5 and 6. At the lowest temperature a field of 1.25 $H_c$ for the 15 percent and 2 $H_c$ for the 20 percent was needed to obtain nearly complete flux penetration.

A further set of induction measurements was made on the 20 percent single crystal specimen quenched from a high temperature. For this experiment the sample was held at a temperature of 110°C for three hours in an inert atmosphere and then quickly transferred to a bath of liquid nitrogen. In 55 seconds it had cooled to the boiling point of nitrogen and was then quickly transferred to the helium bath and the induction measurements taken. It was thought possible that in the slow cooling of specimens, as was previously done, there might be a beginning of separation into phases stable at lower temperatures and that the width of transition might be due to this effect. However, the induction curves in the quenched specimen were very similar to

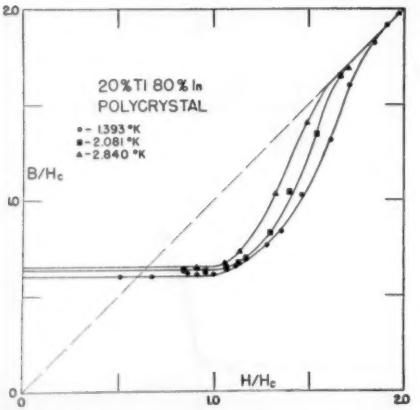


FIG. 8. Reduced magnetic induction *versus* reduced field.

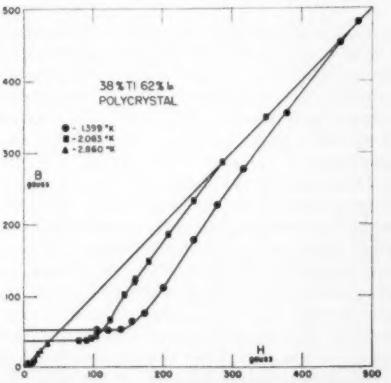


FIG. 10. Magnetic induction *versus* magnetic field.

those shown in Fig. 6. X-ray diffraction measurements made at liquid nitrogen temperatures show no evidence of phases other than the face-centered tetragonal one for the 20 percent composition.

The results of induction measurements on 15 and 20 percent polycrystalline specimens are shown in Figs. 7 and 8. The critical fields used in calculating $B/H_c$ and $H/H_c$ are those obtained from measurements on the single crystal specimens of the same composition. In general, the over-all breadth of the transition for the polycrystalline specimens is similar to that for the single crystals; however, the trapped flux in zero field is very much larger and the initial penetration gradual, so that it would be very difficult to define a critical field from these curves alone. In Figs. 9, 10, and 11 are shown the magnetic induction, $B$, plotted against field for the 30,

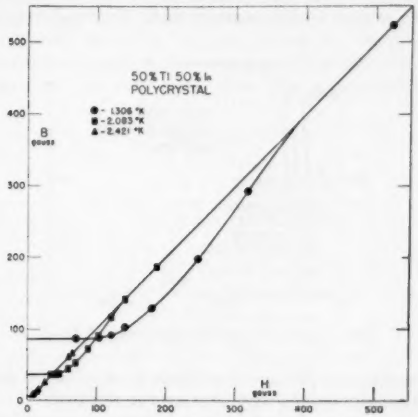


FIG. 11. Magnetic induction *versus* magnetic field.

38, and 50 percent polycrystalline specimens. In these samples there is as much as a factor of 3 between the field strengths when flux penetration begins and is complete. Because of the gradual initial penetration of flux, it was not possible to choose a critical field with any precision and the data are consequently not given in terms of $B/H_c$ and $H/H_c$. There is no great variation in the width of transition or shape of the curves in these three samples.

### THE RESISTANCE MEASUREMENTS

These measurements were made on the same samples as were used for the induction measurements. The resistance-temperature curves for the single crystal specimens are shown in Fig. 12 and for the polycrystalline specimens in Figs. 13 and 14. These curves were all taken with slow cooling in the earth's magnetic field (0.4 gauss) and the observed data have been corrected to zero field. The measuring currents used are indicated

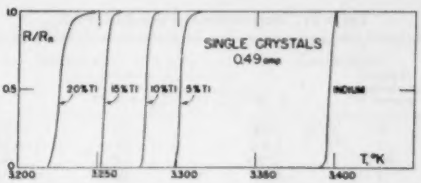


FIG. 12. Reduced resistance *versus* temperature.

on the figures. The ordinate on the plots is the ratio of the observed resistance, $R$, to the resistance, $R_n$, when the sample is completely nonsuperconducting. During a cooling curve the samples were under continuous observation, and the curves drawn represent a large number of points all lying on the curve. A few measurements, indicated as points, were taken for the polycrystalline specimens at different measuring currents. These points, which are definitely not on the curve, show a decrease in apparent transition temperature with larger measuring currents. The effects are larger by factors of 20 to 100 than would be calculated from Silsbee's hypothesis.

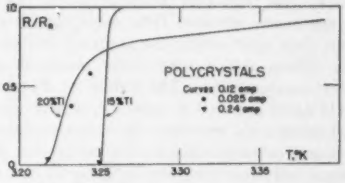


FIG. 13. Reduced resistance *versus* temperature.

The transitions for the single crystal specimens are all quite sharp, and although there is a gradual increase in breadth in going from the pure indium to the 20 percent specimen, even for the latter the major drop in resistance occurs within 0.01°. The polycrystalline 15 percent specimen has a transition curve practically identical with the single crystalline one. The polycrystalline 20 percent specimen begins to acquire resistance at the same temperature as the single crystal, but the curve is much broader and has a very long high temperature tail. The transitions in the 30 and 38 percent polycrystalline specimens occur over a range

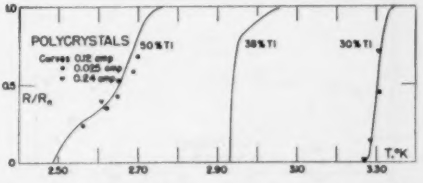


FIG. 14. Reduced resistance *versus* temperature.

TABLE IV. Temperature at which $R/R_n = 0.5$.

| Single crystals | | Polycrystals | |
|---|---|---|---|
| Nominal composition percent Tl | $T$, °K | Nominal composition percent Tl | $T$, °K |
| 0 | 3.396 | 15 | 3.254 |
| 5 | 3.302 | 20 | 3.233 |
| 10 | 3.280 | 30 | 3.304 |
| 15 | 3.254 | 38 | 2.938 |
| 20 | 3.226 | 50 | 2.652 |

of temperature of about 0.1°. The wide transition curve covering about 0.25° and the unusual shape of the curve for the 50 percent sample may be because in this specimen the stable room temperature structure was formed by a reaction in the solid state between face-centered and body-centered cubic phases rather than directly by crystallization from the melt.[4] Although no evidence of two phases was found by metallographic examination of the annealed sample, nor was any indicated by the induction measurements, an extremely small amount of a different phase might affect the resistance measurements, which are sensitive to traces of superconducting impurities.

The zero field transition temperatures for the single crystal specimens obtained from extrapolation of the induction data agree within the accuracy of the extrapolation (about 0.01°) with those observed in the resistance measurements. The values of $T_0$ given in Table III agree less well because a quadratic function does not adequately represent the induction data. The temperatures corresponding to the restoration of half the normal resistance are given in Table IV and represented graphically in Fig. 15. For comparison, the data of Meissner, Franz, and Westerhoff[5] on polycrystalline

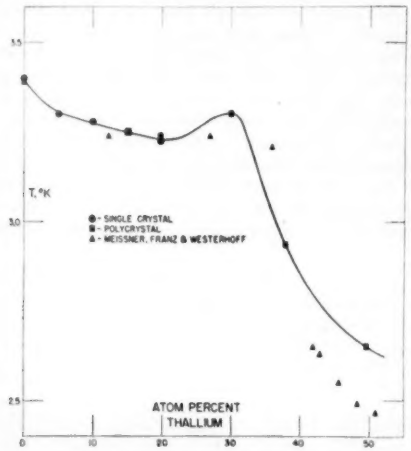


FIG. 15. Transition temperature in zero field *versus* composition.

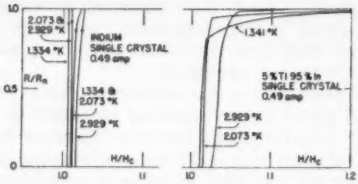


FIG. 16. Reduced resistance *versus* reduced field.

specimens are shown. From measurements of the electrical resistance at higher temperatures reported elsewhere[9] we believe that at the temperatures of liquid helium the specimens ranging in composition from indium through 30 percent thallium have a face-centered tetragonal structure, whereas the 38 and 50 percent compositions are face-centered cubic. The rapid drop in

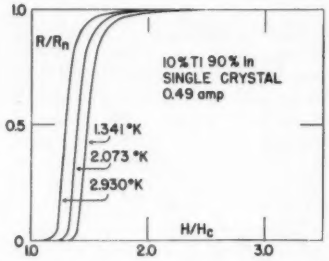


FIG. 17. Reduced resistance *versus* reduced field.

transition temperature that begins between our 30 and 38 percent samples may be related to this fact.

The restoration of electrical resistance upon the application of an external magnetic field is shown in Figs. 16–19 for the single crystal specimens and in Figs. 20–24 for the polycrystal ones. For the specimens up to 20 percent thallium the fraction of the resistance in the normal state is plotted against the reduced field,

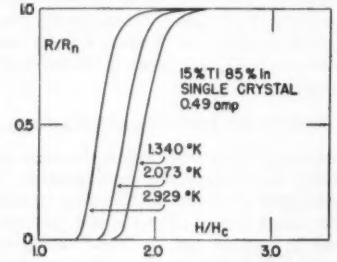


FIG. 18. Reduced resistance *versus* reduced field.

[9] J. W. Stout and L. Guttman, Phys. Rev. **88**, 713 (1952).

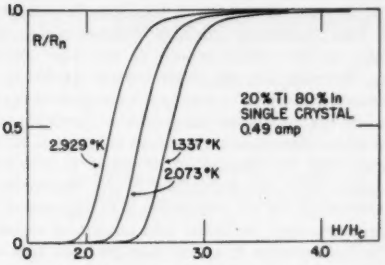


FIG. 19. Reduced resistance *versus* reduced field.

$H/H_c$, where the appropriate critical field was calculated from the induction measurements on the single crystal specimens. In the case of the 30, 38, and 50 percent specimens where the critical field could not be accurately estimated, we have plotted the fractional resistance against the measured field. For all samples measurements were made with both increasing and

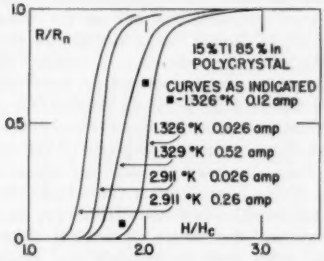


FIG. 20. Reduced resistance *versus* reduced field.

decreasing field. For the pure indium the resistance is restored sharply at a field 1 to 2 percent larger than the critical field for flux penetration. A slight hysteresis of about 1 percent in field was observed in the pure indium sample between the increasing field at which the normal resistance was restored and the decreasing field at which the resistance suddenly dropped to zero. Within the

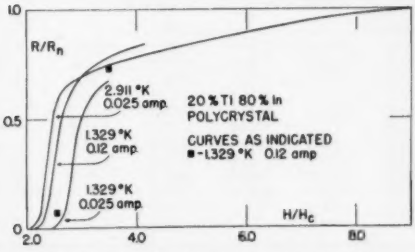


FIG. 21. Reduced resistance *versus* reduced field.

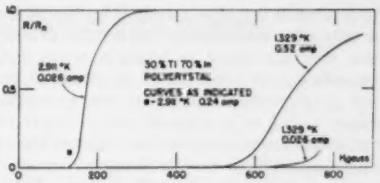


FIG. 22. Reduced resistance *versus* field.

accuracy of the measurements there was no hysteresis in the other samples.

The restoration of resistance in the 5 percent single crystal occurred at a value of $H/H_c$ comparable with that for pure indium except at the highest temperature where a field about 3 percent greater than $H_c$ was required. The curves for the 10, 15, and 20 percent single crystal specimens show increasing breadth of transition and increasing values of $H/H_c$ for a given restoration of resistance as the amount of thallium in the alloy increases. In these specimens the value of $H/H_c$ to obtain a certain restoration of resistance

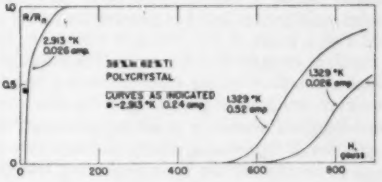


FIG. 23. Reduced resistance *versus* field.

increases as the temperature is lowered. The polycrystalline specimens containing 15 and 20 percent thallium show curves resembling those of the single crystal specimens, except that there is a break and a long tail on the high resistance side for the 20 percent sample. This high resistance tail was also noted in the resistance-temperature data in zero field for the same specimen; the reason for it is not clear. In the polycrystalline specimens several measuring currents were used and it was found that increasing measuring current appreciably reduced the field necessary to restore a given fraction of the normal resistance. Each curve

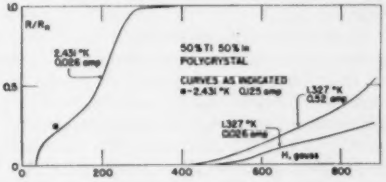


FIG. 24. Reduced resistance *versus* field.

shown represents many points which are not indicated. When only a few measurements were taken at a certain current, they are shown as separate points and the corresponding curve is not drawn. In the 30, 38, and 50 percent polycrystalline specimens the restoration of resistance begins at a magnetic field comparable to that at which flux penetration was found in the induction measurements to be substantially complete, and extends over a wide range of field strengths. The curve for the 50 percent specimen reflects the behavior found for this specimen in the resistance-temperature data previously discussed.

## DISCUSSION

The measurements show that the single crystals resemble pure metals much more closely than has been found previously[1] for alloys. In particular, the field at which flux penetration begins is sharply defined, and most of the flux is expelled on decreasing the applied field to zero. As one goes from pure indium to 20 percent thallium the breadth of the region over which flux penetration occurs upon the isothermal application of a magnetic field gradually increases. The restoration of resistance begins at a field greater than that required for substantially complete flux penetration and is completed over a range of field which is greater the larger the thallium content of the sample. The effect of the addition of thallium on the superconducting properties is, however, much more gradual than the effect on the normal electrical resistivity at low temperatures.[9] Thus the addition of 5 percent thallium produces very little change in breadth of the superconducting transitions but increases the resistivity at the boiling point of helium by a factor of 16. In the single crystal specimens the trapped flux in zero field is 15 to 20 percent of the flux that would be present in a specimen of unit permeability at the field where penetration begins. If the field at which flux penetration begins is taken as the true critical fields, the samples exhibit therefore a Meissner effect of 80 percent or more. The breadth of the flux penetration *versus* magnetic field curves for polycrystalline specimens in which the crystals were grown in the solid state is similar to that for the single crystals; however, the polycrystalline specimens showed a much larger trapped flux, or smaller Meissner effect.

The increase of breadth of transition in a magnetic field with increasing thallium content of the alloy appears to be a characteristic of the solid solution. Since, however, for the single crystal specimens the resistance transitions in zero field were quite sharp and to a first approximation the magnetic transition curve for a given concentration scales as the critical field, it appears that the breadth of transition is principally connected with the mechanism of the destruction of superconductivity by a magnetic field. Because of the finite penetration depth the field to destroy superconductivity is greater in a thin filament than in a bulk specimen. To explain the sharp transitions in a longitudinal magnetic field observed in pure metals, it is necessary to postulate a surface energy between the normal and superconducting regions which makes the formation of small superconducting filaments energetically unfavorable.[10] If the surface energy decreases with increasing thallium content in the alloys, one would expect a widening of the magnetic field transitions. In such a case the field at which flux penetration begins should correspond to the thermodynamic critical field, and when this point is sharply defined as it was in our single crystal specimens one may use the critical fields so obtained to deduce (using well-known thermodynamic formulas) the difference in entropy and heat capacity between the normal and the superconducting state. By assuming the parabolic relation (Eq. (1)) and with the further assumption that there is no term linear in temperature in the heat capacity of the superconducting state, one may calculate the electronic heat capacity of the normal metal. This heat capacity is given by $C_n=\gamma T$, where $\gamma=VH_0^2/2\pi T_0^2$. In making the calculation, the lattice parameters observed by Guttman[4] were used to calculate the gram-atomic volume $V$. The values of $\gamma$ calculated from the values of $H_0$ and $T_0$ are given in Table III.

We are indebted to Mr. Stanley Reed for assistance in preparing the specimens and with the measurements, to Mr. K. K. Ikeuye for help in the growing of the polycrystalline specimens, and to the members of the analytical chemistry section for making the chemical analyses.

[10] F. London, *Superfluids* (John Wiley and Sons, Inc., New York, 1950), Vol. I, p. 125.

# The Electrical Resistivity of Indium-Thallium Solid Solutions

J. W. STOUT AND LESTER GUTTMAN
*Institute for the Study of Metals, University of Chicago, Chicago, Illinois*
(Received July 28, 1952)

Electrical resistivity measurements on indium-thallium solid solutions in the composition range from indium to 50 atom percent thallium and from the boiling point of helium to room temperature are described. An anomalous behavior of the resistivity of a specimen containing 30 atom percent thallium indicates that it probably undergoes a transformation from face-centered cubic to tetragonal in the temperature interval 45–60°K.

IN connection with experiments on the superconducting properties of indium-thallium solid solutions,[1] we have made some measurements of the electrical resistance of these alloys at higher temperatures which will be briefly presented here. The samples used and the method of measurement are the same as previously described.[1] The single crystal specimens covered the composition range from indium to 20 percent thallium and the polycrystal specimens ranged from 15 to 50 percent thallium. The specific resistances at the ice point were calculated from the dimensions and observed resistances of the samples. The accuracy of specific resistances is estimated as 1 to 2 percent except in the case of the 10 percent single crystal specimen where the error is greater because the specimen was diverted to another use before accurate dimensional measurements were made. The specific resistance data at the ice-point are given in Table I. They are in fairly good agreement with the data of Meissner, Franz, and Westerhoff.[2]

TABLE I. Specific resistance of In—Tl solid solutions at $T=273.16$°K.

| Single crystals | | | Polycrystals | | |
|---|---|---|---|---|---|
| Composition, atom percent thallium | | $\rho\times10^6$ | Composition, atom percent thallium | | $\rho\times10^6$ |
| Nominal | Actual | ohm cm | Nominal | Actual | ohm cm |
| 0 | 0 | 7.9 | 15 | 15.07 | 11.8 |
| 5 | 5.05 | 9.5 | 20 | 19.96 | 13.0 |
| 10 | 10.07 | 10.5* | 30 | 30.07 | 15.1 |
| 15 | 15.09 | 12.0 | 38 | 37.94 | 16.3 |
| 20 | 19.89 | 13.1 | 50 | 49.68 | 17.6 |

* Low accuracy, see text.

TABLE II. Resistance ratios, $R/R_{273.16}$, for single crystal specimens.

| | Nominal composition, atom percent thallium | | | | |
|---|---|---|---|---|---|
| $T$, °K | 0 | 5 | 10 | 15 | 20 |
| 77.6 | 0.223 | 0.306 | 0.368 | 0.409 | 0.452 |
| 4.2 | 0.0080 | 0.106 | 0.179 | 0.240 | 0.287 |

TABLE III. Resistance ratios, $R/R_{273.16}$ for polycrystal specimens.

| | Nominal composition, atom percent thallium | | | | |
|---|---|---|---|---|---|
| $T$, °K | 15 | 20 | 30 | 38 | 50 |
| 4.20 | 0.2347 | 0.2811 | 0.3617 | 0.3855 | 0.3950 |
| 10.15 | 0.2384 | 0.2844 | 0.3650 | 0.3884 | 0.3973 |
| 13.98 | 0.2433 | 0.2899 | 0.3700 | 0.3930 | 0.4020 |
| 16.26 | 0.2471 | 0.2930 | 0.3736 | 0.3965 | 0.4051 |
| 18.17 | 0.2510 | 0.2962 | 0.3769 | 0.3993 | 0.4079 |
| 20.34 | 0.2556 | 0.3012 | 0.3808 | 0.4028 | 0.4120 |
| 46.81 | 0.3234 | 0.3622 | 0.4346 | 0.4590 | 0.4672 |
| 55.14 | 0.3452 | 0.3835 | 0.4576 | 0.4768 | 0.4849 |
| 63.26 | 0.3670 | 0.4042 | 0.4810 | 0.4950 | 0.5018 |
| 70.14 | 0.3853 | 0.4214 | 0.4965 | 0.5098 | 0.5163 |
| 77.41 | 0.4053 | 0.4391 | 0.5135 | 0.5257 | 0.5308 |
| 297.0 | 1.088 | 1.083 | 1.073 | 1.072 | 1.072 |

On the single crystal specimens measurements of resistance were taken at the boiling points of helium and nitrogen. The temperature at the nitrogen boiling point was obtained from the resistance of a copper coil calibrated against vapor pressures of oxygen. The data are shown in Table II. The ratio of the resistance at each temperature to that of the same sample at 273.16°K is given. The residual resistance of the indium specimen corresponds to an impurity content equivalent to 0.3 atom percent thallium. A spectrographic analysis of the material used showed the following impurities in *weight* percent: Mg, 0.01; Ca, 0.003; Cu, 0.002; Sn, 0.01; Pb, 0.001; Sb, 0.01; Si, 0.01; Fe, 0.002, Al, trace.

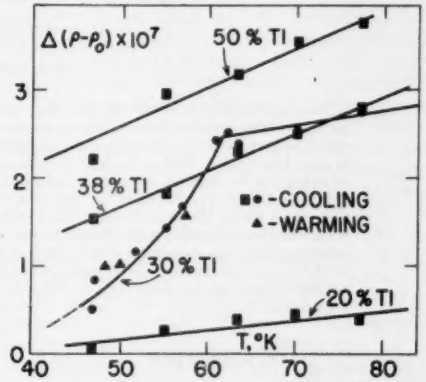


FIG. 1. Temperature variation of relative resistivity of indium-thallium solid solutions.

[1] J. W. Stout and L. Guttman, Phys. Rev. 88, 703 (1952).

[2] Meissner, Franz, and Westerhoff, Ann. Physik [5] 13, 505 (1932).

These add up to about 0.13 *atom* percent of total detected impurity.

A more extensive series of measurements was made on the polycrystal specimens. Hydrogen or nitrogen was condensed in the inner Dewar which was ordinarily used for helium. This Dewar was surrounded by a bath of nitrogen so that heat leak into the inner dewar was very small and the temperature stability was excellent. The temperatures of the samples were calculated from the observed vapor pressure of nitrogen or hydrogen. At room temperature and the ice point the temperature was measured with a copper-constantan thermocouple. The ratio of the resistance at various temperatures to that at the ice point is given in Table III. The precision of the resistance measurements was about 0.1 percent.

An anomalous behavior of the resistivity of the 30 percent thallium specimen was observed in the nitrogen range. This is shown in Fig. 1. The ordinate is the thermal part of the specific resistance, $\rho(T)-\rho(0°\mathrm{K})$, for the 20, 30, 38, and 50 percent samples, less the corresponding quantity for the 15 percent sample, which was arbitrarily taken as a standard for comparison. Although because of possible errors in the dimensional measurements the specific resistance is known only to 1 or 2 percent, for a given sample its fractional variation with temperature is known much more accurately. The anomaly in the temperature variation of the 30 percent specimen occurring over the range 45–60°K is very likely an indication that in this temperature interval the specimen is changing from a high temperature face-centered cubic form to a low temperature face-centered tetragonal one. Such an assumption fits well an extrapolation of the composition-temperature curve for the cubic-tetragonal transformation found by Guttman.[3]

[3] L. Guttman, J. Metals (Trans. Am. Inst. Mining Met. Engrs. **188**, 1472 (1950)).

PHYSICAL REVIEW VOLUME 88, NUMBER 4 NOVEMBER 15, 1952

# Paramagnetic Resonance in Phosphors*

W. D. HERSHBERGER AND H. N. LEIFER
*University of California, Los Angeles, California*

(Received July 7, 1952)

Paramagnetic studies at 9375 Mc have been made on 32 inorganic phosphors containing paramagnetic activators. The sample is contained in a transmission cavity and the spectrum is obtained by a sweeping technique that yields the derivative of the absorption curve. Less than $10^{-11}$ mole of $Mn^{++}$ may be detected in cubic host crystals. The specimen in the cavity may be illuminated by ultraviolet light for observations on changes in its spectrum under these conditions, but, when illuminated, the changes observed may be attributed largely to photoconduction. The phosphors containing $Mn^{++}$ as an activator under no illumination yield a variety of spectra. Seven of these phosphors display a single absorption line 750 to 1000 gauss wide, while four phosphors with different host crystals but all having cubic symmetry display line spectra consisting of six lines seven gauss wide but with spacings between members of from 68 to 88 gauss depending on the host crystal. Finally, two phosphors display 30-line spectra which arise because the crystal field and the applied field together serve to remove both the $I$ and $S$ degeneracy, whereas for cubic crystals only the $I$ degeneracy is removed.

## INTRODUCTION

EXPERIMENTAL methods for observing paramagnetic resonance[1] at microwave frequencies provide means for obtaining precise and detailed information on the energy levels occupied by electrons in solids. In general, depending on the experimental technique employed, line spectra will be observed only when an adequate number of electrons with unpaired spins occur in a material and when the various factors which determine line width are favorable, such as, for example, the lifetime of the state under study or the magnitude and character of the interactions between ions and the crystal field. Such spectra should be particularly instructive when found in phosphors and other semiconductors. For example, in phosphors, the set of transitions involved in the processes of fluorescence and phosphorescence are at present imperfectly understood in any quantitative sense. Experiments on photoinduced changes in paramagnetism have been reported both for organic[2] and inorganic[3] phosphors, but these experiments make use of bulk ponderomotive effects. In the present study, the paramagnetic spectra of a number of inorganic phosphors were taken at 9375 Mc requiring magnetic fields in the 3000–3500 gauss range. The emphasis has been placed on phosphors in which small proportions of doubly ionized manganese ($Mn^{++}$) are used as activators in a variety of host crystals. $Mn^{++}$ is

* Work supported in part by the ONR.

[1] E. Zavoisky, J. Phys. (U.S.S.R.) **9**, 211, 245, 447 (1945); **10**, 170, 197 (1946); R. L. Cummerow and D. Halliday, Phys. Rev. **70**, 443 (1946); D. M. S. Bagguley and J. H. E. Griffiths, Nature **160**, 532 (1947).

[2] G. N. Lewis and M. Calvin, J. Am. Chem. Soc. **67**, 1232 (1945).

[3] P. D. Johnson and F. E. Williams, J. Chem. Phys. **17**, 435 (1949).

in an $S$-state, its $3d$-shell consists of five unpaired electrons, and as a result of low spin-orbit coupling we may expect long relaxation times and relatively narrow line spectra. The changes observed in the phosphors under irradiation may at present be attributed largely to photoconduction, but changes in paramagnetism under irradiation should exist and be observable if conditions favorable for the excitation of a sufficient number of luminescent centers can be met.

The spectra of unirradiated phosphors are sufficiently interesting and varied to warrant a separate treatment. In the present paper, the experimental method in use is described, and results on the spectra of some thirty unirradiated phosphors are reported together with a discussion of their most interesting features.

## EXPERIMENTAL METHOD

Observations on the phosphors are carried on at a fixed frequency of approximately 9375 Mc. The sample itself often was in the form of a wafer, perhaps $\frac{1}{4}$ inch in diameter and $\frac{1}{32}$ inch thick and was placed to intersect the axis of a resonant cavity operating in the circular electric or $TE_{011}$ mode. Again, a thin layer of phosphor was placed in a shallow cup in the cavity. The $TE_{011}$ mode was chosen, in part, because it is the low-loss or high $Q$ mode, and in part, because an aperture for sample illumination may readily be cut in the end of the cavity without appreciably disturbing the field. The loaded $Q$ of the cavity with the sample in position was of the order of 10,000. Further, in this mode, the rf magnetic field is concentrated along the axis of the cavity yielding high sensitivity with a small sample and at the same time the condition for resonance—rf field perpendicular to the external magnetic field—may readily be satisfied. The magnet has 8-inch diameter pole pieces, and a $2\frac{1}{2}$-inch gap was used so the effect of field inhomogeneity on line width is negligible.

In searching for paramagnetic spectra, the magnetic field is swept over a 500-gauss range in perhaps 4 minutes and is simultaneously swept 2 to 5 gauss at a 40-cycle rate. The low speed wide range sweep is accomplished by varying the set point on an electronically regulated supply furnishing power for the main magnet coils, while separate low inductance coils are employed for injecting the low amplitude 40-cycle sweep. The band width of the detection system is approximately 3 cycles. As a result of the method employed in collecting information from the sample, the derivative of the paramagnetic absorption curve or curves is obtained. Changes in power transmitted through the cavity containing the sample are detected and recorded using either a square law detector or a phase detector following a 40-cycle amplifier. Signal to noise ratios in excess of 1000 are obtained with a 10-mg sample of cubic zinc sulfide activated with manganese present to 1 part in $10^6$, indicating that less than $10^{-11}$ mole of manganese may be detected.

Magnetic field strength is measured by comparing the frequencies of two equipments used simultaneously in the same magnet. The cavity of one equipment contains the phosphor under study, while the second cavity, operating at a different frequency, contains a small quantity of diphenyl-trinitrophenyl-hydrazyl.[4] Since the $g$-value of the hydrazyl is given as $2.0036 \pm 0.0002$ and is quite accurately known,[5] a frequency comparison is sufficient to determine the positions of the peaks of the paramagnetic spectrum of the phosphor. Field strength is measured with an accuracy of $\pm 1$ gauss.

In taking the spectra of irradiated samples, sources rich in either 2537A or 3640A were used depending on the characteristics of the phosphor under study. In one procedure, steady illumination is used and both the slow wide range magnetic sweep and the 40-cycle sweep are used. The original spectrum characteristic of an unilluminated sample is found—masked somewhat by photoconduction in some instances—and a search is made for a new spectrum which could perhaps arise from trapped electrons or a modified manganese ground state. The failure to detect such spectra may mean only that trapping or other changes occur to an insufficient degree in the phosphors studied in view of the detection sensitivity now available, or that the spectra are too broad to be observed readily. In a second procedure, only the slow wide range sweep is employed, but intermittent 40-cycle illumination is used on the phosphor in an attempt to detect differences between spectra characteristic of an illuminated and an unilluminated phosphor sample. The only conclusion one can reach from the negative result for a phosphor in which a signal to noise ratio of 100 is observed for the unilluminated sample, is that less than 1 percent of the contributing manganese ions experience changes in their paramagnetic properties on illumination, or that in some instances, changes in paramagnetism may be masked by changes in conductivity produced by the illumination. These latter changes of course occur at all values of the magnetic field, including zero.

The changes in dielectric constant in phosphors on illumination which have been reported,[6] probably have little effect on microwave transmission, since the relaxation time associated with these changes is of the order of $10^{-7}$ second, which is long compared with the period of the microwaves. In the transmission experiments reported here, susceptibility changes cannot be differentiated from changes in conductance as in more complicated experimental procedures. However, these latter methods would be particularly valuable when photoconduction masks the permeability changes sought.

---

[4] Furnished by A. N. Holden of Bell Telephone Laboratories.
[5] A. N. Holden *et al.*, Phys. Rev. **77**, 147 (1950).
[6] G. F. J. Garlick, *Luminescent Materials* (Oxford Press, London, 1949), Chapter V.

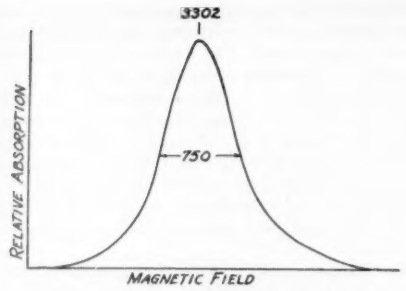


FIG. 1. Absorption of tetr. $ZnF_2$:Mn (0.04).

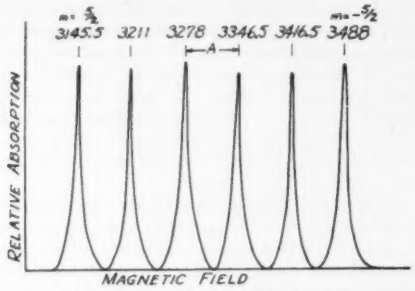


FIG. 4. Absorption of cub. ZnS:Mn (0.001).

## EXPERIMENTAL RESULTS

The phosphors investigated have been classified into five groups according to their observed spectra. The first four groups contain all the manganese activated phosphors; the fifth group contains all others.[7]

The members of group one are: tetr. $ZnF_2$:Mn (0.04); rbhdl. $Zn_2SiO_4$:Mn (16); rbhdl. $8ZnO \cdot BeO \cdot 5SiO_2$:Mn (0.25); rbhdl. $Zn_2GeO_4$:Mn (0.01); rbhdl. $Zn_3(PO_4)_2$:Mn (0.05); rhomb. $CdSiO_3$:Mn (0.018); rhomb.

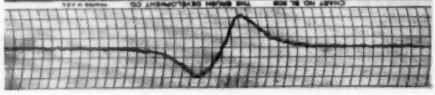

FIG. 2. Experimental record tetr. $ZnF_2$:Mn (0.04).

$Mg_2GeO_4$:Mn (0.01). The spectrum of each member of this group is a single broad absorption curve, 750–1000 gauss wide, as typified in Fig. 1. This curve was constructed using data from Fig. 2 which is an experimental record taken with tetr. $ZnF_2$:Mn (0.04) as the phosphor.

The members of group two are: cubic ZnS:Mn (0.001); cubic $ZnAl_2O_4$:Mn (0.001); MgO:Mn (0.1 mole percent) [197–2]:MgO:Mn (0.1 mole percent) [200–2]. Each member of group two displays a six-peaked hyperfine spectrum as typified in Figs. 3 and 4. Of interest is the very large ($A''$ gauss) and isotropic hyperfine spectrum for $S$ state $Mn^{++}$. It should also be noted that the hyperfine splitting, $A$, differs for each material as shown in Table I. Finally, the absorption signal for MgO:Mn [200–2] is 10 percent, in magnitude, of MgO:Mn [197–2], both having the same manganese concentration.

There are two members in group three: hex. ZnS:Mn (0.01) and ZnS:Tb (0.04):Mn (0.005). The 30-peak spectrum of these two phosphors is a superposition of fine and hyperfine splitting shown in Figs. 5 and 6.

The members of group four are: rbhdl. $Zn_2SiO_4$:Mn (0.25); rbhdl. $Zn_2SiO_4$:Mn (1); rhomb. $CdSO_4$:Mn (0.006); rhomb. $ZnSO_4$:Mn (0.006); $ZnO \cdot B_2O_3$:Mn (0.05). None of these phosphors yielded an observable spectrum.

Group five has as members: hex. ZnS:Cu (0.3); cubic ZnS:Cu (0.03); hex. ZnS:Cu (0.003); cubic ZnS:[Zn]; cubic $ZnAl_2O_4$:Cr (0.25); tricl. $Ca_2MgSiO_7$:Ce (0.05) monocl. $CaMg(SiO_3)_2$:Ti (0.02); $Ca_2P_2O_7$:Dy; ZnS:Cu (0.1); ZnS:Cu (0.3); ZnS:Cu (2.0). These are all the nonmanganese activated phosphors investigated, and none of them yielded an observable spectrum.

## INTERPRETATION

As a point of departure, we assume that, to a first approximation, we have free ions all of which exist in a common ground state in the absence of a field. When a steady magnetic field is applied, these ions will occupy $2J+1$ equally spaced Zeeman levels according to the

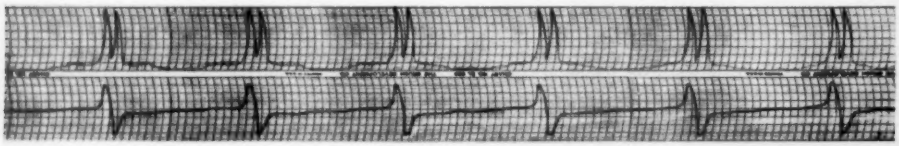

FIG. 3. Experimental record cub. ZnS:Mn (0.001).

[7] Twenty-six of the phosphor samples were furnished by H. W. Leverenz of RCA Laboratories and six by F. E. Williams of the General Electric Research Laboratory.

TABLE I. Calculated values for absorption lines of Mn-activated phosphors. Spectra display "hyperfine" structure only.

| Material | $H_{5/2}$ | $H_{3/2}$ | $H_{1/2}$ | $H_{-1/2}$ | $H_{-3/2}$ | $H_{-5/2}$ | $A$ | $K$ | $H_0$ | $\nu$(Mc) | $g$ |
|---|---|---|---|---|---|---|---|---|---|---|---|
| Cub. ZnS:Mn | 3145.5 | 3211 | 3278 | 3346.5 | 3416.5 | 3488 | 68.5 | 0.75 | 3318.5 | 9290 | 2.0 |
| Cub. $ZnAl_2O_4$:Mn | 3116 | 3194 | 3274 | 3356 | 3440 | 3526 | 82 | 1.0 | 3324 | 9290 | 2.0 |
| MgO:Mn(197–2) | 3097 | 3181.5 | 3267.5 | 3355 | 3444 | 3534.5 | 87.5 | 0.75 | 3319 | 9290 | 2.0 |
| MgO:Mn(200–2) | 3138 | 3211 | 3286 | 3363 | 3442 | 3523 | 77 | 1.0 | 3333 | 9290 | 2.0 |

*Accuracies:* $H$: ±1 gauss; $A$: ±1 gauss; $K$: ±0.05 gauss.

Boltzmann distribution. All transitions take place within the ground state of the ion, and adjacent levels are separated in energy by

$$\Delta E = g\beta H,$$

where $g$ = spectroscopic splitting factor, $\beta$ = Bohr magneton = $eh/4\pi mc$, and $H$ = externally applied magnetic field.

If now a radiofrequency magnetic field of frequency $\nu$ impinges on the ions at right angles to the static field, the probability of an ion making a transition from the level it occupies to an adjacent level, is a maximum when the condition

$$h\nu = g\beta H$$

is satisfied. This is the magnetic resonance condition.

Transition probabilities to a higher and lower level are the same but the lower levels are more highly populated and there is, therefore, a greater absorption than emission. For usual microwave power values, the Boltzmann distribution is retained and there is a net absorption.

The "$g$" value of the paramagnetic ion can be determined from the values of the frequency, $\nu$, and the magnetic field, $H$, at absorption.

When incorporated in a crystalline solid, the paramagnetic ion is subjected to strong internal electric fields. The major interactions to which the ion is then subject arise from

1. an internal electric field;
2. *LS* coupling;
3. external magnetic field;
4. electronic-nuclear spin interaction.

This interaction is proportional to the concentration and tends to broaden the sharply defined levels by producing a large number of close-lying neighboring levels. It may be interpreted as arising from an internal magnetic field, whose value is not the same at all ions because of the statistical distribution of the paramagnetic ion dipole orientations. At the low concentrations used in this research, dipole-dipole broadening is negligible.

The second contribution is an exchange interaction between spin systems, which Van Vleck[8] has shown tends to broaden an absorption line at the wings and sharpen its peak, or in effect, to narrow the line. This "exchange narrowing" may be looked upon as a rapid energy exchange between spin systems resulting in diminished localized or internal magnetic field spread. As is to be expected, the effect disappears at very dilute concentrations of the magnetic ion.

The third contribution is that of spin-lattice relaxation and is the mechanism by which an ion in an excited state returns to its unexcited state. When the relaxation occurs in an exceptionally short time, the energy level, and hence the absorption line, is broadened to such an extent as to make the spectrum unobservable. The mechanism of the relaxation process has been given by Kronig[9] and Van Vleck[10] as follows: Transfer of heat of magnetization between the magnetic spin system and the crystal lattice is provided by the Stark effect of the electric field of the lattice. The thermal vibrations of the crystal lattice produce periodic variations in the electric field acting on the ions which affect the energies of the orbital levels. Through spin-orbit coupling these effects provide an interaction between the spins and the lattice. Thus long relaxation times may be realized either by large crystal field splittings which break down *LS* coupling or by the use of low temperatures to reduce crystal lattice vibrations.

The fourth contribution to line width is anisotropy-energy broadening. For low symmetry crystal fields, the energy of a paramagnetic ion in a magnetic field

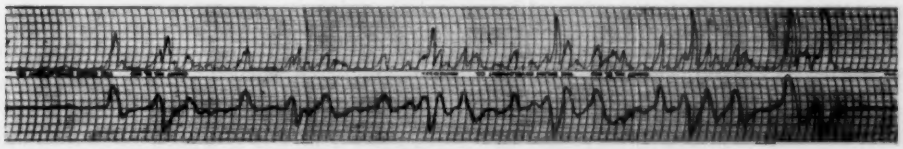

FIG. 5. Experimental record hex. ZnS:Mn (0.001).

[8] J. H. Van Vleck, Phys. Rev. **57**, 426 (1940).
[9] R. de L. Kronig, Physica **6**, 33 (1939).
[10] J. H. Van Vleck, Phys. Rev. **74**, 1168 (1948).

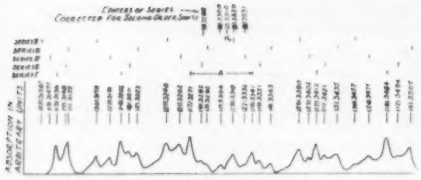

FIG. 6. Absorption of hex. ZnS:Mn (0.001).

is a function of the orientation of the crystal axis with respect to the external field. The angular dependence varies as $(3\cos^2\theta-1)$.[11] If the material under investigation is a powder in which the crystal axes are oriented at random in a magnetic field, it is possible that the energy differences associated with the various orientations are sufficient to broaden the absorption lines to the extent that they are no longer observable.

## MANGANESE PHOSPHORS

As indicated, $Mn^{++}$ is of particular interest[11,12] because it is, in many respects, the ideal paramagnetic substance; and further, the study has yielded certain unexpected results. $Mn^{++}$ has five unpaired $3d$-electrons, in addition to filled shells, with a total electron spin $S=5/2$ and nuclear spin $I=5/2$.

Its ground state is ${}^6S_{5/2}$, so the "quenching" of orbital angular momentum need not arise and it should behave very much as a free spin magnetic dipole. The crystal field can affect the electronic spin only indirectly through interaction with $L$ and spin-orbit coupling. Since only second order spin-orbit coupling is present, the relaxation times should be long enough so that undue broadening of the magnetic resonance spectrum of $Mn^{++}$ in any compound should not occur. The "$g$" factor should be isotropic and almost exactly 2. Similarly any crystal field splitting must necessarily be small and because of the spherical symmetry of the electronic distribution, there should be no electronic-nuclear spin interaction. Finally, electric quadrupole and external magnetic field-nuclear spin interactions are too small to be observable; this is so since, to the first order, they merely shift each of the hyperfine levels, becoming observable only under violation of the selection rule $\Delta m=0$.

Experimentally, the most striking feature of the spectra is the existence of a pronounced isotropic hyperfine structure. Also the crystal field splitting is greater than would be expected from the symmetry of the field in which the $Mn^{++}$ has been investigated.

In attempting to account for hyperfine structure where none is expected, the mechanism suggested thus far[13] is that of an admixture to the $3s^23p^63d^5$ configuration of a small fraction of a configuration in which one $3s$-electron has been promoted to a $4s$-state. The overall state is still assumed to be ${}^6S_{5/2}$ and to retain the parity of the main configuration. This mechanism would predict that the hyperfine structure is a property of the free ion and does not arise from the crystal field.

The crystal splitting (where it has appeared) has likewise been unexpected. To account for the relatively large splitting, it has been proposed[13] that electric fields of axial symmetry in conjunction with spin-spin interaction may be expected to give rise to a second-order contribution to the Hamiltonian of the form $D[S_z^2-\frac{1}{3}S(S+1)]$. The proposal is that the field produces a slight ellipsoidal deformation of the otherwise spherically symmetric electronic distribution and that then the mutual energy of the spin magnetic moments will no longer be isotropic but will depend upon their orientation relative to the symmetry axis. The cubic field may well still contribute; however, it is such a high order coupling as to have a coefficient small compared to the second-order process described. The direct interaction between the nuclear magnetic moment and the $3d$ electron shell which arises because of the proposed distortion of the electron distribution is very small and contributes at best a slight anisotropy to the hyperfine structure.

The Hamiltonian of the $Mn^{++}$ system may be represented as follows:

$$\mathcal{H}=g\beta HS+D'[S_z^2-\tfrac{1}{3}S(S+1)]+A'S\cdot I. \quad (1)$$

Here $g$ is the spectroscopic splitting factor, $\beta$ the Bohr magneton, $H$ the external magnetic field, $S$ the electron spin operator, and $I$ the nuclear spin operator. The first term denotes the interaction between external magnetic field and magnetic moment of electron spin, and in fields of the order of 3000 gauss, it is the dominant term.

The energy levels for each $M$ and $m$ (magnetic quantum numbers of electronic and nuclear spin, respectively) are

$$E_{M,m}=g\beta HM+D'[M^2-\tfrac{1}{3}S(S+1)]+A'Mm +K'\{M[I(I+1)-m^2]-m[S(S+1)-M^2]\}.$$

The last term is the result of a second-order perturbation calculation on the term $A'S\cdot I$ where $K'$ is given by $A'^2/2h\nu$. Figure 7 illustrates this over-all splitting and resultant absorption spectrum.

Since the selection rules for absorption are $\Delta M=1$, $\Delta m=0$, the energy difference, rearranged in terms of gauss, is

$$H=H_0-D(2M-1)-Am-K[I(I+1)-m^2], \quad (2)$$

where $H_0=h\nu/g\beta$, while $D$, $A$ and $K$ are $D'$, $A'$ and $K'$ divided by $g\beta$ respectively. A term $-Km(2M-1)$ has been neglected, since the resultant splitting is less than the line width and the center of gravity remains unchanged.

[11] B. Bleaney and D. J. E. Ingram, Proc. Roy. Soc. (London) **A205**, 336 (1951).
[12] E. E. Schneider and T. S. England, Physica **XVII**, 221 (1951).
[13] A. Abragam and M. H. L. Pryce, Proc. Roy. Soc. (London) **A205**, 135 (1951).

### Group One

The spectra of group one correspond to transitions between the unperturbed Zeeman levels, $g\beta HM$, and have a width so large as to make other effects unobservable.

Since the concentration of paramagnetic ions in the phosphors is very low, the broadening arising from dipole-dipole interaction may be neglected. Further, since the ions are all $Mn^{++}$, $LS$ coupling is small and the spin-lattice relaxation times too long to broaden the spectra significantly. The major contribution to the line width arises from the anisotropy energy broadening of the relatively low symmetry crystals in powdered form. This is borne out by the resolution in groups two and three where the crystal symmetries are high. The "$g$" values are all very nearly 2, in agreement with the ions being in an $S$ ground state.

### Group Two

The spectra of group two phosphors, corresponding to transitions between the shifted hyperfine levels are given by Eq. (2) neglecting the term $D(2M-1)$. The crystal symmetries are high so there is no undue anisotropy broadening but also no crystal field splitting.

Table I indicates the fit of theory with experiment and the values of the constants involved. Of note, is the variation in the value of the hyperfine splitting constant which is not in quantitative agreement with the mechanism proposed[13] to account for the splitting.

The spectra of this group are consistent with the spin of the manganese nucleus of 5/2.

### Group Three

The spectra of these two phosphors correspond to transitions as given by Eq. (2) and shown in Fig. 7. The crystal symmetries are slightly lower than those of group two—sufficiently lower to produce crystal field splitting but not low enough to broaden the spectra unduly.

The five series (fine structure) of six unequally spaced hyperfine lines for the spectrum of Fig. 6 are tabulated in Table II showing the fit of theory with experiment and giving the values of the constants involved.

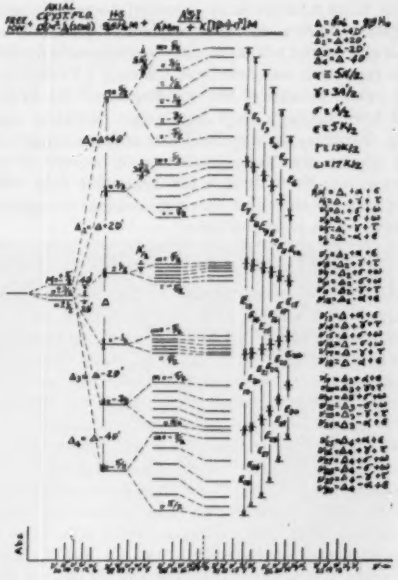

FIG. 7. Energy level diagram hex. ZnS:Mn.

### Group Four

All members of group four are manganese activated phosphors yielding no observable spectra. Since all crystal symmetries are low, the lack of spectra has been attributed to the anisotropy broadening of the powdered samples. In general, phosphors are not available in single crystals as a result of the methods currently in use in making them, but studies with such crystals would be useful in furnishing further checks on the correctness of the present interpretation.

## NONMANGANESE PHOSPHORS

### Group Five

The iron group members of group five with the exception of $Ti^{+++}$ all exist in high symmetry crystal

TABLE II. Calculated values for absorption lines of Mn-activated phosphors. Spectra display both "fine" and "hyperfine" structure.
$H=H_0-D(2M-1)-Am-K[I(I+1)-m^2](2)$
Hex. ZnS:Mn.

| Series I | Series II | | Series III | | Series IV | | Series V | |
|---|---|---|---|---|---|---|---|---|
| $M=-\frac{1}{2}\rightarrow\frac{1}{2}$ | $M=\frac{1}{2}\rightarrow\frac{3}{2}$ | $2D$ | $M=-\frac{3}{2}\rightarrow-\frac{1}{2}$ | $2D$ | $M=\frac{3}{2}\rightarrow\frac{5}{2}$ | $4D$ | $M=-\frac{5}{2}\rightarrow\frac{3}{2}$ | $4D$ |
| $H_{13}=3136$ | $H_7=3148$ | 12 | $H_{19}=?$ | ? | $H_1=3152$ | 16 | $H_{25}=?$ | ?? |
| $H_{14}=3202$ | $H_8=3211$ | 9 | $H_{20}=3191$ | 11 | $H_2=3222$ | 20 | $H_{26}=3178$ | 24 |
| $H_{15}=3271$ | $H_9=3282$ | 11 | $H_{21}=3262$ | 9 | $H_3=3292$ | 21 | $H_{27}=3248$ | 23 |
| $H_{16}=3341$ | $H_{10}=3351$ | 10 | $H_{22}=3332$ | 9 | $H_4=3363$ | 22 | $H_{28}=3318$ | 23 |
| $H_{17}=3412$ | $H_{11}=3421$ | 10 | $H_{23}=3402$ | 9 | $H_5=3435$ | 24 | $H_{29}=3390$ | 21 |
| $H_{18}=3484$ | $H_{12}=3494$ | 10 | $H_{24}=3471$ | 11 | $H_6=3507$ | 23 | $H_{30}=3457$ | 27 |

$A=70\pm1$ gauss; $H_0=3310\pm1$ gauss;
$K=0.5\pm0.05$ gauss; $g=2.0\pm0.05$;
Average $D=5$ gauss.

fields. Since none are in an $S$ ground state, their orbital angular momenta will be incompletely "quenched" and their spin-lattice relaxation times correspondingly short. The rare earth members have a strong $LS$ coupling in any event, because of the shielding about the $4f$-shell, and have similarly short spin-lattice relaxation times. It is, therefore, not surprising that at room temperature the spectra should be unobservable because of such broadening. $Ti^{+++}$ is in a low symmetry field, which lengthens the relaxation time but broadens the spectrum because of its powdered form.

## VALENCY CONSIDERATIONS

An alternative mechanism may exist for the lack of spectra with copper activated phosphors. It is the possibility of copper existing as $Cu^{+}$ rather than $Cu^{++}$. $Cu^{+}$ has only filled shells and is not paramagnetic. The evidence is not conclusive that this is the case; however, other investigations[14] have suggested this possibility on purely optical and chemical grounds.

Of a more definite character is the difference in magnetic spectra between the phosphors MgO:Mn(197–2) and MgO:Mn(200–2). These phosphors are identical in composition, concentration and presumably crystal structure. They differ in luminescence spectra, and it was suspected on that basis that No. 197–2 contains only $Mn^{++}$ while No. 200–2 contains 20 percent $Mn^{++}$ and 80 percent $Mn^{4+}$. Arguing that $Mn^{4+}$ will not yield an observable spectrum because of a short spin-lattice relaxation time (see $Cr^{+++}$), the ratio of spectra magnitudes of 10:1 indicates that No. 200–2 contains 10 percent $Mn^{++}$ and 90 percent $Mn^{4+}$, in close agreement with expectations from luminescence data. In short, paramagnetic spectra may well prove useful, in conjunction with other data, in determining the valence state of paramagnetic ions dissolved in a host material.

[14] R. H. Bube, J. Chem. Phys. **19**, 985 (1951).

## CRYSTAL STRUCTURE AND SPECTRA

In this research, manganese was available as an activator in low concentrations in both cubic zinc sulfide and hexagonal zinc sulfide giving rise to markedly different spectra as shown in Figs. 4 and 6. Such evidence serves to illustrate the utility of the method of paramagnetic resonance for determining crystal structure. A spectrum similar to that shown in Fig. 6 was reported by Schneider and England[14] for manganese in zinc sulfide, but no indication was given of the crystal structure. It seems reasonable to suspect that the material used by these English workers was hexagonal or a mixture of cubic and hexagonal crystals. At least this hypothesis makes their results consistent with those reported here.

## SUMMARY

The work with dilute paramagnetic materials outlined above demonstrates to some degree the utility as well as the limitations of the paramagnetic resonance method. Much of the information we now have on electrons in solids depends upon their mobility and in many cases on surface conditions, as in thermionic and photoelectric emission and in contact rectifiers. On the contrary, in the paramagnetic resonance method, electron mobility may sometimes be an experimental handicap, and, in any event, the electrons seen by the method make themselves known solely by their spin and magnetic moment. Deep-lying rather than surface electrons are seen and the interactions between spin and environment which give rise to anomalous $g$-values, to line broadening, and to "fine" and "hyperfine" structure yield a fund of information on the fields inside of a material, as well as the valence state of an ion for which the paramagnetic effects are observed.

# Plastic Deformation of Germanium and Silicon

C. J. GALLAGHER
*General Electric Research Laboratory, Schenectady, New York*
(Received June 18, 1952)

Single crystals of germanium and silicon have been plastically deformed at elevated temperatures. Germanium becomes ductile above 500°C, and silicon requires temperature above 900°C. At temperatures below 600°C, germanium exhibits an induction period at constant load. Deformed germanium, originally *n*-type, remains *n*-type. The resistivity is increased by deforming, and the lifetime of photo-injected carriers is drastically reduced.

PLASTIC deformation has been observed in single crystals of germanium. Deformation occurs in the temperature range above 500°C with applied stresses of the order of several kg/mm². The temperature range is well below the melting point of 941°C. The specimens studied were single crystal bars of *n*-type germanium of approximately 1-mm square cross section, with a purity corresponding to a resistance range of 2- to 20-ohm cm. These bars were bent and also subjected to tension. Right angle bends can be obtained over a length of 6 mm without fracture. Strains of 0.06 have been measured in tensile specimens subjected to stresses of 2 kg/mm² at 600°C. Slip lines have been observed in both bent and tensile specimens. A typical tensile specimen is shown in Fig. 1. These slip lines are in 111 planes, as might be expected from the packing in the diamond-type cubic lattice of germanium. The slip direction has not yet been definitely established. In

FIG. 1. A typical tensile specimen of Ge.

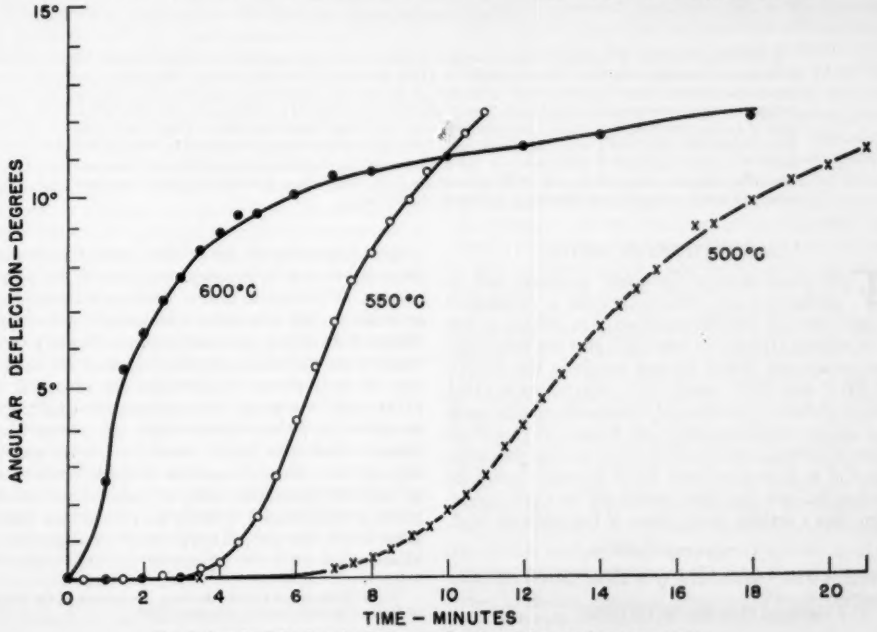


FIG. 2. Angular deflection of a Ge bar as a function of time, at three temperatures.

several specimens, two sets of slip lines have been observed intersecting at angles corresponding to 111 planes. The slip lines disappear when the specimen is etched. Laue patterns of the deformed regions of bent specimens show asterism, but the material retains its single crystal character over the range of strain observed. When larger specimens are bent drastically, audible clicks can be heard.

At the lower end of the temperature range, the deformation exhibits a time delay or induction period of the order of minutes. When a constant load is applied at constant temperature, the time delay decreases with increasing temperature, as shown in the curves of Fig. 2. Each curve represents the angular deflection *versus* time for a bar, 1 mm square, clamped at one end and loaded with 100 grams at a point 1 cm distant. Above 600°C, the time delay was too short to be observed with the loading method used.

The electrical behavior of the deformed material is of interest, particularly in view of results obtained by other workers on the effect of heat treating germanium.[1,2] It has been found that *n*-type germanium heated above 550°C and then quenched to room temperature is left with a permanent increase in resistivity and a decrease in carrier lifetime, probably due to the introduction of acceptor-type defects. A similar effect is found with deformed germanium. For bent specimens, the resistivity is higher in the region of bending, and the lifetime of photo-injected carriers is considerably lower. The germanium, originally *n*-type, was still *n*-type after deformation. Work is in progress to determine possible relations of defects introduced by deformation to those introduced by heat treatment.

Silicon single crystals have also been plastically deformed at temperatures above 900°C with somewhat higher stresses than for germanium. Slip lines have been observed along [111] planes. The writer is indebted to F. H. Horn for furnishing silicon crystals.

[1] Fuller, Theurer, and van Roosbroeck, Phys. Rev. **85**, 678 (1952).
[2] W. DeSorbo and W. C. Dunlap, Jr., Phys. Rev. **83**, 879 (1951).

PHYSICAL REVIEW VOLUME 85, NUMBER 4 NOVEMBER 15, 1952

# The Plasticity of Silicon and Germanium

FREDERICK SEITZ
*University of Illinois, Urbana, Illinois*
(Received July 28, 1952)

A qualitative analysis of Gallagher's measurements of plastic flow in germanium and silicon is made. It is reasonable to suppose the slip occurs by motion in {111} planes of dislocations having a Burger's vector equal to an allowed translation in the $(1\bar{1}0)$ direction. It is suggested, following current thought, that the observed temperature-dependent incubation time for plastic flow is related to the freeing by thermal fluctuations of locking points of the Cottrell type associated with the broken bonds which occur along nearly pure screw dislocations that have a small edge component. It is proposed that foreign atoms reside at the broken bonds in normal materials. A discrepancy in the coefficient of the Boltzmann factor indicates, however, that these concepts cannot be applied in the most simple form. The analogy between Gallagher's measurement and those of Kramer and Maddin in $\beta$-brass is pointed out.

## I. DISLOCATIONS IN LATTICE

THE recent work of Gallagher[1] on plastic flow in germanium and silicon provides a remarkable insight into the ductility of materials in general, as well as of valence crystals. In brief Gallagher has found that germanium and silicon become ductile in the vicinity of 500°C and 900°C, respectively. Slip occurs in {111} planes with the production of well-developed slip bands for stresses somewhat above $10^8$ dynes/cm$^2$. One of the most interesting features of the flow process is the occurrence of an incubation time. From Gallagher's data for germanium one concludes tentatively that this incubation time $\tau$ satisfies an equation of the following kind:

$$\tau = \tau_0 \exp(Q/RT), \qquad (1)$$

where $\tau_0 = 10^{-8}$ second and $Q$ is about 28,000 cal/mole.

[1] C. J. Gallagher, Phys. Rev. **88**, 721 (1952).

It is interesting to see to what extent Gallagher's observations can be explained in terms of the present concepts of dislocation theory. The simplest assumption to make is that the active dislocations move in slip planes of the {111} type and possess a Burger's vector equal to an allowed translational distance of the $(1\bar{1}0)$ type in such planes. Neighboring slip planes of the {111} type, which are also common cleavage planes, are linked by valence bonds which run normal to the planes. Since these bonds would be broken and not reformed if a dislocation whose Burger's vector is not an allowed translation were to pass across the slip plane, it seems highly unlikely that the active dislocations break into partial components[2] as is possible in close-packed cubic or hexagonal lattices, where the

[2] R. D. Heidenreich and W. Shockley, *Conference on the Strength of Solids* (Physical Society, London, 1948).

energies of twin surfaces are relatively low. In this respect valence crystals probably resemble the simple salts, such as the alkali halides.[3]

A pure Taylor-Orowan dislocation of the type assumed above can be formed, geometrically, by removing two neighboring $\{1\bar{1}0\}$ half-planes which contain an equal mixture of the two types of atom in the unit cell, much as in the alkali halides. There will be a row of broken bonds at the edge of each of the half-planes removed. Screw, or Burger's dislocations, can be formed without generating broken bonds but by bending existing bonds instead. The screw axis of such dislocations will, in the ideal case, run through the familiar channels of hexagonal cross section characteristic of the diamond lattice. A mixed Burger's and Taylor-Orowan dislocation will have a linear density of broken bonds along the dislocation line proportional to the degree of Taylor-Orowan character.

## II. LOCKING POINTS

We may expect the unbonded atoms associated with the Taylor-Orowan character to provide ideal condensation points for foreign atoms which like to form valence bonds. These regions should provide locking points of the type proposed by Cottrell and Koehler for many atoms, including those such as hydrogen, carbon, and nitrogen which may enter interstitially. Interstitial atoms or vacancies of the parent material may also be bonded at such locking points.

It is natural to suppose that the observed slip bands are produced by Frank-Read generators which are initially locked because foreign atoms are found at points along the generating dislocation, where broken bonds occur. The stress required to free the locking points without the aid of thermal fluctuations is so great that it can not be applied without rupturing the crystal, whence the material is brittle at low temperatures. At higher temperatures, however, thermal fluctuations may supply sufficient energy to break the dislocations free of the locked points and permit the generators to operate. According to this view, the activation energy $Q$ in (1) is the energy required to free the dislocation from the locked point.

From the information available at the present time, it is not possible to say whether the incubation time for start of plastic flow is strongly dependent on the time the specimen is held at temperature without application of stress. For the purpose of the present discussion we shall assume that the incubation time is essentially independent of such holding time and shall conclude tentatively that the freeing of bonds requires the application of shear stress as well as temperature. This in turn suggests that the dislocations which can be set in motion are those for which the separation of locking points is sufficiently great that the dislocation is able to move at least one atom distance under the applied stress when the lock is broken by thermal fluctuations. These presumably are dislocations in which the locked points are separated from one another by distances of the order of 100 atom spaces or more. This suggests further that the active generators are nearly pure screw dislocations with a small component of edge type. It is conceivable that a nearly perfect edge-type dislocation would not be locked if the material were very free of foreign atoms. However, it seems most reasonable, at present, to assume that there is a sufficient number of foreign atoms present to lock most of the unbonded ends.

Since pure screw dislocations have no unbonded atoms, one might ask why they cannot act as generators without the need of an incubation time. Three replies seem possible: (1) Such dislocations may be exceedingly rare. (2) Any stationary dislocation running perfectly parallel to a crystallographic direction may be difficult to free because of the high value of the Peierls-Nabarro stress. Some edge admixture may be a valuable addition to a screw dislocation because mixed dislocations are easier to move.[4] (3) Even pure screw dislocations may be locked by impurities, in spite of the absence of broken bonds.

It seems difficult to say whether or not the migration along the dislocation of the broken bonds associated with the edge component is a process requiring thermal activation energy. At present the writer is inclined to believe that this motion does not require thermal activation energy provided the dislocation is moving sufficiently rapidly. This does not mean that it is necessary for the dislocation line to move normal to itself with a velocity nearly equal to that of sound. The phase-like motion of a broken bond may be more rapid than the dislocation, in a nearly pure screw dislocation, since the bond moves essentially parallel to the dislocation line. It is possible that a thermal activation energy or a large stress concentration is needed to start the phase-like motion of the broken bond; however, this activation energy may be considerably smaller than the value $Q$ in (1). Thus the time required to set the broken bond in motion would become the observable, limiting time for initiation of flow only in very pure materials.

If the typical Frank-Read generator is $10^4$ atom distances long and contains 100 locking points, one might suppose that $\tau_0$ in (1) would be of magnitude $100\times10^{-12}=10^{-11}$ second. The much larger observed value, namely, $10^{-8}$ second, seems to propose an interesting problem. It may be noted that $\tau_0$ would be about $10^{-8}$ second if the relaxation time involved were that required for locking atoms to diffuse out of the area, about $10^4$ atoms on an edge, over which the generators presumably act. $Q$ would then represent an activation energy for diffusion. In this case, however, as with other conceivable mechanisms, one might expect the incubation time to be dependent on the time the specimen is

[3] F. Seitz, Phys. Rev. **80**, 239 (1950).

[4] See, for example, Pittsburgh Symposium on Plastic Deformation (Government Printing Office PB104,604), page 13.

held at temperature before applying the load, in contradiction with the assumptions made previously.

Cottrell and Bilby[5] have called attention to similar delays in initiating flow in polycrystals of the iron-carbon system and have suggested that it may be necessary to await the formation of avalanches of moving dislocations before flow becomes macroscopically visible. One might hope to eliminate delays of this type by using single crystals with relatively free glide planes; however, this possibility remains for investigation.

### III. EXPERIMENTS OF KRAMER AND MADDIN

The experiments of Kramer and Maddin[6] on time delay of plastic flow in $\beta$-brass seem to be at least qualitatively related to the foregoing work. These investigators have measured the stress required to initiate plastic flow in $\alpha$-brass, aluminum, and $\beta$-brass when the load is applied for relatively short times varying from $8\times10^{-5}$ second to $6\times10^{-3}$ second, and for several temperatures (25°C, −50°C, −190°C). No measurable effects of the high rate of strain were observed in the face-centered cubic metals aluminum and $\alpha$-brass. In these materials the results seem to conform closely to static measurements.

At the temperatures of −50°C and −190°C it was found necessary to increase the stress in the case of $\beta$-brass when the time for which it was applied was less than a critical value $\tau_c$, the increase being a continuous function of time. Apparently if the load is applied for times longer than $\tau_c$, the shear stress required to induce plastic flow is closely the same as the static value. Within the accuracy of the measurements of Kramer and Maddin, the critical stress for plastic flow does not appear to be strongly temperature dependent when the time of application is longer than the $\tau_c$. This result seems to be in contrast with those for the face-centered metals, where there is a gradual rise of yield stress with decreasing temperature.

It is possible to compare the results obtained by Kramer and Maddin for $\beta$-brass with those obtained by Gallagher by making the following assumptions. It will be assumed that the generators for plastic flow in $\beta$-brass are locked, as in the case for those of silicon and germanium. As long as the stress is applied for time greater than $\tau_c$, thermal fluctuations are adequate to free the generating dislocations from the pinning points. An increase in applied stress is necessary to decrease the activation energy for freeing the generating dislocations from the pinning points when the time of application of the load is less than $\tau_c$. With this assumption, $\tau_c$ becomes essentially equivalent to $\tau$ in Eq. (1), providing a measure of the time required for the dislocations to become free without the need for lowering the activation barrier. From the data given in Fig. 10 of the paper by Kramer and Maddin, one may conclude, in rather rough approximation, that $\tau_c=8.0\times10^{-5}$ seconds at −190°C and $\tau_c=4.0\times10^{-3}$ at −52°C. Using an equation of the form

$$\tau_c=\tau_{0c}\exp(Q/RT), \tag{2}$$

one finds $Q$ to be of the order of 180 cal/mole and $\tau_{0c}$ $3\times10^{-3}$ second. The relation (2) is apparently only roughly in agreement with the observations. For example, according to (2) the minimum possible value of $\tau_c$ would be about $3\times10^{-3}$ second if the parameters have the values just given. Actually Kramer and Maddin did not seem to observe a critical time at room temperature even when the load was applied for timest as short as $6.2\times10^{-4}$ second. Nevertheless, it is clear that $Q$ is approximately 100 times smaller in the case of $\beta$-brass than in the cases of silicon or germanium. It is also clear that an appropriate value of $\tau_{0c}$ is much larger than $10^{-11}$ second and is actually comparable to the value found in (1). Conversely, the very large values of $Q$ for silicon and germanium make it seem unlikely that the incubation time observed by Gallagher in these solids can be diminished measurably by the application of stresses only a factor two or three larger than those he employed.

The writer is indebted to Dr. J. D. Eshelby and Dr. William Heller for discussions of this topic. He is particularly obligated to C. T. Gallagher for the privilege of seeing his manuscript prior to publication.

[5] A. H. Cottrell and B. H. Bilby, Proc. Phys. Soc. (London) **A62**, 49 (1949).
[6] I. R. Kramer and R. Maddin, J. Metals **4**, 197 (1952).

# Meson Theory of Nuclear Forces and Low Energy Properties of the Neutron-Proton System*

MAURICE M. LÉVY
*Institute for Advanced Study, Princeton, New Jersey*
(Received August 7, 1952)

A detailed analysis is made of the neutron-proton interaction yielded by the symmetrical pseudoscalar meson theory, with pseudoscalar coupling, using the Tamm-Dancoff nonadiabatic method which has been extended to include nucleon pair creation and higher order effects in the exchange of mesons. It is found that, in the nonrelativistic region, the second- and fourth-order terms provide the main contribution to the interaction, the remaining part of the potential giving only a small correction. In the relativistic region, little can be said about the convergence of the interaction, but there are indications that it becomes strongly repulsive at distances comparable with the nucleon Compton wavelength ($\hbar/Mc$). The radiative corrections to the potential are calculated in the nonrelativistic limit, using the equation of Bethe and Salpeter, which has been transformed into a one-time equation by means of a method which has been given previously. It is shown that the corrections arising from vertex parts and closed loops in the Feynman diagrams are at most of the order of $(G^2/4\pi)(\mu/2M)^2$ times the term which they correct. There exists, however, a class of finite self-energy terms which give a contribution to the interaction having the same analytical form as the fourth-order potential, times a numerical factor which can be expressed as a power series in $G^2/4\pi$.

The low energy properties of the neutron-proton system are discussed, using the nonrelativistic potential which is calculated in this paper, and replacing the interaction in the relativistic region by a boundary condition prescribing that the wave function tends to zero at a finite distance $r_c$. It is found that a good agreement with experiment can be achieved by choosing $G^2/4\pi=9.7\pm1.3$ and $r_c=(0.38\pm0.03)(\hbar/\mu c)$. Finally, an investigation of the neutron-proton scattering at 40 Mev shows that the same potential leads to a satisfactory description of the available experimental data.

## I. INTRODUCTION

THE pseudoscalar meson field[1] theory has not yet progressed very far in the quantitative description of nuclear forces, mainly because of the two following difficulties:

(1) The calculation of the nucleon-nucleon interaction, to the second order in the coupling constant[2] $G$, leads to a static approximation which is too strongly singular near the origin to permit the existence of stationary states. It is clear, however, that this singularity has no physical meaning, since the static interaction is no longer valid for distances of the order of the nucleon Compton wavelength ($1/M$).

(2) The high value of $G^2/4\pi$ which is obtained by fitting the simplest low energy properties of the neutron-proton system casts strong doubts on the validity of any perturbation expansion of the interaction. Unfortunately, it appears very difficult to treat the pseudoscalar meson field by other methods ("strong" or "intermediate" coupling), since the nucleons cannot be replaced, in this case, by infinitely massive extended sources, because of the importance of nucleons pair creation.[3]

It should be noted, however, that few serious attempts have been made so far to determine to what extent these difficulties are real.[4] The nonstatic effects might, for example, lower the singularity of the interaction, or even change its sign at very small distances. On the other hand, the creation of virtual nucleon pairs might improve, at least in some region, the convergence of the perturbation expansion, the effective expansion parameter being, in that region, much smaller than $G^2/4\pi$.

It is the purpose of the present paper to investigate critically the above difficulties by means of a term by term analysis of the interaction expansion yielded by a weak coupling treatment of the symmetrical pseudoscalar meson theory, with pseudoscalar coupling. This analysis includes not only the finite parts of the interaction, but also the radiative corrections in which the

* A preliminary report on the results of this paper has appeared in Phys. Rev. **86**, 806 (1952); **87**, 1143 (1952).

[1] Only the pseudoscalar coupling will be considered in this paper, since it is only in this case that the intrinsic field theoretical infinities can be separated and re-interpreted consistently. See J. C. Ward, Phys. Rev. **84**, 897 (1951); A. Salam, Phys. Rev. **84**, 426 (1951); **86**, 731 (1952).

[2] The physical evidence having considerably reduced in recent years the possibilities of different types of $\pi$-meson fields and couplings, it seems useful to replace the conventional nomenclature [see for example, L. Rosenfeld, *Nuclear Forces* (North Holland Publishing Company, Amsterdam, 1948), p. 322] by a simplified system of notations. We denote by $G$ the pseudoscalar coupling constant of a pseudoscalar field (suggesting by this choice that this constant is expected to be big!) and by $g$ the quantity $G(\mu/2M)$, which can be considered as an equivalent pseudovector coupling constant in the cases where the equivalence theorem is valid [see, E. C. Nelson, Phys. Rev. **60**, 830 (1941); F. J. Dyson, Phys. Rev. **73**, 929 (1948); K. M. Case, Phys. Rev. **76**, 14 (1949)]. Both $G^2/4\pi$ and $g^2/4\pi$ are expressed in the same units as the fine structure constant in electrodynamics. A system of units where $\hbar=c=1$ is used in this paper.

[3] It is an essential feature of the $\gamma_5$ coupling that the matrix elements which simply create or annihilate a meson are, in the nonrelativistic limit, much smaller than those which, in addition, create or annihilate a pair of nucleons.

[4] The fourth-order interaction and its influence on nuclear forces have been discussed by several authors, for example: H. A. Bethe, Phys. Rev. **76**, 191 (1949); K. M. Watson and J. V. Lepore, Phys. Rev. **76**, 1157 (1949); Y. Nambu, Prog. Theor. Phys. **5**, 614 (1950); G. Wentzel, Phys. Rev. **86**, 802 (1952); etc. Nobody has, however, investigated seriously the behavior of the remaining parts of the static interaction and the effect of the nonstatic corrections.

mass and coupling constant have to be renormalized explicitly. In order to carry out this program, use has been made of the nonadiabatic treatment of Tamm[5] and Dancoff[6] which, in a previous paper,[7] has been extended to include the creation of virtual nucleon pairs and the exchange of an arbitrary number of mesons. In the framework of this formalism, it is necessary to give first the definition of an interaction operator having a general validity. This operator, which is defined in Sec. II, is similar to the "velocity dependent potential" introduced by Wheeler,[8] but has the added feature that it depends explicitly on the total energy of the system.

In Sec. III, the part of the interaction which contains no contribution arising from radiative processes will be analyzed term by term. It will be shown that, in the nonrelativistic region,[9] even if $G^2/4\pi$ is of the order of 10, there exists a finite number of terms (namely, the second-order and the largest part of the fourth-order potential) which can be used as the starting basis of a perturbation treatment, all the remaining portions of the interaction being considered as small corrections. In the relativistic region, the effective expansion parameter is $G^2/4\pi$, and little can be said about the convergence of the interaction. There are, however, some indications that it becomes repulsive at short distances, the lowest order terms of the potential being dominated by the so-called "contact" terms, which actually have a range of order $\hbar/Mc$. On the other hand, the pseudoscalar meson theory should not be expected to give too reliable results in that region, on account of the existence of heavier mesons than $\pi$-mesons, isobaric states of nucleons, etc. . . .

The contributions to the interaction arising from the radiative processes will be calculated in Sec. IV, starting from the equation of Bethe and Salpeter[10] and transforming it into a one-time equation by means of a method which has been given previously.[7] It will be found that the correction contributed by vertex parts and closed loops in the irreducible Feynman diagrams are at most of the order of $(G^2/4\pi)(\mu/2M)^2$ times the interaction term which they correct ($\mu$ and $M$ are respectively the meson and nucleon masses). There exists, however, a class of finite self-energy terms, which give a contribution to the interaction which is not negligible. In the nonrelativistic region this contribution has the same analytical form as the fourth-order potential, times a numerical factor which can be expressed as a power series in $G^2/4\pi$.

[5] I. Tamm, J. Phys. (USSR) **9**, 449 (1945).
[6] S. M. Dancoff, Phys. Rev. **78**, 382 (1950).
[7] M. Lévy, Phys. Rev. **88**, 72 (1952). This paper will be referred to as (*A*) in the following.
[8] J. A. Wheeler, Phys. Rev. **50**, 643 (1936).
[9] By "nonrelativistic region" is meant the part of the momentum distribution in which the nuclear recoils can be neglected ($|p| \ll M$). In coordinate space, this part of the interaction coincides with the static potential which still depends, however, on the total energy of the system.
[10] E. Salpeter and H. A. Bethe, Phys. Rev. **84**, 1232 (1951); M. Gell-Mann and F. Low, Phys. Rev. **84**, 350 (1951). This equation will sometimes be referred to as (B.S.) in the following.

The preceding features of the pseudoscalar interaction permit a semiquantitative description of the neutron-proton system at low and intermediate energies. In the nonrelativistic region the exact potential calculated in this paper can be used, the relativistic part of the interaction being arbitrarily replaced by a boundary condition, prescribing that the wave function tends to zero at a finite distance $r_c$. Considering the relatively large value of the ratio $(\mu/M)$, the separation of a nonrelativistic region where the potential can be calculated exactly is, to a certain extent, arbitrary. It can therefore be expected that the corresponding semiquantitative treatment becomes less and less satisfactory as the energy of the system increases. It will be shown, in Sec. V, that a good agreement with the low energy properties of the neutron-proton system can be achieved by choosing $G^2/4\pi = 9.7 \pm 1.3$ and $r_c = (0.38 \pm 0.03)(\hbar/\mu c)$. The same constants lead to a good description of the available experimental data on the neutron-proton scattering at 40 Mev.

## II. DEFINITION AND GENERAL PROPERTIES OF THE INTERACTION

In the nonadiabatic treatment of the two-body problem,[7] the state vector of the system is defined by means of a set of probability amplitudes $a_\lambda^{(m,n)}$ of the free states where $m$ mesons and $n$ nucleon pairs are present; the two initially interacting nucleons are treated separately, and $\lambda$ is a variable which specifies the momenta, spins, isotopic spins, etc., of the particular free state which is considered.

The set $[a_\lambda^{(m,n)}]$ satisfies a system of simultaneous integral equations which has been discussed in detail in (*A*). If, in particular, one eliminates all the amplitudes except $a_\lambda^{(0,0)}$ by means of successive substitutions, one obtains the general equation (A, 6) which we now write in the center-of-mass system as follows:

$$(W-2E_p)a^{(0,0)}(\mathbf{p},-\mathbf{p}) = (2\pi)^{-3}\int K(\mathbf{p},\mathbf{p}';W)a^{(0,0)}(\mathbf{p}',-\mathbf{p}')d\mathbf{p}', \quad (1)$$

in which $W$ is the total energy of the system and $E_p = (p^2+M^2)^{\frac{1}{2}}$. The kernel $K(\mathbf{p},\mathbf{p}';W)$ is expressed as a power series of $G^2$:

$$K(\mathbf{p},\mathbf{p}';W = \sum_n G^{2n}K_{2n}(\mathbf{p},\mathbf{p}';W). \quad (2)$$

Multiplying both sides of (1) by $(W+2M)^{-1}(W+2E_p)$ and defining $\epsilon = W-2M$ as the binding energy (or, for an unbound state, the total nonrelativistic energy in the center-of-mass system), we obtain the equation

$$\left(\frac{p^2}{M_\rho}-\epsilon\right)u^{(0,0)}(\mathbf{p}) = -(2\pi)^{-3}\int \frac{[(2E_p+W)(2E_{p'}+W)]^{\frac{1}{2}}}{4M_\rho} \times K(\mathbf{p},\mathbf{p}';W)u^{(0,0)}(\mathbf{p}')d\mathbf{p}', \quad (3)$$

where we have set $\rho=1+\epsilon/4M$ and introduced the amplitude[11]

$$u^{(0,0)}(\mathbf{p})=\left[\frac{4M\rho}{2E_p+W}\right]^{\frac{1}{2}}a^{(0,0)}(\mathbf{p},-\mathbf{p}). \quad (4)$$

Transforming Eq. (3) into coordinate space, we get

$$\left(\frac{\nabla^2}{M\rho}+\epsilon\right)\phi^{(0,0)}(\mathbf{r})=\int U(\mathbf{r},\mathbf{r}';W)\phi^{(0,0)}(\mathbf{r}')d\mathbf{r}', \quad (5)$$

where

$$\phi^{(0,0)}(\mathbf{r})=(2\pi)^{-\frac{3}{2}}\int u^{(0,0)}(\mathbf{p})e^{i\mathbf{p}\mathbf{r}}d\mathbf{p} \quad (6)$$

is the Fourier transform of $u^{(0,0)}(\mathbf{p})$ and $U(\mathbf{r},\mathbf{r}';W)$ the interaction operator

$$U(\mathbf{r},\mathbf{r}';W)=\sum_n G^{2n}U_{2n}(\mathbf{r},\mathbf{r}';W)$$
$$=\sum_n\frac{G^{2n}}{(2\pi)^3}\int\frac{[(2E_p+W)(2E_{p'}+W)]^{\frac{1}{2}}}{4M\rho}$$
$$\times K_{2n}(\mathbf{p},\mathbf{p}';W)e^{i\mathbf{p}\mathbf{r}-i\mathbf{p}'\mathbf{r}'}d\mathbf{p}d\mathbf{p}'. \quad (7)$$

Equation (5) is an ordinary Schrödinger equation for a particle of reduced mass $M\rho$ and energy $\epsilon$, and, therefore, the interaction operator of the right hand side is unambiguously defined. By writing, on the right-hand side of (7), $\mathbf{p}\mathbf{r}-\mathbf{p}'\mathbf{r}=\frac{1}{2}[(\mathbf{p}+\mathbf{p}')(\mathbf{r}-\mathbf{r}')+(\mathbf{p}-\mathbf{p}')(\mathbf{r}+\mathbf{r}')]$, one sees easily that, for a given value of $|\mathbf{r}+\mathbf{r}'|$, $U(\mathbf{r},\mathbf{r}';W)$ is a function of $|\mathbf{r}-\mathbf{r}'|$ of the Gaussian type, the width of which becomes more and more narrow when $|\mathbf{r}+\mathbf{r}'|$ increases. We have in fact, for $|\mathbf{r}+\mathbf{r}'|\gg(1/M)$:

$$U_{2n}(\mathbf{r},\mathbf{r}';W)\rightarrow\delta\left(\frac{\mathbf{r}-\mathbf{r}'}{2}\right)V_{2n}\left(\frac{|\mathbf{r}+\mathbf{r}'|}{2}\right). \quad (8)$$

Consequently, when $r$ *or* $r'$ is large compared with the nucleon Compton wavelength, the interaction operator reduces to a usual potential.

For small values of $r$, the analysis of the interaction becomes a relatively complicated problem,[12] since its value at a given point $\mathbf{r}$ cannot be separated from that of the wave function in a certain volume around $\mathbf{r}$. It is clear, however, that the main contribution to the right-hand side of (5) arises, in this case, from the part of the right-hand side of (3) in which both the momentum $|\mathbf{p}|$ and the momentum transfer $|\mathbf{p}-\mathbf{p}'|$ are large compared with the meson mass $\mu$. In the case where $\phi^{(0,0)}(\mathbf{r})$ is finite at (and does not vary too rapidly in the neighborhood of) the origin, the extreme relativistic behavior of the right-hand side of (7) can therefore be expressed as follows:

$$\int U(\mathbf{r},\mathbf{r}';W)\phi^{(0,0)}(\mathbf{r}')d\mathbf{r}'$$
$$\rightarrow\frac{\phi^{(0,0)}(0)}{(2\pi)^3}\int\left(\frac{2E_p+W}{4M\rho}\right)^{\frac{1}{2}}K(\mathbf{p},0;W)e^{i\mathbf{p}\mathbf{r}}d\mathbf{p}. \quad (9)$$

In the case where $\phi^{(0,0)}(\mathbf{r})$ is not finite at the origin (in particular, when it tends to zero on account of a strong repulsion at short distances), Eq. (9) still corresponds to a good approximation, if $\phi^{(0,0)}(0)$ is replaced by a suitable constant of the form $\int F(\mathbf{p}')u^{(0,0)}(\mathbf{p}')d\mathbf{p}'$, provided that the wave function is mainly concentrated in the nonrelativistic region, which it is likely to be in this particular case.

## III. ANALYSIS OF THE INTERACTION (WITHOUT RADIATIVE CORRECTIONS)

In this section, a detailed study of the interaction will first be made in the nonrelativistic region (with the exception of the radiative corrections which will be considered in the next section). A discussion of the behavior of the interaction in the relativistic region will follow.

### A. Nonrelativistic Region

As was seen in the preceding section, the interaction reduces in this case, to an ordinary potential $V(r)$, which is obtained[13] by setting, in the expression of $K(\mathbf{p},\mathbf{p}';W)$, as well as on the right-hand side of (7): $E_p=E_{p'}=M$. Consequently, $u^{(0,0)}(\mathbf{p})$ and $a^{(0,0)}(\mathbf{p},-\mathbf{p})$ are, in this case, identical, and $\phi^{(0,0)}(\mathbf{r})$ is simply the Fourier transform of $a^{(0,0)}(\mathbf{p},-\mathbf{p})$. Furthermore, the total energy of the system $W$ wil be equaled to $2M$, since only the low energy properties of the nucleon-nucleon system are considered in this paper. A remark will however be made at the end of this section on the influence of the energy dependence of the interaction on the high energy nucleon-nucleon scattering.

#### 1. *Second-order potential*

The first term in the expansion (2) can be written [see Eq. (A, 7)]:

$$K_2(\mathbf{p},\mathbf{p}';W)=-G^2(\boldsymbol{\tau}_1\cdot\boldsymbol{\tau}_2)\frac{(M+E_p)(M+E_{p'})}{4E_pE_{p'}}$$
$$\times\frac{(\boldsymbol{\sigma}_1\cdot\mathbf{R})(\boldsymbol{\sigma}_2\cdot\mathbf{R})}{\omega(\mathbf{p},\mathbf{p}')[\omega(\mathbf{p},\mathbf{p}')+E_p+E_{p'}-W]}, \quad (10)$$

[11] This new amplitude is introduced in order to preserve the symmetry of the interaction operator with respects to the variables $\mathbf{r}$ and $\mathbf{r}'$.

[12] Except in the particular case where the kernel $K(\mathbf{p},\mathbf{p}';W)$ can be broken into a product of two functions of $\mathbf{p}$ and $\mathbf{p}'$, respectively.

[13] In the calculation of the different terms of the kernel $K_n(\mathbf{p},\mathbf{p}';W)$ there will occur integrations over some intermediate momenta, such as $\mathbf{p}''$. In principle, these integrations must be carried out exactly; it can easily be shown, however, that, by setting also in those terms $E_{p''}=M$, only corrections of order $(\mu/M)^2$ are neglected, except when the corresponding integral becomes divergent if this approximation is made. In this case, the terms involving $\mathbf{p}''$ must evidently be left untouched.

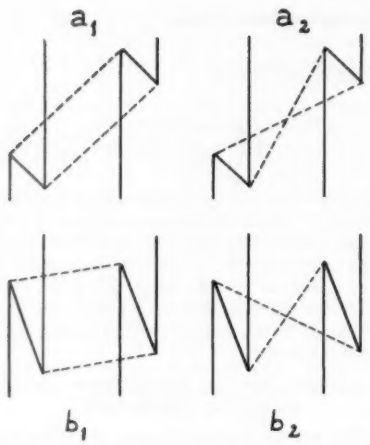


FIG. 1. The virtual processes which give the main contribution to the fourth-order interaction, and which involve the creation of two nucleon pairs in the intermediate states.

where use has been made of the notation:

$$\omega=[|\mathbf{p}-\mathbf{p}'|^2+\mu^2]^{\frac{1}{2}},$$

and

$$\mathbf{R}=\mathbf{p}'/(M+E_{p'})-\mathbf{p}/(M+E_p). \tag{11}$$

For distances which are large compared with $(1/M)$, one obtains, using (7) and (8):

$$V_2(r)=-\frac{G^2}{(2\pi)^3}\frac{\boldsymbol{\tau}_1\cdot\boldsymbol{\tau}_2}{(2M)^2}\int\frac{(\boldsymbol{\sigma}_1\cdot\mathbf{k})(\boldsymbol{\sigma}_2\cdot\mathbf{k})}{\omega_k{}^2}e^{i\mathbf{k}\mathbf{r}}d\mathbf{k}, \tag{12}$$

which gives the well-known expression:

$$V_2(r)=\tfrac{1}{3}(\boldsymbol{\tau}_1\cdot\boldsymbol{\tau}_2)\frac{G^2}{4\pi}\left(\frac{\mu}{2M}\right)^2\times\left\{(\boldsymbol{\sigma}_1\cdot\boldsymbol{\sigma}_2)+S_{12}\left[1+\frac{3}{\mu r}+\frac{3}{(\mu r)^2}\right]\right\}\frac{e^{-\mu r}}{r}, \tag{13}$$

where $S_{12}=3(\boldsymbol{\sigma}_1\cdot\mathbf{r})(\boldsymbol{\sigma}_2\cdot\mathbf{r})/r^2-(\boldsymbol{\sigma}_1\cdot\boldsymbol{\sigma}_2)$. On the right-hand side of (13) we have omitted the so-called "contact" term: $\frac{1}{3}(\boldsymbol{\sigma}_1\cdot\boldsymbol{\sigma}_2)(\boldsymbol{\tau}_1\cdot\boldsymbol{\tau}_2)(2M)^{-2}\delta(\mathbf{r})$, which gives no contribution in the region under consideration. We shall return to this term in paragraph $(B)$ of this section.

### 2. *Fourth-Order Potential*

Because of the special properties of the matrix element of $\gamma_5$ (see footnote 3), the main contribution to a given order of the interaction arises, in the nonrelativistic region, from the virtual processes which involve the creation and annihilation of the maximum number of pairs possible to that order. The main part of the fourth order potential will therefore be provided by the virtual processes involving the presence of two nucleon pairs in the intermediate states. Another feature of the fourth-order potential, which is, however, purely accidental, is that the contribution from the processes involving one nucleon pair in the intermediate states vanishes in the nonrelativistic region, in the case of the symmetrical theory.[14] Finally, the part of the potential which is contributed by the processes involving an ordinary two-mesons exchange (and no pairs) is of the order of $(g^2/4\pi)^2=(G^2/4\pi)^2(\mu/2M)^4$ and can be neglected. The part of the interaction which contains all the contributions up to the order of $(G^2/4\pi)^2(\mu/2M)^3$ has the following expression:

$$V_4(r)=-3\left(\frac{G^2}{4\pi}\right)^2\left(\frac{\mu}{2M}\right)^2\frac{1}{\mu r^2}\times\left\{\frac{2}{\pi}K_1(2\mu r)+\frac{\mu}{2M}\left[\frac{2}{\pi}K_1(\mu r)\right]^2\right\}, \tag{14}$$

where $K_n(x)$ is the $n$th-order Hankel function of imaginary argument.[15]

*a. Two-pair terms.*—These terms are provided by the virtual processes illustrated in diagrams $a_1$, $a_2$, $b_1$, $b_2$ of Fig. 1 (plus those which are symmetrical with respect to particles 1 and 2). Diagrams $a_1$ and $a_2$, which involve a maximum number of two mesons but only one pair at a given time, give the main contribution

$$V_4^{(a)}=-\frac{G^4}{(2\pi)^6}\frac{\tau_\lambda^{(1)}\tau_\mu^{(1)}[\tau_\lambda^{(2)}\tau_\mu^{(2)}+\tau_\mu^{(2)}\tau_\lambda^{(2)}]}{(2M)^2}\times\int\frac{\exp[-i(\mathbf{k}_1+\mathbf{k}_2)\mathbf{r}]}{4\omega_1\omega_2(\omega_1+\omega_2)}d\mathbf{k}_1d\mathbf{k}_2$$
$$+\text{symmetrical term in (1) and (2)}, \tag{15}$$

and consequently $V_4^{(a)}=-3(G^2/4\pi)^2(2M)^{-4}J_1(r)$, where $J_1(r)$ is a function calculated in the Appendix [Eq. (10a)]. Diagrams $b_1$ and $b_2$, where a maximum number of two pairs is present at a given time, give a contribution which is smaller by a factor $(\mu/2M)$:

$$V_4^{(b)}=-\frac{G^4}{(2\pi)^6}\frac{\tau_\lambda^{(1)}\tau_\mu^{(1)}[\tau_\lambda^{(2)},\tau_\mu^{(2)}]_+}{(2M)^3}\int\frac{\exp[-i(\mathbf{k}_1+\mathbf{k}_2)\mathbf{r}]}{4\omega_1\omega_2}d\mathbf{k}_1d\mathbf{k}_2,$$

and, therefore, $V_4^{(b)}=-3(G^2/4\pi)^2(2M)^{-3}(2/\pi)[I_0(r)]^2$, where $I_n(r)$ is defined by Eq. (5a) of the Appendix. In Eqs. (15) and (16) we have set $\omega_i=(k_i{}^2+\mu^2)^{\frac{1}{2}}$. Adding the expressions of $V_4^{(a)}$ and $V_4^{(b)}$ gives Eq. (14).

*b. One-pair terms.*—These processes (plus those which are symmetrical with respect to (1) and (2)) are illustrated in Fig. 2. Diagrams $(2a_1)$ and $(2a_2)$ give

$$V_4^{(a')}=\frac{G^4}{(2\pi)^6}(2M)^{-2}\int\{\tau_\lambda^{(1)}\tau_\mu^{(1)}[\tau_\lambda^{(2)},\tau_\mu^{(2)}]_+(\boldsymbol{\sigma}_1\cdot\mathbf{k}_1)(\boldsymbol{\sigma}_2\cdot\mathbf{k}_2)$$
$$+\tau_\lambda^{(2)}\tau_\mu^{(2)}[\tau_\lambda^{(1)},\tau_\mu^{(1)}]_+(\boldsymbol{\sigma}_2\cdot\mathbf{k}_1)(\boldsymbol{\sigma}_2\cdot\mathbf{k}_2)\}$$
$$\times\frac{\exp[-i(\mathbf{k}_1+\mathbf{k}_2)\mathbf{r}]}{4\omega_1{}^2\omega_2{}^2}d\mathbf{k}_1d\mathbf{k}_2$$
$$=-\frac{3G^4}{(2\pi)^6}(2M)^{-2}\int\frac{\mathbf{k}_1\cdot\mathbf{k}_2\exp[-i(\mathbf{k}_1+\mathbf{k}_2)\mathbf{r}]}{\omega_1{}^2\omega_2{}^2}d\mathbf{k}_1d\mathbf{k}_2. \tag{17}$$

[14] This result is only true in the symmetrical theory. The neutral theory, for example, gives the repulsive potential: $(G^2/4\pi)^2\times(\mu/2M)^3(\mu r^2)^{-1}[1+(\mu r)^{-1}]^2e^{-2\mu r}$.

[15] For the properties of these functions, see G. N. Watson, *Theory of Bessel Functions* (Cambridge University Press, Cambridge, 1922).

The contribution of $(2b_1)$ and $(2b_2)$ is, on the other hand,

$$V_4^{(b')}=-\frac{3G^4}{(2\pi)^6}(2M)^{-3}\int\frac{\exp[-i(\mathbf{k}_1+\mathbf{k}_2)\mathbf{r}]\mathbf{k}_1\cdot\mathbf{k}_2}{\omega_1^2\omega_2(\omega_1+\omega_2)}d\mathbf{k}_1d\mathbf{k}_2, \quad (18)$$

and that of diagrams $(2c_1)$ and $(2c_2)$:

$$V_4^{(c')}=-\frac{3G^4}{(2\pi)^6}(2M)^{-3}\int\frac{\exp[-i(\mathbf{k}_1+\mathbf{k}_2)\mathbf{r}]\mathbf{k}_1\cdot\mathbf{k}_2}{\omega_1\omega_2^2(\omega_1+\omega_2)}d\mathbf{k}_1d\mathbf{k}_2. \quad (19)$$

It can easily be verified that $V_4^{(a')}+V_4^{(b')}+V_4^{(c')}=0$.

*c. No-pair terms.*—These are the customary two meson exchange terms (with or without crossing of the meson lines) which have been discussed in detail in (*A*, Sec. 2.22). In the case of the pseudoscalar interaction, they can easily be brought, in the nonrelativistic region, into the following form:

$$V_4''=-\frac{G^4}{(2\pi)^6}\frac{(\boldsymbol{\tau}_1\cdot\boldsymbol{\tau}_2)^2}{(2M)^4}\times\int\frac{(\boldsymbol{\sigma}_1\cdot\mathbf{k}_1)(\boldsymbol{\sigma}_2\cdot\mathbf{k}_1)(\boldsymbol{\sigma}_1\cdot\mathbf{k}_2)(\boldsymbol{\sigma}_2\cdot\mathbf{k}_2)\exp[-i(\mathbf{k}_1+\mathbf{k}_2)\mathbf{r}}{\omega_1^2\omega_2^2}\times d\mathbf{k}_1d\mathbf{k}_2-\frac{3G^4}{(2\pi)^6}(2M)^{-4}\int\frac{\boldsymbol{\sigma}_1\cdot[\mathbf{k}_1\times\mathbf{k}_2]\boldsymbol{\sigma}_2\cdot[\mathbf{k}_1\times\mathbf{k}_2]}{\omega_1^2\omega_2(\omega_1+\omega_2)}\times\left(\frac{2}{\omega_1}+\frac{1}{\omega_2}\right)\exp[-i(\mathbf{k}_1+\mathbf{k}_2)\mathbf{r}]d\mathbf{k}_1d\mathbf{k}_2. \quad (20)$$

This part of the fourth-order potential is of the order $(G^2/4\pi)^2\times(\mu/2M)^4$ and can be neglected for the time being. It contains, however, a "contact" term which will be discussed in paragraph (*B*) of this section.

We conclude this paragraph by a few remarks on the potential of Eq. (14), which is spin and isotopic spin independent and attractive in all states. The first term of the right-hand side is $G^2/4\pi$ times bigger than $V_2(r)$, which, if $G^2/4\pi$ is of the order of 10, is of the same order as the second term of (14). However, $V_4(r)$ has a range $(1/2\mu)$, since, the asymptotic value of $K_n(x)$ being $(\pi/2x)^{\frac{1}{2}}e^{-x}$, its behavior for large distances is defined by the following expression:

$$V_4(r)\sim-3\left(\frac{G^2}{4\pi}\right)^2\left(\frac{\mu}{2M}\right)\frac{1}{\mu r^2}\times\left[1+\frac{\mu}{M}(\mu r)^{-1}\right](\mu r)^{-\frac{1}{2}}e^{-2\mu r}. \quad (21)$$

For small values of $x$, $K_1(x)$ is roughly equal to $1/x$, and therefore, the two terms of Eq. (14) behave respectively like $r^{-3}$ and $r^{-4}$ at short distances.

It is finally not without interest to note the connection of the results of this paragraph with the remarks made by Lepore[16] and Wentzel,[17] who have shown that, by means of the canonical transformation used by Dyson,[18] the pseudoscalar interaction term of the nucleon-meson Hamiltonian can be brought into the following form:

$$-iG\bar{\psi}\gamma_5\tau_\alpha\psi\phi_\alpha\rightarrow-\tfrac{1}{2}i(G/M)\bar{\psi}'\tau_\beta\psi'\boldsymbol{\sigma}\cdot\boldsymbol{\nabla}\phi_\beta-\tfrac{1}{2}(G^2/M)\bar{\psi}'\psi'\phi_\beta^2, \quad (22)$$

where only terms of order $(G/2M)^2$ have been neglected. A weak coupling calculation of the nucleon-nucleon potential corresponding to each of the two terms of the right-hand side of (22) yields, in first approximation, $V_2(r)$ and the first part of $V_4(r)$, respectively.

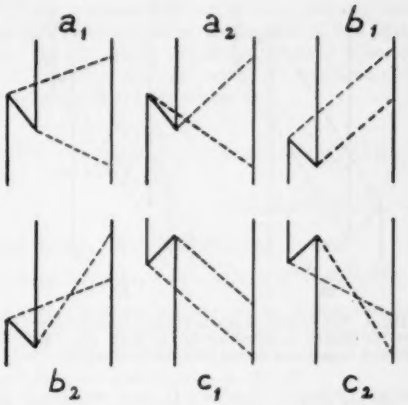


FIG. 2. The virtual processes which involve the creation of one virtual pair in the intermediate states, the contributions of which cancel each other in the nonrelativistic region, in the case of the symmetrical theory.

### 3. *Higher-Order Terms of the Potential*

These terms have the following general properties:

*a. Strength.*—The interaction is characterized, in the non-relativistic region, by two expansion parameters: $\alpha_1=(G^2/4\pi)(\mu/2M)^2$, which corresponds to the exchange of one meson without pair creation;

$$\alpha_2=(G^2/4\pi)^2(\mu/2M)^2,$$

which corresponds to a double mesonic exchange with the creation of two pairs. To the order of $G^{4n}$, the leading term of the nonrelativistic potential is proportional to $\alpha_2^n$, whereas to the order of $G^{4n+2}$, it is proportional to $\alpha_2^n\alpha_1$, and therefore much smaller. If $G^2/4\pi$ is of the order of 10, the expansion parameters have the following numerical values: $\alpha_1\sim0.06$ and $\alpha_2\sim0.6$.

*b. Range.*—A term of order $G^{2n}$ corresponds to a potential of range $(1/n\mu)$. Since the nonstatic effects become predominant at a distance of order $(2/M)\sim(1/3\mu)$, the reduction due to the range becomes effective, in the nonrelativistic region, for the terms of the sixth order in $G$; for the eighth and higher order terms, it influences the convergence of the interaction expansion in a more important way than the reduction due to the strength.

*c. Singularity.*—If it were possible to approximate at short distances the Hankel functions by the first term of their expansion in powers of the argument, the singularity of the potential would increase rapidly with the order of the terms, and the expansion parameters should rather be taken as $\alpha_1'=(G^2/4\pi)(2Mr)^{-2}$ and $\alpha_2'=(G^2/4\pi)^2(2Mr)^{-2}$. However, since the function $K_m(n\mu r)$ can be replaced by $\frac{1}{2}(m-1)!\,(2n\mu r)^{-m}$ only for

[16] J. V. Lepore, Phys. Rev. **87**, 209 (1952).
[17] G. Wentzel, Phys. Rev. **86**, 802 (1952).
[18] F. J. Dyson, Phys. Rev. **73**, 929 (1948).

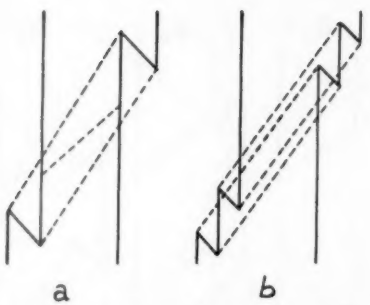


FIG. 3. Two typical diagrams of the virtual processes which give the leading contributions to the sixth- and eighth-order potential, respectively (in the nonrelativistic region).

$r \ll (m-1)^{\frac{1}{2}}(2n\mu)^{-1}$ (for $m>1$) and $r \ll (1/n\mu)$ (for $m=0$, 1), the range in which this approximation is possible is rapidly displaced into the relativistic region, where the static approximation is no longer valid.[19]

The above properties will be illustrated by estimating the leading terms of the sixth- and eighth-order potentials. The magnitude of the latter will, in particular, provide an essential test for the convergence of the interaction expansion, since its strength involves $\alpha_2$ only, and its "apparent" singularity (in the sense explained in paragraph (c) above) is $r^{-5}$.

Sixth-order potential.—The leading term, which is proportional to $\alpha_2\alpha_1$, arises from virtual processes which can be illustrated by joining the nucleon lines of the diagrams $(a_1)$ and $(a_2)$ of Fig. 2 by means of a single meson line in the region where there are already two mesons (and no nucleon pair) present [an example is given in Fig. 3(a)]. By adding the contributions of all possible graphs, the following expression is obtained:

$$V_6(r) = -\left(\frac{G^2}{4\pi}\right)^3 (\boldsymbol{\tau}_1\cdot\boldsymbol{\tau}_2)(2\pi)^{-3}\int \frac{\boldsymbol{\sigma}_1\cdot\mathbf{k}_3\ \exp[-i(\mathbf{k}_1+\mathbf{k}_2+\mathbf{k}_3)\mathbf{r}]}{2\omega_1\omega_2\omega_3(\omega_1+\omega_2)(\omega_1+\omega_2+\omega_3)} \times\left(\frac{3\boldsymbol{\sigma}_2\cdot\mathbf{k}_1}{\omega_1+\omega_2}+\frac{\boldsymbol{\sigma}_2\cdot\mathbf{k}_1}{\omega_2+\omega_3}\right)d\mathbf{k}_1 d\mathbf{k}_2 d\mathbf{k}_3 + \text{symmetrical term with respect to (1) and (2).} \quad (23)$$

Eighth-order potential.—The main contribution to this potential comes from processes involving the exchange of four mesons and the creation of four nucleon pairs (not more than one being present at a given time). One of them is illustrated in Fig. 3(b). All the others can be obtained by allowing the meson lines to cross each other in all possible ways, and by interchanging the role of particles (1) and (2). The resulting expression is given by

$$V_8(r) = -3\left(\frac{G^2}{2M}\right)^4 (2\pi)^{-12}\int \frac{\exp[-i(\mathbf{k}_1+\mathbf{k}_2+\mathbf{k}_3+\mathbf{k}_4)\mathbf{r}]}{\omega_1\omega_2\omega_3\omega_4(\omega_1+\omega_2)} \times\left(\frac{3}{(\omega_1+\omega_2)(\omega_3+\omega_4)}+\frac{1}{(\omega_1+\omega_2)(\omega_2+\omega_4)}\right)d\mathbf{k}_1\cdots d\mathbf{k}_4. \quad (24)$$

In order to estimate the influence of this potential, we remark that the second term between brackets, on the right-hand side, gives roughly one-third of the contribution of the first term, so that $V_8(r)$ can be approximated by

$$V_8(r)\sim -12\left(\frac{G^2}{2M}\right)^4(2\pi)^{-12}\int \frac{\exp[-i(\mathbf{k}_1+\mathbf{k}_2+\mathbf{k}_3+\mathbf{k}_4)\mathbf{r}]}{\omega_1\omega_2\omega_3\omega_4(\omega_1+\omega_2)^2(\omega_3+\omega_4)} = -12(G^2/2M)^4(2\pi)^{-6}J_3(r)J_3(r). \quad (25)$$

Using the definitions of the functions $J_n(r)$, calculated in the Appendix [see Eqs. (10a) and (12a)], one obtains easily:

$$V_8(r)\sim -12\left(\frac{G^2}{4\pi}\right)^4\left(\frac{\mu}{2M}\right)^4\left(\frac{2}{\pi}\right)^3\frac{1}{\mu^3r^3}K_1(2\mu r)\int_{\mu r}^{+\infty}[K_0(x)]^2x\,dx. \quad (26)$$

This potential is plotted as a dotted line in Fig. 5 for $G^2/4\pi=9.7$ (value which will be obtained in Sec. V, from the low energy properties of the neutron-proton system). One sees that its influence is only sensible very near the edge of the relativistic region. Its inclusion in the central part of the total interaction has been found to modify the value of the singlet neutron-proton scattering length at zero energy by about 1 percent.

## B. Relativistic Region

An examination of the expansion of the kernel $K(\mathbf{p},\mathbf{p}';W)$ shows that, for high values of $|\mathbf{p}|$ and $|\mathbf{p}-\mathbf{p}'|$ (and $G^2/4\pi=1$), all its terms are of the same order of magnitude and that the effective expansion parameter is therefore $G^2/4\pi$. Under these circumstances, no definite conclusion can be drawn from a term by term analysis of this kernel. However, even if its magnitude cannot be determined with any certainty in this region, its sign is of crucial importance, because a repulsive interaction, no matter how strong and singular, would still insure the existence of stationary states, since the potential in the nonrelativistic region is sufficiently attractive. What we would like to do here is to show, by means of a rapid discussion of the second- and fourth-order terms of the expansion of $K(\mathbf{p},\mathbf{p}';W)$, that there are some indications that this interaction becomes repulsive for distances of order $(1/M)$.

### 1. *Second-Order Relativistic Interaction*

We first separate out of the kernel defined by Eq. (10) the part which corresponds, in the nonrelativistic region, to the "contact" term which has been omitted in Eq. (13). For this purpose, we write $K_2(\mathbf{p},\mathbf{p}';W)$ as follows:

$$K_2(\mathbf{p},\mathbf{p}';W) = -G^2(\boldsymbol{\tau}_1\cdot\boldsymbol{\tau}_2)\left\{\frac{1}{3}\frac{(\boldsymbol{\sigma}_1\cdot\boldsymbol{\sigma}_2)}{4E_pE_{p'}} \times\left[1-\frac{\mu^2+(E_p-E_{p'})^2+\omega(E_p+E_{p'}-W)}{\omega(\omega+E_p+E_{p'}-W)}\right] + \frac{(M+E_p)(M+E_{p'})}{4E_pE_{p'}}\left[\frac{(\boldsymbol{\sigma}_1\cdot\mathbf{R})(\boldsymbol{\sigma}_2\cdot\mathbf{R})}{R^2} - \frac{1}{3}(\boldsymbol{\sigma}_1\cdot\boldsymbol{\sigma}_2)\right]\frac{R^2}{\omega(\omega+E_p+E_{p'}-W)}\right\}. \quad (27)$$

The term of the third and fourth lines, on the right-hand side, is the relativistic generalization of the tensor force. The first term of the first and second lines gives the

[19] For a process involving the exchange of $m$ mesons, the static interaction itself becomes less singular at distances of order $(m/2M)$, since the quantity $m\omega_k$ cannot then be neglected in comparison with $2M$.

"contact" interaction, which has the following form in co-ordinate space [see Eq. (5a) of the Appendix]:

$$U_c^{(2)}(\mathbf{r},\mathbf{r}')=-\frac{G^2}{3}(\boldsymbol{\tau}_1\cdot\boldsymbol{\tau}_2)(\boldsymbol{\sigma}_1\cdot\boldsymbol{\sigma}_2)\frac{M^2}{rr'}K_1(Mr)K_1(Mr'). \quad (28)$$

Assuming that the integral $\beta=\int r'^{-1}K_1(Mr')\phi^{(0,0)}\times(\mathbf{r}')d\mathbf{r}'$ has a finite value, one sees therefore that the interaction (28) is equivalent to a potential which behaves like $r^{-2}$ at short distances and like $(r^{-\frac{1}{2}}e^{-Mr})$ for large values of $r$ (compared with $1/M$). This interactions acts only if the wave function is spherically symmetrical ($S$ states) and is repulsive in singlet and triplet spin states.

We now investigate the complete behavior of the second-order interaction for small values of $r$, in order to see if the repulsive operator (28) is not compensated by the contribution arising from the attractive part of (27). Using Eq. (9), we may write, for $r\ll 1/\mu$,

$$\int U_2(\mathbf{r},\mathbf{r}';W)\phi^{(0,0)}(\mathbf{r}')d\mathbf{r}'\sim$$

$$-\beta\frac{G^2}{(2\pi)^3}(\boldsymbol{\tau}_1\cdot\boldsymbol{\tau}_2)\int\frac{(\boldsymbol{\sigma}_1\cdot\mathbf{p})(\boldsymbol{\sigma}_2\cdot\mathbf{p})e^{i\mathbf{pr}}d\mathbf{p}}{2E_p(M+E_p)\omega(\omega+E_p-M)}, \quad (29)$$

which can also be written

$$\int U_2(\mathbf{r},\mathbf{r}';W)\phi^{(0,0)}(\mathbf{r}')d\mathbf{r}'\sim M\beta\left(\frac{G^2}{4\pi}\right)\frac{(\boldsymbol{\tau}_1\cdot\boldsymbol{\tau}_2)}{3}$$

$$\times\left\{(\boldsymbol{\sigma}_1\cdot\boldsymbol{\sigma}_2)\left[F''(Mr)+\frac{2F'(Mr)}{Mr}\right]\right.$$

$$\left.+S_{12}\left[F''(Mr)-\frac{F'(Mr)}{Mr}\right]\right\}, \quad (30)$$

where only terms of order $(\mu/M)^2$ have been neglected and where

$$F(Mr)=\frac{1}{2\pi r}\int_0^\infty\left(1-\frac{p}{M+E_p}\right)\frac{\sin prdp}{pE_p}. \quad (31)$$

By expanding $F(Mr)$ as a power series in the neighborhood of the origin, it is not difficult to verify that the central force is still repulsive and that the singularity of both the central and the tensor forces is now $r^{-1}\log(Mr)$. Since the effective coupling constant in the relativistic region is $G^2/4\pi$, the distance at which this repulsion takes place can roughly be estimated as of the order of $(M\mu)^{-\frac{1}{2}}$.

### 2. *Fourth-Order Relativistic Interaction*

The kernel $K_4(\mathbf{p},\mathbf{p}';W)$ being very complicated in the relativistic region, we shall only show that the fourth-order potential contains a repulsive $\delta$-function and give its actual expression at short distances.

In the nonrelativistic fourth-order potential which has been calculated in paragraph (A2) of this section, the only term which contains a "contact" interaction is $V_4''$ given by Eq. (20), where the first term of the right-hand side can be written as

$$V_4''^{(1)}=\frac{G^2}{2\pi^2}\left(\frac{\mu}{2M}\right)^2\frac{(\boldsymbol{\tau}_1\cdot\boldsymbol{\tau}_2)}{3}\{(\boldsymbol{\sigma}_1\cdot\boldsymbol{\sigma}_2)[3K_0(\mu r)-K_2(\mu r)]$$

$$+S_{12}K_2(\mu r)\}V_2(r); \quad (32)$$

consequently, the contact term has the form

$$(G^2/4\pi)^2(4/3\pi)(\boldsymbol{\sigma}_1\cdot\boldsymbol{\sigma}_2)^2(\boldsymbol{\tau}_1\cdot\boldsymbol{\tau}_2)^2(2Mr)^{-2}[\delta(\mathbf{r})/4M^2];$$

it is always repulsive but acts only in $S$ states. Its actual expression, in the relativistic region, is proportional to $(G^2/4\pi)^2(Mr^2)^{-1}K_1(Mr)e^{-Mr}$. It behaves like $r^{-3}$ at very short distances and its range is $(1/2M)$.

*Remark on the energy dependence of the interaction.*—In the case of high energy nucleon-nucleon scattering, the dependence of the potential on $W$ tends to increase the range of the interaction, as can be seen by considering the second-order potential (which is predominant at large distances):

$$V_2(r,\epsilon)=\frac{G^2}{4\pi}\left(\frac{\mu}{2M}\right)^3(\boldsymbol{\tau}_1\cdot\boldsymbol{\tau}_2)(\boldsymbol{\sigma}_1\cdot\boldsymbol{\nabla})(\boldsymbol{\sigma}_2\cdot\boldsymbol{\nabla})\frac{Y(r,\epsilon)}{\mu^3}, \quad (33)$$

where $\epsilon=W-2M$ and

$$Y(r,\epsilon)=\frac{1}{2\pi^3}\int\frac{\exp(i\mathbf{kr})d\mathbf{k}}{\omega_k(\omega_k-\epsilon)}=\frac{1}{2\pi^2}\int\frac{\exp(i\mathbf{kr})d\mathbf{k}}{k^2+\mu^2-\epsilon^2}\left(1+\frac{\epsilon}{\omega_k}\right). \quad (34)$$

The first term of the right-hand side is a Yukawa potential of range $\chi^{-1}=(\mu^2-\epsilon^2)^{-\frac{1}{2}}$. The second term, which is more complicated, behaves roughly like $r^{-\frac{1}{2}}e^{-\chi'r}$ with $\chi'\sim(\chi^2\mu)^{\frac{1}{2}}$. This increase of the potential range with the energy might be useful in interpreting the experimental neutron-proton scattering data, since the customary static potentials have a tendency to predict too small $D$-phase shifts. When $\epsilon\geq\mu$ (which, in the laboratory system, corresponds to a neutron energy of about 280 Mev), the potential (33) begins to oscillate at large distances. For such energies, however, the static approximation should not be considered too seriously.

## IV. RADIATIVE CORRECTIONS

In order to calculate the contribution of the radiative corrections to the effective pseudoscalar interaction, it is first necessary to separate covariantly the infinite renormalization effects of mass and coupling constant. For this purpose, we start from the equation of Bethe and Salpeter,[10] transformed into a one-time equation by means of the method which has been discussed in detail in (*A*). It has been shown that the expression of the effective interaction which is obtained in this way is, in the nonrelativistic region, identical term by term with the expression (2) which results from the Tamm-Dancoff treatment.

In the following, we shall further restrict ourselves to the "ladder" approximation,[7,10] since analogous results can be obtained in a straightforward manner by applying the same method to the other terms of the kernel expansion of the B.S. equation. In this approximation, the amplitude $A_{ij}(\mathbf{p},\mathbf{p}_0)$ $(i,j=1,2)$ which is

defined by Eq. (A.25) obeys, in the center-of-mass system, the following equation:

$$A_{ij}(\mathbf{p}, p_0)=\frac{1}{[\Lambda_i(p)-p_0][\Lambda_j(p)+p_0]}\sum_{k,l}\frac{-iG^2}{(2\pi)^4}$$
$$\times\int\frac{\Gamma_{ik}^{(1)}(\mathbf{p}, \mathbf{p}')\Gamma_{jl}^{(2)}(\mathbf{p}, \mathbf{p}')A_{kl}(\mathbf{p}', p_0')d\mathbf{p}'dp_0'}{\Delta p^2+\mu^2}, \quad (35)$$

where we have set $\Delta p^2=\omega^2(\mathbf{p}, \mathbf{p}')-(p_0-p_0')^2$ and

$$\Gamma_{ik}^{(r)}=\bar{u}_i^{(r)}(\mathbf{p})\gamma_5 u_k^{(r)}(\mathbf{p}'), \quad (36)$$

$u_i^{(r)}(\mathbf{p})$ being the amplitude of the Dirac spinor defined by (A, 26). The quantities $\Lambda_i(p)$ are defined by (A, 29).

The radiative corrections are taken into account: (1) By substituting to $\Delta_F(x)$ [the Fourier transform of which appears in the kernel of Eq. (35)] the function $\Delta_F'(x)$, which has been defined by Dyson[20] and which accounts for all closed loop insertions in the meson lines of the irreducible diagrams of the $S$ matrix; (2) by replacing $\gamma_5$, in the matrix elements of Eq. (36), by the operator $\Gamma_5$, which embodies the contributions arising from the vertex parts of those irreducible diagrams; (3) by introducing in the kernel of the integral equation the remaining contributions of the (finite) irreducible graphs which include self-energy effects.[21]

We shall first calculate the functions $\Delta_F$ and $\Gamma_5$, up to the second order in $G$.

### A. Calculation of $\Delta_F'$

This calculation has been made by Watson and Lepore,[22] with the following result,

$$\Delta_F'(x)=-\frac{2i}{(2\pi)^4}\int\frac{e^{ikx}d^4k}{k^2+\mu^2}\left[1-\frac{G^2}{2\pi^2}U(k^2)\right], \quad (37)$$

in which terms of order $(\mu/M)^2$ have been neglected and the following definition introduced:

$$U(k^2)=\int_0^1\frac{k^2x(1-2x)dx}{k^2x(1-x)+M^2}, \quad (38)$$

the poles of this function being defined as usual by introducing a small negative imaginary part in $M$.

### B. Calculation of $\Gamma_5(p, p')$

This calculation will be made without assuming that the nucleons are free in the initial and final states of momenta $p$ and $p'$. To the second order in $G$, we write

$$\Gamma_5(p, p')=\gamma_5\{1-G^2[C_1(p, p')+C_2(p, p')]\}, \quad (39)$$

where, after some elementary transformation, the functions $C_i$ are found to have the following expressions:

$$C_1(p, p')=-\frac{2i}{(2\pi)^4}\int\frac{k^2d^4k}{[(p+k)^2+M^2][(p'+k)^2+M^2](k^2+\mu^2)}, \quad (40)$$

$$C_2(p, p')=-\frac{2i}{(2\pi)^4}\int\frac{[-i\gamma k(i\gamma p'+M)+(-i\gamma p+M)i\gamma k+(-i\gamma p+M)(i\gamma p'+M)]d^4k}{[(p+k)^2+M^2][(p'+k)^2+M^2](k^2+\mu^2)}. \quad (41)$$

$C_2(p, p')$ is a finite integral which vanishes if the initial and final states are free, $C_1(p, p')$, which is a logarithmically divergent integral can be written as

$$C_1(p, p')=-\frac{2i}{(2\pi)^4}\int\frac{d^4k}{(k^2+M^2)^2}+\frac{2i}{(2\pi)^4}\int\frac{\mu^2d^4k}{[(p+k)^2+M^2][(p'+k)^2+M^2](k^2+\mu^2)}+C_1'(p, p'). \quad (42)$$

The first term on the right corresponds to a coupling constant renormalization; the second term will be incorporated to $C_2(p, p')$; finally, by using Feynman integral representation of product denominators, $C_1'(p, p')$ is found equal to

$$C_1'=-\frac{2i}{(2\pi)^4}\int_0^1\int\frac{\Delta p^2x(1-x)[2(k^2+M^2)+\Delta p^2x(1-x)]d^4kdx}{(k^2+M^2)^2[k^2+M^2+\Delta p^2x(1-x)]^2}=\frac{1}{4\pi^2}U(\Delta p^2). \quad (43)$$

In the same way, after some calculations, $C_2(p, p')$ is found such that

$$\gamma_5C_2(p, p')=\frac{1}{4\pi^2}\int_0^1\int_0^1\frac{ududvK(p, p'; u, v)}{\Delta^2(p, p'; u, v)}, \quad (44)$$

where the second term of $C_1(p, p')$ has been incorporated and the following definitions introduced:

$$K(p, p'; u, v)=(1-u)(i\gamma p+M)\gamma_5(i\gamma p'+M)$$
$$+Mu[\gamma_5(i\gamma p'+M)+(i\gamma p+M)\gamma_5]$$
$$-u\gamma_5[(1-v)(p'^2+M^2)+v(p^2+M^2)]-\mu^2\gamma_5, \quad (45)$$

$$\Delta^2(p, p'; u, v)=u^2[v(1-v)\Delta p^2+M^2]+\mu^2(1-u)$$
$$+u(1-u)[(p^2+M^2)v+(p'^2+M^2)(1-v)]. \quad (46)$$

If the expression (39) of $\Gamma_5$ is substituted to $\gamma_5$ in Eq.

[20] F. J. Dyson, Phys. Rev. **75**, 486 (1949).

[21] The corrections to the interaction due to self-energy effects included in the $S_F'(x)$ function (see reference 20) are very small in the nonrelativistic region, since they vanish when the initial and final states of the nucleons are supposed to be free.

[22] K. M. Watson and J. V. Lepore, Phys. Rev. **76**, 1157 (1949).

(36), the matrix elements $\Gamma_{ik}^{(r)}$ are transformed into

$$\Gamma_{ik}'^{(r)}=\Gamma_{ik}^{(r)}\Big\{1-\frac{G^2}{4\pi^2}U(\Delta p^2)+\frac{G^2}{4\pi^2}\int_0^1\int_0^1\frac{u\,du\,dv}{\Delta_r^2}\times F_{ik}^{(r)}(p,p';u,v)-\sum_{ik}^{(r)}\frac{G^2}{4\pi^2}\times\int_0^1\int_0^1\frac{u^2\,du\,dv}{\Delta_r^2}M[\Delta p_0+E_k(p')-E_i(p)],\quad(47)$$

where $F_{ik}^{(r)}$ and $\Delta_r^2$ are, respectively, equal to

$$F_{ik}^{(r)}(p,p';u,v)=(1-v)[p_0-\epsilon_r\Lambda_i(p)][p_0'-\epsilon_r\Lambda_k(p')]+\mu^2+u\{(1-v)(\mathbf{p}'^2+M^2-p_0^2)+v(\mathbf{p}^2+M^2-p_0^2)-(W^2/4)+W\epsilon_r[(1-v)p_0'+vp_0]\},\quad(48)$$

$$\Delta_r^2=u^2[M^2+v(1-v)\Delta p^2]+(1-u)\mu^2+u(1-v)\{v(E_{p'}^2-p_0^2)+(1-v)(E_{p'}^2-p_0'^2)+W\epsilon_r[vp_0+(1-v)p_0']-(W^2/4),\quad(49)$$

$\epsilon_r$ being defined by $\epsilon_1=+1$, $\epsilon_2=-1$. $\sum_{ik}^{(r)}$ is the matrix element of $-\rho_2^{(r)}=\gamma_5^{(r)}\gamma_4^{(r)}$, namely

$$\sum_{ik}^{(r)}=\bar{u}_i^{(r)}(\mathbf{p})\gamma_5^{(r)}\gamma_4^{(r)}u_k^{(r)}(\mathbf{p}').\quad(50)$$

### C. Corrections to the Interaction Arising from Vertex Parts and Closed Loops

In order to avoid an excessive use of algebra, we shall only give here some details on the main contribution to the interaction arising from these radiative effects, namely the corrections to the terms $V_4^{(a)}$ and $V_4^{(b)}$ of the potential, defined by Eqs. (15) and (16).

After substituting expressions (37) and (47) into (35), one obtains a three-dimensional equation for the amplitude corresponding to equal times of the two nucleons:

$$a_{ij}(\mathbf{p})=\frac{1}{2\pi i}\int_{-\infty}^{+\infty}A_{ij}(\mathbf{p},p_0)\,dp_0,\quad(51)$$

by following exactly the method given in $A$: First, one introduces on the right of (35) the function $A_{kl}^{(1)}(\mathbf{p},\mathbf{p}_0)$, in which the dependence on $p_0$ corresponds to taking only into account the diagrams where the maximum number of mesons present at a given time is one (one of them gives $V_4^{(b)}$):

$$A_{kl}^{(1)}(\mathbf{p},p_0)=-2\epsilon_k\Lambda_k(p)\frac{a_{kk}(\mathbf{p})}{\Lambda_k^2-p_0^2}\delta_{kl}.\quad(52)$$

Then, one iterates Eq. (35) another time, in order to include also the diagrams where the maximum number of mesons is two (one of them leads to $V_4^{(a)}$).

($a$) It is easier to calculate in the first place the corrections arising from $\Delta_r'$ and the $G^2C_1(p,p')$ term in $\Gamma_5$, which involve only $U(\Delta p^2)$. This function is such that, apart from unimportant terms in $(\mu/M)^2$, the corresponding corrections do not modify the analytical form of the kernel of Eq. (35), but substitute an apparent mass $M[x(1-x)]^{-1}$ to the meson mass $\mu$. The correction to order $G^3$ to the interaction $V_4^{(b)}$ is found to be

$$\Delta V_4^{(b)}=-48\left(\frac{G^2}{4\pi}\right)^3\left(\frac{\mu}{2M}\right)^4\frac{\delta(\mathbf{r})}{\mu^3r}K_1(\mu r)+\mathcal{O}[(G^2/4\pi)^3(\mu/2M)^5],\quad(53)$$

whereas the correction to $V_4^{(a)}$ is given by

$$\Delta V_4^{(a)}=-32\left(\frac{G^2}{4\pi}\right)^3\left(\frac{\mu}{2M}\right)^4\frac{\delta(\mathbf{r})}{\mu^3r}\frac{2}{\pi}K_1(\mu r)+\mathcal{O}[(G^2/4\pi)^3(\mu/2M)^5].\quad(54)$$

The leading terms, in both expressions, vanish in the nonrelativistic region. This result might appear a little surprising, especially for the $\Gamma_5$-correction, since the corresponding vertex part has been inserted in a transition from positive to negative energy states, where the four-dimensional $\Delta p$ is of the order of $M$. It can however be interpreted as meaning that the pairs which are created in the intermediate states are moving rather slowly and that the three-dimensional momentum transfer $\Delta\mathbf{p}$ is small compared to the corresponding transfer of energy.

($b$) The leading term of the corrections to $V_4^{(a)}$ arising from $G^2C_2(p,p')$ in $\Gamma_5$ can be found, after elaborate calculations, to be equal to

$$\Delta V_4'^{(a)}=+\frac{64}{9}\left(\frac{G^2}{4\pi}\right)^3\left(\frac{\mu}{2M}\right)^5\log\left(\frac{\mu}{2M}\right)\frac{1}{\mu r^2}\frac{2}{\pi}K_1(2\mu r).\quad(55)$$

The correction to $V_4^{(b)}$ has an analogous form.

### D. Finite Self-Energy Terms[23]

These terms are contributed by a series of irreducible diagrams, the first one of which is illustrated in Fig. 4. (All the others can be obtained by allowing an arbitrary number of mesons to be emitted by one nucleon *before* $k_1$ and $k_2$, and to be reabsorbed by the same nucleon *after* $k_1$ and $k_2$ have been emitted.) In order to calculate the contribution of these diagrams, it is convenient to suppose that the initial and finite states of the interacting nucleons are free. This assumption leads actually to a correct value of the interaction in the nonrelativistic

[23] We are very indebted to Professor N. Kroll for directing our attention to these terms, and for an interesting discussion. We also gratefully acknowledge helpful discussions with Dr. Lepore and Dr. Ruderman on this point. The finite self-energy terms can alternatively be calculated by means of the noncovariant Tamm-Dancoff method; the result is, however, rather ambiguous, since the separation of renormalization parts in the self-energy effects by means of this method is not unique.

region. After some elementary transformations, where terms of order $(\mu/M)^2$ have been neglected, the contribution of the diagram of Fig. 4 is found to have the following expression:

$$\Delta G_4^{(1)} \sim -\int \frac{\psi_{p'} U \psi_p \bar{\psi}_{q'} \gamma_\nu \psi_q k_\nu d^4k}{[(q-k)^2+M^2][k^2+\mu^2][(k-\Delta p)^2+\mu^2]}, \tag{56}$$

with $\Delta p = p'-p$, $U$ being defined by

$$U = \gamma_\mu \int \left[k_\mu + k_\mu' - 2\frac{k_\mu' k_\lambda'(p_\lambda+k_\lambda)}{k'^2+\mu^2}\right] \frac{d^4k'}{[(p+\Delta p-k')^2+M^2][(p+k-k')^2+M^2][(p-k')^2+M^2]}. \tag{57}$$

The integration over $k'$ yields the expression

$$U = \pi^2[i\gamma_\mu k_\mu A + MB], \tag{58}$$

where the following definitions have been introduced:

$$A = \int_0^1\int_0^1\int_0^1 xdxdydz\left[-\frac{1+x-xy}{D^2}+\frac{xy}{D'^2} + \frac{2x^2y(1-y)Q_\lambda(p_\lambda+k_\lambda)}{D'^4}\right],$$
$$B = \int_0^1\int_0^1\int_0^1 xdxdydz\left[-\frac{1}{D^2}+\frac{xy}{D'^2} + \frac{2xy(1-xyz)Q_\lambda(p_\lambda+k_\lambda)}{D'^4}\right], \tag{59}$$

$D^2$, $D'^2$ and $Q_\lambda$ being, respectively, given by

$$\begin{aligned} D^2 &= M^2+x^2y(1-y)(k-\Delta p)^2 \\ &\quad +xy(1-x)\Delta p^2+x(1-x)(1-y)k^2, \\ D'^2 &= M^2(1-xyz)^2+x^2yz(1-y)[(p+k)^2+M^2] \\ &\quad +x^2y(1-y)(1-z)(k-\Delta p)^2 \\ &\quad +xy(1-y)(1-z)\Delta p^2+x(1-y)(1-x)k^2, \\ Q_\lambda &= (1-xyz)p+xy(1-z)\Delta p+x(1-y)k. \end{aligned} \tag{60}$$

The expression for $\Delta G_4^{(1)}$, given by (56) and (58), is now introduced in the equation of Bethe and Salpeter, and the corrections to the interaction are obtained in the same way as in the preceding subsection. In the nonrelativistic region, this leads to the expression

$$\Delta V_4^{(e)} \sim C_1\left(\frac{G^2}{4\pi}\right)^3 \frac{1}{8\pi^6}\sum_{\mu,\nu}\int \prod_\nu^{(2)}(\mathbf{k}_1,\mathbf{k}_2) \times[\prod_\nu^{(1)}(\mathbf{k}_1,\mathbf{k}_2)H_{\mu\nu}^{(1)}(\mathbf{k}_1,\mathbf{k}_2) - iMH_\nu^{(2)}(\mathbf{k}_1,\mathbf{k}_2)] \times\exp[-i(\mathbf{k}_1+\mathbf{k}_2)\mathbf{r}]d\mathbf{k}_1 d\mathbf{k}_2, \tag{61}$$

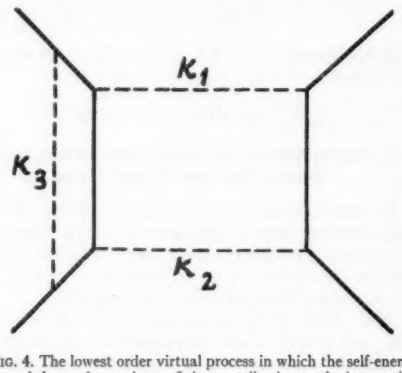


FIG. 4. The lowest order virtual process in which the self-energy of one of the nucleons gives a finite contribution to the interaction in the nonrelativistic region.

where the following definitions have been introduced:

$$\prod_\mu^{(r)}(\mathbf{k}_1,\mathbf{k}_2) = \bar{u}_1^{(r)}(0)\gamma_\mu u_1^{(r)}(\mathbf{k}_1+\mathbf{k}_2), \tag{62}$$

$$H_{\mu\nu}^{(1)} = \lim_{\epsilon\to 0}\frac{(2i\epsilon)^2}{(2\pi i)^3}\int_{-\infty}^{+\infty} \frac{(p_\mu'-p_\mu)(p_\nu'-p_\nu)A_0 dp_0 dp_0' dp_0''}{[\omega_1^2-(p_0'-p_0)^2][\omega_2^2-(p_0''-p_0')^2](p_0^2+\epsilon^2)(p_0''^2+\epsilon^2)(p_0'-i\epsilon)(p_0'-2M)}, \tag{63}$$

$$H_\nu^{(2)} = \lim_{\epsilon\to 0}\frac{(2i\epsilon)^2}{(2\pi i)^3}\int_{-\infty}^{+\infty} \frac{(p_\nu'-p_\nu)B_0 dp_0 dp_0' dp_0''}{[\omega_1^2-(p_0'-p_0)^2][\omega_2^2-(p_0''-p_0')^2](p_0^2+\epsilon^2)(p_0''^2+\epsilon^2)(p_0'-i\epsilon)(p_0'-2M)}, \tag{64}$$

$A_0$ and $B_0$ being obtained from $A$ and $B$ by replacing, in $D^2$ and $D'^2$,

$$\begin{aligned} \Delta p^2 \text{ by } -\Delta p_0^2 &= -(p_0''-p_0')^2, \\ k^2 \text{ by } -k_0^2 &= -(p_0'-p_0)^2, \\ (\Delta p-k)^2 \text{ by } -(p_0''-p_0')^2 &= -(\Delta p_0-k_0)^2, \end{aligned}$$

and by putting $(p+k)^2+M^2 = -(p_0'+i\epsilon)(p_0'+2M)$. The indices $\mu$ and $\nu$ take the values 1, 2, 3, 4 with $\mathbf{p}'-\mathbf{p}=\mathbf{k}_1$ and $p_4'-p_4 = i(p_0'-p_0)$.

The first term of the right-hand side of (61) yields very small corrections to the iteration of the second order potential, and to the fourth-order potential cal-

culated in Sec. III, 2. The second term of (61) gives, for $\nu=1, 2, 3$, small corrections to the "one-pair terms" of the fourth-order interaction. The main correction comes actually from $H_4^{(2)}$, which can be written

$$H_4^{(2)}=\frac{1}{4\pi M^3}\int_{-\infty}^{+\infty}\frac{dp_0'}{(p_0'^2-\omega_1^2)(p_0'^2-\omega_2^2)}$$
$$=\frac{-1}{4iM^3\omega_1\omega_2(\omega_1+\omega_2)}. \quad (65)$$

The main part of $V_4^{(2)}$ is therefore proportional to the potential $V_4(r)$ of Eq. (14), the numerical coefficient being of order $(G^2/4\pi)$. The whole series of diagrams analogous to Fig. 4 will similarly contribute corrections proportional to $V_4(r)$, the entire coefficient being expressed as a power series in $G^2/4\pi$. The practical effect of these corrections will be therefore to modify the strength of the fourth-order potential in an unknown fashion. This can be accounted for by replacing $G$, in Eq. (14), by a new coupling constant $G_1$, to be determined from experiment.

## V. LOW ENERGY PROPERTIES OF THE NEUTRON-PROTON SYSTEM

In order to discuss the low energy properties of the neutron-proton system, it is possible to use, in the nonrelativistic region, the potential which has been calculated in Section (IIIA). At very short distances, it is not advisable to take the second- and fourth-order relativistic interactions which have been discussed in Sec. (IIIB), since the higher order terms of the expansion (as well as the contribution from heavier mesons, isobaric states of nucleons, etc.) would probably modify them seriously. We shall however retain the qualitative features of these interaction terms, which are repulsive and strongly singular, in prescribing that the "wave function" $\phi^{(0,0)}(\mathbf{r})$, defined in Sec. II, must satisfy the boundary condition: $\phi^{(0,0)}(\mathbf{r}_c)=0$, $r_c$ being some finite distance of order $(M\mu)^{-1}$. This boundary condition, which is equivalent to assuming that the central force includes an infinitely repulsive core of radius $r_c$, introduces certainly an over-simplification in the actual behavior of the wave function; it can, however, be justified further by means of the two following arguments.

(a) If the pseudoscalar potential is used in the nonrelativistic region, the only type of relativistic interaction which leaves any possibility of agreement with the low energy experimental data must be strongly repulsive. This argument, which has already been pointed out by Brueckner and Low,[24] is based on the fact that the static pseudoscalar potential, being very singular, leads to a much too small neutron-proton (singlet or triplet) effective range, unless the wave function tends rapidly to zero in the neighborhood of the nucleon Compton wavelength.

[24] K. Brueckner and F. Low, Phys. Rev. **83**, 461 (1951).

(b) It can be expected that the low energy properties of the neutron-proton system are not very sensitive to the shape of this short range repulsive interaction, provided that it is sufficiently strong.

### A. The Experimental Data

The latest values of the low energy experimental data on the neutron-proton system, as quoted or calculated by Salpeter,[25] are as follows:

Binding energy in the triplet ground state (deuteron):

$$\epsilon=(-2.227\pm0.003)\text{ Mev}.$$

Zero energy singlet scattering length:

$$a_s=(-23.68\pm0.06)10^{-13}\text{ cm}=(-16.91\pm0.38)(1/\mu).$$

Singlet effective range:

$${}^1r_0=(2.7\pm0.5)10^{-13}\text{ cm}=(1.93\pm0.41)(1/\mu).$$

Triplet effective range:

$${}^3r_0=(1.704\pm0.030)10^{-13}\text{ cm}=(1.217\pm0.047)(1/\mu).$$

Electric quadrupole moment:

$$Q=(2.738\pm0.016)10^{-27}\text{ cm}^2.$$

Proportion of $D$ state:[26]

$$0.02\lesssim p_D\lesssim0.06.$$

### B. The Potential

Taking only the main terms of the nonrelativistic interaction calculated in Sec. III, and putting $x=\mu r$, the potential for $x\geq x_c=\mu r_c$ has the following expression:[27]

$$V(x)=\mu[V_c(x)+S_{12}V_t(x)], \quad (66)$$

where the central and tensor forces are respectively defined by

$$V_c(x)=-\frac{G^2}{4\pi}\left(\frac{\mu}{2M}\right)^2\frac{e^{-x}}{x}-3\left(\frac{G^2}{4\pi}\right)^2\left(\frac{\mu}{2M}\right)^3\frac{1}{x^2}$$
$$\times\left\{\frac{2}{\pi}K_1(2x)+\frac{\mu}{2M}\left[\frac{2}{\pi}K_1(x)\right]^2\right\}, \quad (67)$$

$$V_t(x)=-\frac{G^2}{4\pi}\left(\frac{\mu}{2M}\right)^2\left(1+\frac{3}{x}+\frac{3}{x^2}\right)\frac{e^{-x}}{x}. \quad (68)$$

[25] E. Salpeter, Phys. Rev. **82**, 60 (1951).

[26] The nonrelativistic expression of the deuteron magnetic moment $\mu_D=\mu_N+\mu_P-\frac{3}{2}(\mu_N+\mu_P-\frac{1}{2})p_D$ leads to $p_D=0.04$. The relativistic corrections are, however, usually estimated as about 2 percent.

[27] We neglect, for the time being, the influence of the radiative corrections, discussed in Sec. IV, 5, which modify the strength of the fourth order part of the central force, by introducing (in this part of the potential only) a new coupling constant $G_1$, which is an unknown function of $G$. Since a good agreement with experiment is obtained by putting $G_1=G$, it is to be expected that a direct determination of $G_1$ by comparison with experiment would lead to a numerical value very close to that of $G$.

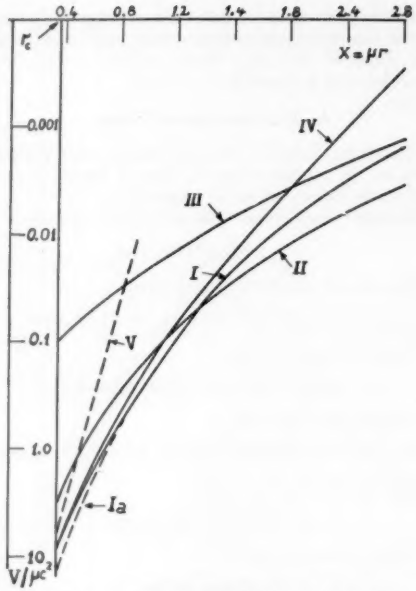


FIG. 5. Plot of the potential corresponding to the constants of Eq. (74) as a function of the distance $r$. Curve I represents the total central force, defined by (67) and curve II the tensor force, defined by (68). The dotted curve (Ia) represents the central force when the eighth-order corrections are taken into account. Curves III, IV, V represent the respective contributions of the second-, fourth-, and eighth-order central parts of the potential.

### C. Determination of $G^2/4\pi$ and $x_c$

The two constants which define the interaction have been calculated by fitting exactly the binding energy of the deuteron and the singlet scattering length, in the following way:

(a) For the $^1S$ state of zero energy, the radial function obeys the equations

$$v(x_c)=0,$$
$$d^2v/dx^2=(M/\mu)V_c(x)v(x) \text{ for } x\geqslant x_c. \tag{69}$$

These equations have been integrated numerically[28] for several values of $G^2/4\pi$, starting from the asymptotic form $v(x)\sim 1+x(\mu a_s)^{-1}$ and determining in each case the value of $x$ at which the wave function goes to zero. The initial integrating point was 4.5 and the difference interval $\Delta x=0.1$. This procedure permits to draw point by point the curve $x_c=f_1(G^2/4\pi)$ which results from an exact fitting of the zero energy scattering length.

[28] The integration method which has been used allows the calculation of the solution at one point from its value at the two preceding ones. The error at a point $x$ is equal to $(1/120)(\Delta x)^8 \times u^{(8)}(x)$. We are indebted to Dr. R. Christian for valuable advice in the numerical calculations.

(b) For the $(^3S+^3D)$ state, the wave function may be written[29]

$$\phi^{(0,0)}(\mathbf{r})=(1/r)[u(x)+(1/8^{\frac{1}{2}})S_{12}w(x)]\chi_m, \tag{70}$$

where $\chi_m$ is the spin function with magnetic quantum number $m$, $u(x)$ and $w(x)$ being solutions of the following system of equations:

$$\frac{d^2u}{dx^2}=\left[\eta^2+\frac{M}{\mu}V_c(x)\right]u(x)+2^{\frac{1}{2}}\frac{M}{\mu}V_t(x)w(x),$$
$$\frac{d^2w}{dx^2}=\left[\eta^2+\frac{M}{\mu}V_c(x)-\frac{2M}{\mu}V_t(x)+\frac{6}{x^2}\right]w(x)+2^{\frac{1}{2}}\frac{M}{\mu}V_t(x)u(x), \tag{71}$$

with the secondary condition

$$u(x_c)=w(x_c)=0, \tag{72}$$

$\eta^2$ being equal to $-M\epsilon/\mu$. The system of equations (71) has similarly been integrated numerically for several values of $G^2/4\pi$, starting from the asymptotic form

$$u(x)\sim e^{-\eta x}, \quad w(x)\sim \rho e^{-\eta x}\left[1+\frac{3}{\eta x}+\frac{3}{(\eta x)^2}\right], \tag{73}$$

where $\rho$ is adjusted by repeated integrations so that both $u(x)$ and $w(x)$ go to zero at the same point. This procedure yields a curve $x_c=f_2(G^2/4\pi)$, resulting from an exact fitting of the deuteron binding energy.

(c) The required values of $x_c$ and $G^2/4\pi$ are determined by the relations $x_c=f_1(G^2/4\pi)=f_2(G^2/4\pi)$, which gives[30]

$$r_c=x_c/\mu=(0.38\pm 0.03)(1/\mu), \quad G^2/4\pi=9.7\pm 1.3. \tag{74}$$

The corresponding potential functions are drawn in Fig. 5, together with the eighth-order correction to the central force, which is defined by Eq. (26). When this correction is incorporated into $V_c(x)$, it has been found that the value of $x_c$ which results from an exact fitting of the zero energy scattering length is modified by about 1 percent.

### D. Calculation of the Derived Quantities

Using the numerically integrated function $v(x)$ corresponding to the constants (74), the singlet effective range is calculated as follows:

$$^1r_0=\frac{2}{\mu}\int_0^\infty\left[\left(1+\frac{x}{\mu a_s}\right)^2-v^2(x)\right]dx=1.78(1/\mu). \tag{75}$$

Similarly, the numerically integrated functions $u(x)$ and $w(x)$ corresponding to the same constants yield a

[29] H. Feshbach and J. Schwinger, Phys. Rev. 84, 194 (1951).

[30] The value of $r_c$ is in agreement with our estimate of the distance at which the interaction (30) becomes important.

triplet effective range

$$^3r_0=\frac{2}{\mu}\int_0^\infty\left[e^{-2\psi^2}-\frac{u^2(x)+w^2(x)}{1+\rho^2}\right]dx=1.185(1/\mu), \quad (76)$$

an electric quadrupole moment

$$Q=\frac{2^{\frac{1}{2}}}{10\mu^2}\int_0^\infty x^2[uw-8^{-\frac{1}{2}}w^2]dx\Big/\int_0^\infty(u^2+w^2)dx$$
$$=2.08\times10^{-27}\text{ cm}^2, \quad (77)$$

and a proportion of $D$ state:

$$p_D=\int_0^\infty w^2(x)dx\Big/\int_0^\infty(u^2+w^2)dx=0.051. \quad (78)$$

A quantity of physical interest is the mean value of the square of the momentum in the ground state

$$\left\langle\frac{p^2}{\mu^2}\right\rangle=-\frac{\int_0^\infty\left[u\left(\frac{d^2}{dx^2}\right)u+w\left(\frac{d^2}{dx^2}-\frac{6}{x^2}\right)w\right]dx}{\int_0^\infty(u^2+w^2)dx}=1.76, \quad (79)$$

which corresponds to a mean value of the kinetic energy of 18.5 Mev per nucleon. This result indicates that the momentum distribution is mainly concentrated around $\mu$, and is therefore not too sensitive to the shape of the interaction at distances of order $(1/M)$.

The preceding results are in good agreement with experiment, except the quadruple moment, which is too small by about 20 percent. This quantity is, however, sensitive to an increase of the tensor force, and can probably be improved by including the remaining portion of the fourth-order interaction, $V_4''(r)$ defined by (20), and the sixth-order potential [Eq. (23)].

### E. Neutron-Proton Scattering at 40 Mev

The neutron-proton scattering cross section for a neutron energy of 40 Mev in the laboratory system has been calculated, using the potential $V(r)=V_2(r)+V_4(r)$ defined by (13) and (14) for $r\geqslant r_c$, a repulsive core of radius $r_c$, and the constants (74). For the ($^1S$) and ($^3S+^3D$) scattering states, the wave equation has been integrated numerically, starting at the point $x=x_c$ (in the case of the $^3S+^3D$ state, two numerical integrations were necessary, for the $S$ and $D$ dominant modes, respectively). The phase shifts corresponding to $P$ and $D$ singlet and triplet states were calculated by means of the Born approximation, the coupling (due to the tensor force) with states corresponding to $L>2$ being neglected. Due to the presence of the repulsive core, the phase shift corresponding to a state $(J, L, s)$ in the Born approximation is given by the equation

$$\tan{}^s\delta_{J,L}=-\frac{M}{\mu k}\int_{x_c}^\infty[g_{L+1}(\xi)-\rho(x_c)g_{-(L+1)}(\xi)]^2$$
$$\times{}^sV_{J,L}(\xi)d\xi-(-1)^l\rho(x_c), \quad (80)$$

with $k^2=\frac{1}{2}ME$ ($E$ is the neutron energy in the laboratory system),

$$g_\nu(x)=(\tfrac{1}{2}\pi kx)^{\frac{1}{2}}J_\nu(x), \text{ and } \rho(x_c)=g_{L+1}(x_c)/g_{-(L+1)}(x_c).$$

The calculated value of the total cross section is equal to $\sigma_t=216$ millibarns. The corresponding mean value of the two experimentally measured cross sections[31] is $\sigma_t=194\pm20$ millibarns. The agreement is therefore satisfactory.

The angular distribution of the cross section in the center-of-mass system, represented in Fig. 6, shows very little asymmetry around 90 degrees. This is due to the fact that, for odd states, the weak long range second order potential (13) becomes repulsive, whereas the strong short-range fourth-order potential (14) remains attractive. The phase shifts corresponding to odd states

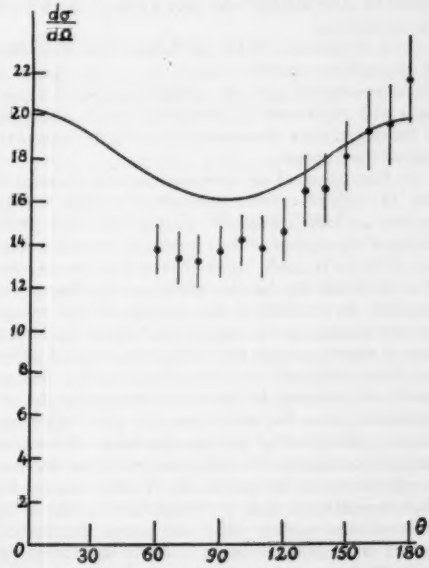


FIG. 6. Angular distribution of the differential cross section (in millibarns per steradian) in the center-of-mass system for scattering of 40-Mev neutrons by protons. The experimental points are those of Hadley *et al.* (reference 31), normalized in order to make the total cross section agree with the mean experimental value. An arbitrary experimental error of 10 percent has been assumed at each point.

[31] Hadley, Kelly, Leith, Segrè, Wiegand, and York, Phys. Rev. **75**, 351 (1949); R. H. Hildebrand and C. E. Leith, Phys. Rev. **80**, 842 (1950).

are therefore greatly reduced. In the particular case of the 40-Mev $n$–$p$ scattering, there is the additional helpful fact that the singlet and triplet $P$-phase shifts turn out to have opposite signs. The main defect of the theoretical angular distribution curve is that the $D$ phase shifts are somewhat too small, the curve being consequently too flat by about 20 percent. This can be greatly improved, however, by taking into account the energy dependence of the potential which, as was shown at the end of Sec. III, increases the range of the interaction. For a neutron energy of 40 Mev, the effect would be of the order of 15 percent.

## VI. CONCLUDING REMARKS

The fact that the pseudoscalar interaction calculated in this paper leads to a good agreement with the low energy experimental data on the neutron-proton system, might perhaps appear not too surprising, if one remarks that this interaction contains a certain number of features which were actually qualitatively predicted on the basis of other investigations:

(a) A phenomenological treatment of the nuclear forces[29] has led to the conclusion that the central force should be more singular and have a shorter range than the tensor force.

(b) A detailed analysis of nucleon-nucleon scattering at intermediate energies[32] shows that, in the case of a phenomenological Yukawa potential, a better agreement with experiment is obtained by choosing a range of the central force corresponding to a higher mass than that of the $\pi$-meson.

(c) Discussions of the nucleons' magnetic moments[33] and of multiple meson production in high energy nucleon-nucleon collisions[34] suggest that the probability of the presence of two mesons in the field around the nucleons is much higher than that of one meson. A more severe test for the validity of the theory will probably be provided by the analysis of high energy nucleon-nucleon and meson-nucleon scattering. In the case of neutron-proton scattering, the potential which has been obtained here contains an added feature which will probably be helpful in interpreting the experimental data: For odd states, the weak long range second order potential becomes repulsive, whereas the strong short-range fourth-order force remains attractive; as was shown at the end of Sec. V, this reduces the $P$-phase-shifts and leads to angular distributions in the center-of-mass system which are nearly symmetrical around 90 degrees. However, it is the opinion of the writer that it would not be very consistent to use the same potential at very high energies,[35] because the shape of the repulsive interaction would then become a significant factor. Moreover, the dependence of the potential on the total energy $W$ should then carefully be taken into account.

In the case of meson-nucleon scattering, a weak coupling treatment of the interaction Hamiltonian (22) would probably lead to a serious disagreement (see reference 17) with recent experimental data.[36] It is, however, not unreasonable to think that the role of the radiative corrections is much more important in this case than in the nucleon-nucleon interaction.

The author would like to express his gratitude to Professor Oppenheimer for his kind hospitality at the Institute for Advanced Study. This work could not have been concluded without his continued encouragement and his stimulating criticisms and suggestions. The author is also very indebted to Professors Pais and Peierls, and to Dr. F. Low, for numerous and valuable discussions. His thanks are finally due Professors Bethe and Weisskopf, for two illuminating conversations.

## APPENDIX

1. The functions $I_n(r)$. We have

$$I_n(r)=(2\pi)^{-\frac{1}{2}}\int\frac{e^{i\mathbf{k}\mathbf{r}}}{\omega_k^{2n+1}}d\mathbf{k}=\left(\frac{2}{\pi}\right)^{\frac{1}{2}}\frac{1}{r}\int_0^\infty\frac{\sin krkdk}{(k^2+\mu^2)^{n+\frac{1}{2}}}. \tag{1a}$$

By using the integral representation of the Hankel functions of imaginary argument (see reference 15, p. 172):

$$K_n(\mu r)=\pi^{-\frac{1}{2}}\Gamma(n+\tfrac{1}{2})\left(\frac{2\mu}{r}\right)^n\int_0^\infty\frac{\cos krdk}{(k^2+\mu^2)^{n+\frac{1}{2}}}, \tag{2a}$$

$I_n(r)$ can easily be put into the form

$$I_n(r)=-\left(\frac{2}{\pi}\right)^{\frac{1}{2}}\frac{1}{r}\frac{d}{dr}\left[\frac{\pi^{\frac{1}{2}}}{\Gamma(n+\frac{1}{2})}\left(\frac{r}{2\mu}\right)^n K_n(\mu r)\right]. \tag{3a}$$

Taking into account the relations (reference 15, p. 79)

$$\begin{aligned}-2K_n'(x)&=K_{n-1}(x)+K_{n+1}(x),\\ -2(n/x)K_n(x)&=K_{n-1}(x)-K_{n+1}(x),\end{aligned} \tag{4a}$$

one finally obtains

$$I_n(r)=\left(\frac{2}{\pi}\right)^{\frac{1}{2}}\frac{2^n n!}{(2n)!}\left(\frac{r}{\mu}\right)^{n-1}K_{n-1}(\mu r). \tag{5a}$$

2. The functions $J_n(r)$. These functions are defined by

$$\begin{aligned}J_n(r)&=(2\pi)^{-3}\int\frac{e^{-i(\mathbf{k}_1+\mathbf{k}_2)\mathbf{r}}}{\omega_1\omega_2(\omega_1+\omega_2)^n}d\mathbf{k}_1d\mathbf{k}_2\\ &=\frac{2}{\pi r^2}\int_0^\infty\int_0^\infty\frac{\sin k_1r\sin k_2r}{\omega_1\omega_2(\omega_1+\omega_2)^n}k_1k_2dk_1dk_2.\end{aligned} \tag{6a}$$

[32] G. Breit, Phys. Rev. **84**, 1053 (1951).
[33] R. G. Sachs, Phys. Rev. **87**, 1100 (1952).
[34] H. W. Lewis (private communication).
[35] An estimate of the order of energy at which the potential is still valid is provided by the mean value of the kinetic energy in the deuteron ground state, calculated in Sec. V. In the laboratory system, it corresponds to about 37 Mev.
[36] H. L. Anderson *et al.*, Phys. Rev. **85**, 936 (1952); **86**, 793 (1952).

(a) $n=1$: We multiply the numerator and the denominator of the integrand by $(\omega_1-\omega_2)$:

$$J_1(r)=\frac{2}{\pi r^2}\int_0^\infty\int_0^\infty\left(\frac{1}{\omega_2}-\frac{1}{\omega_1}\right)\frac{\sin k_1 r\sin k_2 r k_1 k_2}{k_1^2-k_2^2}dk_1dk_2. \tag{7a}$$

By exchanging the integrations over $k_1$ and $k_2$ in the second part of the right-hand side, we obtain

$$J_1(r)=\frac{4}{\pi r^2}\int_0^\infty\frac{\sin k_2 r}{\omega_2}F_1(k_2,r)k_2dk_2, \tag{8a}$$

where the function $F_1$ is defined by

$$F_1(k_2,r)=\int_0^\infty\frac{\sin k_1 r k_1}{k_1^2-k_2^2}dk_1=\frac{\pi}{2}\cos k_2 r \text{ for } r>0. \tag{9a}$$

It follows, therefore, that

$$J_1(r)=\frac{1}{r^2}\int_0^\infty\frac{\sin 2k_2 r}{\omega_2}k_2dk_2=\frac{\mu}{r^2}K_1(2\mu r), \tag{10a}$$

where use has been made of the definition of $I_0(r)$ in the previous paragraph.

(b) $n=2$: We differentiate $J_2(\mu r)$ with respect to $\mu$:

$$\frac{\partial}{\partial\mu}J_2(\mu r)=-\frac{\mu}{(2\pi)^3}\int\frac{e^{-i(\mathbf{k}_1+\mathbf{k}_2)r}}{\omega_1^3\omega_2^3}d\mathbf{k}_1d\mathbf{k}_2$$

$$=-\mu[I_1(r)]^2=-\frac{2\mu}{\pi}[K_0(\mu r)]^2. \tag{11a}$$

Since $J_2(\mu r)\to 0$ for $\mu\to\infty$, it follows therefore that

$$J_2(\mu r)=\frac{2}{\pi r^2}\int_{\mu r}^\infty[K_0(x)]^2xdx. \tag{12a}$$

PHYSICAL REVIEW VOLUME 88, NUMBER 4 NOVEMBER 15, 1952

# $C^{12}(p,pn)C^{11}$ Cross Section from Threshold to 340 Mev*

R. Lee Aamodt,† Vincent Peterson,‡ and Robert Phillips
*Radiation Laboratory, Department of Physics, University of California, Berkeley, California*

(Received April 28, 1952)

The excitation function for the reaction $C^{12}(p,pn)C^{11}$ has been measured from threshold to 340 Mev using the Berkeley 40-ft linear accelerator and 184-in. cyclotron. Absolute cross-section measurements were made at various energies, using a Faraday cup and calibrated beta-counter. The threshold occurs at 18.5±0.3 Mev. The cross section has a broad maximum of 100 millibarns near 45 Mev and decreases to 43 millibarns at 340 Mev.

## I. INTRODUCTION

THE formation of radioactive $C^{11}$ from $C^{12}$ by high energy particles (protons, neutrons, deuterons, and alpha-particles) has been widely used at this laboratory as a monitor and detector.[1–6] These reactions have thresholds near 20 Mev and therefore discriminate against low energy background. The positron activity of $C^{11}$(0.97 Mev, 20.5 min)[7] is convenient for short activation and counting periods. Carbon targets are readily available in the form of graphite or polystyrene.

Knowledge of the variation of cross section with energy and the absolute value of the cross section is important to the extensive use of such reactions. The $C^{12}(p,pn)C^{11}$ reaction is of particular interest because of the number of existing proton accelerators. A considerable amount of work, both experimental and theoretical, has already been done at the Radiation Laboratory on this reaction. Before the 184-in. cyclotron was converted from deuteron to proton acceleration, Chupp and McMillan[8] measured the relative excitation curve up to 140 Mev using protons "stripped" from 190-Mev deuterons inside the cyclotron vacuum tank. By using this proton source, McMillan and Miller[9] determined the absolute cross section at 62 Mev. More recently Panofsky and Phillips,[10] working with the Berkeley 32-Mev proton linear accelerator, established the excitation curve up to 27 Mev. In particular they studied the region just above the threshold in

* This work was sponsored by the AEC.

† Now at Los Alamos Scientific Laboratory, Los Alamos, New Mexico.

‡ Now at California Institute of Technology, Pasadena, California.

[1] Helmholz, McMillan, and Sewell, Phys. Rev. **72**, 1003 (1947).

[2] Chupp, Gardner, and Taylor, Phys. Rev. **73**, 742 (1948).

[3] Cook, McMillan, Peterson, and Sewell, Phys. Rev. **75**, 7 (1949).

[4] Bratenahl, Fernbach, Hildebrand, Leith, and Moyer, Phys. Rev. **77**, 597 (1950).

[5] S. B. Jones and R. S. White, Phys. Rev. **78**, 12 (1950).

[6] W. J. Knox, Phys. Rev. **81**, 687 (1951).

[7] E. Siegbahn and E. Born, Arkiv Mat. Astron. Fysik **30B**, No. 3 (1944).

[8] W. W. Chupp and E. M. McMillan, Phys. Rev. **72**, 873 (1947).

[9] E. M. McMillan and R. D. Miller, Phys. Rev. **73**, 80 (1948).

[10] W. K. H. Panofsky and R. Phillips, Phys. Rev. **74**, 1732 (1948).

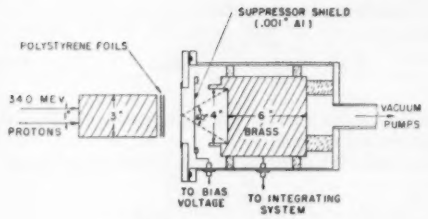


FIG. 1. Deflected beam geometry.

detail where the reaction was shown to be $C^{12}(p,d)C^{11}$. Heckrotte and Wolff[11] have calculated the excitation curve to be expected for both the $(p,pn)$ and $(n,2n)$ reactions up to 100 Mev using a model of the nucleus proposed by Serber.

The new experimental work described here was performed mainly after an external deflected beam of 340-Mev protons became available from the 184-in. cyclotron. Absolute measurements of the $(p,pn)$ cross section at proton energies of 340 Mev and below were then possible with a well-collimated beam. Additional work with the linear accelerator has extended the previous excitation curve up to 32 Mev, and an absolute determination of the cross section at 32 Mev has been made with improved accuracy. Considerable effort has been spent in the preparation and calibration of a beta-ray standard in order to establish the absolute values of the cross section over the entire energy range. Preliminary results of this work have been published.[12]

## II. EXPERIMENTS USING 340-MEV PROTONS

### A. Description of Apparatus

The experimental arrangement used in the high energy absolute cross-section determinations is shown in Fig. 1. A well-collimated beam of 340-Mev protons from the Berkeley 184-in. cyclotron was used to activate thin foils of polystyrene. The proton current incident on the foils was then collected by a Faraday cup and integrated. The $C^{11}$ activity produced in the foils was counted with an end-window Geiger-Mueller counter and compared to the activity of various calibrated beta-ray sources (see Sec. IV).

If the incident proton flux were to remain constant while traversing its range in an absorber, the relative activities of foils interspersed in the absorber could be used to construct an excitation function. However, the range of 340-Mev protons is such ($\sim$93 g/cm$^2$ in copper) that nuclear processes significantly attenuate the flux. Supplementary measurements indicate that the flux is reduced to about one-half in 90 g/cm$^2$ of copper. Therefore it was necessary to determine the activation flux for each point at high energies.

The energy of the proton beam was reduced by interposing copper absorbers before the target foils. The initial angular spread (about 0.004 radian) and diameter (1 in.) of the beam is thereby increased as the energy is reduced, due to multiple Coulomb scattering. Calculations of the root-mean-square plane projected scattering angle and lateral displacement show that at a residual mean energy of 100 Mev, the values in copper are 5.4° and 0.35 cm, respectively. The exposure pattern observed on x-ray films sandwiched in the absorber stack confirmed that the spreading out of the beam is not yet serious at this energy. The angular spread, however, increases rapidly with decreasing residual range and it becomes difficult to collect all the current. Furthermore, the statistical straggling in range of protons initially nearly monochromatic produces an energy spread which is about 5 percent (rms) at 100 Mev and rises very steeply at lower residual energies. Therefore absolute measurements made with the high energy proton beam were not extended below a minimum energy of 93 Mev.

The Faraday cup[13] used to collect the proton current was a 6-in. long brass cylinder 6 inches in diameter mounted on insulators inside a vacuum chamber (see Fig. 1). The proton beam enters through a 2-mil Be-Cu window. The collected current was integrated using calibrated condensers and a null-method electrometer-tube voltmeter. Loss of protons from the cup due to nuclear scattering was found to be negligible by placing nuclear emulsions around the outside surface. The pressure inside the cup-chamber was kept below 0.1 micron, a factor of 100 below the pressure at which ionization effects were observed to become important. Numerous experiments were made to measure the emission of secondary electrons from the internal surfaces of the cup both by the use of a suppressor foil to which bias voltages were applied and by means of magnetic fields. It was concluded that the correction to the current measured without electrical bias or magnetic field was less than 1 percent for full energy protons.

Considering all sources of error in making an absolute measurement of charge collected by the Faraday cup, it is felt that the results are good to $\pm 2$ percent. In relation to the difficulties in determining the absolute number of beta-particles emitted by the radioactive foils (discussed in Sec. IV), the charge measurement is a minor source of error in determination of the absolute cross section.

### B. Experimental Results—340 Mev to 93 Mev

Five-mil polystyrene $(C_8H_8)_n$ foils, placed behind copper absorbers as close as possible to the Faraday

[11] W. Heckrotte and P. Wolff, Phys. Rev. **73**, 264, 265 (1948).
[12] Aamodt, Peterson, and Phillips, Phys. Rev. **78**, 87 (1950); and Aamodt, Peterson, and Phillips, University of California Radiation Laboratory Report 526 (1949) and University of California Radiation Laboratory Report 1400 (1951) (unpublished).
[13] Details concerning the Faraday cup and its use in measuring currents of high energy charged particles will be included in an article submitted to the *Review of Scientific Instruments*.

cup window, were bombarded for periods of 10 to 20 minutes with proton currents of $10^{-10}$ to $10^{-12}$ ampere. The resulting $C^{11}$ activity was counted for several half-lives, and extrapolated back to the end of bombardment in the usual manner. In later runs, the calculation of the cross section was simplified by adjusting the RC of the integrating circuit to equal the mean life of the $C^{11}$ activity. In this case fluctuations in the proton current during bombardment do not enter, and

$$\sigma(mb) = 0.00612R(t)/Q(t)w,$$

where $w$ is the foil thickness in mg/cm², $R(t)$ the number of $C^{11}$ disintegrations per second determined at the same time as the charge $Q(t)$ (in microcoulombs).

The decay curves showed no evidence for contaminating radioactivity, agreeing well with the published half-life.[7] In particular, foils placed adjacent to the copper absorber showed the same activity as foils protected by an additional 5 mils of polystyrene.

Neutrons are certainly produced in the 48-in. brass collimator and in the copper absorbers by the incident protons. Since the $C^{12}(n,2n)C^{11}$ cross section[14] is comparable to the $(p,pn)$ cross section, one might expect an appreciable background activity. However the high threshold energy discriminates against neutrons below 20 Mev, and the angular distribution of neutrons produced by high energy protons is quite broad.[15] Experimentally the $C^{11}$ activity produced by neutrons is about 2 percent of the initial activity, as measured by foils placed beyond the end of the proton range.

Absolute measurements of the $C^{12}(p,pn)C^{11}$ cross section were made at 8 different proton energies at or below 340 Mev. The values are given in Table I, and are plotted in Fig. 6. The probable errors of the mean value given are due mainly to counting statistics and do not include the absolute error involved in beta-source calibration.

### C. Intermediate Energy Region—32 Mev to 100 Mev

The energy spread of the proton beam from the Berkeley cyclotron rapidly increases at degraded energies so that only the general outlines of the excitation curve can be observed. Fortunately, N. M. Hintz has investigated the $C^{12}(p,pn)C^{11}$ reaction using magnetically focused 110-Mev protons in the Harvard cyclotron. This proton energy is ideally suited to provide data in the region 32 to 100 Mev, and Hintz has kindly consented to allow us to include his results. The relative excitation curve was corrected for nuclear absorption in brass absorbers taken to be one-half the total cross section for 70-Mev neutrons in copper (1.1 barns).[16] It was then fitted to the Berkeley data. For the fit, both curves were plotted using a logarithmic scale for the cross section and a linear scale for the energy. Adjustment was made along both cross section and energy scales to achieve the best match of the shapes in the steeply rising region from 20 to 30 Mev. When this is done, the curve also agrees within the probable error with the Berkeley cyclotron data at 93 Mev. The composite curve is shown in Fig. 6.

TABLE I. Absolute cross-section measurements (Berkeley cyclotron).

| Proton energy (Mev) | Number of runs | Cross-section mean value (millibarns) | P.E. of mean (millibarns) |
|---|---|---|---|
| 340 | 12 | 41.2 | 0.6 |
| 313 | 1 | 47.6 | 2.1 |
| 293 | 5 | 47.7 | 1.0 |
| 263 | 1 | 50.5 | 2.6 |
| 245 | 4 | 49.8 | 1.2 |
| 194 | 3 | 52.0 | 1.5 |
| 144 | 3 | 56.5 | 1.5 |
| 93 | 1 | 70.5 | 3.6 |

[14] E. M. McMillan and H. F. York, Phys. Rev. **73**, 262 (1948); R. L. Mather and H. F. York (private communication). The $(n,2n)$ cross section is 20±4 millibarns for neutrons of mean energy of 90 Mev.

[15] Miller, Sewell, and Wright, Phys. Rev. **81**, 374 (1951).

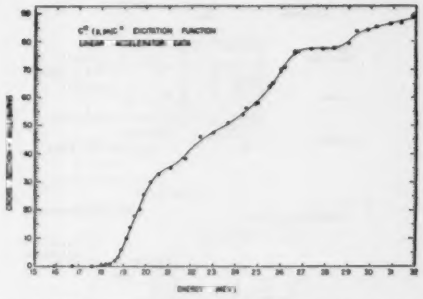

FIG. 2. $C^{12}(p,pn)C^{11}$ excitation function linear accelerator data.

## III. EXPERIMENTS WITH 32-MEV PROTONS

### A. Relative Excitation Curve

Previously reported measurements[10] include data on the relative excitation curve from threshold (18.5±0.3 Mev) to 27 Mev using the Berkeley 32-Mev proton linear accelerator. Using the same stacked foil technique the excitation curve has now been extended up to full beam energy.

Stacks of 0.010-in. polystyrene foils were bombarded by the full energy beam, and the foils were then counted with an end-window Geiger counter. In order to obtain good counting statistics, only enough foils were counted to obtain a sufficient overlap with the previously established curve. The curve of the run which yielded the highest activity, fitted to the data from threshold to 27 Mev is shown in Fig. 2. The probable errors resulting from counting statistics are too small to be shown on the scale used for Fig. 2. The two curves overlap for about 2½ Mev in a region where a bend permits accurate activity and energy normalization.

[16] J. DeJuren, Phys. Rev. **81**, 919 (1951).

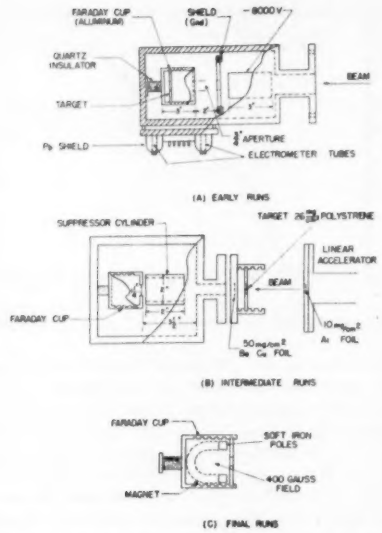


FIG. 3. Faraday cup geometry for measurements at 32 Mev.

The fitting of the two curves does not permit a shift of more than ±0.15 Mev, which introduces an uncertainty of only 2 millibarns at the full energy. Although the incident energy of the beam may vary downward as much as 1 Mev, the best fit results from assuming the incident energy to be the same as for the lower part of the curve (32.0±0.1 Mev).

A foil placed beyond the proton range as a neutron monitor showed that error from this source could be considered negligible.

Because of the comparatively small thicknesses of absorbers used to slow down 32-Mev protons, no nuclear absorption correction has been applied to the activity curves. Furthermore due to the small beam diameter ($\frac{1}{4}$ in.) relative to foil diameter (1 in.), no scattering loss is expected.

### B. Absolute Cross Section at 32 Mev

The absolute cross section measurements at 32 Mev previously reported[10] have been extended and improved, primarily as regards beta-standardization (Sec. IV) and determination of the effects of secondary electrons. Thin (0.010-in.) polystyrene foils were bombarded at full beam energy, and the current was collected in a Faraday cup. Due to high average beam intensity ($\sim 10^{-8}$ amp) it is possible to use short bombardments (6 to 120 sec) and therefore render negligible any error due to inconstancy of the beam current. The electrometer tubes and integration condensers are contained within the cup vacuum chamber.

A total of 34 separate runs were made on the absolute cross section at full beam energy. Three different target Faraday cup arrangements were used as shown in Fig. 3 in order to assess and eliminate the error due to secondary electron emission. In the early runs as illustrated in Fig. 3(a), a cylinder at high (8000 v) negative potential removed most low energy charged particles from the beam before it entered the Faraday cup. The cup aperture was only $\frac{3}{4}$-in. diameter, with the target foil inside. Since the solid angle of this aperture to particles emitted from the target area is only $1\frac{1}{2}$ percent (of $4\pi$), this geometry might be expected to trap nearly all of the secondary electrons. However, it does not readily provide a means of measuring the magnitude of the effect.

Intermediate runs as shown in Fig. 3(b) were made with the target foil outside the cup chamber and a secondary-suppressing cylinder before the cup. The cylinder bias was kept at 200 to 400 volts negative. A series of foils was bombarded with different voltages on the cylinder. The results indicate that secondary electron emission from the Faraday cup decreases by approximately 5 percent as the bias is increased from 0 to 400 volts. This figure agrees with the secondary emission check made by Cork[17] for 32-Mev protons.

The final runs as shown in Fig. 3(c) were made with a permanent magnet which produced a field of 400 gauss inside the Faraday cup. A variation of suppressor voltage from 0 to 400 volts produced no observable change in the cross section.

The average values of the measured cross section using the three methods of integration are shown in Table II. The agreement between methods, combined with the voltage effects noted above, indicates that most of the secondary electrons are of low energy and that the suppression measures employed were adequate. The estimated systematic error in cross section due to secondary electron effects is 3 percent.

The finally adopted value at 32 Mev is

$$\sigma_{32\ \mathrm{Mev}} = 89 \pm 4 \text{ millibarns.}$$

The uncertainty includes errors due to integration and counting statistics but does *not* include the probable error in beta-standard calibration.

## IV. ABSOLUTE BETA-ACTIVITY DETERMINATION

The absolute values of the cross section are dependent on a knowledge of the number of $C^{11}$ nuclei produced

TABLE II. Average values of the measured cross section at 32 Mev.

| Method | Number of runs | Mean value (millibarns) | P.E.[a] (millibarns) |
|---|---|---|---|
| A | 23 | 88.1 | 1.5 |
| B | 4 | 84.0 | 4.6 |
| C | 7 | 92.6 | 1.6 |
| Combined | | 88.5 | 1.0 |

[a] Probable error of mean from spread in measured values.

[17] B. Cork, Phys. Rev. **80**, 321 (1950).

in the target foil, and therefore, the disintegration rate at a later time. This rate is found by comparing the counting rate of the target foils with the counting rate of various $\beta$-emitters of known disintegration rate under identical geometrical conditions.

Ideally, foils used for absolute beta-activity determination should be very thin to minimize self-absorption and scattering in the source. The necessity for sufficient activity in short bombardments sets a lower limit on foil thickness, however, and 0.005-in. ($\sim$13 mg/cm$^2$) and 0.010-in. polystyrene foils were used in the cyclotron and linear accelerator runs. The foils were counted on the lower shelves of an end-window Geiger-Mueller counter of 2 mg/cm$^2$ window thickness. The geometry is shown in Fig. 4.

Significant corrections for absorption and scattering of low energy beta-particles in the source, air, and counter window must be made if the geometry or beta-spectrum of the target foil and standard are different. These corrections are difficult to assess and involve dubious extrapolations to zero thickness. Here such corrections have been avoided by choosing beta-standards of nearly the same energy as $C^{11}$ and counting them in geometries as nearly like that of the $C^{11}$ foil as possible. Half-thicknesses of polystyrene foils were placed above and below the active deposit in counting standards, and the same foil holders were used. Since the standards were effective point sources, a small geometrical correction for the finite extent of the active

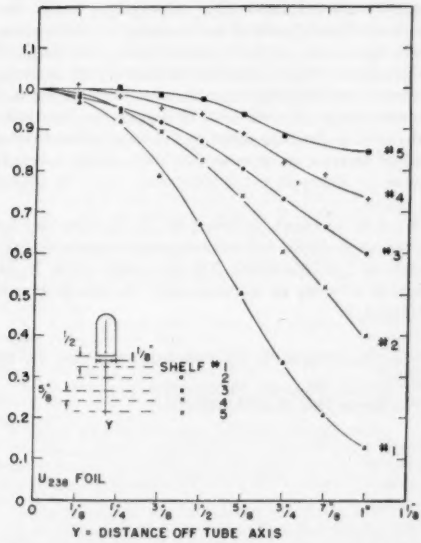


FIG. 4. Relative variation of counting efficiency with lateral displacement of a point source at various distances from a counter window.

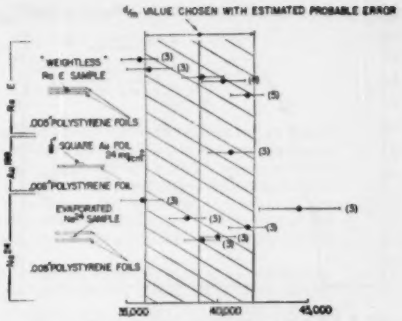


FIG. 5. Equiv. $d/m$ of $UO_3$ Secondary $\beta$-Std for primary standards shown. Numbers in parenthesis indicate shelf on which counting was done.

region of the cyclotron-bombarded foils had to be made. This correction was based on a series of measurements, as shown in Fig. 4, of counting rate as a function of lateral position off the counter axis, made by Mrs. Beverly Lee in this Laboratory. The counting rate of a uniform distribution of activity over a one-in. diameter centered circle, as compared to a point source on the axis is 6 percent low on the third shelf, and 3 percent low on the fourth shelf.

Several beta-standards of energies bracketing that of $C^{11}$(0.97 Mev) were used: $Au^{198}$(0.92 Mev.), RaE(1.17 Mev), and $Na^{24}$(1.4 Mev).[18] Both $Au^{198}$ and $Na^{24}$ have well-established simple decay schemes[19] which make them suitable for calibration by the beta-gamma coincidence method.[20] The RaE was calibrated by counting the alphas form the daughter RaF in a standard geometry alpha-counter. The alpha-count was made several times over a period of four half-lives to insure that the RaF was in equilibrium with the RaE. Each of these standards was then used to calibrate the beta-counter for $C^{11}$ betas under specific conditions of geometry and foil thickness.

If the standard is calibrated at $N_s$ disintegrations per minute, and counts at the rate of $N_1$c/m, as compared with $N_2$c/m for the $C^{11}$ foil, then we say $(N_2/N_1)N_s=N_c$, the disintegration rate of the $C^{11}$ foil. It is convenient to interpose a long-lived secondary standard assigning it a number of "equivalent" $d/m$. If it counts at a rate $N_3$ $c/m$ we say this number $N_{eq.}=(N_3/N_1)N_s$. Then, if at a later time the $C^{11}$ is counted in the same geometry, it is satisfactory to say $N_c=(N_2/N_3)N_{eq.}$ since this equals $(N_2/N_3)$ $(N_3/N_1)N_s$ $=(N_2/N_1)N_s$ as before.

[18] G. T. Seaborg and I. Perlman, Revs. Modern Phys. **20**, 585 (1948).
[19] C. L. Peacock and R. G. Wilkinson, Phys. Rev. **74**, 297 (1948); Cook, Jurney, and Langer, Phys. Rev. **70**, 985 (1946).
[20] W. Siri, *Isotopic Tracers and Nuclear Radiations* (McGraw-Hill Book Company, Inc., New York, 1949), Chap. 13. The $Na^{24}$ sample was kindly made available by Dr. C. A. Tobias, as was the coincidence-counting equipment.

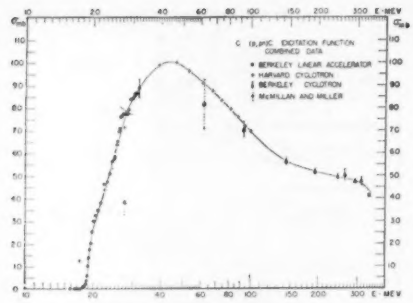


FIG. 6. $C^{12}(p,pn)C^{11}$ excitation function combined data.

Obviously this number $N_{eq.}$ must be redetermined when the target thickness or the geometry is changed.

Values of $N_{eq.}$ for the various standards with geometry shown appear in Fig. 5, where the probable errors, including the standardization statistical probable error, are shown. It is assumed that the proper value of $N_{eq.}$ for a known $C^{11}$ activity would lie somewhere in the shaded area ($\pm 7.5$ percent probable error).

## V. DISCUSSION OF RESULTS

The combined data from the Berkeley linear accelerator, Havard cyclotron, and Berkeley cyclotron is plotted in the final curve of Fig. 6. The probable errors shown are those of absolute measurements but only relative to one another, i.e., they do not include the probable error of $7\frac{1}{2}$ percent in beta-standard calibration.

An independent absolute measurement at 62 Mev by McMillan and Miller,[9] in which the present uranium "intermediate" beta-standard was used as the primary standard, may be corrected in view of a more accurate calibration of the equivalent $C^{11}$ beta-activity of the uranium. The corrected value is $82 \pm 11$ millibarns and is plotted for comparison in Fig. 6.

The earlier experiments of Chupp and McMillan,[8] using stacks of graphite plates bombarded internally in the cyclotron with protons stripped from deuterons, indicated that the excitation curve was flat from 140 to 60 Mev. No correction for nuclear absorption was made in these earlier experiments. However, a correction based on a nuclear absorption cross section as large as 0.5 barn (approximately the average total cross section for neutrons in this energy region)[12,16] in carbon apparently is not sufficient to account for the discrepancy. The remaining discrepancy results from some other source of error, probably a contamination of the proton beam inside the cyclotron tank from lower energy particles.

The shape of the excitation curve has several features of interest. As shown earlier by Panofsky and Phillips,[10] the low threshold energy provides definite evidence for the existence of a $(p,d)$ reaction in this region. Evidence for the persistence of the $(p,d)$ reaction with good probability for protons of 32 Mev occurs in the independent experiments of Levinthal *et al.*[21] In this energy range the $(p,pn)$ and $(p,d)$ reactions represent inelastic processes best described by the theory of the compound nucleus. The low energy excitation curve, Fig. 2, exhibits irregularities which are experimentally significant but difficult to analyze in terms of the capture process. The peak of the curve occurs at 45 Mev, in agreement with the calculations of Heckrotte and Wolff,[11] but the width of the peak is considerably greater than their evaporation theory estimates.

Furthermore, at higher energies where noncapture processes may be expected to become more important, the experimental curve does not show a plateau but decreases with energy approximately as $E^{-\frac{1}{2}}$. This energy dependence is very similar to that of the neutron total cross section in carbon.[16]

The dip in the $C^{12}(p,pn)C^{11}$ cross section at 340 Mev is apparently real. This was checked by bombarding foils placed on both sides of the first absorber. The results, corrected for nuclear absorption, verify the dip. A calculation based on measurements of the neutron production cross section[6] and angular distribution[22] and checked by Serber's theory[23] indicates that neutrons formed in the absorber can at most account for a 2 percent change. No evidence of copper recoil activity was found in the beta-counting. This deviation from a gradual decrease in cross section with energy makes it unwise to extrapolate the excitation curve to higher energies.

We wish to thank Professor W. K. H. Panofsky for his constant advice and encouragement throughout the history of this experiment. The generosity of Dr. N. M. Hintz in allowing us to incorporate his data is greatly appreciated.

[21] Levinthal, Martinelli, and Silverman, Phys. Rev. **78**, 199 (1950).
[22] J. DeJuren, Phys. Rev. **81**, 458 (1951).
[23] R. Serber, Phys. Rev. **72**, 1008 (1947).

# Pair Production by Electrons*

M. Camac†
*Cornell University, Ithaca, New York*
(Received August 1, 1952)

Pair production by electrons was observed by measuring the positrons emitted from thin copper targets irradiated directly by the synchrotron electron beam (230±20 Mev energy). The positrons were produced in either of two ways: either (1) directly by the electron beam, or (2) through a double process in which bremsstrahlung was first produced which then materialized in pairs in the same target. By measuring the positron rate as a function of target thickness a direct comparison of the two modes of production was obtained. The thickness of copper from which the positron yield was the same for both processes was 0.0043±0.001 inch (0.0073±0.0017 radiation lengths). The positrons had about 0.80 of the energy of the incident electron beam.

The results of this experiment is shown to be in agreement with the Weizsaker-Williams approximation. In this approximation the formula for the number of virtual quanta associated with an incident electron contains a constant of the order of unity. Using the results of this experiment and the Bethe-Heitler formulas for the double process this constant was calculated to be 1.6±0.2.

## I. INTRODUCTION

With the recent development of high energy electron accelerators detailed measurements of electromagnetic interactions are being extended to the several hundred million electron volt region. Measurements of the differential energy cross sections for bremsstrahlung[1] and pair production by gamma-radiation[2] were shown to be in agreement with the Bethe-Heitler formulas[3] modified slightly.[4] For the similar phenomenon of direct pair production by an electron, however, there were few quantitative measurements. In fact, this process was first observed[5] only recently in photographic plates irradiated in the upper atmosphere by cosmic radiation. With four events Hooper, King, and Morrish[6] obtained a rough measurement of the total cross section which was in agreement with the theoretical work of Racah and others.[7]

In the period from 1934 to 1941 there were several experimental attempts to measure direct pair production by electrons.[8–12] Except in two cases[9,10] cloud chambers were used. In the more conclusive experiments[11,12] only upper limits to the cross section were obtained and these were not in disagreement with the theory. For example, Crane and Halpern[12] used a cloud chamber with ½-mm lead plate in the center and an external source of beta-particles with energies ranging from 1 to 7 Mev. No events were observed in 1337 traversals of the plates. Recently there have been several abstracts on this phenomenon.[13]

The high energy electron accelerators furnish well-collimated, monochromatic electron beams and are ideally suited to measure pair production by electrons. Such measurements made with the Cornell synchrotron are described in this paper. The results are then compared to the theoretical work of Bhabha[7] and shown to be in agreement with the Weizsaker-Williams approximation.[14]

## II. EXPERIMENTAL APPARATUS

A schematic section in the median plane of the synchrotron indicating the detecting apparatus and the modifications in the donut-shaped vacuum system is shown in Fig. 1.

The well-collimated[15] electron beam expanded outward from its accelerating orbit and irradiated a thin copper target. The expanded beam was used in order to minimize the time that the outgoing positrons spent in the strong magnetic field, which decreased their energy dispersion. The predominant radiation produced in the target (electrons, positrons and bremsstrahlung) initially travelled in the direction of the incident beam. The components were then separated by the strong magnetic field: the electrons circled inward; the gamma radiation went tangent to the orbit; and the positrons

* This research supported jointly by the ONR and AEC.
† Now at the University of Rochester, Rochester, New York.
[1] J. W. DeWire and L. A. Beach, Phys. Rev. **83**, 476 (1951).
[2] G. D. Adams, Phys. Rev. **74**, 1707 (1948); R. L. Walker, Phys. Rev. **76**, 527 (1949); J. L. Lawson, Phys. Rev. **75**, 433 (1949); Powell, Hartsough, and Hill, Phys. Rev. **81**, 213 (1951); DeWire, Beach, and Ashkin, Phys. Rev. **83**, 233, 476, 505 (1951); **82**, 447 (1951).
[3] W. Heitler, *The Quantum Theory of Radiation* (Oxford University Press, London, 1944).
[4] L. C. Maximon and H. A. Bethe, Phys. Rev. **87**, 156 (1952); Handel Davies and H. A. Bethe, Phys. Rev. **87**, 156 (1952).
[5] Bradt, Kaplon, and Peters, Helv. Phys. Acta **23**, 43 (1950); **24**, 23 (1950); G. P. S. Occhialini, Nuovo cimento Supp. **6**, 3, 413 (1949).
[6] Hooper, King, and Morrish, Phil. Mag. **42**, 304 (1951).
[7] G. Racah, Nuovo cimento **14**, No. 3, 93 (1937); H. J. Bhabha, Proc. Roy. Soc. (London) **152**, 559 (1935); D. G. Ravenhall, Proc. Phys. Soc. (London) **113**, 1177 (1950); (private communication).
[8] Sizoo, Barendregt, and Griffioen, Physica **7**, 860 (1940).
[9] J. R. Feldmeier and G. B. Collins, Phys. Rev. **58**, 200 (1940).
[10] N. Feather and J. V. Dunworth, Proc. Cambridge Phil. Soc. **34**, 435 (1938).
[11] Hans Staub, Helv. Phys. Acta **9**, 306 (1939).
[12] H. R. Crane and J. Halpern, Phys. Rev. **55**, 838 (1939).
[13] Cleland, Konneker, and Hughes, Phys. Rev. **79**, 229 (1950); M. Camac, Phys. Rev. **83**, 207 (1951); N. J. Shiren and R. F. Post, Phys. Rev. **86**, 617 (1952).
[14] C. F. v. Weizsaker, Z. Physik **88**, 612 (1934); E. J. K. Williams, Kgl. Danski Videnskab. Selskab, Matt.-fys. Medd. **13**, 4 (1935); Phys. Rev. **45**, 729 (1934).
[15] In the region of the target the beam was approximately 2 mm high and 4 mm wide.

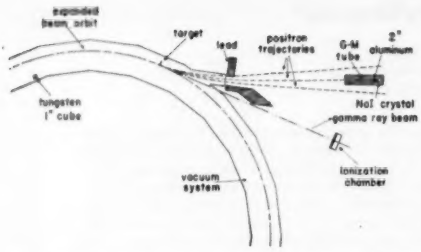


FIG. 1. Experimental arrangement indicating the modifications in the vacuum system of the synchrotron, shielding and the radiation detectors.

spiraled outward and were separated in energy. Trajectories for three different energies are shown in Fig. 1. The path with the least curvature is for a positron with the same energy as the primary electron. The next is for 0.8 of the initial energy and the most curved one is for 0.6. The position of the target was chosen so that the high energy positrons left the vacuum system through a thin $\frac{1}{32}$-inch aluminum exit port.

The target and target holder used in the final runs are shown in Fig. 2. The targets were copper strips $\frac{1}{4}$ inch in the vertical direction, 0.050 inch in the radial direction, and a range of thicknesses in the azimuthal direction, 0.0012, 0.0040, 0.0104, and 0.0160 inch. The copper targets were cemented to polystyrene strips 0.020 inch by 0.010 inch which were mounted on 0.040-inch "C" shaped Lucite rings. A coating of Aquadag was placed on all plastic parts to avoid electrical charging. There were provisions (1) for rotating this target assembly out of the beam and (2) moving it azimuthally in the donut.

The positron detector was a lead shielded counter telescope consisting of a thin walled G-M tube, 2 inches of aluminum, and a 4-cm by 4-cm NaI scintillation detector set to record signals greater than about 15-Mev energy. A charged particle at minimum ionization must have had at least 40-Mev energy to produce a coincidence pulse in the two detectors. The coincidence system served two purposes: (1) It set an energy bias on the particles to be measured, and (2) it discriminated against gamma-radiation. The positron detector was mounted on a bakelite table between the synchrotron magnet coils and the back column of a magnet yoke. Two selsyn drives remotely controlled (1) the rotation and (2) the azimuthal translation of the telescope.

The bremsstrahlung beam from the target was measured with an ionization chamber with $\frac{1}{4}$ inch of lead in front of it.

The electronic circuits were of standard design. The positron detector was sensitive to radiation only during the target irradiation time.

Radiation shielding was placed around the exit port and inside the donut (see Fig. 1). The lead at the port shielded against gammas and low energy positrons from the target. The tungsten cube prevented the degraded electrons from striking the portion of the inner wall of the donut from which gamma-rays would go in the direction of the positron detector.

## III. IDENTIFICATION OF THE POSITRONS

The identification of the positrons was obtained with two complementary measurements. It was ascertained (1) that the particles had the curvature in the magnetic field and intensity distribution that was theoretically predicted for positrons, and (2) that they came from the target. For thick targets a calculated distribution was possible since the pairs were produced mainly through the double process with the intermediate bremsstrahlung beam.

The measurements were made as follows. A 0.040-inch tungsten wire was used for the target. The azimuthal positions of the target and positron telescope detector were fixed. The counting rate in the positron counters was measured as a function of the telescope rotation for a constant integrated bremsstrahlung beam. Typical data are shown in Fig. 3. The abscissa is plotted in degrees of rotation with 0° for the telescope pointing to the center of the synchrotron. At the setting of the peak, about 30°, the telescope pointed towards the exit port.

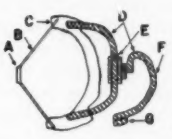


FIG. 2. Target and target holder. *A*: copper target; *B*: 0.010-inch polystyrene strips; *C*: 0.040-inch Lucite; *D*: stainless steel; *E*: target rotated in and out of beam on this axis; *F*: this point rested against wall of vacuum system; and *G*: shaft to exit port plate to support target assembly.

Next, the counter telescope was moved azimuthally to observe positrons of different energies. For each translational position the telescope was rotated to determine the rate at the peak of the curve. In Fig. 4 the counting rates at the peak of the curves are plotted as a function of the azimuthal position of the counter telescope. Each point is normalized to the same integrated gamma-ray beam. Also shown in Fig. 4 is the theoretically expected distribution for thick targets, such as the 0.040-inch tungsten wire. The agreement is very good. This distribution was obtained by folding the Bethe-Heitler differential energy formulas for the double process with the energy dispersion curves for the synchrotron magnetic field. The degree markers plotted along the abscissa represent the angle between the positron detector and the target with the vertex at the center of the synchrotron. 37.75° was the detector position for positrons with the same energy as the synchrotron beam.

Experimental data represented in Fig. 4 were repeated for different azimuthal positions of the target. The angular shift of the curve as shown in Fig. 4 corresponded to the angular motion of the target. Thus, the

37.75° end point remained the same. From the above measurements we concluded that we were observing positrons.

## IV. THEORY OF THE MEASUREMENTS

There are only two important ways in which positrons can be created in the target by the electron beam: (1) by direct pair production by electrons and (2) by the double process in which the bremsstrahlung gamma-rays produce pairs in the same target. The yield from the direct process varies linearly with target thickness. For the double process the variation is quadratic. Thus, by measuring the positron rates for different target thicknesses the two processes were separated. This simple theory was applied to the measurements as follows.

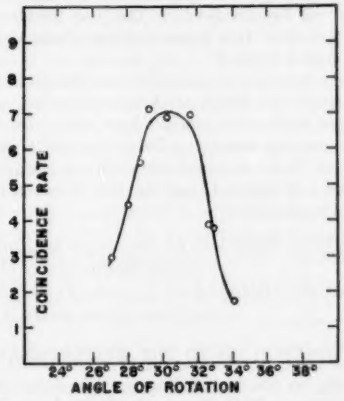


FIG. 3. Coincidence counting rate as a function of angle of rotation of positron detector for fixed positions of the target and detector. All points normalized in the same integrated bremsstrahlung beam. At the rotation angle of 0° the detector pointed to the center of the synchrotron.

Let $P$ be the total positron count arising from both processes.

$$P = (\text{direct process}) + (\text{double process}). \quad (1)$$

$$P = (e_s StB) + (\tfrac{1}{2} e_d D t^2 B), \quad (2)$$

where $e_s$ and $e_d$ are the detection efficiencies for the direct and double process; $S$ and $D$ are the cross sections per radiation length of target for producing positrons by the direct and double process, respectively; $t$ is the target thickness and $B$ is the integrated incident beam. The factor of $\frac{1}{2}$ in the term for the double process arises since the same target is used for the two interactions. Since all the positrons leave the target in the same direction, we cannot determine directly from which process they were produced. Thus, they will be detected with equal efficiency, i.e., $e_s = e_d$. The formula

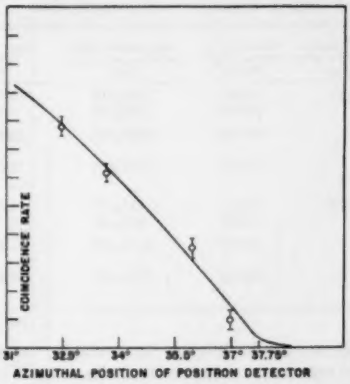


FIG. 4. Experimental points indicate the coincidence rates at the peaks of the detector rotation curves for different azimuthal positions of the positron detector. The angle notation on the abscissa axis is the angle between the target and the detector with the vertex at the center of the synchrotron. The curve is the theoretical distribution of the positrons.

for $P$ becomes

$$P = e_s tB(S + \tfrac{1}{2} Dt). \quad (3)$$

The total gamma-ray counts, say $G$, was

$$G = gtB, \quad (4)$$

where $g$ is the total gamma-ray counts per radiation length of target; $t$ and $B$ are the same as in Eq. (2).

In this experiment the ratio $P/G$ was measured:

$$P/G = e_s tB(S + \tfrac{1}{2} Dt)/Bgt. \quad (5)$$

$$P/G = (e_s/g)(S + \tfrac{1}{2} Dt). \quad (6)$$

Note that the expression for $P/G$ varies linearly with target thickness. The parenthesis in Eq. (6) does not contain terms that depend upon the detection efficiency. This enormously simplified the experiment. The final results are independent of the efficiencies of the positron and gamma ray detectors.

If we extrapolate the linear curve of Eq. (6) to the point where $P/G = 0$, then the value of the parenthesis is zero. Let $t = t_0$ at this extrapolated point. We obtain the relation for the cross section for direct pair production:

$$S = -\tfrac{1}{2} Dt_0. \quad (7)$$

A physical interpretation can be given to $t_0$. The probability for an electron to create a positron of a definite energy in passing through a target thickness $t_0$ is the same for the direct and double process.

The cross sections for the double process have been experimentally determined[1,2] and are given by the Bethe-Heitler formulas[3] modified slightly.[4] The value of $t_0$ was obtained in this experiment. Thus, the absolute value of the pair production by electrons differential

TABLE I. Measurements of pair production.

| Ratio of positron to incident electron energy | Thickness of copper target (inches) | Uncorrected data including standard error | Corrected data |
|---|---|---|---|
| 0.83 | 0.0012 | 390±15 | 390±15 |
| | 0.0040 | 510±15 | 510±15 |
| | 0.0104 | 1050±15 | $1060^{+55}_{-15}$ |
| | 0.0160 | 1320±20 | $1420^{+130}_{-100}$ |
| 0.78 | 0.0012 | 455±10 | 455±10 |
| | 0.0040 | 675±20 | 675±20 |
| | 0.0104 | 1170±20 | $1181^{+60}_{-20}$ |
| | 0.0160 | 1750±20 | $1890^{+180}_{-140}$ |

cross section can be obtained by combining the results of this experiment with the formulas for the double process.

## V. MEASUREMENTS

In the analysis of this experiment it is convenient to express the energy of the positron in two steps:

(1) the energy of a positron relative to that of its incident beam electron, and
(2) the energy of the incident electron.

The trajectories of the positions depended only on the relative energy and were independent of the energy of the electron beam.

The synchrotron beam irradiated the target for one millisecond starting at the time that the expanded beam conditions set in. Although about 315 Mev was available with the contracted beam, the expanded beam was limited to 250-Mev energy. Since the magnetic field was decreasing during the irradiation time, the beam energy dropped proportionately to about 210 Mev. Thus, the energy of the electron beam was 230±20 Mev. These values were obtained by comparing the magnitude of the magnetic field at the top of the magnetic cycle to that at the time of the target irradiation. At the top of the cycle the magnetic field was measured in two ways: (1) directly and (2) by an analysis of the data on the bremsstrahlung spectrum.

The ratio of a positron's energy to its incident beam electron was not obtained directly by measurements, but from the calculation of the positron spectral yield as a function of the positron telescope position as shown in Fig. 3. The uncertainty in the energy determination by this method was about 5 percent.

Consistent data was obtained with the positron detector at two azimuthal positions corresponding to energies of about 0.83 and 0.78 of the energy of the incident electron beam. It was difficult to obtain data with positrons of other energies. For a ratio of energies significantly greater than 0.83 insufficient shielding from the gamma-radiation from the target and the small counting rates were the limiting factors. For energies lower than 0.78, the positron trajectories were either too curved to leave the small two-inch exit port of the vacuum system or they met obstacles in the region of the magnet coils.

The results of the measurements of the cross section for pair production are shown in Table I. Four copper foils of different thicknesses were used for targets: 0.0012, 0.0040, 0.0104, and 0.0160 inch.

The positron count *versus* telescope rotation was taken for each azimuthal setting and each target thickness, and the intensity at the peak of the curve was determined within a few percent statistics. The values at the peak together with their standard error are shown in Table I under the column heading "Uncorrected data." These were normalized to a constant integrated bremsstrahlung beam.

Corrections to this data for (1) background, (2) multiple scattering of the incident beam and positrons in the target, (3) target misalignment, and (4) other sources will be discussed in the next section. The results including these corrections are tabulated in the last column of Table I.

These corrected positron counts are plotted in Fig. 5 as a function of target thickness. According to the discussion in Sec. IV, straight lines should be drawn between readings taken at a fixed translational setting.

For the limits of uncertainty of the extrapolated thickness $t_0$ determined from the data shown in Fig. 5, the final results are

$|t_0| = 0.0046 \pm 0.0008$ inch for the ratio of positron to incident electron energy of 0.78;

$|t_0| = 0.0043 \pm 0.0010$ inch for the ratio of positron to incident electron energy of 0.83.

## VI. CORRECTIONS TO THE MEASUREMENTS

In this section the following corrections to the measurements will be discussed: (1) background, (2) multiple scattering in the target, (3) target misalignment with respect to synchrotron beam, and (4) other corrections. These corrections were included in the last column of Table I.

(1) Background: All background was produced by gamma-radiation either from the target or from electrons striking other parts of the donut. By removing the target from the beam it was found that less than 3 percent of the counts were produced by radiation from other parts of the donut. By an analysis of the data taken with lead and without lead at the exit port it was found that the number of gamma-ray counts was not larger than the statistical error of about 5 percent. The main background radiation varied linearly with the thickness of the target and, thus, increased the measured value of the direct positron production. Thus, the values for $t_0$ determined in Sec. V are upper limits.

(2) Multiple scattering in the target: Multiple scattering in the target of the incident electrons and outgoing positrons spread the positron trajectories at

the detector. Multiple scattering in the median plane of the synchrotron did not produce a change in the counting rate because of the contribution of positrons of neighboring energies. However, this produced a spread in the energy of the positrons entering the detector. Multiple scattering in the vertical direction (normal to the median plane) did produce a loss of positrons for thick targets. The loss was determined by varying the vertical aperture of the detector. There were no losses for the 0.0012- and 0.0040-inch targets, about 1 percent loss for the 0.0104-inch target, and $8\pm6$ percent loss for the 0.0160-inch target.

(3) Misalignment of target: When this experiment was started it was felt that one of the major limitations would be the determination of the thickness of the target. The radial expansion of the beam was so slow compared to the time for an orbit revolution that on the average one would expect a radial penetration of about 0.0001 to 0.0002 inch. One could not hope to prepare thin foils with edges that were uniform in regions of this size and then to line up the foils perpendicular to the beam to fractions of a degree.

A systematic set of measurements (to be published elsewhere) were made to determine the irradiation pattern of the foil, and they showed that the picture of the previous paragraph was incorrect. On the contrary, not only did the beam radially penetrate well into the foil, but especially for the thin targets a large region of the donut, up to an inch in diameter, was irradiated. In fact, minimization of the radiation from the target supports became an important problem.

In the primary traversal of the target the vertical extension of the beam was roughly two millimeters. In the primary traversal of the target the beam irradiation decreased almost exponentially with radial penetration —a drop by a factor 2 in from 0.002 to 0.003 inch becoming negligible at about 0.015 inch. During the first traversal the beam was multiply scattered and spread out. It was then able to irradiate a greater region of the target and even the target holder in the subsequent traversals. The subsequent traversals in the 0.0012, 0.0040, 0.0104, and 0.0160 inch foils were 9, 3.2, 0.6, and 0.3, respectively. Thus, we see that for the thin foils the primary traversal was a small part of the total irradiation.

From the above measurements it was shown that the effects of the target supports were most important for the thinnest target. With the design used the target supports produced a 1 percent effect for the 0.0012-inch target and was negligible for the others.

Misalignment of the target with respect to the synchrotron beam did not change the direct positron production but decreased the yield from the double effect for a constant integrated bremsstrahlung beam. The effect was more important for the thick targets. Unfortunately the target was not aligned directly with the synchrotron beam, but on a model of the synchrotron donut. While the alignment with the model was better than 3° an over-all misalignment uncertainty of about 5° was used. This introduced uncertainties of 0 percent, 1 percent, 4 percent, and 9 percent for the 0.0012, 0.0040, 0.0104, and 0.0160 inch targets, respectively.

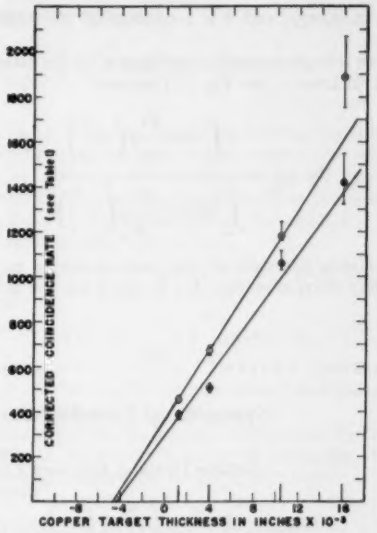


FIG. 5. Corrected positron counting rate as a function of the target thickness. Data taken from the last column of Table I. Upper curve: data for positrons with 0.78 of the energy of the incident beam. Lower curve: data for positrons with 0.83 of the energy of the incident electron beam.

(4) Other sources of errors were considered, such as electronics stability, beam fluctuations, etc., but no corrections were needed for them.

## VII. CONCLUSIONS

The results of this experiment were compared to the theoretical work of Bhabha.[7] He showed that within the accuracy of his calculations the Weizsaker-Williams approximation gave the same result as the usual quantum mechanical treatment.

In this approximation one essentially compares the virtual quanta spectrum associated with the incident electron for producing the direct pair production to the bremsstrahlung gamma-rays for the double process. It is assumed that the cross section for pair production is the same for the virtual and real gamma-rays.

The virtual gamma-ray spectrum is given by the formula:

$$N(\gamma)d\gamma=\frac{2\pi}{137}\frac{d\gamma}{\gamma}\log\left(\frac{k}{\gamma}\right), \tag{8}$$

where $N$ is the number of quanta with energy between $\gamma$ and $\gamma+d\gamma$; $\gamma$ is the ratio of the quanta to the incident

electron energy; and $k$ is a constant of the order of unity.

With this approximation the formula for the extrapolated thickness $t_0$ [see Eq. (7)] becomes

$$|t_0| = \frac{2S}{D} = \frac{2\int_n^1 N(\gamma)\frac{d\gamma}{\gamma}\phi\left(\gamma,\frac{n}{\gamma}\right)}{\int_n^1 \Psi(E_s,\gamma)\frac{d\gamma}{\gamma}\phi\left(\gamma,\frac{n}{\gamma}\right)}, \quad (9)$$

where $n$ is the ratio of the positron energy to the incident electron energy, $E_s$; $\Psi$ and $\phi$ are the Bethe-Heitler formulas[3,4] for bremsstrahlung and pair production, respectively; and $N$ and $\gamma$ are the same as in Eq. (8). Substituting the result of this experiment for $t_0$ the arbitrary constant $k$ in the formula for the virtual quanta spectrum was calculated:

$$k = 1.6 \pm 0.2. \quad (10)$$

This is in agreement with the Weizsaker-Williams approximation.

I wish to thank Professor R. R. Wilson for his continuous interest and guidance. The author is also indebted to Professor D. R. Corson for measuring the beam energy for this experiment.

PHYSICAL REVIEW VOLUME 88, NUMBER 4 NOVEMBER 15, 1952

# Symmetrical Pseudoscalar Meson Theory of Nuclear Forces*

JOSEPH V. LEPORE
*Radiation Laboratory, Department of Physics, University of California, Berkeley, California*

(Received July 25, 1952)

Nuclear forces yielded by the symmetrical pseudoscalar theory are discussed in terms of a perturbation expansion. It is shown that, up to terms in the square of the coupling constant, the pseudoscalar coupling is equivalent to a scalar pair coupling of the pseudoscalar field plus a pseudovector coupling of that field. The dominant contribution to the fourth-order nucleon potential is then obtained in a simple way by using this result.

## INTRODUCTION

THE nuclear force given by the symmetrical pseudoscalar meson theory with pseudoscalar coupling has been re-examined in recent years by a number of authors[1] treating the meson-nucleon interaction as weak. They have shown that the contribution to these forces due to processes involving transport of momentum between nucleons by a pair of mesons are larger than those due to a single meson. The pseudoscalar character of the meson implies that simultaneous emission or absorption of $S$-state meson pairs by a single nucleon cannot involve nucleon spin change. Similarly the symmetrical theory implies that there can be no isotopic spin change for these processes. As a consequence the forces due to them are spin and charge independent.

The importance of these effects suggests that one should be able to exhibit them explicitly in the meson-nucleon interaction Hamiltonian. In what follows the nuclear forces are obtained in a simple manner by taking advantage of this possibility. Besides having the aforementioned properties it is shown that these forces are highly singular and have a range of half the meson Compton wavelength.

* This work was performed under the auspices of the AEC.

[1] K. M. Watson and J. V. Lepore, Phys. Rev. **76**, 193 (1949) and Phys. Rev. **76**, 1157 (1949); H. A. Bethe, Phys. Rev. **76**, 191 (1949); Y. Nambu, Prog. Theoret. Phys. **5**, 4, 614 (1950); R. P. Feynman, California Institute of Technology lecture notes (unpublished).

## I. TRANSFORMATION OF THE HAMILTONIAN

The equation of motion, in the interaction representation,[2] of the state vector, $\Psi[\sigma]$, of the coupled meson and nucleon fields is determined by the coupling Hamiltonian

$$H(x) = if\bar{\psi}(x)\gamma_5\tau_a\psi(x)\phi_a(x). \quad (1)$$

Here and in the following $\psi$, $\bar{\psi}$, $\phi$ represent the nucleon and meson field variables, $\tau_a$ is the nucleon isotopic spin and $\gamma_5 = \gamma_1\gamma_2\gamma_3\gamma_4$ is the Dirac pseudoscalar. Units are chosen so $\hbar = c = 1$ and the meson and nucleon masses are $\mu$ and $K_0$, respectively.

If one now applies the transformation $e^{iS[\sigma]}$ used by Dyson,[3]

$$S[\sigma] = -\frac{if}{2K_0}\int d\sigma_\mu\bar{\psi}(x)\gamma_\mu\gamma_5\tau_a\phi_a(x)\psi(x), \quad (2)$$

to the state vector $\Psi[\sigma]$,

$$\Psi[\sigma] = e^{iS[\sigma]}\Psi'[\sigma], \quad (3)$$

one finds that the new Hamiltonian is, up to terms in $f^3$,

$$H'(x) = H(x) - i[S[\sigma], H(x)] + \frac{\delta S[\sigma]}{\delta\sigma(x)} - \frac{i}{2}\left[S[\sigma], \frac{\delta S[\sigma]}{\delta\sigma(x)}\right]. \quad (4)$$

[2] J. S. Schwinger, Phys. Rev. **74**, 1439 (1948).
[3] F. J. Dyson, Phys. Rev. **73**, 929 (1948).

The choice of $S[\sigma]$ insures that the new Hamiltonian contains no term in $H(x)$, since

$$\frac{\delta S[\sigma]}{\delta\sigma(x)}=-H(x)-\frac{if}{2K_0}\bar{\psi}(x)\gamma_\mu\gamma_5\tau_\alpha\partial_\mu\phi_\alpha(x)\psi(x). \quad (5)$$

If this expression for $\delta S[\sigma]/\delta\sigma(x)$ is inserted in Eq. (4) one finds that the commutators can be readily evaluated to give[4]

$$\begin{aligned}H'(x)&=(f^2/2K_0)\bar{\psi}(x)\psi(x)\phi_\alpha{}^2(x)\\&-(if/2K_0)\bar{\psi}\gamma_\mu\gamma_5\tau_\alpha\partial_\mu\phi_\alpha(x)\psi(x)\\&+\tfrac{1}{2}(f/2K_0)^2[\eta_\mu\bar{\psi}(x)\gamma_\mu\gamma_5\psi(x)]^2\\&-(f/2K_0)^2\bar{\psi}(x)\gamma_\mu\epsilon_{\alpha\beta\gamma}\tau_\alpha\phi_\beta(x)\partial_\mu\phi_\gamma(x)\psi(x). \quad (6)\end{aligned}$$

The main terms in $H'(x)$ correspond to a scalar pair coupling of a pseudoscalar field plus two terms corresponding to the usual pseudovector coupling. The important thing to notice is that only a single power of the nucleon rest mass is contained in the denominator of the pair coupling. A similar result has been obtained by Foldy[5] using a different canonical transformation. It can also be shown that the scalar pair coupling yields the dominant contribution to the nuclear forces in a strong coupling approximation.[6]

## II. DETERMINATION OF THE NUCLEAR FORCES

The interaction Hamiltonian, $H'(x)$, may now be treated by standard Feynman-Dyson techniques to yield the nuclear forces. The second-order nuclear force due to the pseudovector coupling has been obtained by many authors[7] so only the force yielded by the pair coupling will be discussed here.

The term in the scattering matrix corresponding to the lowest order effect involving two nucleons of the scalar pair coupling is

$$S_4=\frac{-3f^4}{16K_0^2}\int dx_1\int dx_2\bar{\psi}(x_1)\psi(x_1)\bar{\psi}(x_2)\psi(x_2)\times\Delta_F{}^3(x_1-x_2). \quad (7)$$

$\Delta_F(x)$ is the Feynman $\Delta$-function as defined by Dyson.[8]

The nuclear force may be inferred from this expression by replacing all quantities in Eq. (7) by their appropriate nonrelativistic approximation. One finds, in the center of momentum system, for initial and final nucleon momenta $P_\mu$, $Q_\mu$; $P_\mu'$, $Q_\mu'$:

$$S_4=-2\pi i\delta(P_0'+Q_0'-P_0-Q_0)(P'Q'|V_4(r)|PQ), \quad (8)$$

where

$$V_4(r)=-\frac{3f^4}{16K_0^2}\int_{-\infty}^{\infty}dt\Delta_F{}^2(t^2-r^2), \quad (9)$$

and $(r, t)=(x_1-x_2, t_1-t_2)$, the relative coordinates of the two nucleons.

The integral in Eq. (9) may be evaluated by transforming to momentum space or by using one of the integral representations[8] for $\Delta_F(x)$. One finds

$$V_4(r)=-\left(\frac{f^2}{4\pi}\right)^2\left(\frac{\mu}{2K_0}\right)^2\frac{3\mu}{\pi(\mu r)^2}\int_{\mu r}^{\infty}K_0(2\lambda)d\lambda+\text{contact term} \quad (10)$$

for the pair-exchange nuclear potential. There are, of course, other terms in the nuclear potential proportional to $f^4$; these are, however, much smaller and contribute less than ten percent to the nucleon-nucleon interaction.

At small distances $V_4(r)$ represents a highly singular potential:

$$V_4(r)\sim(\mu r)^{-1}\ln(\mu r), \quad (11)$$

whereas for large distances it has half the range of a Yukawa potential:

$$V_4(r)\sim(\mu r)^{-5/2}e^{-2\mu r}. \quad (12)$$

This potential has been studied by Lévy[9] in connection with a hard core model for the nuclear forces.

[4] J. V. Lepore, Phys. Rev. **87**, 209 (1952).
[5] L. L. Foldy, Phys. Rev. **84**, 168 (1951).
[6] J. V. Lepore, Phys. Rev. **82**, 310 (1951).
[7] W. Pauli, *Meson Theory of Nuclear Forces* (Interscience Publishers, Inc., New York, 1948), p. 7.
[8] F. J. Dyson, Phys. Rev. **75**, 486 (1949).
[9] M. Lévy, Phys. Rev. **86**, 806 (1952).

# Proton Triton Interaction*,†

J. S. McIntosh, R. L. Gluckstern, and S. Sack
*Yale University, New Haven, Connecticut*

(Received July 10, 1952)

A phase shift analysis of the Los Alamos data on $p$-T scattering for incident protons of 0.708 to 2.548 Mev is carried out using singlet and triplet $s$ and $p$ phase shifts. The large $p$ wave phase shifts obtained are shown to be consistent with the suggested $^1P$ resonant level of the $\alpha$-particle. The effect of absorption associated with the $T(p,n)He^3$ reaction is taken into account by means of a schematic resonance model. A satisfactory fit is obtained with attractive singlet and triplet potentials of depths ~46 Mev and ~11 Mev, respectively. The singlet depth is chosen to give the observed bound state of the $\alpha$-particle.

## INTRODUCTION

DURING the last few years extensive experimental investigations of the interactions of protons and tritons have been carried out at Los Alamos and the University of Minnesota. Differential cross sections for elastic scattering, $T(p,p)T$, have been reported by Hemmendinger *et al.*[1,2] for proton energies in the range 0.708 to 2.548 Mev. The energy range has been extended to 3.5 Mev by Claasen *et al.*[3] The angular distribution of neutrons from the reaction $T(p,n)He^3$, which becomes energetically possible for proton energies above 1.019 Mev, has been reported by Jarvis *et al.*[4] for proton energies up to 2.487 Mev. Argo *et al.*[5] have obtained the angular distribution and energy dependence for the reaction $T(p,\gamma)He^4$.

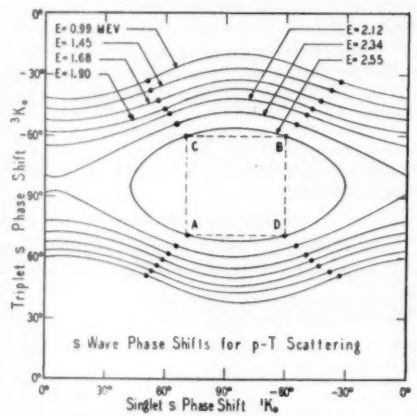


FIG. 1. Triplet $s$ phase shift, $^3K_0$, *vs* singlet $s$ phase shift, $^1K_0$.

In Sec. I a phase shift analysis of the scattering data previously reported[6] is carried out. The differential cross section is fitted with singlet and triplet $s$ and $p$ wave phase shifts with tensor and spin-orbit forces neglected. The absorption of protons from the incident beam, connected with the reaction $T(p,n)He^3$, is ignored in the present treatment, but the effect of absorption on the $s$ wave scattering is considered in Sec. III using the schematic resonance treatment of Breit.[6]

In Sec. II the large $^1P$ phase shifts resulting from the phase shift analysis are related to the resonant state of $He^4$ suggested by Jarvis *et al.*[4] from the $T(p,n)He^3$ data and by Argo *et al.*[5] from the $T(p,\gamma)He^4$ data.

The contents of this paper have been presented in part at the 1952 Washington meeting of the American Physical Society.[7]

## I. PHASE SHIFT ANALYSIS

As a first attempt to fit the $p$-T scattering data, it is assumed that there is a spin dependent central force between the proton and triton which allows for a different interaction in singlet and triplet spin states. A serious defect in this model is that no account is taken of the reaction $T(p,n)He^3$ which competes with elastic scattering for incident proton energies above 1.019 Mev. A schematic resonance treatment to take account of the absorption due to the reaction is discussed in Sec. III.

On the assumption of only spin dependent central forces the cross section for $p$-T scattering may be written as

$$\sigma(\theta)=\tfrac{1}{4}\cdot{}^1\sigma(\theta)+\tfrac{3}{4}\cdot{}^3\sigma(\theta), \qquad (1)$$

where

$$^i\sigma(\theta)=|-(\eta/2ks^2)+k^{-1}\sum_{L=0}^{\infty}(2L+1)P_L(\cos\theta)\sin{}^iK_L \times\exp i[{}^iK_L+2(\sigma_L-\sigma_0)+\eta\ln s^2]|^2, \quad j=1,3 \qquad (2)$$

and $\theta$ = scattering angle in the center-of-mass system, $v$ = velocity of incident proton, $\mu$ = reduced mass of

* Assisted by the joint program of the ONR and AEC.

† Part of a dissertation submitted by J. S. McIntosh for the degree of Doctor of Philosophy at Yale University.

[1] Taschek, Jarvis, Hemmendinger, Everhart, and Gittings, Phys. Rev. **75**, 1361 (1949).

[2] Hemmendinger, Jarvis, and Taschek, Phys. Rev. **76**, 1137 (1949).

[3] Claasen, Brown, Freier, and Stratton, Phys. Rev. **82**, 589 (1951).

[4] Jarvis, Hemmendinger, Argo, and Taschek, Phys. Rev. **79**, 929 (1950).

[5] Argo, Gittings, Hemmendinger, Jarvis, and Taschek, Phys. Rev. **78**, 691 (1950).

[6] G. Breit, Phys. Rev. **69**, 472 (1946).

[7] McIntosh, Gluckstern, and Sack, and Freeman, Phys. Rev. **87**, 237 (1952).

TABLE I. $p$-T scattering phase shift fits for possibilities $A$, $B$, $C$, $D$. All angles are expressed in degrees.

| $E_{Mev}$ | $^1K_0$ | $^1K_0$ | $^3K_1$ | $^1K_1$ | $^3K_1$ | $^1K_1$[a] |
|---|---|---|---|---|---|---|
| | | | Possibility $A$ | | | |
| 0.990 | 51 | 51 | −15½ | 25 | 2 | −38½ |
| 1.108 | 49½ | 49½ | −8 | 19 | 4½ | −23 |
| 1.236 | 49 | 49 | −10½ | 21½ | 4 | −28 |
| 1.450 | 52½ | 52½ | −11½ | 24 | 4 | −31 |
| 1.678 | 56½ | 56½ | −12½ | 23 | 3½ | −32 |
| 1.900 | 60 | 60 | −14 | 25 | 3 | −36 |
| 2.117 | 62 | 62 | −16 | 33 | 4 | −46 |
| 2.335 | 66 | 66 | −17 | 32 | 2 | −47 |
| 2.548 | 71 | 71 | −18 | 34 | 1 | −52 |
| | | | Possibility $B$ | | | |
| $E_{Mev}$ | $^1K_0$ | $^1K_0$ | $^3K_1$ | $^1K_1$ | $^1K_1$ | $^1K_1$[a] |
| 0.990 | −33 | −33 | 19 | −10 | 5½ | 34½ |
| 1.108 | −32 | −32 | 11 | −3 | 4 | 18½ |
| 1.236 | −33 | −33 | 13 | −6 | 4 | 23 |
| 1.450 | −37½ | −37½ | 14½ | −10 | 3 | 27½ |
| 1.678 | −42½ | −42½ | 15½ | −12 | 3 | 30 |
| 1.900 | −46½ | −46½ | 17½ | −15 | 3 | 35 |
| 2.117 | −49½ | −49½ | 20 | −23 | 2 | 45 |
| 2.335 | −54½ | −54½ | 21 | −21 | 3½ | 47 |
| 2.548 | −60 | −60 | 23 | −23 | 4 | 51 |
| | | | Possibility $C$ | | | |
| $E_{Mev}$ | $^3K_0$ | $^1K_0$ | $^3K_1$ | $^1K_1$[a] | $^3K_1$ | $^1K_1$ |
| 0.990 | −33 | 51 | 2½ | −28½ | 22 | 16 |
| 1.108 | −32 | 49½ | 2½ | −13 | 13 | 13 |
| 1.236 | −33 | 49 | 3 | −19 | 15 | 15 |
| 1.450 | −37½ | 52½ | 1½ | −24 | 16 | 18 |
| 1.678 | −42½ | 56½ | 1 | −28 | 16½ | 18 |
| 1.900 | −46½ | 60 | 1½ | −32 | 18 | 20 |
| 2.117 | −49½ | 62 | 0 | −42 | 20 | 29 |
| 2.335 | −54½ | 66 | 1½ | −43½ | 22 | 24 |
| 2.548 | −60 | 71 | 2 | −49 | 24 | 26 |
| | | | Possibility $D$ | | | |
| $E_{Mev}$ | $^3K_0$ | $^1K_0$ | $^3K_1$ | $^1K_1$[a] | $^3K_1$ | $^1K_1$ |
| 0.990 | 51 | −33 | −1½ | 44 | −12½ | −18 |
| 1.108 | 49½ | −32 | 3 | 28 | −7 | −11 |
| 1.236 | 49 | −33 | 3 | 32 | −9 | −13 |
| 1.450 | 52½ | −37½ | 3 | 35 | −10½ | −16 |
| 1.678 | 56½ | −42½ | 2 | 35 | −12 | −18 |
| 1.900 | 60 | −46½ | 1 | 38 | −13½ | −19 |
| 2.117 | 62 | −49½ | 2 | 49 | −15 | −29 |
| 2.335 | 66 | −54½ | 0 | 49 | −17 | −27 |
| 2.548 | 70 | −60 | −2 | 52 | −18 | −31 |

[a] "Resonance" fits (see Sec. II).

system $= M_P M_T/(M_P+M_T) \cong \frac{3}{4}M$, $k=\mu v/\hbar$, $\eta=e^2/\hbar v$, $s=\sin(\theta/2)$, $L=$ orbital angular momentum, $^jK_L=$ phase shift for $L$ and $j=1, 3$, $\sigma_L=$ Coulomb phase shift.

It is not possible to fit the data with $s$ wave phase shifts alone because of the large observed cross section for backward scattering. For this reason $p$ wave phase shifts ($^1K_1$, $^3K_1$) have to be included in the analysis in addition to the two $s$ wave phase shifts ($^1K_0$, $^3K_0$), and the total of four adjustable parameters is available to fit the data.

The scheme for determining the best phase shifts at each energy is as follows:

(a) The cross section at $\theta=90°$, where the $p$ wave contributions vanish, determines a relation between the two $s$ wave phase shifts at each energy. Curves of $^1K_0$ *vs* $^3K_0$, with minor adjustments explained in (c), are plotted in Fig. 1 for the experimental proton energies.

(b) Calculations for the best $p$ wave phase shifts are then carried out by trial and error for various points on each $^1K_0$ *vs* $^3K_0$ curve of Fig. 1. Four arbitrary pairs of $^1K_0$, $^3K_0$ chosen for convenience are the two pairs for $^1K_0=^3K_0$ (points denoted by $A$ and $B$) and the two corresponding pairs for $^1K_0$ and $^3K_0$ opposite in sign (points denoted by $C$ and $D$, with $^1K_0(C)=^1K_0(B)$, $^3K_0(C)=^3K_0(A)$ and $^1K_0(D)=^1K_0(A)$, $^3K_0(D)=^3K_0(B)$. For each pair ($^1K_0$, $^3K_0$), two distinct pairs ($^1K_1$, $^3K_1$) are found which fit the data within the quoted experimental error.

(c) Slight readjustments are made in $^1K_0$, $^3K_0$, $^1K_1$ and $^3K_1$ (as mentioned in (a)) to minimize the mean square deviation of the calculated fits from the experimental cross sections.

The adjusted values of $^1K_0$, $^3K_0$ are the ones plotted in Fig. 1 and the values of ($^1K_0$, $^3K_0$), ($^1K_1$, $^3K_1$) for possibilities $A$, $B$, $C$, $D$ are given in Table I. Additional calculations have been carried out at $E=0.990$, 1.450 and 2.548 Mev to determine the values of ($^1K_1$, $^3K_1$) for values of ($^1K_0$, $^3K_0$) other than those corresponding to

TABLE II. $p$-T scattering phase shift fits for $E=0.990$, 1.450, 2.548 Mev. All angles are expressed in degrees.

| $^3K_0$ | $^1K_0$ | $^3K_1$ | $^1K_1$ | $^3K_0$ | $^1K_0$ | $^3K_1$ | $^1K_1$ |
|---|---|---|---|---|---|---|---|
| | | | $E=0.990$ Mev | | | | |
| −42 | 9 | 10 | −26 | −42 | 9 | 9 | 35 |
| −33 | 51 | 2½ | −28½ | −33 | 51 | 22 | 16 |
| −22 | −81 | 16½ | −19½ | −22 | −81 | 19 | 22½ |
| −33 | −33 | 19 | −10 | −33 | −33 | 5½ | 34½ |
| 60 | 9 | −1½ | −35 | 60 | 9 | −1½ | 45 |
| 51 | 51 | 2 | −38½ | 51 | 51 | −15½ | 25 |
| 40 | −81 | −10½ | −24 | 40 | −81 | −13½ | 27½ |
| 51 | −33 | −12½ | −18 | 51 | −33 | −1½ | 44 |
| | | | $E=1.450$ Mev | | | | |
| $^3K_0$ | $^1K_0$ | $^3K_1$ | $^1K_1$ | $^3K_0$ | $^1K_0$ | $^3K_1$ | $^1K_1$ |
| −47 | 7½ | 8 | −22 | −47 | 7½ | 6 | 29 |
| −45 | 27½ | 2 | −23½ | −45 | 27½ | 13½ | 22 |
| −37 | 52 | 1½ | −24 | −37 | 52 | 16 | 18 |
| −30 | 77½ | 7 | −23 | −30 | 77½ | 15 | 19 |
| −28 | −82½ | 11½ | −17½ | −28 | −82½ | 12½ | 22 |
| −30 | −62½ | 14 | −13 | −30 | −62½ | 8½ | 26½ |
| −37½ | −37½ | 14½ | −10 | −37½ | −37½ | 3 | 27½ |
| −40 | −30 | 14½ | −10 | −40 | −30 | 2 | 27½ |
| −45 | −12½ | 14 | −12½ | −45 | −12½ | 2 | 28 |
| 43 | −82½ | −7½ | −22½ | 43 | −82½ | −9 | 26½ |
| 45 | −62½ | −10½ | −17½ | 45 | −62½ | −4½ | 32½ |
| 52½ | −37½ | −10½ | −16 | 52½ | −37½ | 3 | 35 |
| 60 | −12½ | −8 | −21½ | 60 | −12½ | 4½ | 35 |
| 62 | 7½ | −½ | −29½ | 62 | 7½ | 1 | 36 |
| 60 | 27½ | 4½ | −30½ | 60 | 27½ | −7 | 30½ |
| 52½ | 52½ | 4 | −31 | 52½ | 52½ | −11½ | 24 |
| 45 | 77½ | −2½ | −29 | 45 | 77½ | −11½ | 23½ |
| | | | $E=2.548$ Mev | | | | |
| $^3K_0$ | $^1K_0$ | $^3K_1$ | $^1K_1$ | $^3K_0$ | $^1K_0$ | $^3K_1$ | $^1K_1$ |
| 71 | 71 | 1 | −52 | 71 | 71 | −18 | 35 |
| 71 | −60 | −18 | −30 | 71 | −60 | −2 | 52 |
| −85 | −30 | −21 | 24 | −85 | −32 | −22 | 30 |
| −60 | −60 | 4 | 51 | −60 | −60 | 23 | −23 |
| −60 | 71 | 24 | 26 | −60 | 71 | 2 | −49 |
| −85 | 42 | 22 | 28 | −85 | 42 | −21 | −21 |
| 71 | 71 | 1 | −52 | 71 | 71 | −18 | 35 |

TABLE III. Rough calculation of phase shifts from Minnesota data. All angles are expressed in degrees.

| $E_{Mev}$ | $^3K_0$ | $^1K_0$ | $^3K_1$ | $^1K_1$ | $^3K_0$ | $^1K_0$ | $^3K_0$ | $^1K_1$ |
|---|---|---|---|---|---|---|---|---|
| 2.55 | 64 | 64 | −16 | 46 | 64 | 64 | 3 | −60 |
| 2.74 | 66 | 66 | −17 | 49 | 66 | 66 | 1 | −65 |
| 3.03 | 66 | 66 | −8 | 68 | 66 | 66 | 4 | −73 |
| 3.25 | 67 | 67 | −2 | 87 | 67 | 67 | −2 | −92 |
| $E_{Mev}$ | $^3K_0$ | $^1K_0$ | $^3K_1$ | $^1K_1$ | $^3K_0$ | $^1K_0$ | $^3K_1$ | $^1K_1$ |
| 2.55 | −53 | 64 | −4 | −53 | −53 | 64 | 19 | 41 |
| 2.74 | −55 | 66 | −4 | −58 | −55 | 66 | 18 | 45 |
| 3.03 | −55 | 66 | −9 | −60 | −55 | 66 | 9 | 62 |
| 3.25 | −57 | 67 | −8 | −69 | −57 | 67 | 6 | 73 |
| $E_{Mev}$ | $^3K_0$ | $^1K_0$ | $^3K_1$ | $^1K_1$ | $^3K_0$ | $^1K_0$ | $^3K_1$ | $^1K_1$ |
| 2.55 | −53 | −53 | 18 | −39 | −53 | −53 | −2 | 55 |
| 2.74 | −55 | −55 | 18 | −42 | −55 | −55 | −1 | 59 |
| 3.03 | −55 | −55 | 11 | −58 | −55 | −55 | −6 | 63 |
| 3.25 | −57 | −57 | 9 | −67 | −57 | −57 | −4 | 71 |
| $E_{Mev}$ | $^3K_0$ | $^1K_0$ | $^3K_1$ | $^1K_1$ | $^3K_0$ | $^1K_0$ | $^3K_1$ | $^1K_1$ |
| 2.55 | 64 | −53 | 0 | 60 | 64 | −53 | −16 | 43 |
| 2.74 | 66 | −55 | −1 | 64 | 66 | −55 | −17 | 46 |
| 3.03 | 66 | −55 | 2 | 72 | 66 | −55 | −11 | 62 |
| 3.25 | 67 | −57 | −1 | 81 | 67 | −57 | −8 | 73 |

points $A$, $B$, $C$, $D$. The results are given in Table II.

In the case of scattering without a Coulomb field there is an indeterminacy in the sign of the calculated phase shifts. Specifically, if the data are fitted by

$$(^1K_0, ^3K_0), (^1K_1, ^3K_1),$$

they will be equally well fitted by

$$(^1K_0, -^3K_0), (^1K_1, -^3K_1);$$
$$(-^1K_0, -^3K_0), (-^1K_1, -^3K_1);$$
$$(-^1K_0, ^3K_0), (-^1K_1, ^3K_1).$$

An analogous situation exists when a Coulomb field is present. Because of the interference between the nuclear and Coulomb scattered waves, the phase shifts of one class are not so simply related to those of another class and corresponding fits in different classes are not equally good. Thus the presence of the Coulomb field

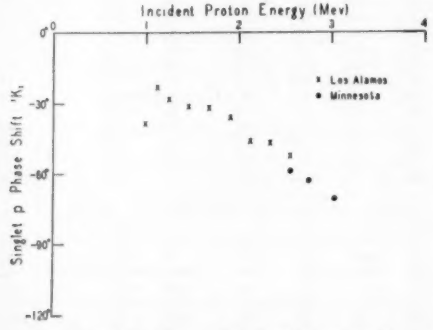


FIG. 2. Singlet $p$ "resonant" phase shift vs energy for $^3K_0=^1K_0>0$ (possibility $A$).

appears to offer the possibility of choosing between the many possible values of the phase shifts.

Unfortunately it does not prove possible to choose a "best" set of phase shifts on the basis of the "best" fit to the experimental data. As was previously mentioned, all sets of phase shifts given in Tables I and II fit the data within the experimental error. However, the various fits do differ from one another significantly at low angles. (At $E=1.450$ Mev and $\theta=15°$ the possible phase shift fits lead to cross sections which differ by as much as a factor of two.) It therefore seems likely that data below $\theta=59°$ will eliminate many of the fits in Tables I and II. In addition it is expected that small $d$ waves (up to 5°) will be necessary in order to obtain satisfactory fits to the low angle data.

The presence of spin-orbit and tensor interactions has been neglected. The introduction of a tensor force, for example, would split the triplet $p$ phase shift into three, giving two additional fitting parameters. The

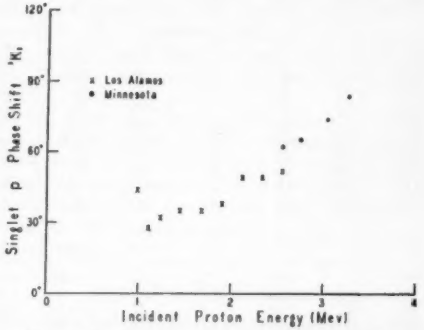


FIG. 3. Singlet $p$ "resonant" phase shift vs energy for $^3K_0=^1K_0<0$ (possibility $B$).

accuracy of the experimental data does not seem to warrant an elaborate investigation employing $p$ wave splitting at the present time.

## II. POSSIBLE $^1P$ RESONANT LEVEL OF $He^4$

A feature of the results in Tables I and II which is surprising is that the magnitude of the $p$ wave phase shifts required for the best fits is considerably larger than would be expected for scattering from a simple potential well. However, these $p$ phase shifts may not be unreasonable if there exists a $^1P$ resonant state of $He^4$ as suggested by Argo *et al.*[5] from considerations of the $T(p,\gamma)He^4$ reaction data. Subsequent measurements of Falk and Phillips[8] are not in agreement with the results of Argo *et al.* and seem to indicate that if a resonant state exists, it occurs at a proton energy above 3.5 Mev. The disagreement may be due to a difference in targets and to the choice of the type of curve

[8] C. E. Falk and G. C. Phillips, Phys. Rev. **83**, 468 (1951).

drawn through the experimental points. In addition Flowers and Mandl[9] have shown that it may be possible to explain the large slope of the yield *vs* energy curve without assuming a resonance. Thus although the existence of the resonant state is far from certain, it may prove helpful to determine whether the large $p$ waves are consistent with the resonance. Such a $^1P$ resonant state would permit large values of $^1K_1$ but would require small $^3K_1$. Half of the fits in Table I (denoted by *) are of this character and are referred to as "resonance" fits, while the others are called "non-resonance" fits.

In order to investigate the variation of $^1K_1$ with energy for the "resonance" fits, rough calculations have been performed with the data of Claasen *et al.*[3] at proton energies from 2.12 to 3.5 Mev. For simplicity calculations were performed only for regions *A*, *B*, *C*, *D* although it is quite unlikely that the true variation of $^1K_0$ and $^3K_0$ with energy will follow any of these possibilities exactly. The results are given in Table III and they join reasonably well with the results obtained from the Los Alamos data.[2]

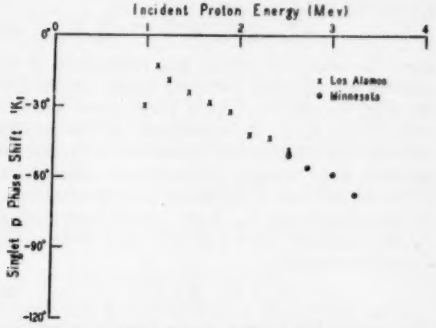


FIG. 4. Singlet $p$ "resonant" phase shift *vs* energy for $^3K_0<0$, $^1K_0>0$ (possibility *C*).

The "resonant" values of $^1K_1$ are plotted against energy in Figs. 2–5 for possibilities *A*, *B*, *C*, *D*. Although wide variation of $^1K_1$ is evident, the absence of points above 3.5 Mev does not permit any definite conclusions about the resonant state. If such a state does occur the variation of $^1K_1$ with energy suggests that it occurs at about 3–4 Mev with a half-width of about 1 Mev. However only possibilities *B* and *D* seem consistent with the usual expectation of a phase shift which increases as the energy increases through the resonance.

From Figs. 3 and 5 it may be seen that possibilities *B* and *D* imply that the singlet $s$ phase shift $^1K_0$ should be negative (equivalent to values between 90° and 180°), but do not imply a restriction on $^3K_0$. It can be shown that the singlet potential well necessary to permit the known ground state of $He^4$ leads to negative values of $^1K_0$ in the energy range 0–5 Mev, so that on the basis of the assumed model, a $^1P$ excited state of $He^4$ is consistent with the information used thus far.

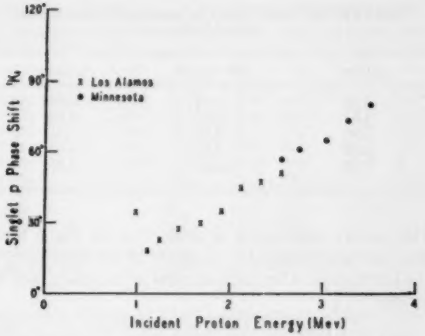


FIG. 5. Singlet $p$ "resonant" phase shift *vs* energy for $^3K_0>0$, $^1K_0<0$ (possibility *D*).

Another point consistent with the "resonance" fits comes from consideration of the strong cusps in the $\sigma(\theta)$ *vs* $E$ curves in Fig. 4 of Hemmendinger *et al.*[2] for low angle scattering. It has been pointed out by Wigner[10] that at the threshold of a reaction, the energy dependence of the elastic scattering cross section may show a cusp. In the present case the cusp is approximately located at 1 Mev, the threshold of the $T(p,n)He^3$ reaction. One expects that near threshold, the neutrons, which are predominantly $s$ wave, come directly from the $s$ wave protons, and therefore the cross section for scattering should break sharply downward. This is not the case for $T(p,n)He^3$, where the scattering cross section seems to increase sharply. The increase can be accounted for by the removal of a large destructive $s$–$p$ interference term which arises from large $p$ waves. This is indeed the case for angles less than 90° for the "resonance" fits. These fits correspond to values of $^1K_0$ and $^1K_1$ which are always opposite in sign, while $^3K_1$ is sufficiently small so that the triplet $s$–$p$ interference may be neglected for the immediate purpose.

Consideration of the angular distribution of neutrons from the reaction $T(p,n)He^3$ furnishes further evidence favoring the "resonance" fits. Jarvis *et al.*[4] in their paper reporting the experimental results, analyzed the angular distribution in a power series in $\cos\theta$ and found that the coefficient of $\cos^2\theta$ rises rapidly with energy, suggesting a $p$ wave resonance. The question may be examined more quantitatively with the use of a schematic resonance treatment. It is assumed for the energies here considered (<1.35 Mev above threshold) that only $s$ and $p$ wave protons contribute to the reaction, although as pointed out in Sec. III, there is probably some $d$ wave contribution for the higher energies.

[9] B. H. Flowers and F. Mandl, Proc. Roy. Soc. (London) **A206**, 131 (1951).

[10] E. Wigner, Phys. Rev. **73**, 1002 (1948).

TABLE IV. Resonance widths for assumed $^1P$ resonance at $E^R=2.0$ Mev.

| $E$(Mev) | $(E^R-E')/\Gamma_p$ | $\Gamma_p$(Mev) |
|---|---|---|
| 1.62 | 1.10 | 0.73 |
| 1.83 | 0.81 | 0.80 |
| 2.05 | 0.58 | 0.83 |
| 2.20 | 0.45 | 0.82 |
| 2.36 | 0.31 | 0.81 |

The further assumption is made that all the $p$ wave neutrons are produced by a single $^1P$ resonant level of the $He^4$ system. The reaction cross section may then be written

$$^1\sigma_{pn}(\theta)=(1/k^2)\,|\,a_0+3\cos\theta a_1\,|^2, \tag{3}$$

where $a_0$ is the $s$ wave contribution and $a_1$ is given by

$$a_1=(\Gamma_p\Gamma_n)^{\frac{1}{2}}\exp i(\delta_p+\delta_n)/(E^R-E'-i(\Gamma_p+\Gamma_n)), \tag{4}$$

where $\Gamma_p$ and $\Gamma_n$ are the level widths for protons and neutrons, respectively, $\delta_p$ and $\delta_n$ are protons and neutron phase shifts, $E^R$ is the resonant energy associated with the compound level, and $E'$ is the energy in the center-of-mass system. The effects of the $s$ wave are eliminated by considering

$$^1\sigma_{pn}(45°)+{}^1\sigma_{pr}(135°)-2\,{}^1\sigma_{pn}(90°)=(9/k^2)\,|\,a_1\,|^2. \tag{5}$$

For the "resonance" fits, $^3K_1\approx 0$ and therefore

$$^3\sigma_{pn}(45°)+{}^3\sigma_{pn}(135°)-2\,{}^3\sigma_{pn}(90°)\cong 0. \tag{6}$$

Since $\sigma_{pn}=(3/4)\,{}^3\sigma_{pn}+(1/4)\,{}^1\sigma_{pn}$,

$$\sigma_{pn}(45°)+\sigma_{pn}(135°)-2\sigma_{pn}(90°)=(9/4k^2)\,|\,a_1\,|^2$$
$$=(9/4k^2)(\Gamma_n/\Gamma_p)(\Gamma_p^2/[(E^R-E')^2+\Gamma_p^2]), \tag{7}$$

where $\Gamma_p$ is written in place of $\Gamma=\Gamma_p+\Gamma_n$ since $\Gamma_n\cong 0$ near threshold. One now writes

$$\Gamma_n/\Gamma_p\approx(v_n/v_p)^{2L+1}/[(1+\eta^2)2\pi\eta/(\exp 2\pi\eta-1)], \tag{8}$$

where the factor in $\eta$ is related to the Coulomb barrier factor $C_l^2$ for $p$ waves. In view of other uncertainties no attempt is being made to be precise about taking into account the correction factor for the Coulomb field. Substitution of (8) into (7) gives a roughly constant value of $\Gamma_p$ if $E^R$ is set equal to 2.0 Mev, corresponding to a laboratory energy of 2.7 Mev as shown in Table IV.

The angular distribution of the reaction neutrons thus suggests a broad $^1P$ resonance at a laboratory energy of $\sim$2.7 Mev with $\Gamma_p$ in the laboratory system $\approx$1.1 Mev. These figures are consistent with the broad resonance, $\Gamma\approx$1 Mev indicated by the "resonance" fits of the $p$-T scattering data [Figs. 2–5]. The above calculation further agrees with the scattering analysis in placing the $^1P$ resonant level of $He^4$ somewhat higher than the 2.5 Mev suggested by Argo *et al.*[b] and Jarvis *et al.*[4] The possibility of $d$ wave contributions to the neutron cross section, discussed in Sec. III, makes the numerical results somewhat uncertain.

## III. SCHEMATIC RESONANCE TREATMENT OF THE $S$ WAVES

For incident protons of energy 1.019 Mev and higher, neutrons from the reaction $T(p,n)He^3$ are observed among the outgoing particles.[4] The reaction cross section rises sharply with energy, and for 2.5-Mev protons it is over 20 percent of the scattering cross section. Thus the effect of absorption from the proton beam is large, and the phase shift analysis of the preceding sections must be modified to take the reaction into account. It has been shown by Ostrofsky, Breit, and Johnson[11] and others[12] that the effect of absorption may be accounted for by the introduction of a complex potential energy, which leads to complex phase shifts. A somewhat more definite model is provided by the schematic resonance treatment of Breit.[6,13] From this point of view the total singlet or triplet cross section, in the case of no Coulomb field, for a particle incident in the $p$th mode and leaving in the $q$th mode is given by

$$\sigma_{p\to q}=(2L+1)(\Lambda_p^2/\pi)\,|\,\delta_{pq}\exp(-i\delta_p)\sin\delta_p$$
$$+\textstyle\sum_j G_{qj}G_{pj}/(E_j^R-E'-i\sum_q\Gamma_{qj})\,|^2, \tag{9}$$

where the effects of relative spin orientations of the particles are neglected. Here the $p$ and $q$ modes may be taken to refer to $s$ wave protons and neutrons, respectively, $\Lambda_p$ is the wavelength of the incident protons, $\delta_p$ is the phase shift produced by the effective potential, $E'$ is the energy in the center-of-mass system, $E_j^R$ is the real part of the energy corresponding to the $j$th compound level, $\Gamma_{qj}$ is the partial level width of the $q$th mode and the $j$th level, and $G_{qj}$ is related to the $\Gamma_{qj}$ by the equation:

$$|G_{qj}|^2=\Gamma_{qj}\textstyle\sum_r|\,\xi_j^r\,|^2. \tag{10}$$

The sum of the squares of the transformation coefficients[6] $\sum_r|\,\xi_j^r\,|^2$ is never less than unity, reducing to unity in the one-level case. It is seen from Eq. (9) that the model gives a scattered wave consisting of two parts, one of which is such as would take place from a potential and another consisting of contributions associated with resonance levels. The manner in which the resonance

TABLE V. Values of $^1T$, $^3T$ for $R=(^3T)^2/(^1T)^2=0.5$, 1.0, 2.0.[a]

| Incident energy | $R=0.5$ | | $R=1.0$ | | $R=2.0$ | |
|---|---|---|---|---|---|---|
| | $^1T$ | $^3T$ | $^1T$ | $^3T$ | $^1T$ | $^3T$ |
| 0.990 Mev | 0.309 | 0.223 | 0.244 | 0.244 | 0.185 | 0.262 |
| 1.108 | 0.328 | 0.236 | 0.259 | 0.259 | 0.196 | 0.277 |
| 1.236 | 0.346 | 0.249 | 0.273 | 0.273 | 0.206 | 0.293 |
| 1.450 | 0.381 | 0.275 | 0.301 | 0.301 | 0.228 | 0.322 |
| 1.678 | 0.416 | 0.300 | 0.329 | 0.329 | 0.249 | 0.352 |
| 1.900 | 0.450 | 0.325 | 0.356 | 0.356 | 0.269 | 0.381 |
| 2.117 | 0.483 | 0.348 | 0.381 | 0.381 | 0.288 | 0.409 |
| 2.335 | 0.517 | 0.374 | 0.409 | 0.409 | 0.310 | 0.439 |
| 2.548 | 0.551 | 0.398 | 0.435 | 0.435 | 0.329 | 0.467 |

[a] See Eqs. (17) and (18) for definitions of $^3T$ and $^1T$.

[11] Ostrofsky, Breit, and Johnson, Phys. Rev. **49**, 22 (1936).
[12] H. A. Bethe, Phys. Rev. **57**, 1125 (1940).
[13] Breit, Condon, and Present, Phys. Rev. **50**, 825 (1936).

level parameters $G$, $E^R$, $\Gamma$ are connected with the initial parameters of the model does not matter in the present application, the form of the answer being the main feature used below. The equations are applied here to $s$ wave scattering, and it is assumed that $s$ wave neutrons are produced by incident $s$ wave protons. The subscripts $p$ and $n$ are henceforth used for the proton and neutron $s$ wave modes, respectively. To obtain the $s$ wave cross section the reaction data are taken at 90°, where the $p$ wave contributions vanish. Introduction of Coulomb terms then leads to the differential cross section at 90°:

$$\begin{aligned}\sigma_{p\to q}(90°)=k^{-2}\{&\tfrac{3}{4}|-\eta\exp[i(\eta\ln 2-2{}^3\delta_0)]\\&+\exp(-i\,{}^3\delta_0)\sin({}^3\delta_0)\\&+\textstyle\sum_j({}^3G_{pj})^2/({}^3E_j{}^R-E'-i\sum_q{}^3\Gamma_{qj})|^2\\&+\tfrac{1}{4}|-\eta\exp[i(\eta\ln 2-2\,{}^1\delta_0)]\\&+\exp(-i\,{}^1\delta_0)\sin({}^1\delta_0)\\&+\textstyle\sum_k({}^1G_{pk})^2/({}^1E_k{}^R-E'-i\sum_q\Gamma_{qk})|^2\}.\end{aligned}\tag{11}$$

$$\begin{aligned}\sigma_{p\to n}(90°)=k^{-2}\{&\tfrac{3}{4}|\textstyle\sum_j({}^3G_{nj})({}^3G_{pj})/({}^3E_j{}^R-E'-i\sum_q{}^3\Gamma_{qj})|^2\\&+\tfrac{1}{4}|\textstyle\sum_k({}^1G_{nk})({}^1G_{pk})/({}^1E_k{}^R-E'-i\sum_q{}^1\Gamma_{ak})|^2\}.\end{aligned}\tag{12}$$

Since it would be hopeless to attempt to ascertain the parameters $G$, $E^R$, $\Gamma$ for all terms in the expansion, the resonance terms are lumped into ${}^3T(E')\exp[i\,{}^3\tau(E')]$ and ${}^1T(E')\exp[i\,{}^1\tau(E')]$, and it is assumed that one may approximate

$$G_{nj}/G_{pj}=(v_n/v_p){}^1C_0{}^{-1},\tag{13}$$

where $v_n$ and $v_p$ are the neutron and proton velocities and

$$C_0{}^2=(2\pi\eta)/[\exp(2\pi\eta)-1].\tag{14}$$

Equation (13) is reasonable since the $G$'s vary approximately as $v^{\frac{1}{2}}$ [see Breit,[6] Eq. (5.4)] and $C_0{}^2$ is included to approximate the effects of the Coulomb barrier for protons. One then has

$$\begin{aligned}\sigma_{p\to p}(90°)=k^{-2}\{&\tfrac{3}{4}|-\eta\exp[i(\eta\ln 2-2\,{}^3\delta_0)]\\&+\exp(-i\,{}^3\delta_0)\sin({}^3\delta_0)+{}^3T\exp(i\,{}^3\tau)|^2\\&+\tfrac{1}{4}|-\eta\exp[i(\eta\ln 2-2\,{}^1\delta_0)]+\\&+\exp(-i\,{}^1\delta_0)\sin({}^1\delta_0)+{}^1T\exp(i\,{}^1\tau)|^2\},\end{aligned}\tag{15}$$

$$\sigma_{n\to p}(90°)=k^{-2}(v_n/v_pC_0{}^2)\{\tfrac{3}{4}({}^3T)^2+\tfrac{1}{4}({}^1T)^2\},\tag{16}$$

where

$$\begin{aligned}&{}^3T(E')\exp[i\,{}^3\tau(E')]\\&\quad=\textstyle\sum_j({}^3G_{pj})^2/({}^3E_j{}^R-E'-i\sum_q{}^3\Gamma_{qj}),\end{aligned}\tag{17}$$

and

$$\begin{aligned}&{}^1T(E')\exp[i\,{}^1\tau(E')]\\&\quad=\textstyle\sum_k({}^1G_{pk})^2/({}^1E_k{}^R-E'-i\sum_q{}^1\Gamma_{qk}).\end{aligned}\tag{18}$$

Six parameters, ${}^1\delta_0$, ${}^3\delta_0$, ${}^1T$, ${}^3T$, ${}^1\tau$, ${}^3\tau$ must now be determined from the experimental information available. It is assumed for the present that

$$R=({}^3T)^2/({}^1T)^2\tag{19}$$

TABLE VI. Values of ${}^1\tau$, ${}^3\tau$ for $R=({}^3T)^2/({}^1T)^2=0.5$, 1.0, 2.0.[a]

| Incident energy | $R=0.5$ | | $R=1.0$ | | $R=2.0$ | |
|---|---|---|---|---|---|---|
| | ${}^1\tau$ | ${}^3\tau$ | ${}^1\tau$ | ${}^3\tau$ | ${}^1\tau$ | ${}^3\tau$ |
| 0.990 Mev | 18.0° | 12.9° | 14.1° | 14.1° | 10.7° | 15.2° |
| 1.108 | 19.1° | 20.3° | 22.4° | 22.4° | 16.7° | 24.0° |
| 1.236 | 35.5° | 24.7° | 27.3° | 27.3° | 20.2° | 29.5° |
| 1.450 | 44.9° | 30.6° | 33.9° | 33.9° | 25.0° | 36.5° |
| 1.678 | 54.0° | 35.7° | 39.8° | 39.8° | 28.9° | 43.2° |
| 1.900 | 64.0° | 40.5° | 45.3° | 45.3° | 32.5° | 49.6° |
| 2.117 | 79.1° | 45.1° | 50.8° | 50.8° | 35.9° | 56.3° |
| 2.335 | ··· | 50.3° | 57.2° | 57.2° | 39.6° | 64.4° |
| 2.548 | ··· | 55.7° | 64.4° | 64.4° | 43.1° | 75.7° |

[a] See Eqs. (17) and (18) for definitions of ${}^1T$, ${}^3T$, ${}^1\tau$, and ${}^3\tau$.

is a constant, that is, that the singlet and triplet resonance terms vary in the same way with energy. Actually this restriction is not a critical one and will be relaxed later. It is made temporarily in order not to deal with too many parameters at once. For any value of $R$, ${}^3T$ and ${}^1T$ can then be calculated and other quantities entering into the equation may be obtained from the known energies. The values of ${}^3\tau$ and ${}^1\tau$ are fixed for any given $R$ by conservation of particles. Since it is assumed that there is no mixing between singlet and triplets, the wave function for protons with either spin state is given by

$$\begin{aligned}&\sin(k_pr_p)+\exp(ik_pr_p)\{\exp(i\delta)\sin\delta+T\exp[i(2\delta+\tau)]\}\\&\quad=-(2i)^{-1}\exp(-ik_pr_p)+\exp(ik_pr_p)\\&\qquad\times\{(2i)^{-1}\exp(2i\delta)+T\exp[i(2\delta+\tau)]\}.\end{aligned}\tag{20}$$

For the practical case the Coulomb field is screened, so its contribution merely adds to $\delta$, which drops out in the final result. Therefore one may here neglect the Coulomb term. Equating incoming and outgoing particle fluxes, one obtains

$$\sin\tau=T\{1+(v_n/v_pC_0{}^2)\}\tag{21}$$

separately for singlets and triplets. Since a choice of $R$ fixes both ${}^1T$ and ${}^3T$, it also fixes both ${}^1\tau$ and ${}^3\tau$. Table V gives ${}^1T$ and ${}^3T$ for $R=\frac{1}{2}$, 1, 2, and Table VI gives the corresponding values of ${}^1\tau$ and ${}^3\tau$ for these choices of $R$.

The phase shifts ${}^1\delta_0$ and ${}^3\delta_0$ remain to be calculated. To find ${}^1\delta_0$, a square well potential model for the singlet $s$ state of $He^4$ is employed. The range of force is taken to be

$$r_0{}^{(1)}=1.5\times10^{-13}\times4^{\frac{1}{2}}=0.238\times10^{-12}\text{ cm}.$$

The depth is chosen to give the bound ${}^1S_0$ state of $He^4$ at 20.5 Mev below the threshold of $T(p,n)He^3$ or 19.75 Mev below $p+T$, as determined by the mass differences. The well depth so determined is $V=-46$ Mev. Various triplet well depths with $r_0{}^{(3)}=r_0{}^{(1)}$ are assumed in order to calculate ${}^3\delta_0$. For all reasonable repulsive wells and for attractive wells, $V=0$ to $\sim-9$ Mev, the phase shifts are too small to reproduce the experimental values of the scattering cross section at 90° for any value of $R$. If the attractive well were deeper than $\sim-14$ Mev, there would exist a bound ${}^3S_0$ level of $He^4$, which is

TABLE VII. Values of triplet well depth necessary to fit the 90° scattering data.

| Incident energy (Mev) | Depth of potential well (Mev) |
|---|---|
| 0.990 | −11 |
| 1.108 | −11 |
| 1.236 | −11 |
| 1.450 | −12 |
| 1.678 | −13 |

unlikely. This limits the triplet well depth to between −9 and −14 Mev. For the lower proton energies and for values of $R$ ranging from $\frac{1}{2}$ to 2, the value of $V$ which reproduces the 90° scattering cross section is $V\cong-11$ Mev. The variation of this triplet well depth with energy is given in Table VII.

In the present analysis the potential well is a substitute for the main effect of many body forces acting inside the nucleus. It takes account of general effects, varying smoothly with energy, while the resonance term is concerned with additional effects caused by the possibility of formation of a semistable "compound" state. It would not be reasonable to demand strict constancy of the depth and range parameters of the well since it is a substitute for many-body effects. One expects nevertheless a $d\mathfrak{F}/\mathfrak{F}dr$ monotonically decreasing with energy and an approximate fit to the known stable states of the four-particle system.

It may be noted from Table VII that for energies greater than 1.450 Mev the well appears to deepen. It is in fact not possible to obtain a reasonable fit for energies greater than 2 Mev. However, the calculations do not hold for these energies since the assumption that the 90° cross section is due to $s$ waves alone may no longer be valid. Jarvis *et al.*[4] have shown that for the reaction T($p$,$n$)He$^3$ the coefficient of $\cos^3\theta$ in the expansion of $\sigma(\theta)$ in powers of $\cos\theta$ may not be neglected above 1.45 Mev and becomes larger above 2 Mev. The indication of $d$ waves in the reaction cross section at higher energies as well as the probable existence of $d$ wave contributions to the scattering cross section above 2 Mev makes the simple calculation incorrect at these energies. For energies where the $d$ waves are less important the well depth appears quite constant. For $^3V\cong-11$ Mev the potential phase shift, $^3\delta_0$ varies from +43° to +45° in the energy range 0.990 to 2.548 Mev.

It is now necessary to examine Tables V and VI to see if a reasonable variation of $T$ and $\tau$ with energy can be obtained. If $R$ is chosen equal to unity for all energies, $^1\tau$ and $^3\tau$ are equal and increase from 14° at 0.990 Mev to 45° at 1.900 Mev. If a single resonant level is assumed, the variation of $\tau$ with energy indicates an $s$ wave resonance level at ~3.5 Mev with a width of ~1 Mev. If the resonant terms are due to several levels, some of these levels must be located at low energies (less than 4 Mev) in order to account for the rapid variation of the $\tau$'s in the region from 1 to 2 Mev. The fact that these levels must be wide would probably make their detection by scattering methods impractical.

If the artificial restriction of identical singlet and triplet resonant terms ($R=1$) is removed, the qualitative features of the resonances still remain. For example if $R=2$, the one-level assumption leads to a singlet level of width ~2 Mev located at ~5 Mev and a triplet level of width ~1 Mev located at ~3 Mev. If the further restriction of constant $R$ is removed either the singlet or triplet $s$ wave level may be moved to higher energies by choosing entries in Table VI which give slow variations of $^1\tau$ or $^3\tau$ with energy. However the other $s$ wave level will be moved to lower energies corresponding to more rapid variation of $\tau$.

The presence of $d$ waves should not alter the qualitative features of the above discussion although the resonant level energies will probably change somewhat.

It therefore seems that the schematic resonance model leads to one or more broad low energy $s$ levels superposed on a slowly varying background in order to satisfy scattering and reaction data simultaneously.

## IV. SUMMARY AND CONCLUSIONS

From the study of the angular distribution of the $p$-T scattering and the T($p$,$n$)He$^3$ reaction cross sections the following conclusions have been reached:

(1) The elastic scattering data may be fitted within experimental error in the angular range available by singlet and triplet $s$ and $p$ phase shifts, $^1K_0$, $^3K_0$, $^1K_1$, $^3K_1$, for all incident proton energies up to 2.5 Mev. There are an infinite number of $s$ wave phase shift pairs possible, for each of which there are two $p$ wave phase shift pairs. The values of the phase shifts for four arbitrary $s$ wave pairs are given in Table I for each energy. Additional fits at three of the energies are given in Table II.

(2) The $p$ wave phase shifts are in all cases larger than expected from potential scattering but one of the fits is consistent with the $^1P$ resonant level of He$^4$ suggested from the T($p$,$\gamma$)He$^4$ data. These fits, denoted by (*) in Table I, are called "resonance" fits and have large values of the singlet $p$ phase shift, $^1K_1$, and reasonably small values of the triplet $p$ phase shift, $^3K_1$.

(3) The results of a rough phase shift analysis of the Minnesota scattering data are given in Table III and the singlet $p$ "resonance" phase shifts are shown to be consistent with the suggested singlet $p$ resonant level at about 3 to 4 Mev, with a width of about 1 Mev.

(4) The asymmetry of the T($p$,$n$)He$^3$ reaction data was taken into account using the one-level resonance formulation. The results of this calculation are also consistent with the suggested singlet $p$ resonant level of He$^4$ corresponding to incident protons of about 3 Mev.

(5) The schematic resonance treatment of Breit[6] is used to combine the $p$-T scattering data and the T($p$,$n$)He$^3$ reaction data. The model divides both the singlet and triplet scattering amplitudes into a contribution due to resonant levels $[T\exp(i\tau)]$ and a con-

tribution due to potential scattering, while the reaction amplitude is due only to the resonant term. The values of ${}^1T$ and ${}^3T$ for different assumptions of the relative contribution of the singlet and triplet levels are given in Table V and the corresponding values of ${}^1\tau$ and ${}^3\tau$ (related to ${}^1T$ and ${}^3T$ by conservation requirements) are given in Table VI. It is found that the large values of the reaction cross section lead to values of $T$ and $\tau$ which require that there be one or more broad ($\sim$1 Mev) low energy ($<$4 Mev) resonant $s$ levels.

(6) The singlet potential scattering is obtained from a square well chosen to give the known singlet bound state of He$^4$. The triplet phase shifts, obtained from the schematic resonance model, are shown to be consistent with an attractive triplet well about $\frac{1}{4}$ as deep as the singlet well. The variation of the calculated well depth with energy is shown in Table VII.

The authors wish to express their thanks to Professor G. Breit for suggesting the problem and for numerous helpful discussions throughout the course of the work. They are especially indebted to him for calling attention to the possible connection of the large size of $p$ wave phase shifts with resonances and for the formulation of the treatment in Sec. III in terms of a nonresonant background for the two cases. The authors also wish to thank Dr. B. E. Freeman, Dr. W. de Marcus, and Mr. A. E. Woodruff for their assistance in the preliminary stages of the work.

PHYSICAL REVIEW VOLUME 88, NUMBER 4 NOVEMBER 15, 1952

# Small Angle X-Ray Scattering from Compact Identical Particles*

R. M. FRANK AND K. L. YUDOWITCH†
*Physics Department, Florida State University, Tallahassee, Florida*
(Received July 3, 1952)

A general expression is deduced for the intensity distribution of x-rays scattered at small angles from a compact system of identical particles. The scattering element selected for this derivation includes several near neighbors with the origin particle, thus taking cognizance of short-range order. An inherently positive intensity distribution may then be deduced for any such system describable by an "average" radial electron density which may be approximated by linear segments. This approximation for a compact system of impenetrable spheres compares favorably with the meager data available.

SMALL angle scattering theory[1] indicates that the intensity of scattering from a dilute system of particles may be expressed as a simple sum of the intensities scattered by the individual particles. Theoretical and experimental considerations both reveal the error in extension of this simple summation to compact systems. Early attempts to evaluate the scattering of x-rays at small angles by a compact system have not proven wholly adequate. The first attempt[2] gave qualitative agreement with experiment, predicting the observed maximum of scattered intensity at a small angle. This theory, based on the earlier work of Debye,[3] shares the glaring fault of that work in predicting negative intensities for sufficient compactness. A second attempt,[4] although avoiding this negative intensity, seems to predict the intensity maximum at rather too small values of angle.[5]

We have undertaken to deduce an expression for the amplitude of the electric field scattered from any system for which a radial electron density $\rho$ is conceivable. Such a theory is not confined to a two-phase system of fixed electron density, but may involve any number of fixed or varying electron densities. A system having a radial electron density which is significant for only a few particle radii is, as will be evident, a fair approximation to a typical system of particles. We can then conceive of a specimen composed of volume elements, each one containing a particle surrounded by its neighbors. If we integrate the scattering from the electrons within each volume element and square, we will then have an expression for the intensity scattered from each volume element, which, when added for $M$ volume elements, gives us the intensity scattered by the specimen.

The scattered amplitude from one such volume element is given by

$$A = A_e \int_v \exp(-ikr\cos\alpha)dV, \tag{1}$$

where $A_e$ = amplitude scattered per electron, $k = (4\pi/\lambda) \times \sin(\epsilon/2)$, $\lambda$ = radiation wavelength, $\epsilon$ = angle between incident and scattered rays, $r$ = magnitude of radius vector from the origin, and $\alpha$ = angle between $r$ and the line bisecting the incident and the scattered rays.

* This paper is based on work sponsored in part by the Biological Department, Chemical Corps, Camp Detrick, Frederick, Maryland, under contract with the Florida State University.
† Present address: Armour Research Foundation, Chicago, Illinois.
[1] A. Guinier, Ann. phys. **12**, 161 (1939).
[2] K. L. Yudowitch, J. Appl. Phys. **20**, 174 (1949).
[3] P. Debye, Ann. Physik **46**, 809 (1915).
[4] G. Fournet, Compt. rend. **228**, 1421 (1949).
[5] K. L. Yudowitch, Amer. Cryst. Assn. No. G-2, Tamiment, Pennsylvania (June, 1952).

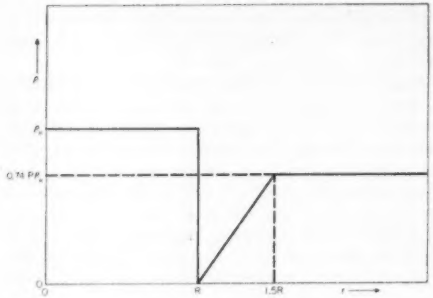


FIG. 1. Approximation of radial electron density ($\rho$) within one volume element of a compact system of identical, homogeneous spheres of radius $R$.

Using cylindrical coordinates,

$$A=A_e\int_{-x}^{x}\exp(-ikz)dz\int_0^{\pi}d\phi\int_{|z|}^{x}r\rho dr, \qquad (2)$$

where $z=r\cos\alpha$, and $\phi$=azimuthal angle.

If we now restrict our electron density to linear variation, such that

$$\rho=\gamma_p+\beta_p r, \qquad (3)$$

where $\gamma_p$ and $\beta_p$ are constants for any region $r_p\leqslant r\leqslant r_{p+1}$, and divide our range of integration into these regions, we can perform the integration. We then find

$$A=(4\pi A_e/3)\textstyle\sum_q[r_{p+1}{}^4\Psi(kr_{p+1})-r_p{}^4\Psi(kr_p)]$$
$$-\textstyle\sum_q(\Delta\rho)_q r_q{}^2\Phi(kr_q), \qquad (4)$$

where

$$\Phi(X)=3X^{-3}(\sin X-X\cos X),$$
$$\Psi(X)=3X^{-3}(\sin X+2X^{-1}\cos X),$$

and $r_q$ are points where $\rho$ has discontinuities of magnitude $(\Delta\rho)_q$.

In order to evaluate this expression, values of $\Phi$ and $\Psi$ have been tabulated. The evaluation in a particular instance depends, of course, on the system chosen. A simple system of considerable interest is one consisting of uniform, homogeneous spheres of radius $R$ and density $\rho_0$. If we approximate the radial electron density within a volume element of such a system by the function shown in Fig. 1, the amplitude scattered by this volume element is given by

$$A(NA_e)^{-1}=\Phi(kR)+1.48P[5.06\Psi(1.5kR)-\Psi(kR)], \qquad (5)$$

where

$$N=4\pi R^3\rho_0/3,$$

and $P$ has the significance indicated in Fig. 1. For impenetrable spheres,

$$0<P<1.$$

Squaring and multiplying by the number $M$ of such scattering elements, we obtain for the inherently positive scattered intensity $I$

$$I(MN^2I_e)^{-1}$$
$$=\{\Phi(kR)+1.48P[5.06\Psi(1.5kR)-\Psi(kR)]\}^2. \qquad (6)$$

For a sufficiently dilute system, $P$ vanishes, and Eq. (6) approaches the expression derived[1] for $M$ independent spherical particles.

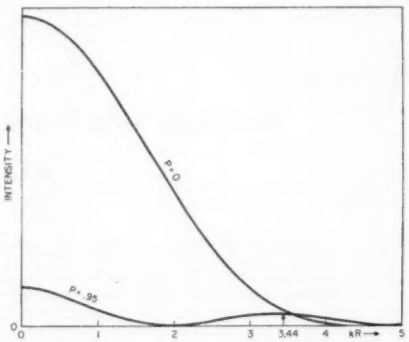


FIG. 2. Intensity distribution as given by Eq. (5) for a specimen described by the radial electron density of Fig. 1—for 95 percent maximum ($P=0.95$) and minimum ($P=0$) packing.

Figure 2 shows the intensity distribution given by Eq. (6) for $P=0$ and $P=0.95$. Comparison of this intensity distribution with experimental Latex data[6] justifies the well-defined peak at $kR=3.44$. The data shows the peak at 3.6; the earlier theories predict peaks at 2.9[2], 2.4[3], and 2.5[4]. The predicted peak at $kR=3.44$ also compares favorably with the deductions from liquid mercury data,[6] which place the peak at 3.5 for an atomic radius of 1.6A.[7]

[6] G. Oster and D. P. Riley, Acta Cryst. **5**, 1 (1952).
[7] P. Debye and H. Menke, Ergeb. Tech. Röntgenk. **2**, 1 (1931).

# The Electronic Component at Low Altitudes Produced by $\pi$-Meson Decay*†

E. D. PALMATIER‡
*Cornell University, Ithaca, New York*

(Received July 14, 1952)

The intensity of the electronic component at low altitudes produced by $\pi$-meson decay (designated as the $E_\pi$ component) has been obtained as a function of zenith angle and altitude by subtracting from the experimentally observed soft component those electrons arising from the collision and decay processes of $\mu$-mesons (designated as $E_\mu$ electrons). Extensive auxiliary studies of the corrections required in such soft component studies are described, and experimental requirements are stated for a precise telescopic study of the soft component. In particular, it is shown that the usual method of correcting a Geiger counter telescope for side showers is incorrect, and also that the effect of wall-generated secondaries should be considered. It is shown that the $E_\pi$ component of energy greater than 30 Mev can be represented as a function of zenith angle $\theta$ and atmospheric depth $h$ by the expression

$$I(E_\pi, h, \theta) = 0.70 \exp(-h/160 \cos\theta) \text{ cm}^{-2} \text{ sec}^{-1} \text{ sterad}^{-1},$$

for $\theta \leqslant 60°$ and $h \geqslant 700$ g cm$^{-2}$.

## I. INTRODUCTION

ALTHOUGH the bulk of the electronic component at low altitudes arises as a secondary radiation from $\mu$-mesons by collision and decay processes,[1–5] the strong dependence of the soft component intensity on zenith angle and altitude[6–8] and the small disagreement between observed and predicted electron rates on the basis of two or three particle $\mu$-meson decay schemes all indicate the presence of another electronic component[9, 10] which is now understandable in terms of the decay properties of the $\pi$-meson. In order to separate these components, the electron intensity at low altitudes was determined by Geiger counter telescope as a function of zenith angle, altitude, and energy. This was done for the entire electronic portion of the soft component by first measuring the total intensity as a function of zenith angle and altitude and then subtracting meson and proton intensities as observed in independent measurements. The dependence upon these factors for the electronic components lying in various energy intervals was obtained by the use of carbon absorbers. A separation of the electronic component into two subcomponents was then effected by the use of a computed $E_\mu$ spectrum, the latter being based on the known properties and spectrum of the $\mu$-meson.

## II. EXPERIMENTAL ARRANGEMENT AND PROCEDURE

The counter telescopes and absorbers were arranged as shown in Fig. 1. In order to reduce scattering and absorption of the soft electrons, aluminum-walled Geiger counters of 0.016-inch wall thickness and one-inch outer diameter were used throughout. Counters *a* to *g* (small counters) were of ten inch over-all length with an effective length of 7.75±0.05 inches, while the *h* counters (large counters) were eighteen inches long with an effective length of sixteen inches. This type of counter has been described elsewhere.[11] The solid angle of each telescope was defined by counter *c* and those counters above *c*, while underneath counter *c* was placed a curved carbon absorber. Absorber thicknesses of 2.62, 5.62, and 8.18 g cm$^{-2}$ were used. It was also possible to insert 4.28 g cm$^{-2}$ of carbon absorber above counter *c*; this, however, led to an increase in the effective width of counter *c*, which will be considered later (Sec. III-L). Tray *h*, located beneath the carbon absorber, was arranged so that a particle traversing the absorber

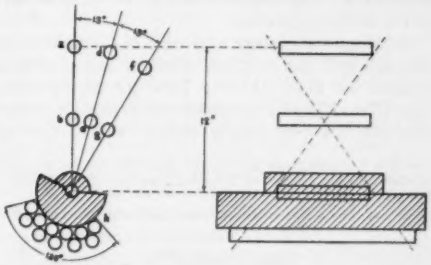

FIG. 1. Axial and side views of arrangement of Geiger counter telescopes and carbon absorbers.

* This project was supported in part by an ONR contract and in part by a Research Corporation grant.

† This work was done in partial fulfillment of the requirements for the Ph.D. degree at Cornell University.

‡ Now at the University of North Carolina, Chapel Hill, North Carolina.

[1] W. Heitler, Proc. Roy. Soc. (London) **161**, 261 (1937).
[2] H. Euler and W. Heisenberg, Ergeb. exakt. Naturw. **17**, 1 (1938).
[3] B. Feretti, Ricerca sci. 7–8, 736 (1939).
[4] H. J. Bhabha, Proc. Roy. Soc. (London) **164**, 256 (1938).
[5] D. Lyons, Physik. Z. **42**, 166 (1941).
[6] K. Greisen, Phys. Rev. **61**, 212 (1942).
[7] (a) Bernardini, Cacciapuoti, Feretti, Piccioni, and Wick, Phys. Rev. **58**, 1017 (1940); (b) Bernardini, Cacciapuoti, and Querzoli, Phys. Rev. **73**, 328 and 335 (1948).
[8] Azimov, Veksler, Dobrotin, Zhdanov, and Lubimov, J. Phys. (U.S.S.R.) **10**, 507 (1946).
[9] K. Greisen, Phys. Rev. **63**, 323 (1943).
[10] B. Rossi and K. Greisen, Phys. Rev. **61**, 121 (1942).
[11] D. R. Corson and R. R. Wilson, Rev. Sci. Instr. **19**, 207 (1948).

could undergo a deflection of at least 45° from its original path and still be detected by the tray.

The material in the vicinity of the telescope was minimized as follows. The framework of the telescope was constructed of pressed wood (0.4 g cm$^{-2}$) located at the extreme ends of the counters. The whole apparatus was housed at Ithaca (275 meters) in a small wooden hut with walls and roof of pressed wood (0.4 g cm$^{-2}$). The hut projected from a top window of the laboratory and the telescope was located four feet from the walls of the building; the top counters being on the same level as the flat roof of the building. At Echo Lake (3240 meters) the wooden hut was replaced by a canvas tent 0.03 g cm$^{-2}$ thick.

The following coincidence rates were observed: threefold, *abc*, *dec*, and *fgc*; fourfold, *abch*, *dech*, and *fgch*; displaced center counter rates, *aec*, *dbc*, *dgc*, and *fec*. These latter rates were used to obtain a correction for the effects of extensive air showers. The electronic circuits were of standard form, the resolving time of each channel being four microseconds, while the dead time of the mechanical recorders was 0.07 second.

For each of the four absorber thicknesses, measurements were made at two separate telescope positions, an upper position where the zenith angles for the *abc* and *fgc* telescopes were 0° and 30°, respectively, and a lower position, where these angles were 30° and 60°, respectively.

Measurements in the upper telescope position were carried out for approximately one-hundred hours with each absorber (yielding a standard statistical error of somewhat less than one percent in the total intensity measurements at zero zenith angle) and for approximately seventy hours with each absorber in the lower position of the telescope. The total data for each particular arrangement of the telescope and absorber were obtained in several different runs during the course of the measurement rather than in one continuous run. This was done in the expectation that the fluctuations arising from meteorological causes would sometimes compensate one another. Furthermore, the similarity of the data obtained in several different setting of a given set of experimental conditions served as a check on the over-all operation.

At Ithaca the counter axes were in the north-south direction and the principal telescope axis was tilted towards the East. At Echo Lake the measurements were all made with the counter axes in the north-south direction, but were equally divided between east and west inclinations of the principal telescope axis. As no statistically significant differences were observed, the readings for these two settings at Echo Lake were combined.

TABLE I. Average rates ($n$) and resultant dead time inefficiencies for Geiger counters, resulting from counter dead time of 300 microseconds.

| | Ithaca | | Echo Lake | |
|---|---|---|---|---|
| | $n$(sec$^{-1}$) | Dead time inefficiency | $n$(sec$^{-1}$) | Dead time inefficiency |
| Small counters | 2.5 | <0.10% | 4.5 | 0.15% |
| Large counters | 5.0 | 0.15% | 9.0 | 0.30% |

## III. TREATMENT AND CORRECTION OF THE OBSERVED DATA

The following factors were considered in the correction of the observed data.

### A. Meteorological Fluctuations

Owing to large barometric fluctuations existing at sea level, the Ithaca data were not corrected by the use of the barometric coefficient, but by the use of data from a wide-angled monitor telescope which ran with a counting rate of one hundred times the greatest counting rate observed with the arrangement of Fig. 1. The reduction of the Ithaca data to a mean intensity was accomplished by multiplying the number of coincidences during a given run by the ratio of the average monitor rate during the whole measurement to the average monitor rate during the given run.

At Echo Lake the average barometric pressure during any given run never deviated from the long time average by more than 1.7 mm Hg (and in most cases the deviation was much less than this); hence, no meteorological corrections were applied.

### B. Variation of Zenith Angle over the Telescope

The conversion of observed coincidence rates into absolute intensities is dependent not only upon the telescope geometry but also upon the zenith angle of the radiation. For telescopes of the dimensions used here, the observed coincidence rate $N(\theta)$sec$^{-1}$ is related to the absolute intensity $I(\theta)$cm$^{-2}$ sterad$^{-1}$ sec$^{-1}$ by the expression[6]

$$N(\theta)=kI(\theta)=kI(0)\cos^n\theta,$$

where $k=2.37$; 2.28; 2.22; 2.17; and 2.12 for $n=0$, 1, 2, 3, and 4, respectively. For nonintegral values of $n$, $k$ is obtained by interpolation.

### C. Failure of the Particle to Produce an Ion Pair in the Counter

For our counters, with an average primary specific ionization of thirty ion pairs cm$^{-1}$ atmosphere$^{-1}$ and a pressure of 0.13 atmosphere, a calculation similar to that performed by Montgomery,[12] but including a very small correction to allow for the inclination of the particle paths to the telescope axis, yields an inefficiency of 1.2 percent per counter. This type of inefficiency is normally offset by the effect of particles lying just outside the solid angle of the telescope creating secondaries in the counter walls.[13] Owing to the thinness of our walls, there was considerable uncertainty as to the

[12] R. A. Montgomery, Phys. Rev. **75**, 1407 (1949).
[13] K. Greisen and N. Nereson, Phys. Rev. **62**, 316 (1942).

magnitude of this compensation; hence an auxiliary study of the generation of secondaries in thin strips of material was made by means of cloud chamber and Geiger counter telescope.[14] From these studies the contribution of wall-generated secondaries to apparent increase in the Geiger counter efficiency can readily be shown to amount to only 0.1 percent in the case of our thin-walled aluminum counters; hence the final correction to be applied is +1.1 percent per counter. This correction is not applicable to the middle counters of our three counter telescopes, since relatively few particles lying in the telescope traverse the edges of these counters; nor does it apply to the counters of tray *h*, owing to overlapping of the edges of those counters.

### D. Dead Time of Counters

The dead time of these counters was 300 microseconds; the inefficiencies introduced here are as shown in Table I. For the counters of tray *h*, where three-quarters of the particles traversed two counters, this inefficiency will be negligible.

### E. Chance Coincidences

Chance coincidences were negligible, in the worst case amounting to no more than 0.1 percent of the total rate.

### F. Circuit Inefficiencies

The finite resolving time of the mechanical recorders was approximately 0.07 sec in all cases. This never gives rise to a correction of more than 0.2 percent at sea level.

### G. Special Correction for Tray *h*

Owing to the overlapping of the counters of the bottom tray in addition to their being electrically isolated from one another, an inefficiency in this tray of less than 0.1 percent is expected. It was observed, however, when all the absorber was removed from the telescope (both at Ithaca and Echo Lake) that the number of particles traversing the top telescope and not detected by tray *h* was greater than this and was practically independent of zenith angle. This portion amounted to about one percent of the vertical rate and is interpreted as an extremely soft portion of the soft component, which fails to penetrate the walls of tray *h* counters, and which is so strongly scattered that it no longer possesses an observable zenith angle dependence.

### H. Extensive Shower Correction

In order to obtain the contribution from extensive showers in the conventional manner (by displacement of the center counter out of the solid angle of the telescope) the following coincidence rates were observed: *ace*, *dbc*, *dgc*, and *fec*. Each of these four arrangements can be considered as being derived from some simple three counter telescope by a slight displacement of the center counter from its normal position. We shall refer to a given arrangement as being inclined at a certain zenith angle, namely, that of the telescope from which it is derived. Thus the *dgc* arrangement with the lower telescope position is derived from the *dec* telescope in the lower position; hence the former will be said to possess a zenith angle of 45°

Table II. Displaced center counter rates for various telescope zenith angles as observed at Ithaca and Echo Lake. The second column under each location shows the value given by the analytical expression adopted for that location.

| Zenith angle of telescope | Ithaca | | Echo Lake | |
|---|---|---|---|---|
| | Observed rate ($hr^{-1}$) | Analytical expression ($0.45\ hr^{-1} + 2.4\cos^2\theta\ hr^{-1}$) | Observed rate ($hr^{-1}$) | Analytical expression ($4.5\ hr^{-1} + 6.2\cos^2\theta\ hr^{-1}$) |
| 0° | 2.83±0.1 | 2.85 | 10.4±0.3 | 10.7 |
| 15° | 2.7 ±0.1 | 2.6 | 10.9±0.3 | 10.3 |
| 30° | 2.5 ±0.1 | 2.2 | 8.9±0.2 | 9.2 |
| 45° | 1.5 ±0.2 | 1.6 | 7.6±0.3 | 7.6 |
| 60° | 1.3 ±0.1 | 1.0 | 5.2±0.25 | 6.0 |

Now as will be seen from the data (Table II) the displaced center counter rate varies rather strongly with zenith angle, but only by a factor of 4 with altitude. Were this rate due to extensive showers, we would expect little if any zenith angle variation, but a rather strong altitude variation (factor of 10 between the two stations). The observed behavior is, however, quite reasonable if it is considered to arise primarily from secondaries generated in the roof, telescope, and counter walls by the total component. Since extensive showers increase by approximately tenfold between Ithaca and Echo Lake,[15] whereas the total component is observed to increase by a factor of 2.6 only, we may expect to fit the observed data by the expressions

$$c + d\cos^2\theta \text{ for Ithaca,}$$

and

$$10c + 2.6d\cos^2\theta \text{ for Echo Lake,}$$

where $c$ refers to the contribution from extensive showers and $d$ to the contribution from locally generated secondaries. Indeed, such expressions do fit the displaced counter data very well for the values $c = 0.45$ $hr^{-1}$ and $d = 2.4$ $hr^{-1}$ as is shown in Table II. It is quite apparent that any interpretation which assigns a large portion of the displaced counter rate at Ithaca to extensive showers must predict a displaced counter rate at Echo Lake which greatly exceeds that observed. We are forced to conclude that the standard method of displacing the center counter to estimate the shower rate leads to a considerable overcorrection.

The above conclusions are confirmed by the following independent considerations:

(a) Extensive shower measurements by Cocconi and Tongiorgi[15] show that the threefold coincidence rate for

[14] Brown, McKay, and Palmatier, Phys. Rev. **76**, 506 (1949).

[15] G. C. Cocconi and V. Cocconi Tongiorgi, Phys. Rev. **75**, 1058 (1949).

counters of 50 cm² area at sea level and separated by 4 m is 0.3 hr⁻¹. This must certainly be a lower limit for our counters.

(b) The displaced center counter rate *ace*, when the zenith angle of our telescope is zero, is 2.8 hr⁻¹, whereas the rate of *acf* is 0.5 hr⁻¹. Were the *ace* rate due entirely to extensive showers, we would expect no appreciable difference in the two rates; hence we may take 0.5 hr⁻¹ as an upper limit to the extensive shower rate.

(c) Whenever a fourfold coincidence rate is observed in this experimental arrangement, such that no three counters are in line, we obtain a coincidence rate (which we may now more reasonably assume to be entirely due to extensive showers) of 0.25 hr⁻¹. It has been observed experimentally[16] that for counters of 54 cm² area, the ratio of threefold to fourfold shower coincidence rate is 1.6; this yields a threefold shower coincidence rate of 0.4 hr⁻¹ for our counters, in good agreement with the two previous limits. Owing to the small solid angle of our telescope, only an extremely small portion of what we consider as the extensive shower correction will actually consist of shower particles with paths parallel to the axis of the telescope; thus overcorrection on this account need not be considered.

We conclude from all these considerations that for our telescopes the extensive shower rate at Ithaca is 0.4 hr⁻¹ for any orientation of the telescope, while for Echo Lake (where the extensive shower rate is ten times as great as at Ithaca) the rate is 4.0 hr⁻¹.

### I. Losses Arising from the Simultaneous Traversal of the Telescope by Several Particles

The resolving time of the mechanical recorder was 0.07 second; hence two or more particles traversing the telescope within this time interval will be recorded as one particle only. For random events this effect is negligible (correction $F$). For genetically related particles also, the following considerations show that the effect is negligible.

The *fac* rate was observed to be $0.53\pm0.05$ hr⁻¹. Since the known contributions comprise the major portion of this rate (0.4 hr⁻¹ from extensive showers and 0.04 hr⁻¹ from counter wall- and roof-generated secondaries) we can say that at most a contribution of 0.1 hr⁻¹ arises from the simultaneous traversal of *ac* and *f* by two genetically related particles travelling in parallel paths. When we further restrict the paths of these particles to the solid angle of the telescope, it is apparent that the rate will be negligible. Montgomery[12] has reached the same conclusion by the use of two parallel telescopes.

### J. Contribution of Secondaries Generated in the Roof and Counter Walls

Using our uncorrected total intensity data, the known distribution of secondaries,[14] and the geometry of a telescope located about four inches below the thin wooden roof, we have estimated the contribution from various roof and wall sources. Owing mainly to the scattering of the low energy secondaries in the counter walls, it is found that the only appreciable contribution arises when a cosmic-ray particle traverses the two upper counters (not the bottom one) and generates a secondary electron in the center counter wall, which then enters the bottom counter. This effect is found to give rise to a correction of $-0.3\cos^2\theta$ hr⁻¹ at Ithaca and $-0.8\cos^2\theta$ hr⁻¹ at Echo Lake for our type of counter walls and geometry. These corrections are to be applied to both the threefold and fourfold rates.

### K. Effect of Counter Walls upon Soft Component Intensity

In order to extrapolate to zero wall thickness, an auxiliary study was made of the counting rate as a function of aluminum wall thickness. It was found that an excellent fit of the data for the particular three counter telescope used in this auxiliary experiment was given by $R(t)=(70+50e^{-0.18t})$ hr⁻¹ where $R(t)$ is the soft component coincidence rate (in counts per hour) corrected for meteorological fluctuations only, and $t$ is the wall thickness (for each wall) in mils of aluminum. This expression is valid for values of $t$ from 16 to 140. Now on theoretical grounds the electron spectrum is not expected to diverge rapidly at low energies; hence over the small range of $t$ the extrapolation to zero wall thickness does not seem unreasonable. We therefore consider that an approximate increase of ten percent in the soft component intensity (or three percent of the total intensity) results when all the counter wall thicknesses are reduced from 16 mils to 0.

### L. Errors Arising from the Use of Carbon Absorber above the *c* Counter

When carbon absorbers were located both above and below counter *c*, the absorption was considered as occurring in two stages. The true absorption occurring in the top section (4.28 g cm⁻² above *c*) was assumed to be equal to the absorption measured by placing an equal thickness of carbon below counter *c* with no absorber above *c*. This latter quantity is obtained directly from a linear interpolation between the rates obtained with the 2.62 g cm⁻² and the 5.62 g cm⁻² carbon absorbers in the bottom position. The absorption occurring in the bottom section (below *c*) was assumed to be equal to the difference of the *abc* and *abch* rates with both parts of the absorber in place. This seems quite a reasonable assumption, since any effects arising from the presence of the carbon absorber above *c* will occur almost identically in both telescopes.

That is, if $x$ represents the amount of absorber above *c* and $y$ the amount of absorber between *c* and *h*, then the total absorption occurring in a thickness $x_1+y_1$ is

[16] Cocconi, Loverdo, and Tongiorgi, Phys. Rev. **70**, 841 (1946).

equated to

$$abc-abch\Big\}_{y=x_1}^{x=0} + abc-abch\Big\}_{y=y_1}^{x=x_1}$$

in which the first term refers to the absorption in $x_1$ and the second term to the added absorption in $y_1$.

### M. Contribution of Soft Mesons to the Soft Component

The meson contribution to our telescope rates at Ithaca with 12 g cm$^{-2}$ of carbon absorber has been determined from Kraushaar's measurements[17-18] as $-0.4\cos^3\theta$ hr$^{-1}$. In view of the slight disagreements in the published measurements of the variation of soft meson intensity with altitude, we consider that the delayed coincidence method, which excludes the proton component, is the most reliable method for determining this factor. Using Kraushaar's value of 2, we obtain a meson correction to the soft component rate in our telescopes of $-0.8\cos^3\theta$ hr$^{-1}$ at Echo Lake. The corrections to be applied for the other absorber thicknesses will then be proportional to the absorber thickness.

The mesons contained in the entire soft component (all particles of range less than 80 g cm$^{-2}$ air equivalent) were determined from Kraushaar's measurements. From the differential proton spectrum presented in the next section we estimate that his differential vertical intensity of mesons of range 105 g cm$^{-2}$ air equivalent (which was obtained by an absorption method) contains a six percent contribution from protons. This correction, though quite insignificant for our purpose has been included in the final correction which is then $-3.0\cos^3\theta$ hr$^{-1}$ for our telescope rates at Ithaca.

The Echo Lake correction amounting to $-6.0\cos^3\theta$ hr$^{-1}$ is then obtained as before from the results of the delayed coincidence methods and should contain no appreciable contribution from protons.

### N. Contribution of Soft Protons to the Soft Component

The proton spectrum for Ithaca, which we have used to obtain the correction, is presented in Fig. 2. No great accuracy can be claimed for this spectrum owing to the uncertainties of interpretation of proton intensity measurements, especially in those instances where absorption and production of protons may occur in material above the apparatus. Owing to the small number of protons present at low altitudes, however, it seems reasonable that future revisions of this proton spectrum will not appreciably influence our final corrected intensities for the soft component. For momenta above 1000 Mev/$c$ the observations of Mylroi and Wilson[19] have been used. The observations of Todd *et al.*[20] obtained at an altitude of 3400 meters, when converted to lower altitudes by the use of an absorption length of 130 g cm$^{-2}$ yield a vertical differential intensity at Ithaca of $6\times10^{-8}$ (Mev/$c$)$^{-1}$ sec$^{-1}$ sterad$^{-1}$ cm$^{-2}$ for momenta of around 400 Mev/$c$. This latter value is in good agreement with the early measurement of Rochester and Bound,[21] whose observations yield a vertical differential intensity of $5\times10^{-7}$ g$^{-1}$ sec$^{-1}$ sterad$^{-1}$ for protons of range 20 g cm$^{-2}$ in Pb (or $7\times10^{-8}$(Mev/$c$)$^{-1}$ cm$^{-2}$ sec$^{-1}$ sterad$^{-1}$ at momenta of around 460 Mev/$c$). For the lower momenta values, the observations of Franzinetti[22] indicate that the number of protons is quite small as is expected on the basis of ionization loss considerations.

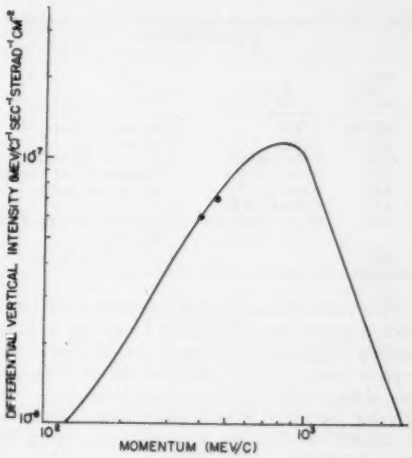


FIG. 2. Differential vertical intensity spectrum of protons at Ithaca as used in correction $N$.

In order to correct for protons at various zenith angles, the $\cos^3\theta$ zenith angle dependence computed by Mylroi and Wilson[19] has been used. The soft component corrections to be applied to our observed rates are finally obtained as $-0.4\cos^3\theta$ hr$^{-1}$ at Ithaca and $-4.0\cos^3\theta$ hr$^{-1}$ at Echo Lake

## IV. HARD COMPONENT INTENSITY AT ITHACA

In order to ensure that the soft component could properly be obtained as the difference between the total intensities from our measurements and the hard component intensities from other measurements, a separate determination of the hard component vertical intensity was made at Ithaca. The arrangement of counters and lead was the same as shown in Fig. 1 with the exception

[17] W. Kraushaar, Phys. Rev. **76**, 1045 (1949).
[18] W. Kraushaar, thesis, Cornell (1948).
[19] M. G. Mylroi and J. G. Wilson, Proc. Phys. Soc. (London) **A64**, 404 (1951).
[20] Todd, Henderson, Miller, and Potter, Phys. Rev. **76**, 590 (1949).
[21] G. D. Rochester and M. Bound, Nature **146**, 745 (1940).
[22] C. Franzinetti, Phil. Mag. **41**, 86 (1950).

TABLE III. Classification of observed coincidences according to ranges of particles.

| Type | Minimum range (gm cm$^{-2}$) | Maximum range (g cm$^{-2}$) | Type of correction applied |
|---|---|---|---|
| 1 | 0.03 air | 0.55 Al | Discussed in Sec. III K |
| 2 | 0.55 Al | 0.77 Al | Discussed in Sec. III G |
| 3 | 0.55 | 0.55+2.62 C | *A, B, C, M, N.* Latter three corrections just compensate for one another |
| 4 | 0.55 | 0.55+5.62 C | |
| 5 | 0.55 | 0.55+8.18 C | |
| 6 | 0.55 | 0.55+12.46 C | *A, B, L* |
| 7 | 0.55 | 80 air equivalent | Corrections for type 8 plus *M* and *N* |
| 8 | 0.55 | $\infty$ | *A, B, C, D, F, H, J* |

that the vertical telescope only was used and 10 cm of lead was placed between counter *c* and tray *h*. In the following paragraph the observed data and corrections are given in some detail to illustrate the relative magnitudes of the various corrections used throughout.

During the period from October 30th to December 1st, 22,363 coincidences were observed during 317 hours of operation. This yields an observed rate of 70.5±0.5 hr$^{-1}$, to which the following corrections (as discussed in the previous section) were applied:

| | | Correction |
|---|---|---|
| Meteorological | −0.5 percent | +1.45 hr$^{-1}$ |
| Failure to produce an ion pair | +2.2 percent | |
| Dead time inefficiencies | +0.2 percent | |
| Circuit inefficiencies | +0.15 percent | |
| Extensive showers (owing to the large area of the bottom tray the shower correction here will be the same as with our previous arrangement) | | −0.4 hr$^{-1}$ |
| Knock-on secondaries from roof and counter walls | | −0.2 hr$^{-1}$ |
| Back-scattered secondaries from lead absorber (calculated from information of reference 13) | | −0.3 hr$^{-1}$ |
| | Total correction | +0.5 hr$^{-1}$ |

Applying this correction and converting to a minimum range of 80 g cm$^{-2}$ of dense air[14] we obtain

$$I_v(80 \text{ g cm}^{-2} \text{ dense air}) = (0.886 \pm 0.006) \times 10^{-2} \text{ cm}^{-2} \text{ sterad}^{-1} \text{ sec}^{-1}.$$

To compare this properly with Kraushaar's published value, we must apply a slight correction for his counter inefficiencies after the manner of Sec. III C. This calculation yields a correction of +0.4 percent per counter or +0.8 percent for his telescope. Our final corrected value of his result is

$$I_v(80 \text{ g cm}^{-2} \text{ dense air}) = (0.894 \pm 0.005) \times 10^{-2} \text{ cm}^{-2} \text{ sterad}^{-1} \text{ sec}^{-1}.$$

The excellent agreement of these two intensity measurements lends support to the general validity of our scheme of correcting for showers and secondaries.

## V. TREATMENT OF DATA

In analyzing these data it was found convenient to divide the observed coincidences into classes according to the type of absorber used. In Table III these classes are defined and the types of corrections which have been applied to each class are indicated. Those types of corrections not included are considered to be negligible.

While we shall not present all the observations and corrections, but only the final intensities, it seems worth while to illustrate the procedure and the order of magnitude of these corrections for one component; hence in Table IV we have summarized the procedure followed in obtaining the type 7 component which consists essentially of all electrons with ranges between 0.55 g cm$^{-2}$ of Al and 80 g cm$^{-2}$ of air equivalent.

In Fig. 3 the corrected rates are shown for types 2 to 7 of the soft spectrum as obtained at Ithaca. The solid curves, which fit the data within the standard deviations, have the property that the differences of the ordinates of any two adjacent curves are expressible by some power of cos$\theta$. This is convenient, for we may now readily express our corrected rates as intensities for various energy intervals by the method of Sec. III B. In Table V the results of this conversion are given.

For the Echo Lake observations the corrected rates

TABLE IV. Summary of data (counts/hour) and corrections to data which were used in obtaining the type 7 component for Ithaca (electronic component of the soft spectrum), namely, those electrons capable of penetrating 0.55 g cm$^{-2}$ of Al but with ranges $\leq$80 g cm$^{-2}$ of air equivalent.

| No. of item | Item | 0° | 15° | 30° | 45° | 60° |
|---|---|---|---|---|---|---|
| 1 | Observed rate for type 8, corrected only for meteorological fluctuations | 100.2±0.6 | 91.0±0.6 | 70.2±0.4 | 45.1±0.5 | 21.5±0.3 |
| 2 | Correction *C* | 2.2 | 2.0 | 1.6 | 1.0 | 0.5 |
| 3 | Correction *D* | 0.2 | 0.2 | 0.15 | 0.1 | 0.05 |
| 4 | Correction *F* | 0.2 | 0.15 | 0.1 | 0.04 | — |
| 5 | Correction *H* | −0.4 | −0.4 | −0.4 | −0.4 | −0.4 |
| 6 | Correction *J* | −0.3 | −0.27 | −0.20 | −0.15 | −0.07 |
| 7 | Type 8 (corrected) | 102.1±0.6 | 92.7±0.6 | 71.4±0.4 | 45.0±0.5 | 21.6±0.3 |
| 8 | Hard component of range $\geq$80 g cm$^{-2}$ of air | 70.6±0.4 | 65.6±0.4 | 52.2±0.3 | 34.1±0.2 | 16.5±0.1 |
| 9 | Experimentally defined soft component (item 7–item 8) | 31.5±0.7 | 27.1±0.7 | 19.2±0.5 | 11.6±0.6 | 5.1±0.3 |
| 10 | Mesonic and protonic component of soft spectrum correction *M* and *N* | 3.4±0.3 | 3.0±0.3 | 2.1±0.2 | 1.2±0.1 | 0.4±0.05 |
| 11 | Type 7 electronic component of soft spectrum item 9–item 10 | 28.1±0.8 | 24.1±0.8 | 17.1±0.6 | 10.4±0.6 | 4.7±0.3 |

TABLE V. Summary of corrected rates and absolute intensities of various difference components at Ithaca.

| Component | Rate ($hr^{-1}$) | $K$ | Absolute intensity ($cm^{-2}$ $sec^{-1}$ $sterad^{-1}$) |
|---|---|---|---|
| 7–6 | $13.0\cos^{2.6}\theta$ | 2.12 | $0.170\times10^{-2}\cos^{2.6}\theta$ |
| 6–5 | $3.8\cos^{2.7}\theta$ | 2.18 | $0.048\times10^{-2}\cos^{2.7}\theta$ |
| 5–4 | $2.2\cos^{2.5}\theta$ | 2.19 | $0.028\times10^{-2}\cos^{2.5}\theta$ |
| 4–3 | $4.3\cos^{2.4}\theta$ | 2.20 | $0.054\times10^{-2}\cos^{2.4}\theta$ |
| 3–2 | $3.2\cos^{1.9}\theta$ | 2.22 | $0.040\times10^{-2}\cos^{1.9}\theta$ |
| 2 | 1.0 | 2.37 | $0.010\times10^{-2}$ |
| 1 | 3.0 | 2.37 | $0.035\times10^{-2}$ |
| 8 | $102.2\cos^{2.55}\theta$ | 2.19 | $1.29\times10^{-2}\cos^{2.55}\theta$ for $0\leq\theta\leq30°$ |
| | $96.5\cos^{2.14}\theta$ | 2.21 | $1.21\times10^{-2}\cos^{2.14}\theta$ for $30°\leq\theta\leq60°$ |

are shown in Fig. 4, while the analytical expressions for the rates and absolute intensities are given in Table VI.

## VI. VALIDITY OF RESULTS AND COMPARISON WITH OTHER MEASUREMENTS

### A. Estimated Validity of the Final Intensities

It is considered that the greatest source of error in the whole experiment is associated with the scattering of the soft component particles in the absorber. In this section, where we shall compare our results with those of other workers, this error does not enter, since the comparison will be made in terms of absorber thickness. It will be considered later, however, when our range spectrum is converted to an energy spectrum.

From a consideration of the relative magnitudes of the various remaining errors and the cross-checks used in the experiment, we have placed the following estimates on the validity of our results

*Observed Rates*

Types 1 and 2: The error here is probably no greater than 20 percent, although it must be recognized that the process of extrapolation to zero wall thickness may contain some unrecognized error.

Types 3, 4, 5, 6, and 8: The determinate errors are considered to be no greater than the standard deviations; thus we estimate the total errors to be no greater than 1.5 times the standard deviations.

Type 7: An error of from 5 to 10 percent (several times the standard deviation) may arise here, owing to the location of the carbon absorber above the $c$ counter.

TABLE VI. Summary of corrected rates and absolute intensities of various difference components at Echo Lake.

| Component | Rate ($hr^{-1}$) | $K$ | Absolute intensity ($cm^{-2}$ $sec^{-1}$ $sterad^{-1}$) |
|---|---|---|---|
| 7–6 | $61\cos^{4.7}\theta$ | 2.095 | $0.81\times10^{-2}\cos^{4.7}\theta$ |
| 6–5 | $20\cos^{3.6}\theta$ | 2.14 | $0.26\times10^{-2}\cos^{3.6}\theta$ |
| 5–4 | $12\cos^{2.9}\theta$ | 2.16 | $0.15\times10^{-2}\cos^{2.9}\theta$ |
| 4–3 | $21\cos^{3.1}\theta$ | 2.21 | $0.26\times10^{-2}\cos^{3.1}\theta$ |
| 3–2 | $14.5\cos^{2.1}\theta$ | 2.21 | $0.18\times10^{-2}\cos^{2.1}\theta$ |
| 2 | 2.5 | 2.37 | $0.029\times10^{-2}$ |
| 1 | 8.8 | 2.37 | $0.103\times10^{-2}$ |
| 8 | $261\cos^{3.55}\theta$ | 2.19 | $3.31\times10^{-2}\cos^{3.55}\theta$ $0\leq\theta\leq45°$ |
| | $235\cos^{2.36}\theta$ | 2.205 | $2.96\times10^{-2}\cos^{2.36}\theta$ $45°\leq\theta\leq60°$ |

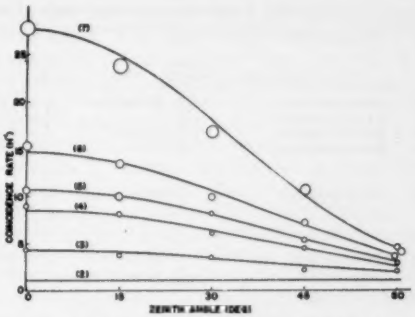


FIG. 3. Corrected rates for zenith angles out to 60° of types 2 to 7 of the electronic component at Ithaca.

*Analytical Expressions for Rates and Intensities*

Owing to the manner in which data for many of the components were obtained (as the difference of two simultaneously observed rates) many of the errors are quite small. We consider that the average error in the expressions of the form $R\cos^n\theta$ is no greater than 10 percent in the amplitude ($R$) and no greater than 15 percent in the exponent ($n$). For those components of large magnitude, the accuracy may be slightly better; for those of small magnitude it will possibly be worse.

### B. Comparison with other Measurements

In Table VII we have presented for comparison with our results, other observations which contain enough of the experimental details to permit correction in accordance with our scheme. It will be observed that good agreement is obtained among the first seven experiments, provided the correction for extensive showers is re-evaluated as explained above, instead of using directly the displaced center counter rate.

In the last four measurements of Table VII, a rather large error appears. This discrepancy, which is of the order of 20 percent of the soft component, is far greater

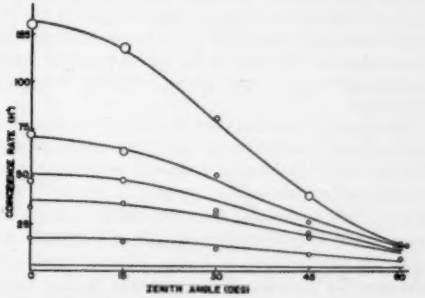


FIG. 4. Corrected rates for zenith angles out to 60° of types 2 to 7 of the electronic component at Echo Lake.

TABLE VII. Comparison of corrected results of various observers. *P* refers to results of this measurement.

| | Type of component | Altitude (meters) | Observer | Intensity $I$ in units of cm$^{-2}$ sec$^{-1}$ sterad$^{-1}$ $J_2$ in units of cm$^{-2}$ sec$^{-1}$ | | Comments on corrections |
|---|---|---|---|---|---|---|
| 1. | Hard-vertical | 275 | Kraushaar[a] | $I_v=(0.894\pm0.005)\times10^{-4}$ | 1. | Correction $C$ applied |
| 2. | Hard-vertical | 275 | *P* | $I_v=(0.886\pm0.006)\times10^{-4}$ | | |
| 3. | Hard-integrated | 275 | Greisen[b] | $J_2=(1.803\pm0.012)\times10^{-2}$ | | |
| 4. | Hard-integrated | 275 | *P* | $J_2=(1.811\pm0.12)\times10^{-2}$ | 4. | Obtained from our observed vertical intensity and well established zenith angle dependence for mesons (17) |
| 5. | Total vertical | 0 | Montgomery[c] | $I_v=(1.215\pm0.01)\times10^{-4}$ | 5. | A shower correction of $-1.0$ percent (rather than $-5.0$ percent) and a $-0.5$ percent correction for wall-generated secondaries have been applied |
| 6. | Total vertical | 0 | *P* | $I_v=(1.23\pm0.01)\times10^{-4}$ | 6. | Corrected to sea level |
| 7. | Total vertical | 0 | Greisen[d] | $I_v=(1.22\pm0.01)\times10^{-4}$ | 7. | This component has been corrected to sea level, to zero wall thickness and for an overcorrection made in the shower correction. Owing to the uncertainties of these corrections, the excellent agreement obtained is fortuitous |
| 8. | Integrated total of range 2.2 g cm$^{-2}$ brass | 275 | Greisen[b] | $J_2=2.51\times10^{-2}$ | | |
| 8(a). | Integrated total of range 2.2 g cm$^{-2}$ brass | 275 | Greisen | $J_2=2.44\times10^{-2}$ | 8(a). | Recorrected by removal of shower correction |
| 9. | Integrated total of range 2.2 g cm$^{-2}$ brass | 275 | *P* | $J_2=2.38\times10^{-2}$ | | |
| 10. | Soft-integrated | 275 | Greisen[b] | $J_2=0.71\times10^{-2}$ | 10. | Measurements 8–3 |
| 10(a). | Soft-integrated | 275 | Greisen | $J_2=0.64\times10^{-2}$ | 10(a). | Measurements 8a–3 |
| 11. | Soft-integrated | 275 | *P* | $J_2=0.57\times10^{-2}$ | 11. | Measurements 9–4 |

[a] See reference 17.
[b] See reference 9.
[c] See reference 12.
[d] See reference 6.

than can be expected on the basis of statistical fluctuations of the observations. Since the hard component results of these measurements are in such good agreement (measurements 3 and 4 of Table VII) it appears that the trouble is in some way associated with the soft component. Considerations of the effects of extensive showers and secondaries enable us to indicate in a reasonable manner how these results may be reconciled; it has not been possible, however, to make a precise correction.

As shown in Sec. I of part III, Greisen's shower effect (two particles with parallel paths simultaneously traversing the telescope) has been found to be negligible by Montgomery[12] and ourselves. A computation of the contribution to be expected on the basis of extensive shower observations[18] confirms this conclusion. When Greisen's shower correction is made negligible his observed electronic component is decreased by 10 percent. This makes no difference to his hard component measurement, however, as the shower correction was negligible there.

The empirical method used by Greisen to determine his "collision" correction is based on the assumption that secondary electrons and showers originating in an absorber will not diverge to any great extent from their primary before emerging from the absorber; hence the arrangement of several counters used to determine this correction should form a highly efficient "collision" detector. We consider this assumption to hold quite well in the case of Pb and Fe; with carbon absorbers, however, it is probable that this assumption is not strictly valid, and that the detector has a low efficiency. Such an effect will lead to an underestimation of the collision correction and an overestimation of the electronic component. It has not been possible to determine the value of the correction; we can only say that a further reduction of 10 percent in the soft component on this basis is not unreasonable.

## VIII. CONVERSION OF RANGES TO ENERGY LIMITS

The number of electrons, $N_0(t)$, observed to traverse a telescope and absorber (of combined thickness $t$) in unit time is given by

$$N_0(t)=-\int_0^\infty P(R',t)\frac{dN(R')}{dR'}dR',$$

where $N(R)$ is the number of electrons of total range $R$ or greater arriving in the solid angle of the telescope in unit time and $P(R,t)$, the penetration probability, is the probability that an electron capable of traveling a total path length $R$ in the absorber, actually traverses a thickness $t(t<R)$ and is detected by the apparatus. In order to obtain an energy spectrum we must first convert $N_0(t)$ to $N(t)$ where the latter represents the number of electrons arriving in the solid angle of the telescope in unit time for which the total range is $t$ g cm$^{-2}$ (the actual thickness of absorber). The conversion to an energy spectrum is then made in a straightforward manner by means of a standard relationship between energy and total range. The initial step is

carried out by correcting $N_0(t)$ for the number of absorbed electrons as follows:

$$N(t)=N_0(t)-\int_0^\infty\{1-P(R',t)\}\frac{dN(R')}{dR'}dR'.$$

Now if the penetration probability is known, $N(t)$ may be determined by the usual process of successive substitution of $N_0(t)$ for $N(t)$ in the integral, then the first-order corrected spectrum, and so on. It was found that the magnitude of the correction term to be applied to each observed rate depends primarily on the form of the penetration probability and that the differences between successive order correction terms varied in geometric progression. Thus the total correction term to be applied in each case could readily be ascertained.

The penetration probability was obtained as follows: For a thin beam of monoenergetic electrons of total range $R$ in carbon, incident perpendicularly on a carbon plate, the radial distribution function $F(t,r)$ for those particles lying at a depth $t$ and possessing a perpendicular displacement $r$ from the axis of the beam is found to be[23,24]

$$F(t,r)dr=\frac{1}{2A_2(R,t)}\exp\left(-\frac{r^2}{4A_2(R,t)}\right)rdr,$$

where

$$A_2(R,t)=\int_0^t\frac{(t-\eta)^2}{W^2(\eta)}d\eta \quad \text{and} \quad W(t)=\frac{2\rho\beta}{E_s}.$$

At each depth $t$ there will exist an effective maximum displacement $D(R,t)$ such that

$$P(R,t)=\int_0^{D(R,t)}F(t,r)dr.$$

While the correct value of $D(t)$ is not known, it is certainly less than $(R^2-t^2)^{\frac{1}{2}}$. We have taken $D(t)=[R(R-t)]^{\frac{1}{2}}$, which is the form obtained by Fowler *et al.*[25] We have used their method of correcting for the effect of radiation upon the penetration probability, i.e., by the use of a factor of the form $\exp(-ht)$ where $h=0.018$ g$^{-1}$ cm$^2$ for carbon. Thus our method is essentially the same as Fowler's with the added feature that the variation of energy loss has been handled by the method of Eyges.[24] The final form of the penetration probability is

$$P(R,t)=\exp(-ht)\{1-\exp[-R(R-t)/4A_2]\}.$$

The actual computation was carried out for initial energies 5, 10, 15, 20, 26, 33, and 40 Mev. A total range $R$ was obtained for these energies by means of Greisen's calculations[26] of the maximum ranges of electrons in aluminum. These results were used as they agreed rather closely with experimental determinations of this quantity at lower energies.[27] The value of $A_2(R,t)$ as a function of $t$ was then obtained by numerical integration. The final curves for $P(R,t)$ for various initial energies (or ranges) are shown in Fig. 5. The results for intermediate energies are readily obtained by interpolation. It must be noted that we have neglected the straggling of electrons about the maximum range $R$ and have not considered the occasional increase in range occurring by production of photons which release new electrons at greater thicknesses.

The final results of our computations are given in Table VIII as energy limits to be associated with the absorber thicknesses and correction factors to be applied to the observed integrated intensities to obtain the integrated intensities for electrons of these lower energy limits. In Table IX are given the absolute intensities of the four most energetic groups of electrons at each altitude obtained by application of the previous results to the observed intensities of Tables V and VI.

## IX. SEPARATION OF THE HIGH ENERGY ELECTRONIC COMPONENTS

As we have indicated initially, the $E_\tau$ component can be obtained by removal of the computed $E_\mu$ component from the total electronic component. This procedure was carried out as follows. Using the meson intensity measurements of Kraushaar[17] and the computations of Bernardini *et al.*,[7] corrected for a meson mass of 108 Mev/$c^2$, a half-life of $2.2\times10^{-6}$ sec, and a three-particle $\mu$-meson decay scheme, the integrated vertical intensity of the $E_\mu$ component of energy $\gtrsim 30$ Mev is readily obtained for both altitudes. Since our altitudes were identical with those of Kraushaar and quite close to those used by Bernardini and co-workers, a linear interpolation was used with the latter for the small altitude corrections required. These vertical $E_\mu$ intensities were then subtracted from the total vertical electronic intensities obtained by taking the difference of the observed rates of types 6 and 7, correcting as

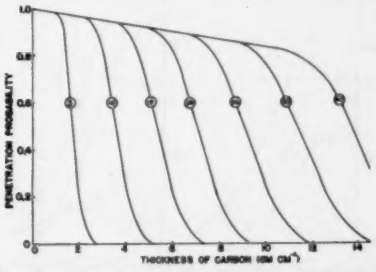


FIG. 5. Penetration probability to various depths in carbon absorber for electrons of initial energies of 5, 10, 15, 20, 26, 33, and 40 Mev.

[23] B. Rossi and K. Greisen, Revs. Modern Phys. **13**, 243 (1941).
[24] L. Eyges, Phys. Rev. **74**, 1534 (1948).
[25] Fowler, Lauritsen, and Lauritsen, Revs. Modern Phys. **20**, 265 (1948).
[26] K. I. Greisen, thesis, Cornell (1943).
[27] F. L. Hereford and C. P. Swann, Phys. Rev. **78**, 728 (1950).

TABLE VIII. Correction factors for conversion of integral range spectra to integral energy spectra.

| Thickness of carbon absorber (g cm$^{-2}$) | Lower energy limit Mev | Correction[a] factor |
|---|---|---|
| 0.00 | 0.00 | 1.00 |
| 2.62 | 6.5 | 1.14 |
| 5.62 | 13.3 | 1.26 |
| 8.18 | 19.6 | 1.35 |
| 12.46 | 30.8 | 1.47 |

[a] This multiplying factor is to be applied to the integrated vertical electronic component for the given absorber, for both Ithaca and Echo Lake.

described previously and multiplying by the factor 1.47 to adjust the observed intensities to this energy limit (as discussed in the previous section). The procedure for the nonvertical directions was similar, the additional assumption being introduced that the $E_\mu$ component varies as $\cos^2\theta$. This amounts essentially to neglecting the effect of multiple air scattering upon the zenith angle distributions of the high energy electronic components. We believe that this assumption does not lead to any considerable error for not only are most of the electrons of rather high energy, but as will be indicated later, the effect of scattering upon the zenith angle distribution is not very great at higher energies. In Fig. 6 the computed $E_\mu$ component is shown by a solid line, while the $E_\tau$ and total electronic components obtained by use of the data are indicated along with their standard deviations. The solid lines used to fit the data have been obtained in an identical manner from the smoothed out data of Figs. 3 and 4. The results at large angles of such a procedure are of uncertain value; owing to the large uncertainties in the small quantities involved, we obtain slightly negative values at 60°.

The high energy $E_\tau$ component is seen to possess a very steep zenith angle distribution (steeper at Ithaca than at Echo Lake). The results for the two altitudes may be related by plotting the logarithm of all the $E_\tau$ intensities from 0° to 45° on one figure (Fig. 7) as a function of $h/\cos\theta$. The line joining the two vertical intensity points as obtained from the smoothed out data gives an excellent fit of the data, and we obtain for the absolute integrated intensity of the $E_\tau$ component, at low altitudes, at atmospheric depth $h$, and zenith angle $\theta$ for energies greater than 30 Mev, the following expression:

$$I_{E_\tau}(h,\theta)=0.70\exp(-h/160\cos\theta)\ \text{cm}^{-2}\ \text{sec}^{-1}\ \text{sterad}^{-1}.$$

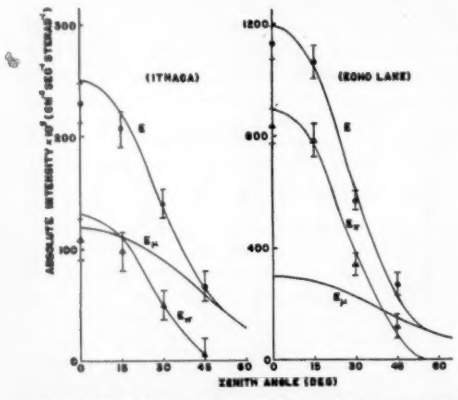


FIG. 6. Absolute intensities (multiplied by $10^3$) for zenith angles out to 45° of the $E$, $E_\tau$, and $E_\mu$ electronic components of energy greater than 30.8 Mev at Ithaca and Echo Lake.

## X. SEPARATION OF THE LOW ENERGY ELECTRONIC COMPONENTS

The electronic components of the remaining bands, which are composed entirely of low energy electrons, have undergone rather severe atmospheric scattering, and cannot be separated without consideration of this phenomenon. The effect of multiple scattering upon the zenith angle distributions has been determined for two groups of 100-Mev electrons initially with $\cos^2\theta$ and $\cos^6\theta$ dependences, representing, respectively, the $E_\mu$ and $E_\tau$ components of greater energies. The computation, which was performed numerically, consisted essentially in the repeated application of the standard scattering formulas[22] to obtain the zenith angle dependence at successively lower energies. In Table X are given the final results of the computations; the details will be given in a later publication dealing with the scattering of the extreme soft component. From Table X we may readily determine how the relative abundance of the $E_\mu$ and $E_\tau$ components, now known for energies greater than 30 Mev, changes as we proceed to the lower energy groups. This information, along with the computed zenith angle distribution for the $E_\mu$ component, allows a separation to be effected. In Fig. 8 the total electronic component and the separated electron components for the three most energetic electron bands of the lower energy groups are shown for both altitudes. The resultant $E_\tau$ curves compare favorably with the curves (shown by dotted lines) obtained by extending the computed $E_\tau$ vertical intensity to large zenith angles in accordance with the results of our scattering calculations as summarized in Table X.

TABLE IX. Absolute intensities of four most energetic bands of the electronic component at Ithaca and Echo Lake.

| Energy limits of components (Mev) | Absolute intensities (cm$^{-2}$ sec$^{-1}$ sterad$^{-1}$) Ithaca | Echo Lake |
|---|---|---|
| 6.5–13.3 | $(0.032\times10^{-3})\cos^{2.4}\theta$ | $(0.15\times10^{-3})\cos^{2.1}\theta$ |
| 13.3–19.6 | $(0.016\times10^{-3})\cos^{2.5}\theta$ | $(0.10\times10^{-3})\cos^{2.2}\theta$ |
| 19.6–30.8 | $(0.044\times10^{-3})\cos^{2.7}\theta$ | $(0.25\times10^{-3})\cos^{2.4}\theta$ |
| 30.8– | $(0.25\times10^{-3})\cos^{2.5}\theta$ | $(1.19\times10^{-3})\cos^{4.7}\theta$ |

## XI. CONCLUSIONS

Our conclusions can readily be arranged into two groups: those dealing with the experimental technique associated with a soft component study and those dealing with the properties of the various electronic components in the lower atmosphere. The first group are summarized in the following list of conditions which should be observed in any measurement of the soft component. This is an extension and in some places a modification of a list published by Azimov and his collaborators.[8]

(a) The multiple scattering of low energy electrons, both in the air and in the apparatus, must be considered throughout the analysis of the data. This effect leads to the most serious errors encountered in soft component measurements.

(b) Counter walls must be thin and of a low $Z$ material, and all absorbers should be below the counters defining the solid angle of the telescope.

(c) A large solid angle of the telescope should be used; this will in general diminish the effects of side showers and scattering, although the angular resolution required will place an upper limit on the allowed solid angle.

TABLE X. Calculated zenith angle distributions of the electronic component slowed down to various energies from 100 Mev. The representations hold for $\theta \leqslant 60°$.

| Energy, Mev | Original form of $1.00\cos^{2}\theta$ | Original form of $\cos^{6}\theta$ |
|---|---|---|
| 100 | $1.00\ \cos^{2}\theta$ | $1.00\ \cos^{6}\theta$ |
| 68 | $0.98\ \cos^{1.9}\theta$ | $0.965\ \cos^{5.9}\theta$ |
| 40 | $0.96\ \cos^{1.8}\theta$ | $0.908\ \cos^{4.8}\theta$ |
| 30 | $0.94\ \cos^{1.7}\theta$ | $0.865\ \cos^{4.4}\theta$ |
| 20 | $0.91\ \cos^{1.5}\theta$ | $0.793\ \cos^{3.8}\theta$ |
| 15 | $0.88\ \cos^{1.4}\theta$ | $0.733\ \cos^{3.2}\theta$ |
| 12.25 | $0.84\ \cos^{1.3}\theta$ | $0.688\ \cos^{2.8}\theta$ |
| 10.35 | $0.815\ \cos^{1.1}\theta$ | $0.647\ \cos^{2.1}\theta$ |

(d) The hard and soft components must be corrected for side (extensive) showers. The best correction can be obtained directly from extensive shower measurements.[15] Determinations by simple "out of line" coincidence methods are seriously wrong.

(e) Corrections must be applied for locally generated showers and secondaries.[14]

(f) Meteorological corrections should not be made on the basis of barometric pressure changes only, unless the measurements have been taken continuously over a long period.

(g) Geiger counters of large cross section or high pressure with thin walls will reduce the corrections required for short path lengths in the gas.

With regard to the properties of the two electronic components, our assumption of two components and our method of separation are such that the discrepancies mentioned in the introduction now appear as the expected behavior of the soft component, at least for energies greater than 30 Mev. For energies lower than this value it is also necessary to consider the effect of multiple scattering in the air in order to account for the zenith angle distributions. That the scheme is reasonable, however, is indicated by the result that the absorption length (160 g cm$^{-2}$) obtained for the $E_\tau$ component is certainly in accord with what is expected from our present knowledge of the altitude variation of

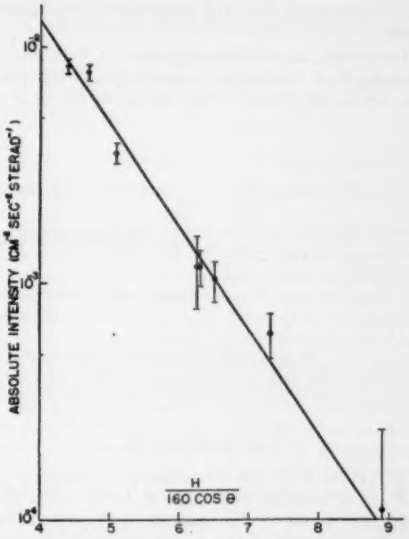


FIG. 7. Absolute intensity of $E_\tau$ component of energy greater than 30.8 Mev at Ithaca and Echo Lake for zenith angles out to 45° plotted against $h/160\cos\theta$.

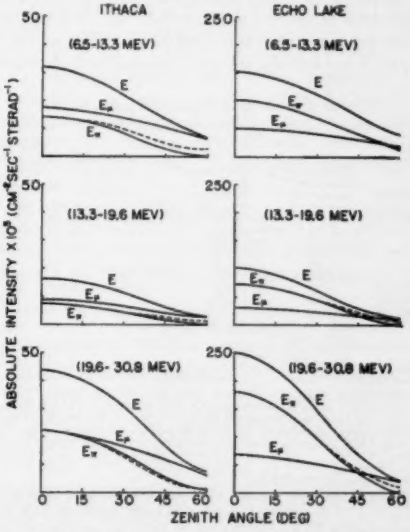


FIG. 8. Absolute intensities (multiplied by $10^3$) for zenith angles out to 45° of the $E$, $E_\mu$, and $E_\tau$ electronic components of various energies less than 30.8 Mev at Ithaca and Echo Lake.

the $N$ component and the properties of the neutral meson.

The author, in conclusion expresses his gratitude to Professor K. I. Greisen for his suggestion of this problem, and for his extensive help during the course of its investigation. Professor R. P. Feynman and Dr. G. Cocconi and Dr. V. Cocconi Tongiorgi contributed helpful advice. Further acknowledgment is due Dr. Iona and Dr. Cohn of Denver University and the Inter-University High Altitude Laboratory.

PHYSICAL REVIEW VOLUME 88, NUMBER 4 NOVEMBER 15, 1952

# Six-Millimeter Spectra of OCS and $N_2O$†

S. J. TETENBAUM*
*Sloane Physics Laboratory, Yale University, New Haven, Connecticut*
(Received July 25, 1952)

The $J=3\rightarrow4$ pure rotational transition of OCS and the $J=1\rightarrow2$ transition of $N_2O$ have been investigated. The molecules were in their normal isotopic abundances. The results are compared with those of previous investigators. Quadrupole hyperfine structure, $l$-type doubling, and Fermi resonance effects are analyzed.

## I. INTRODUCTION

BOTH the $J=3\rightarrow4$ pure rotational transition of the linear molecule OCS and the $J=1\rightarrow2$ rotational transition of the linear molecule $N_2O$ occur in the wavelength region around 6 mm. These spectra have been measured using the apparatus previously described.[1]

## II. CARBON OXYSULFIDE

The OCS molecule has been extensively investigated at wavelengths longer than 6 mm, and some work has been done at shorter wavelengths. The OCS was prepared by the action of $NH_4SCN$ on $H_2SO_4$ in water.[2] All OCS isotopic species were observed in their normal abundances. Ground-state lines were measured at $T=195°K$, and excited vibrational state lines were measured at room temperature. The pressure was kept at about $2\times10^{-3}$ mm Hg. Line positions were measured to an accuracy of $\pm0.1$ Mc/sec.

TABLE I. $J=3\rightarrow4$ rotational spectrum of OCS.

| Molecule | Vibrational state and $F$ transition | Experimental frequency in Mc/sec | Previously determined frequency in Mc/sec | Calculated intensity[b] at 300°K in $10^{-8}$ $cm^{-1}$ |
|---|---|---|---|---|
| $O^{16}C^{12}S^{32}$ | 0 0 0 | 48,651.40 ±0.10 | 48,651.64 ±0.05[a] | 436 |
| | 1 0 0 | 48,506.24 | | 7.0 |
| | 0 $1_0$ | 48,710.80 | | 34.9 |
| | 0 $1_0$ | 48,761.55 | | 34.9 |
| | 0 $2_0$ | 48,801.08 | | 2.7 |
| | 0 $2_0$ | 48,819.92 | | 5.2 |
| $O^{16}C^{13}S^{32}$ | 0 0 0 | 47,462.20 | 47,462.40 ±0.05[a] | 17.8 |
| $O^{16}C^{12}S^{34}$ | 0 0 0 | 48,494.76 | | 4.7 |
| $O^{18}C^{12}S^{32}$ | 0 0 0 | | | |
| | $3/2\rightarrow5/2$ | 48,038.19 | | 1.0 |
| | $5/2\rightarrow7/2$ | | | |
| | $7/2\rightarrow9/2$ | 48,039.13 | | 1.8 |
| | $9/2\rightarrow11/2$ | | | |

[a] Strandberg, Wentink, and Kyhl, Phys. Rev. **75**, 270 (1948).
[b] Calculated using intensity relation of P. Kisliuk and C. H. Townes, J. Research Natl. Bur. Standards **44**, 611 (1950). $\Delta\nu=6$ Mc/sec, and the dipole moments given in R. G. Shulman and C. H. Townes, Phys. Rev. **77**, 500 (1950). Those moments not measured were taken equal to 0.7085 debye.

Table I presents the experimental results obtained. No attempt was made to measure intensities, the relative intensities only being used as an aid in identifying the lines.

Only two quadrupole hyperfine components due to the $O^{16}C^{12}S^{32}$ molecule were found. Using the value of the coupling constant $(eqQ)=-29.07\pm0.01$ Mc/sec obtained by Eshbach, Hillger, and Strandberg,[3] and the center of gravity $\nu_0=48{,}038.86$ Mc/sec, the calculated line positions agree almost exactly with those observed.

The calculated rotational constants and $l$-type doubling constant are shown in Table II. A value of $1.28\pm0.05$ kc/sec for $D_0$, the centrifugal distortion coefficient in the ground vibrational state of $O^{16}C^{12}S^{32}$, was used in the calculation. This value is obtained from the data of Johnson, Trambarulo, and Gordy.[4] Strandberg, Wentink, and Kyhl[5] obtained a value of $D_0$ in $O^{16}C^{12}S^{32}$ of $1.60\pm0.05$ kc/sec. The first value agrees very closely with the theoretically determined value. $D_v$ in excited vibrational states and in all isotopes was taken equal to $D_0$ in $O^{16}C^{12}S^{32}$. The values of $\alpha_1$ and $\alpha_2$ were obtained from the excited state data, corrections being made for Fermi resonance (see below). The value of $\alpha_3$ was obtained from an analysis of the frequency shifts for isotopic changes of the masses of each of the three atoms of OCS. Townes, Holden, and Merritt obtained the relationship[6]

$$\alpha_1+2\alpha_2+\alpha_3=0.00856B_0,$$

† Assisted by the ONR.
* This paper, together with reference 1, is part of a dissertation submitted to the Faculty of the Graduate School of Yale University for the Ph.D. degree.
[1] S. J. Tetenbaum, Phys. Rev. **86**, 440 (1952).
[2] Stock, Siecke, and Pohland, Ber. deut. chem. Ges. **57**, 719 (1924).
[3] Eshbach, Hillger, and Strandberg, Phys. Rev. **85**, 532 (1952).
[4] Johnson, Trambarulo, and Gordy, Phys. Rev. **84**, 1178 (1951).
[5] Strandberg, Wentink, and Kyhl, Phys. Rev. **75**, 270 (1949).
[6] Townes, Holden, and Merritt, Phys. Rev. **74**, 1113 (1948).

TABLE II. Rotational constants of OCS (all quantities in Mc/sec).

| Molecule | $B_0$ | $\alpha_1$ | $\alpha_2$ | $\alpha_3$ | $q_l$ |
|---|---|---|---|---|---|
| $O^{16}C^{12}S^{32}$ | 6081.466±0.013 | 20.56±0.04[a] | $\left.\begin{matrix}-10.594\pm0.022\\-10.533\pm0.009\end{matrix}\right\}$[b] | 52.6[a] | 6.344±0.018 |
| $O^{16}C^{12}S^{33}$ | 6004.899±0.007 | | | | |
| $O^{16}C^{12}S^{34}$ | 5932.816±0.013 | | | | |
| $O^{16}C^{13}S^{32}$ | 6061.886±0.013 | | | | |

[a] Calculated using $\alpha_3 = -10.563 \pm 0.02$ Mc/sec.
[b] Upper value computed from (0 0 0) and (0 $1^0$0) vibrational states. Lower value computed from (0 0 0) and (0 $2^0$0) vibrational states.

from which $\alpha_3$ can be computed. The $l$-type doubling constant $q_l$ agrees well with the theoretical value of 6.34 Mc/sec obtained by Nielsen.[7]

Fermi resonance perturbation effects have previously been detected in OCS[8] and discussed in greater detail in the molecule BrCN.[1] The $J=3\rightarrow4$ transition has been analyzed,[9] and the results are shown in Table III. The two levels which perturb each other are the (1 $0^0$0) and (0 $2^0$0) levels. The energy separation between these levels in their unperturbed states ($\delta$) can be obtained from the experimental infrared data of Bartunek and Barker.[10] (The $2_0$ and $2_2$ levels should be interchanged from the positions of Bartunek and Barker because Fermi resonance would push the $2_0$ level up and the level corresponding to $\omega_1$ down. This also necessitates a change in their value of $X_{lk}$.) Using their data, we get $\delta=163.6$ cm$^{-1}$. The values of $\alpha_2$ obtained using different pairs of unperturbed vibrational state lines are unequal. This is due to the use of a first-order approximation formula relating the $B$'s and the $\alpha$'s. In the calculation of $\alpha_1$ an average value of $\alpha_3=-10.563\pm0.02$ Mc/sec was used. The computed value of the interaction energy $W_{12}$ is 43.2 cm$^{-1}$. The correction to the rotational frequency due to Fermi resonance perturbations is given by $2(J+1)(B-B^0)$. For the interacting levels bracketed together in Table III the correction is 19.33 Mc/sec.

## III. NITROUS OXIDE

The molecule $N_2O$ has a relatively small electric dipole moment, resulting in a rotational spectrum of small absolute intensity. Thus far, pure rotational transitions have been observed only in the ground vibrational state. This has precluded the observation of Fermi resonance and $l$-type doubling effects in the microwave data of $N_2O$, although an appreciable Fermi resonance effect has been found in the infrared spectrum.[11]

The microwave spectrum of $N_2O$ was first observed by Coles, Elyash, and Gorman.[12] They studied the molecules $N^{14}N^{14}O^{16}$ and $N^{15}N^{14}O^{16}$ in the $J=0\rightarrow1$ pure rotational transition. They also observed and analyzed the hyperfine structure due to the electric quadrupole moment of the $N^{14}$ nucleus. Since the two-quadrupole theory of Bardeen and Townes[13] had not yet been developed, they could only estimate the quadrupole coupling constant of the $N^{14}$ nucleus in the end position. The coupling constant for the central nitrogen was computed from the hyperfine structure of $N^{15}N^{14}O^{16}$.

The quadrupole hyperfine structure of $N^{14}N^{14}O^{18}$ in the $J=0\rightarrow1$ transition has also been investigated by Smith, Ring, Smith, and Gordy.[14] Using the previously determined value of $(eqQ)$ for central $N^{14}$, they determined the value of the end $N^{14}$ coupling constant so as to give the best fit with the two-quadrupole theory.[13] In their theoretical plot of this spectrum, the authors have left out a third line which belongs with the central group of the pattern.

The $J=3\rightarrow4$ and $J=4\rightarrow5$ spectra have been observed in $N^{14}N^{14}O^{16}$.[4] No hyperfine structure is mentioned in this paper.

The author has observed and analyzed the $J=1\rightarrow2$ rotational transition of $N^{14}N^{14}O^{16}$ in its ground state. Because there is quadrupole splitting of the $J=2$ level as well as of the $J=1$ level (as compared to only the $J=1$ level being split in the $J=0\rightarrow1$ transition), and also because the relative separation of the hyperfine components is only about one-half that in the lowest rotational transition, it is considerably more difficult to obtain accurate values of the quadrupole coupling constants.

At low pressures the absorption line was seen to consist of three separate components. The large central line was measured with the marker system. The relative positions and amplitudes of the three components were

TABLE III. Fermi resonance perturbations in the $J=3\rightarrow4$ transition of $O^{16}C^{12}S^{32}$.

| Vibrational state | Experimental $B$ value in Mc/sec[a] | Unperturbed $B$ value in Mc/sec[b] |
|---|---|---|
| 0 0 0 | 6081.466±0.013 | — |
| 0 $1^1$0 | 6092.060±0.018 | — |
| 0 $2^2$0 | 6102.521±0.013 | — |
| 1 $0^0$0 | 6063.321±0.013 | 6060.906 |
| 0 $2^0$0 | 6100.176±0.013 | 6102.592 |

[a] Center of gravity used when $l$-type doubling present. $B_0$ calculated using $D_0=1.28\pm0.05$ kc/sec for all vibrational states.
[b] Calculated using $\alpha_1=20.56$ Mc/sec and $\alpha_2=-10.563$ Mc/sec.

[7] H. H. Nielsen, Phys. Rev. **78**, 296 (1950).
[8] W. Low and C. H. Townes, Phys. Rev. **79**, 244 (1950).
[9] I should like to thank Professor C. H. Townes for making available an unpublished analysis of Fermi resonance in linear triatomic molecules.
[10] P. F. Bartunek and E. F. Barker, Phys. Rev. **48**, 516 (1935).
[11] G. Herzberg and L. Herzberg, J. Chem. Phys. **18**, 1551 (1950).
[12] Coles, Elyash, and Gorman, Phys. Rev. **72**, 973 (1947).
[13] J. Bardeen and C. H. Townes, Phys. Rev. **73**, 97 (1948).
[14] Smith, Ring, Smith, and Gordy, Phys. Rev. **73**, 633 (1948).

TABLE IV. The $J=1\rightarrow2$ transition of $N^{14}N^{14}O^{16}$.

| Transition ($F_{1t}$, $F_1\rightarrow F_{1f}$, $F_f$)[a] | | Observed relative intensity | Calculated relative intensity[b] |
|---|---|---|---|
| (2,1→2,2), (2,3→2,2), (2,1→2,1), (2,3→2,3), (2,2→2,2), (0,1→1,1), (2,2→2,3), (0,1→1,2), (2,2→2,1), (0,1→1,0) | 50,245.63±0.15 | 2 | 2 |
| (1,1→2,2), (2,3→3,3), (1,2→2,2), (1,1→2,1), (2,2→3,3), (1,2→2,3), (2,1→3,2), (2,3→3,4), (1,2→2,1), (2,3→3,2), (1,0→2,1), (2,2→3,2), (2,1→1,1), (2,1→1,2), (2,3→1,2), (2,1→1,0), (2,2→1,1), (2,2→1,2) | 50,246.03±0.10 | 8 | 8.2 |
| (1,1→1,1), (1,2→1,1), (1,1→1,2), (1,2→1,2), (1,0→1,1), (1,1→1,0) | 50,246.53±0.15 | 1 | 1 |

[a] Notation used is that of J. Bardeen and C. H. Townes, Phys. Rev. **73**, 97 (1948).
[b] Calculated assuming $|(eqQ)_{\text{end}}| \gg |(eqQ)_{\text{center}}|$.

TABLE V. Rotational constants of $N^{14}N^{14}O^{16}$.

| Spectrum | Center of gravity | $B_0$ in Mc/sec | $D_0$ in kc/sec |
|---|---|---|---|
| $J=0\rightarrow1$[a] | 25,123.25 | 12,561.64[b] | |
| $J=1\rightarrow2$[a] | 50,246.01 ±0.10 | 12,561.55 ±0.025[b] | |
| $J=3\rightarrow4$[d] | 100,491.76 ±0.25 | 12,561.65 ±0.023[b] | 5.67 ±0.05 |
| $J=4\rightarrow5$[d] | 125,613.68 ±0.30 | | |
| Vibrational bands from 0.8 to 1.2$\mu$[e] | | 12,564.1[f] | 5.7[g] |
| Vibrational bands near 4.5$\mu$[g] | | 12,565.3 ±4.5 | |

[a] Coles, Elyash, and Gorman, Phys. Rev. **72**, 973 (1947).
[b] Computed using $D_0=5.67$ kc/sec.
[c] Present work.
[d] Johnson, Trambarulo, and Gordy, Phys. Rev. **84**, 1178 (1951).
[e] G. Herzberg and L. Herzberg, J. Chem. Phys. **18**, 1551 (1950).
[f] $B_1=12,563.2$ Mc/sec.
[g] H. W. Thompson and R. L. Williams, Proc. Roy. Soc. (London) **A208**, 326 (1951).

interpolated from an enlarged photograph of the face of the cathode-ray oscilloscope. Frequency modulation sidebands were placed on the 3.5-cm klystron carrier,[1] and their frequency and amplitude were adjusted so that the main marker and one sideband straddled the pattern on the scope. Table IV shows the results obtained. The total spread is 0.9±0.1 Mc/sec, and the relative spacing from the low frequency component to the high frequency one is 0.4±0.05 Mc/sec and 0.5±0.05 Mc/sec.

The observed frequencies and calculated rotational constants for the $J=1\rightarrow2$ transition and previously investigated rotational transitions are shown in Table V. The results of recent infrared investigations are also included. It is seen that our $B_0$ value is somewhat smaller than that obtained in other microwave transitions.

TABLE VI. Quadrupole coupling constant of the end $N^{14}$ in $N^{14}N^{14}O^{16}$.

| Transition | $(eqQ)$ in Mc/sec | Reference |
|---|---|---|
| $J=0\rightarrow1$ | −0.78[a] | b |
| $J=0\rightarrow1$ | −1.03±0.10 | c |
| $J=1\rightarrow2$ | −1.05±0.20 | |

[a] Calculated using the line frequencies of reference b and the two-quadrupole theory of J. Bardeen and C. H. Townes, Phys. Rev. **73**, 97 (1948).
[b] Coles, Elyash, and Gorman, Phys. Rev. **72**, 973 (1947).
[c] Smith, Ring, Smith, and Gordy, Phys. Rev. **73**, 633 (1948).

Table VI shows the calculated quadrupole coupling constant for the end $N^{14}$ nucleus and compares it with previously determined values. In all cases, the coupling of the central $N^{14}$ nucleus was taken equal to −0.27 Mc/sec, the value obtained by Coles, Elyash, and Gorman.[11] The coupling constant for the $J=1\rightarrow2$ transition has a much larger probable error than that calculated from the $J=0\rightarrow1$ transition, but it seems to be closer to the value given in footnote b.

I wish to thank Professor Robert Beringer for his helpful advice and criticism throughout the course of this work.

# Precision Measurements of Nuclear $\gamma$-Ray Wavelengths of $Ir^{192}$, $Ta^{182}$, RaTh, Rn, $W^{187}$, $Cs^{137}$, $Au^{198}$, and Annihilation Radiation*

DAVID E. MULLER, HARRY C. HOYT, DAVID J. KLEIN,† AND JESSE W. M. DUMOND
*California Institute of Technology, Pasadena, California*

(Received July 14, 1952)

The sensitivity of the curved crystal gamma-ray spectrometer has been improved (1) by replacing the multicellular Geiger counter formerly used as a detector with a sodium iodide crystal scintillation counter and (2) by doubling the thickness of the quartz crystal which is used for diffraction of gamma-rays. Certain minute nonlinearities in the spectrometer have been detected and corrected in a recent calibration. An analysis of the precision of the instrument based on this calibration and a systematic treatment of errors due to random variations in counting rate is presented. Verification of the quoted precision is achieved by comparisons of wavelengths measured in various orders and by consistency of Ritz combinations.

Precision measurements of the wavelengths and energies of nuclear gamma-rays and x-rays which follow the decay of iridium 192, tantalum 182, radiothorium, radon, tungsten 187, cesium 137, and gold 198, as well as the annihilation radiation from copper 64, are tabulated. A topological system is used to enumerate all possible level schemes agreeing with a given set of Ritz combinations. This method is applied to determine possible level schemes for iridium 192 and tantalum 182. After all corrections, the measured wavelength of the annihilation radiation from copper 64 agrees, within the precision of the measurements, with the present "best" value of $h/m_e c$ (for electrons) as obtained by entirely independent methods. It is concluded that to a part in $10^4$ there is no evidence for any difference in mass between positive and negative electrons.

## I. INTRODUCTION

METHODS of measuring gamma-ray energies have advanced in two directions in the past few years. Much progress has been made in the measurement of extremely weak gamma-rays by the use of scintillation spectrometers of the type used by Hofstadter.[1] On the other hand, the method of crystal diffraction has been used to obtain highly precise measurements of relatively intense gamma-rays. Measurements of the latter type were made from 1947 to 1949 on a number of gamma-rays with the focusing crystal gamma-ray spectrometer of DuMond,[2–5] although at this time it was possible to obtain few sources of gamma-radiation in sufficient specific activity to allow measurements. Since then neutron irradiated sources of much higher specific activity have become available to us through the use of reactors with higher neutron flux than that available at Oak Ridge. Furthermore, the sensitivity of the spectrometer itself has been improved manyfold (1) by replacing the multicellular Geiger counter previously used for detecting the gamma-rays[6] with a sensitive scintillation counter using a thallium-activated sodium iodide crystal, and (2) by use of a 2-mm thick quartz crystal for diffracting the gamma-rays instead of a 1-mm crystal. Through such improvements in sensitivity and luminosity, a large number of gamma-rays which previously lay beyond the reach of this precise method may now be measured directly.

The scintillation counter which is employed as a detector contains a rectangular 3×3×1 in. single sodium iodide crystal as the scintillating element, so placed that it intercepts the 3×3 in. gamma-ray beam which is reflected from the quartz crystal. In order to protect the sodium iodide from the effects of the moisture in the air, it is immersed in a medium of resin and enclosed in a glass box. Scintillations from this crystal are detected by means of two RCA 5819 photomultiplier tubes making optical contact with two opposite 3×1 in. faces of the crystal through Plexiglas light conductors. These photomultipliers are operated in coincidence so as to reduce the amplitude of the random shot noise from the photomultipliers which, were it not reduced in this fashion, would produce pulses in the counting circuit similar to those produced by low energy gamma-rays. A drawing of the assembly of two photomultiplier tubes and scintillation counter, the latter with the front cover removed, is shown in Fig. 1.

Pulses from the coincidence circuits whose magnitudes fall within a chosen range are selected by means of adjustable upper and lower pulse-height discriminators, thus providing a means of rejecting pulses due to cosmic rays (which are generally very large) and some unwanted gamma-rays. As will appear later, this pulse-height discriminator also serves the valuable purpose of identifying the crystal order in which a line is reflected since it yields independent information regarding line energies.

## II. CALIBRATION OF THE SPECTROMETER

Since the curved crystal spectrometer is designed primarily to achieve high precision, it is of importance to include here a rather detailed description of (1) the most recent calibration which makes this precision

* This work was performed and financed under the joint sponsorship of the ONR and AEC by contract with the California Institute of Technology.

† Now with North American Aviation, Inc., Downey, California.

[1] J. A. McIntyre and R. Hofstadter, Phys. Rev. **78**, 617 (1950).

[2] DuMond, Lind, and Watson, Phys. Rev. **73**, 1392 (1948).

[3] DuMond, Lind, and Watson, Phys. Rev. **75**, 1226 (1948).

[4] Lind, Brown, Klein, Muller, and DuMond, Phys. Rev. **75**, 1544 (1949).

[5] Lind, Brown, and DuMond, Phys. Rev. **76**, 1838 (1949).

[6] D. A. Lind, Rev. Sci. Instr. **20**, 233 (1949).

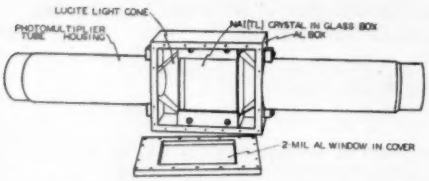


FIG. 1. The scintillation counter with front cover removed, exposing the crystal.

possible, and (2) certain auxiliary optical equipment which has recently been installed to permit correction for certain mechanical flexures in parts of the instrument.

An illustration of the basic geometry of the curved crystal spectrometer may be seen in Fig. 2. The crystal used for diffraction of the gamma-rays, which is shown schematically at $C$, consists of a slab of quartz 2 mm thick. It is bent elastically so that its (310) atomic planes, which are normal to the face of the crystal, converge toward the point $\beta$, 2 meters away. The reason for bending the crystal in this way is to allow all rays from a line source of gamma-radiation at $R$ to make the same angle $\theta$ with the crystal planes, thus making use of the entire crystal at once. It may be seen from simple geometry that this is approximately accomplished as long as the source $R$ lies on the circle passing through $C$ and $\beta$ and having a center at O. This imaginary circle on which the source $R$ must lie is called the focal circle.

Reflection of gamma-rays from the crystal planes occurs when $\theta$ equals the Bragg angle for the radiation being studied. Since the reflected radiation leaves the crystal planes at the angle of incidence, it diverges as though it were coming from the virtual focus point $V$. This divergent beam is separated from the heterogeneous radiation passing directly through the crystal by means of the tapered lead sheets (called the collimator) at $A$, and is detected by the scintillation counter at $G$.

The mechanism of the spectrometer shown in the perspective line drawing of Fig. 3 is designed to serve three purposes. (1) It permits accurate measurement of the sine of the angle $\theta$, which is the Bragg angle whenever reflection occurs. (2) It constrains the source $R$ to move on the focal circle, thus satisfying the focusing condition. (3) It moves both source and crystal in such a way that the Bragg reflected radiation remains fixed in space. This feature makes it unnecessary to move the heavy collimator and detector shown at $A$ and $G$.

In Fig. 3 the crystal is shown at $C$, while the source in its lead shielding lies at $R$. Those elements of the mechanism which rotate with the crystal frame of reference are (1) the lower beam $F$, which is connected to the crystal by means of a shaft; (2) the center of the focal circle $O$, lying on $F$; (3) the swinging track $T$, which pivots about the point $V'$; (4) the long carriage $Q$ which is driven on the track $T$ by a screw in the lower part of $Q$. $Q$ is prevented from rotating with respect to $F$ by means of a $1\frac{1}{2}$-inch rod $B'$ terminating $F$, which passes in and out through bearings on either side of $Q$ in a direction perpendicular to the motion of $Q$.

In order that the reflected radiation remain fixed in space, the source $R$ and the source beam $U$ upon which it rides must rotate about the crystal pivot at twice the angular speed of the crystal. This is accomplished by driving the small carriage $L$ (which supports $U$) along $Q$ at the same rate that $Q$ is being driven on $T$. $L$ is driven by means of a precision screw in the upper part of $Q$ having the same pitch as the lower screw which is geared directly to it. While the upper beam $U$ is moving, the source $R$ travels lengthwise on $U$ so as to stay on the focal circle to which it is constrained by the radius arm $OR$.

Since the beam $F$ is held perpendicular to the direction of travel of $Q$ and $L$, it is possible to measure a distance proportional to the sine of the angle of incidence with the precision screw. Thus a scale proportional to wavelengths can be read directly in terms of rotation of the screw because of the form of Bragg's

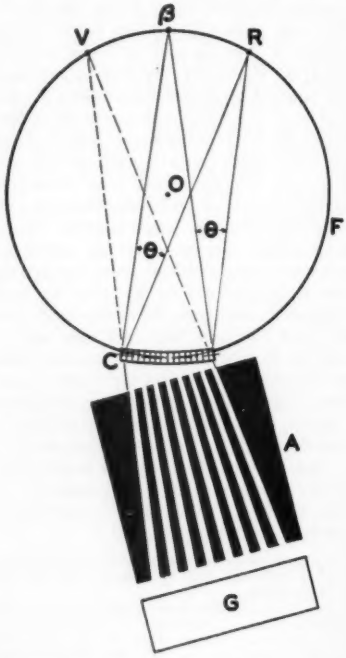


FIG. 2. Basic geometry of the gamma-ray spectrometer. The crystal appears at $C$ and the source at $R$ on the focal circle $F$. The reflected radiation appears to diverge from the virtual focus $V$ as it passes through the collimator $A$ to the detector at $G$.

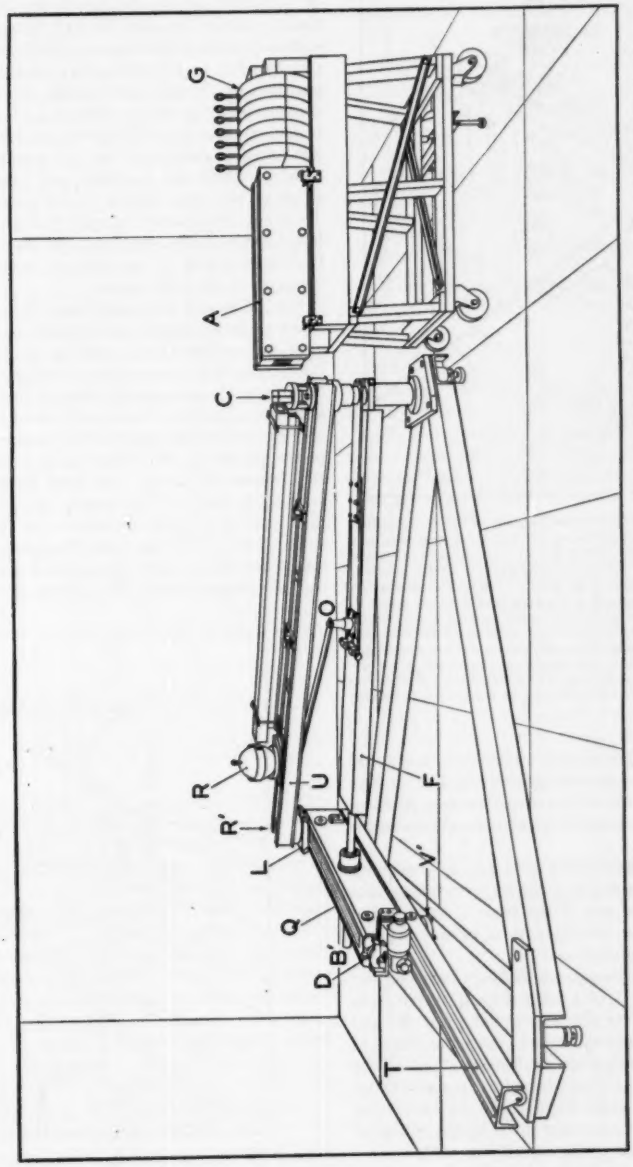


FIG. 3. Perspective line drawing of the gamma-ray spectrometer showing the curved crystal at *C* and the source in its shielded holder 2 meters from it at *R*.

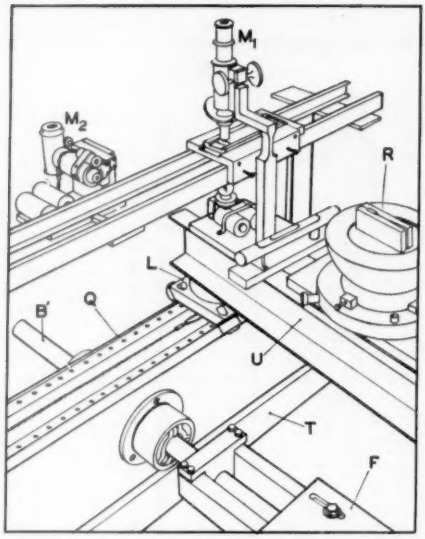


FIG. 4. Arrangements for the calibration of the spectrometer. A pair of rails rigidly supported on the long screw carriage carry a small carriage provided with a Bureau of Standards calibrated precision glass scale. A vertical microscope $M_1$, rigidly attached to the upper (source supporting) beam $U$, views the glass scale. The focus of the microscope is at the same height as the source $R$ and is directly above the pivot of the small carriage $L$, supporting the upper beam. The horizontal elbow microscope $M_2$ and tiny light source used in conjunction with the 6-inch concave mirror to detect any anomalies in the motion of the crystal pivot are mounted at the center of the rails. The source holder $R$, standing on the lower half of the lead bomb used for shielding, can be seen at the right center.

law, $n\lambda = 2d \sin\theta$. Gamma-ray wavelengths are measured by comparing the positions of the line profiles taken *on opposite sides* of the central source position, thus eliminating the need for a well-defined zero on the machine.

To calibrate the instrument, it is necessary to check as completely as possible that the screw measurements do correspond to the sine of the angle of incidence of the gamma-radiation on the curved crystal. This is done in a two-step procedure.

First, precision displacements, measured with respect to the long carriage $Q$, of a point defined by the focus of a microscope vertically above the pivot $R'$ and rigidly fixed to the source beam at the same height as the source, were calibrated against rotation of the screw, and second, the deflections of the curved crystal $C$ with respect to a point fixed in the system $Q$ were studied. In this way a complete check on the motion of the source with respect to the crystal was made.

In order to carry out the first mentioned part of the calibration, a framework to support a pair of steel rails was built on the long carriage $Q$. A 100-power microscope, $M_1$, mounted exactly above the pivot $R'$ on a bracket rigidly attached to the source beam was used to observe the scratches in a Bureau of Standards calibrated glass decimeter scale which was set on these rails (see Fig. 4). By setting the glass scale at particular positions on the rails and reading the screw positions corresponding to various scratches on the glass scale, it was possible to calibrate the precision screw. Care was taken to make sure that the height on the instrument at which the scratches were observed was the same as the mean height of the gamma-ray source. Thus any reproducible minute rocking of the source beam (around its long axis), because of departures from straightness in the ways, for example, would be corrected in the calibration.

For the second mentioned part of the calibration, in which a check was made on the alignment of the crystal with an invariable point fixed on the long carriage, a 6-inch spherical concave mirror having a 90-inch radius of curvature was mounted in place of the curved crystal, and with its center of curvature located centrally on the long carriage at the height of the source. A second 100-power microscope $M_2$ visible in Fig. 4 was mounted on the framework, which had been built on the long carriage in such a position that its focus was located just below the center of curvature of the 6-in. mirror, while a tiny set of cross hairs, illuminated from behind, was mounted just above the center of curvature. In this way the image in the 6-in. mirror of the cross hairs

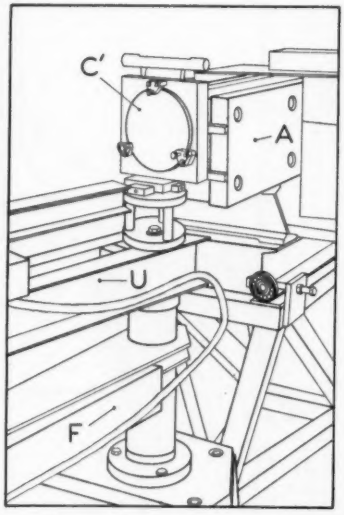


FIG. 5. The 6-inch precision-figured concave mirror $C'$, mounted on the crystal pivot in place of the crystal, where it served, along with the elbow microscope $M_2$ and light source of Fig. 4, to check the fidelity with which the turning of the crystal pivot followed the motion of the long screw carriage.

appeared at the focus of the second microscope. Slight angular motions of the crystal pivot with respect to the long carriage, produced by flexures in the parts of the spectrometer, were measured by observing deflections of the image of the cross hairs on a scale located in the eyepiece of the second microscope. By observing the image of the cross hairs at approximately the height of the gamma-ray source, the sine of the angle of incidence of gamma-rays on the curved crystal may be measured to an accuracy of about $10^{-6}$ independently of slight tilts of any of the carriages or pivots. In Fig. 4 may be seen the calibration framework and microscopes, while in Fig. 5 the 6-inch mirror may be seen mounted above the crystal pivot.

Since the glass decimeter scale would only cover $\frac{1}{10}$ of the one meter screw at a time, it was necessary at intervals to slide the scale along the rails, while maintaining the spectrometer in a fixed position, and match the terminal scratches on the scale. In this way the entire screw was calibrated in steps of one decimeter.

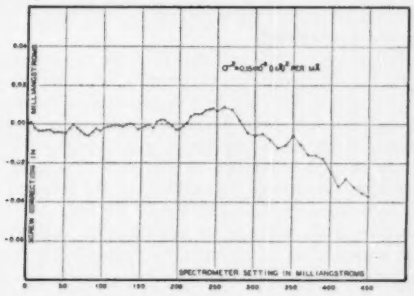

FIG. 6. The wavelength correction necessitated by nonlinearity of the screw. Quasi-periodic correction has been subtracted.

Within each decimeter, points were taken either every 5 or every 10 millimeters, depending on the region being calibrated. In addition to this over-all calibration, the deviations from linearity of the screw which occur in single revolutions of the screw were studied by replacing the decimeter scale with a second calibrated glass scale having scratches every tenth of a millimeter over a distance of one millimeter. Such single revolutions were calibrated every ten revolutions within the interesting range and a quasi-periodic error was thus eliminated.

Results of both the screw calibration and the alignment of the crystal with the long carriage are plotted in Figs. 6 and 7, respectively. Both of these corrections are zero at 208.996 milliangstroms, the wavelength of the tungsten $K\alpha_1$ x-ray line, since this line, which has been measured with high precision,[7] is used for fixing the scale of the screw in terms of wavelength units and therefore represents a known point on the screw. An inspection of these curves shows that the latter

[7] Watson, West, Lind, and DuMond, Phys. Rev. 75, 505 (1949).

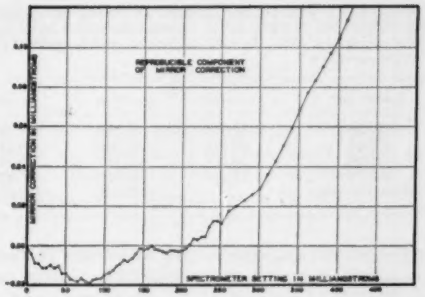

FIG. 7. The wavelength correction necessitated by misalignment of the crystal with the long carriage.

correction (the one observed with the concave mirror) is by far the greater. We have shown that it is chiefly due to two influences: (1) a slight variable flexure of the $1\frac{1}{4}$-inch rod which terminates the lower beam ($B'$, Fig. 4), and (2) minute flexures in the base of the instrument (caused by the shifting of the weight of the screw carriage, as the wavelength scale is explored, which tilts the crystal pivot (in a nonlinear way) clearly detectable by the sensitive level mounted on top of the six inch mirror. That part of the correction due to the flexure of the $1\frac{1}{4}$-inch rod has been entirely explained by an analysis of the effects of known forces and torques which are present in the instrument. We have also observed that this "mirror correction" exhibits considerable hysteresis, i.e., its magnitude depends on the history of the sequence of wavelength settings which have been made just previous to the observation. This is undoubtedly due to nonreproducible flexure of the $1\frac{1}{4}$-inch bar which determines the orientation of the long carriage $Q$ and the track $T$. The combined correction plotted in Fig. 8 shows, furthermore, that within the range of settings corresponding to gamma-ray wavelengths, this correction is never greater than 0.025

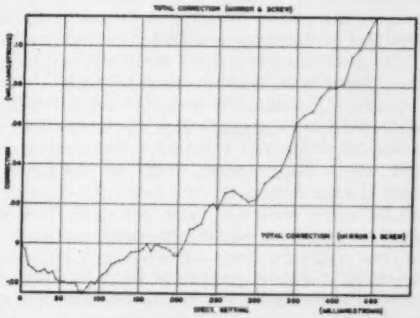

FIG. 8. The sum of screw and mirror corrections, representing therefore the total correction to be applied to measurements in the range of wavelengths from 0 to 450 milliangstroms.

TABLE I. Wavelengths (in milliangstroms) of five intense lines from iridium 192 as measured in various orders after being corrected using the older, inferior calibration which ignored the "mirror-correction."

| Energy, kev | 3rd order | 2nd order | 1st order |
|---|---|---|---|
| 295.94 | 41.898 | 41.894 | 41.909 |
| 308.45 | 40.191 | 40.205 | 40.214 |
| 316.46 | 39.174 | 39.183 | 39.197 |
| 467.98 | 26.496 | 26.503 | 26.515 |
| Iridium $K\alpha_1$ x-ray | | 190.993 | 191.025 |

milliangstrom. To visualize the minuteness of these corrections, one must realize that 0.02 milliangstrom corresponds to a motion of the gamma-ray source of less than 0.02 millimeter, or to a deviation in the sine of the Bragg angle of less than $10^{-5}$.

In our earlier work with this instrument up to the spring of 1951, we had indeed corrected for periodic and aperiodic errors in our screw, but these calibration curves were much less carefully observed and also took no account of the then unsuspected "mirror correction." The scale in this earlier calibration was, furthermore, not supported at the same height as the source so that the calibration did not correct for minute rocking of the source beam.

The first definite internal evidence of slight residual nonlinearity in our supposed linear wavelength scale came when, thanks to greatly improved sensitivity secured by replacing our earlier "multicellular" Geiger counters with a sodium iodide scintillation crystal, we were able to observe one and the same wavelength in three different orders of reflection from the curved quartz crystal for four different intense nuclear gamma-ray lines emitted by an exceptionally strong source of iridium 192. We were also able to observe the intense $K\alpha_1$ x-ray line from iridium in first- and second-order reflection. These results (see Table I) exhibited a very definite systematic trend: Wavelengths computed from higher order reflections were (in every case but one) slightly shorter. These disagreements, however, were not sufficient to establish a very reliable correction curve by themselves. Nevertheless, it was because of them that the intensive recalibration and study of the minute causes of nonlinearity in the instrument (lasting over a period of six months) was undertaken.

An idea of the reliability of the new calibration may be gleaned from a comparison of the intense lines of iridium 192 which were measured in first, second, and third orders. These results, which are compared in Table II after making the new calibration correction and the mirror correction, agree well within their assigned errors and correspond to measurements made at one, two, and three times the wavelength settings of these lines. It is interesting to note that even the measurements on the intense iridium $K\alpha_1$ line, which was obtained in the second as well as the first order, agree quite well in spite of the fact that corrections in this case were relatively large.

At present the calibration equipment is to be used to provide still higher precision than was possible before. By permanent installation of the 6-inch mirror above the curved crystal, the alignment of the crystal with the long carriage is now and henceforth checked at the time and every time that the gamma-rays are actually being measured. In this way, any possible hysteresis or nonreproducibility present in this motion is automatically taken into account. Similar methods are used for checking the behavior of the screw.

With the use of these improvements a further exceedingly satisfactory check has been made on the reliability of the calibration by observing in three different orders of reflection the 412-kev line from a strong source of gold 198. Wavelength measurements in the first, second and third orders of reflection are $30.102 \pm 0.0038$, $30.105 \pm 0.0033$, and $30.107 \pm 0.0028$ milliangstroms, respectively. Disagreement between these measurements lies well within the assigned errors, thus confirming even more satisfactorily the reliability of the calibration. This is definitely not the case in the data obtained before the screw calibration and mirror corrections were applied.

By making multiple calibrations of the spectrometer, it was possible to estimate the errors which arose during the calibration. This was done by determining the mean square deviations from the mean and dividing by the number of degrees of freedom. A random walk analysis of the over-all calibration of the screw was used to determine the error of the calibration. For this part of the calibration $\sigma^2 = 0.15 \times 10^{-6} (\text{mA})^2$ per mA. A determination of the errors in the quasi-periodic calibration was accomplished by repeating the calibration of single turns of the screw. Random variations in screw readings and in the "mirror correction" were treated in a similar fashion. Results of these calculations indicate that the errors to be expected in wavelength measurements made subsequent to the calibration are less than 0.005 milliangstrom because "mirror" readings are taken at the time the gamma-rays are measured. Measurements made prior to the calibration are subject to the somewhat larger uncertainty of about 0.01 milliangstrom because no check had been made at that time of the alignment of the crystal with the long carriage. In order to correct these older measurements the curve shown in Fig. 7 (which was obtained during the calibration) had to be used.

TABLE II. Wavelengths (in milliangstroms) of five intense lines from iridium 192 as measured in various orders after being corrected using the latest calibration.

| Energy, kev | 3rd order | 2nd order | 1st order |
|---|---|---|---|
| 295.94 | 41.891 | 41.885 | 41.887 |
| 308.45 | 40.187 | 40.190 | 40.191 |
| 316.46 | 39.172 | 39.172 | 39.175 |
| 467.98 | 26.486 | 26.491 | 26.495 |
| Iridium $K\alpha_1$ x-ray | | 191.041 | 191.031 |

### Theory of Errors in Wavelength Measurement Resulting from Random Variations in Counting Rate Alone

For wavelength measurement, plots are made of the two line profiles obtained by use of internal reflection from opposite sides of the crystal planes. A typical pair of such plots is shown in Fig. 9. Since the wavelength of the line corresponds to the number of screw divisions of displacement between such opposite plots, the following system has been devised for determining such displacement with high precision. A composite line profile is drawn from the superposition of several such plots. This composite line profile is then matched as carefully as possible to the two opposite plots of a line. By measuring the displacement of this composite profile in going from one plot to the opposite one, a measurement of wavelength can be made with an error which is a small part of the actual breadth of a line.

In order to analyze the error[8] resulting from the above procedure, it is necessary to derive an expression for the precision with which a composite profile can be fitted to the plot of a line, assuming that a least squares fit is obtained.[9] Let $L(u)$ be the average counting rate at spectrometer setting $u$. $L(u)$, therefore, represents a line profile if $u$ covers a range of settings which include a line. If a series of measurements of counting rate is made lasting $\tau$ minutes each at a set of positions $u_i$, $i=1, \cdots, n$ the expected number of counts at each point will then be given by $\tau L(u_i)$, and the standard variation of each such point from its expected number of counts will be $[\tau L(u_i)]^{\frac{1}{2}}$ if the normal distribution is used to approximate to the Poisson distribution. Each counting rate measurement at a point $u_i$ may be thought of as constituting an independent measurement of the position of the composite profile, since the profile, once obtained, could conceivably be fitted to a single point. As such, the standard error of the position measurement corresponding to a run at $u_i$ lasting $\tau$ minutes is $[\tau L(u_i)]^{\frac{1}{2}}/\tau L'(u_i)$, provided that the slope $L'(u)$ of the curve $L(u)$ does not change appreciably over the vertical interval $[\tau L(u_i)]^{\frac{1}{2}}$, so that the error in fitting the composite profile horizontally may also be considered normal. The combined effect of the measurements of counting rate at all $n$ points can be regarded as a combination of independent measurements, each contributing with a weight inversely proportional to the square of its standard error. Hence, if $\sigma$ is the standard error of the fitting of the composite profile to all points, we obtain

$$1/\sigma^2 = P = \sum_{i=1}^{n} \tau[L'(u_i)]^2/L(u_i). \tag{1}$$

$P=1/\sigma^2$ is a convenient measure of the precision of fit.

Regarding the setting $u$ as a function of time $t$, we may let $n$ increase indefinitely, and replacing $\tau$ by $dt$ we obtain another representation of Eq. (1),

$$1/\sigma^2 = P = \int \{[L'(u)]^2/L(u)\}dt, \tag{2}$$

which is somewhat more general than Eq. (1) since it holds regardless of how the interval is traversed. It should be reiterated that Eqs. (1) and (2) were based on the following approximations:

1. All counting intervals contain enough counts so that the Poisson distribution may be approximated by a normal distribution.

2. All errors are small enough so that, within their range, the curve $L(u)$ does not change slope appreciably.

Of these two approximations the second one is the more serious since it tends to break down when one considers extremely weak lines. Nevertheless, this assumption is necessary for a systematic analysis of these errors.

In order to obtain an explicit expression for the errors in fitting a particular profile we make the following additional approximations:

3. Points on the profile are uniformly spaced and sufficiently closely spaced that a continuous distribution of points may be used to approximate the actual discrete distribution.

4. The line profile has the shape of an isosceles triangle, its apex representing the line peak, and the extended background representing its base.

This simple profile seems to be very nearly the shape of the actual one in many cases (see Fig. 9) and certainly is not so far wrong as to cause a greatly incorrect estimate of $P$.

Assigning a base width $W$ to the line and a peak height $H$ above background $B$, we obtain $[L'(u)]^2 = 4H^2/W^2$ over the profile so that if a total time $T$ is required to cross the line, then

$$P = \frac{2T}{W}\int_0^{W/2} \frac{4H^2/W^2}{(2Hl/W)+B}dl,$$

giving

$$P = 1/\sigma^2 = (4HT/W^2)\log[(H+B)/B]. \tag{3}$$

Actual lines which have been investigated have $\sigma$'s as calculated by Eq. (3) which are less than 0.001 milliangstrom in almost all cases, and for this reason we feel that errors due to random variations in counting rate are considerably smaller than instrumental errors.

[8] This analysis only aims to give that component of the total error in the wavelength determination which comes from one cause alone, the statistical fluctuations of counting.

[9] In actual practice the composite profile is fitted to the observed points on the profile of a given line, not by the laborious numerical method of least squares, but by a visual estimate of the "best" fitting position. It is found by actual test that this can be judged with remarkable accuracy in accord with the least squares criterion. Hence for this analysis a least squares fit is assumed. Errors resulting from imperfect visual fitting of the composite profile have been studied and have been found experimentally to be of the same order or less than those due to statistical fluctuations of counting.

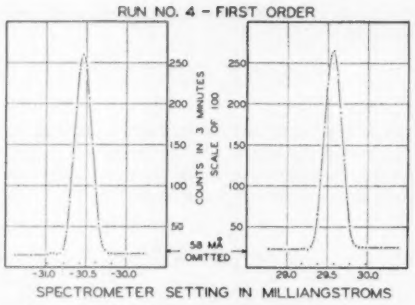


FIG. 9. A typical pair of line profiles. This pair of profiles was obtained for the 412-kev gamma-radiation following decay of gold 198. The wavelength is found by first forming a composite profile by superposition of all profiles (plotted to the same scale) obtained with the same source and then matching each profile individually to the composite profile. The difference in screw readings for the two members of a pair corresponding to a fiducial mark on the composite profile gives twice the wavelength, before corrections.

### III. IRIDIUM 192

Iridium 192 has been found to decay with a half-life of 70 days by both $\beta^-$ emission and $K$ capture.[10] The end point of the $\beta^-$ spectrum as measured by Mandeville and Scherb and others[11–13] corresponds to an energy of about 0.6 Mev, the exact end point being difficult to measure because it is obscured by internal conversion lines. A simple spectrum is thought to exist, however, since the ratio of beta-gamma coincidence counting rate to $\beta$-counting rate does not seem to vary as $\beta$-absorber is placed in front of the $\beta$-counter. Mandeville and Scherb have also found by means of coincidence measurements that each $\beta$-ray is followed on the average by 0.6 Mev of gamma-radiation.

We infer from the presence of osmium $K$ x-rays, along with those from iridium and platinum, in the spectrum from a neutron activated source of iridium 192 that iridium 192 also decays by the process of $K$ capture to osmium 192 with the possible emission of gamma-rays following this decay. $K$ capture leaves the atom of osmium ionized in the $K$ shell, thus giving rise to $K$ x-rays. Cork[10] has confirmed this conclusion by detecting Auger electrons corresponding to osmium x-rays.

A list of our measured x-ray lines from a neutron-activated source of iridium 192 is given in Table III, where present measurements of wavelengths are compared with those of Ingelstam.[14] Intensities of the $K$ spectra of osmium, iridium, and platinium were observed to lie in the ratio 1:1.7:1.3. While $K$ lines of iridium are, no doubt, excited by fluorescent absorption of gamma-rays in the source material, those of platinium must be produced by internal conversion of the gamma-rays following $\beta^-$ decay. Since the needed internal conversion coefficients are not known, it is not possible to determine quantitatively, from a comparison of x-ray intensities, the relative probabilities of $K$ capture and $\beta^-$ decay. On the other hand, we can be certain that the latter has the greater probability, since osmium x-rays are the least intense of all.

By studying characteristics of the peaks obtained during the search for lines from iridium 192, it is possible to make an interpretation of them in terms of gamma-rays and x-rays appearing in the first, second, and third orders of reflection from the quartz crystal.

X-ray lines may be identified in a number of ways. In the first place, their wavelengths are fairly well known so that by accurate measurement alone a positive identification can be made. Second, the natural breadths of the $K$ lines are quite comparable to instrumental breadths of the spectrometer so that they appear detectably broader than gamma-lines, whose natural breadth is quite negligible. Finally, the x-ray lines appear in characteristic series having definite intensity ratios, so that a complete series may be expected and the positions of the lines predicted in advance.

Second and third orders of intense gamma- and x-ray lines appear at spectrometer settings corresponding to two and three times the wavelength of the first-order reflections. Intensities of first- to second- to third-order reflections were found to lie in the ratio of 1:0.013:0.005 [quartz (310) planes]. Identification of the various orders was thus achieved by comparing spectrometer settings and intensities. A positive identification could also be made in all cases by use of the scintillation counter as a low resolution spectrometer operating in tandem with the crystal diffraction spectrometer to separate orders of reflections. Gamma- and x-ray lines will thus produce scintillation pulse-height spectra corresponding to the energy of the reflected photons and independent of the order of reflection. Using the

TABLE III. Wavelengths (in milliangstroms) of x-rays which follow decay of iridium 192.

| Designation | Present measurement | Measurement by Ingelstam |
|---|---|---|
| Os $K\alpha_2$ | 201.620 | 201.627 |
| Os $K\alpha_1$ | 196.771 | 196.783 |
| Ir $K\alpha_2$ | 195.869 | 195.889 |
| Ir $K\alpha_1$ | 191.031 | 191.033 |
| Pt $K\alpha_2$ | 190.362 | 190.372 |
| Pt $K\alpha_1$ | 185.485 | 185.504 |
| Os $K\beta_3$ | 174.418 | 174.424 |
| Os $K\beta_1$ | 173.584 | 173.607 |
| Ir $K\beta_3$ | 168.524 | 168.533 |
| Pt $K\beta_3$ | 164.463 | 164.489 |
| Ir $K\beta_2^{II}$ | 164.009 | 164.139 |
| Ir $K\beta_2^{I}$ | | 163.944 |
| Pt $K\beta_1$ | 163.661 | 163.664 |
| Pt $K\beta_2^{II}$ | 159.257 | 159.374 |
| Pt $K\beta_2^{I}$ | | 159.184 |

[10] Cork, LeBlanc, Stoddard, Childs, Branyan, and Martin, Phys. Rev. **82**, 258 (1951).
[11] C. E. Mandeville and M. V. Scherb, Phys. Rev. **73**, 1434 (1948).
[12] L. J. Goodman and M. L. Pool, Phys. Rev. **71**, 288 (1947).
[13] P. W. Levy, Phys. Rev. **72**, 352 (1947).
[14] E. Ingelstam, Nova Acta Regiae Soc. Sci. Upsaliensis **73**, 812 (1948).

above methods, it was possible to pick out from the 38 peaks originally noted, 11 distinct nuclear gamma-rays lying between the energies of 136.33 kev and 612.87 kev. Of these eleven, the four gamma-rays having energies of 467.98 kev, 316.46 kev, 308.45 kev, and 295.94 kev were five to ten times as intense as any other lines present and were all obtained in the second and third orders as well as in the first order. Four much weaker lines of higher energy were also measured at energies of 484.75 kev, 588.40 kev, 604.53 kev, and 612.87 kev, the last pair comprising a fairly close doublet which had to be separated by use of a composite profile.

A complete list of gamma-ray wavelengths and energies, together with their approximate intensities and estimated errors is given in Table IV, while a comparison of these measurements with results previously obtained by use of beta-ray spectrometers is given in Table V. For the sake of consistency, only first-order measurements are listed in these tables.

TABLE IV. Wavelengths and quantum energies of gamma-rays following decay of iridium 192.

| Identification letter[a] | Wavelength in milliangstroms | Energy in kev | Relative intensity[c] |
|---|---|---|---|
| *A* | 20.227±0.020[b] | 612.87 ±0.61 | 50 |
| *B* | 20.506±0.020[b] | 604.53 ±0.59 | 140 |
| *C* | 21.068±0.010 | 588.40 ±0.28 | 110 |
| | 25.573±0.010 | 484.75 ±0.19 | 110 |
| *D* | 26.489±0.004 | 467.984±0.061 | 3000 |
| *E* | 39.172±0.004 | 316.462±0.034 | 9900 |
| *F* | 40.189±0.004 | 308.454±0.033 | 3700 |
| *G* | 41.888±0.004 | 295.942±0.031 | 3800 |
| | 60.254±0.011 | 205.736±0.038 | 750 |
| | 61.580±0.011 | 201.306±0.037 | 100 |
| *H* | 90.929±0.012 | 136.331±0.019 | 40 |

[a] Only those lines which can be assigned to platinum 192 have been given identification letters. This identification was made by Cork and his co-workers from $\beta$-ray spectrometer studies.
[b] Errors in these two measurements are greater because the line profiles overlapped and had to be separated by using the composite profile.
[c] Relative intensities of lines having greatly different energies cannot be compared reliably because the variation of sensitivity of the spectrometer with energy is not accurately known for this source.

TABLE V. A comparison of present measurements with various other determinations of gamma-ray energies in kev from iridium 192.

| Present measurement | Cork *et al.*[a] | H. & M.[b] | Levy[c] | Cork[d] | Deutsch[e] |
|---|---|---|---|---|---|
| | | | | 651 | |
| 612.87 | 611.2 | | 615 | 610 | |
| 604.53 | 603.7 | | 607 | 601 | 603 |
| 588.40 | 588.6 | | 591 | 586 | |
| 484.75 | 484 | | 488 | 477 | |
| 467.98 | 467.4 | | 468 | 466 | 467 |
| | 415.1 | | | | |
| 316.46 | 316.1 | 317 | 316 | 315 | |
| 308.45 | 307.7 | 308 | 307 | 306 | 307 |
| 295.94 | 294.9 | 296 | 295 | 294 | |
| | 283 | | | 269 | |
| 205.74 | 205.7 | 208 | 209 | | |
| 201.31 | 201.1 | | | | |
| 136.33 | 135.9 | 137 | | | |

[a] See reference 10.
[b] R. D. Hill and W. E. Meyerhof, Phys. Rev. **73**, 812 (1948).
[c] See reference 13.
[d] J. M. Cork, Phys. Rev. **72**, 581 (1947).
[e] M. Deutsch, Phys. Rev. **64**, 265 (1943).

A level scheme involving all but the four gamma-lines at 201.31 kev, 205.74 kev, 484.75 kev, and 588.40 kev may be constructed as shown in Fig. 10, in which different Ritz combinations of the various lines agree in energy to better than their estimated errors. This scheme is also in good agreement with observed intensities and is essentially the same as the one proposed by Cork in 1951.[10] Its construction was permitted by the use of the following energy combinations:

$$\begin{aligned} &295.94 \text{ kev} + 308.45 \text{ kev} = 604.53 \text{ kev};\\ &136.33 \text{ kev} + 467.98 \text{ kev} = 604.53 \text{ kev};\\ &295.94 \text{ kev} + 316.46 \text{ kev} = 612.87 \text{ kev}. \end{aligned} \qquad (4)$$

Gamma-ray energies combine with such exactness (well within their assigned errors, given in Table IV) that the validity of these combinations seems practically certain. The level scheme of Fig. 10 which was derived from these combinations is, however, by no means unique, since by permuting the orders of the various lines within the combinations, it is possible to arrive at other level schemes. Level schemes obtained in this way, such as the one in Fig. 11, involve the same combinations, but are otherwise quite different. The level scheme of Fig. 11 has the advantage over the first level scheme of agreeing with the assertion of Mandeville and Scherb that 0.6 Mev of gamma-radiation follows beta-emission, but the disadvantage not present in the first scheme of disagreeing decidedly with the intensity ratios noted during the present measurements.[15]

## Topological Method of Enumerating Level Schemes

Since various energy level schemes may be constructed from a given set of Ritz combinations, it is of interest to see how many ways a given set of combina-

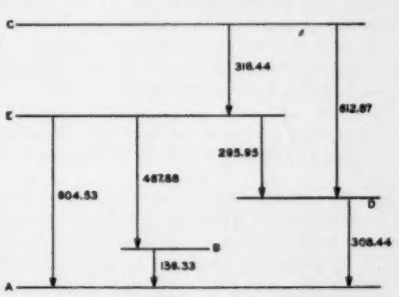


FIG. 10. Proposed energy level scheme for platinum 192.

[15] Intensities of the lines at 295.94 kev and 308.45 kev are about the same, while the intensity of the one at 316.46 kev is more than twice this. In the scheme of Fig. 11, one would expect the intensity of the 295.94 kev line to be greater than the sum of the other two.

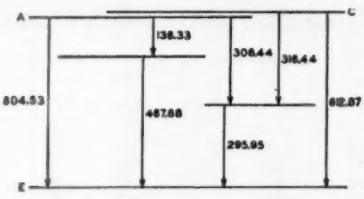


FIG. 11. Alternate energy level scheme for platinum 192.

tions may be permuted to give different level schemes, and to attempt to devise a system for enumerating these schemes quickly and easily. Physical considerations such as intensity ratios, coincidence studies, multiplicity of $\beta$-rays, and multipolarity of gamma-radiation provide the basis for determining the most likely of the several permutations.

In a general scheme consisting of $N$ levels, $L$ gamma-lines, and $C$ algebraically independent Ritz combinations, let us concentrate on a particular combination such as one of Eqs. (4). Taking an arbitrary line of this combination, we discover that the level from which it originates has one, and only one other line of the combination, either passing to it or away from it. This line in turn passes either away from, or to another level where a third line of the combination has its terminus, so we may pass in a circuit around the various lines of the combination until we arrive at the original line where we started. Such a circuit may be represented graphically on a topological diagram as a loop with the various levels appearing as dots or points and the gamma-lines as the connecting lines between these points. Other combinations, involving perhaps some of the same gamma-rays, form other circuits containing points (or levels) and lines in common with this one and the whole is thus represented as a network. In this topological network the lengths of the various lines in no way correspond to gamma-ray energies, and consequently this representation conveys no numerical information concerning the combinations, but instead may be used to show at a glance their topology. The topological network representation of the iridium level scheme is shown in the upper drawing of Fig. 12.

Given such a network, it is possible to construct the associated decay scheme if one knows the line energies and the signs to be attached to these energies in each circuit.[16]

Once the network representation for a level scheme has been obtained, it is possible to arrive at other level schemes having the same independent combinations (or circuits) by permuting the orders of lines appearing in the various circuits in such a way as to avoid changing the lines appearing in any circuit. In the lower drawing of Fig. 12, lines $a$ and $b$ have been interchanged, thus changing the level scheme from the one appearing in Fig. 10, represented by the upper drawing of Fig. 12, to the one appearing in Fig. 11. Clearly, still other level schemes could be constructed by interchanging $c$ and $d$ or by interchanging both $c$ and $d$, and $a$ and $b$. Still more schemes may be constructed by inverting the orders of all lines in all the circuits thus effecting a mirror transformation. This type of transformation corresponds to turning the entire level scheme upside down, and is always possible, even when no other permutations are permitted. By considering all possible permutations of the scheme in Fig. 12, eight different networks of this type having the circuits of the original scheme, may be constructed. Two of these additional schemes may be obtained by inverting those of Figs. 10 and 11, while the remaining four result from the interchange of the 467.98-kev and the 136.33-kev lines. An inspection of any network of this type will disclose which permutations of lines may be made without destroying the existing circuits and the resulting level schemes may be constructed.

[16] A positive sign may be arbitrarily attached to a line in a combination if, as one passes around a circuit, one goes from the final to the initial state, while a negative sign may be attached if one goes from the initial to the final. The algebraic sums of the lines contained in any circuit is therefore zero.

## IV. TANTALUM 182

The radiations from tantalum 182 and its daughter tungsten 182 have been studied by several groups.[17–24] With the single exception of reference 20, where absorption and coincidence methods were used, all of these investigations were made with $\beta$-ray spectrometers. In reference 23 Beach, Peacock, and Wilkinson reported the presence of at least one group of beta-particles (with end point at 0.525 Mev), 3 intense gamma-rays in the neighborhood of 1.2 Mev, and 17 low energy gamma-rays ($<$0.33 Mev). The most recent paper[24] by the Michigan group gives 14 to 18 low energy gamma-rays; this same paper proposes a nuclear energy level scheme of 8 levels to account for these gamma-ray lines. No attempt was made to fit the 3 high energy lines into this scheme.

The great number of gamma-ray lines produced in the decay of tantalum 182 has made it difficult to construct nuclear energy level schemes with certainty, especially in view of the limited accuracy of the beta-ray spectrometers used. This isotope was therefore selected for a precision investigation using the curved crystal gamma-ray spectrometer. This investigation has been carried out during the past two years. A total of 16 gamma-ray lines was detected and measured. These lines can be fitted together into several tentative energy level schemes.

[17] Zumstein, Kurbatov, and Pool, Phys. Rev. **63**, 59 (1943).
[18] W. Rall and R. G. Wilkinson, Phys. Rev. **71**, 321 (1947).
[19] J. M. Cork, Phys. Rev. **72**, 581 (1947).
[20] C. E. Mandeville and M. V. Scherb, Phys. Rev. **73**, 340 (1948).
[21] Cork, Keller, Sazynski, Rutledge, and Stoddard, Phys. Rev. **75**, 1778 (1949).
[22] C. H. Goddard and C. S. Cook, Phys. Rev. **76**, 1419 (1949).
[23] Beach, Peacock, and Wilkinson, Phys. Rev. **76**, 1585 (1949).
[24] Cork, Keller, Rutledge, and Stoddard, Phys. Rev. **78**, 95 (1950).

Two different sources of neutron irradiated tantalum were used during the investigations. Only the results obtained with the second of these sources are reported here, since we feel that these are the more reliable. With this source 18 gamma-rays were detected in the preliminary search runs. In addition, the $K\alpha_1$, $\alpha_2$, $\beta_1$, $\beta_3$, and $\beta_2$ x-rays of tungsten and the $K\alpha_1$, $\alpha_2$, $\beta_1$, and $\beta_3$ x-rays of tantalum were detected. The x-rays of hafnium were not detected; thus there is no evidence for $K$ capture in tantalum 182. The detection of the W $K\alpha_1$ x-ray line permitted the instrument to be calibrated without the installation of the heavy x-ray tube and its stiff high voltage cables, which could easily produce mechanical flexures in the spectrometer. Such a calibration was performed both before and after the gamma-ray measurements. This method of calibration was used in connection with all of the measurements reported in this paper.

Satisfactory measurements were obtained for 16 of the gamma-ray lines. The final results are presented in Table VI. One of the remaining two lines, at about 108 kev, was so weak that it could not be detected sufficiently well for a good measurement. The other line, at about 250 kev, appeared as a strong line during two different search runs, but decayed below the minimum intensity for measurement during the one month interval between the searches and the measurements. This is definitely contrary to the known half-life of 112 days of tantalum 182. Since the two searches in which the line was detected were about a week apart and on opposite sides of the instrument, it is difficult to explain this effect by a freakish behavior of the spectrometer.

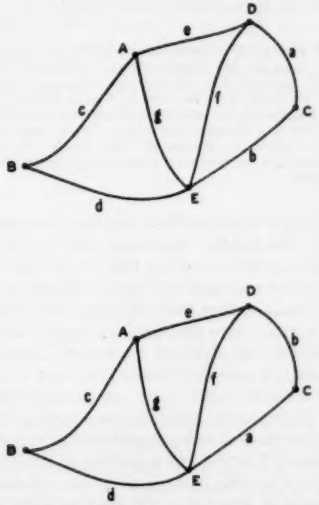


FIG. 12. Topological representation of the energy level schemes of Figs. 10 (above) and 11 (below).

TABLE VI. Wavelengths, energies, and relative intensities[a] of gamma-radiation following decay of tantalum 182. The uncertainties given are standard deviations.

| Identification letter | Wavelength in milliangstroms | Energy in kev | Relative intensity[a] |
|---|---|---|---|
| *A* | 10.134±0.010 | 1223.25±1.21 | 334 |
| *B* | 10.437±0.015 | 1187.74±1.70 | 157 |
| *C* | 11.057±0.010 | 1121.14±1.02 | 352 |
| *D* | 46.941±0.011 | 264.086±0.060 | 27 |
| *E* | 54.070±0.011 | 229.266±0.046 | 24 |
| *F* | 55.827±0.011 | 222.051±0.044 | 45 |
| *G* | 62.512±0.011 | 198.305±0.036 | 9 |
| *H* | 69.115±0.011 | 179.360±0.030 | 19 |
| *I* | 79.277±0.012 | 156.369±0.024 | 14 |
| *J* | 81.337±0.012 | 152.408±0.023 | 43 |
| *K* | 106.500±0.013 | 116.398±0.014 | 2 |
| *L* | 109.071±0.013 | 113.655±0.014 | 9 |
| *M* | 123.851±0.014 | 100.092±0.012 | 46 |
| *N* | 146.414±0.015 | 84.667±0.009 | 6 |
| *O* | 183.010±0.018 | 67.736±0.007 | 100 |
| *P* | 188.643±0.018 | 65.714±0.006 | 9 |

[a] All factors except internal conversion have been taken into account in calculating the relative intensities.

We have not been able to identify the line with any *known* impurity in the source sample. A comparison with the adjacent 264-kev line in the two search runs indicates a half-life of about 7–10 days for the 250-kev line. We plan to investigate this effect with a new source of tantalum 182 in the near future.

Since the measurements of the 16 gamma-ray lines of Table VI were made prior to the new calibration reported above, it was necessary to use a calibration curve to correct for the mirror correction. The hysteresis effects known to be present cannot be included in such a curve, and hence the measurements might be more in error than is indicated by the consistency of successive measurements. Consequently, the arbitrary value of 0.010 screw division was assigned as the error. This value is believed to be large enough to account for errors due to hysteresis. In the case of the line designated by the letter *B*, the source was so wide that although the line could be resolved from the adjacent line *A* with the aid of the composite profile, the accuracy of the determination was seriously impaired. Therefore, the following procedure was adopted: The wavelength of line *A* was determined from the data obtained with the second source; then the difference, $\lambda_B - \lambda_A$, determined with the first source, was added to the wavelength of line *A* to get the wavelength of line *B*. The first source was about one-third as wide as the second source; consequently the lines were clearly resolved for this source, since the resolution of the spectrometer was much better. The value obtained in this manner is believed to be more reliable; however, a larger error (0.015 screw division) has been assigned to this line. The errors were assigned before conversion to milliangstroms; consequently, the errors given in Table VI are somewhat larger, since there also is an error associated with the factor for converting from screw divisions to milliangstroms.

TABLE VII. Equations[a] for determining the energy level scheme for tungsten 182.

| I | II | III Discrepancy: column I − column II in kev[b] | IV Standard deviation in kev | V Identification number |
|---|---|---|---|---|
| $G+P=D$ | | −0.067 | 0.070 | (1) |
| $I+P=F$ | | −0.059 | 0.068 | (2) |
| $L+N=G$ | | +0.017 | 0.039 | (3) |
| $L+P=H$ | | +0.009 | 0.034 | (4) |
| $N+O=J$ | | −0.005 | 0.025 | (5) |
| $C+O=B$ | | +1.14 | 1.99 | (6) |
| $M+C=A$ | | −2.02 | 1.58 | (7) |
| $A+G=B+E$ | | +4.55 | 2.09 | (8) |
| $A+K=B+I$ | | −4.46 | 2.09 | (9) |
| $A+K=B+J$ | | −0.50 | 2.09 | (10) |
| $A+E=B+D$ | | +0.69 | 2.09 | (11) |
| $A+L=B+J$ | | −3.24 | 2.09 | (12) |
| $A+N=B+K$ | | +3.78 | 2.09 | (13) |
| $A+M=C+G$ | | +3.90 | 1.58 | (14) |
| $B+J=C+F$ | | −3.04 | 1.99 | (15) |
| $B+K=C+H$ | | −3.64 | 1.99 | (16) |
| $C+P=B$ | | −0.89 | 1.99 | (17) |

[a] Only independent equations are listed here.
[b] Equations containing two of lines *A*, *B*, and *C* have been rejected if the discrepancy was over 5 kev. Equations not containing any of the lines *A*, *B*, and *C* have been rejected if the discrepancy was more than 5 times the standard deviation.

Energy values and relative intensities are also given in Table VI. The energies were found from the wavelengths by using the conversion factor 12396.44±0.25 kev-milliangstroms.[25] To determine the relative intensities, the observed intensities (measured by the heights of the peaks above background) were corrected for (1) the reflection coefficient of the crystal, which is proportional to $\lambda^2$, (2) self-absorption in the source, and (3) counter efficiency, which is assumed to depend only on the absorption of the gamma-ray beam in traversing the 1-inch thickness of the scintillation crystal. Internal conversion could not be taken into account because neither the nature of the radiation nor the internal conversion coefficients (for the lower energies) are known.

The topological method for determining and enumerating level schemes described above was also used in an attempt to find a level scheme for tungsten 182. From all possible sums and differences of two gamma-ray energies, the equations of Table VII were selected for possible use in determining level schemes. The criteria used in selecting these equations were as follows: (1) only independent equations were to be listed; (2) equations containing the lines *A*, *B*, and *C*, which have large errors, could not have a discrepancy over 5 kev; (3) equations not containing any of the lines *A*, *B*, and *C* could not have discrepancies greater than 5 times the corresponding standard deviations. Clearly it will be impossible to use all of these equations in formulating a level scheme, since some are incompatible with others. Undoubtedly some of the equations are accidental, and these must be determined by trial and error and rejected. The first five equations of Table VII were chosen as a starting nucleus, since none of them has a discrepancy of more than 100 electron-volts. Furthermore, the discrepancies for these equations are all

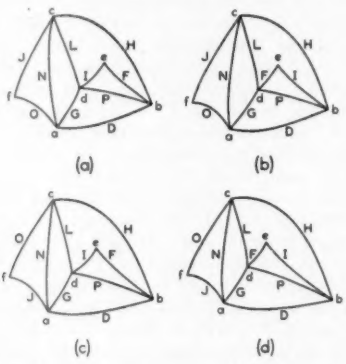


FIG. 13. Topological maps representing four possible energy level schemes for ten gamma-ray lines from tungsten 182. The lines are identified by the upper case letters assigned to them in Table VI. Lower case letters at the intersections represent energy levels. The four permutations are obtained by interchanging lines *F* and *I* and lines *J* and *O* as indicated. The corresponding energy level schemes are given in Fig. 14.

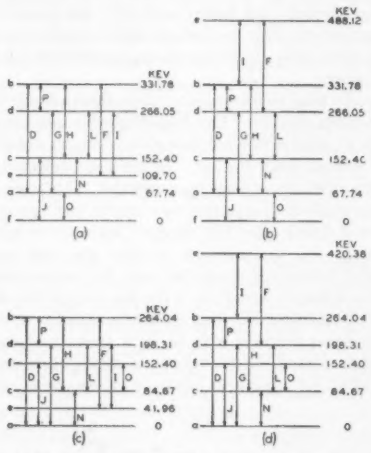


FIG. 14. Four possible energy level schemes for ten gamma-ray lines from tungsten 182. These schemes correspond to the four topological maps of Fig. 13 and are designated in the same manner. The lowest level has been arbitrarily assigned the value zero. An additional four possible level schemes can be found by inverting the four schemes shown here. One of these eight level schemes for these ten gamma-ray lines should, we believe, be incorporated into the final level scheme for tungsten 182 when it is determined.

[25] J. W. M. DuMond and E. R. Cohen, Report to the National Research Council Committee on Constants and Conversion Factors of Physics, December, 1950; Phys. Rev. 82, 555 (1951).

less than the corresponding standard deviations. The resulting topological maps for the 10 gamma-ray lines contained in these 5 equations are shown in Fig. 13. There are 4 possibilities to be considered, since lines $F$ and $I$ or lines $J$ and $O$ may be interchanged without affecting the equations from which the maps are constructed. The energy level schemes corresponding to these maps are shown in Fig. 14. Four additional level schemes can be obtained by inversion of those given in the figure, since the choice of the ground state is (so far) arbitrary. The schemes presented in Figs. 13 and 14 have been determined solely on the basis of the Ritz combinations given in the first 5 equations of Table VII. It is impossible to choose between the 8 possibilities represented here without the use of additional equations and other information such as relative intensities, known $\beta$-rays associated with the decay process, internal conversion coefficients, etc.

Attempts to extent the level schemes by including more lines, for the most part, have not been very satisfactory. Using only the 16 lines which we have measured, it seems impossible to obtain a level scheme containing all of these lines. This is not unreasonable, since there are undoubtedly a number of lines which we have not been able to detect with the gamma-ray spectrometer, and these lines could conceivably be just those needed to complete the level scheme. We have succeeded in obtaining several topological maps containing 14 or 15 of the measured lines, each of which has 24 or more permutations. Eliminations of these different maps must be made on the basis of relative intensities, known beta-rays, internal conversion coefficients, etc., and the unsatisfactory nature of this information to date makes such eliminations difficult. Furthermore, our results for the high energy lines $A$, $B$, and $C$ are not sufficiently accurate to enable one to choose the proper equations from the large number in Table VII which contain these lines. For these reasons we have been unable to formulate with reasonable certainty any level scheme which contains the three high energy lines. The maps for two of perhaps half a dozen different possibilities are given in Fig. 15. Until more, and more accurate, information is available, it seems unlikely that the actual level scheme can be determined. A program for future work on tantalum 182 at this laboratory has been outlined, and we plan to begin work in the very near future. Use of the gamma-ray spectrometer in conjunction with the axial focusing homogeneous magnetic field $\beta$-ray spectrometer,[36] the construction of which was completed only recently, is expected to provide the additional information necessary for the completion of the level scheme.

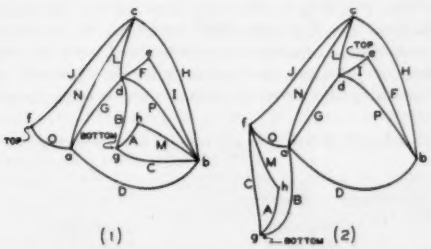


FIG. 15. Topological maps for two possible energy level schemes for 14 gamma-ray lines from tungsten 182. These two maps clearly point out the need for greater precision in the 1-Mev region, since on the basis of present accuracy and the present state of additional information on beta-ray spectra and internal conversion one cannot decide between Eqs. (6) and (17) of Table VII. These two equations give the two topological maps shown here. Several other possible energy level schemes for 14 or 15 gamma-ray lines can also be obtained from the information now available.

TABLE VIII. Energies and intensities of gamma-rays of the thorium series.

| Line energy as measured by other investigators, in kev | Present observed energy in kev, and standard error | Present observed intensity |
|---|---|---|
| | ThB−ThC transition | |
| 238.61±0.08[a] | 238.595±0.032 | 1 |
| | ThC−ThC′ transition | |
| 726[b] | 729.3±1.7 | 0.15 |
| | ThC″−ThD transition | |
| 276.5[b] | 277.350±0.063 | 0.05 |
| 510.90±0.09[a] | 510.75 ±0.15 | 0.15 |
| 582.3[b] | 582.978±0.27 | 0.4 |
| | Unassigned | |
| | 240.984±0.033 | 0.1 |

[a] See reference 29.
[b] See reference 28.

## V. NATURAL THORIUM SERIES

A 150-millicurie sample of radiothorium[37] was used for the measurement of certain lines of ThC, ThC′, and ThD. The results of these measurements are tabulated in Table VIII. The relative intensities of the lines have been estimated by correcting for the change in sensitivity of the scintillation counter with wavelength (assumed equal to the change in absorption of the scintillating crystal), the self-absorption of the source and its platinum-iridium capsule, and the change in reflecting power of the crystal. The tabulated error has been evaluated by combining the standard deviation given by the consistency (reproducibility) of the instrument in repeating observations of a given gamma-ray line with the errors associated with the calibration and conversion factors. These gamma-ray lines have been measured by other investigators[28–30] and the most precise of their results, expressed in terms of quantum energy, have been included in the table for comparison.

[36] DuMond, Bogart, Kohl, Muller, and Wilts, Special Technical Report No. 16, California Institute of Technology, March, 1952 (unpublished).

[37] We are indebted to R. B. Holt and N. F. Ramsey of the Radiation Laboratory, Harvard University, for the generous loan of this source.

[28] See Rutherford, Chadwick, and Ellis, *Radiations from Radioactive Substances* (Cambridge University Press, Cambridge, 1930).

[29] G. Lindstrom, Phys. Rev. **83**, 465 (1951).

[30] H. Craig, Phys. Rev. **85**, 688 (1952).

TABLE IX. Energies and intensities of gamma-rays of the radium series.

| Ellis *et al.* energy, kev | Present observed energy in kev, together with standard error | Present observed relative intensity |
|---|---|---|
| | RaB−RaC transition | |
| 52.9 | 53.226±0.0014 | |
| 240.6 | 241.924±0.030 | 0.2 |
| 293.7 | 295.217±0.039 | 0.55 |
| 349.9 | 351.992±0.062 | 1 |
| | RaC−RaC′ transition | |
| 606.7 | 609.37±0.16 | 1.6 |
| | Po $K\alpha_1$ x-ray line 79.290±0.015 | |

For this purpose the data of Lindstrom (expressed as electron momentum in gauss-cm) have been converted to electron kinetic energy in electron kilovolts through the use of the latest values of the atomic constants and conversion factors.[25] To these quantum energies were added appropriate binding energies through the use of the values of the Bi $L_{\rm I}$ and Pb $K$ absorption edges published by Cauchois and Hulubei,[31] as well as the value of $E_K-E_{L\rm I}$ for Bi given by Cauchois.[31] The limits of error correspond to estimated probable error given by Lindstrom. The present results agree with those of Lindstrom well within the experimental error. This agreement was not encountered with our older results.

Many other lines have been reported but careful search has shown them to be too weak to measure with the present instrument. The source was not of optimum shape for the curved crystal spectrometer, being a cylinder 2 mm in diameter and 4 mm long encased in a capsule 0.5 mm thick. This resulted in a large background contribution and a weak beam, since it was necessary to mask the source in order to obtain resolution. Carefully designed masking jaws were used but with no success in detecting the 2.6-Mev gamma-ray of ThD.

The observed line of energy 240.98 kev has not been identified. It is close to the 241.92-kev line of RaC but the difference between them far exceeds the limits of error. Since this line is only one-tenth as strong as the 238.59-kev line of ThC and only one percent different in energy, the $\beta$-ray spectrometers may have failed to resolve it.

## VI. RADIUM C AND RADIUM C′

The gamma-ray spectrum of the radium series was studied by the use of the emanation radon. Several sources of approximately 100-millicurie strength were employed,[32] and it was possible to make measurements even after the source had decayed to 8 millicuries.

The results of measurement of four lines of RaC and of one line of RaC′ are given in Table IX. The uncertainties are standard errors based on consistency of repeated observations, since the error due to all unknown systematic errors is thought to be small. Three or four measurements were made on each of these lines and the results averaged. The standard error of a single measurement was obtained by the usual formula,[33]

$$\sigma_{x_i}=\{[\Sigma(\delta x_i)^2]/(n-1)\}^{\frac{1}{2}}, \tag{5}$$

for each of the gamma-ray lines. Since it is felt that the uncertainty in wavelength of a single observation is independent of wavelength, the weighted rms value of these deviations $\sigma_{x_i}$ was determined. The standard error of the determination of wavelength of a line was taken to be this value divided by $\sqrt{n}$ where $n$ is the number of observations, in accord with the usual expression for the standard error of the mean of $n$ observations,

$$\sigma_{x_m}=\{[\Sigma(\delta x_i)^2]/[n(n-1)]\}^{\frac{1}{2}}. \tag{6}$$

In the energy determinations, the uncertainty of knowledge of the W $K\alpha_1$ calibrating line introduced additional error. This completely masked the above-mentioned internal consistency uncertainty in the case of the 52-kev line, and had a slight effect on some of the others.

The estimated relative intensities were determined by correcting for the efficiency of the scintillation detector, for the reflection coefficient of the crystal, and for decay of the source between measurements. Uncertainty of the counter sensitivity at 52 kev prevented a comparison of its intensity with the other lines.

A single close relation was expected to occur between the 52-kev line, the 242-kev line, and the 295-kev line. It runs as follows:

$$(241.924\pm0.030)+(53.226\pm0.0014)-(295.217\pm0.039)=0.067\pm0.049,$$

thus tending to verify the accepted decay scheme.[34]

The following x-rays were detected and identified: Bi $K\alpha_2$, $K\alpha_1$, $K\beta_2$, $K\beta_1$, $K\beta_2^{\rm II}$, and $K\beta_2^{\rm I}$. An additional x-ray line was measured and is believed to be the $K\alpha_1$ line of polonium. Its wavelength was obtained by measuring the difference between its wavelength and

TABLE X. Wavelengths and quantum energies of tungsten 187 $\gamma$-ray lines.

| Wavelengths in milliangstroms | Energy in kev |
|---|---|
| 18.069±0.010 | 686.06±0.38 |
| 20.030±0.010 | 618.89±0.31 |
| 25.852±0.010 | 479.52±0.19 |
| 92.341±0.012 | 134.25±0.018 |
| 172.174±0.017 | 72.00±0.007 |

[31] Y. Cauchois and H. Hulubei, *Longeurs d'Onde des Emissions X* (Herman & Cie, Paris, 1947).

[32] We are greatly indebted to Dr. C. Emery and Dr. G. L. Locher of the Emery Tumor Group, Los Angeles, and Western Radiation Laboratories, Los Angeles, for making these Rn samples available to us.

[33] *Handbook of Chemistry and Physics* (Cleveland Chemical Rubber Publishing Company, Cleveland, 1944). See the explanation of the Mathematical Tables.

[34] M. Stern, Revs. Modern Phys. **21**, 316 (1949).

that of Bi $K\alpha_1$, listed in the tables.[31] The wavelength of the Po $K\alpha_1$ line is thus found to be 156.343±0.030 milliangstroms.

### VII. TUNGSTEN 187

Results of the measurements of the five known gamma-rays of 24-hour tungsten 187 are in essential agreement with previous measurements[33–37] (see Table X).

The decay scheme of Beach, Peacock, and Wilkinson[35] appears to be correct in so far as the combination of 72.00 kev+134.25 kev+479.52 kev=686.06 kev checks well within instrumental errors, but the line at 618.89 kev does not combine with the 134.25-kev and 479.52-kev lines, as indicated in their decay scheme The corrected decay scheme for tungsten 187 shown in Fig. 16 does not include the 618.89-kev line, which apparently represents an independent transition.

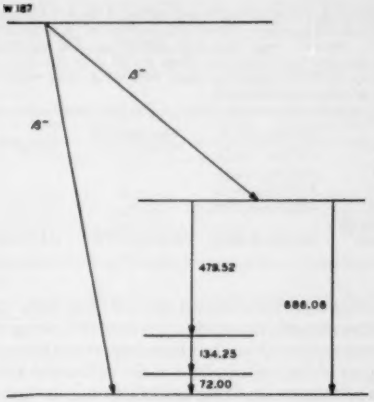


FIG. 16. Proposed decay scheme for tungsten 187.

### VIII. CESIUM 137 AND GOLD 198

Measurements of the gamma-rays from cesium 137, gold 198, and the annihilation radiation from copper 64 were carried out after the calibration described above. Since the spectrometer was equipped with the 6-inch mirror at the time these measurements were made, it was possible to check the alignment of the long carriage with the crystal during the measurements. As a result, two to three times the precision otherwise attainable was possible.

The wavelength and energy of the single gamma-ray following decay of cesium 137 has been determined from the average of 6 measurements. The resultant values are λ=18.737±0.004 milliangstroms; $E$=661.60 ±0.14 kev.[38]

Several gamma-rays follow the decay of gold 198.[39–43] Of these, the strongest is the 412-kev gamma-ray line, which accompanies 99.7 percent of the decay processes. The fairly large neutron absorption cross section of gold 197 (96.4 barns), combined with this, makes it possible to obtain a source of sufficient activity to observe second- and third-order reflections for this gamma-ray line from our bent quartz crystal. It was hoped that, in addition to this, the high activity would be sufficient to permit measurement of one or more of the other lines from gold 198, as well as some of the gamma-ray lines following decay of gold 199, which is produced by neutron capture in gold 198.[44]

The source, a piece of 24-carat gold foil, was irradiated in the reactor at the Argonne National Laboratory, and had an activity of approximately 5 curies on arrival in Pasadena. Preliminary searches with the spectrometer showed that, as expected, the second- and third-order reflections of the 412-kev line could be detected; in addition, the 159-kev gamma-ray line following decay of gold 199 was found to be strong enough for a wavelength measurement. Unfortunately, however, it was necessary to confine all measurements to the 412-kev line.

A total of two runs in the third order, one run in the second order, and ten runs in the first order was made. Counting intervals were chosen so that one percent statistics or better were obtained at the peak of the profiles. A typical pair of profiles for the first order is shown in Fig. 9. To determine the composite profile, only the profiles obtained from the first-order runs were used. Decay corrections were not necessary, since only 2½ hours or less was required to cross each line profile. The second- and third-order profiles were also matched to this composite, after decay corrections had been made.[45]

The final results of the experiment are given in Table XI. The average of the wavelengths (in screw divisions) obtained in each order are listed separately.

[31] Beach, Peacock, and Wilkinson, Phys. Rev. **75**, 211 (1949).
[32] C. L. Peacock and R. G. Wilkinson, Phys. Rev. **74**, 601 (1948).
[33] Hole, Benes, and Hedgran, Arkiv. Mat. Astron. Fysik. **35A**, No. 35 (1948).
[34] We are much indebted to A. F. Rupp of Oak Ridge for preparation of a suitable source of cesium 137.
[35] R. W. Pringle and S. Standil, Phys. Rev. **80**, 762 (1950).
[36] L. G. Elliott and J. L. Wolfson, Phys. Rev. **82**, 333 (1951).
[37] Bross, Ketelle, Zeldes, and Fairstein, Phys. Rev. **84**, 586 (1951).
[38] Cavanagh, Turner, Booker, and Dunster, Proc. Phys. Soc. (London) **A64**, 13 (1951).
[39] Patrick E. Cavanagh, Phys. Rev. **82**, 791 (1951).
[40] P. M. Sherk and R. D. Hill, Phys. Rev. **83**, 1097 (1951).

[41] The half-life of gold 198 has been determined by L. M. Silver, Phys. Rev. **76**, 589 (1949). The half-life of gold 198 was also calculated from the data for the first-order reflections. To do this, the height of the profile peak above background and the corresponding time at which the peak was reached were used. The values were obtained by using a least squares process to find the slope of the straight line representing the decay function when plotted in its logarithmic form. Because of a slight asymmetry in the profiles obtained on opposite sides of the spectrometer (the heights are not equal), there are two separate sets of data to be analyzed. The average of the two values is

$$\tau_{\frac{1}{2}} = 2.74 \pm 0.04 \text{ days.}$$

This agrees with Silver's value of 2.69±0.015 days.

TABLE XI. The wavelength and energy of the 412-kev gamma-ray line following decay of gold 198, as obtained by measurements of first-, second-, and third-order reflections. The uncertainties given are standard deviations; these are given to one extra place to avoid incorrect weighting when combining these values with those of other experimenters.

| Order | Wavelength in screw divisions | Wavelength in milliangstroms | Energy in kev |
|---|---|---|---|
| 1 | 30.016±0.0028 | | |
| 2 | 30.019±0.0023 | | |
| 3 | 30.021±0.0016 | | |
| Weighted mean | 30.019±0.0012 | 30.105±0.0026 | 411.770±0.036 |

The final value is a weighted mean of these three values. This wavelength was used to calculate the energy of the gamma-ray line. The errors were determined by a careful analysis of the contributions of the calibration and correction factors, counting statistics, etc., to the total error of a measurement.

## IX. THE ANNIHILATION RADIATION FROM COPPER 64

It is well known that positrons decay by the process of annihilation of positron-electron pairs. The energy released by the disappearance of the masses of the two particles appears as radiation. In most cases this radiation appears as two quanta, each having an energy of approximately 510 kev. One-quantum and three-quantum annihilation also take place, but the frequency of occurrence of such events is so low as to make a study of these effects impossible with the curved crystal spectrometer. Hence our studies have been limited to two-quantum annihilation.

If both positron and electron are at rest in the c.m. system of coordinates, the equivalence of mass and energy yields Eq. (7) below:

$$(m_+ + m_-)c^2 = 2h\nu = 2hc/\lambda_A. \tag{7}$$

In this relation $m_+$ and $m_-$ are the rest masses of the positron and electron, respectively, $c$ is the velocity of light, $h$ is Planck's constant, $\nu$ is the frequency of the annihilation radiation, and $\lambda_A$ is the wavelength. Rearranging (7), the wavelength is found to be

$$\lambda_A = 2h/(m_+ + m_-)c. \tag{8}$$

This is the wavelength in the c.m. system; in the lab coordinate system the observed wavelength will be altered by a Doppler shift due to the motion of the center of mass. However, there is no reason to assign a preferred direction to the motion of the center of mass; and therefore, when one considers all of the electron-positron pairs annihilating in a given time interval, the effect is a broadening of the observed line rather than a shift in the center of the line. If there should be a residual kinetic energy in the c.m. system, or if the potential energies of the two particles should not be equal in magnitude and opposite in sign, a shift in wavelength would result. It has been shown[46] that such effects, if present, are negligible. The observed wavelength then is that given by Eq. (8).

One of the principal problems in the measurement of the annihilation radiation wavelength with the curved crystal spectrometer is the source of positrons to be used. First, a fairly strong source of radiation is necessary; the radiation should correspond to an activity of 10 millicuries or better at all times. Second, only naturally radioactive or neutron-activated materials are economically feasible because of the source strength requirement. On this basis copper 64 was selected as the source material. Even with this most advantageous choice, however, additional difficulties are encountered. These follow: (1) copper 63 comprises only 69 percent of natural copper; (2) the neutron absorption cross section of copper 63 is relatively low—2.82 barns; (3) copper 64 has a short half-life for our purpose—12.8 hours; (4) copper 64 decays by three competing processes—$K$-capture, $\beta^-$ emission, and $\beta^+$ emission—and positron emission occurs in only 17.5 percent of all cases; (5) as explained in greater detail in a previous paper,[46] the relatively long range of positrons before annihilation requires that the source be defined by a slit, thereby severely limiting the effective volume of the source. The steps taken to make the most of the available activity will be described in the following paragraphs.

Two problems must be considered in the design and construction of the slit jaws used to define the source: (1) The part of the source which the crystal "sees" must be limited by the slit; otherwise the source would appear to be rather large and diffuse because of the long range of the positrons before annihilation and the fact that the positrons are annihilated in the material surrounding the radioactive sample as well as in the sample itself. (2) Radiation penetrating the sides of the slit jaws causes the so-called source window to have "tails," which will also appear in the observed line profiles. From the discussion of the effect of counting statistics on the accuracy of measurement given above, it can be seen that the accuracy can be increased considerably by eliminating or minimizing these "tails," i.e., by causing the line profile to have the greatest possible steepness over the widest possible range of wavelength settings. The best solution to these two problems can be obtained by use of the design of Fig. 17 and by

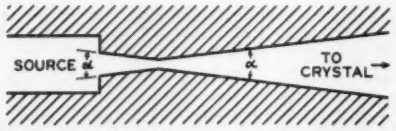


FIG. 17. Design for uranium slit jaws used to define $Cu^{64}$ source in annihilation radiation experiment. $\alpha = 1.45°$. Width at narrowest point = 0.2 mm. Distance between source and narrowest point = 1 cm. The sketch is not to scale.

[46] DuMond, Lind, and Watson, Phys. Rev. **75**, 1226 (1949).

making the slit jaws of a material having a very large absorption coefficient for the particular radiation which is to be studied. For the experiment reported here, uranium was chosen as the absorbing material. Sufficient uranium for the slit jaws was kindly made available to this project by the Atomic Energy Commission, and the slit jaws were made at the Brookhaven National Laboratory.

The source for the experiment was a rectangular block of copper, 0.080×0.497×1.25 in. This was irradiated at high neutron flux density in the reactor at the Argonne National Laboratory. Transportation to Pasadena was by special U. S. Navy plane. The activity of the source on arrival was approximately 7 curies; the useful activity (that is, that which resulted in annihilation radiation in the part of the source "seen" by the crystal) was equivalent to about 250 millicuries.

It had been hoped that the annihilation radiation line could be measured by second- and third-order reflection from the crystal planes, thereby increasing the precision of the measurements. However, preliminary calculations had shown that if the line were detected at all in these higher order reflections, it would be too weak to use successfully. Measurements immediately after installation of the source confirmed this. Consequently, all measurements were confined to the first-order reflections.

A 5-minute counting interval at each wavelength setting was chosen as a satisfactory value. This interval was kept fixed throughout the entire experiment. Thus all the profiles obtained were subject to the same distortion due to decay of the source. Since the important quantity is the difference in wavelength settings between corresponding points on the two members of a pair of profiles, the decay correction was not necessary for proper interpretation of the data. This eliminated possible errors due to additional arithmetic operations. Furthermore, the decay correction for the 3-hour interval required to cross a single profile is quite small. A total of nine pairs of profiles was obtained before the source had decayed below its useful limit. The results of the experiment are given in Tables XII and XIII.

TABLE XII. Illustration of the removal of the effect of hysteresis and the reproducibility of measurements. The values of 2λ (twice the wavelength), in screw divisions, for the annihilation radiation from copper 64 are given below. Comparison of the values before and after the mirror correction is applied indicates that the determination of the mirror correction for each run at the time of the experiment does indeed improve the reproducibility of the measurements.

| Run No. | 2λ Before mirror correction | 2λ After mirror correction |
|---|---|---|
| 1 | 48.328 | 48.383 |
| 2 | 48.352 | 48.390 |
| 3 | 48.338 | 48.388 |
| 4 | 48.320 | 48.381 |
| 5 | 48.332 | 48.385 |
| 6 | 48.328 | 48.378 |
| 7 | 48.326 | 48.384 |
| 8 | 48.336 | 48.390 |
| 9 | 48.344 | 48.392 |

TABLE XIII. Results on annihilation radiation. The uncertainties given after each ± are standard deviations. These are given to one extra place to avoid incorrect weighting when combining these values with those of other experimenters.

| | |
|---|---|
| Wavelength: | |
| 1. $\lambda_A = 24.262 \pm 0.0033$ mA | $Cu^{64}$ direct measurement of $\lambda_A$ |
| 2. $\lambda_A = 24.263 \pm 0.0033$ mA | $Au^{198}$ expt.+Hedgran and Lind |
| 3. $\lambda_c = 24.26067 \pm 0.00048$ mA | DuMond and Cohen least squares analysis |
| Energy: | |
| 1. $E_A = 510.941 \pm 0.067$ kev | $Cu^{64}$ direct measurement of $\lambda_A$ |
| 2. $E_A = 510.920 \pm 0.070$ kev | $Au^{198}$ expt.+Hedgran and Lind |
| 3. $m_-c^2 = 510.969 \pm 0.015$ kev | DuMond and Cohen least squares analysis |
| Positron mass: | |
| 1. $(m_- - m_+)/m_- = (1.61 \pm 1.85) \times 10^{-4}$ | $Cu^{64}$ direct measurement of $\lambda_A$ |
| 2. $(m_- - m_+)/m_- = (1.92 \pm 2.80) \times 10^{-4}$ | $Au^{198}$ expt.+Hedgran and Lind |

Table XII illustrates the slight variation in results due chiefly to flexure and mechanical hysteresis in the 1¼-inch bar linking the crystal to the long screw carriage in the spectrometer, and how this effect is corrected by the use of optical methods (6-inch concave mirror and microscope) at the time of the experiment. The first column gives the value of 2λ between settings for reflections from opposite sides of the crystal planes, after all corrections *except the mirror correction* have been made (the values have not been converted from screw divisions to milliangstroms, however). The second column gives the values after the mirror correction has been applied. These values are in much better agreement than those of the first column.

Table XIII lists the results of the wavelength measurements. These are listed in three different forms: the wavelength of the annihilation radiation, the energy of this radiation, and a comparison of the masses of the positron and the electron. Since there has been, to date, no precise method of obtaining a comparison of the masses of the positron and the electron other than measuring the wavelength of the annihilation radiation, we have interpreted the experiment as a measurement of the mass of the positron. A second measurement of the annihilation radiation has been made by Hedgran and Lind,[47] who determined the energy difference between the annihilation radiation and the 412-kev line following decay of gold 198. Using the most recent measurement of the 412-kev line (described above), the energy of the annihilation radiation can be determined. This energy value, together with the corresponding wavelength value and electron-positron mass difference, is also listed in Table XIII. As a further comparison, the values of $\lambda_c = h/m_-c$ and $m_-c^2$ obtained by DuMond and Cohen in their most recent least squares adjustment of fundamental constants[28] are given in the table.

[47] Arne Hedgran and David A. Lind, Phys. Rev. **82**, 126 (1951).

As a conclusion from these results, we believe it may now be stated that no experimental evidence exists for any difference in the masses of negative and positive electrons greater than a part in ten thousand.

Some additional information can be gleaned from the data for the annihilation radiation line profiles. It is possible to get an idea of the momentum distribution of the centers of mass of the annihilating pairs. This then tells which atomic electrons take part in the annihilation process and to what extent they enter into the reaction.[48]

Since the primary purpose of the experiment was to measure the wavelength of the radiation, we have not attempted an exhaustive study of the shape of the line profile. Such a study would best be undertaken as a separate experiment. It has been possible to calculate

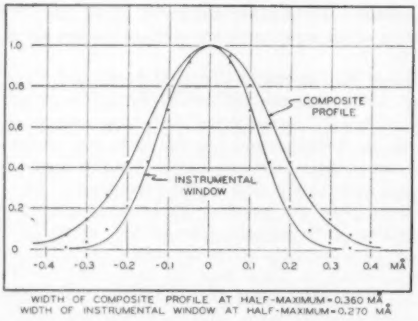


FIG. 18. Showing the effect of Doppler broadening on the observed line profile for the annihilation radiation from copper 64. The composite profile formed by superposition of all observed line profiles is compared with the calculated instrumental window. The dots represent Gaussian functions, $e^{-k^2x^2}$, having the same widths at half-maximum as the solid curves. The composite profile has not been corrected for decay of the source during the time required to obtain a single profile, since such corrections are only slight.

a good approximation to the instrumental "window" profile of the gamma-ray spectrometer[49]; and when the observed line profile is compared with this window curve, the Doppler broadening is readily apparent (see Fig. 18). If we assume that the two curves are Gaussian, then the widths at half-maximum can be combined in quadrature to find the width at half-maximum of the natural line profile. Such an assumption is not, of course, rigorously accurate. Nevertheless, a good estimate of the order of magnitude of the velocities of the centers of mass of the annihilating pairs can be obtained in this manner. Since the calculated instrumental window has a width at half-maximum of 0.270 milliangstrom and the width of the observed line profile at half-maximum is 0.360 milliangstrom, the corresponding width at half-maximum of the natural line profile is 0.238 milliangstrom. Using the nonrelativistic relation for the Doppler shift, this width (one must use half of the above value, or 0.119 milliangstrom in such a calculation) corresponds to a momentum

$$p = 9.8 \times 10^{-3}\, m_e c.$$

This value is in good agreement with the results of the previous experiment performed in this laboratory[46] and with the experiments of DeBenedetti *et al.*[50] This value for the momentum indicates that, for the most part, only the conduction electrons take part in the annihilation process. *M* electrons might also play a small role in the process. These conclusions are discussed in more detail in references 46 and 50.

## X. ACKNOWLEDGMENTS

It is a pleasure to acknowledge the interest in our work and the most helpful criticisms of Professor Richard Feynman, particularly in the case of our studies of iridium 192 in which certain complex line structures looking like very complicated close multiplets appeared. We jumped to the conclusion that these were nuclear lines since they resembled nothing known to us in the x-ray spectrum until Dr. Feynman pointed out that the spacing and intensities of the multiplet could be completely explained as the superposition of two similar symmetrical partially overlapping quadruplets with about 2:1 intensity ratio and a spacing of about 4.9 milliangstroms between them. These two quadruplets are in fact, respectively, the $K\alpha_1$ and $K\alpha_2$ fluorescent lines of lead excited on the edges of the lead slit jaws which we used in the source holder. Each quadruplet consisted of (1) two strong closely adjacent "lines" in the center of the pattern of about equal intensity formed by exciting radiation from the sample falling directly *on* the surface of each slit jaw right at its sharp edge, and (2) two weaker broader and more widely separated fluorescent "lines" formed by exciting radiation which came *through* the jaws from the back. Because of the bevel of the slit jaws, there occurs a point on each at which the depth of penetration for the exciting radiation from behind is optimum for excitation of the greatest fluorescent intensity emerging from the front surface.

The work here reported on tantulum 182 is a continuation of work started by James Brown on this

[48] The half-life of copper 64 was determined in the same manner as was that of gold 198. The final value obtained is $12.77 \pm 0.14$ hours. This is in good agreement with Silver's value of $12.88 \pm 0.045$ (see reference 45).

[49] The instrumental window was calculated by means of a "fold" taking into account (1) the finite opening of the uranium slit jaws, (2) the penetration of the radiation into the edges of the slit jaws, and (3) the estimated window ascribable to the crystal (intrinsic diffraction pattern and aberration of focusing) as determined by measurements on very thin sources with spectrally very narrow lines (e.g., cesium 137).

[50] DeBenedetti, Cowan, and Konneker, Phys. Rev. **76**, 440 (1949); DeBenedetti, Cowan, Konneker, and Primakoff, Phys. Rev. **77**, 205 (1950).

isotope with the 2-meter crystal spectrometer in 1949 and 1950, which formed part of his thesis for the doctorate. The first mentioned of the two sources, the narrower and the weaker of the two, was the one used by him. Actually all the wavelengths have been remeasured with the second source because certain changes in the spectrometer in the meanwhile have rendered the applicability of our present calibration to this older data too uncertain. Nevertheless, Brown's pioneering study on this isotope has been of the greatest value to us, and it is a pleasure to acknowledge here our indebtedness to him.

PHYSICAL REVIEW VOLUME 88, NUMBER 4 NOVEMBER 15, 1952

# Penetration and Diffusion of X-Rays: Calculation of Spatial Distributions by Semi-Asymptotic Methods*

L. V. SPENCER
*National Bureau of Standards, Washington, D. C.*
(Received June 20, 1952)

Methods are presented for calculating x-ray spectra in an infinite homogeneous medium. These methods are particularly useful for calculating spectra at great distances from the radiation source. The transport equation is solved numerically by characterizing angular and spatial distributions with a small number of suitable parameters. Attention is called to a mathematical technique which is extremely useful for this purpose, whereby a function may be approximated from a knowledge of moments, derivatives, or values. Sample numerical applications include spectral intensities at various distances from a plane monodirectional 10.22-Mev x-ray source in Pb and a plane monodirectional 5.11-Mev source in Fe.

## I. INTRODUCTION

THE very deep penetration of photons which experience multiple Compton scattering[1] has been studied previously in a number of papers.[2–4] These treatments—all completely analytic—have been designed to yield information about the asymptotic form of the x-ray penetration law. In this paper we shall present a numerical approach which makes use of these asymptotic penetration laws; therefore, in Appendix A we summarize these earlier results and discuss briefly some unpublished work of the same kind.

The complicated nature of actual x-ray cross sections militates strongly against the usefulness of purely analytical methods in finding realistic spectral intensities in specific situations. Numerical methods hold much more promise. One such numerical method has been presented[5–7] which relies an expansions in suitable spatial and directional polynomial systems. The diffusion equation is reduced through these expansions to a form suitable for ordinary numerical integrations. This polynomial method has proved very useful for penetrations up to 16–24 mean free paths of the hardest spectral component; but it is in no sense asymptotic since the burden of the numerical integrations tends to increase rapidly with the penetration.

We present here a method for numerical calculations which might be called "semi-asymptotic." It is capable of yielding as much information as the polynomial method, while the numerical work involved is nearly independent of the penetration. This method relies upon a Fourier-Laplace transformation in the spatial variable. In Sec. II the diffusion equation is presented and is reduced, through this spatial transformation and through integrations over photon directions, to an interlinked system of integral equations. Section III describes schematically an approach to the solution of this system. Section IV presents the method which was actually used. The success of this method is largely due to a new mathematical technique for approximating functions. In order to preserve continuity of thought, this technique is described in Appendix B rather than in the body of the text. In Sec. VII the inversion of the Fourier-Laplace transform is discussed. The details of the inversion are given in Appendix C.

The results of actual calculations for the following three problems are presented and discussed in Sec. VIII: (1) a plane monodirectional 10.22-Mev source in Pb; (2) a plane monodirectional 5.11-Mev source in Fe; (3) a plane isotropic 5.11-Mev source in Fe. Spectral intensities are given for penetrations up to 160 mean free paths in the first case and 50 mean free paths in

* Work supported by the ONR.

[1] At the low energy end of the spectrum, where the energy shift of the scattered photons can be disregarded or treated as a small correction, the diffusion of photons has been studied by S. Chandrasekhar (*Radiative Transfer*, Oxford University Press, London, 1950), but without specific reference to very deep penetrations. At the very high energy end, where large amounts of x-rays are regenerated by secondary electrons, a full development of the shower theory is required. Pair production will be treated here as a mechanism for outright absorption. (The results of this paper can be applied to the tail end of showers.)

[2] Bethe, Fano, and Karr, Phys. Rev. **76**, 538 (1949).

[3] U. Fano, Phys. Rev. **76**, 739 (1949).

[4] Fano, Hurwitz, and Spencer, Phys. Rev. **77**, 425 (1950).

[5] L. V. Spencer and U. Fano, Phys. Rev. **81**, 464 (1951).

[6] L. V. Spencer and U. Fano, J. Research Natl. Bur. Standards **46**, 446 (1951).

[7] L. V. Spencer and Fannie Stinson, Phys. Rev. **85**, 662 (1952).

the second. The calculations for the third case are more restricted.

## II. THE DIFFUSION EQUATION

We consider the penetration, degradation, and diffusion of x-rays in an infinite medium with a plane source. Under conditions of plane symmetry the spectral energy density $Y$ of the x-rays depends only on the distance $x$ from the source, on the obliquity $\omega_x$ of the direction of propagation $\omega$, and on the wavelength $\lambda$ (in Compton units). This energy density obeys the transport equation

$$\omega_x\partial Y(x,\omega_x,\lambda)/\partial x+\mu(\lambda)Y(x,\omega_x,\lambda)$$
$$=\int_0^\lambda d\lambda' k(\lambda',\lambda)\int_{4\pi}d\omega' 1/2\pi\delta(1-\lambda+\lambda'-\omega\cdot\omega')$$
$$\times Y(x,\omega_x',\lambda')+\text{source}, \quad (1)$$

where $\mu(\lambda)$ represents the total attenuation coefficient, $k(\lambda',\lambda)$ represents the differential Klein-Nishina probability for Compton scattering of a photon of wavelength $\lambda'$ into the interval from $\lambda$ to $\lambda+\Delta\lambda$,[7a] and the Dirac $\delta$-function represents the Compton condition.

As in references 3 and 4 we represent the solution of (1) as a superposition of space distributions which decay in depth exponentially, by the method of the Fourier-Laplace transformation. The "transform" of $Y$, i.e.,

$$y(p,\omega_x,\lambda)=\int_{-\infty}^{\infty}dx e^{px}Y(p,\omega_x,\lambda),$$

obeys the equation

$$[\mu(\lambda)-p\omega_x]y(p,\omega_x,\lambda)$$
$$=\int_0^\lambda d\lambda' k(\lambda',\lambda)\int_{4\pi}d\omega' 1/2\pi\delta(1-\lambda+\lambda'-\omega\cdot\omega')$$
$$\times y(p,\omega_x',\lambda')+\text{source}. \quad (2)$$

We are primarily interested in calculating the quantity

$$y_0(p,\lambda)=(1/2\pi)\int_{4\pi}d\omega y(p,\omega_x,\lambda).$$

The inversion of $y_0(p,\lambda)$ to obtain the depth distribution will be discussed in Sec. VII.

The "topography" of $y$ as a function of $p$ is as follows: $y$ is defined on a strip parallel to the imaginary axis such that $-\mu_s\leq \mathrm{Re}\,p\leq+\mu_s$, where $\mu_s$ is the attenuation coefficient of the hardest scattered x-rays. (For $|\mathrm{Re}\,p|>\mu_s$, the integral defining $y$ diverges.) The singularities of $y$ are related to the vanishing of the factor $[\mu(\lambda)-p\omega_x]$. This occurs, within the strip of definition, only if $\mu(\lambda)\to\mu_s$, $\omega_x\to1$. Thus, $y$ has singularities at $\pm\mu_s$, i.e., on the real axis. (The type of singularity which $y$ may have at $+\mu_s$ is given in Appendix A.) Because of the location of the singularities, for every set of values $(x,\omega_x,\lambda)$ there must exist a saddle on the real axis for some value $|p|<\mu_s$. For large $x$, this saddle will be close to $+\mu_s$, while for small or negative $x$, the saddle will lie at small or negative values of $p$. Since we are primarily interested in evaluating $y$ near the saddle point, we want to assign to $p$ real values within the range of definition.

Clearly those components are most penetrating which have the smallest attenuation coefficient and which travel directly away from the source. The components which control the deep penetrations tend to have directional distributions strongly peaked at $\omega_x=1$. Now, any sharply peaked distribution requires many spherical harmonics for its description. This means that spherical harmonics are not the most convenient quantities to use in describing the directional distribution of the deeply penetrating radiation.[6] A more convenient quantity to use in characterizing these directional distributions is the "angular moment" defined as follows:

$$y_n(p,\lambda)=\frac{1}{2\pi}\int_{4\pi}d\omega(1-\omega_x)^n y(p,\omega_x,\lambda). \quad (3)$$

In order to find equations for these angular moments, we multiply (2) by $(1-\omega_x)^n$ and integrate over all directions. The result is the following system of equations:

$$[\mu(\lambda)-p]y_n(p,\lambda)+py_{n+1}(p,\lambda)$$
$$=\int_0^\lambda d\lambda' k(\lambda',\lambda)\sum_{n'=0}^{n}(\lambda-\lambda')^{n-n'}S_n^{n-n'}(\lambda-\lambda')\cdot$$
$$\times y_{n'}(p,\lambda')+\text{source}, \quad (4)$$

where $S_n^{n'}(z)$ are polynomials of degree $(n-n')$,[8]

$$(-1)^{n'}[2^{n-n'}n'!(n-n')!]S_n^{n'}(z)$$
$$=(d^n/dz^n)[z^{n-n'}(2-z)^n]. \quad (5)$$

Notice that the set of Eqs. (4) is interlinked by the term $y_{n+1}(p,\lambda)$ in such a way that the whole system must be solved simultaneously. Every $y_n$ depends upon every other $y_n$. If $p/(\mu-p)$ is small enough, it is feasible to break the interlinkages by expanding the $y_n$ in powers of $p$ or perhaps $p/(\mu_s-p)$. Such a procedure is equivalent to the polynomial method.[6] However, we are interested in solving for $y_n(p,\lambda)$ at values of $p$ large enough so that such an expansion converges very slowly; hence we must now consider the simultaneous solution of Eqs. (4).

## III. DISCUSSION

In order to solve Eqs. (4) simultaneously, we may resort to trial and error methods. We may define a

[7a] Since $Y$ refers to energy density rather than number density, the function $k(\lambda',\lambda)$ referred to here differs from that in reference 6 by a factor $(\lambda/\lambda')$.

[8] These (Jacobi type) polynomials are self-adjoint over the interval $0\leq z\leq2$ with respect to the weight function $z^{n'}$.

function $g_1(p,\lambda)=y_1(p,\lambda)/y_0(p,\lambda)$. If we guess this function, the whole chain of equations can be unraveled and values for all the $y_n$'s can be obtained. However, these values for the angular moments will correspond to a well-behaved function[9] only if $g_1(p,\lambda)$ has been guessed correctly. Thus $g_1(p,\lambda)$ plays the role of an "eigenvalue."[10] This suggests that if it is possible to determine whether or not a set of values for the $y_n(p,\lambda)$ correspond to the moments of a well-behaved function, it may be possible to determine whether or not any estimated $g_1(p,\lambda)$ is correct.

Because Compton scattering always increases the photon wavelength $\lambda$, the integration of (4) proceeds naturally from smaller to larger $\lambda$'s. As a matter of fact, if $y(p,\omega_z,\lambda')$ is known for all $\lambda'<\lambda$, then $y(p,\omega_z,\lambda)$ must be completely determined. Thus, if a numerical integration could be made of the whole infinity of Eqs. (4) simultaneously, using infinitely small integration steps, it would yield automatically the correct solution; and no "eigenvalue problem" would exist. Such an idealized procedure can be outlined in the angular moment scheme as follows: If the infinity of quantities $y_n(p,\lambda')$, $\lambda'<\lambda$, are known, the right-hand sides of Eqs. (4) are completely determined except for a single infinitesimal interval which can be neglected. Furthermore, according to (2) the right sides of Eqs. (4) are the angular moments of the quantity $R(p,\omega_z,\lambda)=[\mu(\lambda)-p\omega_z]y(p,\omega_z,\lambda)$. Because we know an infinity of these moments, we can determine $R(p,\omega_z,\lambda)$ and thereby $y(p,\omega_z,\lambda)$ exactly.

In practice such a perfect integration scheme is impossible, of course. It is necessary to use finite steps of integration and a finite number of equations. This means that incomplete information about $y(p,\omega_z,\lambda')$, for $\lambda'<\lambda$, must suffice in our determination of $y(p,\omega_z,\lambda)$. The problem is thus to find a procedure for making such "educated estimates" of $g_1(p,\lambda)$ that no harm arises from the lack of complete information about $y(p,\omega_z,\lambda')$ for $\lambda'<\lambda$.

The critical information which apparently must be included in any such procedure is the fact that $y(p,\omega_z,\lambda)$ and therefore $R(p,\omega_z,\lambda)$ are well-behaved functions of $\omega_z$. Thus, our method of solution (which is outlined in greater detail in the next section) is to determine at each step of a progressive numerical integration in $\lambda$, an approximate function $\bar{R}(p,\omega_z,\lambda)$. This function has three properties:

(a) The first $r$ angular moments of $\bar{R}$ agree with the right sides of the first $r$ Eqs. (4).

(b) $\bar{R}$ is well-behaved.

(c) The first $r$ approximate angular moments $\bar{y}_n(p,\lambda)$ which occur on both sides of (4), are given by the relations

$$\bar{y}_n(p,\lambda)=\int_{-1}^{1}d\omega_z(1-\omega_z)^n\frac{\bar{R}(p,\omega_z,\lambda)}{\mu(\lambda)-p\omega_z}. \tag{6}$$

These approximate values, $\bar{y}_n(p,\lambda)$, then enter into the integrals in (4) for all further integrations.

The accuracy of this method depends upon the integration technique and also upon how well we can describe $R$ with $r$ angular moments. Section V is a discussion of this point.

## IV. AN ITERATION PROCEDURE

Having decided to use numerical procedures to integrate Eqs. (4), we now write the integrals as sums:

$$[\mu(\lambda_l)-p]\bar{y}_n(p,\lambda_l)+p\bar{y}_{n+1}(p,\lambda_l)$$
$$=\sum_{i=0}^{l}\Delta\lambda_i a_i k(\lambda_i,\lambda_l)\sum_{n'=0}^{n}(\lambda_l-\lambda_i)^{n-n'}$$
$$\times S_n{}^{n-n'}(\lambda_l-\lambda_i)\bar{y}_{n'}(p,\lambda_i)+\text{source}. \tag{7}$$

The $a_i$ are the weights associated with some integration formula or combination of integration formulas. The $\Delta\lambda_i$ need not be all the same size. The bar over the various quantities indicates that we are working now with approximate quantities limited in accuracy by the finiteness of the integration intervals and by the number of moment equations used. If we separate the $l$th term from the sum on the right, we have

$$[\mu(\lambda_l)-p]\bar{y}_n(p,\lambda_l)+p\bar{y}_{n+1}(p,\lambda_l)$$
$$=[\Delta_l a_l k(\lambda_l,\lambda_l)\bar{y}_n(p,\lambda_l)]$$
$$+\sum_{i=0}^{l-1}\Delta\lambda_i a_i k(\lambda_i,\lambda_l)\sum_{n'=0}^{n}(\lambda_l-\lambda_i)^{n-n'}$$
$$\times S_n{}^{n-n'}(\lambda_l-\lambda_i)\bar{y}_{n'}(p,\lambda_i)+\text{source}. \tag{8}$$

Consider a situation in which we have determined $\bar{y}_n(p,\lambda_i)$ for $0\leqq\lambda_i\leqq\lambda_{l-1}$. We are now in a position to calculate the right hand side of Eqs. (8) except for the term in brackets. This term can be made small relative to the other terms on the right by taking $\Delta\lambda_l$ sufficiently small. Furthermore, since the $y_n$'s must be continuous functions a good estimate can be made of this term. We now perform the following sequence of operations:

(a) We estimate the $\bar{y}_n(p,\lambda_l)$ and call our estimate $\bar{y}_n{}^0(p,\lambda_l)$.

(b) We insert the $\bar{y}_n{}^0(p,\lambda_l)$ into the bracketed terms of (8) and thus calculate the right sides of (8). We call these quantities $\bar{R}_n{}^0(p,\lambda_l)$. These $\bar{R}_n{}^0(p,\lambda_l)$ are the zero'th approximation to the moments of

$$\bar{R}(p,\omega_z,\lambda_l)=[\mu(\lambda_l)-p\omega_z]\bar{y}(p,\omega_z,\lambda_l).$$

[9] By "well-behaved function" we mean a function which is positive and finite (except possibly for known $\delta$-function terms) and agrees with as much of our other *a priori* information, such as number and location of maxima and discontinuities, as it is feasible to consider.

[10] Other combinations of the $y_n$'s can be used as well in this connection. The function $g_1(p,\lambda)$ is chosen here because of other advantages discussed in Sec. VI.

(c) We construct a well-behaved function $\bar{R}^0(p,\omega_x,\lambda_l)$, whose first moments are the quantities $\bar{R}_n{}^0(p,\lambda_l)$. This is our main problem. Methods for doing it are discussed later in this section and in Appendix B. In problems involving a plane, monodirectional source, where $r$ equations are used, we have taken

$$\bar{R}^0(p,\omega_x,\lambda_l)=\sum_{m=1}^{r/2}\frac{\eta_m}{\beta_m}e^{-(1-\omega_x)/\beta_m}+D(p,\omega_x,\lambda_l), \quad (9)$$

where $D(p,\omega_x,\lambda_l)$ represents essentially the effect of low orders of scattering, which we can calculate exactly. The $r$ parameters, $\eta_m$ and $\beta_m$, are so chosen that the first $r$ moments of $\bar{R}^0(p,\omega_x,\lambda_l)$ are equal to the $\bar{R}_n{}^0(p,\lambda_l)$. Various other forms for $\bar{R}^0$ have proved convenient under different circumstances.

(d) We calculate the quantities

$$\bar{y}_n{}^1(p,\lambda_l)=\int_0^\infty d(1-\omega_x)(1-\omega_x)^n\frac{\bar{R}^0(p,\omega_x,\lambda_l)}{\mu(\lambda_l)-p\omega_x}. \quad (10)$$

The upper limit of this integration is actually 2, but it can be taken as $\infty$ if the source is monodirectional and if $\lambda_l-\lambda_0\ll 2$. This is a convenient, though unnecessary approximation.

(e) We insert the $\bar{y}_n{}^1(p,\lambda_l)$ into the bracketed terms of (8) and call the new approximation to the right sides so obtained $\bar{R}_n{}^1(p,\lambda_l)$.

Since this last step corresponds to step (b) we have a closed cycle defining an iteration procedure. This cycle of operations is repeated until it yields negligible change in the quantities $\bar{y}_n(p,\lambda_l)$. These values are then used in exactly this same way to calculate the $\bar{y}_n(p,\lambda_{l+1})$.

This iteration procedure can be used to calculate the $\bar{y}_n(p,\lambda_1)$. For this first interval it may be convenient to take $\bar{R}^0(p,\omega_x,\lambda_1)=D(p,\omega_x,\lambda_1)$ in the first iteration, since the low orders of scattering always predominate very close to the smallest wavelength for the problem.

As was mentioned in the third step of the iteration cycle, the main problem of this method of solution is that of determining a well-behaved function corresponding to $r$ approximately known moments. The most widely used general procedure for solving such a moment problem is that of combining the moments into coefficients of some orthogonal polynomial system. (For a discussion of this, see reference 6.) This polynomial method is especially useful if a proper "weight function" can be ascertained from available information about the distribution. Experience indicated that our knowledge of $R$ and the $R_n$ is insufficient to make use of the polynomial method. We could devise no polynomial system which gave adequate convergence, and were forced to seek new methods for approximating functions.

The form of $\bar{R}^0$ given in (9) corresponds to a different method of using moments to approximate a distribution function. This method, which proved very satisfactory, is described in Appendix B. It is a generalization of a type of numerical integration due to Gauss. (Szego[11] and Chandrasekhar[1] give good discussions of this type of numerical integration.) Gauss' type of numerical integration may be regarded as a method for approximating some standard function by a sum of Dirac $\delta$-functions. The generalization which we use substitutes continuous functions such as the exponentials of (9) for the $\delta$-functions. This procedure is particularly accurate and flexible when integrals of a function are desired in terms of moments of the function. This is just what we need, since we must evaluate the integrals (10).

## V. ACCURACY OF THE CALCULATIONS

Of the two types of approximations involved, the use of finite integration steps is less troublesome than the use of a finite number of moment equations. It is always possible to decrease the interval size or use a better integration procedure to obtain the desired accuracy. Since the $y_n$ are all continuous functions of $\lambda$, no special difficulties arise. It is quite advantageous to make use of our *a priori* knowledge of the $y_n$ to decrease the number of intervals or to increase the accuracy of the integration. Thus, near the singularity the $y_n$ will change rapidly with $\lambda$ and fine integration intervals should be used; whereas if $p$ and $\lambda$ are such that the singularity is far away in the $(p,\lambda)$ plane, coarse integration intervals can be used. Also, in plane, monodirectional, monoenergetic problems the $y_n$ behave as $(\lambda-\lambda_0)^n$ near $\lambda_0$. The integration should be weighted to take advantage of this knowledge.

With regard to the use of a limited number of moment equations and therefore limited information about $R$, we may say several things:

(a) All of our present knowledge of photon directional distributions indicates that oscillations or sharp discontinuities which would require many moments for their description are not an essential feature of this problem. It is true that if the source is monodirectional and monoenergetic the first scattered beam is indeed a $\delta$-function; the second scattered beam contains a step function discontinuity; and in general the $n$'th order of scattering contains a discontinuity in the $(n-2)$ derivative.[12] However, these discontinuities are a feature of a particular source type, and they tend to wash out as the penetration increases.[13]

(b) Our feeling that a relatively small number of moment Eqs. (8) may suffice is strengthened by examination of the fourth step in the iteration procedure.

[11] G. Szego, *Orthogonal Polynomials* (American Mathematical Society, Colloquium Publications, 1939), vol. 23.

[12] L. V. Spencer and Fannie Jenkins, Phys. Rev. **76**, 1885 (1949).

[13] In practice, the first scattered beam may be calculated separately; and the step function discontinuity in the second scattered beam may be easily reduced to a harmless discontinuity in the derivative by subtracting out and calculating separately a rectangular directional distribution whose ordinate is the same as that of the second scattering discontinuity.

Since the $\bar{y}_n(p, \lambda_l)$ are to be obtained by evaluating integrals, they will tend to be insensitive to the fine features of $R(p, \omega_z, \lambda_l)$.

(c) These deep penetrations are a heretofore unsolved problem, and no independent results exist which can serve as a check. We can, however, consider a sequence of approximations using 1, 2, 3, $\cdots$ equations and see how rapidly it converges.

(d) An estimate of the accuracy obtained by using $r$ moment equations can be made by calculating the eigenvalues of simplified problems with the methods discussed here.[14] These can be compared with the values given by standard eigenvalue procedures. This was done in a preliminary investigation. In the homogeneous Wick equations corresponding to constant and linear mean free paths we approximated $R$ with Gaussians (i.e., $\bar{R}=\sum_m(\eta_m/\beta_m)\exp(-\frac{1}{2}\theta^2/\beta_m)$). The surprising result was that as few as two moment equations yielded the eigenvalue at least as accurately as any of the eigenvalue methods of reference 4.

Because of this result, it seemed reasonable in monodirectional source problems to use only two moment equations and to approximate $R$ by a single exponential of the form given by (9).

On the other hand, in plane isotropic source problems the angular distribution has a long and very strong tail. For these problems it was necessary to use four moment equations, in order to describe both the peak at $\omega_z=1$ and the tail. Here the approximation was of the form

$$R=\frac{\eta_0}{\beta_0+(1-\omega_z)}+\frac{\eta_1}{\beta_1+(1-\omega_z)}. \tag{11}$$

(This analytic form is exact for the unscattered radiation.)

## VI. THE "MEAN SQUARE DEFLECTION" PARAMETER

The parameter $g_1(p, \lambda)=y_1(p, \lambda)/y_0(p, \lambda)$ is a very useful quantity which has some physical significance. From the definition of the angular moments, we see that for small deflections $\theta$, $g_1(p, \lambda)=\langle 1-\omega_z\rangle_{\omega}\cong\langle\theta^2/2\rangle_{\omega}$. Thus, the $g_1(p, \lambda)$ is essentially a mean square deflection and measures the angular "spread."

The $g_1(p, \lambda)$ has a number of very convenient properties. It is a smooth, positive, bounded, slowly varying function of $p$ and $\lambda$. As mentioned in Sec. III, the $g_1$ can be regarded as playing the role of an eigenvalue. A knowledge of the $g_1(p, \lambda)$ makes it possible to reduce the system of Eqs. (4) to a single equation, similar to Eq. (3) of reference 3, for the flux $y_0(p, \lambda)$. If $y_1(p, \lambda)$ is expressed as $g_1(p, \lambda)y_0(p, \lambda)$, the first of Eqs. (4) ($n=0$) becomes

$$[\mu(\lambda)-p+pg_1(p, \lambda)]y_0(p, \lambda)=\int_0^{\lambda}d\lambda' k(\lambda, \lambda')y_0(p, \lambda')+\text{source}.$$

The asymptotic solution of the equation, for $\mu\sim\mu_s$ is

$$[\mu(\lambda)-p+pg_1(p_1\lambda)]y_0(p, \lambda)=\exp\left[C\int^{\lambda}d\lambda'\frac{1}{\mu(\lambda')-p+pg_1(p, \lambda')}\right], \tag{12}$$

where $C=k(\lambda, \lambda)$.[3,15]

Equation (12) differs from Eq. (3) reference 3 by the additional term $pg_1y_0(p, \lambda)$. This term disappears if one assumes a "straight ahead" approximation, i.e., $g_1=0$, as in reference 3. The equation without the term $pg_1y_0(p, \lambda)$ also pertains to a somewhat different problem. If one regards the variable $x$ in (1) as the total path length traveled, rather than as the distance attained from the source, then $\omega_z$ must be replaced by 1 in this equation and the coefficient $g_1$ never appears. Accordingly the factor $pg_1$ in (12) represents an additional absorption due to obliquity of path, which makes the depth of penetration shorter than the path length traveled.

## VII. INVERSION OF THE FOURIER-LAPLACE TRANSFORM

In order to obtain the spectral density as a function of penetration away from the source, it is necessary to evaluate numerically the complex integral

$$Y_0(x, \lambda)=\frac{1}{2\pi i}\int_{-i\infty}^{i\infty}dp e^{-px}y_0(p, \lambda). \tag{13}$$

We have a number of pieces of information with which to work in making this inversion:

(a) We have values of $\bar{y}_0$ for four or five real values, $p_i$, of $p$. These numbers are approximations, as discussed earlier.

(b) $y_0(p, \lambda)$ is a smooth function of $p$ and $Y_0(x, \lambda)$ is a smooth function of $x$. The values $p_i$ will have been chosen conveniently for interpolation.

(c) Both $y_0$ and $Y_0$ are positive functions.

(d) $\text{Exp}(-px)y_0(p, \lambda)$ has a saddle point on the real axis as discussed earlier.

(e) We know approximately the variation of both $y$ and $Y$ for small $p$ and small $x$.

(f) All singularities of $y_0(p, \lambda)$ are located on the real axis, as discussed earlier.

(g) We know the type as well as the location of the singularities of $y_0(p, \lambda)$ and the corresponding asymptotic form of $Y_0(x, \lambda)$.

[14] Such problems would be the homogeneous equations with constant or linear total cross section. These problems were first treated by Wick. See reference 4 and Appendix A.

[15] The eigenvalue $\bar{C}$ mentioned in Appendix A is related to $g_1$ by

$$\bar{C}=C/[1+pg_1/(\mu-p)].$$

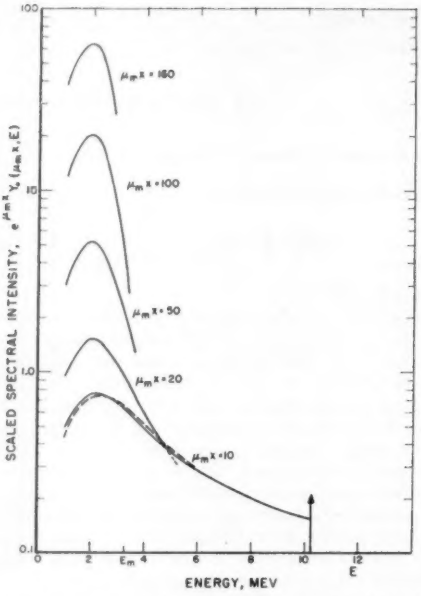


FIG. 1. Scaled differential x-ray intensity in units (Mev/cm²sec)/Mev at various distances $x$ from a plane monodirectional source of 10.22-Mev photons in Pb. The factor $\exp(-\mu_m x)$ has been divided out. The strength of the source is 10.22 Mev/cm² sec. The narrow beam attenuation coefficient of the source radiation is 0.561 cm$^{-1}$, while that of the most penetrating component is 0.466 cm$^{-1}$.

The method of inversion which first suggests itself is saddle point integration, because of (d) and (f). In order to do such an integration, we would fit an approximate curve or curves to the points $\bar{y}_0(p_i, \lambda)$, determine the function and a few derivatives at the saddle point, and substitute in the proper formula. In so doing we would be taking no advantage of important information [e.g., item (g)] which we might have about higher derivatives of $y_0$.

In general, we can expect that most accurate results can be obtained by an inversion process which incorporates a maximum of the available information. The inversion technique which we actually used is described in Appendix C. Basically it consisted of fitting the values with smooth, positive functions which have both the correct type of singularity and the correct behavior for small $p$. These functions were then inverted exactly. The results were considered reliable for that range of $x$ where the saddle point method could have been used.

## VIII. NUMERICAL APPLICATIONS

In order to explore the range of application of these methods, we made calculations for both a monotonic attenuation coefficient and an attenuation coefficient which has a minimum within the range of integration. We also made calculations for both plane monodirectional and plane isotropic source types. The attenuation coefficients were furnished by White,[16] and the full Klein-Nishina differential scattering cross section was used.

The calculations were not extended to include components below 1 Mev in energy. Also, the isotropic source calculation was limited to a single value of $p$. Economy of effort was the main reason for these limitations. If desired, low energies (which come quickly into relative equilibrium) and small values of $p$ can perhaps be more easily calculated by the polynomial method.[6]

### A. Plane Monodirectional 10.22-Mev Source in Pb

In this problem, $y_0(p, \lambda)$ was calculated for $p/\mu_m = 0$, 0.65, 0.85, 0.95, and 0.98. The Fourier-Laplace transform was inverted as in Appendix C. Figure 1 presents the resulting spectra, for penetrations up to $\mu_m x = 160$.[17] The dashed line gives for comparison the results of a polynomial calculation for $\mu_m x = 10$. The same attenuation coefficients were used for both calculations. The agreement is within about 3 percent.

Notice that the ordinate is $\exp(+\mu_m x) Y_0(\mu_m x, E)$ rather than the exponentially decreasing $Y_0(\mu_m x, E)$. (If $Y_0$ had been plotted, it would have been necessary to use 70-cycle log paper!)

The main characteristics of the x-ray spectra of Fig. 1 are as follows: There is a $\delta$-function source at 10.22 Mev, represented by the arrow. At 10.22 Mev there is a singly scattered component which varies as $\mu_0 x \exp(-\mu_0 x)$. Since we have discounted an exponential, this component behaves, in Fig. 1, as $\mu_m x \exp[-(\mu_0 - \mu_m)x]$. In general the components with energies above $E_m$ ($E_m$ corresponds to the minimum attenuation coefficient) behave asymptotically as $(\mu_m x)^{-\bar{C}/\dot{\mu}(\lambda)} \exp[-(\mu - \mu_m)x]$.[18] As the energy approaches $E_m$ from above, the exponential factor becomes weaker and $(\bar{C}/\dot{\mu})$ becomes larger. At $E_m$, the exponential factor becomes unity and the build-up is maintained asymptotically at approximately the rate $x^{-5/6} \exp(\frac{1}{2}\delta x^{1/3})$.[18]

At low energies a relative equilibrium is established. (This means that at low energies the spectrum does not change shape as the penetration increases.) All components "build up" together over the exponential at approximately the rate $x^{-5/6} \exp(\delta x^{1/3})$.[18] The more penetrating the scattered component, the greater the

[16] G. R. White, Natl. Bur. Standards Rep. 1003, 1952 (unpublished).

[17] At high energies and great penetrations, the spectrum is not given. This is because the singularity for $\lambda < \lambda_m$ is located at $\phi = \mu(\lambda) > \mu_m$. Since we did no calculations for $\phi > 0.98\mu_m$ we did not, in general, approach very closely to the singularity for $\lambda < \lambda_m$. Thus, the saddle point for deep penetrations at these high energies lay outside the range of our calculations.

[18] Refer to Appendix A for a summary of asymptotic penetration laws.

penetration at which this relative equilibrium is established.

Since the low energy components "build up" as $x^{-5/8}\exp(\delta x^{1/3})$, whereas the $E_m$ component "builds up" as $x^{-5/8}\exp(\frac{1}{2}\delta x^{1/3})$, there must be an energy region in which a transition occurs from one asymptotic penetration law to the other. This nonequilibrium region becomes narrower with increasing penetration, and the difference between the penetration laws becomes more serious. Thus the spectrum becomes enormously steep at energies near $E_m$.

Perhaps the most striking feature of the spectra is a maximum at an energy substantially below $E_m \approx 3$ Mev. This maximum is apparently a feature of the equilibrium spectrum.[19] It is located about at the energy at which the sum of the photoelectric and pair creation cross sections is a minimum. Whereas the steeply rising portion of the curve is determined by the minimum in the total cross section, the maximum may be determined by the interplay of photoelectric absorption and pair creation.

The $\bar{g}_1(p, \lambda)$ given by these calculations is presented in Fig. 2. The linear rise near $\lambda_0 = 0.05$ represents first scattering. The dip at $\lambda \sim 0.2$ illustrates the fact that the components controlling the deep penetration have directional distributions strongly peaked at $(1-\omega_x)=0$.

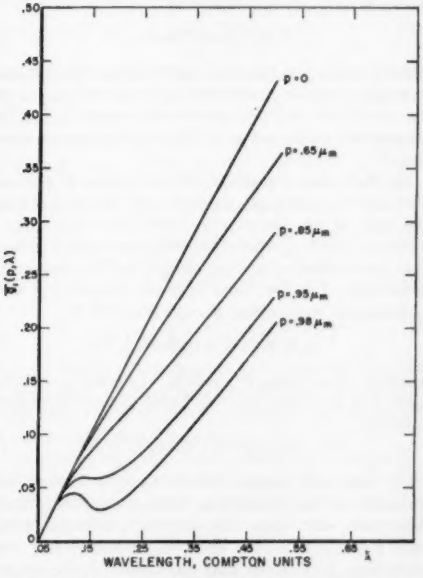


FIG. 2. The "mean square deflection" parameter $\bar{g}_1(p, \lambda)$ for the Pb calculation.

[19] In water there is a maximum in the equilibrium spectrum at about 70 kev which is determined by the interplay of scattering and photoelectric absorption. (See references 5 and 6.)

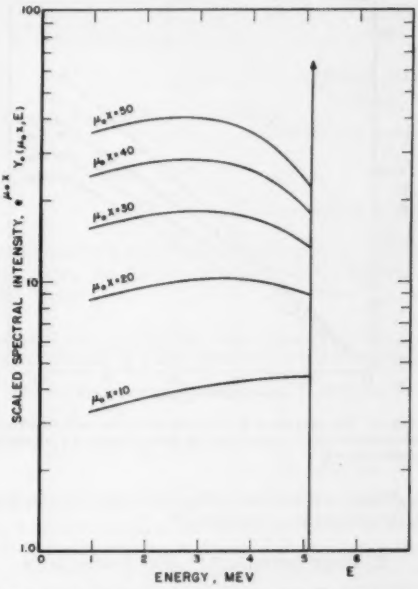


FIG. 3. Scaled differential x-ray intensity in units (Mev/cm²sec)/Mev at various distances $x$ from a plane monodirectional source of 5.11-Mev photons in Fe. The factor $\exp(-\mu_0 x)$ has been divided out. The source strength is 5.11 Mev/cm² sec and the attenuation coefficient of the source radiation is 0.246 cm⁻¹.

Finally, at large $\lambda$ the curves for different $p$ have nearly the same shape, indicating relative equilibrium in the directional distributions, as well as the flux, of the low energy components.

### B. Plane Monodirectional 5.11-Mev Source in Fe

Calculations of $\bar{y}_0(p, \lambda)$ were made at the values $p/\mu_0 = 0$, 0.65, 0.85, and 0.95. Figure 3 presents the calculated spectral intensities for various penetrations.

The ordinate is $\exp(\mu_0 x) Y_0(\mu_0 x, E)$ rather than $Y_0(\mu_0 x, E)$. Since $\mu_0$ is the smallest attenuation coefficient, all scattered components increase in Fig. 3. The lowest energy components reach relative equilibrium at relatively small penetrations. These equilibrium components "build up" at the rate $(\mu_0 x)^{\bar{C}/\dot{\mu}_0}$, $\bar{C}/\dot{\mu}_0 > 1$. Just below the source energy $E_0$ is a nonequilibrium region of the spectrum which narrows as the penetration increases. Since the trend of the build-up changes from $x$ to $x^{\bar{C}/\dot{\mu}_0}$ in this nonequilibrium region, the spectrum becomes increasingly steep.

The solid curves in Fig. 4 give the $\bar{g}_1(p, \lambda)$ for this problem. They behave like $(\lambda - \lambda_0)$ near $\lambda_0$, indicating single scattering. For large $\lambda$ and for $p$ near $\mu_0$, the curves tend to become parallel, indicating an approach

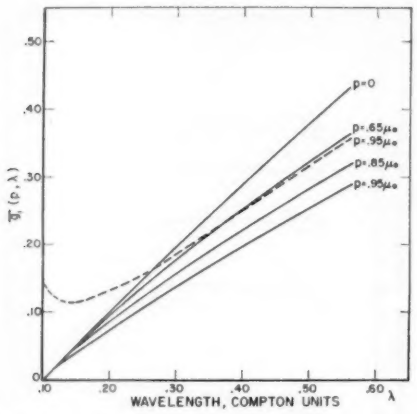


FIG. 4. The parameter $\bar{g}_1(p, \lambda)$ for the plane monodirectional Fe calculation (solid curves) and the plane isotropic Fe calculation (dashed curve).

to relative equilibrium in the directional distributions of the low energy components.[20]

### C. Plane Isotropic 5.11-Mev Source in Fe

This calculation was made only for the value $p/\mu_0 = 0.95$. The dashed line in Fig. 4 gives the resulting $\bar{g}_1$. Notice that it starts at a finite value corresponding to once scattered radiation. It then dips, indicating a concentration of scattered radiation with directions near $\theta = 0$. Finally, it tends to become parallel with the solid curves, indicating the establishment of equilibrium.

In this isotropic problem, four moment equations were used, whereas only two were used in the corresponding monodirectional problem. This gives rise to a slight difference in the slope of the $\bar{g}_1$ in the equilibrium region of wavelengths. (The comparison is between the two curves with $p/\mu_0 = 0.95$.) The effect of this on the asymptotic penetration law is to change the exponent of the build-up factor by perhaps two or three percent.

## IX. REMARKS

In conclusion it may be worth noting that the work required to accomplish a second calculation like the Pb calculation of Fig. 1 would be of the order of three or four man weeks.

As mentioned in the first footnote, pair production has been considered as being simply a mechanism for absorption. Cascade processes have been neglected. One may wonder at what source energy (for a given material) cascade processes become sufficiently important to make this a poor approximation. Some work has been done on this problem by Cohen and Plesset,[21] who attempt a rough calculation of the effect in Pb and U. It is our intention to concentrate some effort on this and related problems in the future.

In this paper we have concentrated on great penetrations. These methods of calculation can probably also be used effectively to study the spectral distributions of those x-rays which reverse their direction and penetrate back to and behind the source.

The writer wishes to thank Dr. U. Fano for many discussions and suggestions, and to acknowledge the able assistance of Mrs. Fannie Stinson, who did most of the numerical work for this paper.

## APPENDIX A. SUMMARY OF CALCULATIONS OF ASYMPTOTIC PENETRATION LAWS

(a) The initial work on this problem followed the "straight ahead" approximation method, i.e., it disregarded the small deflections which accompany Compton scattering with small changes of wavelength. In addition to this, reference 2 assumed, in particular, that the total ("narrow beam") attenuation coefficient $\mu(\lambda)$ increases steadily as the photon wavelength increases in the course of successive Compton scatterings. Under these assumptions the spectral energy density $Y(x, \lambda)$ was shown to vary asymptotically as

$$Y(x, \lambda) \propto x^{C/\dot{\mu}_0} e^{-\mu_0 x}, \tag{1}$$

where $C = k(\lambda, \lambda)$ is the probability density for Compton scattering without wavelength change and $\mu_0$, $\dot{\mu}_0$ are the zero'th and first derivatives with respect to $\lambda$ of the attenuation coefficient $\mu$ at the smallest source wavelength.

(b) Reference 3 removed the restriction of a monotonically increasing attenuation coefficient and treated the case of an attenuation coefficient which has a minimum value $\mu_m = \mu(\lambda_m)$ at some wavelength greater than the smallest source wavelength $\lambda_0$. The asymptotic penetration law for those spectral components with wavelengths greater than $\lambda_m$ was found to be

$$Y(x, \lambda) \propto [x^{-5/6} \exp(bx^{1/3})] e^{-\mu_m x}, \tag{2}$$

where $b = 3[\pi^2 C^2/2\ddot{\mu}_m]^{1/3}$, and $\ddot{\mu}_m = (d^2\mu/d\lambda^2)_m$. Surprisingly, the $\lambda_m$ component was found to vary asymptotically as

$$Y(x, \lambda_m) \propto [x^{-5/6} \exp(\tfrac{1}{2} bx^{1/3})] e^{-\mu_m x}. \tag{3}$$

(c) The small angular deflections have a substantial influence on the intensity at deep penetrations. These deflections were taken into account in reference 4, but only for a $\mu(\lambda)$ which increases monotonically with increasing $\lambda$. The resulting asymptotic behavior was found to be

$$Y(x, \omega_x, \lambda) \propto x^{\bar{C}/\dot{\mu}_0} e^{-\mu_0 x}, \tag{4}$$

[20] Since the attenuation coefficient is nearly linear, the slope $\dot{\bar{g}}_1 = \partial g_1/\partial\lambda$ for the equilibrium portions of the curves is related to Wick's eigenvalue in the following way:

$$\bar{C} = C/(1 + p\dot{\bar{g}}_1/\dot{\mu}).$$

(See footnotes 14 and 15 and Appendix A.)

[21] S. T. Cohen and E. H. Plesset, Rand Corporation Report RAD-264, May 20, 1948 (unpublished).

where $(-\bar{C})$ is the lowest eigenvalue of a certain Schrödinger type equation. The resemblance to (1) is apparent, and indeed $C$ is an upper limiting value to $\bar{C}$. This progress represents an application of a method used by Wick[23] in solving the analogous problem of neutron penetration.

(d) The case of a constant attenuation coefficient has importance even though it is physically nonexistent. Application of the methods of references 2 and 3 is straightforward in the "straight ahead" approximation, and the result is

$$Y(x, \lambda) \propto \exp[2(C(\lambda-\lambda_0)x)^{\frac{1}{2}}]e^{-\mu_0 x}. \quad (5)$$

Angular deflections can be taken into account by the method of Wick, which yields the asymptotic form

$$Y(x, \omega_x, \lambda) \propto \exp[2(\bar{C}(\lambda-\lambda_0)x)^{\frac{1}{2}}]e^{-\mu_0 x}, \quad (6)$$

where $(-\bar{C})$ is again the lowest eigenvalue of a Schrödinger type equation.

(e) The situation in which the attenuation coefficient decreases monotonically has never been discussed even though it is pertinent if $\lambda<\lambda_m$. The asymptotic penetration law in straight ahead approximation is

$$Y(x, \lambda) \propto x^{-C/\dot{\mu}(\lambda)}e^{-\mu(\lambda)x}. \quad (7)$$

Angular deflections change this to

$$Y(x, \omega_x, \lambda) \propto x^{-\bar{C}/\dot{\mu}(\lambda)}e^{-\mu(\lambda)x}, \quad (8)$$

where $(-\bar{C})$ is the lowest eigenvalue of a Schrödinger type equation very similar to that associated with expression (4).

(f) To complete the picture, we must discuss (b) generalized to include angular deflections. A study of this problem has been made by Fano.[23a] The asymptotic penetration law behaves like

$$Y(x, \omega_x, \lambda) \propto [x^{-5/6}\exp(\bar{b}x^{1/3})]e^{-\mu_m x}, \quad (9)$$

where $\lambda>\lambda_m$. The $\lambda_m$ component obeys the asymptotic law

$$Y(x, \omega_x, \lambda_m) \propto [x^{-5/6}\exp(\tfrac{1}{2}\bar{b}x^{1/3})]e^{-\mu_m x}, \quad (10)$$

where $\bar{b}=b(C)$, $b$ has the meaning previously ascribed in paragraph (b), and $\bar{C}$ is the eigenvalue of a constant mean free path problem obtained by completely ignoring variations of $\mu$ near $\mu_m$.

(g) Associated with each asymptotic penetration law is a singularity in the spatial Fourier-Laplace transform variable $y(p, \omega_x, \lambda)$. The following is a list of these singularities:

$$y(p, \omega_x, \lambda) \propto \left[\frac{1}{\mu_0-p}\right]^{\xi} \quad \text{(monotonically increasing } \mu(\lambda)),$$

$$y(p, \omega_x, \lambda) \propto \left[\frac{1}{\mu(\lambda)-p}\right]^{\xi(\lambda)}$$

(monotonically decreasing $\mu(\lambda)$),

$$y(p, \omega_x, \lambda) \propto \{\exp[(\lambda-\lambda_0)/(\mu_0-p)]\}^{\xi}$$

(constant $\mu$, $\mu=\mu_0$),

$$y(p, \omega_x, \lambda) \propto [\exp(\mu_m-p)^{-1}]^{\xi}$$

($\mu(\lambda)$ with minimum at $\lambda_m$).

The parameter $\xi$ must be determined, in every case, by determining the lowest eigenvalue of a Schrödinger type equation.

## APPENDIX B. A METHOD FOR APPROXIMATING A FUNCTION FROM A KNOWLEDGE OF ITS MOMENTS

We want to approximate a distribution function $H(x)$ by a sum of terms

$$H(x) \approx \eta_1 f(x, \beta_1)+\eta_2 f(x, \beta_2)+\eta_3 f(x, \beta_3) +\cdots+\eta_n f(x, \beta_n), \quad (1)$$

where the $\eta_i$ and $\beta_i$ are parameters to be fitted so that the first $2n$ moments of the approximate function agree with the corresponding moments of $H(x)$. (Notice that in contrast to the polynomial method, each term on the right involves two constants to be determined instead of one, and that all the terms have the same form.) This can be accomplished for a broad class of functions $f(x, \beta_i)$.

### 1. The Gauss Method of Numerical Integration

According to this well-known integration technique, if an integral

$$\int_c^d H(x)S(x)dx \quad (2)$$

is to be evaluated, $H(x)$ and all its moments over the interval being known, the most accurate $n$ point numerical integration that can be performed is to take

$$\int_c^d H(x)S(x)dx \approx \sum_{i=1}^{n} \eta_i S(\beta_i), \quad (3)$$

where the $\beta_i$ are the zeros of a polynomial $h_n(x)$, which is the $n$'th self-adjoint polynomial associated with the weight function $H(x)$. The $\eta_i$ are the so-called Christoffel numbers, which may be calculated from the formula

$$\left(\frac{dh_n}{dx}\right)_{\beta_i}\eta_i=\int_c^d \frac{H(x)h_n(x)}{x-\beta_i}dx. \quad (4)$$

(In Gauss' original scheme, $H(x)=1$, $c=-1$, $d=1$.)

The reason for the accuracy of this approximation is that in this procedure we are actually replacing $H(x)$ by

[23] G. C. Wick, Phys. Rev. **75**, 738 (1949).

[23a] This material is part of a comprehensive report on the subject to be published in the J. Research Natl. Bur. Standards.

a much more manageable function, namely,

$$H(x)\approx\sum_{i=1}^{n}\eta_i\delta(x-\beta_i). \tag{5}$$

The scheme for choosing the $\beta_i$, $\eta_i$ is such that the first $2n$ moments of the sum of Dirac delta-functions are made to agree with the first $2n$ moments of $H(x)$.

From our standpoint the most remarkable feature about this method of describing $H(x)$ is the fact that the $\beta_i$ and $\eta_i$ are all determined from a knowledge of the moments of $H(x)$, rather than from the function itself. Thus the $\delta$-function is one of the functions which can be used in the approximation (1).

### 2. Generalization to Other Types of Functions

If we multiply (5) by $x^m$ and integrate over $x$, we obtain the following set of equations, where $H_m=\int_c^d x^m H(x)dx$:

$$\begin{array}{lllll}
\eta_1 & +\eta_2 & +\cdots+\eta_n & = H_0\\
\eta_1\beta_1 & +\eta_2\beta_2 & +\cdots+\eta_n\beta_n & = H_1\\
\eta_1\beta_1^2 & +\eta_2\beta_2^2 & +\cdots+\eta_n\beta_n^2 & = H_2\\
\cdot & \cdot & \cdots & \cdot & \cdot\\
\cdot & \cdot & \cdots & \cdot & \cdot\\
\cdot & \cdot & \cdots & \cdot & \cdot
\end{array} \tag{6}$$

$$\eta_1\beta_1^{2n-1}+\eta_2\beta_2^{2n-1}+\cdots+\eta_n\beta_n^{2n-1}=H_{2n-1}.$$

These are $2n$ equations in $2n$ unknowns. The equations are nonlinear in half of the unknowns.

Since the first $n$ self-adjoint polynomials can be obtained from a knowledge of the first $2n$ moments of the weight function, the polynomial $h_n(x)$ is determined by the known constants $H_m$. The zeros of $h_n(x)$ and the relations (4) determine the $\beta_i$ and $\eta_i$ which satisfy this nonlinear system of equations.

A set of equations with exactly the same form as (6) can be shown to obtain if we take moments of the relation (1), where $f(x, \beta_i)$ may be one of the following group of functions:

(a) $f(x/\beta_i)$, $c\leqslant x/\beta_i\leqslant d$, where $f(x/\beta_i)$ is any function, and $c$, $d$ are arbitrary constants such that moments of $f(x/\beta_i)$ over this range exist.

(b) $x^{\beta_i}e^{-x}$, $0\leqslant x\leqslant\infty$.

(c) $e^{-x}\,{}_1F_1(-\beta_i;1;-x)$, $0\leqslant x\leqslant\infty$, where ${}_1F_1$ is the confluent hypergeometric function.

(d) $x^{\beta_i}(1-x)^{A-\beta_i}$, $0\leqslant x\leqslant 1$, $A$ arbitrary.

### 3. Illustration

As a very simple illustration, suppose we have four moments $H_m$ of a function $H(x)$, $0\leqslant x\leqslant\infty$, and we want to approximate $H(x)$ by two exponentials. We write

$$H(x)\approx\frac{\eta_1}{\beta_1}e^{-x/\beta_1}+\frac{\eta_2}{\beta_2}e^{-x/\beta_2}.$$

Taking moments, we have the relations (6) for this simple problem:

$$\begin{array}{ll}
\eta_1 \quad +\eta_2 \quad = H_0/0! = H_0^*,\\
\eta_1\beta_1+\eta_2\beta_2 = H_1/1! = H_1^*,\\
\eta_1\beta_1^2+\eta_2\beta_2^2 = H_2/2! = H_2^*,\\
\eta_1\beta_1^3+\eta_2\beta_2^3 = H_3/3! = H_3^*.
\end{array}$$

Using "orthogonality relations" we obtain the polynomial which is "self-adjoint" with respect to the "weight function" whose "moments" are the $H_m^*$:

$$h_2^*(x)=x^2-ax+b,$$

where

$$a=\frac{H_3^*H_0^*-H_2^*H_1^*}{H_2^*H_0^*-H_1^{*2}};\qquad b=\frac{H_3^*H_1^*-H_2^{*2}}{H_2^*H_0^*-H_1^{*2}}.$$

The roots of the equation $h_2^*(x)=0$ are

$$\beta_0=\tfrac{1}{2}[a-(a^2-4b)^{\frac{1}{2}}];\quad \beta_1=\tfrac{1}{2}[a+(a^2-4b)^{\frac{1}{2}}].$$

For the corresponding "Christoffel" numbers, we have

$$\eta_1=\frac{1}{2\beta_1-a}\int_0^\infty(x-\beta_2)H_0^*(x)dx=\frac{\beta_2H_0^*-H_1^*}{(a^2-4b)^{\frac{1}{2}}};$$

$$\eta_2=\frac{1}{2\beta_2-a}\int_0^\infty(x-\beta_1)H_0^*(x)dx=\frac{\beta_1H_0^*-H_1^*}{(a^2-4b)^{\frac{1}{2}}}=H_0^*-\eta_1.$$

## APPENDIX C. INVERSION OF THE FOURIER-LAPLACE TRANSFORM

### 1. Approximating a Function if Several Values of the Function are Known

If we have several values $H_m=H(x_m)$ of a function $H(x)$, we may make the same type of approximation as in Appendix B, provided the $H_m$ are properly spaced. The useful function types in general differ from those of Appendix B. (This method has been worked out independently and applied to a similar problem by a UCLA group.)[23]

As an example, suppose we choose four values $H_0$, $H_1$, $H_2$, $H_3$ of a function which we want to approximate by exponentials. The approximate function must agree with the exact one at the values $(H_m, x_m)$. The $x_m$ are so chosen that $(x_{m+1}-x_m)=(x_m-x_{m-1})$. We write

$$H(x)\approx\eta_0e^{-\beta_0x}+\eta_1e^{-\beta_1x}.$$

Next, we define $\beta_0^*=e^{-\beta_0(x_1-x_0)}$; $\beta_1^*=e^{-\beta_1(x_1-x_0)}$; $\eta_0^*=\eta_0e^{-\beta_0x_0}$; $\eta_1^*=\eta_1e^{-\beta_1x_0}$. The set of equations which must be solved to pass the approximate function through the values $(H_m, x_m)$ is thereby reduced to the form (6) of Appendix B.

A class of functions most useful in making this type of approximation is the class $[W(x)]^\beta$, where $W(x)$ is any function and $\beta$ is a constant. All the singularities which may determine the asymptotic form of $Y_0(x, \lambda)$ are of this type.

[23] Greenfield, Specht, Kratz, and Hand, J. Opt. Soc. Am. 42, 6 (1952).

### 2. Numerical Applications

In order to make the best possible use of our information about $y_0(p, \lambda)$ we accomplish the inversion in the following ways:

(a) Where the controlling singularity has the form $(\mu_0-p)^{-\beta}$, as in the problem of a monodirectional source in Fe, we made the approximation

$$y_0(p, \lambda) \approx e^{-dp}[\eta_1(\mu_0-p)^{-\beta_1}+\eta_2(\mu_0-p)^{-\beta_2}].$$

Here, $d$ is an arbitrary constant which is chosen to make the approximate function as smooth as possible. We chose this method of introducing such a smoothness parameter because it does not make the exact inversion more difficult or complicated. The inverted function $Y_0(x, \lambda)$ is then given by the relation

$$Y_0(x, \lambda) \approx e^{-\mu_0(x+d)}\left[\frac{\eta_1}{\Gamma(\beta_1)}(x+d)^{\beta_1-1}+\frac{\eta_2}{\Gamma(\beta_2)}(x+d)^{\beta_2-1}\right].$$

Notice that the $d$ merely introduces a shift in the penetration.

(b) In the problem of a monodirectional source in Pb, for $\lambda<\lambda_m$, where the controlling singularity has the form $(\mu-p)^{-\beta(\lambda)}$, we made the approximation

$$(\mu_0-p)^2 y_0(p, \lambda) \approx e^{-dp}[\eta_1(\mu-p)^{-\beta_1}+\eta_2(\mu-p)^{-\beta_2}].$$

Here, $d$ is again chosen for smoothness. Notice the factor $(\mu_0-p)^2$ on the left. This discounts features of $y_0$ which are characteristic of the source and which tend to obscure the approach to asymptoticity. (The unscattered component of the radiation is not included in $y_0$.) Taking this factor into account explicitly in this way gives greater accuracy by introducing one more piece of our information. When this approximation is inverted, the flux is given by the expression

$$Y_0(x, \lambda) \approx e^{-\mu(x+d)} \sum_{i=1,2} \frac{\eta_i}{\Gamma(\beta_i+2)}(x+d)^{\beta_i+1} \times {}_1F_1[2; 2+\beta_i; -(\mu_0-\mu)(x+d)].$$

(c) Finally, in the problem of a monodirectional source in Pb, for $\lambda>\lambda_m$, where the singularity has the form $[\exp(\mu_m-p)^{-1}]^\beta$, we use the approximation

$$(\mu_0-p)^2 y_0(p, \lambda) \approx e^{-dp}\{\eta_1 \exp[\beta_1/(\mu_m-p)^{\frac{1}{2}}] + \eta_2 \exp[\beta_2/(\mu_m-p)^{\frac{1}{2}}]\},$$

with $d$ again chosen for smoothness. The behavior of $y_0(p, \lambda)$ for small $p$ is again taken into account explicitly.

In order to obtain the flux in this last case, we must find the inverse transform of the function $(\mu_0-p)^{-2}\exp[\beta_i/(\mu_m-p)^{\frac{1}{2}}]$. There are various ways in which this inversion can be accomplished, but the one which turned out to be most convenient was to expand the exponential and invert term by term. This yields a strongly converging sum:

$$\frac{1}{2\pi i}\int_{-i\infty}^{i\infty} dp e^{-p(x+d)}(\mu_0-p)^{-2}\exp[\beta_i/(\mu_m-p)^{\frac{1}{2}}] = e^{-\mu_m(x+d)} \sum_{n=0}^{\infty} \frac{\beta_i^n (x+d)^{\frac{1}{2}n+1}}{n!(\frac{1}{2}n+1)!} \times {}_1F_1[2; \tfrac{1}{2}n+2; -(\mu_0-\mu_m)(x+d)].$$

Some idea of the convergence can be gained from the fact that in the Pb problem it took about 15 terms to give an accurate answer for a penetration of 180 mean free paths. This is not so much work as it seems, because the alternate terms of the sum can be readily derived from each other. Using the formulas connecting the various ${}_1F_1$'s we made tabulations and graphs of the first 16 of these functions.

This expansion into a sum of ${}_1F_1$'s has physical significance. Since the constant $\beta$ in the exponent contains, asymptotically, the factor $k(\lambda, \lambda)=C$,[3] this is actually a sort of expansion in orders of scattering. Thus, the fact that 15 terms suffice at 180 mean free paths means that as few as 15 orders of scattering are important at this penetration!

# States of Light Nuclei from the *jj* Coupling Model*

D. KURATH
*Argonne National Laboratory, Chicago, Illinois*
(Received July 17, 1952)

The ordering of energy levels is presented for $1p$ shell nuclei in the *jj* coupling model. Comparison of the *jj* and *LS* model predictions with experiment are given for angular momenta and magnetic moments of the ground states as well as for the shape of the binding energy curve. No decisive favoring of either model is evident.

## INTRODUCTION

THE ordering of energy levels for nuclei in the $1p$ shell, which extends from $He^4$ to $O^{16}$, has been investigated by Feenberg and Wigner[1] and Feenberg and Phillips.[2] These authors performed a Hartree method calculation under the assumption that spin-orbit coupling forces are negligibly small. As a result the orbital angular momenta of the individual nucleons $\mathbf{l}_i$ are coupled to give the total angular momentum $\mathbf{L}$ of the nucleus as a good quantum number. The same holds for the individual spins $\mathbf{s}_i$ and the total spin $\mathbf{S}$, so the model is referred to as the *LS* coupling model.

In the present calculation the opposite assumption is made about spin-orbit forces, namely, that they are large. As a result the individual nucleon $\mathbf{l}$ and $\mathbf{s}$ are coupled to give a resultant angular momentum $\mathbf{j}$. The $\mathbf{j}_i$ are then coupled to give the total angular momentum $\mathbf{I}$ of the nucleus. A Hartree method calculation is carried out for this, the *jj* coupling model of the nucleus, and the results are presented in a form that facilitates comparison with the earlier calculation for the *LS* model.

## PROCEDURE

In both models each individual particle is assumed to move in a central potential well representing the average effect of the other nucleons. For the *jj* model there is assumed to be an additional term in the potential, proportional to $\mathbf{l}_i \cdot \mathbf{s}_i$, which couples the spin and orbital angular momentum for each individual particle to give it total angular momentum $j=l\pm\frac{1}{2}$. The sign of this single-particle coupling term is chosen to give the state $1p_{\frac{1}{2}}$ lower in energy than the state $1p_{\frac{3}{2}}$, and the contribution of spin-orbit coupling to the potential energy for a configuration of nucleons is then an additive term depending solely on the number of nucleons present in each shell. The $1p$ shell is thereby split into two parts, the region from $He^4$ to $C^{12}$ consisting of configurations of $1p_{\frac{1}{2}}$ nucleons, while from $C^{12}$ to $O^{16}$ the $1p_{\frac{3}{2}}$ nucleons are filled in.

The radial dependence of the individual particle function is chosen to be that of a three-dimensional harmonic oscillator, namely,

$$R_p = N_p r \exp[-(r/r_p)^2].$$

The attractive forces acting between nucleons are assumed to be charge independent and sufficiently greater than the Coulomb repulsion of the protons so that the isotopic spin $T$ is a good quantum number. In the Hartree approximation the nuclear wave function is represented by a function consisting of products of individual particle functions. These product functions are then made antisymmetric to the complete exchange of any two nucleons, and the further stipulation of total angular momentum $I$ and isotopic spin $T$ serves to determine the wave function uniquely for all but one nuclear configuration.[3] The splitting of the energy levels under various interactions is then calculated as a first-order perturbation using the wave functions determined in the above manner as zero-order functions.

The potential energy of interaction of the $1p$ shell nucleons, exclusive of the Coulomb contribution, is the term that determines the separation of the possible levels for each nucleus. Matrix elements are calculated for the four possible types of exchange[4] that represent the general interaction under restriction to a static central-force potential:

$$V_{12} = [1 \text{ or } P_{12} \text{ or } Q_{12} \text{ or } P_{12}Q_{12}]J(r_{12}), \qquad (1)$$

where $P_{12}$ and $Q_{12}$ are, respectively, space and spin exchange of particles 1 and 2. These types of exchange in the order in which they appear in Eq. (1) are customarily called Wigner, Majorana, Bartlett, and Heisenberg interactions. The range dependence used is the negative Gaussian $J(r_{12}) = A \exp[-(r_{12}/r_0)^2]$. The matrix elements are given in terms of the same integrals $L$ and $K$, which are defined in reference 1. In terms of the parameters present in $J(r_{12})$ and $R_p$ the integrals are

$$\begin{aligned} K &= \tfrac{1}{4}A(r_p/r_0)^4[1+(r_p/r_0)^2]^{-7/2}, \\ L/K &= 3+4(r_0/r_p)^4[1+(r_p/r_0)^2]. \end{aligned} \qquad (2)$$

The contributions to the potential energy due to $1p$ shell interactions are given for the various nuclei in Table I. For nuclei between $He^4$ and $C^{12}$ the table

* Work done in part at the University of Chicago, Chicago, Illinois.

[1] E. Feenberg and E. Wigner, Phys. Rev. **51**, 95 (1937).

[2] E. Feenberg and M. Phillips, Phys. Rev. **51**, 597 (1937).

[3] The two states of $I=2$, $T=0$ in $Be^8$ must be resolved by solution of a secular equation.

[4] E. Wigner and L. Eisenbud, Proc. Natl. Acad. Sci. **27**, 281 (1941).

TABLE I. Matrix elements and quantum numbers for the potential energy of interaction in the $1p$ shell.

| Nucleus | State $J$ | State $T$ | Matrix elements all have factor 1/9 $P_{12}$ | 1 | $P_{12}Q_{12}$ | $Q_{12}$ |
|---|---|---|---|---|---|---|
| $He^6$ | 2 | 1 | $-3L+15K$ | $9L-21K$ | $-9L+21K$ | $3L-15K$ |
| | 0 | 1 | $3L+21K$ | $9L+3K$ | $-9L-3K$ | $-3L-21K$ |
| $Li^8$ | 3 | 0 | $9L-9K$ | $9L-9K$ | $9L-9K$ | $9L-9K$ |
| | 2 | 1 | $-3L+15K$ | $9L-21K$ | $-9L+21K$ | $3L-15K$ |
| | 1 | 0 | $-L+21K$ | $9L-9K$ | $9L-9K$ | $-L+21K$ |
| | 0 | 1 | $3L+21K$ | $9L+3K$ | $-9L-3K$ | $-3L-21K$ |
| $Li^7$, $Be^7$ | 7/2 | 1/2 | $9L+9K$ | $27L-45K$ | $18K$ | $18L-36K$ |
| | 5/2 | 1/2 | $2L+30K$ | $27L-45K$ | $18K$ | $11L-15K$ |
| | 3/2 | 3/2 | $-6L+48K$ | $27L-51K$ | $-27L+51K$ | $6L-48K$ |
| | 3/2 | 1/2 | $12L+30K$ | $27L-15K$ | $-12K$ | $6L-30K$ |
| | 1/2 | 1/2 | $-6L+54K$ | $27L-45K$ | $18K$ | $3L+9K$ |
| $Li^9$ | 3 | 1 | $6L+54K$ | $54L-90K$ | $-18L+54K$ | $24L-72K$ |
| | 2 | 1 | $6L+66K$ | $54L-78K$ | $-18L+42K$ | $18L-66K$ |
| | 1 | 1 | $-4L+84K$ | $54L-90K$ | $-18L+54K$ | $14L-42K$ |
| | 0 | 2 | $-12L+96K$ | $54L-102K$ | $-84L+102K$ | $12L-96K$ |
| $Be^9$ | 4 | 0 | $14L+30K$ | $54L-90K$ | $36K$ | $32L-60K$ |
| | 3 | 1 | $6L+54K$ | $54L-90K$ | $-18L+54K$ | $24L-72K$ |
| | 2 | 1 | $6L+66K$ | $54L-78K$ | $-18L+42K$ | $18L-66K$ |
| | 2 | 0 | $72K$ | $54L-90K$ | $36K$ | $18L-18K$ |
| | 2 | 0 | $18L+54K$ | $54L-54K$ | $0$ | $18L-54K$ |
| | 1 | 1 | $-4L+84K$ | $54L-90K$ | $-18L+54K$ | $14L-42K$ |
| | 0 | 2 | $-12L+96K$ | $54L-102K$ | $-84L+102K$ | $12L-96K$ |
| | 0 | 0 | $24L+60K$ | $54L-30K$ | $-24K$ | $12L-90K$ |
| $Be^9$, $B^9$ | 7/2 | 1/2 | $15L+81K$ | $90L-144K$ | $-18L+72K$ | $42L-108K$ |
| | 5/2 | 1/2 | $8L+102K$ | $90L-144K$ | $-18L+72K$ | $35L-87K$ |
| | 3/2 | 3/2 | $120K$ | $90L-150K$ | $-45L+105K$ | $30L-120K$ |
| | 3/2 | 1/2 | $18L+102K$ | $90L-114K$ | $-18L+42K$ | $30L-102K$ |
| | 1/2 | 1/2 | $126K$ | $90L-144K$ | $-18L+72K$ | $27L-63K$ |
| $B^{10}$ | 3 | 0 | $21L+135K$ | $135L-207K$ | $-27L+99K$ | $57L-153K$ |
| | 2 | 1 | $9L+159K$ | $135L-219K$ | $-45L+129K$ | $51L-159K$ |
| | 1 | 0 | $11L+165K$ | $135L-207K$ | $-27L+99K$ | $47L-123K$ |
| | 0 | 1 | $15L+165K$ | $135L-195K$ | $-45L+105K$ | $45L-165K$ |
| $Be^{10}$, $C^{10}$ | 2 | 1 | $9L+159K$ | $135L-219K$ | $-45L+129K$ | $51L-159K$ |
| | 0 | 1 | $15L+165K$ | $135L-195K$ | $-45L+105K$ | $45L-165K$ |
| $B^{11}$, $C^{11}$ | 3/2 | 1/2 | $18L+216K$ | $189L-297K$ | $-54L+162K$ | $72L-216K$ |
| $C^{12}$ | 0 | 0 | $24L+288K$ | $252L-396K$ | $-72L+216K$ | $96L-288K$ |
| $B^{12}$, $N^{12}$ | 2 | 1 | $24L+273K$ | $252L-411K$ | $-90L+258K$ | $90L-282K$ |
| | 1 | 1 | $16L+297K$ | $252L-411K$ | $-90L+270K$ | $94L-282K$ |
| $C^{12}$, $N^{13}$ | 1/2 | 1/2 | $30L+360K$ | $324L-522K$ | $-108L+324K$ | $120L-360K$ |
| $N^{14}$ | 1 | 0 | $41L+432K$ | $405L-660K$ | $-135L+420K$ | $149L-432K$ |
| | 0 | 1 | $33L+456K$ | $405L-660K$ | $-153L+444K$ | $147L-456K$ |
| $O^{14}$, $C^{14}$ | 0 | 1 | $33L+456K$ | $405L-660K$ | $-153L+444K$ | $147L-456K$ |
| $O^{15}$, $N^{15}$ | 1/2 | 1/2 | $45L+540K$ | $495L-810K$ | $-180L+540K$ | $180L-540K$ |
| $O^{16}$ | 0 | 0 | $54L+648K$ | $594L-972K$ | $-216L+648K$ | $216L-648K$ |

includes only configurations of $p_{\frac{1}{2}}$ nucleons. Such configurations should provide the low-lying levels, but when the excitation energy is more than about 2 Mev, nuclei in this region may have excited levels given by configurations of mixed $p_{\frac{1}{2}}$ and $p_{\frac{3}{2}}$ nucleons. The mixed configurations are not included in the table. The table can be compared with that constructed for the *LS* coupling model;[2] the values $K=0.82$ Mev and $L=5.63$ Mev used in that calculation provide reasonable orders of magnitude for numerical evaluation.

### 1. Nuclear Spins and Magnetic Moments

The singlet-triplet potential difference of the deuteron, as determined from low energy neutron-proton scattering, indicates that the central potential interaction has a weight of about 0.80 for space dependence (1 and $P_{12}$) and about 0.20 for spin dependence ($Q_{12}$ and $P_{12}Q_{12}$). Table II gives the experimental nuclear spins as well as the spins of the ground states obtained from the two models with a potential whose space dependence is predominantly $P_{12}$ and with nuclear parameters such that $4<L/K<9$. The observed magnetic moments, together with calculated values for each case where a model gives the correct ground state spin, are also included. Even-even nuclei are not included since all results give a spin of zero for the ground states.

The models are both in agreement with the experimental spins for all the nuclei except $Li^6$, $B^{10}$, $B^{11}$, and $B^{12}$. The *LS* model gives the experimentally observed value of 1 for the spin of $Li^6$, and the magnetic moment calculated from this ground state[5] is much closer to the experimental moment than that obtained[6] from the *jj* model state of spin 1 ($\mu=0.63$ nm). However, for $B^{10}$ the situation is reversed and only the *jj* model gives the measured spin of 3 as well as a good value for the magnetic moment.[7] For $B^{11}$ the observed spin of $\frac{3}{2}$ is given correctly by the *jj* model, while the *LS* model predicts the state $^2P_{\frac{1}{2}}$. In order to have an allowed beta-decay from $B^{12}$ to the $C^{12}$ ground state (spin zero), the spin of $B^{12}$ should be 0 or 1. This can be obtained from the *LS* model, but the *jj* model gives a spin of 2 unless $L<3.5K$ which is not likely.

From the magnetic moments listed in Table II, it is evident that in cases where both models give the experimental spin, the *jj* model usually gives a better value[8] for the magnetic moment. For nuclei in this category the *jj* values are within 10 percent of the experimental values. The cases in which the spin predictions disagree include the previously discussed $Li^6$ and $B^{10}$ plus $B^{11}$. In $B^{11}$ the spin is given correctly by the *jj* model, but the calculated magnetic moment is considerably larger

TABLE II. Ground-state nuclear spins and magnetic moments.

| Nucleus | Nuclear spins Exp | *LS* | *jj* | Magnetic moments (Nuclear magnetons) Exp | *LS*[a] | *jj*[b] |
|---|---|---|---|---|---|---|
| $Li^6$ | 1 | 1 | 3 | 0.822 | 0.88 | ··· |
| $Li^7$ | 3/2 | 3/2 | 3/2 | 3.257 | 3.10 | 3.03 |
| $Li^8$ | (2)[c] | 2 | 2 | | | |
| $Be^9$ | 3/2 | 3/2 | 3/2 | −1.178 | −1.56 | −1.15 |
| $B^{10}$ | 3 | 1 | 3 | 1.801 | ··· | 1.88 |
| $B^{11}$ | 3/2 | 1/2 | 3/2 | 2.689 | ··· | 3.79 |
| $B^{12}$ | (1 or 0)[c] | 1 or 0 | 2 | | | |
| $C^{13}$ | 1/2 | 1/2 | 1/2 | 0.702 | 1.10 | 0.64 |
| $N^{14}$ | 1 | 1 | 1 | 0.404 | 0.88 | 0.37 |
| $N^{15}$ | 1/2 | 1/2 | 1/2 | −0.283 | −0.26 | −0.26 |

[a] Values of reference 5 corrected for the present values of $\mu_p=2.79$ and $\mu_n=-1.91$ nuclear magnetons.
[b] E. Feenberg, Phys. Rev. **76**, 1275 (1949); M. Mizushima and M. Umezawa, Phys. Rev. **85**, 37 (1952); these contain most of the *jj* calculations.
[c] Inferred from beta-decay.

[5] M. E. Rose and H. A. Bethe, Phys. Rev. **51**, 205 and 993 (1937).
[6] M. G. Mayer, Phys. Rev. **78**, 16 (1950).
[7] Feenberg and Phillips have suggested (see reference 2) that the ground state of the *LS* model is a $^3D$ due to repulsion of two low-lying $^3D$ states. However, since spin-orbit coupling does not split the $^3D_{3,2,1}$ states, it is not evident that the ground state of $B^{10}$ should be 3.
[8] The *LS* value for $N^{14}$ in Table II is for the $^3S_1$ ground state. It has been suggested in reference 2 that the ground state is really $^3D_1$, which has a magnetic moment of 0.31 nm.

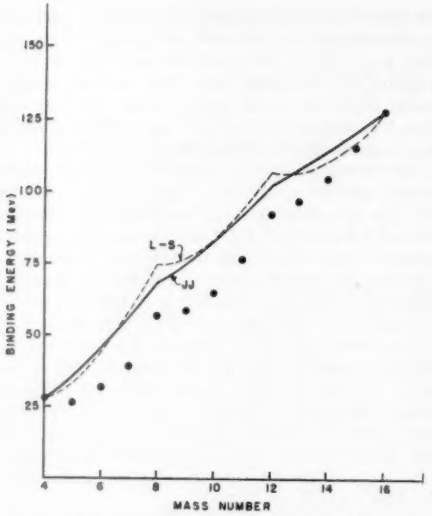


FIG. 1. Binding energy as function of mass number for the $1p$ shell. The curves for the $LS$ model and the $jj$ model are given under the assumption that the integrals $L$ and $K$ are independent of mass number. Circles are experimental points.

than observed. The $LS$ state, $^2P_{\frac{1}{2}}$, gives a moment of 3.44 nm which is somewhat smaller than the $jj$ value but still considerably larger than experiment, which leaves $B^{11}$ as the only nucleus for which neither model comes close to the observed moment.

The general conclusion from comparison of spins and magnetic moments with experiment is that both models give a considerable amount of agreement. However, for the points wherein they disagree neither model is favored consistently by the experimental results.

## 2. Energy Comparisons

Futher tests for the models are provided by the experimental isobar differences and by the structure of the experimental binding energy curve for stable nuclei. The points for comparison of the models are three:

(A) The isobar differences for mirror nuclei, which depend only on a Coulomb term, and are thus independent of the interaction integrals $L$ and $K$, but do depend on the parameter $r_p$ in the oscillator wave function.

(B) The four-shell structure in the binding energy curve, whose features depend on the type of interaction among the $p$-shell nucleons and also depend on the magnitude of the integrals $L$ and $K$.

(C) The isobar differences between odd-odd and even-even nuclei, which involve the interaction integrals $L$ and $K$ as well as a Coulomb term.

### (A) *Mirror Isobars*

For these isobars the difference in binding energy is obtained from the electrostatic repulsion of $p$-shell protons by the $s$-shell protons plus the matrix elements for Coulomb interaction of $p$-shell protons with each other. Only the latter contribution is dissimilar for the $jj$ model and $LS$ model calculations. The matrix elements from the $LS$ model are given in Table IV of reference 2 in terms of the Coulomb integrals $L_c$ and $K_c$. However, since[1] $L_c=49/3\ K_c$, the value is determined largely by the $L_c$ term which is the same for all isotopes of a given element. Therefore, the matrix elements agree within a few percent for the ground states of all nuclei having the same $Z$. In terms of the value for the $Be^7$ ground state in $LS$ coupling $C$, defined as $C=L_c+2/3K_c=17K_c$, the matrix elements are given in Table III for the two models. It is apparent that the Coulomb matrix elements are nearly identical for the two models, so that for the mirror isobars the calculated binding energy differences are substantially the same. The constants used in the $LS$ calculation[1,2] give $C=0.47$ Mev and for the interaction of a $p$-shell proton with the two $s$-shell protons, $C_{sp}=0.84$ Mev. These numbers result in theoretical values for the nine mirrors that are about 20 percent to 30 percent lower than the experimental values. This point will be discussed in Sec. C.

### *B. Binding Energy Curve*

The total binding energy as calculated with Hartree wave functions has a very unsatisfactory magnitude, a failing that is attributed to the limitations of such product-form wave functions. However, the potential energy of interaction within the $p$-shell, including the Coulomb term, superimposes a structure on the general trend of the binding energy curve. This can be compared for the two models with the structure evident in the experimental curve.

The experimental binding energy curve of the most tightly bound nuclei at each mass number has maxima at $He^4$, $Be^8$, $C^{12}$, and $O^{16}$ with pronounced dips between the peaks which become shallower with increasing mass number. Of the four static central-force interactions in Table I, only the $P_{12}$ (Majorana) type presents a comparable structure.[9] Since this is true for both models,

TABLE III. Coulomb matrix elements within the $p$-shell.

| Element | $LS$ model | $jj$ model |
|---|---|---|
| Be | $C$ | $0.95C$ |
| B | $2.60C$ | $2.55C$ |
| C | $5.25C$ | $5.10C$ |
| N | $8.45C$ | $8.45C$ |
| O | $12.65C$ | $12.65C$ |

[9] Wigner interaction does have the type of four-structure desired in the limit of vanishing range of interaction where Majorana and Wigner interactions become identical. However, for the ranges expected physically the Wigner four-structure is very slight.

the Majorana term should be dominant in the interaction. The degree to which the four-structure is accented depends on the exact interaction used, and also it depends quite strongly on the ratio $L/K$. The $LS$ model contains the possibility of having very pronounced four-structure, but the $jj$ model suppresses this feature to a large extent. While there is a peak at $A=8$ in the $jj$ model, the peak at $A=12$ is due almost wholely to the spin-orbit coupling term which is assumed to contribute about $+2$ Mev of binding energy for every $p_{\frac{3}{2}}$ nucleon and $-4$ Mev for every $p_{\frac{1}{2}}$ nucleon, the $p_{\frac{1}{2}}$ shell coming above $C^{12}$. As an example of the comparative amount of four-structure available from the models, the calculated binding energies, fitted at $He^4$ and $O^{16}$ by adding a linear amount of binding as in the previous $LS$ calculation, are given in Fig. 1. The particular interaction is $V_{12}=(0.8\,P_{12}+0.2\,P_{12}Q_{12})J(r_{12})$, with the numerical values $L=5.63$ Mev and $K=0.82$ Mev. The dips between peaks of binding energy are much deeper for the $LS$ model than for the $jj$ model. However, they tend to become more pronounced with increasing $A$ in the $LS$ model which is contrary to the experimental result. This behavior is probably due to the fact that $L$ and $K$ were assumed constant throughout the $p$ shell. From their dependence on the oscillator parameter $r_p$, which is related to the size of the nucleus, one would expect them to decrease considerably between $A=4$ and 16, giving decreased four-structure at larger $A$. Assuming that $r_p$ is proportional to $A^{\frac{1}{3}}$ and that $L=5.63$ Mev and $K=0.82$ Mev at $He^4$ leads one to the curves in Fig. 2 which have a behavior much more similar to the experimental one than those of Fig. 1.

Quantitative comparisons are on speculative ground, owing to lack of knowledge of the nuclear interaction, the uncertainty in the nuclear parameters, and the use of Hartree wave functions. However, the conclusion can be drawn that $LS$ coupling is indicated by the shape of the experimental binding energy curve, certainly for the lower half of the shell. While the $jj$ model could give reasonable agreement for the heavier nuclei by using a larger $L/K$ ratio, it would then fit the light nuclei rather poorly.

The source of the four-structure in the $LS$ model has been pointed out to be the symmetry structure of the spatial part of the wave functions. Maximum symmetry and maximum binding energy for Majorana interaction occur simultaneously whenever a group of four is completed. The suppression of the four-structure by the $jj$ model is due to the fact that the spin-orbit coupling mixes states of different spatial symmetry properties and thus destroys the structure to a large extent. Hence for the light nuclei, $jj$ coupling does not seem likely.

### C. *Even-Even and Odd-Odd Isobars*

The differences in binding energy between even-even and odd-odd isobars involve a Coulomb term plus a term involving $L$ and $K$. These isobars occur at mass numbers 6, 8, 10, 12, and 14 which involve most of the points where one or the other model gives a spin differing from the observed value. In view of the uncertainties in the interaction and nuclear constants it does not seem feasible to attempt a quantitative comparison. In the earlier $LS$ calculation, a fair agreement with four-structure and these isobar differences was obtained at the expense of using nuclear parameters that give differences for mirror isobars lying from 20 percent to 30 percent lower than observation, as mentioned before. The use of these nuclear parameters for the cases where the spin is obtained correctly in the $jj$ model gives differences between even-even and odd-odd isobars that have the same order of magnitude as the $LS$ results, although the agreement with experimental values is not as good. However, the uncertainties mentioned above plus the fact that the Coulomb term cannot be simultaneously satisfied with the parameters used make quantitative comparison for this group of isobars a rather dubious test.

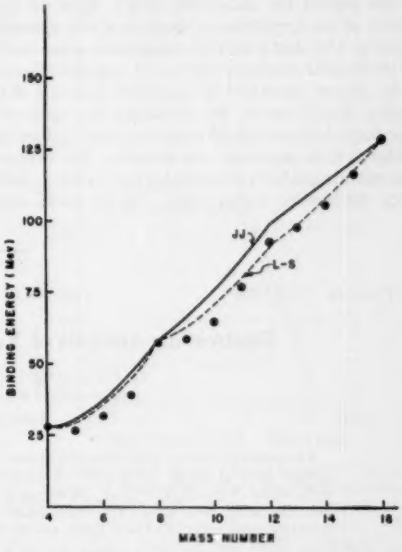


FIG. 2. Binding energy as functions of mass number $A$ under the assumption that the oscillator parameter $r_p$ is proportional to $A^{\frac{1}{3}}$. Circles are experimental points.

## CONCLUSIONS

In so far as the Hartree method is used in both models, it would not be expected that the quantitative separation of levels is given correctly. However, the approximation should be good enough to give the order of levels and the relative binding for neighboring nuclei.

In this respect the calculation should serve for comparison of the hypotheses of weak or strong spin-orbit coupling. The chief points for comparison of the models are the angular momenta (spins) and magnetic moments of the ground states and the four-shell structure of the binding energy curve. In comparing the spins with experiment both models give some incorrect values, and neither is to be preferred over the other. The magnetic moments are generally somewhat better for the $jj$ model. From the binding energy curve, the $LS$ model seems preferable since it contains a pronounced four-structure. It is possible that there is a transition from $LS$ coupling in the early part of the shell to $jj$ coupling in the latter part, which would remove most of the spin difficulties and not affect the binding energies seriously. The present influx of experimental data on energy levels of the $1p$-shell nuclei should help greatly to clarify the problem.

The author wishes to express his appreciation to Professor M. G. Mayer for discussion and guidance in the course of this work.

PHYSICAL REVIEW VOLUME 88, NUMBER 4 NOVEMBER 15, 1952

# Electrostatic Analysis of Nuclear Reaction Energies. II*

D. S. Craig,† D. J. Donahue, and K. W. Jones
*University of Wisconsin, Madison, Wisconsin*

(Received July 29, 1952)

Electrostatic analysis of incident and product particle energies has been used to measure the following ground state $Q$-values: $O^{18}(d,\alpha)N^{14}$ (3.113±0.0035 Mev), $B^{10}(p,He^3)Be^8$ (−0.536±0.003 Mev), and $B^{10}(p,\alpha)Be^7$ (1.147±0.0025 Mev). The energy of the lowest level in $B^{10}$ has been determined to be 719±1.6 kev; that of $Be^7$ to be 429±3 kev. Approximate cross sections are given for the above reactions and upper limits for $O^{18}(d,\alpha)N^{14*}$ (2.3-Mev level), and for $B^{10}(p,p')B^{10*}$ (2.1- and 1.7-Mev levels).

## I. INTRODUCTION

FURTHER accurate measurements of nuclear $Q$-values have been made using the equipment and procedure described in earlier articles.[1,2] It will suffice here to say that a cylindrical electrostatic analyzer[3] was used for measuring the energy of the bombarding particles ($T_1$), and a spherical electrostatic analyzer[1] for measuring the energy of the product particles ($T_2$). A redetermination of the angle of observation with respect to the incoming beam, necessitated by a realignment of the spherical analyzer collimating apertures, was made using the measured positions of the apertures as described previously,[1] and by scattering deuterons from $Li^6$. The mean angle was found to be 134°33′±3′.

The nichrome resistor stack used in our earlier measurements was replaced with a new stack consisting of sixty one-megohm Shallcross Evenohm resistors, Type BX116E, whose temperature coefficient is less than 0.002 percent/°C. These were mounted with corona shields inside Lucite cylinders in which dried air was circulated by a blower. Several low voltage taps were provided to facilitate regulating and measuring the voltage over a wide range of values.

Several appendices are included with this paper. The first one consists of errata to paper I.[2] The second displays the form of the relativistic correction terms used in I and in II. The third appendix is concerned with the masses used in the calculations.

## II. RESULTS AND DISCUSSION

### $O^{18}(d,\alpha)N^{14}$

This $Q$-value is an important link in the group of reactions used by Li *et al.*,[4] in determining the masses of the light nuclei, as it is the only convenient connection to $O^{16}$, the standard of atomic masses.

Two determinations of this $Q$-value were made. The first was made using a target of 0.001-inch aluminum foil which had been heated in air to form the oxide. Because of the thickness of the aluminum it was impossible to scatter deuterons from the target in order to check the amount of contamination and the amount of oxygen. The observed counting rates of the doubly ionized alpha-particles are shown in Fig. 1. For a second run a target of beryllium oxide was prepared by heating in air a thick tantalum foil onto which had been evaporated beryllium. Since these targets were used immediately after putting them into the analyzer, it is reasonable to assume that the contamination on them is negligible. The rate at which carbon is deposited on a 1000A Ni foil was checked during the present measurements, and over a six-and-a-half-hour period of bombardment with a beam of the same magnitude as that used

* Supported by the Wisconsin Alumni Research Foundation and the AEC.

† Now with Atomic Energy of Canada, Ltd., Chalk River, Ontario, Canada.

[1] Browne, Craig, and Williamson, Rev. Sci. Instr. **22**, 952 (1951).

[2] Williamson, Browne, Craig, and Donahue, Phys. Rev. **84**, 731 (1951). This article will be referred to as I.

[3] Warren, Powell, and Herb, Rev. Sci. Instr. **18**, 559 (1947).

[4] Li, Whaling, Fowler, and Lauritsen, Phys. Rev. **83**, 512 (1951).

throughout this work, 0.2 microamperes, less than 0.01-kev thickness of carbon for a 1-Mev proton was deposited. This slow rate of build-up may be attributed to the fact that the targets were maintained at about 200°C, and that a triple-collision, liquid-air-cooled baffle was kept over the diffusion pump. The results for the two targets are as follows:

| Target | Bombarding voltage ($T_1$) in Mev | $Q$ (Mev) |
|---|---|---|
| $Al_2O_3$ | 0.893 | 3.1125±0.0035 |
| BeO | 0.847 | 3.1133±0.0035 |
| | Average value: | 3.113 ±0.0035 |

Table I displays the component errors determining the uncertainty in the values quoted above. The differential cross section at 134°33′ is of the order of $9\times10^{-27}$ cm² per steradian.

The individual values are in agreement with the values of 3.112±0.006 Mev,[5] and 3.119±0.005 Mev,[4] as determined at the Massachusetts Institute of Technology and the California Institute of Technology, respectively.

### $O^{16}(d,\alpha)N^{14*}$(2.3-Mev level)

Alpha-particles going to a level in $N^{14}$ with an excitation energy between 2.0 and 2.8 Mev were undetected when using a deuteron energy of 2.877 Mev. Assuming a target of $Al_2O_3$, the differential cross section must be less than $1.4\times10^{-27}$ cm²/steradian; otherwise, this level would have been detected. This result is in agreement with work of Ashmore and Raffle,[6] and Burrows *et al.*,[7] who did not see any alpha-particles corresponding to this level when $O^{16}$ was bombarded with 6.8- and 8-Mev deuterons, respectively.‡

TABLE I. Tabulation of errors for the $O^{16}(d,\alpha)N^{14}$ reaction energy. $Q=3.113\pm0.0035$, $T_1$ (deuteron energy) $=0.8933$ Mev, $T_2$ (alpha energy) $=2.6729$ Mev.

| Source of error | Magnitude | Error in $Q$ Mev |
|---|---|---|
| Relative calibration of the analyzers | ±0.03 percent of $T_1$ | 0.0002 |
| | ±0.03 percent of $T_2$ | 0.0011 |
| Angle of observation | ±3′ | 0.0004 |
| Location of half-value of alpha-edge | ±0.0006 Mev | 0.0008 |
| Absolute calibration of $Li^7(p,n)Be^7$ threshold | ±0.1 percent of $Q$ | 0.0031 |
| Limit of error of measurement ($dQ_m$)[a] | | 0.0025 |
| Total limit of error[a] | | 0.0056 |
| Total probable error[a] | | 0.0035 |

[a] Notation as in reference 2: "limits of error" $=\Sigma_i|\epsilon_i|$, and probable error $=(\Sigma_i\epsilon_i^2)^{\frac{1}{2}}$.

[5] Straight, Van Patter, Buechner, and Sperduto, Phys. Rev. **81**, 747 (1951).

[6] A. Ashmore and J. F. Raffle, Proc. Phys. Soc. (London) **A64**, 754 (1951).

[7] Burrows, Powell, and Rotblatt, Proc. Roy. Soc. (London) **A209**, 478 (1951).

‡ Recent work by Van de Graaff, Sperduto, Buechner, and Enge (Phys. Rev. **86**, 966 (1952)) using 2-Mev deuterons on $O^{16}$ also gave no indication of alpha-particles corresponding to $N^{14}$ being left in an excited state.

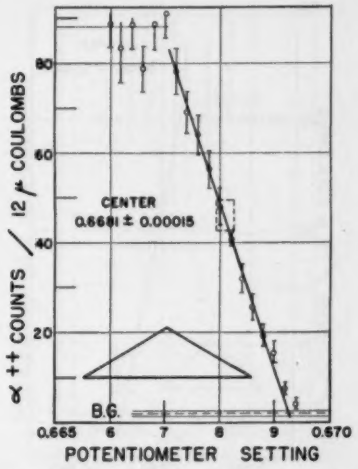


FIG. 1. Doubly ionized alphas from $O^{16}(d,\alpha)N^{14}$. The bombarding energy is 0.893 Mev. The potentiometer setting is approximately ½ alpha-energy.

The low upper limit on this cross section is compatible with isotopic spin selection rules imposed by the assumption of charge independence of nuclear forces. Adair[8] discusses this subject more fully in a forthcoming publication. It should be pointed out, however, that the spins of the ground state and the 2.3-Mev level are expected to differ by one unit of angular momentum; thus even from the requirement of conservation of spin and parity the yield to this level would be expected to be less than to the ground state.

### $B^{10}$ Reactions

The same $B^{10}$ target was used for each of the following reactions. It consisted of a boron layer, approximately 4 kev thick for protons of 0.94 Mev, evaporated onto a 1000A Ni backing. The exact composition of this target is uncertain, but scattered protons indicated that it contained considerable oxygen. The nitrogen content was not checked; however, our experience with other boron targets indicates that some nitrogen may be present. Since the composition of the target is so uncertain, the differential cross sections given are only an indication of the order of magnitude, assuming $B_2O_3$ targets. The boron, obtained from the AEC, was approximately 96 percent $B^{10}$. It was possible to check for carbon build-up by elastically scattering protons. Since this target was in the analyzer for many days, carbon build-up occurred, necessitating a small correction to the $Q$-values of all $B^{10}$ reactions.

[8] R. K. Adair, Phys. Rev. **87**, 1041 (1952).

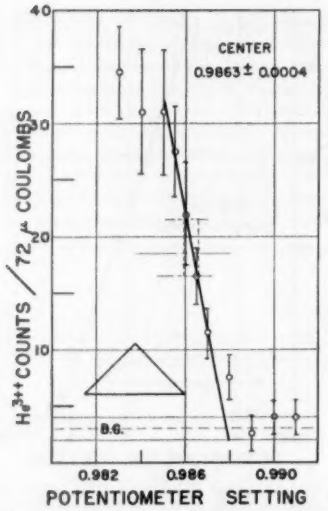


FIG. 2. Doubly ionized $He^3$ from $B^{10}(p, He^3)Be^8$. The bombarding energy is 3.421 Mev. The potentiometer setting is approximately $\frac{1}{4}$ $He^3$ energy.

### $B^{10}(p,He^3)Be^8$

Edges were taken using protons of 3.421 and 3.216 Mev. The observed counting rates of the doubly ionized $He^3$ are shown in Fig. 2, for 3.421-Mev protons. Since a change in bombarding energy ($T_1$) will cause a change in the energy of the reaction product ($T_3$), with the amount dependent on the particular reaction, the agreement in the $Q$-values, $-0.536\pm0.003$ and $-0.535\pm0.004$ Mev, is a check that the particles being measured were from this reaction. A contamination correction of $1\pm0.5$ kev has been applied to $T_3$. The differential cross section at 134°33 is of the order of $1\times10^{-27}$ cm²/steradian. The $Q$-value is $-0.536\pm0.003$ Mev probable error; $\pm0.004$ Mev limit of error.

There are no other observations of this reaction. However, its $Q$ value can be calculated from other reaction cycles. For example, a value of $-0.536\pm0.008$ Mev is obtained from the following cycle[9]: $Li^7(p,n)Be^7$, $Be^9(d,\alpha)Li^7$, $Be^9(p,d)Be^8$, $D(d,p)T$, $T(\beta^-)He^3$, $H^1-n$, and $B^{10}(p,\alpha)Be^7$.

### $B^{10}(p,\alpha)Be^7$

Using a bombarding energy of 3.333 Mev a $Q$-value of $1.147\pm0.0025$ Mev probable error, $\pm0.0044$ Mev limit of error, was found. A contamination correction of $0.6\pm0.3$ kev has been included. This value is in agreement with the values of $1.148\pm0.006$ (California Institute of Technology),[10] $1.152\pm0.004$ (MIT),[11] and $1.147\pm0.010$ (Cambridge).[12] The differential cross section is of the order of $2\times10^{-28}$ cm²/steradian.

### $B^{10}(p,\alpha)Be^{7*}$

Three determinations of this $Q$-value were made and are listed in Table II. The first two have a carbon correction of $0.6\pm0.15$ kev applied to $T_3$ and the latter $0.5\pm0.15$ kev. The differential cross section is of the order of $1\times10^{-28}$ cm²/steradian.

On subtracting the average of these $Q$-values (0.718 Mev), from that for the ground state, a value of $429\pm3$ kev is obtained for the first level in $Be^7$. This value is in agreement with the values summarized by Brown *et al.*,[10] and the more recent measurements of Johnson and Barschall[13] ($431\pm5$ kev), but does not quite overlap that of Willard and Preston[14] ($434\pm1$ kev with no assigned error due to calibration).

### $B^{10}(p,p')B^{10*}$(719-kev level)

The energy of the lowest detected level in $B^{10}$ was measured by the inelastic scattering of protons to be $719\pm1.6$ kev probable error, $\pm3$ kev limit of error. The observed counting rates of the protons are shown in Fig. 3. The bombarding protons had an energy of 2.191 Mev, at which energy the differential cross section was of the order of $3\times10^{-27}$ cm²/steradian.

The value of $719\pm1.6$ kev agrees with the California Institute of Technology values of $716.6\pm1$ kev[15] and $718\pm5$ kev,[16] obtained by measuring the energy of the gamma-rays from $Be^9$ $(d,n)B^{10*}$ and $B^{10}(p,p')B^{10*}$, respectively. Rasmussen *et al.*, applied a Doppler correction to their measured value of 716.6 kev, yielding a final value of $713\pm1.5$ kev. However, some doubt existed as to the necessity of this correction,[17] and our value indicates that no correction is necessary. Therefore, the lifetime for gamma-emission must be longer than the time required to stop the recoiling $B^{10}$ nucleus ($\sim10^{-13}$ sec).

TABLE II.

| $T_1$ Mev | $Q$ Mev | $dQ_m$ Mev | $dQ$ limit Mev | $dQ$ probable Mev |
|---|---|---|---|---|
| 3.333 | 0.717 | 0.0036 | 0.0043 | 0.0026 |
| 3.333 | 0.717 | 0.0036 | 0.0043 | 0.0026 |
| 1.460 | 0.720 | 0.002 | 0.003 | 0.002 |

[9] Suggested by Dr. D. M. Van Patter in a private communication.

[10] Brown, Snyder, Fowler, and Lauritsen, Phys. Rev. **82**, 159 (1951).
[11] Van Patter, Sperduto, Strait, and Buechner, Phys. Rev. **79**, 900 (1950).
[12] W. E. Burcham and J. M. Freeman, Phil. Mag. **41**, 337 (1950).
[13] C. H. Johnson and H. H. Barschall, Phys. Rev. **81**, 317 (1951).
[14] H. B. Willard and W. M. Preston, Phys. Rev. **81**, 480 (1951).
[15] Rasmussen, Hornyak, and Lauritsen, Phys. Rev. **76**, 581 (1949).
[16] R. B. Day and T. Huus, Phys. Rev. **85**, 761 (1952).
[17] V. K. Rasmussen, Ph.D. thesis, California Institute of Technology (1950) (unpublished).

### Other Levels in $B^{10}$

Despite an extensive search at several bombarding energies, ranging up to 4.2 Mev, no inelastically scattered protons from higher levels in $B^{10}$ were observed. Therefore, at these bombarding energies, an upper limit of about $3\times10^{-28}$ cm² per steradian for other inelastic scattering cross sections is indicated.

The authors wish to thank Professor H. T. Richards for suggesting this work and for his subsequent advice. Messrs. M. T. McEllistrem and R. E. Benenson helped in part of the experimental work. Dr. Fay Ajzenberg provided the $Li^6$ target.

## APPENDIX

### A. Errata to I [Phys. Rev. 84, 731 (1951)][2]

1. Fig. 2: The ordinates should read $P$ counts per 0.2 microcoulomb, instead of per 0.1 microcoulomb.

2. Recalculation of the contamination corrections to the $Q$-values for the $Be^9(p,\alpha)Li^6$ reaction, when the $Li^{6++}$ and $Li^{6+++}$ particles were observed, gives values of 2.126 and 2.127 Mev, respectively, in line with the other measurements.

### B. Relativistic Correction Terms

Dr. R. M. Williamson (Ph.D. thesis, University of Wisconsin, unpublished) has expressed the energy of the recoil particle in terms of the classical expression plus a correction term which is obtained when the relativistic expression for momentum is used,

$$\text{Recoil energy } (T_3)=1/M_3[M_1T_1+M_2T_2 -2(M_1M_2T_1T_2)^{\frac{1}{2}}\cos\theta]+V,$$

where the relativistic correction $V$ is given by

$$V=\frac{1}{2E_3}\left[T_1^2+T_2^2-T_3^2-\cos\theta(E_1E_2T_1T_2)^{\frac{1}{2}}\left(\frac{T_1}{E_1}+\frac{T_2}{E_2}\right)\right],$$

correct to the first power of $T/E$.

The energy of particles of mass $M_1$ elastically scattered from target nuclei of mass $M_0$ through an angle $\theta$ is given by

$$\frac{T_2}{T_1}=\left(\frac{M_1}{M_1+M_0}\cos\theta+\left\{\frac{M_0-M_1}{M_0+M_1}+\left(\frac{M_1}{M_1+M_0}\right)^2\cos^2\theta-L\right\}^{\frac{1}{2}}\right)^2,$$

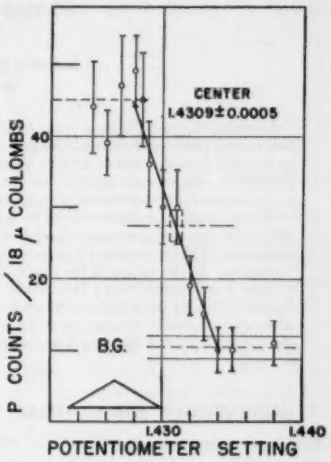


FIG. 3. Protons from $B^{10}(p,p')B^{10*}$ (719-kev level). The bombarding energy is 2.191 Mev. The potentiometer setting is approximately ½ proton energy.

where

$$L=\frac{T_2'}{E_0}-\frac{\cos\theta}{2E_0}\left(\frac{T_2'}{T_1}\right)^{\frac{1}{2}}(T_1+T_2')$$

is the relativistic correction calculated to the first power of $T/E$.

Subscripts 0, 1, 2, and 3 refer to the target, bombarding, measured product, and recoil particles, respectively; $T$ is the energy of the particle; $M$ is the mass; $E=Mc^2$; $\theta$ is the angle between incident and product particles; and $T_2'$ is the energy obtained using the formula with no relativistic correction.

### C. Masses Used

Nuclear masses were used for $M_1$ and $M_2$. The mass used for the recoil particle $M_3$ was its nuclear mass plus the mass of the electrons carried along with it. The number of electrons attached to the recoiling nucleus was estimated by comparing the orbital velocities of the electrons with the linear velocity of the nucleus, as is discussed by Bohr in "The Penetration of Atomic Particles Through Matter".[18]

The error introduced in the $Q$-values by neglecting the electrons accompanying the recoil particle reactions would be less than 0.5 kev.

[18] N. Bohr, Kgl. Danske Videnskab. Selskab, Mat.-fys. Medd. 18, No. 8 (1948).

# Photon-Induced Reactions*

D. C. PEASLEE
*Columbia University, New York, New York*
(Received July 11, 1952)

A detailed derivation is given of the Breit-Wigner formula for the case where one particle is a photon. The half-width $\Gamma_\gamma$ is found to have all the qualitative properties of a heavy particle half-width: It is proportional to the level spacing $D$ and to $XP_l(X)$ where $X=\kappa R$ and $P_l$ is the penetration probability for an uncharged particle. $\Gamma_\gamma$ also depends explicitly on the details of the many-particle structure of the compound state, so that single-particle estimates of $\Gamma_\gamma$ appear to be of limited applicability.

The formulas are applied to recent $\gamma-n$ measurements on $O^{16}$, $N^{14}$, and $F^{19}$. The breaks in the $O^{16}$ excitation curve are due to resonances in $O^{16}$, except for the threshold, which presumably does not represent a resonance. At higher energies the giant $\gamma-n$ electric dipole resonances are interpreted as indicating a certain "coherence" in the motion of the compound state, classically represented as countercurrent neutrons and protons. It is suggested that a flat shoulder in the excitation curves below the giant resonance may represent incoherent electric dipole excitation rather than coherent magnetic dipole and electric quadrupole excitation. The matrix elements necessary to fit the measured magnitudes are surprisingly large, which suggests that the one-particle wave functions have quite similar shapes in the ground state and in highly excited states.

## I. INTRODUCTION AND SUMMARY

RECENT precision measurements[1,2] of $\gamma-n$ reactions on $O^{16}$ have shown a number of interesting features. In the region a Mev or so above threshold, sharp breaks are observed in the activation curve, which are attributed to individual resonance levels. The lowest such "level" corresponds to the threshold energy. In the region about 1 to 4 Mev above threshold, the average cross section shows a tendency to level off at about 1 mb or slightly less. At higher energies the cross section increases rapidly to a maximum of about 12 mb at a gamma-energy of $E=24$ Mev, in the fashion of the well-known "giant resonances."

It is the object of the present note to discuss these features in terms of the compound nucleus model of nuclear reactions. Although the discussion is directed to the case of $\gamma-n$ on $O^{16}$, it should have general validity. In a simple treatment of nuclear reactions[3] the partial half-width $\Gamma_\gamma$ for photons is generally introduced by analogy rather than by strict derivation. The derivation of an explicit formula for $\Gamma_\gamma$ is attempted here, using a perturbation treatment for the initial photon absorption and a boundary-fitting approach where necessary for the emitted heavy particle. The magnitude of $\Gamma_\gamma$ depends essentially on the structure of the excited level in the compound nucleus; this dependence is sufficiently complex to suggest that one-particle models for estimating $\Gamma_\gamma$ can apply only to rather special cases.

The observed resonances in $O^{16}$ $\gamma-n$ then appear to correspond to levels of the excited compound nucleus $O^{16*}$, except that the cutoff at the threshold energy probably does not in general indicate a resonance level at this energy. To obtain the large maximum of the giant resonance at 24 Mev, (1) electric dipole matrix elements are required in which the overlap between initial and final states is almost complete, and (2) the excited compound state must have a particular structure that corresponds to coherent excitation of the neutrons and protons into counter current oscillation. In accordance with this picture of the giant resonance, the flat cross section between threshold and the resonance seems perhaps more likely to arise from incoherent electric dipole excitation than from magnetic dipole or electric quadrupole excitation, which would necessarily be coherent to achieve the observed magnitude.

## II. FORMULATION

Only excitation of single nucleons is considered. The coherent excitation of groups like the deuteron, triton, or $\alpha$-particle can be obtained by specializations of the resulting expression. Two assumptions are involved: (1) the $\gamma$-interaction is a weak, one-particle interaction; (2) the ground state can be described, in accordance with shell model ideas, as a single product of independent particle wave functions. Assumption (1) is essential to the perturbation treatment of the transition, while (2) is not so essential but simplifies the discussion and may be fairly realistic for our purposes.

According to (2), the wave function of the ground state is written

$$\Phi=\prod_{j=1}^{A}\varphi_j(r_j), \tag{1a}$$

where each $\varphi_j$ is normalized to unit integral over volume. The wave function of the excited state, written in corresponding fashion, is

$$\Psi=\sum_c f_c\psi_c(r_i)\prod_{j\neq i}^{A}\varphi_c(r_c), \tag{1b}$$

where the sum over $c$ includes all possible exit channels

* This work was performed under the research program of the AEC.
[1] Johns, Horsley, Haslam, and Quinton, Phys. Rev. **84**, 856 (1951).
[2] Haslam, Katz, Horsley, Cameron, and Montalbetti, Phys. Rev. **87**, 196 (1952).
[3] Feshbach, Peaslee, and Weisskopf, Phys. Rev. **71**, 145 (1947).

(combinations of spins and orbital momenta) for the particle $i$ consistent with angular momentum and parity conservation. Photoelectric matrix elements between $\Phi$ and $\Psi$ exist only if they differ by at most one single-particle wave function. This makes it unnecessary to antisymmetrize Eqs. (1), which would involve exchange of pairs of single-particle functions. In (1b) the $\psi_e$ are normalized per unit energy, and the normalization of $\Psi$ as a whole requires that

$$\sum_e |f_e|^2 = 1. \tag{2}$$

There are three types of single-particle matrix elements to consider, according as $\psi_e$ represents (1) a free particle of the type whose cross section is under consideration; (2) a free particle, not of the type under consideration; (3) a bound particle. The "type under consideration" may be limited specifically as to channel or more generally to a sum over neutron (proton) channels. It is possible for $\psi_e(\mathbf{r}_e)$ to represent a bound particle in case $\varphi_i$ corresponds to an orbit near the bottom of the Fermi well, even though the $\gamma$-energy exceeds the minimum threshold for particle emission.

Consider the cross section for $f_e = \delta_{eC}$, with $C$ a type (1) orbit:

$$\sigma_{\gamma C} = \pi\lambda^2 S_0 |M_C|^2, \tag{3}$$

$$M_C = \{8\kappa^3 k\kappa_0 \alpha S_{l\gamma}(S_C/S_0)\}^{\frac{1}{2}} \int_0^\infty U_C^* r^m U_\gamma r^2 dr.$$

Here $4\pi S_C$ is a statistical factor, and the standard factor for taking a system from initial spin $I$ to final spin $J$ by means of a quantum with two states of polarization is $S_0 = (2J+1)/2(2I+1)$. The constant $S_{l\gamma}$ depends on the type and multipole order of the electromagnetic transition, with $m = l$ or $l-1$, and $\alpha = e^2/\hbar c$. The emitted particle wave number is $k$, that of the $\gamma$-ray is $\kappa = 1/\lambda = E/\hbar c$, and $\kappa_0 = Mc/\hbar$ is the nucleon wave number. The $U$'s are suitably normalized radial functions.

The final state of this photoelectric excitation could be conversely regarded as a particle $C$ incident on an initial nucleus to produce a resonant compound state. To show this resonant character explicitly, write

$$U_C = (kr)^{-1} U(r)(u\cos\delta + v\sin\delta), \tag{4}$$

where $u$ and $v$ are evaluated at the phenomenological nuclear radius $R$ and $U(R) = 1$. The respective functions $u$ and $v$ are the regular and irregular solutions of wave number $k$ in the centrifugal and/or Coulomb potential external to $R$, and $\delta$ is a nuclear phase shift. The function $U$ is not dependent on the external potentials for $r < R$, and for $r > R$ the integral over $U$ does not depend strongly on the external potential; therefore, $U$ is written without subscript. Then

$$|M_C|^2 \sim \frac{1}{k^2} \left| \int U^* r^{m+1} U_\gamma dr \right|^2 |\sin^2(\delta+\delta_0)|\,(u^2+v^2), \tag{5}$$

where $\tan\delta_0 = u/v$. In terms of the logarithmic derivative,[3]

$$RU_{C'}/U_C|_R = f = f_0 - ih,$$

one has

$$\frac{2ix/(u^2+v^2)}{(f_0-\Delta) - i[h + x/(u^2+v^2)]} = \left(\frac{v+iu}{v-iu}\right) e^{2i\delta} - 1$$
$$= e^{2i(\delta+\delta_0)} - 1, \tag{6}$$

where $x = kR$. To obtain isolated resonances, assume that the excited state is in an energy region close above the threshold, where it is possible to expand $f_0$ about $f_0(E_0) = 0$, $f_0 = (E-E_0)\partial f_0/\partial E_0 + \cdots$. The conventional half-widths are defined by $\Gamma_C = 2xP[-\partial f_0/\partial E_0]^{-1}$, $\Gamma - \Gamma_e = 2h[-\partial f_0/\partial E_0]^{-1}$. The penetration probability is $P = (u^2+v^2)^{-1}$, and an order-of-magnitude argument[3] indicates that $[-\partial f_0/\partial E_0]^{-1} \approx D/\pi KR$, where $K \approx 1 \times 10^{13}$ cm$^{-1}$ is a wave number appropriate to the motion of a nucleon in the Fermi well. Thus in the neighborhood of a resonance,

$$|M_C|^2 = 8\kappa^3\kappa_0\alpha S_{l\gamma}(S_C/S_0)|J|^2(D/\pi K)\tfrac{1}{2}\Gamma_C \times\{(E-E_0)^2 + (\Gamma/2)^2\}^{-1}, \tag{7}$$

$$J = \int_0^\infty U^* r^{m+1} U_\gamma dr.$$

The appearance of the resonance denominator comes from considering the final state of the first-order or "direct" photoelectric process to be strongly coupled with other configurations of the same energy, forming a compound state.

The formation of a compound nucleus as the final state of the photoelectric process is responsible for the entire contribution of matrix elements (2) and (3) to $\sigma_{\gamma C}$. Consider case (2), where the directly excited particle $C'$ differs from the emitted particle $C$ under consideration. For excitation of $C'$ an expression analogous to (7) is obtained. The ratio of $C$ emission to $C'$ emission from the resulting compound state is $\Gamma_C/\Gamma_{C'}$, so that the matrix element for $C$ emission by $C'$ excitation is

$$|M_C(C')|^2 = 8\kappa^3\kappa_0\alpha S_{l\gamma}(S_{C'}/S_0)|J|^2 \times(D/\pi K)\tfrac{1}{2}\Gamma_C\{(E-E_0)^2 + (\Gamma/2)^2\}^{-1}. \tag{8}$$

In case (3) the one-particle state $C''$ is bound, and the corresponding matrix element becomes

$$|M_C(C'')|^2 = 4\pi\kappa^3\alpha S_{l\gamma}(S_{C''}/S_0) \times\left| \int U_{C''}^* r^{m+2} U_\gamma dr \right|^2 \frac{\hbar c}{D_0}, \tag{9}$$

where $U_{C''}$ is normalized per unit volume and $1/D_0$ is the density of one-particle levels. For a single particle in a volume of radius $R$, the level spacing is of order $D_0 \approx \pi[\partial(KR)/\partial E]^{-1} = \pi\hbar c K/\kappa_0 R$. To obtain a resonant energy denominator, we allow the energy of

the excited state to have the complex value $E_0-\frac{1}{2}i\Gamma$. Then in the usual perturbation expression for the transition probability the factor $\delta(E-E_0)$ is replaced by a resonance denominator; for this factor in (9) we insert $(\Gamma/2\pi)D/\{(E-E_0)^2+(\Gamma/2)^2\}$, where the constants are chosen to make the average $\int dE/D$ over the actual levels equal to unity. As in case (2), the relative probability of $C$ emission from the compound state is $\Gamma_C/\Gamma$, so that

$$|M_C(C'')|^2=8\kappa^3\kappa_0\alpha S_{l\gamma}(S_{C''}/S_0)|J_0|^2 \times(D/\pi K)\tfrac{1}{2}\Gamma_C\{(E-E_0)^2+(\Gamma/2)^2\}^{-1}, \quad (10)$$

$$|J_0|^2=\tfrac{1}{2}R\left|\int U_{C''}r^{m+2}U_i^*dr\right|^2.$$

The total cross section for $C$ emission with an arbitrary set of $f_c$ is

$$\sigma_{\gamma C}=\pi\lambda^2 S_0|M_C|^2, \quad (11)$$

$$|M_C|^2=8\kappa^3\kappa_0\alpha S_{l\gamma}(\bar{S}/S_0)|J|^2|F|^2 \times(D/\pi K)\tfrac{1}{2}\Gamma_C\{(E-E_0)^2+(\Gamma/2)^2\}^{-1},$$

$$F=\textstyle\sum_c f_c(S_c/\bar{S})^{\frac{1}{2}}(J_c/J),$$

$$\bar{S}|J|^2=N^{-1}\textstyle\sum_c S_c|J_c|^2,$$

$$N=\textstyle\sum_c 1.$$

Thus one obtains an explicit derivation of the Breit-Wigner formula for the case where one of the particles is a photon, using perturbation theory for the photon and boundary fitting for the heavy particles. Expression (11) can be written

$$\sigma_{\gamma C}=\pi\lambda^2 S_0\Gamma_\gamma\Gamma_C\{(E-E_0)^2+(\Gamma/2)^2\}^{-1}, \quad (12a)$$

$$\Gamma_\gamma=(4/\pi)\kappa^3(\kappa_0/K)\alpha S_{l\gamma}(\bar{S}/S_0)|J|^2|F|^2D. \quad (12b)$$

The form (12b) for $\Gamma_\gamma$ displays all the qualitative features of the heavy-particle $\Gamma_C$: It is proportional to $D$, to $X=\kappa R$, and to the photon penetration probability $P_l(X)$, where $l$ is the multipole order of the transition. This last can be seen by noting that $\kappa^3 S_{l\gamma}$ is proportional to $\kappa^{2l+1}$ or to $(\kappa R)^{2l+1}$ if a factor $R^{-(2l+1)}$ is absorbed into $|J_c|^2$. For $X=\kappa R\ll l$, however, $P_l(X)\sim X^{2l}$, so that $\kappa^3 S_{l\gamma}\sim XP_l(X)$. From this rather special point of view the photon behaves like an uncharged, spinless particle for which the orbital momentum $l=0$ is forbidden.

## III. DISCUSSION

The magnitude of $\Gamma_\gamma$ depends essentially on the factor $|F|^2$, in which the coefficients $f_c$ specify the detailed structure of the excited nuclear state under consideration. Nothing specific is known about the $f_c$, but because of the normalization in (11) the limits of $|F|^2$ are $0\leqslant|F|^2\leqslant N$. The maximum value arises when all the exit channels $c$ add "coherently"; when the phases of $f_c$ are random and the channels add incoherently, $|F|^2=1$. Examples approaching the coherent upper limit are provided by the giant $\gamma-n$ resonances observed in the 15–30 Mev region. In an electric dipole transition the sign of $f_c$ for a given particle depends on the product of its effective charge and its displacement operator. Since the effective charges of proton and neutron have opposite sign and approximately equal magnitude, their displacements must be equal and opposite in sign to make $|F|^2\approx N$. On a classical picture this corresponds to countercurrent motion of the neutrons and protons, as in the original model[4] for these resonances. Other factors being equal, $N$ is in approximately constant ratio to $A$ for any given multipole transition, so that the peak cross section of the giant resonances should increase roughly with $A$ throughout the periodic table, except for fluctuations that depend on specific details of nuclear structure. Although the present model gives only a certain interpretation after the experimental fact, the orderly way in which the $f_c$ must fall into line to produce a giant resonance is suggestive that the resonance should be describable in terms of some simple, specific mechanism.

The excitation of deuterons and heavier subunits is described by choosing proper ratios for the $f_c$ of the particles making up the subunits.

Equation (12) can be manipulated in the usual fashion of compound-nucleus expressions. For example, the cross section for inelastic emission of a particle $C'$ that leaves some excitation in the residual nucleus results from replacing $\Gamma_C$ in (12) by an appropriate $\Gamma_{C'}$. The direction of the reaction can also be reversed, and the cross section for radiative capture of a particle $C$ into the ground state of the final nucleus is by detailed balance

$$\sigma_{C\gamma}=\pi\lambda_C^2 S'\Gamma_C\Gamma_\gamma\{(E-E_0)^2+(\Gamma/2)^2\}^{-1}, \quad (13)$$

where $S'$ is an appropriate statistical factor and $\lambda_C$ is the wavelength of the particle $C$. For the total capture cross section $\Gamma_\gamma$ is replaced by $\sum\Gamma_\gamma$, where the summation is over all possible final states. The small magnitudes observed for $\Gamma_\gamma$ among some of the light elements indicates that in practice $|F|^2$ approaches its lower limit of 0 as well as its upper limit of $N$.

The known features of the capture cross section (13) may be used to help interpret the observed $\gamma-n$ cross section at threshold. If the particles $C$ in (13) are $s$-wave neutrons, $\sigma_{n\gamma}$ shows a $1/v\sim\Gamma_\gamma\lambda_n^2$ law as $E_n\to 0$. Conversely, for the production of $s$-neutrons by $\gamma$-excitation, the cross section just above threshold will be proportional to $\Gamma_n\sim(E_n)^{\frac{1}{2}}$. Thus a suitably extrapolated cross section measurement will lead to $\sigma_{\gamma n}=0$ just at the threshold $E_n=0$. This result is invalidated only if the resonance nearest the threshold does not satisfy $|E_0|/\Gamma\gg 1$. In light nuclei where $\Gamma$ is small and the level spacing wide, failure of this condition is especially unlikely.

In special cases it may be possible to estimate $\Gamma_\gamma$

[4] M. Goldhaber and E. Teller, Phys. Rev. 74, 1046 (1948).

by assuming only a few terms to be dominant in the sum for $F$. This seems most reasonable for very light nuclei and very low excitation energies: The number of particles is small, and for most of them $f_c \approx 0$ because the excitation energy is not great enough to lift them out of the occupied region of the Fermi well. In the particular case of $Li^8$ with a threshold of about 2 Mev, we might expect roughly one neutron and one proton to be excitable from $p_{3/2}$ to $s_{1/2}$, $d_{3/2}$ and $d_{5/2}$ states by electric dipole transitions. There are then six terms in the term for $F$, all with rather similar values of $S_c|J_c|^2$. If they are assumed to add incoherently, $|F|^2 \approx 1$, and the entire $\gamma-n$ or $n-\gamma$ cross section can be estimated from $\bar{S}|J|^2$ for the $p_{3/2}-s_{1/2}$ neutron transition.[5] For more complex cases in heavier nuclei, however, there are no present indications against $f_c \neq 0$ for a large number of channels.

## IV. APPLICATIONS TO $O^{16}$ AND LIGHT NUCLEI

Numerical estimates of $\Gamma_\gamma$ can be compared with the absolute measured $\gamma-n$ cross section[1] on $O^{16}$, extending from the threshold at about 16 Mev through a giant resonance at about 24 Mev. The measured value of this peak is just below 12 mb. Here individual resonance levels are not observed, and the average of (12a) over many levels is[6]

$$\bar{\sigma}_{\gamma n} = \int \frac{dE}{D} \sigma_{\gamma n} = 2\pi^2 \lambda^2 S_0 \left(\frac{\Gamma_\gamma}{D}\right)\left(\frac{\Gamma_n}{\Gamma}\right). \tag{14}$$

The quantity $\Gamma_n/\Gamma$ has been estimated from the statistical model for nuclear reactions[7] and is about $\frac{1}{2}$ for $O^{16}$ at 24 Mev. With $I=0$, $J=1$ for electric dipole transitions, the measured value is $\Gamma_\gamma/D \approx 2\times 10^{-3}$.

To obtain an order-of-magnitude value of $|J|^2$ in $\Gamma_\gamma$, consider $J_0$ for a bound orbit $\psi_c$ and take $U_c = U_i = N_i r^n e^{-\mu r}$. The coefficients $n$ and $\mu$ are not independent, but fixed to give the mean square value $r^2 = R^2$. Then

$$J_0^2 = \tfrac{1}{2}R\left|\int_0^\infty U_c^* r^3 U_i dr\right|^2 = \tfrac{1}{2}R^8 \frac{2n+3}{2n+4} \approx \tfrac{1}{2}R^8.$$

Taking this as a representative value for $|J|^2$ with $R = 3.7\times 10^{-13}$ cm, we have $\bar{S}=2/15$, $S_{1\gamma}=\frac{1}{4}$, $\Gamma_\gamma/D \approx \frac{1}{2}\ 10^{-4}|F|^2$. Thus at the peak cross section $|F|^2 \approx 40$. For electric dipole transitions on $O^{16}$, the number of final channels is $N=40$, so that this value of $|F|^2$ is not impossible but indicates a high degree of coherence, as expected. On a classical picture of oppositely moving fluids, one might expect the $f_c$ to add coherently for separate particles and incoherently for the different channels available to a single particle. In this case $|F|^2 = A = 16$, which is not in disagreement with observation because of the large uncertainty in estimating $|J|^2$.

Below the giant resonance in $O^{16}$ there is a "shoulder" where the measured $\gamma-n$ cross section remains roughly constant at 1 mb over the range 17–20 Mev. In a region so close to the threshold of a light nucleus the statistical model may no longer be very reliable, but one may certainly expect that $\Gamma_n/\Gamma$ (19 Mev) $< \Gamma_n/\Gamma$ (24 Mev). Since the observed ratio of $\sigma_{\gamma n}$ at these two energies is about $\frac{1}{3}$, the ratio of $\Gamma_\gamma(19)/\Gamma_\gamma(24) > \frac{1}{3}$ or $\approx \frac{1}{4}$, if the statistical model is taken seriously. The question arises whether this flat shoulder is due to electric dipole or magnetic dipole plus electric quadrupole transitions. Using the same procedure as above, one finds that for MD and EQ transitions $\bar{S}S_{1\gamma}|J|^2$ is about $\frac{1}{10}$ as large as the same factor for ED transitions. Therefore if the shoulder is EQ+MD, these transitions must be highly coherent to achieve the observed magnitude of $\sigma\Gamma_n$. On the other hand, the shoulder could be due to relatively incoherent ED transitions, with $|F|^2$ not quite an order of magnitude smaller than the value at the giant resonance peak. In the absence of a specific model for the giant resonances, no definite conclusions can be drawn. It seems a less stringent requirement, however, for a model to give coherent and incoherent ED excitation than to allow for two coherent excitations of different character at nearby energies.

It is of interest to compare the $N^{14}$ $\gamma-n$ excitation curve.[1] In this case the shoulder is even more pronounced and is again somewhat more than $\frac{1}{10}$ as large as the giant resonance peak, suggesting an incoherent ED or possibly a coherent MD+EQ mechanism. The shoulder shows a tendency to decrease as the energy is increased above the rather low $(\gamma, np)$ threshold at about 13 Mev, in good accord with the statistical model for competing reactions. Then at 16–17 Mev this decrease is abruptly broken by the rise of the giant resonances to a peak at 24 Mev. This again seems to imply that some specific mechanism is responsible for the coherence that suddenly obtains at the giant resonances while the shoulder at lower energy is due to a nonspecific mechanism. The interpretation of peak $\sigma_{\gamma-n}$ for $N^{14}$ is made uncertain by the strong $\gamma-n$, $p$ competition. Crude estimates based on extrapolation of the statistical model[8] to this case suggest that $\Gamma_n/\Gamma \approx 1/7$. If we then take $R = 3.3\times 10^{-13}$ cm in evaluating $|J|^2$ as before, the requisite value of $|F|^2$ to fit the measurement turns out to be about $|F|^2 \approx 32 \approx N$. The relation of the peak $|F|^2$ to $N$ or $A$ is the same as for $O^{16}$, so that the degree of coherence appears to be of the same order in each resonance.

For $F^{19}$, on the other hand, the $\gamma-n$ peak[8] has the relatively low value of 3.5 mb at about 20 Mev. The effect of $\gamma-p$, $\gamma-(n,p)$, and $\gamma-2n$ competition of this

[5] R. G. Thomas, Phys. Rev. **84**, 1061 (1951).

[6] In general when $I \neq 0$, we should write $\sigma/(2\pi^2\lambda^2) = \Sigma_J S_0(I,J) \times \Gamma_\gamma^J/D_J \Gamma_n^J/\Gamma_J$, but if $\Gamma_n^J/\Gamma_J$ is assumed independent of $J$, the sum over $J$ is independent of $I$. Hence in all cases we replace $\Sigma_J$ by $S_0(0,I) = \frac{1}{3}$ for dipole excitation.

[7] J. Heidmann and H. A. Bethe, Phys. Rev. **84**, 274 (1951).

[8] Horsley, Haslam, and Johns (to be published).

energy yields $\Gamma_n/\Gamma \approx \frac{1}{2}$ on the statistical model. With the same estimate of $|J|^2$ as for $O^{16}$, this gives $|F|^2 \sim \frac{1}{4}N$ at the peak of the giant resonance. The shoulder at lower energy, however, has the same order of $|F|^2$ as for $N^{14}$ and $O^{16}$. Incoherent ED excitation need not be affected by partial breakdown of the coherent mechanism.

It should perhaps be remarked that the matrix elements $|J|^2$ are exceptionally large. They are computed on the assumption that the wave functions of the initial and final states in the photoelectric transition overlap perfectly. Any deviations from this correspondence would in general reduce the magnitude of $|J|^2$, which could not be tolerated in the face of the measured cross sections. Although such perfect overlap may seem reasonable in low energy $\gamma$-transitions considered in the shell model, it is rather a surprise to find one-particle wave functions so much alike for ground and highly excited states.

It is a pleasure to record a stimulating conversation with Professor L. Katz.

PHYSICAL REVIEW VOLUME 88, NUMBER 4 NOVEMBER 15, 1952

# Solar "Enhanced Radiation" and Plasma Oscillations

HARI K. SEN
*National Bureau of Standards, Washington, D. C.*
(Received July 3, 1952)

The dispersion relation for a plasma oscillating in a static magnetic field is derived by the Laplace transform method. The plasma oscillations are found to be unstable in frequency bands around multiples of the gyrofrequency. A numerical application to spot magnetic fields at coronal distances indicates sufficient amplification to make plausible the theory of the origin of solar "enhanced radiation" in plasma oscillations of electrons gyrating round the magnetic field of sunspots.

THE sun is known to emit radiofrequency radiation in the meter range of wavelengths which maintains a high but variable level for periods of hours or days.[1] This "enhanced radiation" proceeds from the direction of sunspots and shows circular polarization. An attempt is made in this paper to ascribe this phenomenon to motion of solar material (prominence or corpuscles) in the magnetic field of sunspots.[2] In the highly conductive corona, the prominence (or corpuscles) will move along the lines of magnetic force. The transverse component of any tendency to oblique motion of the material will set the electrons (and ions) gyrating round the lines of force with a peaked velocity distribution.

Malmfors[3] was the first to point out the similarity between the conditions in the solar corona and in a trochotron and ascribe the origin of solar noise storms to plasma oscillations of electrons in the spot magnetic field. When the current exceeds a certain limit, noise and negative current are observed in the trochotron. Ordinary collision processes cannot explain the effect. The physical picture seems to be that any distortion of the distribution of the electrons is repeated with the gyro-period of the electrons. The space charge electric field varies with the same period, achieving an effect similar to what obtains in a cyclotron.

In a later paper, Malmfors[4] has given a more detailed treatment by the hydrodynamic equation of motion of the states of oscillation in a system of electrons moving with uniform speed in circular paths perpendicular to a magnetic field, and has found that the system is unstable.

Plasma oscillations in electric and magnetic fields have been treated by Bailey[5] with Maxwell's transfer equations. The Maxwell transfer equations (the so-called "hydrodynamic approximation") are easier to apply than the Boltzmann equation, and it is fortunate that they lead in most cases to qualitatively correct conclusions (particularly at long wavelengths). However, to obtain accurate results one must apply the more general Boltzmann equation. One may thus obtain not only quantitatively more accurate results, but also qualitatively new ones, e.g., the heavy damping at wavelengths near the Debye length.

Gross[6] by a kinetic theory treatment has obtained a dispersion relation different from Malmfors'.[7] Gross

[1] J. P. Wild, Australian J. Sci. Res. **A4**, 36 (1951).
[2] A thermal origin cannot satisfactorily explain this "enhanced radiation" which must be distinguished from the slowly varying component, at frequencies of 600 Mc/sec and above, that is closely correlated with sunspot area. See J. H. Piddington and H. C. Minnett, Australian J. Sci. Res. **A4**, 131 (1951).
[3] H. Alfven *et al.*, "Theory and application of trochotrons," Kgl. Tekniska Hogskolans Handlingar **No. 22** (1948).
[4] K. G. Malmfors, Arkiv. fys. **1**, 569 (1950).
[5] V. A. Bailey, Phys. Rev. **83**, 439 (1951).
[6] E. P. Gross, Phys. Rev. **82**, 232 (1951).
[7] In the opinion of the author, the reason for the discrepancy between Malmfors' and Gross' results in the following. Malmfors (see reference 3) has used the same vectorial angle $\phi$ in his Fig. 1, which refers to velocity space, and in his equation of perturbation, in Sec. 3, of the $x$ coordinate, which refers to ordinary space. Making correction for this error (changing $\phi$ into $\frac{1}{2}\pi+\phi$ in Malmfors' continuity equation), the author finds that the two results check.

finds from his dispersion equation the existence of gaps in the spectrum at frequencies that are approximately multiples of the gyrofrequency. The magnitude of the gap depends on the temperature of the gas, being proportional to it for long wavelengths. This leads him to the prediction of selective reflection of waves impinging on a plasma with frequency in the forbidden range.

On account of certain singularities[8] appearing in Gross' treatment, the author has thought it worth while to reconsider the Boltzmann equation in a magnetic field by the Laplace transform method used by Landau[9] in an analogous problem. The analysis confirms Gross'[6] dispersion equation. But it is found that the system is unstable in frequency bands around multiples of the gyrofrequency.

We consider an electron plasma gyrating with a uniform speed $v_0$ round a static magnetic field of strength $H_0$.

Let $f(\mathbf{r}, \mathbf{v}, t)$ be the distribution function of the plasma, satisfying the Boltzmann equation[10]

$$\frac{df}{dt} \equiv \frac{\partial f}{\partial t} + \mathbf{v}\cdot\nabla f + \frac{e}{m}\left(\mathbf{E} + \frac{\mathbf{v}\times\mathbf{H}_0}{c}\right)\cdot\nabla_{\mathbf{v}} f = 0. \quad (1)$$

$\mathbf{E}$ is the electric field due to the space charge. We assume the absence of static electric fields and neglect collisions.[11] For oscillations of small amplitude, we may put

$$f(\mathbf{r}, \mathbf{v}, t) = f_0(\mathbf{v}) + f_1(\mathbf{r}, \mathbf{v}, t), \quad (2)$$

where $f_0(\mathbf{v})$ is the equilibrium distribution, and $f_1 \ll f_0$.

In this approximation the Boltzmann equation is linear and reduces to

$$\frac{\partial f_1}{\partial t} + \mathbf{v}\cdot\nabla f_1 - \frac{e}{m}\nabla\phi\cdot\nabla_{\mathbf{v}} f_0 + \frac{e}{mc}(\mathbf{v}\times\mathbf{H}_0)\cdot\nabla_{\mathbf{v}} f_1 = 0, \quad (3)$$

where the electric potential $\phi(\mathbf{r}, t)$ satisfies the Poisson equation[12]

$$\nabla^2\phi = -4\pi e\int f_1 d\tau \quad (d\tau = dv_x dv_y dv_z). \quad (4)$$

The equilibrium distribution $f_0(\mathbf{v})$ satisfies the equation

$$\mathbf{v}\times\mathbf{H}_0\cdot\nabla_{\mathbf{v}} f_0 = 0. \quad (5)$$

A solution of (5) is $f_0(\mathbf{v}) = f_0((v_x^2+v_y^2)^{\frac{1}{2}}, v_z)$, where $\mathbf{H}_0$ is assumed to be in the $Z$ direction. The Maxwellian distribution can therefore be an equilibrium one in a static magnetic field.[13]

Assume that Eqs. (3) and (4) have solutions of the form

$$f_1 = f_1(\mathbf{v}, t)e^{jkz}, \quad \phi = \phi(t)e^{jkz}. \quad (6)$$

Then (3) and (4) reduce to

$$\frac{\partial f_1}{\partial t} + jkv_z f_1 + \omega_c\left[v_y\frac{\partial f_1}{\partial v_x} - v_x\frac{\partial f_1}{\partial v_y}\right] - jk\frac{e}{m}\phi\frac{\partial f_0}{\partial v_z} = 0, \quad (7)$$

and

$$k^2\phi(t) = 4\pi e\int f_1 d\tau. \quad (8)$$

Here,

$$\omega_c = eH_0/mc \quad (9)$$

is the gyrofrequency.

Following the Laplace transform method,[14] we define the function $f_p(\mathbf{v})$ by

$$f_p(\mathbf{v}) = \int_0^\infty f_1(\mathbf{v}, t)e^{-pt}dt, \quad (10)$$

where

$$f_1(\mathbf{v}, t) = \frac{1}{2\pi j}\int_{-j\infty+\gamma}^{+j\infty+\gamma} f_p(\mathbf{v})e^{pt}dp. \quad (11)$$

We suppose on physical grounds that $f_1(\mathbf{v}, t)$ has a continuous derivative and that $|f_1(\mathbf{v}, t)| < Ke^{ct}$, where $K$ and $c$ are positive constants. Then $\gamma$ in (11) $> c$.

Multiply both sides of Eqs. (7) and (8) by $e^{-pt}$ and integrate over $t$. This yields

$$(p+jkv_z)f_p + \omega_c\left[v_y\frac{\partial f_p}{\partial v_x} - v_x\frac{\partial f_p}{\partial v_y}\right] - jk\frac{e}{m}\phi_p\frac{\partial f_0}{\partial v_z} = g(\mathbf{v}), \quad (12)$$

and

$$k^2\phi_p = 4\pi e\int f_p d\tau, \quad (13)$$

where

$$g(\mathbf{v}) \equiv f_1(\mathbf{v}, 0). \quad (14)$$

On transformation into cylindrical coordinates,

$$v_x = \rho\cos\delta, \quad v_y = \rho\sin\delta, \quad v_z = v_z, \quad (15)$$

Equation (12) reduces to

$$(p+jk\rho\cos\delta)f_p - \omega_c\frac{\partial f_p}{\partial\delta} - jk\frac{e}{m}\phi_p\frac{df_0}{d\rho}\cos\delta = g(\mathbf{v}). \quad (16)$$

On account of the axial symmetry, we shall henceforth suppose the dependence on $z$ of the physical variables to have been taken out by integration over $z$, and shall consider only the polar variables $(\rho, \delta)$.

[8] Gross' distribution function ($f_1$) (see reference 5) has singularities at multiples of the gyrofrequency ($\omega_c$). When $\omega = n\omega_c$, $f_1$ cannot be made periodic in $\delta$ (vectorial angle), except for the trivial case of vanishing ac electric field. The Laplace transform method, as we shall see, enables us to work directly with the electric potential which happens to be nonsingular.

[9] L. Landau, J. Phys. (U.S.S.R.), **Vol. X, No. 1**, 25 (1946).

[10] S. Chapman and T. G. Cowling, *The Mathematical Theory of Non-Uniform Gases* (Cambridge University Press, Cambridge, 1939), p. 322, Sec. 18.2.

[11] We suppose the ions to be stationary, on account of their large mass, and smeared into a uniform charge distribution sufficient to cancel the static negative charge of the electrons. We also consider the atmosphere to be rarefied enough to justify the neglect of collisions.

[12] It is true that in a static magnetic field there is a strong coupling of longitudinal and transverse motions and we should, in strictness, use not the Poisson equation but the full set of Maxwell's equations. The use of the Poisson equation is, however, justified for the limiting case of separation of plasma from electromagnetic waves, i.e., when $ck \gg \omega_p$ and $ck \gg \omega_c$, where $\omega_p$ and $\omega_c$ are, respectively, the plasma and gyrofrequencies, $k$ is the wave number and $c$ the velocity of light (see reference 5).

[13] See Appendix I.

[14] H. S. Carslaw and J. C. Jaeger, *Operational Methods in Applied Mathematics* (Oxford University Press, London, 1941), p. 72.

If we regard (16) as a linear differential equation in ($\delta$), the solution is

$$f_p(\rho,\delta)=A(\rho)e^{(p\delta+jk\rho\sin\delta)/\omega_c}-e^{(p\delta+jk\rho\sin\delta)/\omega_c}\int_0^{\delta}e^{-(p\delta+jk\rho\sin\delta)/\omega_c}\times\frac{g(\mathbf{v})+jk(e/m)\phi_p(df_0/d\rho)\cos\delta}{\omega_c}d\delta, \quad (17)$$

where $A(\rho)$ is an arbitrary function of $\rho$, which must be determined from the physical consideration that $f_p$ must be periodic in $\delta$ with the period $2\pi$.

Let the initial perturbation

$$g(\mathbf{v})\equiv\sum_l A_l(\rho)e^{jl\delta}. \quad (18)$$

We use the expansion

$$e^{jz\sin\delta}=\sum_{n=-\infty}^{+\infty}J_n(z)e^{jn\delta}, \quad (19)$$

and set (18) into (17). Thus we obtain

$$f_p(\rho,\delta)=e^{(p\delta+jk\rho\sin\delta)/\omega_c}\left[A(\rho)-\frac{1}{\omega_c}\sum_l\sum_n A_l(\rho)\times J_n\left(-\frac{k\rho}{\omega_c}\right)\frac{e^{[-p/\omega_c+j(l+n)]\delta}-1}{-p/\omega_c+j(l+n)}+\sum_n J_n\left(-\frac{k\rho}{\omega_c}\right)jk\frac{e}{2m\omega_c}\phi_p\frac{df_0}{d\rho}\left\{\frac{e^{[-p/\omega_c+j(n+1)]\delta}-1}{-p/\omega_c+j(n+1)}+\frac{e^{[-p/\omega_c+j(n-1)]\delta}-1}{-p/\omega_c+j(n-1)}\right\}\right]. \quad (20)$$

The condition that $f_p$ given by (20) must be periodic in $\delta$ with period $2\pi$ gives

$$A(\rho)=-\frac{1}{\omega_c}\sum_l\sum_n A_l(\rho)J_n\left(-\frac{k\rho}{\omega_c}\right)\left\{\frac{1}{-p/\omega_c+j(l+n)}\right\}-\sum_n jk\frac{e}{2m\omega_c}\phi_p\frac{df_0}{d\rho}J_n\left(-\frac{k\rho}{\omega_c}\right)\left\{\frac{1}{-p/\omega_c+j(n+1)}+\frac{1}{-p/\omega_c+j(n-1)}\right\}. \quad (21)$$

Thus we have

$$f_p(\rho,\delta)=-\frac{e^{jk\rho\sin\delta/\omega_c}}{\omega_c}\times\left[\sum_l\sum_n A_l(\rho)J_n\left(-\frac{k\rho}{\omega_c}\right)\frac{e^{j(l+n)\delta}}{-p/\omega_c+j(l+n)}+\sum_n J_n\left(-\frac{k\rho}{\omega_c}\right)jk\frac{e}{2m}\phi_p\frac{df_0}{d\rho}\left\{\frac{e^{j(n+1)\delta}}{-p/\omega_c+j(n+1)}+\frac{e^{j(n-1)\delta}}{-p/\omega_c+j(n-1)}\right\}\right]. \quad (22)$$

We set (22) back into (13) and obtain

$$\phi_p=\frac{4\pi e}{\omega_c}\frac{\sum_l\sum_n\int\frac{A_l(\rho)J_n(-k\rho/\omega_c)e^{j[(l+n)\delta+k\rho\sin\delta/\omega_c]}}{p/\omega_c-j(l+n)}d\tau}{k^2+jk\frac{2\pi e^2}{m\omega_c}\sum_n\int\frac{df_0}{d\rho}\left\{\frac{e^{j(n+1)\delta}}{-p/\omega_c+j(n+1)}+\frac{e^{j(n-1)\delta}}{-p/\omega_c+j(n-1)}\right\}J_n\left(-\frac{k\rho}{\omega_c}\right)e^{jk\rho\sin\delta/\omega_c}d\tau}, \quad (23)$$

where, in our coordinate system (15), $d\tau=\rho d\rho d\delta$.

We use in (23) the following properties of the Bessel functions of integral order:

$$J_{-n}(z)=\frac{1}{2\pi}\int_0^{2\pi}e^{jn\delta}e^{jz\sin\delta}d\delta,$$
$$J_n(-z)=(-1)^nJ_n(z),\quad J_{-n}(z)=(-1)^nJ_n(z), \quad (24)$$

and obtain

$$\phi_p=\frac{8\pi^2e}{\omega_c}\frac{\sum_l\sum_n\frac{(-1)^l}{p/\omega_c-j(l+n)}\int_0^{\infty}A_l(\rho)J_n\left(\frac{k\rho}{\omega_c}\right)J_{l+n}\left(\frac{k\rho}{\omega_c}\right)\rho d\rho}{k^2-jk\frac{4\pi^2e^2}{m\omega_c}\sum_n\frac{\int_0^{\infty}J_n\left(\frac{k\rho}{\omega_c}\right)\left\{J_{n+1}\left(\frac{k\rho}{\omega_c}\right)+J_{n-1}\left(\frac{k\rho}{\omega_c}\right)\right\}\frac{df_0}{d\rho}\rho d\rho}{-p/\omega_c+jn}}. \quad (25)$$

We shall suppose, on physical grounds, that the functions $A_l(\rho)$ that determine the initial perturbation and the function $f_0(\rho)$ that determines the unperturbed distribution are such that the integrals in (25) are convergent. When $p$ is an integral multiple of $j\omega_c$, both the numerator and the denominator of $\phi_p$ in (25) have singularities that cancel out. Thus $\phi_p$ is a meromorphic function of the complex variable $p$ with poles at the values of $p$ that make the denominator of (25) vanish. In other words, the poles of $\phi_p$ are the roots $p_1, p_2, \cdots p_r, \cdots$ of the equation (in $p$)

$$4\pi^2\frac{je^2}{mk\omega_c}\sum_n \frac{\int_0^\infty J_n\left(\frac{k\rho}{\omega_c}\right)\left\{J_{n+1}\left(\frac{k\rho}{\omega_c}\right)+J_{n-1}\left(\frac{k\rho}{\omega_c}\right)\right\}\frac{df_0}{d\rho}\rho d\rho}{-\frac{p}{\omega_c}+jn}=1. \tag{26}$$

We shall suppose again on physical grounds that $\phi(t)$ has a continuous derivative and that $|\phi(t)|<Ke^{ct}$, where $K$ and $c$ are positive constants. Then, by (11), we have

$$\phi(t)=\frac{1}{2\pi j}\int_{-j\infty+\gamma}^{+j\infty+\gamma}\phi_p e^{pt}dp, \tag{27}$$

where $\gamma>c$.

Now $\phi_p$ in (25) is $O(p^{-1})$. Hence the line integral in (27) can be replaced by the integral over any circle $C$, center the origin, that includes all the poles of $\phi_p$.[15] Thus, by Cauchy's residue theorem,

$$\phi(t)=\sum_r b_r e^{p_r t}, \tag{28}$$

where $p_r$ is a root of Eq. (26), and $b_r$ is the residue of $\phi_p$ at the pole $p_r$.

From (6), the potential $\phi$ is given by

$$\phi=\sum_r b_r e^{jkx+p_r t}. \tag{29}$$

Equation (26) is therefore the required dispersion equation.

The transform of the electron distribution function $f_1(\mathbf{v}, t)$ is the meromorphic function $f_p(\rho, \delta)$ given by (22), which has poles for $p=jn\omega_c$, besides the poles of $\phi_p$ given by (26). The poles at $p=jn\omega_c$ contribute frequencies that are multiples of the gyrofrequency to the distribution function $f_1(\mathbf{v}, t)$ of the electrons.

Before we can apply the dispersion equation (26), we must specify the unperturbed distribution function $f_0(\rho)$. For a system of electrons gyrating round the magnetic field ($Z$ axis) with a uniform speed $v_0$, we may write

$$f_0(\rho)=(n_0/2\pi v_0)\delta(\rho-v_0), \tag{30}$$

where $n_0$ is the electron density and $\delta$ is the Dirac $\delta$-function whose derivative has the integral property

$$\int_{-\infty}^{\infty} f(x)\delta'(x-a)dx=-f'(a). \tag{31}$$

Using (30) and (31), we find that the dispersion equation (26) reduces to the form[16]

$$1=-\frac{\omega_0^2}{2\omega_c^2}\frac{1}{\lambda}\frac{d}{d\lambda}\left[\lambda\sum_{-\infty}^{\infty}\frac{J_n(\lambda)\{J_{n-1}(\lambda)+J_{n+1}(\lambda)\}}{n-\omega/\omega_c}\right], \tag{32}$$

where

$$\lambda=kv_0/\omega_c, \tag{33}$$

and $\omega_0$ is the plasma frequency given by

$$\omega_0^2=4\pi n_0 e^2/m. \tag{34}$$

For the Maxwellian distribution function

$$f_0=n_0\left(\frac{m}{2\pi\kappa T}\right)^{\frac{3}{2}}\exp\left[-\frac{m}{2\kappa T}(v_z^2+\rho^2)\right], \tag{35}$$

the dispersion equation (26) reduces to

$$\omega=4\omega_0^2\frac{\omega_c^2}{k^4}\left(\frac{m}{2\kappa T}\right)^2\int_0^\infty \lambda e^{-\lambda^2/\beta^2}d\lambda\sum_{n=-\infty}^{+\infty}\frac{n^2J_n^2(\lambda)}{n+\omega/\omega_c}, \tag{36}$$

where

$$\lambda=k\rho/\omega_c \quad \text{and} \quad 1/\mu=(m/\kappa T)(\omega_c^2/k^2). \tag{37}$$

The relation (36), which was obtained by Gross,[6] is further considered in Appendix II.

Gross[6] has considered the dispersion relation (32) for small $\lambda$ ($\lambda\ll 1$) and has shown that in this case there are gaps in the spectrum at approximate multiples of the gyrofrequency. He believes that "the same type of consideration would seem to hold for all values of $\lambda$." He has not, however, undertaken a complete study of the dispersion relation (32) (i.e., for large $\lambda$).

The author has thought fit to consider the dispersion equation (32) for $\lambda>1$, and finds that it can be satisfied by complex values of $\omega$, leading to unstable oscillations growing exponentially in time.

We set

$$K=(\omega_0/\omega_c)^2=4\pi N_0 mc^2/H_0^2, \quad \omega/\omega_c=\alpha+j\beta, \tag{38}$$

in the dispersion equation (32), and, equating real and

[15] See reference 14, p. 76.

[16] Gross obtained the dispersion equation in this form from a direct solution of the Boltzmann equation (see reference 5). As Gross assumed the oscillating quantities to vary as $e^{j(kx-\omega t)}$, we have replaced $p$ in (26) by $-j\omega$.

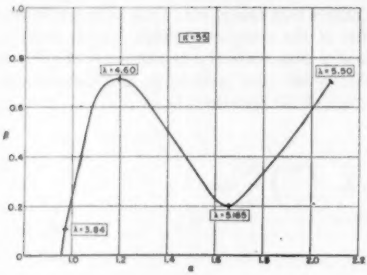


FIG. 1. Curve showing the variations of $\beta$ (amplification) with $\alpha$ (frequency in units of the gyrofrequency).

imaginary parts, obtain

$$\sum_{n=1}^{+\infty} \frac{n(n^2-\alpha^2+\beta^2)}{(n^2-\alpha^2+\beta^2)^2+4\alpha^2\beta^2}(J_{n+1}^2-J_{n-1}^2)=\frac{1}{K}$$
$$\sum_{n=1}^{+\infty} n\frac{J_{n+1}^2-J_{n-1}^2}{(n^2-\alpha^2+\beta^2)^2+4\alpha^2\beta^2}=0. \quad (39)$$

A numerical solution of Eq. (39), for different values of $K$ as a parameter, shows that the equation can be satisfied by real positive values of $\alpha^2$ and $\beta^2$;[17] thus, the dispersion equation (32) can be satisfied by complex $\omega$, indicating amplification of random fluctuations with time.

We will state our results for the particular value of $K=55$, which applies to spot magnetic fields ($H_0\simeq 30$ gauss) at coronal distances ($\simeq 10^{10}$ cm above the photosphere) and to the density of prominance material ($n_0=5\times 10^9$ cm$^{-3}$).

Figure 1 gives the variation of $\beta$ with $\alpha$, and the progression of the $\lambda$-values corresponding to the different points.[18] The curve oscillates round multiples of the gyrofrequency, and fairly large amplifications are available over a wide frequency range. The values of $\beta$ indicate that the amplification will amount to several powers of 10 in a few seconds. We will not quote precise results, as we cannot trust any first-order theory for such large amplitudes. The frequency band width about covers the range of 70–130 Mc/sec in which the Australians[1] have observed "enhanced radiation." Though a nonlinear theory would be required to achieve quantitative accuracy, we believe that the results obtained herein have a qualitative significance, inasmuch as they render plausible the theory of the origin of solar "enhanced radiation" in plasma oscillations of electrons gyrating round the magnetic field of sunspots.

We may note two points in this connection. As the gyrating electrons have a peaked velocity distribution on account of the prominence motion, they do not suffer from the thermodynamic limitation as in the case first treated by Kiepenheuer.[19] Further, amplification is available over a large frequency band width, which will enable the radiation to escape through regions that are normally overdense for the gyrofrequency.[20]

The amplification tends to increase with $K$ as defined by Eq. (38). This tendency may explain the abnormal increases in the enhanced level found at the time of solar flares.[21] The background continuum shows at times short-lived increases to exceptionally high values and of broad band width (tens of megacycles per second). The agency in this case may be the dense corpuscles shot out from sunspots at the time of a solar flare.

The "storm bursts" that occur on the enhanced level[1] have a narrow band width (4 Mc/sec) and seem to owe their origin to a different mechanism that is probably localized in the solar atmosphere, e.g., shock waves due to solar corpuscles moving with supersonic velocity. A physical theory of the propagation of shock waves in an ionized gas subject to a static magnetic field will be relevant to this case.

The author's best thanks are due Miss Loris B. Perry for the numerical solution of Eqs. (39) and the drawing of Fig. 1.

## APPENDIX I

### The Steady-State Solution of the Boltzmann Equation in a Magnetic Field

Let the distribution function $f=f_0(\mathbf{v}, t)$ be a solution of the Boltzmann equation[22] in the magnetic field $H_0$ of gyrofrequency $\omega_c$,

$$\frac{\partial f}{\partial t}+\omega_c\left[v_y\frac{\partial f}{\partial v_x}-v_x\frac{\partial f}{\partial v_y}\right]=B\nabla_v^2 f+3\beta f+\beta\mathbf{v}\cdot\nabla_v f, \quad (1)$$

where

$$B=\beta\kappa T/m, \quad (2)$$

$\kappa$ being the Boltzmann constant and $\beta$ the electronic collision frequency.

Put

$$f'=f_0 e^{-3\beta t}. \quad (3)$$

Then Eq. (1) reduces to

$$\frac{\partial f'}{\partial t}+\omega_c\left[v_y\frac{\partial f'}{\partial v_x}-v_x\frac{\partial f'}{\partial v_y}\right]=B\nabla_v^2 f'+\beta\mathbf{v}\cdot\nabla_v f'. \quad (4)$$

[17] For real $\lambda$, the quantity within the brackets in Eq. (32) is real. It can be reduced to the form:

$$\sum_1^\infty \frac{4n^2J_n^2(\lambda)}{n^2-\alpha^2+\beta^2-2j\alpha\beta}.$$

If this sum is real for any particular $\alpha$, $\beta$, it is real and has the same value for any of the four combinations $\pm\alpha$, $\pm\beta$. Hence the roots of (32) occur in quadruples $\pm\alpha\pm j\beta$.

[18] There seems to be a cut-off near $\lambda=3.84$; see Appendix II.

[19] K. O. Kiepenheuer, Nature **158**, 340 (1946).

[20] M. Ryle, Rept. Prog. Phys. **XIII**, 229 (1950).

[21] Reference 1, p. 42.

[22] S. Chandrasekhar, Revs. Modern Phys. **15**, 35 (1943), Eq. (249).

Change to cylindrical coordinates:

$$v_x=\rho\cos\delta,\quad v_y=\rho\sin\delta,\quad v_z=v_z. \tag{5}$$

Then, Eq. (5) reduces to

$$\frac{\partial f'}{\partial t}-\beta\rho\frac{\partial f'}{\partial\rho}-\omega_c\frac{\partial f'}{\partial\delta}-\beta v_z\frac{\partial f'}{\partial v_z}=B\left[\frac{\partial^2 f'}{\partial\rho^2}+\frac{1}{\rho}\frac{\partial f'}{\partial\rho}+\frac{1}{\rho^2}\frac{\partial^2 f'}{\partial\delta^2}+\frac{\partial^2 f'}{\partial v_z^2}\right]. \tag{6}$$

The left-hand side of (6) equated to zero is a linear, homogeneous first-order partial differential equation, and its solution can be derived from the following Lagrangian subsidiary equations:

$$dt=d\rho/-\beta\rho=d\delta/-\omega_c=dv_z/-\beta v_z. \tag{7}$$

Independent integrals of (7) are

$$\rho e^{\beta t}=c_1,\quad \delta+\omega_c t=c_2,\quad \text{and}\quad v_z e^{\beta t}=c_3. \tag{8}$$

Accordingly, to integrate (6), we make the following change of variables:

$$\rho e^{\beta t}=\xi,\quad \delta+\omega_c t=\eta,\quad v_z e^{\beta t}=\zeta,\quad t=t. \tag{9}$$

Equation (6) reduces, in the new variables $(\xi, \eta, \zeta, t)$, to

$$\frac{\partial f'}{\partial t}=B\left[\frac{\partial^2 f'}{\partial\xi^2}+\frac{1}{\xi}\frac{\partial f'}{\partial\xi}+\frac{1}{\xi^2}\frac{\partial^2 f'}{\partial\eta^2}+\frac{\partial^2 f'}{\partial\zeta^2}\right]e^{2\beta t}. \tag{10}$$

The right-hand side of (10) is the Laplacian of $f'$ in the cylindrical coordinates

$$\xi'=\xi\cos\eta,\quad \eta'=\xi\sin\eta,\quad \zeta'=\zeta. \tag{11}$$

With the substitution (11), Eq. (10) reduces to

$$\partial f'/\partial t=Be^{2\beta t}\nabla_{\xi'}{}^2 f'. \tag{12}$$

We now apply the following lemma:[32]

If $\phi(t)$ is an arbitrary function of time, the solution of the partial differential equation,

$$\partial\chi/\partial t=\phi^2(t)\nabla_\varrho{}^2\chi, \tag{13}$$

which has a source at $\varrho=\varrho_0$ at time $t=0$, is

$$\chi=\frac{1}{\left[4\pi\int_0^t\phi^2(t)dt\right]^{\frac{3}{2}}}\exp\left[-|\varrho-\varrho_0|^2/4\int_0^t\phi^2(t)dt\right]. \tag{14}$$

Applying the above lemma to Eq. (12) and going back to the old variables $(\rho, \delta, v_z, t)$ by means of Eqs. (9) and (11), we find that

$$f_0(\mathbf{v},t)=[(2\pi B/\beta)(1-e^{-2\beta t})]^{-\frac{3}{2}}\exp[-\{\rho\cos(\delta+\omega_c t)-\rho_0\cos\delta_0 e^{-\beta t}\}^2-\{\rho\sin(\delta+\omega_c t)-\rho_0\sin\delta_0 e^{-\beta t}\}^2-(v_z-v_{0z}e^{-\beta t})^2]/[(2B/\beta)(1-e^{-2\beta t})]. \tag{15}$$

[32] See reference 22, p. 34, Lemma I.

As $t\to\infty$, the distribution function given by (15) tends to the Maxwellian one,

$$f_0(\mathbf{v})=\left(\frac{m}{2\pi\kappa T}\right)^{\frac{3}{2}}\exp\left[-\frac{m}{2\kappa T}|\mathbf{v}|^2\right], \tag{16}$$

on substituting (2).

Note that the presence of the magnetic field does not affect the steady-state solution of the Boltzmann equation. Appendix I gives an alternative proof of this well-known result[10] via the Fokker-Planck diffusion equation (1).

## APPENDIX II

### A Closed Expression for the Dispersion Equation (32)

The infinite sum in the dispersion equation (32) can be expressed in a closed form as follows:

Let

$$S(\lambda,\alpha)\equiv\lambda\sum_{n=-\infty}^{\infty}\frac{J_n(\lambda)\{J_{n-1}(\lambda)+J_{n+1}(\lambda)\}}{n-\alpha}, \tag{1}$$

where

$$\omega/\omega_c=\alpha. \tag{2}$$

Then

$$S(\lambda,\alpha)=4\sum_{n=1}^{\infty}\frac{n^2J_n{}^2(\lambda)}{n^2-\alpha^2}=4\sum_1^\infty J_n{}^2(\lambda)+4\alpha^2\sum_1^\infty\frac{J_n{}^2(\lambda)}{n^2-\alpha^2}. \tag{3}$$

Now,[24]

$$(-1)^n J_n{}^2(\lambda)=\frac{2}{\pi}\int_0^{\pi/2}J_0(2\lambda\cos\theta)\cos(2n\theta)d\theta, \tag{4}$$

and

$$\sum_1^\infty(-1)^n\frac{\cos 2n\theta}{n^2-\alpha^2}=\frac{1}{2\alpha^2}-\frac{\pi}{2}\frac{\cos(2\alpha\theta)}{\alpha\sin(\pi\alpha)}. \tag{5}$$

Hence,

$$\sum_1^\infty\frac{J_n{}^2(\lambda)}{n^2-\alpha^2}=\frac{1}{\pi\alpha^2}\int_0^{\pi/2}J_0(2\lambda\cos\theta)d\theta-\int_0^{\pi/2}\frac{J_0(2\lambda\cos\theta)\cos(2\alpha\theta)d\theta}{\alpha\sin(\pi\alpha)}=\frac{1}{2\alpha^2}J_0{}^2(\lambda)-\frac{\pi J_\alpha(\lambda)J_{-\alpha}(\lambda)}{2\alpha\sin(\pi\alpha)}. \tag{6}$$

Also,

$$\sum_1^\infty J_n{}^2(\lambda)=\tfrac{1}{2}-\tfrac{1}{2}J_0{}^2(\lambda). \tag{7}$$

[24] W. Magnus and F. Oberhettinger, *Formulas and Theorems for the Special Functions of Mathematical Physics* (Chelsea Publishers, New York, 1949), p. 28, Sec. 6.

Hence,

$$S(\lambda, \alpha)=2\left\{1-\frac{\pi\alpha}{\sin(\pi\alpha)}J_\alpha(\lambda)J_{-\alpha}(\lambda)\right\}.^{25} \quad (8)$$

From the series expansion[26]

$$J_\alpha(\lambda)J_{-\alpha}(\lambda)=\sum_{m=0}^{\infty}\frac{(-)^m(\frac{1}{2}\lambda)^{2m}(2m)!}{(m!)^2\Gamma(\alpha+m+1)\Gamma(-\alpha+m+1)}, \quad (9)$$

where $\alpha$ is not an integer, we can show that the dispersion equation (32) reduces, when $\lambda\ll 1$, to

$$\frac{2(\alpha^2-4)+3\lambda^2}{2(1-\alpha^2)(4-\alpha^2)}=\frac{1}{K}, \quad (10)$$

where $K$ is given by (38).

Equation (10) gives, for $\lambda=0$, the relation for a static plasma, *viz.*,

$$\omega^2=\omega_0^2+\omega_c^2, \quad (11)$$

where $\omega_0$ is the plasma frequency given by (34).

Setting in Eq. (10),

$$\alpha=\frac{\omega}{\omega_c}=\sqrt{x}+j\sqrt{y}, \quad (12)$$

equating real and imaginary parts, and eliminating $x$, we have

$$16y^2+8(5+K)y+(K-3)^2+6\lambda^2K=0. \quad (13)$$

Neither root of Eq. (13) can be real and positive. Hence the dispersion equation (32) cannot have complex roots for small $\lambda(\ll 1)$. This result is in conformity with Gross' conclusion[6] and the lower cut-off limit for $\lambda$ in our Fig. 1.

## The Dispersion Relation for a Maxwellian Distribution

The integral in the dispersion relation (36) for the Maxwellian distribution function (35) can be expressed in terms of the generalized hypergeometric function[27] ${}_2F_2$:

$$\int_0^\infty \lambda e^{-\lambda^2/2\mu}d\lambda \sum_{n=-\infty}^{+\infty}\frac{n^2J_n^2(\lambda)}{n+\alpha}$$

$$=\alpha\mu[{}_2F_2(1, \tfrac{1}{2}; 1+\alpha, 1-\alpha; -2\mu)-1], \quad (14)$$

where $\alpha$ is given by (2).

Formula (14) follows from Eq. (8) and the following integral relation:[28]

$$\int_0^\infty \lambda \exp(-a\lambda^2)J_\alpha(\lambda)J_{-\alpha}(\lambda)d\lambda$$

$$=\frac{\sin(\pi\alpha)}{2a\pi\alpha}{}_2F_2\left(1, \tfrac{1}{2}; 1+\alpha, 1-\alpha; -\frac{1}{a}\right). \quad (15)$$

We shall assume that

$$\mu/\alpha^2=(\kappa T/m)(k^2/\omega^2)\ll 1. \quad (16)$$

Then using only the first two terms of the series expansion of ${}_2F_2$ in (14), we can reduce the dispersion equation (36) to

$$\omega^2=\omega_c^2+\omega_0^2-3\mu\omega_0^2/(4-\alpha^2). \quad (17)$$

Equation (17) again reduces to (11) for $T\to 0$. In the first approximation, Eq. (11) can be set for $\alpha$ in (17), which will lead to the following relation:

$$\omega^2=\omega_c^2+\omega_0^2-\frac{3\omega_0^2(\kappa T/m)k^2}{3\omega_c^2-\omega_0^2}$$

$$=\omega_c^2+\omega_0^2+3\frac{\kappa T}{m}k^2\left(1+3\frac{\omega_c^2}{\omega_0^2}\right), \quad (18)$$

when $\omega_c^2/\omega_0^2\ll 1$.

Equation (18), which leads to the correct limiting forms for zero magnetic field and/or temperature, should be compared with Gross'[6] Eq. (30).

[25] Formula (8) is due to Dr. J. J. Freeman.

[26] G. N. Watson, *Theory of Bessel Functions* (Cambridge University Press, Cambridge, 1944), p. 147.

[27] Formula (14) is due to Dr. Fritz Oberhettinger.

[28] See reference 26, p. 396.

# Fission Neutron Spectrum of $Pu^{239}$†

NORRIS NERESON
*University of California, Los Alamos Scientific Laboratory, Los Alamos, New Mexico*
(Received July 23, 1952)

The energy distribution of prompt and delayed neutrons originating from thermal fission of $Pu^{239}$ has been measured from 0.5 to 8 Mev with nuclear plates. The spectrum obtained shows a maximum intensity in the 0.6- to 0.8-Mev region and an exponential slope of 4.3±0.2 Mev per decade of intensity in the energy region above 2 Mev.

PREVIOUS measurements on the neutron spectrum from the fission of plutonium by thermal neutrons have been made by Richards[1] and by Staub and Nicodemus.[2] The cloud chamber and half-tone photoplate measurements of Richards showed a spectrum having a broad maximum between 1 and 2 Mev, while the ionization chamber data of Staub and Nicodemus indicated a maximum around 1 Mev or less. The two measurements were in agreement at energies above 2 Mev. The present spectral measurement, performed in 1949 with Ilford C2 nuclear emulsions, was intended to contribute additional information on this spectrum and was carried out mainly for providing a comparison between the unmodified fission spectrum of $Pu^{239}$ and the degraded spectrum emerging from the Los Alamos fast reactor.

The experimental arrangement was very similar to that used in the determination of the fission neutron spectrum of $U^{235}$.[3] The Los Alamos Water Boiler provided a 2-in. diameter thermal neutron beam which bombarded a nickel-coated disk sample of $Pu^{239}$ having dimensions of 0.5-in. diameter and 0.125-in. thick.[4] The C2 nuclear emulsion plates were placed at right angles to the thermal neutron beam at a distance of 20 cm from the plutonium sample. Good geometry was emphasized in the experiment and effort was directed toward eliminating factors which might modify neutron energies such as nearby scattering objects, collimating devices, etc. A 35-hr irradiation at a power of 5.5 kw gave a suitable proton recoil track density in the nuclear plates. Other details of the experimental arrangement are similar to those of reference 3.

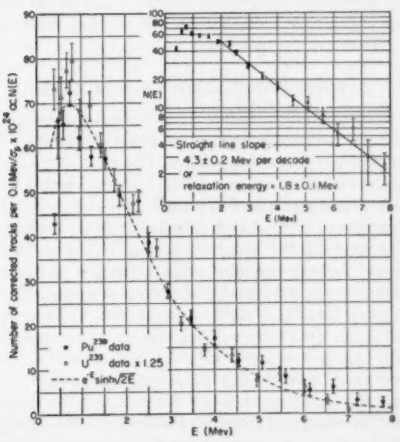


FIG. 1. Fission neutron spectrum of $Pu^{239}$ compared with that of $U^{235}$. Inset: $Pu^{239}$ spectrum plotted on semi-log paper.

The spectrum data were accumulated from a total of approximately 5500 proton recoil tracks measured by two microscopists working independently. The nuclear plate analysis has been discussed previously[3] and only the final results are presented here. The data are shown in Fig. 1 where the relative neutron intensity, $N(E)$, is given as a function of the neutron energy, $E$; the tracks per unit energy interval have been divided by the scattering cross section of hydrogen, $\sigma_p$, and corrected for tracks leaving the emulsion surfaces. The fission spectrum data from $U^{235}$ and Watt's[5] empirical relation, $e^{-E}\sinh(2E)^{\frac{1}{2}}$, where $E$ is in Mev, are given in the figure for comparison purposes. The latter two items were normalized to the $Pu^{239}$ data at 1.5 Mev. This region of the data is considered most reliable since here the statistical errors are quite small, the tracks are of sufficient length to eliminate difficulties associated with the measurement of short tracks, and no correction is required for tracks leaving the emulsion surfaces.

The results show that the fission neutron spectra of $Pu^{239}$ and $U^{235}$ are identical within the statistical errors of the two experiments. Each of these spectra attains a maximum intensity in the 0.6- to 0.8-Mev region and possesses an exponential slope at energies beyond 2 Mev. The slope of the $Pu^{239}$ spectrum data is 4.3±0.2 Mev per decade of intensity, whereas the $U^{235}$ spectrum gave 3.9±0.2 Mev; the two values are just within the limits of experimental error. The average energy, $\bar{E}=\int N(E)EdE/\int N(E)dE$, of the spectrum is 2.0 Mev. The point for $Pu^{239}$ at 0.4 Mev seems unusually low although it has been corrected for emulsion inefficiency at this low energy. Probably this point is not

† This work was performed under the auspices of the AEC.
[1] H. T. Richards (private communications, 1944, 1946).
[2] H. Staub and D. Nicodemus (private communication, 1944).
[3] N. Nereson, Phys. Rev. **85**, 600 (1952).
[4] A thin foil would have provided a better sample geometry but at the time was not available.
[5] B. Watt, Phys. Rev. **87**, 1037 (1952).

too reliable since it represents the lower energy limit at which nuclear emulsion data can be used. Both spectra are represented quite well by the function $e^{-E}\sinh(2E)^{\frac{1}{2}}$. However, there is a tendency for the two sets of data to show somewhat more high energy neutrons than the above empirical relation. It is difficult to know if this is a real effect on account of the small number of proton recoil tracks measured in the high energy region.

The author wishes to thank Julia Carlson and Shirley Suttman for their services in reading the nuclear plates used in this experiment.

PHYSICAL REVIEW VOLUME 88, NUMBER 4 NOVEMBER 15, 1952

# Nuclear Photoprocesses at High Energy*

J. G. Brennan and R. G. Sachs
*Department of Physics, University of Wisconsin, Madison, Wisconsin*
(Received July 28, 1952)

In view of recent interest in the influence of pion production on the high energy photonucleon cross sections, an attempt is made to give a systematic discussion of the background effects, i.e., those high energy effects which are not directly concerned with either the production of pions or relativistic corrections to the nucleon motion. An appropriate definition of each high energy (irreducible) multipole moment is given. It is shown that the Siegert theorem does not apply, so even the electric dipole transition may be affected by (adiabatic) exchange currents. These and other high energy effects are found to contribute about 5 percent to the electric dipole photodisintegration cross section of the deuteron. Larger corrections are anticipated for heavier nuclei. It is shown that the corrections are calculated most readily by using the usual form of the multipole moment operators, rather than the formally correct irreducible operators.

## 1. INTRODUCTION

IT is generally recognized that the possibility of pion photoproduction should have a marked influence on nuclear photodisintegration cross sections at photon energies of the order of 140 Mev or larger.[1] The separation of this influence from the "ordinary" process of photodisintegration can be accomplished only if a reliable theoretical value of the cross section for the ordinary process is available. The natural procedure, and the one that has recently been followed,[2] is to use the electric dipole cross section for this purpose. The dipole moment operator is usually[3] taken to be the static moment operator $D=\sum_a e_a(\mathbf{u}\cdot\mathbf{r}_a)$, where $\mathbf{u}$ is the direction of polarization of the photon. Justification of this procedure has been based on the Siegert theorem, which asserts that that form of the electric moment may be used as long as the dynamics of the nuclear system can be described in terms of nuclear variables alone. Thus any observed deviation from the calculated curve is interpreted as an indication of the effects that depend explicitly on the pion variables, in other words, as the influence of the "pion polarizability" of the system. In particular, this interpretation has recently been given[2] to the deviation of the observed photodisintegration cross section of the deuteron from the calculated curves of Schiff[4] and of Marshall and Guth,[5] curves which are based on the deuteron electric moment, $\frac{1}{2}e(\mathbf{u}\cdot\mathbf{r})$.

Our purpose is to point out that the Siegert theorem is *not* valid at high energy; in fact, for the deuteron it breaks down at energies in the neighborhood of 50 Mev. Therefore, the above interpretation of the data could in principle be erroneous, but we shall see below that the errors are quite small.

## 2. REDUCIBLE MULTIPOLE MOMENTS

To understand the failure of the Siegert theorem, it is necessary to reconsider the problem of defining the multipole moments of a system. The most elementary definition involves an expansion of its interaction with the electromagnetic field in powers of $kr$, where $k$ is the propagation vector of the radiation and $r$ is a distance of the order of the linear dimensions of the radiating nucleus. At low energies, this expansion converges rapidly, so only the lowest of the terms which contribute to a given transition need be considered. That term is fixed by the specification of the angular momentum and parity change associated with the transition. Thus the lowest term contributing to a transition $\Delta j=l$ with parity change equal to $(-1)^l$ is defined as the electric $2^l$ pole moment, and that contributing with the opposite change of parity is the magnetic $2^l$ pole moment. These are the definitions for which the proof of the Siegert theorem has been given.[6]

* This work was supported in part by the AEC and in part by the Wisconsin Alumni Research Foundation.
[1] S. Kikuchi, Phys. Rev. **85**, 1062 (1952).
[2] T. S. Benedict and W. M. Woodward, Phys. Rev. **85**, 924 (1952); R. R. Wilson, Phys. Rev. **86**, 125 (1952); R. Littauer and J. Keck, Phys. Rev. **86**, 1051 (1952); B. Bruno and S. Depkin, Phys. Rev. **86**, 1054 (1952).
[3] J. Levinger, Phys. Rev. **84**, 43 (1951)
[4] L. Schiff, Phys. Rev. **78**, 733 (1950).
[5] J. F. Marshall and E. Guth, Phys. Rev. **78**, 738 (1950).
[6] R. G. Sachs and N. Austern, Phys. Rev. **81**, 705 (1951).

Clearly the above definition fails for radiation of such high energy that $kr$ becomes comparable to unity. Then not only is there a contribution from the aforementioned lowest term, but an infinite series of higher terms must be included for given $\Delta j$ and parity change. Furthermore, the clear separation of electric and magnetic effects no longer follows from the above rule; for example, the above-defined magnetic quadrupole moment contributes to the electric dipole transition $\Delta j=1$, yes. Since the Siegert theorem does not apply to magnetic transitions, it cannot be applicable here.

### 3. REDUCED MULTIPOLE MOMENTS

The multipole moments at high energy are best defined on the basis of the angular momentum and parity of the radiation field produced in the transition. This has the advantage that only a finite number of moments can contribute to a transition of a given $\Delta j$ and parity change, instead of the previously mentioned infinite series. In particular, the transition $j=0$ to $j=l$ can only radiate angular momentum $l$, so only the $2^l$ pole moment plays a role therein.

The assignment of a given angular momentum to the photon requires an expansion of the radiation field in terms of spherical waves.[7] The expansion is usually expressed directly in terms of the solutions $\phi_l^m(kr)$ of the scalar wave equation

$$\phi_l^m=f_l(kr)Y_l^m,$$

where $Y_l^m$ is the spherical harmonic and $f_l$ is the spherical Bessel function.[8] The set of vector potentials which provide the electric multipole fields then have the form[9]

$$\mathbf{A}_l^m(\text{elect})=\text{grad}\chi_l^m+k\mathbf{r}\phi_l^m, \tag{1}$$

with

$$\chi_l^m=k^{-1}[\phi_l^m+(\mathbf{r}\cdot\text{grad}\phi_l^m)]. \tag{2}$$

The magnetic multipole contribution arises from the set

$$\mathbf{A}_l^m(\text{mag})=\text{curl}\mathbf{r}\phi_l^m. \tag{3}$$

If the Hamiltonian of the nuclear system in interaction with the radiation is expanded in powers of the vector potential $\mathbf{A}$, only the linear term $H_1\{\mathbf{A}\}$ is important for the emission and absorption processes with which we are concerned. The transition probability for an electric $2^l$ pole process is proportional to

$$|\langle i|H_1\{\mathbf{A}_l^m(\text{elect})\}|f\rangle|^2,$$

where the matrix element is taken between the initial $(i)$ state and the final $(f)$ state of the radiating system. The electric moment is usually (i.e., at low energies) defined in such a way that its time derivative appears explicitly in the interaction. Therefore, it is convenient to introduce an operator $\dot{E}_l^m$ such that $E_l^m$ plays the role of the electric $2^l$ pole moment. Then $\dot{E}_l^m$ is proportional to $H_1\{\mathbf{A}_l^m(\text{elect})\}$, and the constant of proportionality can be determined by the condition that the result agree in the low energy limit with the definition given on the basis of an expansion in powers of $kr$:[10]

$$\dot{E}_l^m=-ck^{l-1}[2\pi(2l+1)/l(l+1)]^{\frac{1}{2}}H_1\{\mathbf{A}_l^m(\text{elect})\}. \tag{4}$$

Similarly, it is possible to formally relate the $2^l$ pole magnetic moment $M_l^m$ to $H_1$ as

$$M_l^m=k^{-l}[2\pi(2l+1)/l(l+1)]^{\frac{1}{2}}H_1\{\mathbf{A}_l^m(\text{mag})\}. \tag{5}$$

Questions concerning the Siegert theorem are most easily discussed in the formalism of reference 6. There it is shown that gauge invariance of the Hamiltonian has the consequence

$$H_1\{\mathbf{F}+\text{grad}G\}=-c^{-1}\textstyle\sum_a e_a\dot{G}(\mathbf{r}_a)+H_1\{\mathbf{F}\},$$

where $\mathbf{F}(r)$ and $G(r)$ are arbitrary functions and $\mathbf{r}_a$ is the coordinate of a particle (nucleon) of charge $e_a$. Thus introduction of Eq. (1) into Eq. (4) leads to a natural division of the electric moment into the sum

$$E_l^m=P_l^m+S_l^m,$$

where the primary term is

$$P_l^m=k^{-l}[2\pi(2l+1)/l(l+1)]^{\frac{1}{2}}\times[\textstyle\sum_a e_a Y_l^m\{f_l+(\mathbf{r}\cdot\text{grad}f_l)\}]_{\mathbf{r}=\mathbf{r}_a}, \tag{6}$$

and the time derivative of the secondary term is[11]

$$\dot{S}_l^m=-ick^{l-1}[2\pi(2l+1)/l(l+1)]^{\frac{1}{2}}H_1\{\mathbf{r}f_l(kr)Y_l^m\}. \tag{7}$$

The quantity $P_l^m$ has the properties associated with the Siegert theorem; its form is independent of any characteristic of the nucleon other than its charge and position. The secondary term $S_l^m$ depends explicitly on the form of the Hamiltonian. For small $kr$ it is one order smaller than $P_l^m$; hence it is usually neglected. This is the condition under which the Siegert theorem applies. But for $kr\approx 1$, it cannot be neglected; so, then, the form of the electric moment depends explicitly on the form of the Hamiltonian. Under all conditions the magnetic moments depend explicitly on the form of the Hamiltonian.

[7] W. Heitler, Proc. Cambridge Phil. Soc. **32**, 112 (1936).

[8] Normalization of $f_l$ is such that asymptotically as $kr\to\infty$,

$$f_l(kr)\to(kr)^{-1}\sin(kr-\tfrac{1}{2}l\pi).$$

[9] J. A. Stratton, *Electromagnetic Theory* (McGraw-Hill Book Company, Inc., New York, 1941), Chap. VII.

[10] The $E_l^m$ are defined in such a way as to be proportional to $Y_l^m$. Then, for example, the components of the electric dipole moment vector $\mathbf{E}$, are related to the $E_1^m$ by relationships of the form $E_1^{\pm 1}=2^{-\frac{1}{2}}(E_x\pm iE_y)$, etc. The coefficients are most easily obtained by use of the expansion of a plane transverse wave in spherical waves. The required expansion is given in reference 9.

[11] Any given matrix element of $\dot{S}_l^m$ is to be obtained from the matrix element of $\dot{S}_l^m$ by the Heisenberg relation

$$\langle 1|\dot{S}_l^m|2\rangle=i\omega_{12}\langle 1|S_l^m|2\rangle;$$

hence the form of the operator $S_l^m$ can only be obtained from a complete knowledge of the dynamics of the system. An essential feature of the Siegert theorem is that such knowledge is not required to obtain $P_l^m$. It should be emphasized that $\dot{S}_l^m$, not $S_l^m$, is required for the calculation of a transition probability.

## 4. CORRECTIONS TO ELECTRIC MOMENTS AT HIGH ENERGY

Two quite different features of the Hamiltonian lead to contributions to $S_l^m$ which may be important at high energy. One is due to the influence of mesons on the coupling of the nucleons with the electromagnetic field; it is intimately related to the interaction effects on magnetic moments, those effects that lead to non-additive contributions to nuclear moments.[12] The other feature is present whether or not there are meson currents; it is concerned only with the distribution of (additive) electric currents between orbital and spin motion of the nucleon. This is determined by the ordinary part of $H_1$,

$$H_1(\text{ord})=-(2Mc)^{-1}\sum_\alpha[e_\alpha(\mathbf{p}_\alpha\cdot\mathbf{A}_\alpha+\mathbf{A}_\alpha\cdot\mathbf{p}_\alpha)+e\hbar\mu_\alpha(\boldsymbol{\sigma}_\alpha\cdot\text{curl}\mathbf{A}_\alpha)], \quad (8)$$

where $\mathbf{p}_\alpha$ is the momentum of the $\alpha^{\text{th}}$ nucleon, $\mu_\alpha$ is its magnetic moment, and $\mathbf{A}_\alpha=\mathbf{A}(\mathbf{r}_\alpha)$. When Eq. (7) is applied to $H_1(\text{ord})$, the contribution to the secondary electric moment is found to be

$$\hat{S}_l^m(\text{ord})=-ck^{3-l}[2\pi(2l+1)/l(l+1)]^{\frac{1}{2}}\times\sum_\alpha(e_\alpha\hbar/2Mc)\left[\mu_\alpha\boldsymbol{\sigma}_\alpha\cdot(\mathbf{L}Y_l^m)f_l+Y_l^m\left\{3f_l+r\frac{\partial f_l}{\partial r}+2f_l\sigma\frac{\partial}{\partial r}\right\}\right]_{\mathbf{r}=\mathbf{r}_\alpha}. \quad (9)$$

Such terms are included in the expressions for the electric moments given by Weisskopf,[13] but in a quite different form.

The formalism used here is capable of taking into account the meson effects for which the contribution $H_1(\text{exch})$ to $H_1$ depends only on nucleon variables (exchange effects). For example, such a term is known[14] to be associated with the space exchange potential, no matter what the source of the potential. Furthermore, there is very strong evidence[15] for the existence of a spin-exchange current which must be included in $H_1(\text{exch})$. The two effects suggest an $H_1(\text{exch})$ of the form[16]

$$H_1(\text{exch})=(ie/\hbar c)\sum_{\tau,\tau'}\left\{\left(\int_{\mathbf{r}_\tau}^{\mathbf{r}_{\tau'}}A_s ds\right)J(r_{\tau\tau'})P_{\tau\tau'}+(\boldsymbol{\sigma}_{\tau'}\cdot\text{curl}\mathbf{A}_{\tau'}-\boldsymbol{\sigma}_\tau\cdot\text{curl}\mathbf{A}_\tau)\Phi(r_{\tau\tau'})\right\}, \quad (10)$$

where $\mathbf{r}_\tau$ and $\mathbf{r}_{\tau'}$ are neutron and proton coordinates, respectively, $J(r_{\tau\tau'})P_{\tau\tau'}$ is the space exchange potential, and $\Phi(r_{\tau\tau'})$ is a short-range function of the neutron-proton distance which can be normalized in such a way as to give the correct magnetic moment for $H^3$ and $He^3$. The corresponding $\hat{S}_l^m(\text{exch})$ can be obtained directly by means of Eq. (7).

## 5. APPLICATION TO THE DEUTERON

Application of these considerations has been made to the electric dipole photodisintegration of the deuteron with a view to estimating corrections to the Schiff[4] and Marshall-Guth[5] results. In addition to the corrections associated with $S_1^m(\text{ord})$ and $S_1^m(\text{exch})$, it must be noted that $P_1^m$ is not actually equal to $\frac{1}{2}e(\mathbf{u}\cdot\mathbf{r})$ because of the retardation effect. In fact,

$$P_1^m=(3\pi)^{\frac{1}{2}}ek^{-1}Y_1^m\left\{f_1(kr/2)+r\frac{\partial}{\partial r}f_1(kr/2)\right\},$$

and the Schiff and Marshall-Guth curves must be corrected for the difference $P_1^m-\frac{1}{2}eY_1^m$. Furthermore, contributions to the ${}^3S_1\rightarrow{}^3P_1$ transition may arise from the magnetic quadrupole moment, $M_2^m$, and contributions to ${}^3S_1\rightarrow{}^3P_2$ may arise from both $M_2^m$ and the electric octopole term $E_3^m$.

A preliminary exploration of these corrections and the corrections due to $S_1^m$ showed that an expansion of $f_l$ in powers of $kr$ led to a rapidly convergent series of matrix elements even for photon energies as high as 300 Mev. Convergence occurs because, at high energy, the short wavelength $\lambda$ of the outgoing deuteron wave limits the effective value of $kr$ to $k\lambda\approx(E_\gamma/Mc^2)^{\frac{1}{2}}$. The only significant corrections[17] to the cross section turn out to be those of order $k$ and $k^2$.

The validity of an expansion in powers of $kr$ having been established, it is immediately evident that the detailed calculation of corrections is most easily made on the basis of the simple moment operators described in Sec. 2. The corrections then arise from the contributions to the dipole transition of the (reducible) magnetic quadrupole and electric octopole moments. The first of these yields a correction to the dipole matrix element of order $k$, the second of order $k^2$. Corrections of order $k$ to the cross section are then introduced by interference of the magnetic quadrupole term with the usual electric dipole, and the $k^2$ corrections arise both from the magnetic quadrupole and from the interference of electric octopole with electric dipole terms. The great simplicity of this procedure is illustrated by the fact that all corrections associated with the space exchange

[12] N. Austern and R. G. Sachs, Phys. Rev. **81**, 710 (1951).
[13] V. Weisskopf, Phys. Rev. **83**, 1073 (1951).
[14] R. G. Sachs, Phys. Rev. **74**, 433 (1948).
[15] F. Villars, Helv. Phys. Acta **20**, 476 (1943); R. Avery and R. G. Sachs, Phys. Rev. **74**, 1320 (1948); R. G. Sachs and M. Ross, Phys. Rev. **84**, 379 (1951).
[16] The evidence for the spin dependent contribution arises entirely in connection with magnetic dipole moments; hence only the interaction with a uniform magnetic field has known properties. To fix the interaction with a nonuniform field, we have assumed that the spin-exchange moment results from a change in the intrinsic nucleon moments, i.e., that the corresponding current distribution is localized at the nucleon. The form used here then corresponds to the spin-antisymmetric moment of reference 12. See also R. K. Osborne and L. L. Foldy, Phys. Rev. **79**, 795 (1950); A. Bohr, Phys. Rev. **81**, 134 (1951); H. Miyazawa, Prog. Theoret. Phys. **6**, 263 (1951); A. DeShalit, Helv. Phys. Acta **24**, 296 (1951); F. Bloch, Phys. Rev. **83**, 839 (1951).
[17] Note that relativistic corrections to the nucleon motion may become significant at these energies, although they are not considered here.

term in Eq. (10) vanish for the deuteron since the exchange magnetic $2^l$ pole moment operators all vanish.[18] If the problem is formulated in terms of the reduced moments, the elimination of these terms occurs after a detailed calculation through a cancellation between $\hat{S}_l^m$(exch) and $\hat{P}_l^m$.

The magnetic quadrupole moment contains an orbital term, proportional to the orbital angular momentum operator $\mathbf{L}$, a term associated with the intrinsic spin moments, and a spin interaction term, corresponding to the spin-dependent contribution to Eq. (10). The last of these turns out to be negligible, so it will not be discussed further. Only the orbital part of the moment can lead to interference with the electric dipole term. Since the orbital magnetic quadrupole moment is[12]

$$\mathbf{M}_2(\text{orb})=(e/24Mck)[\mathbf{L}(\mathbf{k}\cdot\mathbf{r})+(\mathbf{k}\cdot\mathbf{r})\mathbf{L}],$$

the ratio of its matrix element to the matrix element of the electric dipole moment is independent of any detailed features of the wave function. The relative correction to the dipole cross section due to interference between these terms is just $-E_\gamma/6Mc^2$ which is five percent at 300 Mev.

The spin term in $M_2$ is[19]

$$\mathbf{M}_2(\text{spin})=\tfrac{1}{2}(e\hbar/2Mck)(\mu_p\boldsymbol{\sigma}_p-\mu_n\boldsymbol{\sigma}_n)(\mathbf{k}\cdot\mathbf{r}),$$

so its matrix element is also proportional to that of the electric dipole moment. The interference term vanishes since $(\mathbf{k}\cdot\mathbf{r})$ yields a wave function orthogonal to that produced by $(\mathbf{u}\cdot\mathbf{r})$. The relative correction to the cross section for the ${}^3S\to{}^3P$ transition is $\frac{2}{3}([\mu_p-\mu_n]/4)^2(E_\gamma/Mc^2)^2$, which amounts to 10 percent at 300 Mev. Note that the angular distribution for this term is $\cos^2\theta$, rather than the usual $\sin^2\theta$ electric dipole distribution. The spin term also produces an electric dipole ${}^3S\to{}^1P$ transition, but the corresponding cross section is much smaller.

[18] The magnetic space exchange moments are shown in reference 12 to be proportional to $\mathbf{r}_\pi\times\mathbf{r}_p$, which vanishes for the deuteron since $\mathbf{r}_\pi=-\mathbf{r}_p$.

[19] This moment is obtained from the second term in Eq. (9) by the prescription outlined in reference 6. Its contribution to the transition has been calculated by Marshall and Guth, reference 5, but they failed to include the orbital term in the magnetic quadrupole matrix element.

The interference between the electric octopole and electric dipole terms cannot be obtained so readily, since the one involves the matrix element of $r^3$ while the other involves the matrix element of $r$. However, an estimate of the contribution indicates that it is about 0.1 percent at 300 Mev. Hence the only important correction to the dipole transition is that due to the magnetic quadrupole moment. Since the interference term is negative, the net correction at 300 Mev is only about 5 percent. This is of the same order as the contribution of the electric quadrupole transition,[4,5] Both are quite small compared to the observed deviations from the Schiff and Marshall-Guth curves.

## 6. CONCLUSIONS

At high energy there is some ambiguity as to the meaning of a given multipole moment. This ambiguity has been removed by introducing the "correct" (irreducible) moments of Sec. 3. Nevertheless, it is much more convenient to work with the usual (reducible) moments whenever an expansion in powers of $kr$ can be justified. That is adequately illustrated by the simplicity of the above discussion of the deuteron photodisintegration.

The deuteron problem has been scrutinized for high energy corrections to the calculated photodisintegration cross section because there are large discrepancies between the observations and the calculated curves. However, all effects considered turn out to be small. Nevertheless, effects of the sort discussed here must be kept in mind because they may be appreciably larger for heavier nuclei.[20]

This discussion owes its existence in large part to conversations between the authors and Professor J. H. D. Jensen concerning the "best possible" definition of a multipole moment.

[20] This is suggested by the following facts: the nuclear radii may be larger than the effective radius of the deuteron; exchange contributions vanish just for the deuteron; and the partial cancellation which occurs between the interference term and the magnetic quadrupole cross section is probably a special property of the deuteron.

# The Alpha-Spectra of $Pu^{239}$ and $Pu^{240}$†

FRANK ASARO AND I. PERLMAN
*Radiation Laboratory and Department of Chemistry, University of California, Berkeley, California*
(Received July 30, 1952)

Utilizing a magnetic alpha-particle spectrograph the complex alpha-spectrum of $Pu^{239}$ was found to consist of three groups: $\alpha_0$ (69 percent), $\alpha_{13}$ (20 percent), and $\alpha_{51}$ (11 percent). The spectrum of $Pu^{240}$ consisted of two groups, $\alpha_0$ (76 percent) and $\alpha_{44}$ (24 percent). The nomenclature $\alpha_x$ refers to that alpha-group which leaves the product nucleus with an energy of $x$ kev above the ground state. The alpha-particle energy of $\alpha_0$ of $Pu^{239}$ was measured as 5.150±0.002 Mev and that of $Pu^{240}$ as 5.162±0.004 Mev. These values are correlated with the gamma-rays and conversion electrons observed by other workers to form a partial decay scheme.

## INTRODUCTION

SOON after the availability of $Pu^{239}$ in supra-tracer quantities the alpha-activity was found to be accompanied by gamma-radiation in low abundance.[1,2] These and later measurements will be discussed below where the decay scheme is considered. The complex alpha-spectrum presumed from these data was first observed directly by Rosenblum, Valadares, and Goldschmidt[3] who employed a large permanent magnet spectrograph. They found the highest energy group in highest abundance and a prominent group at 50-kev lower energy. Some evidence was also found for a very weak group 200 kev below the main group. The present study amplifies these results and attempts to explain the gamma-ray spectrum which has been reported by several sources. Samples of plutonium containing measurable $Pu^{240}$ activity have been used to determine its alpha-particle spectrum.

## EXPERIMENTAL RESULTS

### $Pu^{239}$ Alpha-Spectrum

The magnetic alpha-particle spectrograph used for these measurements has been described in other reports.[4,5] The source in each case was prepared by vacuum sublimation from a tungsten filament to a platinum plate of the dried residue from a solution of plutonium (IV) in hydrochloric acid. The platinum plate was masked to give a ½×1 inch band and in the case of $Pu^{239}$ approximately 2 micrograms was deposited. Samples so prepared have the extreme uniformity demanded for alpha-particle spectroscopy.

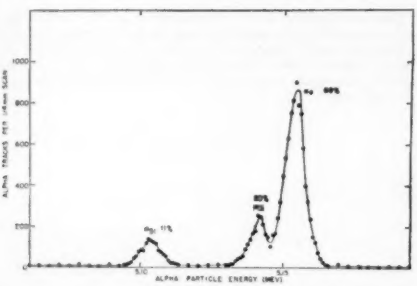


FIG. 1. $Pu^{239}$ alpha-spectrum—peak region.

Figure 1 shows the spectrum of isotopically pure $Pu^{239}$. The source consisted of 2.5 micrograms of $Pu^{239}$ and was exposed for 110 hours. The designations for the alpha-groups follows the same convention previously used in which the highest energy group, presumed to be the ground-state transition, is termed $\alpha_0$ and other groups are shown with subscripts indicating the corresponding energy levels in kilovolts above the ground state. Although no higher energy group than that designated $\alpha_0$ has been detected, there is some evidence to be discussed later which indicates that $\alpha_0$ is not the ground-state transition. If this proves to be so, these designations will have to be revised.

All of the three peaks observed have the same width at half-maximum (~8 kev), and the abundances as indicated were found both by comparing peak heights and by integrating the total alpha-tracks.

In another exposure for 90 hours the slit system was changed to give higher transmission in order to look for rare alpha-groups. The peak widths went up to 21 kev and $\alpha_0$ and $\alpha_{13}$ were no longer clearly resolved. The abundance of $\alpha_{51}$ was found to be 11.7 percent which agrees with the other measurement cited. A careful search was made for other alpha-groups and the data are recorded in Fig. 2. The energy range covered was 4.82–5.57 Mev which extends from 330 kev below the main group to 430 kev above it. No alpha-group was found and the limits can be set as follows: from 25 kev above $\alpha_0$ to 430 kev there is no group in greater than 0.15 percent abundance; from 70 kev below $\alpha_0$ (20 kev below $\alpha_{51}$) to 330 kev there is no group in greater than 0.3 percent abundance. The plate from which Fig. 1 was derived was also counted over an extended range and the results were substantially the

† This work was performed under the auspices of the AEC.
[1] A. Ghiorso, Metallurgical Laboratory Report CK-1511 (April, 1944) (unpublished).
[2] Sullivan, Kohman, and Swartout, Hanford Report HEW-3-1635 (February, 1945) (unpublished).
[3] Rosenblum, Valadares, and Goldschmidt, Compt. rend. **230**, 638 (1950).
[4] F. L. Reynolds, Revs. Sci. Instr. **22**, 749 (1951).
[5] Asaro, Reynolds, and Perlman, Phys. Rev. **87**, 277 (1952).

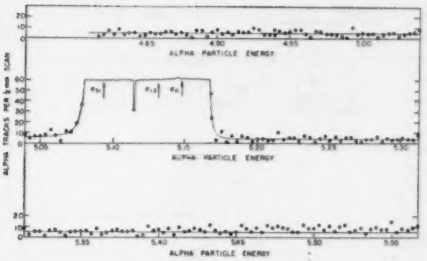


FIG. 2. $Pu^{239}$ alpha-spectrum—high and low energy region.

same although the limits of detection were not so low because of the fewer total tracks recorded.

The energy for $Pu^{239}$ was determined by comparing $\alpha_0$ with $Po^{210}$ as the standard for which the particle energy was taken as 5.298 Mev.[6] The energy for $\alpha_0$ of $Pu^{239}$ was found to be 5.150±0.002 Mev as compared with the other spectrograph value,[3] 5.147, obtained using ThC as a standard.

These spectrograph values are in good agreement with reported values obtained using ionization chambers and range methods. Cranshaw and Harvey[7] using an ionization chamber with a pulse-height analyzer reported 5.159 (±0.005) Mev and Jesse and Forstat[8] obtained 5.140 (±0.005) Mev by measuring total ionization current. An air range determination by Chamberlain *et al.*[9] gave 5.15 Mev.

The energies of the two shorter range groups were obtained from their displacements from the main group using the dispersion of the instrument as described previously.[5] The differences in energy from the main group, $\alpha_0$, were 12.8±0.7 kev and 49.7±0.7 kev. Rosenblum, Valadares, and Goldschmidt[3] resolved $\alpha_{51}$ and found its energy to be 50 kev lower than the main group and our result is in excellent agreement for this group. Adding a correction of 1.7 percent to these alpha-particle energy differences to obtain the spacing between energy levels and rounding off to the nearest kilovolt, the level differences become 13 and 51 kev, hence $\alpha_{13}$ and $\alpha_{51}$. These energies would correspond to gamma-ray energies between the appropriate levels.

### $Pu^{240}$ Alpha-Spectrum

This isotope of plutonium is an alpha-emitter of 6600-year half-life[10] and is best prepared by neutron capture by $Pu^{239}$.[11] Its alpha-energy is known to be very close to that for $Pu^{239}$ and had not previously been resolved for sure.

A sample containing $5\times10^5$ disintegrations per minute of mixed $Pu^{239}$ and $Pu^{240}$ activities was exposed for 46 hours, and the spectrum shown in Fig. 3 was registered. The peaks were readily assigned to their respective isotopes because (1) mass spectrographic analysis indicated that $Pu^{240}$ was in an abundance such that its alpha-activity should predominate,[12] and (2) the energy differences and relative abundances of the three peaks assigned to $Pu^{239}$ were in close agreement with those for pure $Pu^{239}$ (see Fig. 1).

The energy of the main group of $Pu^{240}$ is 12±2 kev greater than that for $Pu^{239}$. Using our value, 5.150 Mev, for the energy of the $\alpha_0$ group of $Pu^{239}$, the energy for $Pu^{240}$ $\alpha_0$ group is 5.162. Since we are fairly certain that the most abundant group of an even-even alpha-emitter represents the ground-state transition we may then calculate the decay energy for $Pu^{240}$ as 5.250 Mev.

The second alpha-group of $Pu^{240}$ is 43.5±2 kev lower energy than the main group; hence it is designated $\alpha_{44}$ signifying that it leads to a state 44 kev above the ground state. Its abundance is 24 percent; therefore the partial alpha half-lives for the two groups, based on the 6600-year measured half-life, are 8700 years and 27,000 years. The half-life *versus* energy relationships for these groups are close to expectations of alpha-decay as can be seen from Fig. 4. The curve is the calculated half-life *versus* energy relationship for plutonium isotopes in which the rigorous one-body decay theory was applied.[13,14] The nuclear radii were taken to follow the function, $r=1.51A^{\frac{1}{3}}\times10^{-13}$ cm, and the effective alpha-energies were obtained by adding to the decay energies 39 kev to account for the change in orbital electron binding as suggested by Ambrosino and Piatier.[15] A similar curve for curium and its method of derivation are shown in another publication.[6]

Figure 4 shows that both $Pu^{240}$ groups are in close agreement with the theory, a situation which we now accept as normal for an even-even nuclide. Similarly

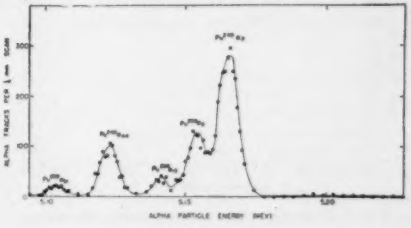


FIG. 3. $Pu^{239,240}$ alpha-spectrum.

[6] M. G. Holloway and M. S. Livingston, Phys. Rev. **54**, 18 (1938).
[7] T. E. Cranshaw and J. A. Harvey, Can. J. Research **A26**, 243 (1948).
[8] W. P. Jesse and H. Forstat, Phys. Rev. **73**, 926 (1948).
[9] Chamberlain, Gofman, Segrè, and Wahl, Phys. Rev. **71**, 529 (1947).
[10] Inghram, Hess, Fields, and Pyle, Argonne National Laboratory Report ANL-4653 (June, 1951) (unpublished).
[11] Ghiorso, James, Morgan, and Seaborg, Phys. Rev. **78**, 472 (1950).
[12] We are indebted to Dr. S. G. Thompson for the plutonium used in this measurement and to Mr. F. L. Reynolds for the mass analysis.
[13] M. A. Preston, Phys. Rev. **71**, 865 (1947).
[14] I. Kaplan, Phys. Rev. **81**, 962 (1951).
[15] G. Ambrosino and H. Piatier, Compt. rend. **232**, 400 (1951).

the groups for $Pu^{239}$ follow the now familiar pattern of hindered decay expected of nuclides with odd nucleons.

## DISCUSSION OF DECAY SCHEME

It will be pointed out that the $Pu^{239}$ alpha-spectrum as observed here cannot explain all features of the gamma-ray and conversion electron spectra which have been reported. First we shall examine the area of agreement which is indicated in Fig. 5.

A gamma-ray of 50 kev was reported early by Ghiorso,[1] and this has been abundantly confirmed. West and Dawson[16] using a proportional counter spectrometer found a 52.3±0.4 kev photon in an abundance of $7\times10^{-5}$ per alpha-particle, Martin[17] in this laboratory has measured this gamma-ray as 53±2 kev with a scintillation spectrometer, while two laboratories[18,19] have found conversion electrons corresponding to a 50-kev gamma-ray in coincidence with alpha-tracks in $Pu^{239}$ impregnated nuclear emulsions. Albouy and Teillac[18] found the electrons to be present to the extent of 16 per 100 total alpha-particles, while Dunlavey and Seaborg[19] found 12.5 electrons per 100 alpha-particles. It seems almost certain that this gamma-ray represents the transition between the levels reached by $\alpha_{51}$ and $\alpha_0$ because of the agreement in energy and moderate agreement in abundance. Rosenblum and co-workers[3] reported a much higher abundance than ours for $\alpha_{51}$, but their resolution would have been more difficult.

West and Dawson[16] also found a gamma-ray of 37.2±0.5 kev in low abundance which corresponds exactly to a transition between $\alpha_{51}$ and $\alpha_{13}$. They also found in low abundance gamma-rays of 59.2 and 32.0 kev. The close agreement in energy of one of these photons with that for the most prominent gamma-ray of $Am^{241}$ (59.78 kev,[20] 59.7 kev[21]) makes it tempting to consider that it is from $Am^{241}$ which grew from $Pu^{241}$.[22] A similar but more extensive series of conversion electron lines has been found by Wagner, Freedman, and Engelkemeir[23] in a sample not isotopically pure $Pu^{239}$. The latter paper reports four weak lines in pure $Pu^{239}$ and these could be interpreted as the $L_I$ or $L_{II}$, $L_{III}$, $M$, and $N$ lines of the 51-kev transitions or two of them could arise from the 38-kev transition.

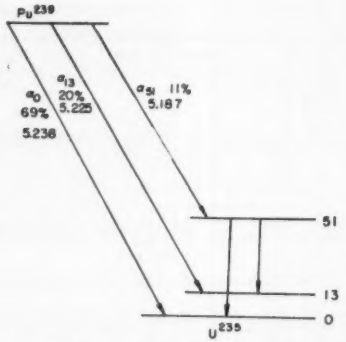


FIG. 5. $Pu^{239}$ partial decay scheme.

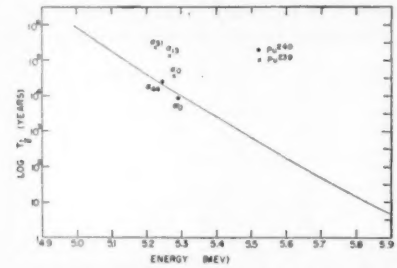


FIG. 4. Theoretical alpha-decay curve for plutonium.

The preceding discussion shows that there need be no sharp disagreement between our alpha-spectrum and the gamma-ray transitions so far considered. However, there is harder gamma-radiation which is more difficult to explain. There have been reported gamma-rays of 300 kev[1] and 420 kev[2] in very low abundance, and these could well correspond to low energy alpha-groups in quantity below our level of detection. Another gamma-ray can be deduced from the work by Albouy and Teillac[18] and by Dunlavey and Seaborg[19] who both measured electron tracks stemming from alpha-tracks in nuclear emulsions. Albouy and Teillac reported theirs as the "$K$ conversion electrons from a 200-kev gamma-ray" which would mean that the electron line was 100 kev and the abundance as 0.1–1 percent of the alpha-particles. It is doubtful that these electrons are $K$ shell converted because the corresponding $K$ x-rays have not been seen in requisite abundance. Dunlavey and Seaborg found similar electrons in the energy range 100±20 kev in 0.5 percent abundance. If the electrons are the $L$ conversion line of an ~120-kev gamma-ray and the abundance is correct, the corresponding alpha-group should have been seen. According to the data of Fig. 3 an alpha-group of lower energy than $\alpha_0$ by 70 kev or more would be detected if present in 0.3 percent

[16] D. West and J. K. Dawson, Proc. Phys. Soc. (London) **64**, 586 (1951).
[17] D. Martin (unpublished data).
[18] G. Albouy and J. Teillac, Compt. rend. **232**, 326 (1951).
[19] D. Dunlavey and G. T. Seaborg, Phys. Rev. **87**, 165 (1952).
[20] C. I. Browne and I. Perlman, Phys. Rev. **85**, 758 (1952).
[21] Beling, Newton, and Rose, Phys. Rev. **86**, 797 (1952).
[22] Dr. West has kindly informed us that another article is in publication showing that the 59-kev gamma-ray is from $Am^{241}$ and that the 32-kev peak may have some other origin.
[23] Wagner, Freedman, and Engelkemeir, AEC Report AECD-3304 (November, 1951) (unpublished).

abundance or greater. The discrepancy between the abundance of the ~120-kev transition and the absence of a corresponding alpha-group is too close to the limits of error in measurement to be considered real at this stage. If it should prove to be real, this may be taken as evidence that the ground-state transition for the alpha-decay of $Pu^{239}$ has not yet been seen.

We wish to acknowledge the assistance of Miss Beverly Turner and Mr. James Vanderveen in counting the alpha-tracks.

PHYSICAL REVIEW VOLUME 88, NUMBER 4 NOVEMBER 15, 1952

# Radioisotopes of Osmium*

J. B. Swan† and R. D. Hill
*Physics Department, University of Illinois, Urbana, Illinois*

(Received July 30, 1952)

Osmium activities of 15-day and 32-hour half-lives have been identified with $Os^{191}$ and $Os^{193}$, respectively. A 14-hour activity, decaying by a 74.2-kev gamma-transition into the 15-day activity, has been assigned to an isomeric state in $Os^{191}$. The decay scheme of $Os^{191}$ has been investigated and a 7/2+ assignment has been made to the 15-day ground state and an $i_{13/2}$ assignment to the 14-hour isomeric state. The 7/2+ state is attributed to a coupling of an odd number of $i_{13/2}$ neutrons.

## INTRODUCTION

OSMIUM has seven stable isotopes, with mass numbers from 184 to 192, except for vacancies at 185 and 191. Three radioisotopes have so far been observed, and these have been allocated to mass numbers 185, 191 and 193.[1–13] We report in the present paper a new activity and a revised assignment of two of the already known activities.

## $Os^{191}$ AND $Os^{191m}$: EXPERIMENTAL OBSERVATIONS

Ordinary osmium, in powdered metallic form, was irradiated by neutrons in the heavy water pile at Argonne. The internal conversion electron spectrum, measured with 180° magnetic spectrographs, showed three groups of conversion lines. Accurate energy determinations, which are given in Table I, indicate that the gamma-transitions of 41.7 and 129.1 kev take place in iridium and that the 74.2-kev gamma-transition occurs in osmium.

Lifetime tests on the individual conversion lines showed that there was an initial rise in the intensity of the 41.7- and 129.1-kev lines, which changed over after a period of several days into a constant decay of 15-day half-life. On the other hand, the 74.2-kev transition lines decayed throughout with a half-life of 14±2 hours. A set of decay curves for a particular source, which was bombarded one day in a pile, is shown in Fig. 1. It is clear that the growth of the 41.7- and 129.1-kev transition intensities is consistent with a partial production of the 15-day activity from a parent of 14-hour half-life.

Osmium was also bombarded by gamma-rays from a 22-Mev betatron, using an internal target arrangement.[14] A conversion spectrum the same as, although weaker than, that from a pile irradiated source was obtained. The 15-day activity is therefore to be identified with mass number 191, instead of 193, and the 14-hour activity is thus an isomer of $Os^{191}$. The present assignment of the 15-day activity is in accord with beta-disintegration energy systematics, as pointed out by Way.[15,‡]

TABLE I. Energies in kev of electron conversion lines from $Os^{191}$ and $Os^{191m}$ activities.

| Gamma-transition | Sub-shell origin of conversion electrons | | | | | | | |
|---|---|---|---|---|---|---|---|---|
| | $K$ | $L_I$ | $L_{II}$ | $L_{III}$ | $M_I$ | $M_{II}$ | $M_{III}$ | $N$ |
| 41.70 kev | | ··· | 28.85 | 30.48 | ··· | 38.80 | 39.19 | 41.15 |
| 74.17 kev | | 61.24 | 61.78 | 63.36 | 71.09 | ··· | 71.72 | 73.45 |
| 129.1 kev | 53.15 | 115.49 | 116.14 | 117.97 | | 126.29 | | 128.76 |

* Assisted by the joint ONR and AEC program.

† Fulbright and University of Illinois Postdoctoral Fellow. On leave from University of Western Australia, Perth, Australia.

[1] Kurtchatow, Latyschew, Nemenow, and Selinow, Physik Z. Sowjetunion **8**, 589 (1935).

[2] E. Zingg, Helv. Phys. Acta **13**, 219 (1940).

[3] G. T. Seaborg and G. Friedlander, Phys. Rev. **59**, 400 (1941).

[4] L. J. Goodman and M. L. Pool, Phys. Rev. **70**, 112 (1946); **71**, 288 (1946).

[5] Cork, Schreffler, and Fowler, Phys. Rev. **72**, 1209 (1947).

[6] L. I. Katzin and M. Pobereskin, Phys. Rev. **74**, 264 (1948).

[7] D. Saxon, Phys. Rev. **74**, 1264 (1948); Atomic Energy Commission Report, AECD, 1860 (1948) (unpublished).

[8] Mandeville, Sherb, and Keighton, Phys. Rev. **74**, 888 (1948).

[9] Bunker, Canada, and Mitchell, Phys. Rev. **80**, 126 (1950); **79**, 610 (1950).

[10] F. K. McGowan, Oak Ridge National Laboratory Report, ORNL-952 (1951) (unpublished); Phys. Rev. **79**, 404 (1950).

[11] T. C. Chu, Phys. Rev. **79**, 582 (1950).

[12] E. Kondaiah, Ark. Fys. **3**, 47 (1951).

[13] *Nuclear Data*, National Bureau of Standards, Circular No. 499 (1950), p. 222.

[14] R. A. Becker, Rev. Sci. Instr. **22**, 773 (1951).

[15] K. Way, private communication and reference 13.

‡ *Note added in proof:*—A revision of the original $Os^{191}$, $Os^{193}$ assignment by Seaborg and Friedlander (see reference 3) was later made by G. Friedlander (quoted in *Table of Isotopes*, Seaborg and Perlman, Revs. Modern Phys. **20**, 585 (1948)). According to J. M. Hollander (private communication) this revision was also made on the basis of γ-irradiations.

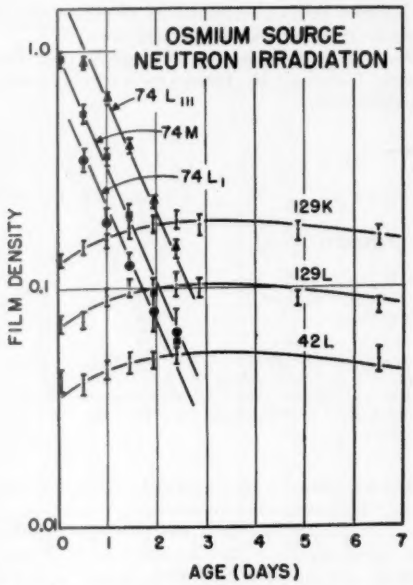


FIG. 1. Decay curves of conversion lines from the 74-kev gamma-transition of $Os^{191m}$ and the 129- and 42-kev gamma-transitions of $Os^{191}$. Bombardment time of the source was one day. Zero time of the abscissa corresponds to the end of the bombardment.

In order to investigate whether there was any beta-decay associated with the 14-hour activity, an osmium source prepared by gamma-irradiation was studied using a lens spectrometer. The spectrum observed several hours after an 8-hour irradiation in the 22-Mev betatron is shown in Fig. 2. We conclude that direct beta-decay from the 14-hour isomeric level in Os does not occur to the extent of 5 percent, if at all, of the isomeric transition intensity from this level.

Investigations of the beta-spectrum of the 15-day $Os^{191}$ activity were also made with lens and 180° spectrometers. However, our results, on account of the too-thick sources, did not lead to accurate values of the conversion coefficient of the 42- and 129-kev radiations. We are essentially in agreement with other workers[7,9,12] that there is a beta-spectrum with an upper end point in the neighborhood of 140 kev.

TABLE II. Relative intensities of conversion lines from $Os^{191}$ and $Os^{191m}$ activities.

| Gamma-transition | Sub-shell origin of conversion electrons | | | | | | | |
|---|---|---|---|---|---|---|---|---|
| | $K$ | $L_I$ | $L_{II}$ | $L_{III}$ | $M_I$ | $M_{II}$ | $M_{III}$ | $N$ |
| 41.70 kev | | ··· | 32 | 40 | ··· | 11 | 18.5 | 9.5 |
| 129.1 kev | 100 | 29.5 | 10.5 | 6.0 | | 11.5 | | 3.5 |
| 74.17 kev | | 42 | 23.5 | 100 | 14 | ··· | 35 | 15 |

The 74.17-kev transition intensities are not directly comparable with the others.

An important question to be resolved in connection with the decay scheme of $Os^{191}$ is whether the 42- and 129-kev transitions decay in cascade or parallel. Experiments to show whether gamma- or x-rays were or were not in coincidence were inconclusive. However, more elaborate experiments using a double slit 180° beta-ray spectrometer[16] showed that the 42-$L$ and 129-$L$ conversion electrons were definitely in coincidence.

The relative intensities of the 74.2- 41.7-, and 129.1-kev transition conversion lines were determined photographically and their values are given in Table II.

## $Os^{191}$: DISCUSSION

The multipolarities of the 129.1- and 41.7-kev transitions have been obtained from the following arguments.

Kondaiah's value[12] of the ratio of the $L$-conversion line intensity to the total $Os^{191}$ beta-intensity, in conjunction with the conversion line intensities of Table II, yields a value of 1.36 for the $K$-conversion coefficient of the 129-kev transitions. Using Rose's tables,[17] this value is in best agreement with an 0.42:0.58 mixture of $M1$:$E2$ multipole radiations. Our value of 2.2 for the $K/L$ ratio of the 129-kev transition agrees excellently with Kondaiah's value of 2.1, and using the empirical $K/L$ ratios of Goldhaber and Sunyar,[18] the ratio of the $M1$:$E2$ mixture is 0.64:0.36. The ratios of the intensities of the $L_I$:$L_{II}$:$L_{III}$ components of the 129-$L$ conversion line, using Gellman's[19] unscreened theoretical $L$-shell conversion calculations, indicate an 0.8:0.2 mixture of $M1$:$E2$.

The multipolarity of the 42-kev transition is more difficult to obtain. Qualitatively, however, both our own scintillation counter experiments and photoelectron spectrometer studies of the 15-day $Os^{191}$ show that the 42-kev transition is highly converted. Beta-conversion electron coincidence experiments[12] also show that the 42-kev gamma transition is certainly of multipole order less than three. One possibility of determining the multipolarity of this transition is through a comparison of theoretical and experimental $L_I$:$L_{II}$:$L_{III}$ ratios. According to Gellman's analysis[19] these ratios are as follows: 1.0:0.68:1.0 for $E1$, 0.03:0.90:1.0 for $E2$, and 1.0:0.065:0.011 for $M1$. The experimental ratios are 0.0:0.81:1.0, which agree well with pure $E2$. An assignment of $M2$, for which there are no theoretical data, can be ruled out on beta- and gamma-transition considerations. The theoretical[19] total $L$-shell conversion coefficient of a 42-kev $E2$ transition is ~200.

If we conclude that the 129-kev transition is a 3:1 mixture of $M1$:$E2$ and the 42-kev transition is pure $E2$, we find that the total intensity of the 129-kev

[16] Katz, Hill, and Goldhaber, Phys. Rev. **78**, 9 (1950).
[17] Rose, Goertzel, Spinrad, Harr, and Strong, Phys. Rev. **83**, 79 (1951); Rose, Goertzel, and Perry, Oak Ridge National Laboratory Report ORNL-1023 (1951) (unpublished).
[18] M. Goldhaber and A. W. Sunyar, Phys. Rev. **83**, 906 (1951).
[19] Gellman, Griffith, and Stanley, Phys. Rev. **85**, 944 (1952).

transition is approximately twice the 42-kev transition intensity. Smaller mixtures of $M1$ in the 129-kev transition would necessarily increase the relative intensity of this transition.

Since it has been shown that the two transitions are in cascade it must be concluded that the 42-kev transition precedes the 129-kev transition. In this case, since the ground state $Ir^{191}$ assignment[20] is $d_{3/2}$, the spins and parities of the 129.1- and 170.8-kev excited states are 5/2+ and 9/2+, respectively. The 5/2+ assignment is in accord with a $d_{5/2}$ shell theory level, but there is no theoretical single-particle assignment for the 9/2+ level.

The $Os^{191}$ beta-transition of energy only 142 kev and half-life 15 days predicates an allowed transition. According to the cascade scheme proposed above, approximately equal intensity beta-branches would proceed to the 170.8-kev and 129.1-kev excited states. Both component spectra would necessarily be allowed, the lower energy component having $\log ft = 5.2$ and the higher energy component having $\log ft = 5.6$. The level assignment of the $Os^{191}$ ground state would then be unequivocally 7/2+.

### $Os^{191m}$: DISCUSSION

The multipolarity of the 74.2-kev transition has been inferred from lifetime considerations. Probably the most uncertain factor in this analysis concerns the internal conversion coefficients, $\alpha_T$, which influence the transition lifetimes, $\tau_\gamma$, through the relationship, $\tau_\gamma = \tau_{exp}(1+\alpha_T)$. Estimates of the internal conversion coefficients have been obtained in the following way.

As the gamma-transition energy is just in excess of the $K$-shell binding energy (73.87 kev), estimates of the threshold $K$-shell conversion coefficients for a number of multipole radiations were obtained from the tables of Spinrad and Keller.[21] Very approximate estimates of the intense $L$-shell conversions were then obtained using the empirical values of the $K/L$ ratios of Goldhaber and Sunyar.[18]

For $E3$ and $E4$ transitions, $\log_{10}(\tau_\gamma \rho^{2l})$ has the values of 9.4 and 11.6, respectively, and for $M3$ and $M4$ transitions, $\log_{10}(\tau_\gamma \rho^{2l-2})$ has the values 8.5 and 10.9, respectively. These values for $E3$ and $M3$ are approximately a factor $10^2$ higher than the "average" observed values for a 74-kev transition of either of these multipoles.[18] For $E4$ and $M4$, the values are a factor of approximately $10^3$ lower than the average observed values. This fact alone probably precludes an $M4$ assignment, since it is generally found that $M4$ transitions lie much closer than a factor of $10^3$ to the average value.

As the $Os^{191}$ ground state has been given a 7/2+ assignment, and as the isomeric transition is very probably an octopole transition, it follows that the spin

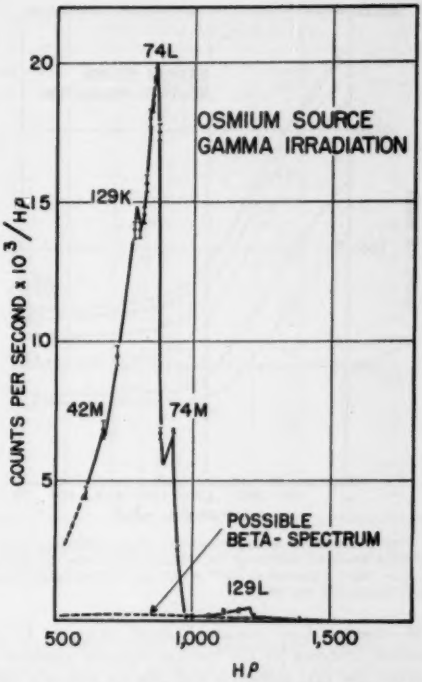


FIG. 2. Beta- and conversion-electron spectra of $Os^{191m}$ and $Os^{191}$.

of the isomeric state is either 1/2 or 13/2. Of the four states having these spins, the even parity, 1/2 spin, state can be ruled out on the grounds of the absence of a direct beta-transition from $Os^{191m}$ to the $Ir^{191}$ ground state. Both the odd parity, 1/2 spin, and even parity, 13/2 spin, states are in accord with $p_{1/2}$ and $i_{13/2}$ levels of nuclear shell theory. An isomeric transition from a $p_{1/2}$ state would be $E3$, and from an $i_{13/2}$ state would be $M3$. A decision on whether this transition is $M3$ or $E3$ can be reached using the empirical $L$ sub-shell conversion ratios determined by Mihelich.[22] For $M3$,

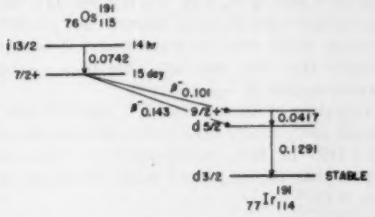


FIG. 3. Proposed decay scheme of $Os^{191m}$ and $Os^{191}$.

[20] Brix, Kopfermann, and Siemens, Naturwiss. **37**, 397 (1950); H. Kopfermann, Naturwiss. **38**, 29 (1951).

[21] B. I. Spinrad and L. B. Keller, Phys. Rev. **84**, 1056 (1951).

[22] J. W. Mihelich, Phys. Rev. **87**, 646 (1952) and private communication.

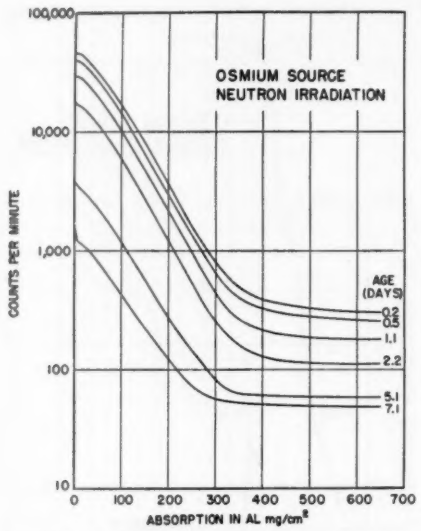


FIG. 4. Aluminum absorption curves of the radiations from a neutron-irradiated source of Os. These curves show the strong 1-Mev beta-component of $Os^{189}$ which has an end point at approximately 350 mg/cm².

the expected $L_{III}$ intensity is about twice the $L_I$ intensity, whereas for $E3$, the $L_{II}$ intensity appears to exceed the $L_{III}$ intensity, with the $L_I$ intensity very weak. The experimental $L_I$:$L_{II}$:$L_{III}$ ratios therefore decide strongly in favor of $M3$. This assignment is shown in Fig. 3.

The existence of a 7/2+ state in the region of $Os^{191}$, which has even $Z$ and 115 neutrons, is not predicted by the independent particle nuclear shell theory. Odd neutron levels in this shell are $h_{9/2}$, $f_{7/2}$, $f_{5/2}$, $p_{3/2}$, $p_{1/2}$, and $i_{13/2}$. As an odd number of neutrons can lead to an even parity state only if they are of even parity, the 7/2+ state is therefore attributed to a coupling of an odd number of $i_{13/2}$ neutrons or possibly a coupling of an $i_{13/2}$ neutron with the nuclear core.

There are two other examples[23] of 7/2+ levels in this region. $W^{183}$ and $W^{185}$, with $N=109$ and 111, respectively, exhibit 7/2+ isomeric states. It was pointed out that these states were anomalous, and it now seems reasonable that they may also arise from a coupling of an odd number of $i_{13/2}$ neutrons.

Systematics of isomer levels[23,24] indicate that $p_{1/2}$ levels are energetically close to $i_{13/2}$ levels in the region of $N=117$. In fact, extrapolation of level trends indicates that the $i_{13/2}$ levels might lie lowest in the region of $Os^{191}$.

[23] M. Goldhaber and R. D. Hill, Revs. Modern Phys. **24**, 179 (1952).
[24] R. D. Hill, Brookhaven Quarterly Report **11**, 18 (1951) (unpublished).

## $Os^{193}$: OBSERVATIONS AND DISCUSSION

The identification of the 32-hour beta-activity as $Os^{193}$ was made on the basis of lifetime and absorption measurements. Osmium sources obtained from pile irradiations exhibited a strong 32-hour beta-activity, and aluminum absorption curves indicated a predominant 1-Mev beta-component which decayed with this half-life. Curves showing the decay of the 1-Mev component are given in Figs. 4 and 5. Osmium sources from betatron irradiations showed an initial decay of 14 hours half-life, with no 32-hour activity observable. Absorption curves also gave no indication of the 1-Mev beta-component associated with the 32-hour activity. Curves showing the decay of the $Os^{191}$ radiations are given in Fig. 6.

In the pile irradiated sources several very weak conversion lines were observed to decay with half-lives intermediate between 14 hours and 15 days. The gamma-transitions identified from $K$ and $L$ conversion lines were of energies 215, 323, and 460 kev. There were also weak intensity lines of 55.2, 59.4, 60.0, and 67.2 kev. The 59.4- and 60.0-kev lines appear to be $L_I$ and $L_{II}$ conversion lines of a 72.4-kev gamma-transition. Some or all of these transitions could have half-lives consistent with 32 hours.

Gamma-transitions associated with the 32-hour activity have been reported previously[4,8,10] at energies

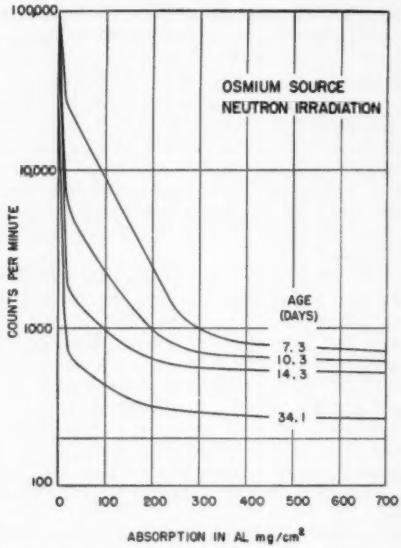


FIG. 5. Aluminum absorption curves of radiations from a neutron-irradiated source of Os. These curves were taken at later times and with the source closer to the counter than in the case of Fig. 4. The curves illustrate the disappearance of the $Os^{193}$ beta-component, as well as the increasing similarity with the curves of Fig. 6, as the Os source ages.

of 1.58, 1.17, 0.22, and 0.065 Mev. If the 59.4- and 60.0-kev conversion lines are to be identified with the 65-kev transition observed in delayed-coincidence by McGowan,[10] then it must be concluded that this transition is only very weak compared with the beta-intensity of $Os^{193}$. McGowan has identified the 65-kev transition as $E2$. According to Gellman *et al.*[19] the total $L$ conversion of such a transition is approximately nineteen. From the measured intensity of the 59.4- and 60.0-kev lines relative to the intensity of the 32-hour beta-spectrum, we conclude that the "65-kev" transition occurs to the extent of less than 2 percent of the beta-decays from $Os^{193}$.

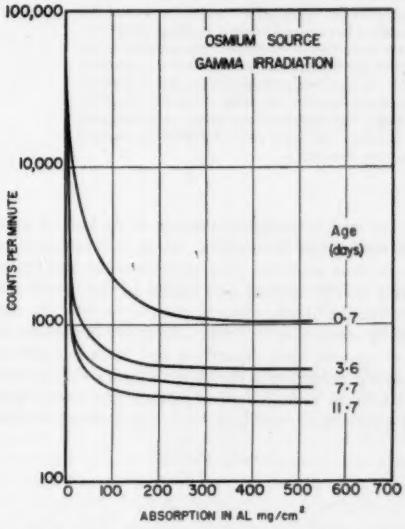


FIG. 6. Aluminum absorption curves of radiations from a gamma-irradiated source of Os. These curves show an electron component of end point approximately 20 mg/cm² which is characteristic of $Os^{191}$.

TABLE III. Internal conversion lines of long half-lives from neutron-irradiated osmium.

| Energy (kev) | Interpretation | $\gamma$-energy (kev) | Activity |
|---|---|---|---|
| 152 | $\gamma_1-L$ in Re | 164 | ? |
| 160 | $\gamma_1-M$ in Re | 163 | ? |
| 163 | $\gamma_2-K$ in Re | 235 | ? |
| 223 | $\gamma_2-L$ in Re | 235 | ? |
| 231 | $\gamma_2-M$ in Re | 234 | ? |
| 219 | $\gamma_3-K$ in Pt | 297 | $Ir^{189}$ |
| 284 | $\gamma_3-L$ in Pt | 297 | $Ir^{189}$ |
| 296 | $\gamma_3-M$ in Pt | 299 | $Ir^{189}$ |
| 231 | $\gamma_4-K$ in Pt | 309 | $Ir^{189}$ |
| 296 | $\gamma_4-L$ in Pt | 309 | $Ir^{189}$ |
| 304 | $\gamma_4-M$ in Pt | 307 | $Ir^{189}$ |
| 240 | $\gamma_5-K$ in Pt | 318 | $Ir^{189}$ |
| 304 | $\gamma_5-L$ in Pt | 317 | $Ir^{189}$ |
| 312 | $\gamma_5-M$ in Pt | 315 | $Ir^{189}$ |
| 391 | $\gamma_6-K$ in Pt | 469 | $Ir^{189}$ |
| 456 | $\gamma_6-L$ in Pt | 469 | $Ir^{189}$ |
| 580 | $\gamma_7-K$ in Re | 652 | $Os^{185}$ |
| 641 | $\gamma_7-L$ in Re | 653 | $Os^{185}$ |
| 653 | $\gamma_7-M$ in Re | 656 | $Os^{185}$ |

## $Os^{185}$: OBSERVATIONS

A two-month old neutron-irradiated Os source was examined in a lens spectrometer and conversion lines corresponding to previously reported[9,25] transitions of 0.65 and 0.88 Mev were observed. Prolonged exposures of the same source in 180° magnetic spectrographs brought out a number of conversion lines of weak intensities and also of long half-lives. An attempt has been made to analyze and identify these lines in Table III.

[25] M. M. Miller and R. G. Wilkinson, Phys. Rev. 82, 981 (1951).

# The Production of Charged Photomesons from Deuterium and Hydrogen. I*

R. S. White, M. J. Jacobson,† and A. G. Schulz‡
*Radiation Laboratory, Department of Physics, University of California, Berkeley, California*
(Received June 30, 1952)

Hydrogen and deuterium gases have been bombarded in a gas target at a temperature of 77°K and at a pressure of about 140 atmospheres by the 318±10 Mev "spread-out" bremsstrahlung photon beam of the Berkeley electron synchrotron. The charged $\pi$-mesons which were produced were collimated at angles of 45°, 90°, and 135° to the beam direction. The $\pi^+$ mesons were detected with *trans*-stilbene scintillation crystals using $\pi\mu$, $\pi\beta$, and $\pi\mu\beta$ delayed coincidences and $\pi^+$ and $\pi^-$ mesons were detected with Ilford C-2 200-micron nuclear emulsions. The ratios of the numbers of $\pi^-$ to $\pi^+$ mesons produced in deuterium were 0.96±0.10, 1.09±0.12, and 1.21±0.17 for the angles of 45°, 90°, and 135°, respectively. No variation of the ratio with meson energy, outside statistics, was observed. Absolute values for the $\pi^+$ meson energy distribution functions from hydrogen and deuterium per "equivalent quantum" have been measured at each of the above production angles. The differential and total cross sections have been obtained by integrating over energy and angle, respectively. The experimental ratios of the deuterium to hydrogen cross sections are in good agreement with the phenomenological theory of Chew and Lewis when the Hulthén deuteron function with $\beta=6\alpha$ is used in the initial state, plane waves are used for the nucleons in the final state, and the bremsstrahlung cutoff is taken into account. The statistics of the data are, however, not sufficient to determine the amount of spin interaction. The excitation functions for hydrogen and deuterium and points on the angular distribution curves in the center-of-mass system have been obtained. An upper limit of 0.08 of the charged $\pi$-meson cross section was obtained for $\mu$-meson production from deuterium.

## I. INTRODUCTION

SINCE the first report of photomeson production,[1] a number of photomeson production experiments have been performed.[2–12] It is quite probable that production experiments with nuclei of a large number of nucleons yield more information about the structure of the nucleus, and the meson interaction with nucleons before leaving the nucleus, than about the initial production of the meson itself. For information concerning the production, therefore, experiments with light nuclei should be performed. Of the light nuclei the photomeson production from the free proton or neutron should be the easiest to interpret theoretically because of the absence of nucleon-nucleon interaction complications. These free nucleon reactions are thought to be

$$\gamma+p\rightarrow n+\pi^+,$$
$$\gamma+n\rightarrow p+\pi^-.$$

The first reaction has been studied by Steinberger, Bishop, and Cook[4–6] and by Feld *et al.*,[11] and the second has not been investigated because of the lack of a concentrated target of neutrons. As an alternative to the free nucleon reactions, this experiment has utilized the loosely bound neutron and proton in the deuteron to compare the above production cross sections. In addition, by comparing the cross sections for the production of $\pi^+$ mesons from deuterium and hydrogen one can study the reduction in the deuteron cross section which results from exclusion effects which was first pointed out by Feshbach and Lax.[13,14] In the deuteron reaction

$$\gamma+d\rightarrow 2n+\pi^+$$
$$\rightarrow 2p+\pi^-,$$
$$^3S,\quad {}^1S, {}^3P, \cdots$$

since the final nucleon state must be antisymmetric, the resulting neutrons or protons can only end in the $^1S$, $^3P$, $\cdots$ states. Since the deuteron is initially in the $^3S$ state, unless the proton flips its spin in the production of a meson the available phase space is reduced relative to that for the production from a free proton, or neutron. Chew and Lewis[15,16] have pointed out that in addition to the above effect the cross section will be further reduced because of the reduction in phase space due to the binding energy of the deuteron. Using a phenomenological approach, they have calculated the ratio of the production cross sections from the deuteron and the proton. Two constants, the amplitude for spin flip and amplitude for nonspin flip appear which can be de-

* Part II of this paper will be *The Production of Charged Photomesons from Helium, Helium-Hydrogen Ratios.*
† Now at University of Washington, Seattle, Washington.
‡ Now at Applied Physics Laboratory, Johns Hopkins University, Silver Springs, Maryland.
[1] E. M. McMillan and J. M. Peterson, Science **109**, 438 (1949).
[2] McMillan, Peterson, and White, Science **110**, 579 (1949).
[3] Peterson, Gilbert, and White, Phys. Rev. **81**, 1003 (1951).
[4] J. Steinberger and A. S. Bishop, Phys. Rev. **78**, 494 (1950).
[5] Bishop, Steinberger, and Cook, Phys. Rev. **80**, 291 (1950).
[6] J. Steinberger and A. S. Bishop, Phys. Rev. **86**, 180 (1952).
[7] R. F. Mozley, Phys. Rev. **80**, 493 (1950).
[8] R. M. Littauer and D. Walker, Phys. Rev. **82**, 746 (1951).
[9] Camac, Corson, Littauer, Shapiro, Silverman, Wilson, and Woodward, Phys. Rev. **82**, 745 (1951).
[10] H. A. Medicus, Phys. Rev. **83**, 662 (1951).
[11] Feld, Frisch, Lebow, Osborne, and Clark, Phys. Rev. **85**, 680 (1952).
[12] Lebow, Feld, Frisch, and Osborne, Phys. Rev. **85**, 681 (1952).
[13] H. Feshbach and M. Lax, Phys. Rev. **76**, 134 (1949).
[14] M. Lax and H. Feshbach, Phys. Rev. **81**, 189 (1951).
[15] C. F. Chew and H. W. Lewis, Phys. Rev. **84**, 779 (1951). For the initial deuteron state, the Hulthén wave function was used. Integration over the final nucleon states was carried out by means of Closure Theorems.
[16] C. F. Chew and H. W. Lewis, unpublished calculations. For the initial deuteron state the Hulthén wave function was used. In the final state the nucleons were treated as plane waves.

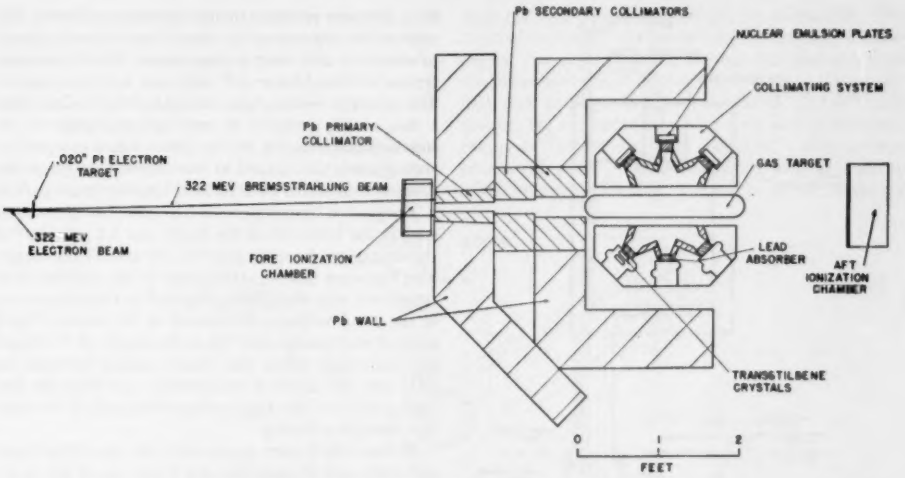


FIG. 1. Schematic layout of the essential experimental components.

termined experimentally by a measurement of these cross sections. This problem has also been treated phenomenologically by other theoretical investigators.[17–19]

An exploratory experiment of Mozley and White,[20] using light and heavy water targets and electronic meson detection indicated that $\alpha^+$ meson production from deuterium, at a production angle of 90°, did not differ greatly from the $\pi^+$ meson production from hydrogen. The present experiment was designed to investigate the production of $\pi^+$ and $\pi^-$ mesons from deuterium as a function of both angle of emission and meson energy, and to measure the ratios of the production cross sections for $\pi^+$ mesons from deuterium and hydrogen.[21] This study has also been made by Lebow, Feld, Frisch, and Osborne.[12]

## II. EXPERIMENTAL PROCEDURE

The source of photons for this experiment was the 318±10 Mev bremsstrahlung "spread-out" beam from the Berkeley electron synchrotron. This beam was generated from the 322±5 Mev electron beam which struck an internal 0.020-inch platinum target. The "spread-out" beam was obtained by modulating the rf accelerating voltage such that the electrons spilled into the target over a period of about 3000 μsec.[22] This occurred in such a way that about half of the electrons hit the target before and after the peak field was reached. The emerging beam had a full width at half-intensity of 0.0135 radian. At 55 inches from the electron target, the beam was defined by a three-quarter inch tapered hole in a nine-inch lead wall, as is shown in Fig. 1. Two secondary collimators were used to absorb the spray of electrons from the walls of the primary collimator.

The beam was monitored by means of an ionization chamber placed in front of the primary collimator. A second ionization chamber placed ten feet behind the rear end of the target was used as a check on the front monitor. The mesons passed through lead absorbers, were stopped, and were detected either in nuclear emulsions or in *trans*-stilbene crystal detectors. The nominal detection angles of 45°, 90°, and 135° were defined by uranium slits. Lead shielding served to prevent electrons and mesons, which were emitted at other angles, from reaching the detectors.

### A. Target

A high pressure, low temperature target was selected for this experiment. The assembly of the target is shown in Fig. 2. The target consisted essentially of 3 concentric

[17] G. Morpurgo, Nuovo cimento **8**, 552 (1951). For the initial deuteron state the ordinary exponential wave function was used. In the final state the nucleons were treated as plane waves.

[18] S. Machida and T. Tamura, Prog. Theor. Phys. **6**, 572 (1951). Calculations are applicable only if the two nucleons end in the $^1S$ state. For the initial deuteron state the Hulthén wave function was used.

[19] Saito, Watanabe, and Yamaguchi, Prog. Theor. Phys. **7**, 103 (1952). For the initial deuteron state the Hulthén wave function was used. In the final state the nucleons were treated as plane waves, as well as distorted $S$-state waves. The results of their plane wave calculation are equivalent to those of Chew and Lewis. (See reference 16.)

[20] R. F. Mozley and R. S. White (unpublished results).

[21] Preliminary results of this experiment have previously been reported. R. S. White, University of California Radiation Laboratory Report UCRL-1319 (1951) (unpublished); White, Jacobson, and Schulz, Phys. Rev. **85**, 770 (1952).

[22] G. Gauer and C. Nunan, University of California Radiation Laboratory Report UCRL-714 (1950) (unpublished).

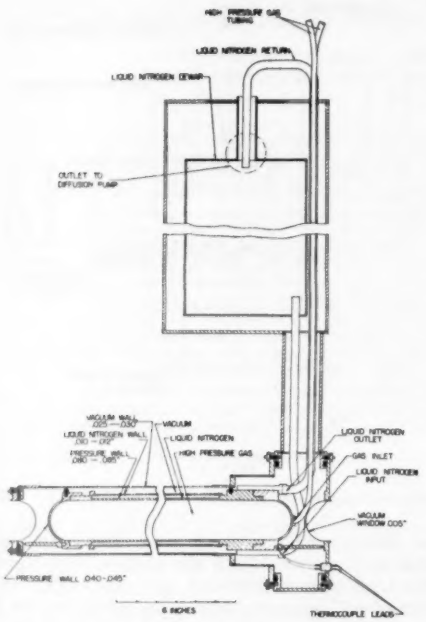


FIG. 2. Section through the gas target assembly.

cylindrical containers. The inside pressure vessel was designed to withstand a pressure of about 5 times the operating pressure of 140 atmospheres at the operating temperature of 77°K, and was tested to 2 times this operating pressure. The liquid nitrogen made direct contact with the pressure wall for most of the length of the target. The vacuum system was for the purpose of lowering heat conduction to the target gas and for conserving the liquid nitrogen.

The liquid nitrogen was stored in a tank above the target and fed to the cooling wall through pipes. Two thermocouples were placed in the tank at different levels and a third was placed on one of the end caps. The signals were sent to an automatic recorder in the counting area so that one had a record of the nitrogen level and the temperature of the pressure wall, and thus the gas, at all times.

One tube from the gas pressure cylinder was led directly to the counting area to a calibrated pressure gauge. From this gauge the pressure of the gas was read at invervals. The densities of the gases were obtained from the experimental curves for the equations of state measured by Johnston *et al.*[23] Their values are given to 0.1 percent accuracy.

An oil pump was used to compress the hydrogen gas from cylinder pressure to the operating pressure. Because of the expense of the deuterium it was necessary to recover it after each bombardment. The oil pumping system of Panofsky *et al.*[24] was used for this purpose. The pressure system was pumped down to less than 1 mm of Hg pressure in each gas exchange to insure negligible mixing of the gases. When comparison among gases was desired at least three changes of the gases were made in each 16 hour bombardment period.

The photon beam traversed 0.89 g per cm² of stainless steel in the front end of the target and 5.2 g per cm² of the deuterium from the front to the rear of the target. The 5 percent photon attenuation in the stainless steel target end was negligible compared to the uncertainty in the absolute beam monitoring of 20 percent. The 2 percent attenuation over the entire length of the target gas that might affect the relative values between the 135° and 45° angles is considerably less than the statistics, and is of the same order of accuracy as the relative beam monitoring.

Mesons which were produced in the gas of the target and were emitted perpendicular to the axis of the target had to penetrate 2.3 g of stainless steel and 0.1 g of liquid nitrogen. The minimum energy of $\pi$-mesons that could penetrate this material was 22 Mev; at 45° and 135° the minimum meson energy was 27 Mev. The energy loss of $\pi$-mesons originating on the center line of the target is less than one Mev in the target gas for all but the lowest energy mesons. This gives a maximum uncertainty in the meson energy, due to the target diameter, of less than 2 Mev. This uncertainty is small compared to the detector energy widths which ranged from 5 to 20 Mev. For the experimental arrangement used, computations showed that the target could be treated as a line source to within 1 percent accuracy.

Mass spectrometer analysis of the deuterium gas showed a 99 percent concentration of deuterium with about a 1 percent contamination of hydrogen.[25] This amount of contamination could be neglected.

### B. Collimators, Slits, and Absorbers

The selection of a gas pressure target with its inherently thick walls required that the target be long so that mesons made in the stainless steel end walls could be shielded out; otherwise, a large subtraction would have been necessitated. Lead was selected for the shielding material as it has a high nuclear charge, $Z$, and consequently is quite effective in stopping electrons and photons in the bremsstrahlung and pair production region.

Two sections through the meson collimating system are illustrated schematically in Fig. 3. In the section perpendicular to the photon beam direction, at the center of the target, are shown the five similar collimating systems arranged azimuthally about the beam

[23] Johnston, Bezman, Rubin, Swanson, Corak, and Rifkin, AEC Report MDDC-850 (unpublished).

[24] Panofsky, Aamodt, and Hadley, Phys. Rev. **81**, 565 (1951).

[25] R. H. Phillips (private communication).

direction. The lower collimating system was used only for the coincidence crystal detectors. The other four identical collimating systems, which were used for the nuclear emulsion detection, allowed the simultaneous measurement of four different energies at each of the three angles of observation.

The angles, as defined by the slits, are shown in the plane section through one of the collimating systems in Fig. 3 and are listed in Table I. From the emulsion data one can obtain a check on the collimation. The channel resolution was folded into the multiple scattering for the mesons passing through the lead and glass absorbers to obtain a distribution in angle of the mesons near their endings. In Fig. 4, for the 45° and 90° collimators, the computed curve for mesons with an initial energy of 70 Mev and final energy of 2 Mev is compared with a set of selected mesons with an average initial energy of 70 Mev. The angle to the collimator

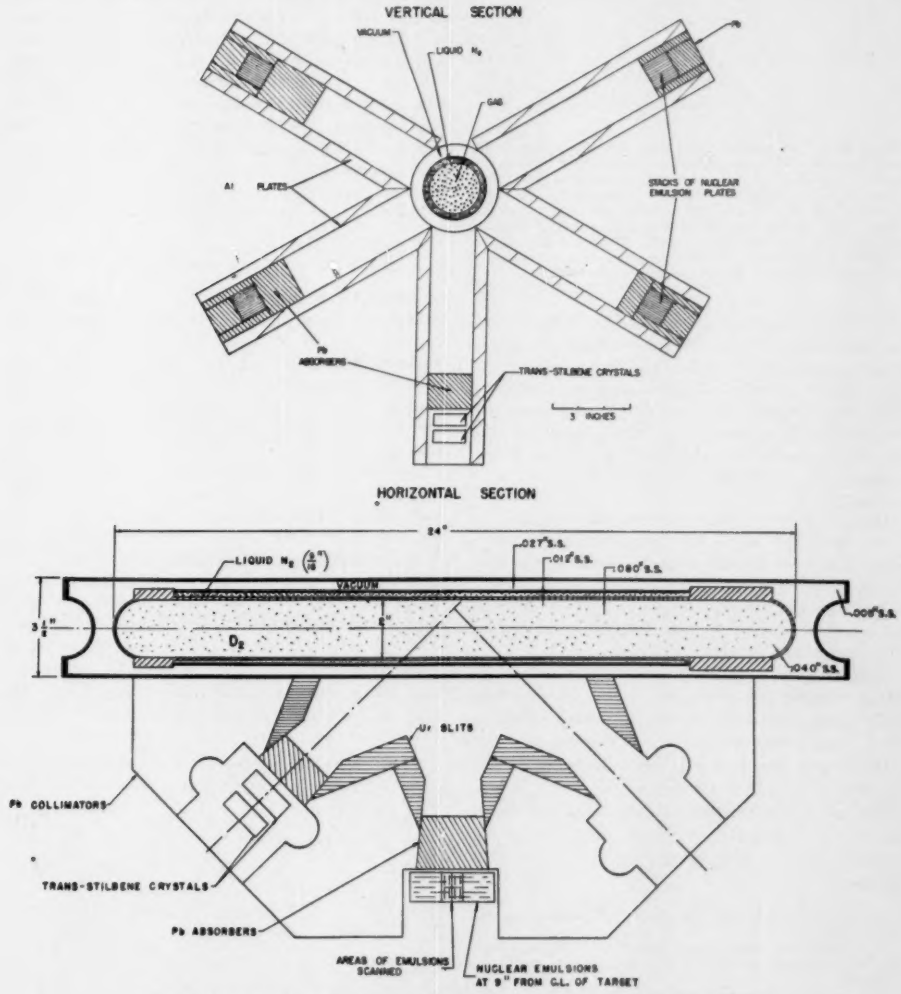


FIG. 3. Schematic drawing of vertical and horizontal sections through the gas target and the collimating system with the detectors in position.

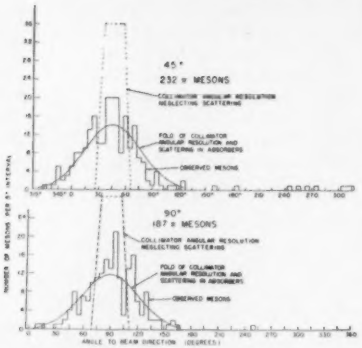
45°
232 π MESONS
COLLIMATOR ANGULAR RESOLUTION NEGLECTING SCATTERING
FOLD OF COLLIMATOR ANGULAR RESOLUTION AND SCATTERING IN ABSORBERS
OBSERVED MESONS
90°
187 π MESONS
COLLIMATOR ANGULAR RESOLUTION NEGLECTING SCATTERING
FOLD OF COLLIMATOR ANGULAR RESOLUTION AND SCATTERING IN ABSORBERS
OBSERVED MESONS
NUMBER OF MESONS PER 5° INTERVAL
ANGLE TO BEAM DIRECTION (DEGREES)

FIG. 4. Plot of the angular distribution of $\pi^+$ and $\sigma$-mesons for the 45° and 90° collimating systems demonstrating the angular resolution. The data was obtained from the emulsions. The mesons had a mean initial energy of 70 Mev and a final energy of 2 Mev; the angles were measured at 200 microns back from the meson endings. The dotted line represents the calculated angular resolution neglecting multiple scattering. This channel resolution was folded into the multiple scattering of the mesons in passing through the absorbers to obtain the solid smooth curve.

direction was measured at 200 microns (2 Mev) back from the meson endings. The calculations of multiple scattering included energy loss in the absorbers.[26]

In order to minimize slit penetration, uranium slits, with a high stopping power per unit length, were used. The low energy gammas from the uranium did not contribute appreciably to the single-grain background on the nuclear emulsions, nor to the background counts in the crystals.

The part of the emulsion which was scanned and most of the crystal in which the mesons stopped were so placed that very few electrons or mesons could be reflected at small angles off the slits into the detectors. The slit was cut away on the side nearest the detector, so that only electrons or mesons reflected from it at large angles could reach the detectors.

Lead was selected for the absorber material. Lead has a large stopping power per unit length and in addition had a large attenuation for the high energy electrons which were made in the ends of the stainless steel envelope and were scattered down the channels from the cylindrical walls of the target.

The energies of the mesons that stopped in the detectors were determined from computed range-energy curves,[27] and the range-energy curves for glass[28] and emulsion.[29]

[26] L. Eyges, Phys. Rev. **74**, 1535 (1948); L. L. Foldy, Phys. Rev. **75**, 311 (1949).
[27] Aron, Hoffman, and Williams, University of California Radiation Laboratory Report. UCRL-121, 2nd revision (1949) (unpublished).
[28] W. A. Aron (private communication).
[29] Bradner, Smith, Barkas, and Bishop, Phys. Rev. **77**, 462 (1950).

## C. Detectors

When photons strike deuterons, both $\pi^+$ and $\pi^-$ mesons are produced. In the presence of matter $\pi^-$ mesons are almost invariably captured as they come to rest. $\pi^+$ mesons, on the other hand, are repulsed by the Coulomb field of the nucleus and decay with a characteristic mean lifetime of $2.5\times10^{-8}$ sec[30,31] into $\mu^+$ mesons with energies of 4 Mev.

For this experiment the characteristic endings were used to distinguish $\pi^+$ and $\pi^-$ mesons in the nuclear emulsions. The $\pi-\mu$ coincidence detection method used by Jakobson, Schulz, and Steinberger,[31] the $\beta^+$ decay of the $\mu^+$ meson used by several experimenters, here called $\pi-\beta$ coincidence detection, and coincidences between these two methods, called $\pi-\mu-\beta$ detection, were chosen for the detection of the $\pi^+$ mesons. The crystal detection was used to obtain detailed statistics of the energy distributions, and the nuclear emulsions for fixing the absolute cross sections and for determination of the deuterium minus-plus ratios.

### *1. Crystal Coincidence Detection*

Some of the $\pi^+$ mesons which left the target passed through the absorber and first crystal and stopped in the second crystal, as illustrated in the block diagram of the electronics, Fig. 5. The individual pulses were viewed by separate photomultipliers and the signals were sent to a Wiegand-type distributed coincidence circuit.[32] The coincidence pulse was delayed 0.025 microsecond by RG63/U cable, and was used to open a gate of $8\times10^{-8}$ sec, duration. If the $\pi^+$ meson decayed into a $\mu^+$ meson during the time interval that the gate was open, a delayed coincidence resulted and the meson was counted on Scaler 2. The accidental background for the $\pi-\mu$ coincidence was obtained by delaying the gate for a time long compared to the $\pi^+$ mean life. In a similar manner, the $\pi-\pi$ coincidence pulse was used to open a series of $\beta$ gates. The beta delayed coincidences were registered on Scalers 7, 8, 9, and 10. As the $\mu^+$ mean life is about $2.2\times10^{-6}$ sec, shaping circuits were used along with the slower coincidence circuits. The first beta-gate was then put into coincidence with the

TABLE I. Angular resolution of the collimating systems.

| Detector | Lab angle |
|---|---|
| Nuclear emulsions | 45°+17° |
| | −15° |
| | 90°±16° |
| | 135°+15° |
| | −17° |
| Crystals | 90°±16° |
| | 135°±19° |

[30] C. Wiegand, Phys. Rev. **83**, 1085 (1951).
[31] Jakobson, Schulz, and Steinberger, Phys. Rev. **81**, 894 (1951).
[32] C. Wiegand, Rev. Sci. Instr. **21**, 975 (1950).

$\pi-\mu$ signal to form the $\pi-\mu-\beta$ coincidence, which was then registered on Scaler 11.

Different counting methods were used to count the same events; therefore, it would appear possible to determine the efficiencies of each of the three methods and the actual number of $\pi^+$ mesons that stopped in the second crystal. This determination is dependent on the fact that all, or a known fraction, of the $\pi^+$ mesons that stopped in the second crystal opened gates. No clear-cut $\pi^+$ meson plateaus were observed for the pulses from the second crystal. Therefore, instead of obtaining efficiencies in this manner, they were calculated from the nuclear emulsion data. This determination showed that at the photomultiplier voltages used, about 1200 volts, only about half of the $\pi^+$ mesons which stopped in the last crystal opened gates. The measured efficiencies and the typical ratios of the background counts to true counts are given in Table II. The counting rate for the $\pi-\mu$ coincidences was of the order of one per minute at the emission angle of 90° and meson energies of 70 Mev. The observed background counting rates were compatible with those calculated.

The following additional evidence may be presented that $\pi^+$ mesons were being detected. (1) When the maximum photon beam energy was reduced below the threshold for meson production no mesons were counted. (2) The shape of the $\pi^+$ meson energy distribution at 90° compares well with the one obtained by Bishop *et al.*[5] (3) The relative shapes of the distributions obtained by each of the counting methods agree, within statistics, at both 90° and 135°. (4) The counter data is in good agreement with the emulsion data for the relative shapes of the spectra and for the deuterium-hydrogen ratios.

A run was made with the experimental setup identical to the usual runs except with an empty pressure chamber. The meson counting rate observed was negligible compared to the normal counting rates with gas in the target.

Recently it was reported[23] that pulses in a photomultiplier were followed by secondary "satellite" pulses which occurred with a definite time rate of build up and decay. The satellite pulses were counted down to one-thirtieth of the minimum main pulse size. For the delayed coincidences of this experiment, on the other hand, the $\mu$-pulses required were about one-tenth of the maximum pulse that might be expected from a stopping proton.

TABLE II. Crystal coincidence detection. Efficiencies and background.

| Detection method | Efficiency | Background counts/ True counts |
|---|---|---|
| $\pi-\beta$ | 0.27 | 2–5 |
| $\pi-\mu$ | 0.077 | 0.10–0.20 |
| $\pi-\mu-\beta$ | 0.027 | ~0.01 |

[23] Godfrey, Harrison, and Keuffel, Phys. Rev. 84, 1248 (1951).

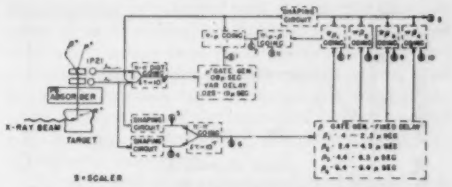


FIG. 5. Block diagram of the electronics used in the crystal coincidence detection.

In order to determine whether or not satellite pulses would be sufficiently large to make a delayed coincidence at the level required by this coincidence circuit, a test was made using protons from the 32-Mev linear accelerator. The pulses from protons passing through the first crystal and stopping in the second were used to open delayed gates. The proton energy loss in the second crystal was about 15 Mev. The number of satellite pulses from the second photomultiplier was found to be negligible compared to the number of mesons which would have been recorded under running conditions of this experiment for that number of gates. Furthermore no mesons were recorded when mesons could have not stopped in the second crystal, i.e., when the maximum energy of the photon beam was reduced below the meson threshold energy.

### 2. *Nuclear Emulsion Detection*

Ilford C-2 nuclear emulsions were selected for detectors as their sensitivity is about optimum for meson detection. They were backed by $1\times3\times1/16$ inch glass plates and were exposed in lead boxes in stacks of five sandwiched between glass plates. This method of exposure was economical of beam time as nuclear emulsions could be pulled at different exposures and blank glass plates inserted. The exposures ranged from 1 to $5\times10^{12}$ equivalent quanta. Only those emulsions which recorded the lowest energy mesons, (thin absorbers) were limited to the low exposures. The single grain background on the emulsions indicated that practically all of the background electrons were coming from the target.

In order to obtain absolute cross sections, it was necessary to have a measurement of the emulsion thickness before development. This was obtained by sending 390 Mev alpha-particles through the emulsions at an angle of 45° to the plane of the emulsion. As the emulsions shrink only in the dimension perpendicular to the plane of the emulsion, the projected track length after development is equal to the original thickness before development. The shrinkage factor obtained by this method was $2.42\pm0.12$. The relative shrinkage factors are considered to be good to 2 percent.

The method of meson identification and classification employed in this experiment have previously been reported.[8]

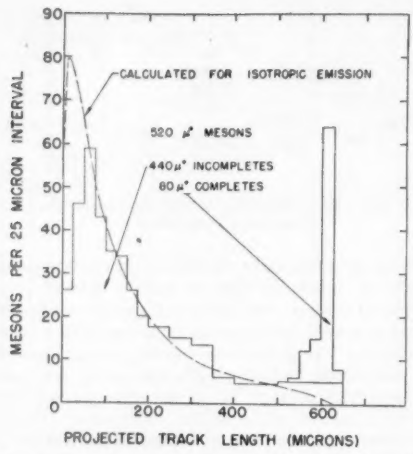


FIG. 6. Projected track length distribution of $\mu^+$ mesons. The track lengths were measured from their endings, back to the point where they entered or left the emulsion to about 10 percent accuracy. The curve on the $\mu^+$ meson range distribution plot is the expected distribution based on normalization between 50 and 500 micron ranges.

The emulsion detection method is subject to several internal checks. (1) In Fig. 4 it was demonstrated that the mesons originated in the target, were collimated and scattered in the absorbers as expected. (2) From a plot of the number of meson endings, of each of the three types, *versus* their depth in the emulsion, the meson emulsion depth acceptance criterion was established. If the mesons end near the surface of the emulsion, or near the glass, the tracks are often shorter and therefore more difficult to identify. In addition, if prongs or mesons are emitted from the ending there is a possibility that they will be missed. Only mesons ending 3 microns or more, after development, from either surface of the emulsion were accepted. This removed about 7 percent of the available emulsion volume. (3) The projected ranges of the mesons, measured from their endings back to the point where they entered or left the emulsion were measured to about 10 percent accuracy. The similarities of the projected track length distributions for mesons with $\sigma$ and $\pi-\mu$ endings indicated a consistent detection efficiency for both types of meson endings. The $\rho$ distribution was compatible with a group of mesons which originated in the target superimposed on a distribution which originated in the immediate vicinity of the emulsion. The distribution of $\mu^+$ mesons from the ends of $\pi^+$ mesons lends itself rather easily to analysis. The expected distribution function for isotropic emission has been included along with observed distribution in Fig. 6. The curve on the plot was normalized in the region of 50 to 500 microns. As $\pi^+$ mesons with very short $\mu^+$ meson decays are more difficult to find than those with long decay tracks or $\pi-\mu$ completes, the lack of $\mu^+$ mesons in the 0–50 micron interval might be expected. The curve fitted in this manner would indicate that about 7 percent of the total $\pi^+$ mesons were not seen. It would also predict 76 $\pi-\mu$ completes, well within the statistics of the 80 observed. The curve was also normalized from 50 microns to infinity (all ranges above 600 microns would be included in the $\pi-\mu$ completes) with similar results. (4) Plots of the angular distribution of all types of mesons from deuterium from the nominal angle of 45° are shown in Fig. 7. The distribution of $\mu^+$ mesons from the $\pi^+$ endings is uniform in angle of emission. The $\pi^+$ and $\pi^-$ mesons are certainly coming from the target. The distribution of $\rho$ endings shows a uniform background of $\mu^+$ mesons plus a hump from the target direction. If this uniform background of $\mu^+$ mesons and the $\mu^+$ and $\mu^-$ mesons due to decay in flight of the $\pi$ mesons are subtracted from the distribution, the remaining number of $\rho$ endings must be from $\pi^-$ mesons which do not form stars plus any $\mu$ mesons that might have been produced in the target. If all of the remaining mesons are considered to be $\pi^-$ mesons which do not form stars, one arrives at the prong distribution of $\pi^-$ mesons shown in Table III. The data of Adelman and Jones, Menon, and Adelman[34] has been included for comparison. If one takes their fraction of $\pi^-$ mesons which do not form stars, the ratio of the cross section for $\mu$ meson production to $\pi$-meson production in deuterium is $-0.04\pm0.08$. Within statistics there were no $\mu$-mesons produced in the target; a similar analysis of the hydrogen data gives the same result. This value is in agreement with the experiment in which carbon was bombarded by photons.[3] If, on the other hand, one assumes no $\mu$-mesons are made in the target, the experimental fraction of $\pi^-$ mesons which give no ionizing tracks at their endings agrees within statistics with the value of Adelman and Jones.[35]

Identical scanning of the same emulsion by different observers indicated that the absolute efficiencies of observers is greater than 90 percent. Analysis of the projected ranges of $\mu^+$ mesons indicated that absolute efficiencies for the observation of $\pi^+$ mesons was greater than 90 percent, but that probably some short $\pi^+$

TABLE III. Fractional number of prongs from $\sigma$-mesons.

| | from 303 $\sigma$-mesons | Aldeman and Jones, Menon *et al.*, Adelman[a] from 3366 $\sigma$-mesons |
|---|---|---|
| $\sigma_0$ | 0.23 ±0.08 | 0.268±0.021 |
| $\sigma_1$ | 0.26 ±0.03 | 0.237±0.007 |
| $\sigma_2$ | 0.28 ±0.03 | 0.239±0.007 |
| $\sigma_3$ | 0.15 ±0.02 | 0.163±0.006 |
| $\sigma_4$ | 0.06 ±0.01 | 0.077±0.004 |
| $\sigma_5$ | 0.02 ±0.01 | 0.014±0.001 |
| $\sigma_6$ | 0.003±0.003 | 0.001±0.001 |

[a] See reference 34.

[34] F. L. Adelman, Phys. Rev. **85**, 249 (1952).
[35] F. L. Adelman and S. B. Jones, Science **111**, 226 (1950).

mesons with short $\mu^+$ meson decays were missed. Some short $\pi^-$ mesons are slightly easier to identify than short $\pi^+$ mesons because of the heavily ionizing tracks at their endings; on the other hand, some of the short $\pi^-$ mesons may be confused with the low energy photo-induced stars in the emulsion and might not be counted. In view of these arguments it is felt that the relative detection efficiencies for $\pi^+$ and $\pi^-$ mesons are about equal, and that if systematic errors are present they would tend to lower the minus-plus ratios slightly. As the absolute efficiencies are not known precisely, the data has not been corrected for observer efficiency. Individual observer error was minimized by dividing the emulsion area to be scanned into two parallel strips, each 1 cm×2.5 cm. Each of the 2 strips was scanned by a different observer. Comparing the data from the two areas showed no systematic error that could be attributed to individual observers.

For the hydrogen exposures at each of the angles, 45° and 90°, the number of $\sigma$-endings observed was less than two percent of the number of $\pi-\mu$ endings. All of the $\sigma$-mesons observed came from the target direction. Since photons on stainless steel should give about as many $\pi^+$ as $\pi^-$ mesons, it follows that the background of $\pi^+$ or $\pi^-$ mesons from the target walls is less than 2 percent of those produced in the gas. However, if all of the mesons came from the target gas, one has the result that the ratio of the number of $\pi^-$ to $\pi^+$ mesons from hydrogen is about 0.02; this alternative is considered quite improbable.

The total volume of emulsion scanned for the deuterium exposures was about 0.9 cm³, for the hydrogen exposures about 0.6 cm³.

## III. RESULTS

### A. Minus-Plus Ratio for Deuterium

A quantity which should be independent of beam monitoring, density of the bombarded gas, and geometry considerations is the ratio of the number of $\pi^-$ to $\pi^+$ mesons produced. In a particular $\pi$ meson energy interval and angle of emission, the minus-plus ratio is simply

$$[\pi^-]/[\pi^+]=1.37[\sigma]/[\pi-\mu],$$

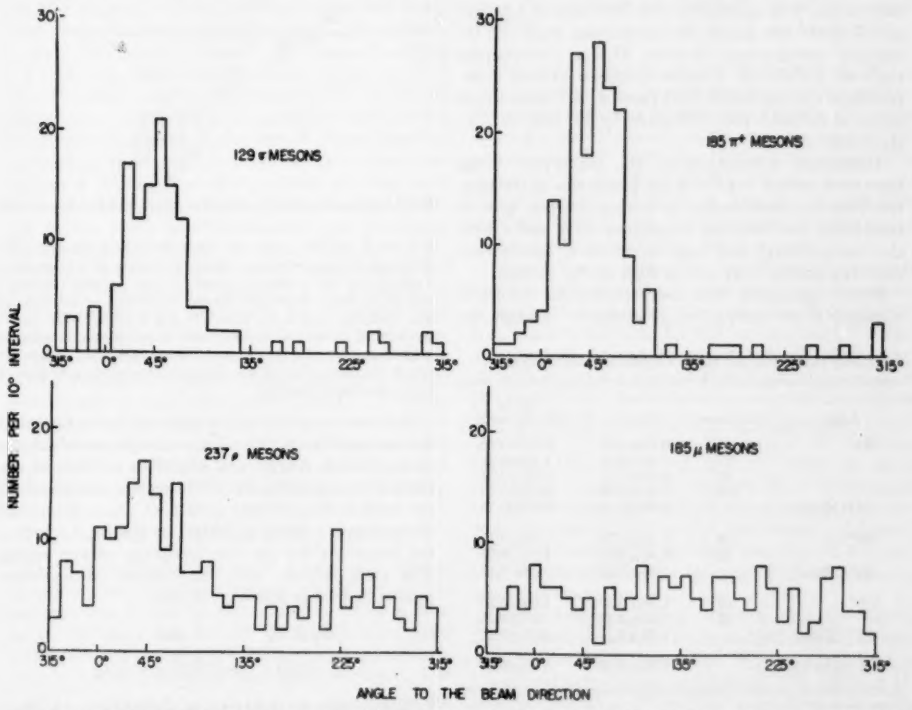


FIG. 7. Distribution in angle of the $\pi-\mu$, $\sigma$, $\rho$, and $\mu^+$ mesons from deuterium for the 45° collimating system. The angles of the tracks were measured at the point where they entered the emulsion, or 200 microns back from their ending, whichever was the shorter. The abscissa is the angle to the beam direction.

where $[\sigma]$, and $[\pi-\mu]$ are the numbers of $\sigma$ and $\pi-\mu$ meson endings found in the volume of emulsion corresponding to the particular $\pi$-meson energy and angle of emission.

An alternate, less reliable, method of obtaining the ratio is of interest in indicating experimental consistency. The value of the ratio is

$$\left(\frac{[\pi^-]}{[\pi^+]}\right)_{\text{Alt}}=\frac{2+f_d}{0.73[T]/[\sigma]-(1+f_d)},$$

where $[T]$ is the total number of meson endings of all types observed, and $f_d$ is the fraction of $\pi$-mesons which decay in flight before reaching the detectors. This method is considered less reliable because a count of the total number of mesons includes $\rho$ endings which are more difficult to identify than either $\sigma$ or $\pi-\mu$ endings as there is no distinguishing event at their endings.

The values for the minus-plus ratios from deuterium are given in Table IV.

It is interesting to note that these ratios are close to one, and are independent of energy or angle, within statistics, for the energies and angles investigated. A ratio of one is in agreement with the value of Littauer and Walker,[8] who found, for the emission angle of 135° and a $\pi^+$ meson energy of about 50 Mev, a minus-plus ratio of $1.19\pm0.12$. Further evidence of this independence was furnished by Lebow *et al.*,[12] who found ratios of $0.5\pm0.5$ and $0.90\pm0.23$ at 90° and 26°, respectively.

Theoretical calculations of the minus-plus ratios have been carried out.[36,18] If the interaction of the photon with the currents due to moving charges, only, is considered, the resulting minus-plus ratio varies with the meson energy and angle of emission and is considerably greater than one for high energy mesons.

Better agreement with the experimental results is obtained if the interaction is primarily through the static magnetic moments of the nucleons. This gives a minus-plus ratio which is essentially independent of the angle of emission or the energy of the meson.

TABLE IV. Minus-plus ratio of $\pi$-mesons from deuterium.

| Angle $\bar{\theta}$ | $E_\pi$ (Mev) | Ratio | Ratio (Alternate method) |
|---|---|---|---|
| 45° | 43 | $0.79\pm0.21$ | $0.75\pm0.22$ |
| | 57 | $1.04\pm0.16$ | $1.15\pm0.21$ |
| | 87 | $0.89\pm0.21$ | $0.91\pm0.24$ |
| | 128 | $0.99\pm0.30$ | $0.73\pm0.26$ |
| 45° (Mean) | | $0.96\pm0.10$ | $0.94\pm0.13$ |
| 90° | 34 | $1.24\pm0.20$ | $1.38\pm0.32$ |
| | 70 | $0.98\pm0.14$ | $1.08\pm0.19$ |
| 90° (Mean) | | $1.09\pm0.12$ | $1.20\pm0.17$ |
| 135° | 39 | $1.37\pm0.22$ | $1.06\pm0.20$ |
| | 57 | $1.05\pm0.18$ | $1.13\pm0.26$ |
| 135° (Mean) | | $1.21\pm0.17$ | $1.08\pm0.16$ |
| All angles (Mean) | | $1.07\pm0.07$ | $1.04\pm0.09$ |

[36] K. A. Brueckner and M. L. Goldberger, Phys. Rev. **76**, 1725 (1949); K. A. Brueckner, Phys. Rev. **79**, 641 (1950); G. Araki, Prog. Theor. Phys. **5**, 507 (1950).

## B. Cross Sections for Hydrogen and Deuterium

For a line source emitting $\pi$-mesons, in the case where there are only two particles in the final state, e.g., photons bombarding protons to give a meson and a neutron, as shown in Fig. 8, the differential cross section can be found from the following formula:

$$\frac{d\sigma(\bar{\theta},k)}{d\Omega}=\frac{1}{\epsilon}\frac{\Delta N}{hdG(\bar{\theta})(dq/dk_0)(dk_0/dE)(dE/dR)n},$$

where $\epsilon$ is the efficiency of the detector; $h$ is the effective height of the detector; $w$ is the effective width of the detector; $d$ is the effective length of the detector; $\Delta N$ are the number of counts observed at a particular meson energy $E$, and average angle of emission, $\bar{\theta}$; $dq/dk_0$ are the number of quanta of energy $k_0$ per unit energy, which contribute to the production of the mesons. This factor depends on the detailed shape of the bremsstrahlung spectrum. $dk_0/dE$ relates the photon energy interval to the meson energy interval. This factor may be obtained from knowledge of

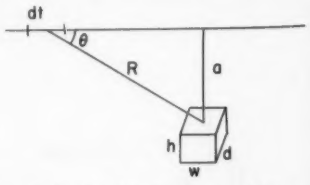


FIG. 8. Schematic drawing of the line source and detector element.

$k_0=f(E,\bar{\theta})$. $dE/dR$ relates the range interval of the detector to the energy interval of mesons leaving the target. It is a function of $\bar{\theta}$ and $E$. $n$ is the number of target particles per unit volume; in this experiment, either the number of protons or neutrons per unit volume. $G(\bar{\theta})=\int\int dwdt/R^2=\int\int dwd\theta/a$. This is the geometrical factor that changes only in going from one average angle to another. $R$ is the distance from an interval of length of the target, $dt$, to the detector. $a$ is the perpendicular distance from the line source to the detector.

If there are more than two particles in the final state, the energy of the $\pi$-meson is not a single valued function of the photon energy, and $dk_0/dE$ is not defined. One method of evaluating data is to replace $(dq/dk_0)dk_0$ by the number of equivalent quanta, $Q$, where the number of equivalent quanta is defined as the total energy in the beam divided by the maximum photon energy. The cross section, with the number of equivalent quanta defined in this way, is then

$$\frac{d^2\sigma(\bar{\theta},E)}{dEd\Omega}=\frac{\Delta N}{\epsilon hdG(\bar{\theta})Q(dE/dR)n}.$$

The differential cross section, $d\sigma(\bar{\theta})/d\Omega$, can be found by integrating $d^2\sigma(\bar{\theta},E)/dEd\Omega$ over $dE$ and the total cross section by integrating the differential cross section

over the solid angle. The data was extrapolated from 0 to 40 Mev to obtain the differential cross sections, and over the angles that were not measured to obtain the total cross sections.

In order to obtain the cross sections, certain corrections were applied to the data. These corrections were: (1) Decay in flight of the $\pi$-mesons. A value for the mean life of the $\pi$-meson was taken to be $2.5\times10^{-8}$ sec.[30,31] This correction is small, varying from 5 percent at low meson energies to 2.5 percent at high. (2) Slit penetration. The geometry factor, $G(\theta)$, was calculated on the basis of perfectly opaque slits to the $\pi$-mesons. This is obviously an oversimplification as some mesons of high energy may penetrate the slit and still have enough energy to reach the detectors; these mesons will then be observed at a lower meson energy. The correction was made by calculating the increase in slit width, and thus the geometrical factor, as a function of the meson energy. (3) Multiple scatter. For the emulsion detection the condition for "poor geometry" was satisfied. The front edge of the emulsion was on contact with the lead absorber. The thickness of the emulsion, about $2\times10^{-2}$ cm, was very small compared to the height of the lead absorber, 4.5 cm, and the absorber and meson beam were wide compared to the width of the emulsion scanned. The rms displacements for mesons traversing the lead and glass absorbers were calculated using methods which consider energy loss of the mesons,[28] and the net loss of $\pi$-mesons to the emulsion detectors was found to be negligible. In the case of crystal detection the poor geometry condition was not entirely satisfied because of the large size of the crystals and their position with respect to the absorbers. The resulting correction factors, which have been applied to all subsequent data, are shown in Fig. 9.

A fourth correction is for nuclear interactions in the absorbers. Because some mesons may be absorbed, or undergo large angle scattering in interacting with nuclei, they will not reach the detector. The evidence, at the present time, indicates that the cross section for nuclear events for $\pi$-mesons in flight traversing matter is of the order of a geometrical nuclear area.[27] The values of nuclear areas found from high energy neutron scattering experiments were used in obtaining these correction factors.[28] This correction varies from about 8 percent at a $\pi$-meson energy of 35 Mev to 85 percent at 150 Mev.

### 1. *Energy Distributions in the Lab System*

The energy distributions for $\pi^+$ mesons with the appropriate corrections have been calculated per equivalent quantum, $Q$, and are plotted in Fig. 10 for each of the production angles, 45°, 90°, and 135°. The crystal data which was obtained by the three detection methods $\pi-\mu$, $\pi-\beta$, and $\pi-\mu-\beta$ have been combined. The

[27] Chedester, Isaacs, Sachs, and Steinberger, Phys. Rev. **82**, 958 (1951).

[28] Cook, McMillan, Peterson, and Sewell, Phys. Rev. **75**, 7 (1949); Fernbach, Serber, and Taylor, Phys. Rev. **75**, 1352 (1949).

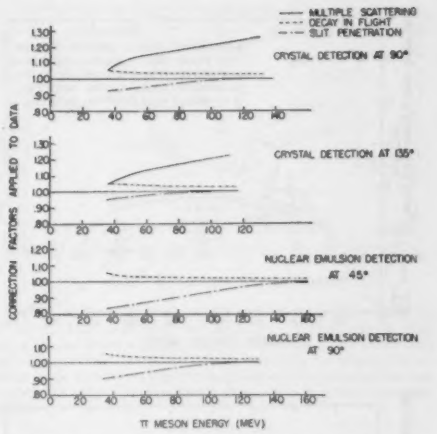


FIG. 9. Curves showing the correction factors applied to the data for time of flight, slit penetration, and multiple scattering. These are given for the coincidence crystal detection at 90° and 135°, and for the emulsion detection at 45° and 90°. No correction for multiple scattering was necessary in the case of emulsion detection.

energy distribution for $\pi^-$ mesons from deuterium is also plotted at 45°. The absolute cross-section scale for the crystal data was fixed by the emulsion data from hydrogen and deuterium at the emission angle of 90° and meson energy of 70 Mev. The relative values of the hydrogen to deuterium energy distributions, as obtained by the crystal detection, were not altered by this emulsion normalization. The agreement between crystal and emulsion data at other points is good.

Smooth curves have been drawn through the data and extrapolated to zero meson energy for the purpose of integration. The dashed curves have been corrected for nuclear interaction. The tails on the energy distributions, which appear at meson energies above that allowed by conservation of energy and momentum at the angles, $\theta$, are due to those mesons which are allowed through the collimating system at angles smaller than $\theta$. The shape of the hydrogen spectrum at 90° compares favorably with that of Bishop *et al.*[5,6] when the tail is taken into account. The absolute value of the peak of the hydrogen spectrum is in agreement with the recently renormalized value of Steinberger and Bishop[8] —hereafter referred to as S.B. From Fig. 10 it is seen that the distributions for hydrogen and deuterium are similar in shape.

The uncertainties in Fig. 10 and in subsequent curves are standard deviations due to statistics only. The relative photon beam integration for the experiment is considered to be as good as 2 percent. The values at 45° relative to those at 90° and 135° are only as good as the normalization of the plate data, about 10 percent. The largest uncertainty in absolute values is that of the

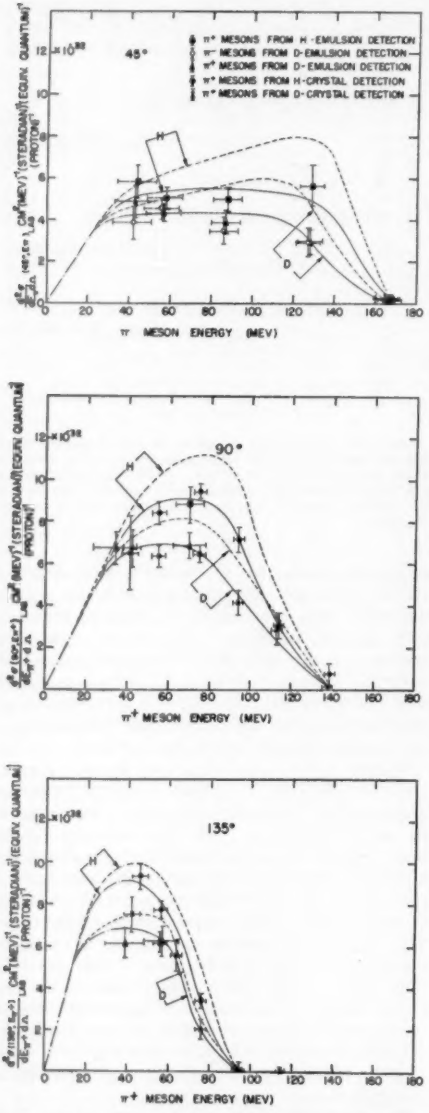


FIG. 10. Energy distributions in the lab system at 45°, 90°, and 135° for $\pi^+$ mesons from deuterium and hydrogen and at 45° for $\pi^-$ mesons from deuterium. The crystal data obtained by the 3 detection methods have been combined. Smooth curves have been drawn through the data and extrapolated to zero for the purpose of integration. The dashed curves have been corrected for nuclear interaction in the absorbers. Uncertainties shown are standard deviations due to statistics only. The horizontal lines are the detector energy widths.

absolute beam integration which may be as large as 20 percent.

### 2. *Differential Cross Sections per Q in the Lab System*

The differential cross sections for $\pi^+$ mesons were found by integrating under the curves of Fig. 10; they are plotted in Fig. 11. The values could be changed somewhat by a different extrapolation to zero meson energy. Smooth curves have been drawn through the data for the purpose of obtaining total cross sections. The dashed curves have been corrected for nuclear interaction.

### 3. *Total Cross Sections per Q*

The total cross sections for $\pi^+$ mesons from hydrogen and deuterium per $Q$ were found by integrating the differential cross sections of Fig. 11 over the solid angle. In addition to the uncertainties listed previously there is the uncertainty due to the extrapolation over angles for which the differential cross sections were not obtained. Since the solid angle approached zero at 0° and 180°, this introduces a small error.

The total cross sections are given in Table V. The uncertainties in Table V are those of the absolute beam integration.

### 4. *Deuterium-Hydrogen Ratios for $\pi^+$ Meson Production*

The ratios of the cross sections for the production of $\pi^+$ mesons from deuterium and hydrogen, as obtained from the energy distributions for several energies at each of the production angles, are plotted in Fig. 12. These ratios are dependent only on the relative beam monitoring, and in the case of emulsions, also on the relative plate thickness. Therefore, the largest uncertainties are given by the statistics.

Chew and Lewis[15,16] and others[17–19] have used an interaction of the form $L+\sigma\cdot\mathbf{K}$ and the impulse approximation to theoretically investigate this deuterium-hydrogen ratio. They point out that in order to calculate the ratio, it is necessary to evaluate certain overlap integrals over the relative momentum of the two outgoing neutrons using the initial deuteron and final di-neutron wave functions. If these functions are known, the calculation is possible. For the initial deuteron wave function, four authors[15,16,18,19] have used the Hulthén wave function

$$\psi_D=\left[\frac{\alpha\beta(\alpha+\beta)}{2\pi(\beta-\alpha)^2}\right]^{\frac{1}{2}}\left(\frac{e^{-\alpha r}-e^{-\beta r}}{r}\right),$$

and one[17] has used the above with $\beta=\infty$. From the low energy $(n, p)$ scattering cross section, and the coherent scattering amplitude of neutrons scattered from hydrogen,[39,40] the value of the effective range, and thus $\beta$ can be obtained. The neutrons in the final state have

[39] J. M. Blatt and J. D. Jackson, Phys. Rev. 76, 18 (1949).
[40] Hughes, Burgy, and Ringo, Phys. Rev. 77, 291 (1950).

TABLE V. Total cross sections per $Q$ for $\pi^+$ mesons from deuterium and hydrogen.

| Target | $\sigma_T$ cm$^2$ $Q^{-1}$ proton$^{-1}$ | $\sigma_T$ corrected for nuclear interaction |
|---|---|---|
| Deuterium | $6.4\pm1.3\times10^{-29}$ | $7.7\pm1.5\times10^{-29}$ |
| Hydrogen | $8.3\pm1.7$ | $10.3\pm2.1$ |

been treated as plane waves[16,17,19] as ending in a $^1S$ state,[18,19] and closure theorems have been involked to perform the integrations over the final state.[15] The plane wave treatment neglects the interaction between the two neutrons which occurs when their relative momentum is small. The $^1S$ state treatment is only valid for low relative momentum between the two nucleons, and the closure method sums over all values of the relative momentum, some of which are not allowed by conservation of energy and momentum, and thus tends to over-estimate the ratio.

Chew and Lewis[15] give the deuterium-hydrogen ratio in the form

$$\left[\frac{(d\sigma/d\Omega)_D}{(d\sigma/d\Omega)_H}\right]_{k_0}=\left[1-\frac{q_0^0}{M}\left(1-\frac{k_0^0\cos\theta}{q^0}\right)\right]\times\int_{m_q}^{q_0^{\max}}\frac{q_0q}{q_0^0q^0}\left[\frac{L^2(F_1-F_2)+K^2(F_1-\frac{1}{2}F_2)}{L^2+K^2}\right]dq_0,$$

where $M$ is the proton rest mass, $q_0$, $q$, and $m_q$ are the meson total energy, momentum, and rest mass, respectively, in units of Mev. $F_1$ and $F_2$[41] are functions of $\theta$, $k_0$, and $q_0$ where $\theta$ is the meson angle with the beam direction and $k_0$ is the photon energy. A super 0, i.e., $q^0$, refers to the kinematics for the free nucleon case. The data has been compared to the theoretical predictions obtained by two different methods.

Method 1: The above indicated numerical integration is evaluated for a given $k_0$. It has been previously pointed out that there is no unique relationship among $\theta$, $k_0$, and $q_0$ for mesons produced from deuterons, as is the case for mesons from protons. If the assumption is made that the deuterium meson energy spectrum from a given $k_0$ is narrow and that the peak occurs at the line spectrum from hydrogen, other photons will not contribute appreciably to the number of mesons at a particular $\theta$, and meson kinetic energy, $E$. The experimental ratio at a given meson kinetic energy can be then compared to the theoretical ratio for a photon

[41] The $F_1$ and $F_2$ of Chew and Lewis (see reference 15) are related to the $F_-$ and $F_+$ of Saito *et al.* (see reference 19) by

$$F_-=\frac{q}{2k_0A^2}(F_1-F_2),$$

$$F_+=\frac{q}{2k_0A^2}\left\{F_1+F_2+\frac{4}{\beta^2-\alpha^2}\ln\left[\frac{(n+1)^2+\alpha^2}{(n-1)^2+\alpha^2}\frac{(n-1)^2+\beta^2}{(n+1)^2+\beta^2}\right]\right\},$$

where

$$A^2=\left[\frac{\alpha\beta(\alpha+\beta)}{2\pi(\beta-\alpha)^3}\right]^{\frac{1}{2}},\quad l=\frac{n_1+n_2}{2},\quad n=\frac{n_1-n_2}{2},$$

and $n_1$ and $n_2$ are the momenta of the two resultant neutrons.

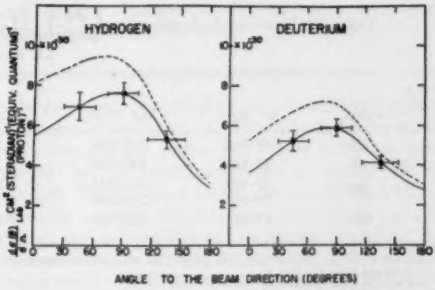


FIG. 11. Differential cross sections per $Q$ in the lab system for $\pi^+$ mesons from deuterium and hydrogen. Smooth curves were drawn for the purpose of integration and extrapolated into 0° and 180°. The dashed curves have been corrected for nuclear interaction in the absorbers. Uncertainties are standard deviations due to statistics only. The horizontal lines are the detector angular widths.

energy obtained by the free particle kinematics. In Fig. 12 are plotted the dotted curves obtained in this manner. Those marked $K^2/L^2=\infty$ refer to all spin interaction, and those marked $K^2/L^2=0$, to no spin interaction. These curves have been evaluated for the Hulthén deuteron function for $\beta=6\alpha$. The experimental

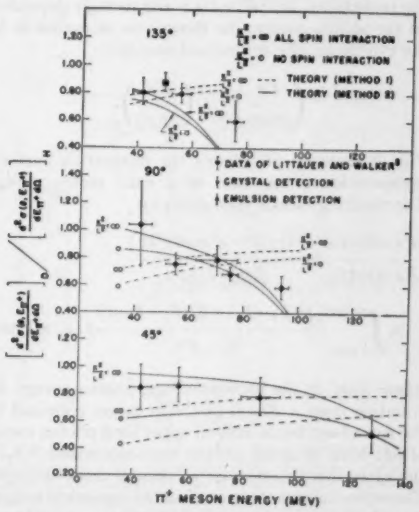


FIG. 12. Deuterium-hydrogen ratios for $\pi^+$ meson production at 45°, 90°, and 135°. The uncertainties are standard deviations due to statistics only. The horizontal lines are the energy widths of the detectors. The curves marked $K^2/L^2=\infty$ and $K^2/L^2=0$ are the theoretical predictions for all spin interaction and no spin interaction, respectively. In the theoretical computations the Hulthen wave function with $\beta=6$ has been used for the initial deuteron state and plane waves have been used for the nucleons in the final state. Method 1 and Method 2 refer to the way the theory has been compared to the data.

TABLE VI. Deuterium-hydrogen ratios, $\left(\frac{d^2\sigma}{dEd\Omega}\right)_D \Big/ \left(\frac{d^2\sigma}{dEd\Omega}\right)_H = \frac{D}{H}$, averaged over the meson kinetic energy interval, $\Delta E$, where data exists.

| $\theta$ (deg) | $\Delta E$ (Mev) | $\Delta k_0$[a] (Mev) | $\overline{[D/H]}_{exp}$ | $\overline{[D/H]}$ theory 1[b] $K^3/L^3=\infty$ | $K^3/L^3=0$ | $\overline{[D/H]}$ theory 2[c] $K^3/L^3=\infty$ | $K^3/L^3=0$ |
|---|---|---|---|---|---|---|---|
| 26 | 65–145 | 212–296 | 0.89±0.17[d] | 0.72 | 0.41 | 0.71 | 0.41 |
| 45 | 38–134 | 190–300 | 0.74±0.08 | 0.76 | 0.57 | 0.84 | 0.63 |
| 90 | 40–105 | 212–322 | 0.64±0.18[d] | 0.81 | 0.73 | 0.80 | 0.72 |
| | 39–93 | 210–300 | 0.74±0.05 | | | | |
| 135 | 37–67 | 230–300 | 0.79±0.06 | 0.82 | 0.77 | 0.71 | 0.64 |

[a] Photon energy interval from free particle kinematics corresponding to $\Delta E$.
[b] Computed by Method 1.
[c] Computed by Method 2.
[d] Data of Lebow *et al.* (see reference 12).

effective range[40] of $1.71\times10^{-13}$ cm fixes the value of $\beta$ to within a few percent. It can be seen from the dotted curves that the theoretical deuterium-hydrogen ratios are less than one and increase with increasing meson energies (photon energies). The data, on the other hand, have a distinct downward trend at each of the angles. This disagreement is a direct consequence of the neglect in the theoretical ratio of the contribution of mesons from other photons in the bremsstrahlung to the detected energy interval. The assumption of a narrow spectrum is only valid for meson angles near 0°.

Method 2: If the assumption is made that the spin flip probability, $K^2/(K^2+L^2)$ is not strongly dependent on the photon energy, the theory can be evaluated for the experimentally determined quantity

$$\left(\frac{d^2\sigma}{dEd\Omega}\right)_D \Big/ \left(\frac{d^2\sigma}{dEd\Omega}\right)_H.$$

This is done by performing the integration over the bremsstrahlung spectrum at a fixed meson energy. The resulting ratio is then given by

$$\frac{(d^2\sigma/dEd\Omega)_D}{d^2\sigma/dEd\Omega)_H} = \frac{[1-(k^0-q^0\cos\theta)/M]}{\mathcal{B}(k_0^0)\,\mathcal{S}(k_0^0)} \times \int_{q_0\,min}^{q_0\,max} \frac{[L^3(F_1-F_2)+K^2(F_1-F_{2/3})]}{(L^2+K^2)} \mathcal{B}(k_0)\,\mathcal{S}(k_0)dk_0,$$

where $\mathcal{B}(k_0)$ is the bremsstrahlung photon energy distribution from a 20-mil platinum target corrected for the spread-out beam with an upper limit photon energy of 322 Mev. $k^0$ is the photon momentum and $\mathcal{S}(k_0)$ is the excitation function for $\pi^+$ mesons from hydrogen. The excitation functions used in the numerical integration of this ratio were those of Steinberger and Bishop,[6] Feld *et al.*[11] and of this paper (see the section on excitation functions) for the angles of 90, 26, and 135 and 45 degrees, respectively. The computed ratio is not very sensitive to the excitation functions used. From the solid curves obtained in this manner it is seen that the theoretical ratio drops rapidly near the upper end of the bremsstrahlung and is equal to zero at maximum photon energy. This drop-off is due to the effect of the cutoff of the photon spectrum and the broad meson spectrum from deuterium for monoenergetic photons.

The solid curves fit the data very well at 90 and 45 deg but drop off too sharply at 135 deg. This departure can be mainly attributed to the effect of the angular uncertainty of ±19 deg in the experimental data. Mesons contributed to the detector from smaller angles tend to increase the ratio which is measured at a given meson energy. The change in meson energy with angle at a fixed photon energy is much more rapid in the backward directions, thus the angle uncertainty has more effect at 135 than at 90 and 45 deg. In addition an uncertainty in the theoretical deuterium meson energy distributions would give the greatest uncertainty in the ratio near the cutoff of the bremsstrahlung.

At each of the angles, the deuterium-hydrogen ratios were averaged over the energy intervals where data exist and are given in Table VI. The theoretical values obtained in the same manner are also given. The values of Lebow *et al.*[12] at 26 and 90 deg have been included.

The agreement between experiment and theory gives strong support for the validity of the impulse approximation. From Fig. 12 and Table VI it can be seen that the statistics of the data are not sufficient to determine the fraction of spin interaction. In order to have a large exclusion effect, and thus large differences in the ratios for all and no spin interaction the relative momentum between the two outgoing neutrons must be small.[12–16] Unfortunately this occurs at small angles to the photon beam direction where the background due to electrons is very high. At these forward angles where the exclusion effect is large, the deuterium spectrum is also sharp and the bremsstrahlung spectrum does not present a problem.

It should be kept in mind that the theoretical ratios are dependent on the initial deuteron and final nucleon wave functions. Computations have been carried out for the case of the Hulthén deuteron wave function in the initial state with $\beta=\infty$, and for plane waves for the nucleons in the final state. The values obtained for the ratio were much lower than the curves of Fig. 12. On the other hand, computations using the Hulthén

function with $\beta=6\alpha$ and closure in the final state give ratios slightly larger than the curves of Fig. 12.

The experimental value of the ratio of the total cross sections is $0.75\pm0.04$. In this case the value is dependent on the relative shapes of the energy spectra at angles which were not measured. Systematic errors due to this could cause uncertainties larger than the statistical uncertainties.

### 5. *Excitation Functions for Hydrogen and Deuterium in the Lab System*

The excitation function for $\pi^+$ mesons from hydrogen per photon of energy $k_0$, has been computed. For the case of deuterium, one can make the assumption of the previous section to calculate $dk_0/dE$ from hydrogen kinematics to get an excitation function for deuterium. Again, this approximation is good only at small meson angles. The excitation functions, so calculated, appear in Fig. 13. The data have been corrected for nuclear interaction. In order to improve the statistics, the $\pi^+$ and $\pi^-$ mesons from deuterium have been combined; a minus-plus ratio of one was taken. The data have been fitted to straight lines, so that it could be used to find points on the angular distribution in the center-of-mass system. The excitation function found by S.B.[6] has been superimposed for the purpose of comparison.

It should be pointed out that this experiment is primarily a survey experiment to compare the deuterium and hydrogen productions and was not designed to investigate the excitation function, or the angular distribution in the manner of the previous experimenters.[6] Although quite inconclusive, the excitation function for hydrogen of this experiment is consistent with that of S.B. for the production angle of 90°. The excitation curves for deuterium show similar trends with somewhat better statistics.

### 6. *Differential Cross Sections for Hydrogen and Deuterium in the Center-of-Mass System*

Points on the angular distribution curves, for various photon energies were obtained by cutting through the excitation function curves at different photon energies. The angles and cross sections were transformed to the center-of-mass system and are plotted in Fig. 14. The angular distribution of S.B. is included for comparison. Three points on an angular distribution curve are obviously not sufficient to determine its shape. The agreement between the data of Fig. 14 for 255-Mev photons on hydrogen and the S.B. data is good. Both sets of data tend to show the apparent peaking at an angle larger than 90° in the center-of-mass system. The curves for other photon energies are drawn only to show a possible trend of the angular distributions as a function of the photon energy.

The theoretical implications of the excitation curves and angular distributions for hydrogen have been treated by S.B. and by Araki.[42]

## IV. CONCLUSIONS

In summary, one can draw the following conclusions from this experiment: (1) The minus-plus ratio for deuterium is close to one, and within statistics, independent of the production angle or energy of the $\pi$-meson. This implies a production interaction which is primarily through the magnetic moments of the nucleons, and independent of the charge carried by the nucleon except to determine the charge of the $\pi$-meson produced. (2) The experimental ratios of the deuterium to hydrogen cross sections are in agreement with the phenomenological theory of Chew and Lewis when the theory is treated in the following way: (a) The Hulthén

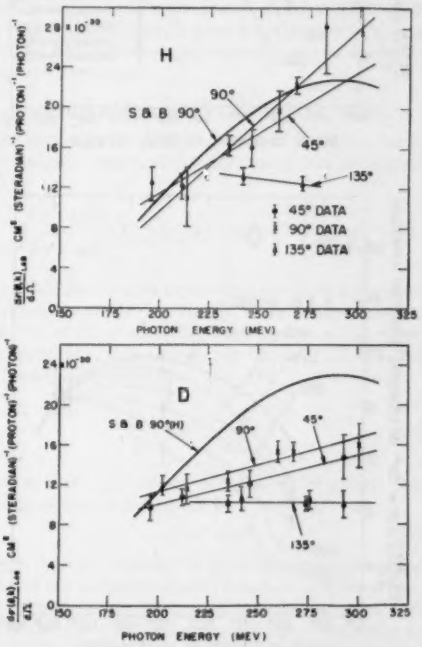


FIG. 13. Excitation functions for hydrogen and deuterium in the lab system. In the case of deuterium, the photon energy was assigned on the assumption that the proton was free. The data has been fitted to straight lines at each of the angles, 45°, 90°, and 135° for the purpose of obtaining points on the differential cross section curves in the center-of-mass system. The excitation function of Steinberger and Bishop (see reference 6) for $\pi^+$ mesons from hydrogen obtained from their data for an emission angle of 90° has been included for comparison. In order to improve the statistics, in the case of deuterium, the $\pi^+$ and $\pi^-$ mesons have been combined; a minus-plus ratio of one was taken. The data have been corrected for nuclear interaction in the absorbers. The uncertainties are standard deviations due to statistics, only.

[42] G. Araki, Phys. Rev. **82**, 959 (1951).

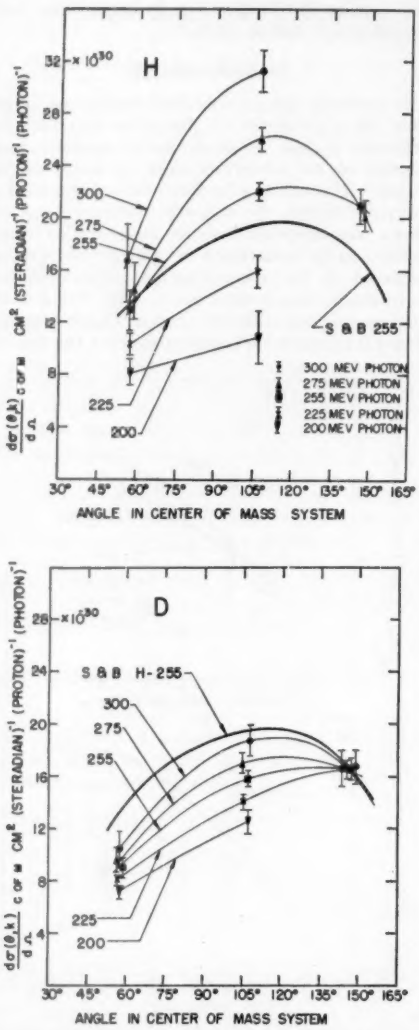


FIG. 14. Differential cross sections for hydrogen and deuterium in the center-of-mass system. Curves have been drawn in to show a possible trend of the angular distribution with the photon energy. Included is the curve of Steinberger and Bishop (see reference 6) for $\pi^+$ mesons for 255-Mev photons on hydrogen. The uncertainties are standard deviations due to statistics only. The data have been corrected for nuclear interaction in the absorbers.

wave function with $\beta=6\alpha$ is used in the initial state; (b) Plane waves are used for the nucleons in the final state; and (c) The bremsstrahlung cutoff is taken into account (Method 2). This agreement gives strong support to the validity of the impulse approximation.

Computations using $\beta=\infty$ in the initial state and plane waves in the final state give values for the ratio much lower than the experiment. Computations using $\beta=6\alpha$ in the initial state and closure in the final state give values slightly higher than the experiment. The treatment of the theory by Method 1 does not give the observed variation of the ratio with meson energy. This method will only be good at small angles to the beam where the meson distribution from deuterium becomes extremely narrow so that the bremsstrahlung spectrum may be neglected. The statistics of the experiment are not sufficient to determine the amount of spin interaction.

(3) The excitation function for hydrogen is consistent with that of S.B. for the production angle of 90°. The excitation curves for deuterium show trends which are similar to those for hydrogen. The points on the angular distribution for $\pi^+$ mesons from hydrogen in the center-of-mass system for a photon of 255 Mev are in agreement with the curve of S.B. with the apparent peaking at an angle larger than 90°. The points from deuterium show similar results to those from hydrogen.

It has been strongly emphasized by Chew and Lewis[15,16] and others that measurements of the spin flip probability for $\pi^+$ meson production from deuterium should be carried out at small angles to the beam direction. Here the exclusion effect is much greater, the assumptions of the theory are better, and the comparison between theory and experiment is more exact. Present investigations are being carried out along these lines.

We wish to express our appreciation to Professor E. M. McMillan for his continued guidance and support. We would like to thank Professor W. K. H. Panofsky and Professor O. Chamberlain and Dr. R. Lelevier for much helpful discussion. We are indebted to D. R. L. Aamodt and Professor W. K. H. Panofsky for the use of the deuterium pumping system, to Professor G. F. Chew and Professor H. W. Lewis for unpublished calculations on photomeson production from deuterons. We wish to thank Mr. Collin Moore and Mr. Bailey for help with the emulsions, Mr. J. A. Winokur and Mr. Robert L. Pexton for numerical computation, and Dr. W. H. Barkas and other members of the Film Group for the use of their facilities. Our sincere thanks go to Mr. George McFarland and members of the synchrotron crew for help in making the bombardments.

# The Density Effect for the Ionization Loss in Various Materials*

R. M. STERNHEIMER
*Brookhaven National Laboratory, Upton, New York*
(Received July 2, 1952)

The density effect for the ionization loss of charged particles has been calculated for a number of metals, scintillating materials, gases at various pressures, and photographic emulsion, using a dispersion model involving an appropriate number of dispersion oscillators for each substance. The results are presented in the form of graphs which can be used to correct the ionization loss for the density effect. The theoretical curves for silver chloride and anthracene are in reasonable agreement with experiments on the ionization loss of $\mu$-mesons. A general derivation of the equations for the density effect is given.

## I. INTRODUCTION

THE reduction in the ionization loss of charged particles due to the polarization of the medium has been first treated quantitatively by Fermi.[1] In Fermi's treatment it was assumed that the dispersive properties of the medium can be described as due to a single type of dispersion oscillator. Halpern and Hall[2] showed that the reduction in ionization loss depends strongly on the description of the dielectric properties of the medium. Fermi's equations were extended to the general case of an arbitrary number of dispersion oscillators by Halpern and Hall,[3] Wick,[4] and the present author.[5,6] Halpern and Hall[3] have given values of the density correction for a few substances. More recently, the reduction in ionization loss has been the object of several experiments.[7] These investigations confirm the existence of the density effect and are in approximate agreement with theory. However, some of the experiments use substances for which the effect has not been calculated, in particular the work of Whittemore and Street[7] on the ionization loss of $\mu$-mesons in a silver chloride crystal and the work of Bowen and Roser[7] on the response of anthracene crystals to $\mu$-mesons. Therefore, it appeared worth while to calculate the density effect for silver chloride, anthracene, and for other substances which are likely to be used in future experiments. The results of this work are presented in the first part of this paper. In addition to values of the density effect correction, we have calculated the ionization loss of $\mu$-mesons and electrons in some of the materials for which the density effect is evaluated. Equations are given from which the ionization loss can be readily calculated for the materials whose density effect has been obtained. The theoretical values of the density effect for silver chloride and anthracene are found to be in reasonable agreement with the experiments.[7] The second part of the paper gives the derivation of the equations for the density effect which has been previously obtained.[5] The derivation involves fewer approximations than are made in the theory of Halpern and Hall[3] and the result obtained is more general, although there are no essential differences between the two results in most practical cases.

## II. CALCULATIONS OF THE DENSITY EFFECT

As shown in the following section, the reduction in the ionization loss $\Delta dE/dx$ ($dE$ = energy loss in distance $dx$) is

$$\Delta\frac{dE}{dx}=\frac{2\pi ne^4}{mv^2}[\textstyle\sum_i f_i \ln[(\bar{\nu}_i^2+l^2)/\bar{\nu}_i^2]-l^2(1-\beta^2)], \quad (1)$$

where $n$ is the number of electrons per cc, $m$ is the electron mass, $v=\beta c$ is the velocity of the passing particle, $f_i$ is the oscillator strength of the $i$th transition, whose frequency is $\bar{\nu}_i$, $l$ is a frequency which is the solution of the following equation:

$$\frac{1}{\beta^2}-1=\textstyle\sum_i \dfrac{f_i}{\bar{\nu}_i^2+l^2}. \quad (2)$$

Here $\bar{\nu}_i$ is to be expressed in terms of the plasma frequency of the medium given by

$$\nu_p=(ne^2/\pi m)^{\frac{1}{2}}. \quad (3)$$

The $\bar{\nu}_i$ must be obtained for each case from the energy levels of the atoms considered. As a first approximation, the frequencies are given by the ionization potentials $h\nu_i$ of the $K$, $L$, $M$, $\cdots$ shells and the $f_i$ are equal to the corresponding occupation numbers divided by the atomic number $Z$. The ionization potentials were obtained from the table given by Sommerfeld.[8] For the outermost shell, the tables of Bacher and Goudsmit[9] were also used. With the $\nu_i$ thus obtained, the geometrical mean $\nu_m$ of the frequencies is calculated; we have

$$\ln\nu_m=\textstyle\sum_i f_i \ln\nu_i. \quad (4)$$

* Work done under the auspices of the AEC.
[1] E. Fermi, Phys. Rev. **57**, 445 (1940).
[2] O. Halpern and H. Hall, Phys. Rev. **57**, 459 (1940).
[3] O. Halpern and H. Hall, Phys. Rev. **73**, 477 (1948).
[4] G. C. Wick, Nuovo cimento (9), **1**, 302 (1943).
[5] R. M. Sternheimer, thesis, University of Chicago (1946) (unpublished).
[6] See also, A Bohr, Kgl. Danske Videnskab. Selskab, Mat.-fys. Medd. **24**, No. 19 (1948).
[7] F. L. Hereford, Phys. Rev. **74**, 574 (1948); W. L. Whittemore and J. C. Street, Phys. Rev. **76**, 1786 (1949); F. Bowen and F. X. Roser, Phys. Rev. **85**, 992 (1952).
[8] A. Sommerfeld, *Atomic Structure and Spectral Lines* (Methuen and Company, London, 1934), third edition, p. 237.
[9] R. F. Bacher and S. Goudsmit, *Atomic Energy States* (McGraw-Hill Book Company, Inc., New York, 1932).

A check on the value of $\nu_m$ is provided by the determination of the average ionization potential $I$ which occurs in the Bethe-Bloch stopping power formula,[10]

$$\frac{dE}{dx}=\frac{4\pi ne^4}{mv^2}\left[\ln\frac{2mv^2}{I(1-\beta^2)}-\beta^2\right]. \tag{5}$$

In their recent measurement of the stopping power of 340-Mev protons, Bakker and Segrè[11] have obtained values of $I$ for a number of elements. According to the Bloch theory $I$ should be proportional to $Z$. Bakker and Segrè confirm this dependence for $Z>26$, where $I$ is approximately given by

$$I=9.4Z \text{ ev}. \tag{6}$$

For smaller $Z$, the values of $I$ are somewhat larger than given by Eq. (6). The mean of the frequencies should equal $I/h$. It was found for all cases that the values of $\nu_m$ obtained from the ionization potentials must be increased by a factor of order 1.3 to give agreement with $I/h$. Thus for Ag, the $\nu_i$ correspond to the following ionization potentials: 1878 ry, 260 ry, 36.3 ry, 4.82 ry, 0.55 ry for the $n=1, 2, 3, 4, 5$ shells, respectively ($n$ =principal quantum number). The $f_i$ are 2/47, 8/47, 18/47, 18/47, 1/47. The resulting $h\nu_m$ is 25.2 ry, which is a factor 1.25 lower than the experimental value[11] of 31.5 ry. To obtain the frequencies to be used in Eq. (1) the $\nu_i$ obtained from the ionization potentials were raised by the factor 1.25. This procedure was carried out for each substance. In the following, the experimental mean frequency is denoted by $\nu_m'$ and the corrected transition frequencies are denoted by $\nu_i'$, so that

$$\nu_i'=(\nu_m'/\nu_m)\nu_i. \tag{7}$$

The factor $\nu_m'/\nu_m$ is perhaps an indication that the average of the states to which the electrons are excited lies in the continuum above the ionization limit. The values of $\bar{\nu}_i$ used in Eq. (1) are obtained from

$$\bar{\nu}_i=\nu_i'/\nu_p. \tag{8}$$

The solids for which the density effect is obtained include gold, photographic emulsion, anthracene, silver chloride, in addition to the metals investigated by Bakker and Segrè.[11] For the gases, we have calculated cases at high pressure for possible application to experiments with diffusion and expansion cloud chambers. The results for $H_2$ and A at 0.2 atmos are included on account of their use in counters. The results are shown in Figs. 1 and 2, in which the quantity in brackets of Eq. (1),

$$\delta=\sum_i f_i\ln((\bar{\nu}_i^2+\bar{P}^2)/\bar{\nu}_i^2)-\bar{P}^2(1-\beta^2), \tag{9}$$

is plotted against $\log_{10}(p/\mu c)$, where $p$ is the momentum and $\mu$ is the mass of the passing particle. This semilog plot was used because $\delta$ is then approximately a straight line at large $p/\mu c$. The data which were used to calculate $\delta$ are given in Table I. In this table are listed the ionization potentials $h\nu_i$ (in ry units), the resulting mean excitation potential $h\nu_m$, the experimental value $h\nu_m'$, and the factor $\nu_m'/\nu_m$ by which the $\nu_i$ are multiplied to give the $\nu_i'$. The table also shows the oscillator strengths $f_i$ and the plasma energy $h\nu_p$. The last two rows give the constants $A$ and $B$ [see Eqs. (13a, b)] which are useful in calculating the ionization loss. In cases for which $\nu_m'$ was not obtained experimentally, it was obtained by interpolation from Table I of Bakker and Segrè.[11]

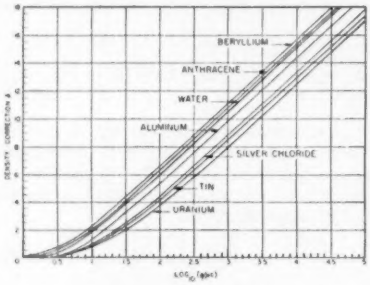


FIG. 1. Density effect correction $\delta$ for condensed materials as a function of the momentum/mass of the passing particle.

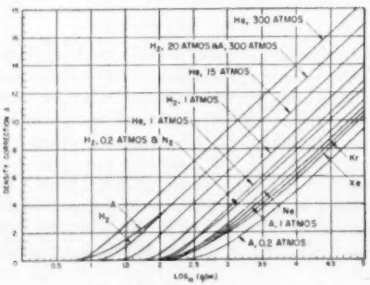


FIG. 2. Density effect correction $\delta$ for gases as a function of the momentum/mass of the passing particle.

In cases of compounds the frequencies for the component atoms are listed. For anthracene and toluene $\nu_1$, $\nu_2$, $\nu_3$ pertain to C, and $\nu_4$ pertains to H. The values of $h\nu_m'$ listed are the geometric means of the $h\nu_m'$ for the component atoms and are the values to be used in the Bethe-Bloch formula. The factors by which the $\nu_i$ are multiplied are given in the tables for graphite and $H_2$. For $H_2O$, $\nu_1$, $\nu_2$, $\nu_3$ pertain to O, and $\nu_4$ pertains to H. For O, we have $h\nu_m=6.14$ ry, $h\nu_m'=7.26$ ry, $\nu_m'/\nu_m=1.18$. For AgCl, $\nu_1$–$\nu_5$ refer to electrons bound in Ag atoms and $\nu_6$–$\nu_8$ refer to Cl. The factor $\nu_m'/\nu_m$ for Ag is 1.25 (see table for silver), while for Cl, $h\nu_m=11.8$ ry, $h\nu_m'=13.5$ ry, so that $\nu_m'/\nu_m=1.14$. Thus $h\nu_1'$ for $n=1$ of Ag is $(1878)(1.25)=2348$ ry, and $h\nu_6'$ for $n=1$ of

[10] M. S. Livingston and H. A. Bethe, Revs. Modern Phys. **9**, 285 (1937).
[11] C. J. Bakker and E. Segrè, Phys. Rev. **81**, 489 (1951).

Cl is (208)(1.14) = 237 ry. The $h\nu_i'$ are then divided by $h\nu_p = 3.33$ ry. In calculating $\delta$ for photographic emulsion, it was assumed that 47 percent of the oscillator strength is due to Ag, 33 percent to Br, and 20 percent to N. The small amount (1.2 percent) iodine was lumped with the silver, and the dispersive characteristics of the light elements, mostly O, C, and H were taken to be those of N. Only the $h\nu_i$ of Br are listed; the frequencies for Ag and the light elements can be found in the tables for silver and $N_2$, respectively. For Br, $h\nu_m = 21.1$ ry, $h\nu_m' = 24.2$ ry, so that the factor $\nu_m'/\nu_m = 1.15$. The value listed $h\nu_m' = 21.0$ ry is the geometric mean appropriate for emulsion.[12] For NaI, $\nu_1$–$\nu_5$ pertain to I, while $\nu_6$–$\nu_8$ pertain to Na. For I, $h\nu_m = 29.7$ ry, $h\nu_m' = 36.6$ ry, so that the values of $\nu_i$ were increased by a factor 1.23. For Na, the corresponding energies are $h\nu_m = 6.73$ ry, $h\nu_m' = 9.57$ ry, so that $\nu_m'/\nu_m = 1.42$.

For a gas at a pressure of $P$ atmos, $h\nu_p$ is $P^{\frac{1}{2}}$ times the value of $h\nu_p$ at 1 atmos, listed in Table I. Correspondingly, $\bar{\nu}_i^2$ in Eq. (2) is reduced by a factor $1/P$. Thus, the value of $\beta$ for which the density effect sets in is raised as $P$ is increased. The appropriate $\beta = \beta_0$ is given by

$$\beta_0 = (1 + \sum_i f_i/\bar{\nu}_i^2)^{-\frac{1}{2}}. \tag{9a}$$

Figure 2 shows the increase of the density effect as the pressure is raised. This effect corresponds to the increase of the polarization as the density is increased.

Figures 1 and 2 also show a general decrease of $\delta$ with increasing $Z$. As the atomic number increases, the electrons are more strongly bound and hence are less effective in polarizing the medium. Thus for two substances with the same $n$, $\delta$ is smaller for the one with larger $Z$. Some of the curves of $\delta$ for condensed materials are not shown in Fig. 1 because they closely coincide with curves that are on this figure. The curve for Li lies ~0.13 below the Be curve in the region of large $p/\mu c$ where $\delta$ is linear. The curve for toluene is ~0.2 below the anthracene curve. It may be noted that stilbene, terphenyl, and phenylcyclohexane ($C_6H_5C_6H_{11}$) have about the same $\delta$ as anthracene, while the toluene curve also applies to benzene. The curve for xylene lies ~0.1 below the anthracene curve. $\delta$ for graphite is 15.6 at $p/\mu c = 10^4$; the curve lies ~0.19 above the anthracene line for large $p/\mu c$. $\delta$ for polyethylene practically coincides with the curve for graphite.

The values of $\delta$ for Fe and Cu lie close to the Al curve. $\delta$ for Fe is about the same as for Al for large $p/\mu c (> 10^2)$ and is ~0.12 higher at $p/\mu c = 10^{1.5}$. The Cu curve lies close to the Al curve for low momenta and is ~0.10 below it for large $p/\mu c (> 10^3)$. $\delta$ for silver is ~0.2 above the AgCl curve. $\delta$ for emulsion is ~0.1 above the AgCl curve. $\delta$ for Au is ~0.07 higher than $\delta$ for Sn, while $\delta$ for W is ~0.18 higher than $\delta$ for Sn. The curve for Pb lies 0.14 below that for U. NaI and LiI have the same $\delta$ within 0.1 as U. This result arises because the smaller $Z$ for iodine which leads to a stronger polarization per electron is compensated by the smaller electronic density of the iodides as compared to uranium.

The values of $\delta$ for the cases of gases which were calculated are shown in Fig. 2 with the exception of $H_2$ at 0.2 atmos. This curve lies close to the curve for

[12] If it is assumed that only the energy loss in the AgBr crystals is detected, the relevant density effect is that for AgBr. [E. Pickup and L. Voyvodic, Phys. Rev. **80**, 89 (1950)]. $\delta$ for AgBr is ~equal to $\delta$ for AgCl. The corresponding values of $A$ and $B$ are $A = 0.0668$ Mev/g cm$^{-2}$, $B = 15.1$.

TABLE I. Data used to calculate the density effect. Energies are given in Rydberg units.

| Material | Li | Be | Graphite | Al | Fe | Cu |
|---|---|---|---|---|---|---|
| $h\nu_1$ | 5.3 | 10.9 | 23.0 | 115 | 524 | 662 |
| $h\nu_2$ | 0.4 | 1.0 | 4.1 | 6.7 | 55.3 | 72.1 |
| $h\nu_3$ | ··· | ··· | 1.3 | 2.4 | 5.0 | 5.4 |
| $h\nu_4$ | ··· | ··· | ··· | ··· | 0.9 | 0.6 |
| $f_1$ | 2/3 | 2/4 | 2/6 | 2/13 | 2/26 | 2/29 |
| $f_2$ | 1/3 | 2/4 | 2/6 | 8/13 | 8/26 | 8/29 |
| $f_3$ | ··· | ··· | 2/6 | 3/13 | 14/26 | 18/29 |
| $f_4$ | ··· | ··· | ··· | ··· | 2/26 | 1/29 |
| $h\nu_m$ | 2.22 | 3.31 | 5.00 | 8.18 | 13.1 | 14.2 |
| $h\nu_m'$ | 2.50 | 4.44 | 5.67 | 11.0 | 17.9 | 20.5 |
| $\nu_m'/\nu_m$ | 1.13 | 1.34 | 1.13 | 1.34 | 1.37 | 1.44 |
| $h\nu_p$ | 1.01 | 1.90 | 2.26 | 2.43 | 4.05 | 4.29 |
| $A$ | 0.0661 | 0.0678 | 0.0765 | 0.0737 | 0.0713 | 0.0698 |
| $B$ | 19.9 | 18.8 | 18.3 | 17.0 | 16.0 | 15.7 |

| Material | Ag | Sn | W | Au | Pb | U |
|---|---|---|---|---|---|---|
| $h\nu_1$ | 1878 | 2150 | 5114 | 5940 | 6463 | 8477 |
| $h\nu_2$ | 260 | 304 | 812 | 975 | 1053 | 1419 |
| $h\nu_3$ | 36.3 | 46.4 | 157 | 193 | 214 | 335 |
| $h\nu_4$ | 4.8 | 6.4 | 22.8 | 24 | 28.1 | 51.6 |
| $h\nu_5$ | 0.6 | 1.3 | 3.6 | 4.1 | 5.8 | 11.3 |
| $h\nu_6$ | ··· | ··· | ··· | ··· | 2.8 | 2.9 |
| $f_1$ | 2/47 | 2/50 | 2/74 | 2/79 | 2/82 | 2/92 |
| $f_2$ | 8/47 | 8/50 | 8/74 | 8/79 | 8/82 | 8/92 |
| $f_3$ | 18/47 | 18/50 | 18/74 | 18/79 | 18/82 | 18/92 |
| $f_4$ | 18/47 | 18/50 | 32/74 | 32/79 | 32/82 | 32/92 |
| $f_5$ | 1/47 | 4/50 | 14/74 | 19/79 | 18/82 | 18/92 |
| $f_6$ | ··· | ··· | ··· | ··· | 4/82 | 14/92 |
| $h\nu_m$ | 25.2 | 26.8 | 43.8 | 42.6 | 45.4 | 51.9 |
| $h\nu_m'$ | 31.5 | 35.2 | 51.3 | 54.6 | 55.6 | 64.8 |
| $\nu_m'/\nu_m$ | 1.25 | 1.31 | 1.17 | 1.28 | 1.22 | 1.25 |
| $h\nu_p$ | 4.53 | 3.72 | 5.90 | 5.89 | 4.49 | 5.69 |
| $A$ | 0.0667 | 0.0644 | 0.0615 | 0.0614 | 0.0606 | 0.0590 |
| $B$ | 14.8 | 14.6 | 13.9 | 13.7 | 13.7 | 13.4 |

| Material | $H_2$ | He | $N_2$ | Ne | A | Kr | Xe |
|---|---|---|---|---|---|---|---|
| $h\nu_1$ | 1.0 | 1.8 | 30.3 | 64 | 235 | 1050 | 2545 |
| $h\nu_2$ | ··· | ··· | 3.5 | 4.0 | 21.6 | 129 | 373 |
| $h\nu_3$ | ··· | ··· | 2.3 | ··· | 2.9 | 11.2 | 61.1 |
| $h\nu_4$ | ··· | ··· | ··· | ··· | ··· | 2.9 | 12.4 |
| $h\nu_5$ | ··· | ··· | ··· | ··· | ··· | ··· | 1.9 |
| $f_1$ | 1 | 1 | 2/7 | 2/10 | 2/18 | 2/36 | 2/54 |
| $f_2$ | ··· | ··· | 2/7 | 8/10 | 8/18 | 8/36 | 8/54 |
| $f_3$ | ··· | ··· | 3/7 | ··· | 8/18 | 18/36 | 18/54 |
| $f_4$ | ··· | ··· | ··· | ··· | ··· | 8/36 | 18/54 |
| $f_5$ | ··· | ··· | ··· | ··· | ··· | ··· | 8/54 |
| $h\nu_m$ | 1.00 | 1.80 | 5.38 | 7.02 | 11.5 | 18.3 | 32.1 |
| $h\nu_m'$ | 1.15 | 1.98 | 6.45 | 8.85 | 14.1 | 25.0 | 37.4 |
| $\nu_m'/\nu_m$ | 1.15 | 1.10 | 1.20 | 1.26 | 1.23 | 1.37 | 1.17 |
| $h\nu_p$ | 0.020 | 0.020 | 0.053 | 0.046 | 0.060 | 0.085 | 0.104 |
| $A$ | 0.153 | 0.0765 | 0.0765 | 0.0759 | 0.0698 | 0.0658 | 0.0629 |
| $B$ | 21.5 | 20.4 | 18.0 | 17.4 | 16.5 | 15.3 | 14.5 |

| Material | Anthracene | Toluene | $H_2O$ | AgCl | Emulsion | NaI |
|---|---|---|---|---|---|---|
| $h\nu_1$ | 23 | 23 | 42.3 | 1878 | 993 | 2448 |
| $h\nu_2$ | 4.1 | 4.1 | 4.0 | 260 | 120 | 356 |
| $h\nu_3$ | 1.3 | 1.3 | 2.9 | 36.3 | 16 | 56.6 |
| $h\nu_4$ | 1.0 | 1.0 | 1.0 | 4.8 | 2 | 10.8 |
| $h\nu_5$ | ··· | ··· | ··· | 0.6 | ··· | 1.4 |
| $h\nu_6$ | ··· | ··· | ··· | 208 | ··· | 96 |
| $h\nu_7$ | ··· | ··· | ··· | 14.8 | ··· | 5 |
| $h\nu_8$ | ··· | ··· | ··· | 4.0 | ··· | 0.4 |
| $f_1$ | 28/94 | 14/50 | 2/10 | 2/64 | 2/35 | 2/64 |
| $f_2$ | 28/94 | 14/50 | 2/10 | 8/64 | 8/35 | 8/64 |
| $f_3$ | 28/94 | 14/50 | 4/10 | 18/64 | 18/35 | 18/64 |
| $f_4$ | 10/94 | 8/50 | 2/10 | 18/64 | 7/35 | 18/64 |
| $f_5$ | ··· | ··· | ··· | 1/64 | ··· | 7/64 |
| $f_6$ | ··· | ··· | ··· | 2/64 | ··· | 2/64 |
| $f_7$ | ··· | ··· | ··· | 8/64 | ··· | 8/64 |
| $f_8$ | ··· | ··· | ··· | 7/64 | ··· | 1/64 |
| $h\nu_m'$ | 4.75 | 4.39 | 5.00 | 25.6 | 21.0 | 28.8 |
| $h\nu_p$ | 1.72 | 1.46 | 1.58 | 3.33 | 2.82 | 2.65 |
| $A$ | 0.0808 | 0.0831 | 0.0851 | 0.0684 | 0.0708 | 0.0653 |
| $B$ | 18.7 | 18.8 | 18.5 | 15.3 | 15.7 | 15.0 |

TABLE II. Values of the coefficients of Eqs. (10) and (10a) for the density correction $\delta$.

| Material | $-C$ | 10$a$ | $m$ | $x_1$ | $x_0$ |
|---|---|---|---|---|---|
| Li | 2.81 | 3.56 | 2.99 | 2 | −0.10 |
| Be | 2.70 | 2.60 | 3.38 | 2 | 0.00 |
| Graphite | 2.82 | 3.18 | 3.15 | 2 | 0.04 |
| Al | 4.06 | 0.38 | 4.25 | 3 | 0.39 |
| Fe | 3.97 | 0.88 | 3.47 | 3 | −0.01 |
| Cu | 4.13 | 0.99 | 3.40 | 3 | 0.00 |
| Ag | 4.88 | 1.62 | 3.10 | 3 | −0.03 |
| Sn | 5.49 | 2.43 | 2.85 | 3 | 0.17 |
| W | 5.33 | 2.14 | 2.93 | 3 | 0.21 |
| Au | 5.45 | 2.54 | 2.80 | 3 | 0.25 |
| Pb | 6.03 | 3.16 | 2.71 | 3 | 0.38 |
| U | 5.86 | 3.27 | 2.64 | 3 | 0.20 |
| $H_2$ | 9.11 | 3.4 | 5.01 | 3 | 1.76 |
| He | 10.19 | 9.8 | 4.11 | 3 | 2.00 |
| Ne | 11.52 | 2.17 | 3.34 | 4 | 2.10 |
| A | 11.92 | 3.89 | 2.80 | 4 | 1.96 |
| Kr | 12.37 | 5.37 | 2.56 | 4 | 2.00 |
| Xe | 12.77 | 7.94 | 2.19 | 4 | 1.72 |
| Anthracene | 3.03 | 4.3 | 2.79 | 2 | 0.09 |
| Stilbene | 3.03 | 4.0 | 2.90 | 2 | 0.09 |
| Toluene | 3.20 | 4.6 | 2.77 | 2 | 0.12 |
| Xylene | 3.14 | 4.5 | 2.77 | 2 | 0.12 |
| $H_2O$ | 3.30 | 3.77 | 3.15 | 2 | 0.08 |
| AgCl | 5.08 | 1.39 | 3.30 | 3 | 0.18 |
| AgBr | 5.14 | 1.60 | 3.18 | 3 | 0.10 |
| Emulsion | 5.02 | 1.56 | 3.17 | 3 | 0.17 |
| NaI | 5.77 | 2.78 | 2.77 | 3 | 0.09 |
| LiI | 5.52 | 2.77 | 2.72 | 3 | −0.07 |
| $N_2$ | 10.60 | 1.12 | 3.84 | 4 | 1.81 |

$N_2$. However, $\delta$ for $H_2$ remains zero up to $\log_{10}(p/\mu c) = 2.11$ instead of the cutoff 1.81 for $N_2$. For large $p/\mu c (> 10^{2.5})$ the $H_2$ line lies $\sim 0.13$ below the $N_2$ line. We note that $\delta$ for $O_2$ lies $\sim 0.1$ below the $N_2$ curve, so that the correction for $N_2$ can also be used for air. Whenever the pressure is not indicated in Fig. 2, the gas is at normal pressure.

In order to give more accurate values of $\delta$, which do not involve the use of Figs. 1 and 2, the calculated values of $\delta$ have been fitted by means of an analytic expression as follows:

$$\delta = 4.606x + C + a(x_1 - x)^m, \qquad (x_0 < x < x_1) \qquad (10)$$

$$\delta = 4.606x + C, \qquad (x > x_1) \qquad (10a)$$

where $x = \log_{10}(p/\mu c)$ and $a$, $m$, $C$ are constants which depend on the substance; $x_0$ is the value of $x$ which corresponds to the momentum below which $\delta = 0$ [see Eq. (9a)]; $x_1$ corresponds to the momentum above which the relation between $\delta$ and $x$ can be considered to be linear. The linearity of $\delta$ at large energies can be seen from Figs. 1 and 2. The linear relationship is given by Eq. (46b) below, from which one obtains

$$C = -2\ln(\nu_m'/\nu_p) - 1. \qquad (10b)$$

The term $a(x_1 - x)^m$ in (10) is introduced in order to correct for the fact that in the intermediate region $\delta$ exceeds the asymptotic value, Eq. (10a). By means of a suitable choice of $x_1$, the resulting expression was made to fit the calculated values of $\delta$ to within 0.2 in all cases, and generally with deviations less than 0.1.

The coefficients $a$ and $m$ were obtained by fitting Eq. (10) to $\delta$ at $x_0$ ($\delta(x_0) = 0$) and at a point near the middle of the range $(x, x_1)$. Table II gives the values of $C$, $a$, $m$, $x_1$ needed to evaluate (10), in addition to $x_0$. The values given for gases pertain to normal pressure. It can be easily shown that $\delta$ at any other pressure $P$ (atmos) can be obtained from $\delta$ at $P = 1$ by means of the relation

$$\delta_P(P^{-1}\lambda) = \delta_1(\lambda), \qquad (10c)$$

where $\delta_{P'}(\lambda)$ denotes $\delta$ for a pressure $P'$ and momentum $\lambda$. To prove Eq. (10c), we consider Eq. (2) and note that an increase of pressure by a factor $P$ decreases $\bar{\nu}_i^2$ by the same factor. The left side of (2) is $(\mu c/p)^2$. Consider a momentum $p$ for the gas at normal pressure; a certain $l$ corresponds to $p$. If the pressure is increased and a new value of $l$, $l' = lP^{-1}$, is considered, the left side of (2) corresponds to a momentum $p' = pP^{-1}$. In this process the values of $(\bar{\nu}_i^2 + \bar{l}^2)/\bar{\nu}_i^2$ are unchanged and hence the first term of Eq. (1). For $\beta \approx 1$, the second term of $\delta$ equals $-\bar{l}^2(\mu c/p)^2$ which is also constant. Thus $\delta_P(p') = \delta_1(p)$. This relation can be used in all cases of interest, since $\beta \approx 1$.

With the values of $\delta$, the ionization loss $dE/dx$ was

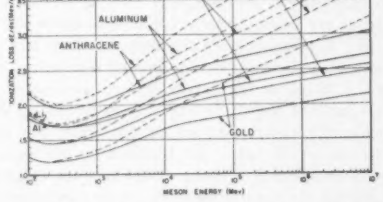


FIG. 3. Ionization loss of $\mu$-mesons in various condensed materials. The broken curve given the values of $(1/\rho)(dE/dx)$ which would be obtained without the density effect.

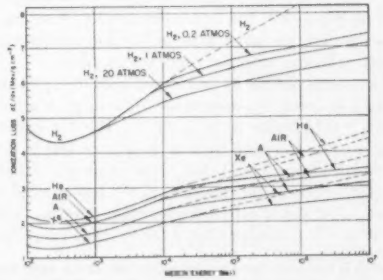


FIG. 4. Ionization loss of $\mu$-mesons in various gases. The broken curves give the values of $(1/\rho)(dE/dx)$ which would be obtained without the density effect.

calculated for several cases. The loss is obtained from the equation[13]

$$\frac{dE}{dx}=\frac{2\pi ne^4}{mv^2}\left[\ln\frac{mv^2T}{(h\nu_m')^2(1-\beta^2)}+1-\beta^2-\delta\right], \quad (11)$$

where $T$ is the maximum energy transfer and is given by[14]

$$T=\frac{E^2-\mu^2c^4}{\mu c^2(\mu/2m+m/2\mu+E/\mu c^2)}. \quad (12)$$

Here $E$ is the energy of the passing particle, whose mass is $\mu$. For $\mu$-mesons, $T$ approaches asymptotically the value $E-\mu^2c^2/2m$. For very large $E(E\gg 200\mu c^2)$. For the ionization loss of electrons, one must use

$$T=\tfrac{1}{2}(E-mc^2) \quad (12a)$$

instead of $E-mc^2$ as given by (12) to take into account the fact that the incident electron and the electron of the atom are indistinguishable.[15] Figures 3 and 4 show the ionization loss of $\mu$-mesons for several solids and gases. For comparison the values of $dE/dx$ which would be obtained without the density effect are also shown (broken curves). Among the solids, anthracene has the largest density effect. Figures 5 and 6 show $dE/dx$ for high energy electrons.

In order to compute the ionization loss, it is useful to write (11) as follows:

$$\frac{1}{\rho}\frac{dE}{dx}=\frac{A}{\beta^2}\left[B+2\ln\frac{p}{\mu c}+\ln T'+1-\beta^2-\delta\right], \quad (13)$$

where

$$A=2\pi ne^4/mc^2\rho, \quad (13a)$$

$$B=\ln[mc^2(10^6\text{ ev})/(h\nu_m')^2], \quad (13b)$$

$T'$ is the energy trasnfer in Mev, $\rho$ is the density, so that $(1/\rho)(dE/dx)$ gives the loss per g cm$^{-2}$. Values of $A$ and $B$ for each substance are given in Table I. At high energies $\beta\approx 1$, and the sum in brackets reduces to four terms. As an example, we calculate $dE/dx$ for $\mu$-mesons of energy $10^6$ Mev in uranium. Equation (12) gives $T=0.91\times 10^6$ Mev. Using $\mu c^2=100$ Mev, one finds $p/\mu c=10^3$ for which Fig. 1 gives a value of $\delta=7.9$. With $A=0.0590$ Mev/g cm$^{-2}$ and $B=13.4$, Eq. (13) gives

$$(1/\rho)(dE/dx)=0.0590[13.4+13.8+11.4-7.9]$$
$$=1.81\text{ Mev/g cm}^{-2}.$$

Equation (13), together with Eq. (12) or (12a) for $T$, applies to any charged particle. However, for electrons, the result can be somewhat simplified on account of (12a). Thus for electrons of high energy ($\beta\approx 1$), (13) can be written

$$\frac{1}{\rho}\frac{dE}{dx}=A\left[B-1.4+3\ln\frac{p}{mc}-\delta\right]. \quad (14)$$

As an example, $dE/dx$ for $10^3$ Mev electrons in $U$ will be calculated. For $p/mc=1960$, Fig. 1 gives $\delta=9.3$. One finds

$$(1/\rho)(dE/dx)=0.0590[12.0+22.7-9.3]$$
$$=1.50\text{ Mev/g cm}^{-2}.$$

For low energy electrons ($\beta<0.95$), the following equation may be used as an alternative to (13),

$$\frac{1}{\rho}\frac{dE}{dx}=\frac{A}{\beta^2}\left[B-1.4+2\ln\frac{\beta}{(1-\beta^2)^{\frac{1}{2}}}+\ln\left(\frac{1}{(1-\beta^2)^{\frac{1}{2}}}-1\right)+1-\beta^2-\delta\right]. \quad (15)$$

For high energy particles which lose energy in a thin target there are appreciable fluctuations of the ioniza-

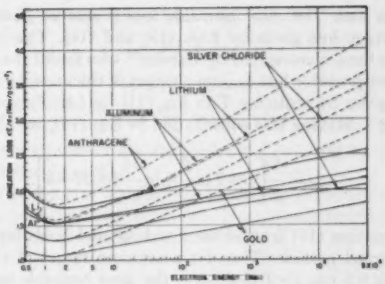


FIG. 5. Ionization loss of electrons in various condensed materials. The broken curves give the values of $(1/\rho)(dE/dx)$ which would be obtained without the density effect.

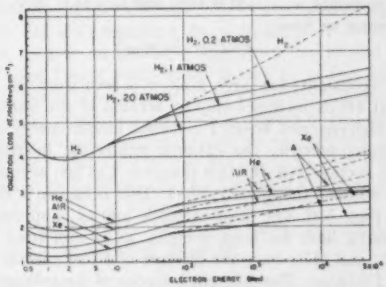


FIG. 6. Ionization loss of electrons in various gases. The broken curves give the values of $(1/\rho)(dE/dx)$ which would be obtained without the density effect.

[13] We note that there is some uncertainty concerning the theoretical expression for $dE/dx$. We choose the same expression as was used by Halpern and Hall (see reference 3) and previously given by W. Heitler, *The Quantum of Radiation* (Oxford University Press, 1936), p. 218, Eq. (1).

[14] H. J. Bhabha, Proc. Roy. Soc. (London) **164**, 257 (1937).

[15] W. Heitler, *The Quantum Theory of Radiation* (Oxford University Press, London, 1936), p. 218.

tion loss. The most probable loss is smaller than the average loss given by Eqs. (13) and (14). This effect has been investigated by Landau[16] who found that the most probable loss $\epsilon_{\text{prob}}$ in a target of thickness $t$ g cm$^{-2}$ is given by replacing $T$ in Eq. (11) by $(At/\beta^2)\exp(0.37+\beta^2)$. Making this substitution in Eq. (13), we obtain

$$\epsilon_{\text{prob}}=\frac{At}{\beta^2}\left[B+2\ln\frac{p}{\mu c}+\ln\frac{At}{\beta^2}+1.37-\delta\right]. \quad (16)$$

Equation (16) is valid for $T\gg At/\beta^2$ and holds for any charged particle. Thus for a uranium target of thickness 0.5 cm, $t=9.35$ g cm$^{-2}$, the most probable loss of $10^5$ Mev mesons is found from Eq. (16) with $At=0.55$ Mev to be 11.1 Mev, while the average loss $\epsilon_{\text{Av}}$ is $(1.81)(9.35)=16.9$ Mev. For $10^3$ Mev electrons in the same target, $\epsilon_{\text{prob}}=11.0$ Mev and $\epsilon_{\text{Av}}=14.0$ Mev.

Since we have

$$\delta=C+2\ln(p/\mu c) \quad (17)$$

($C$ = constant) for large $p/\mu c$, it is seen from Eq. (13) that $dE/dx$ increases only on account of the term $\ln T'$ at high energies. When $T$ is the full kinetic energy of the passing particle, the extreme relativistic increase of the average loss $dE/dx$ is thus only $\frac{1}{3}$ as fast as it would be without the density effect. This behavior is shown in Figs. 3–6. The most probable loss $\epsilon_{\text{prob}}$ approaches a finite limit for large energies, as is seen from Eqs. (16) and (17), since the increase of $\delta$ just cancels that of $2\ln(p/\mu c)$. The different behavior of the average and the most probable loss is due to the possibility of a large energy transfer (up to the maximum $T$) which raises the average energy loss with increasing $E$ but does not affect the most probable loss.[16]

The theoretical values of $\delta$ for AgCl can be compared with the experiment of Whittemore and Street[7] on the ionization loss of $\mu$-mesons in a silver chloride crystal. This investigation confirmed the existence of the density effect. On the basis of the most probable loss in the crystal, the authors obtained a curve of the correction $\delta$ which when applied to the Bethe-Bloch formula gives best agreement with the experimental results (see Fig. 3 of their paper). The experimental values of $\delta$ agree essentially with the curve presented here, although they are larger by $\sim 0.8$ for large $p/\mu c$ than our values. This discrepancy is quite small and may be due partly to experimental uncertainties as well as to uncertainties in the theoretical expression[13] for $dE/dx$ used by Whittemore and Street. We conclude that our values of $\delta$ for AgCl are in reasonable agreement with experiment.

Bowen and Roser[7] investigated the response of an anthracene crystal to high energy $\mu$-mesons. They found no rise in $\epsilon_{\text{prob}}$ with increasing energy in the relativistic region. This result also confirms the existence of the density effect. We note that the curve of $\epsilon_{\text{prob}}$ as a function of meson energy, as obtained from Eq. (16) with our values of $\delta$ for anthracene has a plateau of $\sim 6.0$ Mev for meson energies above 500 Mev, in good agreement with the experimental results of Bowen and Roser. Our curve also agrees (within $\sim 0.1$ Mev) with the $\epsilon_{\text{prob}}$ curve obtained by these authors, using estimated values for $\delta$.

We have compared our values of $\delta$ with those of Halpern and Hall[3] in the cases treated by these authors. The present values of $\delta$ generally agree with those of Halpern and Hall within 1 unit. The small differences between the two results arise because of the use of different frequencies for the dispersion oscillators. The corresponding values of $dE/dx$ agree with those of Halpern and Hall (obtained with $I=13.5Z$ ev) within $\sim 0.1$ Mev/g cm$^{-2}$.

### III. EQUATIONS FOR THE DENSITY EFFECT

In this section we give the derivation of the equations of the density effect which has been previously obtained.[5] If the electric field $\mathbf{E}$ of the passing particle and the polarization $\mathbf{P}$ of the medium are Fourier analyzed, a relation

$$\alpha(\omega)\mathbf{E}_\omega=4\pi\mathbf{P}_\omega \quad (18)$$

is assumed to hold for the Fourier components of frequency $\omega$. $\alpha(\omega)$ is $4\pi$ times the polarizability, for which we write

$$\alpha(\omega)=\frac{4\pi ne^2}{m}\sum_i\frac{f_i}{\omega_i^2-2i\bar{\eta}_i\omega-\omega^2}, \quad (19)$$

where the atomic frequencies $\omega_i$, the damping constants $2\bar{\eta}_i$, and $\omega$ are to be expressed in rad/sec. It was shown by Fermi[1] that the ionization loss to atoms with impact parameter greater than $b$ is given by

$$W_b=\frac{2e^2b}{\pi v^2}\,\mathrm{Rl}\int_0^\infty\left(\frac{1}{1+\alpha}-\beta^2\right)i\omega k^*K_1(k^*b)K_0(kb)d\omega, \quad (20)$$

where $K_0$ and $K_1$ are the modified Bessel functions of the second kind, Rl denotes the real part, and $k$ is the square root with real part $\geqq 0$ of

$$k^2=\frac{\omega^2}{v^2}(1-\beta^2)-\frac{\omega^2\alpha}{c^2}. \quad (20a)$$

Upon using the approximate expressions for $K_0$ and $K_1$,

$$K_0(kb)\approx\tfrac{1}{2}\ln(4/3.17k^2b^2), \quad (21)$$

$$K_1(k^*b)\approx 1/k^*b, \quad (21a)$$

one obtains from Eq. (20)

$$W_b=\frac{4ne^4}{mv^2}\,\mathrm{Rl}\int_0^\infty\left(1-\beta^2-\frac{\alpha}{1+\alpha}\right)\left[\ln\frac{4mv^2}{3.17\pi b^2ne^2(1-\beta^2)}-2\ln\nu-\ln\left(1-\frac{\beta^2\alpha}{1-\beta^2}\right)\right]i\nu d\nu, \quad (22)$$

[16] L. Landau, J. Phys. (U.S.S.R.) **8**, 201 (1944); K. R. Symon, thesis, Harvard University (1948) (unpublished).

where $\nu \equiv \omega(4\pi ne^2/m)^{-\frac{1}{2}}$. In the following, it is assumed that the damping constants $2\eta_j$ and binding frequencies $\nu_j$ are also expressed in units of the plasma frequency, so that the factor $(4\pi ne^2/m)$ of $\alpha$ disappears. In the case where the transition has $\nu_j=0$ (conduction electron), $\eta_j$ is related to the static conductivity $\sigma$ as follows:

$$\eta_j=\frac{nf_je^2}{4\pi m\sigma}\sec^{-1}=\left(\frac{ne^2}{\pi m}\right)^{\frac{1}{2}}\frac{f_j}{4\sigma}(\text{units } \nu_p). \tag{23}$$

In order to evaluate (22), it is useful to write $\alpha/(1+\alpha)$ as a sum of partial fractions,

$$\frac{\alpha}{1+\alpha}=\sum_i\frac{F_i}{l_i^2-2i\xi_i\nu-\nu^2}, \tag{24}$$

where $F_i$, $l_i$, $2\xi_i$ are the modified oscillator strength, frequency, and damping constant, respectively, associated with the $i$th transition. From the expression for $\alpha$ [Eq. (19)] it will be shown that to a good approximation, $F_i=f_i$, $\xi_i=\eta_i$, and

$$l_i=(\nu_i^2+f_i)^{\frac{1}{2}}. \tag{25}$$

It follows from (25) that $l_i\approx\nu_i$, except for $\nu_i<1$, i.e., for the transitions from the most loosely bound electrons. In order to prove these results, we consider a simplified case in which the medium can be represented by only two types of dispersion oscillators. The frequency $\nu_1$ (in units $\nu_p$) is assumed $\gg1$, while $\nu_2<1$. From (19) one obtains

$$\frac{\alpha}{1+\alpha}=\frac{f_1(\nu_2^2-2i\eta_2\nu-\nu^2)+f_2(\nu_1^2-2i\eta_1\nu-\nu^2)}{D}, \tag{26}$$

with

$$D=(\nu_1^2-2i\eta_1\nu-\nu^2)(\nu_2^2+f_2-2i\eta_2\nu-\nu^2)+f_1(\nu_2^2-2i\eta_2\nu-\nu^2). \tag{26a}$$

Alternatively, Eq. (24) gives

$$\frac{\alpha}{1+\alpha}=\frac{F_1(l_2^2-2i\xi_2\nu-\nu^2)+F_2(l_1^2-2i\xi_1\nu-\nu^2)}{(l_1^2-2i\xi_1\nu-\nu^2)(l_2^2-2i\xi_2\nu-\nu^2)}. \tag{27}$$

We equate the denominators of (26) and (27). Equating the coefficients of all powers of $\nu$ gives

$$\xi_1+\xi_2=\eta_1+\eta_2, \tag{28}$$

$$l_1^2+l_2^2=\nu_1^2+\nu_2^2+f_1+f_2, \tag{29}$$

$$\xi_2l_1^2+\xi_1l_2^2=\eta_1\nu_2^2+\eta_2\nu_1^2+\eta_2f_1+\eta_1f_2, \tag{30}$$

$$l_1^2l_2^2=\nu_1^2\nu_2^2+f_1\nu_2^2+f_2\nu_1^2. \tag{31}$$

These equations are satisfied by $\xi_i=\eta_i$ and by Eq. (25) for $l_i$. In (31) the assumption that $\nu_1^2\gg1(>f_1)$ was used. In order to obtain $F_i$ we equate the numerators of (26) and (27). One finds

$$F_1+F_2=f_1+f_2, \tag{32}$$

$$F_1\xi_2+F_2\xi_1=f_1\eta_2+f_2\eta_1, \tag{33}$$

$$F_1l_2^2+F_2l_1^2=f_1\nu_2^2+f_2\nu_1^2. \tag{34}$$

These equations are satisfied by $F_i=f_i$ up to terms of order $f_1f_2\ll f_2\nu_1^2$.

The result of Eq. (25) can be understood by considering the singularity near $\nu=\nu_i$. Near $\nu_i$ only the $i$th term of (19) is of importance, so that

$$\frac{\alpha}{1+\alpha}\approx\frac{f_i(\nu_i^2-\nu^2)^{-1}}{1+f_i(\nu_i^2-\nu^2)^{-1}}, \tag{35}$$

where $\eta_i=0$ has been assumed for simplicity. The denominator of (35) vanishes for $\nu^2=\nu_i^2+f_i$, which agrees with Eq. (24) regarding the singularity at $\nu^2=l_i^2$. In case there is an oscillator with $\nu_i=0$, $l_i=f_i^{\frac{1}{2}}$ and (24) becomes 1 near $\nu=0$, which is seen to be the correct limit from the expression for $\alpha$. The preceding proof of Eq. (25), which was given for a system of two dispersion oscillators, obviously holds for an arbitrary number, since near each $\nu_i$ only the $i$th term of $\alpha$ matters and the replacement of $\nu_i$ by $l_i$ ensures that the singularity of $\alpha/(1+\alpha)$ occurs at the correct $\nu$.

By means of (24) with $F_i=f_i$, $\xi_i=\eta_i$, $W_b$ can be reduced to the following integrals:

$$I_1=\mathrm{Rl}\int_0^\infty i\nu d\nu,$$

$$I_2=\mathrm{Rl}\int_0^\infty i\nu\ln\nu d\nu,$$

$$I_3=\mathrm{Rl}\int_0^\infty i\nu\ln\left[1-\frac{\beta^2}{1-\beta^2}\sum_i\frac{f_i}{\nu_i^2-2i\eta_i\nu-\nu^2}\right]d\nu,$$

$$I_{4j}=\mathrm{Rl}\int_0^\infty\frac{f_j}{l_j^2-2i\eta_j\nu-\nu^2}i\nu d\nu,$$

$$I_{5j}=\mathrm{Rl}\int_0^\infty\frac{f_j}{l_j^2-2i\eta_j\nu-\nu^2}i\nu\ln\nu d\nu,$$

$$I_{6j}=\mathrm{Rl}\int_0^\infty\frac{f_j}{l_j^2-2i\eta_j\nu-\nu^2}i\nu\times\ln\left[1-\frac{\beta^2}{1-\beta^2}\sum_i\frac{f_i}{\nu_i^2-2i\eta_i\nu-\nu^2}\right]d\nu. \tag{36}$$

The path of integration is along the positive real axis. These integrals can be evaluated in the manner shown by Fermi[1] by considering the closed contour consisting of the real axis up to a large distance $R$, a quarter of circle of radius $R$ with center at the origin and the positive imaginary axis from $iR$ to 0. There are no

singularities inside the contour, so that the integral along the real axis is the negative of the integral along the rest of the contour in the counterclockwise direction.

The evaluation of (36) will be illustrated by calculating $I_{aj}$. For large $R$, the contribution from the circle is

$$\mathrm{Rl}\int_0^{\pi/2} f_j \ln\left(1+\frac{\beta^2}{(1-\beta^2)R^2\exp(2i\theta)}\right)d\theta = O(R^{-2}),$$

which goes to zero as $R\to\infty$. The integral along the imaginary axis is

$$I_{aj}' = -\mathrm{Rl}\int_\infty^0 \frac{f_j}{l_j^2+2\eta_j y+y^2} \times \ln\left[1-\frac{\beta^2}{1-\beta^2}\sum_i \frac{f_i}{\nu_i^2+2\eta_i y+y^2}\right] iy\,dy. \quad (37)$$

For large $y$, the bracket $>0$ and the integral has no real part. For $y<l$, where $l$ is defined by

$$\frac{1}{\beta^2}-1=\sum_i \frac{f_i}{\nu_i^2+2\eta_i l+l^2}, \quad (38)$$

the logarithm gives $-i\pi$ so that

$$I_{aj}' = -\pi f_j\int_l^0 \frac{y\,dy}{l_j^2+2\eta_j y+y^2} = \frac{\pi f_j}{2}\ln\left(\frac{l_j^2+2\eta_j l+l^2}{l_j^2}\right)-\pi f_j T_{bj}, \quad (37a)$$

where

$$T_{bj}=\frac{\eta_j}{(l_j^2-\eta_j^2)^{\frac{1}{2}}}\tan^{-1}\frac{l(l_j^2-\eta_j^2)^{\frac{1}{2}}}{l_j^2+\eta_j l}, \quad (l_j>\eta_j) \quad (39)$$

$$T_{bj}=\frac{\eta_j}{(\eta_j^2-l_j^2)^{\frac{1}{2}}}\tanh^{-1}\frac{l(\eta_j^2-l_j^2)^{\frac{1}{2}}}{l_j^2+\eta_j l}. \quad (l_j<\eta_j) \quad (39a)$$

The singularities of the integrand are at

$$\nu=-i\eta_i\pm(\nu_i^2+\eta_i^2)^{\frac{1}{2}}, \quad -i\eta_j\pm(l_j^2+\eta_j^2)^{\frac{1}{2}}, \quad (40)$$

and lie in the lower half-plane outside the contour. Hence $I_{aj}=-I_{aj}'$.

The condition $l_j>\eta_j$ holds in most actual cases, whereas $l_j<\eta_j$ applies only to conduction electrons ($\nu_j=0$) in case there is strong damping (poor conductor). The values of $I_a$ are

$$\begin{aligned} &I_1=I_2=0,\\ &I_3=-\tfrac{1}{2}\pi l^2+\tfrac{1}{2}\pi\beta^2/(1-\beta^2),\\ &I_{4j}=-\tfrac{1}{2}\pi f_j,\\ &I_{5j}=-\tfrac{1}{2}\pi f_j \ln l_j-\tfrac{1}{2}\pi f_j T_{aj},\\ &I_{6j}=-\tfrac{1}{2}\pi f_j \ln[(l_j^2+l^2+2\eta_j l)/l_j^2]+\pi f_j T_{bj}, \end{aligned} \quad (41)$$

where

$$T_{aj}=\frac{\eta_j}{(l_j^2-\eta_j^2)^{\frac{1}{2}}}\tan^{-1}\frac{(l_j^2-\eta_j^2)^{\frac{1}{2}}}{\eta_j}, \quad (l_j>\eta_j) \quad (42)$$

$$T_{aj}=\frac{\eta_j}{(\eta_j^2-l_j^2)^{\frac{1}{2}}}\tanh^{-1}\frac{(\eta_j^2-l_j^2)^{\frac{1}{2}}}{\eta_j}. \quad (l_j<\eta_j) \quad (42a)$$

From Eq. (22) one finds

$$W_b=\frac{4ne^4}{mv^2}\left[I_3(\beta^2-1)-\sum_j I_{4j}\ln\frac{4mv^2}{3.17\pi b^2 ne^2(1-\beta^2)} +\sum_j(2I_{5j}+I_{6j})\right]. \quad (43)$$

Upon inserting the values (41) into (43) one obtains

$$W_b=\frac{2\pi ne^4}{mv^2}\left[\ln\frac{4mv^2}{3.17\pi b^2 ne^2(1-\beta^2)}-\sum_j f_j\ln(l_j^2+l^2+2\eta_j l) -\sum_j 2f_j(T_{aj}-T_{bj})+l^2(1-\beta^2)-\beta^2\right]. \quad (44)$$

The density effect is obtained by comparing $W_b$ with the classical ionization loss $W_{b0}$ to a system of isolated atoms which is given by [10]

$$W_{b0}=\frac{2\pi ne^4}{mv^2}\left[\ln\frac{4mv^2}{3.17\pi b^2 ne^2(1-\beta^2)}-\beta^2-\sum_j f_j\ln\nu_j^2\right]. \quad (45)$$

The reduction of the ionization loss is

$$W_{b0}-W_b=\frac{2\pi ne^4}{mv^2}\left[\sum_j f_j\ln\left(\frac{l_j^2+l^2+2\eta_j l}{\nu_j^2}\right) +2\sum_j f_j(T_{aj}-T_{bj})-l^2(1-\beta^2)\right]. \quad (46)$$

Since damping of the dispersion oscillators is not taken into account in $W_{b0}$, Eq. (46) gives the combined effect of the polarization and damping.[3] For $\beta<\beta_0$ [see Eq. (9a)], $l=0$ and one obtains only a small effect

$$W_{b0}-W_b=\frac{2\pi ne^4}{mv^2}\left(\sum_j f_j\ln\left(\frac{l_j^2}{\nu_j^2}\right)\right). \quad (46a)$$

For the case of a single dispersion oscillator, Eq. (46a) gives $(2\pi ne^4/mv^2)\ln\epsilon$, where $\epsilon$ is the static dielectric constant. This agrees with Fermi's result.[1] For very high energies, $l=(1-\beta^2)^{-\frac{1}{2}}$ and we obtain

$$W_{b0}-W_b=\frac{2\pi ne^4}{mv^2}\left[-\ln(1-\beta^2)-\sum_j f_j\ln\nu_j^2-1\right], \quad (46b)$$

in agreement with the results of Fermi[1] and others.[3,4]

Equation (46) for the density effect is valid for an arbitrary number of dispersion oscillators, each having its own binding and damping characteristics. The $l_j$ can be taken as the excitation frequencies $\nu_j$, except for the conduction electrons for which $l_j=f_j^{\frac{1}{2}}$ should be used. The damping terms $T_{aj}$, $T_{bj}$ are obtained from Eqs. (39) and (42), and $l$ is obtained by solving (38).

In the case in which damping can be neglected for all but one transition ($j=j_0$) and if $\eta_{j0}\gg l_{j0}$, we have

$$T_{aj0}-T_{bj0}\approx\tfrac{1}{2}\ln(1+2\eta_{j0}/l),$$

$$W_{b0}-W_b=\frac{2\pi ne^4}{mv^2}\left[\sum_{j\neq j_0} f_j\ln\left(\frac{l_j^2+l^2}{\nu_j^2}\right)\right.$$
$$\left.+f_{j0}\ln\left(\frac{l+2\eta_{j0}}{\nu_{j0}}\right)^2-l^2(1-\beta^2)\right]. \quad (47)$$

If $\nu_j>1$ for $j\neq j_0$, $l_j$ can be replaced by $\nu_j$ and the result agrees with that of Halpern and Hall.[17] We note that the $\eta_{j0}$ term makes a sizable contribution to $W_{b0}-W_b$ if $f_{j0}$ is appreciable. This contribution does not become zero for low energies when $l=0$. The $\eta_{j0}$ term corresponds to the fact that a strong damping is equivalent to a binding in reducing the ionization loss.

When the mean excitation frequency $\nu_m'$ is determined experimentally as in the work of Bakker and Segrè,[11] $\nu_m'$ includes the effect of damping so that the $\delta$, which must be applied to the Bethe-Bloch formula with the experimental $\nu_m'$, should become zero at low energies. The procedure used in the calculations of Sec. II in which it was assumed that $\eta_k=0$ gives zero correction at low energies (when $l=0$). In all cases (see Table I), the excitation frequencies $\nu_j$ exceed $f_j^{\frac{1}{2}}$ so that $l_j\approx\nu_j$. Thus Eq. (46) reduces to Eq. (1) which was used in the numerical work.

Halpern and Hall[3] have considered the effect of the Lorentz term in the dielectric constant. Thus the polarizability upon inclusion of this term becomes

$$\alpha(\nu)=\frac{\sum_{j\neq j_0}\dfrac{f_j}{\nu_j^2-2i\eta_j\nu-\nu^2}}{1-\frac{1}{3}\sum_{j\neq j_0}\dfrac{f_j}{\nu_j^2-2i\eta_j\nu-\nu^2}}+\frac{f_{j0}}{-2i\eta_{j0}\nu-\nu^2}, \quad (48)$$

where $j_0$ is the transition, if present, for which $\nu_j=0$. If we let $f_j'\equiv-f_j/3$, we may write

$$\alpha(\nu)=-3\frac{\zeta}{1+\zeta}+\frac{f_{j0}}{-2i\eta_{j0}\nu-\nu^2}, \quad (49)$$

where

$$\zeta=\sum_{j\neq j_0}\frac{f_j'}{\nu_j^2-2i\eta_j\nu-\nu^2}. \quad (49a)$$

The first term of (49) is of the same form as $\alpha/(1+\alpha)$. Corresponding to the results obtained above [see Eqs. (24) and (25)], we find

$$\frac{\zeta}{1+\zeta}\approx\sum_{j\neq j_0}\frac{f_j'}{\bar{\nu}_j^2-2i\eta_j\nu-\nu^2}, \quad (50)$$

where

$$\bar{\nu}_j=(\nu_j^2+f_j')^{\frac{1}{2}}=(\nu_j^2-f_j/3)^{\frac{1}{2}}. \quad (j\neq j_0) \quad (51)$$

Upon inserting (50) into (49) it is seen that the effect of the Lorentz term is merely to replace $\nu_j$ by $\bar{\nu}_j$, except when $\nu_j=0$ in which case $\nu_j$ must still be used. The resulting equation for $l_j$ is

$$l_j=(\bar{\nu}_j^2+f_j)^{\frac{1}{2}}=(\nu_j^2+\tfrac{2}{3}f_j)^{\frac{1}{2}}. \quad (j\neq j_0) \quad (52)$$

Equation (46) with $l_j$ as obtained from (52) gives the density effect when the Lorentz term is taken into account. However, since in all cases of Sec. II, the difference between $l_j$ and $\nu_j$ could be neglected, we may conclude that the Lorentz correction is also unimportant for these cases.

I would like to thank Dr. Ernest D. Courant for several very helpful discussions and comments. I am also indebted to Dr. W. L. Whittemore for information concerning his experiment.

[17] See Eq. (17) of reference 3.

# Proton Induced Reactions of Thorium—Fission Yield Curves*

HOWARD A. TEWES† AND RALPH A. JAMES
*Department of Chemistry, University of California, Los Angeles, California*
(Received June 30, 1952)

The fission yields of a number of nuclides produced in proton-induced fission of $Th^{232}$ were determined at several proton energies in the range of 6.7 Mev to 21.1 Mev. At the same time, the relative cross sections of the $(p,n)$ and $(p,3n)$ reactions on $Th^{232}$ were also determined. It was found that, although the fission reaction was predominant at proton energies greater than 8 Mev, competition from the $(p,xn)$ type of reaction was considerable over all energies investigated.

The trough in the fission yield curve becomes shallower with increasing proton energy and this change was quantitatively determined over the energy range investigated. A model is proposed to explain the change in shape of the fission yield curves.

An approximate determination of the excitation function for the $(p,f)$ reaction was made; the shape of the resulting curve was at least qualitatively in agreement with the excitation function predicted from existing theory.

## INTRODUCTION

DURING the past few years all of the work which has been done on the distribution of fission products originating in fission induced with high energy particles has indicated that the probability of symmetrical fission becomes greater at high energies.[1–4] However, none of this work has given fission yield curves of sufficient precision at various energies to give more than qualitative information about this trend toward greater symmetry in the fission process as the excitation energy is increased.

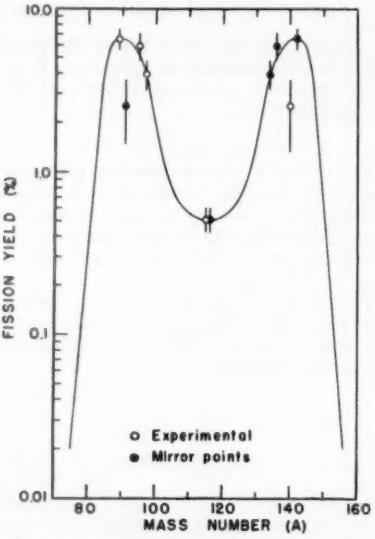


FIG. 1. Fission yield curve. Proton energy, 6.7 Mev.

Considerable work has also been done at very high particle energies which has indicated that the $(d,xnyp)$ and $(\alpha,xnyp)$, i.e., "spallation," reactions may compete favorably with fission,[2,4] but nothing has been published on the relative cross sections of this type of reaction with protons nor on the deuteron and helium ion induced reactions in the energy region just above the threshold for fission where the results would be expected to be more easily interpreted.

The work reported here was undertaken for the following purposes: (1) to ascertain the change in shape of the fission yield curve with increasing proton energies; (2) to determine the variation in the ratio of $(p,f)$ to $(p,n)$ and $(p,3n)$ reactions with increasing proton energies; and (3) to obtain the excitation functions for fission, the $(p,n)$ and $(p,3n)$ reactions of thorium for proton energies below 21 Mev.

## PROCEDURE

All bombardments were made on 0.001-in. or 0.002-in. thorium metal foil. As there was little possibility that any impurities could introduce errors in the determination of the expected bombardment products, no effort was made to analyze or purify the thorium. The targets were mounted on the unshielded probe of the UCLA frequency-modulated cyclotron; individual bombardments were obtained at selected proton energies by adjusting the position at which the target intercepted the beam. The irradiations varied from one to five hours in length with proton currents of approximately 0.1 microampere. In general, a 10- or 20-mg portion of carrier of the element being investigated was added to an aliquot of the hydrochloric acid solution of the target, the element was separated and purified from all others, and the chemical yield was determined by weighing a compound of the recovered carrier. The chemistry used

* This work was supported in part by the joint program of the ONR and AEC.
† Present address—California Research and Development Company, University of California Radiation Laboratory, Berkeley 4, California.
[1] A. S. Newton, Phys. Rev. **75**, 209 (1949).
[2] P. R. O'Connor and G. J. Seaborg, Phys. Rev. **74**, 1189 (1948).
[3] A. Turkevich and J. B. Niday, Phys. Rev. **84**, 52 (1951).
[4] R. H. Goeckermann and I. Perlman, Phys. Rev. **76**, 628 (1949).

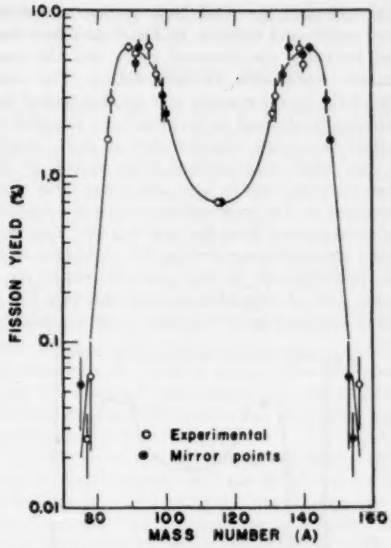


FIG. 2. Fission yield curve. Proton energy, 8.0 Mev.

has been discussed in detail by Meinke[5] and has also been described by other investigators.[1,3,4] An outline of these chemical procedures and a discussion of the nuclides identified are included in the appendix.

The final precipitates were transferred to ~3 cm² area filter papers, which were subsequently mounted on chipboard sample cards and covered with 2.7-mg/cm² cellophane. Radiation measurements were made with a single lead-shielded Geiger-Müller tube with a 2.3-mg/cm² mica (end) window. The background radiation level was subtracted from all measurements; also coincidence corrections were made where high activities were encountered. Partial absorption curves were determined for all isotopes studied this work in order that counting rates could be corrected to zero absorber thickness.

## RESULTS

### Fission Yield Curves

The fission yield curves for protons ranging in energy from 6.7 to 21.1 Mev are given in Figs. 1 to 7, and Table I gives the data from which these curves were constructed. Figure 8 reproduces the fission yield curves obtained by Turkevich and Niday[3] with 2.6-Mev neutrons and by Newton[1] with 37.5-Mev helium ions, along with two of the curves obtained in this work so that a direct comparison can be made. In all of these curves open circles represent the experimental data, and solid circles represent mirror points.[6] The mass numbers of the mirror points ($A'$) were obtained by assuming that two neutrons were given off in the fission process; consequently, $A'=231-A$. The number of neutrons assumed to be given off was arbitrarily chosen to give the smoothest curve in the regions where the fission yields were relatively high, and consequently, fairly reliable. The assumption that the average number of neutrons emitted is independent of the degree of symmetry of that particular fission is open to question. It may be noted that the fission yield curves obtained with proton energies of 18 Mev or less show appreciable scatter of points at the extreme ends of the curves. If, however, the expression used in calculating the mirror points is changed to $A'=233-A$, this scatter at the ends of the curves would be eliminated but would, naturally, introduce more scatter near the maxima. The scatter is completely eliminated if it is assumed that less neutrons are emitted in the very asymmetric fission (and possibly in symmetrical fission) than are emitted when the fission products are those of maximum yield.

### Excitation Functions

Although it was not possible by the methods used here to determine accurately the absolute values of the cross sections for the reactions studied, the ratios of these cross sections at each energy were determined with fair precision as indicated by the data of Table I.

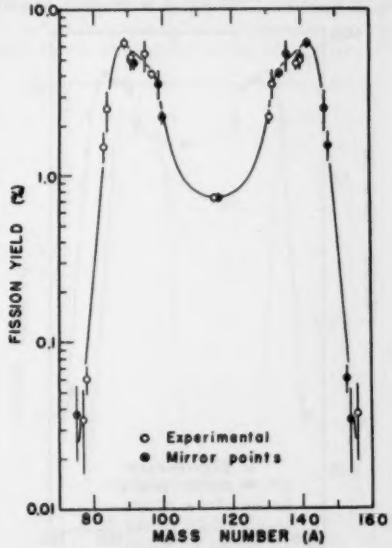


FIG. 3. Fission yield curve. Proton energy, 9.3 Mev.

[5] W. W. Meinke, AEC Reports AECD-2738 (UCRL-432) and AECD-2750 (unpublished).

[6] The use of both experimental and mirror points in the drawing of a fission yield curve is not uncommon; e.g., Turkevich and Niday (reference 3) constructed their fission yield curve in this way.

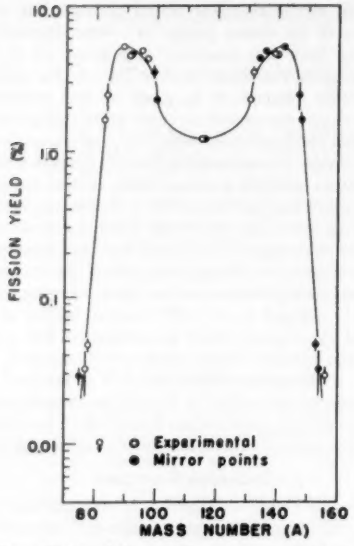


FIG. 4. Fission yield curve. Proton energy, 13.3 Mev.

In order to have some scale on which to present these ratios, the statistical treatment of Weisskopf[7,8] has been used to calculate the total cross section for proton induced reactions of thorium. In Fig. 9 the points were plotted by using the observed ratios and the total calculated cross section at each energy. The cross section of the $(p,2n)$ reaction was not determined but was arbitrarily assumed to have the form indicated. It is unlikely that other reactions such as $(p,\dot{p})$; $(p,pn)$; $(p,\alpha)$, etc. have cross sections large enough at the energies involved here to have any appreciable effect on these curves. The cross sections were also calculated in the usual manner from the yield and the (very inaccurately) measured beam striking the unshielded probe in the cyclotron tank. In most cases the results are of the same order of magnitude as those shown in Fig. 9, but large discrepancies were present in certain instances

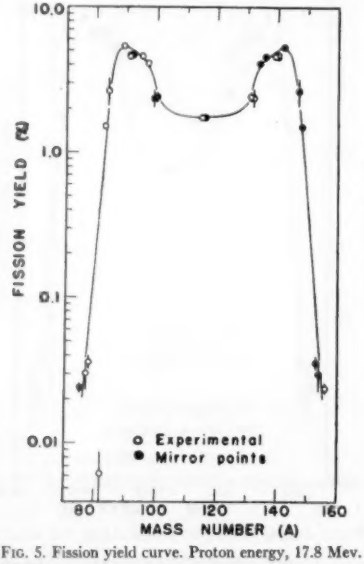


FIG. 5. Fission yield curve. Proton energy, 17.8 Mev.

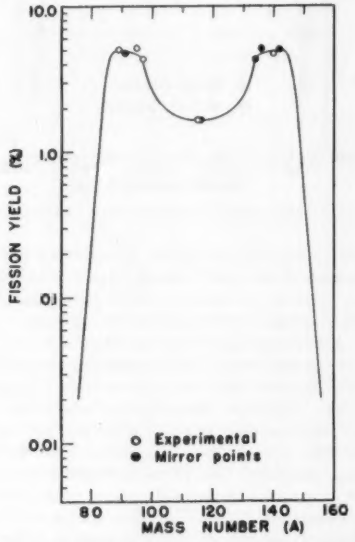


FIG. 6. Fission yield curve. Proton energy, 19.5 Mev.

which are best explained by the large error in proton beam measurement.

It should be noted that, although the $(p,f)$ reaction is predominant at higher particle energies, the $(p,xn)$ reactions account for much of the total proton cross section at all energies. It is highly probable that this is the case for the interaction of any charged particle with heavy nuclei; consequently, the abnormally low fission cross sections which have been observed by Jungerman for helium ions on thorium[9] can reasonably be attributed to the competition of $(\alpha,xn)$ reactions.

A picture which is consistent with the above results on the excitation functions as well as the trend in

[7] V. F. Weisskopf and D. H. Ewing, Phys. Rev. **57**, 472 (1939).
[8] V. F. Weisskopf, unpublished lecture series on nuclear physics (Los Alamos Report No. 24), p. 207.
[9] J. Jungerman, Phys. Rev. **79**, 632 (1950).

degree of symmetry of fission is presented in the discussion of these results.

### Miscellaneous Results

It was found that the ratio of the yields of the two $Cd^{115}$ isomers remained approximately constant over the range of energies at which this quantity could be measured. The average value of the ratio (2.19 day/43 day) in eight bombardments in the energy range 13.3–21.1 Mev was 16.7, the extreme values being 15.1 and 17.4 with no observable trend with increasing energy. It seems probable that all of both of these isomers are formed from a primary fission product of lower $Z$ and that this ratio represents the natural ratio arising from decay of $Ag^{115}$. It is doubtful that the value 16.7 obtained in this work represents a significant departure from the value 14 quoted in the slow neutron fission of uranium,[10] particularly since the half-life of 2.19 days used here differs from that used in calculating the ratio in slow neutron fission.

The fraction of the $As^{77}$ which was formed by the decay of the 59-second $Ge^{77}$ was calculated for those bombardments where sufficient arsenic activity was present to make the computations meaningful. These values were constant within experimental error, the mean value for the ratio (59-sec $Ge^{77}$)/(12−hr $Ge^{77}$) being $1.1\pm0.2$ Here again it is probable that this is the ratio of $Ge^{77}$ isomers resulting from the decay of $Ga^{77}$.

### DISCUSSION OF RESULTS

With regard to the series of fission yield curves resulting from the present investigation, several points are of interest. First, the depth of the trough decreases markedly and in a regular fashion with increasing energy of the incident protons. This trend is clearly shown in Table II and also in Fig. 10 where the ratio of the fission yield of $Cd^{115}$ (the sum of the two isomers) to the yield of $Sr^{89}$ is plotted against the proton energy.

Newton's results[1] are somewhat inconclusive with respect to the depth of the trough; however, the reported ratio of $Cd^{115}/Sr^{89}$ is of the order of 0.5, which is not inconsistent with the value which might have been predicted for 37.5-Mev particles on the basis of this curve. It may be noted that if the $Cd^{115}/Sr^{89}$ yield ratio determined by Turkevich and Niday[3] for the fission of thorium with pile neutrons is plotted in Fig. 10, it lies on the extrapolated curve within experimental error. Consequently, it may be concluded that the nature of the particle which induces fission as well as the nucleus which is considered to be the compound nucleus are not as critical in determining the mode of fission as is the energy imparted to the compound nucleus by the particle.

If one assumes that a compound nucleus is formed with excitation energy determined by the energy of the incident particle and that this compound nucleus may lose its excess energy by the numerous possible modes of fission or by the emission of one or more neutrons, the fraction decomposing by any particular mechanism would then be proportional to the relative rate of that

[10] The Plutonium Project, J. Am. Chem. Soc. 68, 2411 (1948).

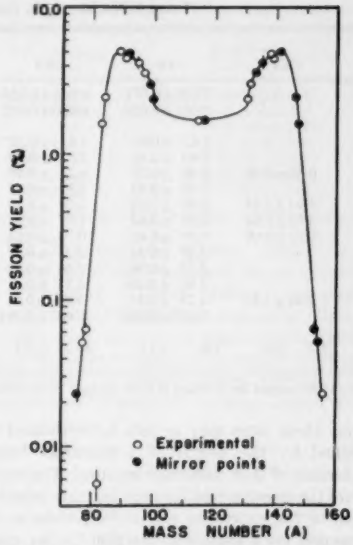


FIG. 7. Fission yield curve. Proton energy, 21.1 Mev.

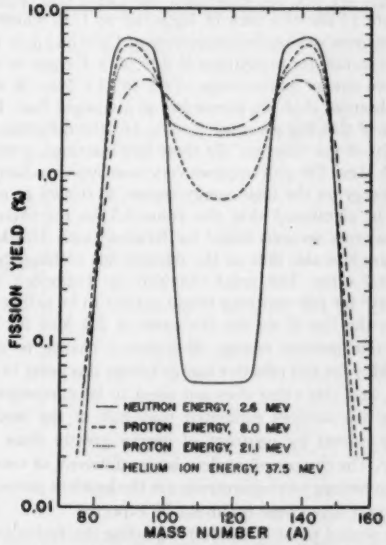


FIG. 8. Fission yield curves for $Th^{232}$.

TABLE I. Nuclide yields, percent (total atoms fissioned = 100 percent).

| Mass No. | Proton energy (Mev) 6.7 | 8.0 | 9.3 | 13.3 | 17.8[a] | 19.5[a] | 21.1 |
|---|---|---|---|---|---|---|---|
| 77 | | 0.026±0.011 | 0.034±0.018 | 0.032±0.011 | 0.030 ±0.007 | | 0.052 ±0.006 |
| 78 | | 0.061±0.039 | 0.060±0.012 | 0.047±0.005 | 0.036 ±0.004 | | 0.064 ±0.006 |
| 82 | | | | 0.010$_3$ (Max) | 0.0062±0.0025 | | 0.0057±0.0014 |
| 83 | | 1.67 ±0.07 | 1.51 ±0.32 | 1.65 ±0.08 | 1.51 ±0.07 | | 1.64 ±0.07 |
| 84 | | 2.90 ±0.50 | 2.53 ±0.69 | 2.44 ±0.53 | 2.66 ±0.56 | | 2.49 ±0.50 |
| 89 | 6.55±0.96 | 6.00 ±0.37 | 6.24 ±0.49 | 5.25 ±0.18 | 5.31 ±0.12 | 5.01±0.14 | 5.07 ±0.14 |
| 91 | | 5.48 ±0.53 | 5.15 ±0.52 | 4.58 ±0.21 | 4.57 ±0.28 | | 4.61 ±0.14 |
| 95 | 5.93±1.14 | 6.05 ±1.05 | 5.29 ±1.10 | 4.93 ±0.18 | 4.57 ±0.22 | 5.14±0.32 | 4.27 ±0.38 |
| 97 | 3.97±0.84 | 4.08 ±0.61 | 4.07 ±0.24 | 4.36 ±0.11 | 4.08 ±0.15 | 4.32±0.20 | 3.63 ±0.09 |
| 115 | 0.51±0.09 | 0.69 ±0.03 | 0.73 ±0.04 | 1.22 ±0.04 | 1.75 ±0.11 | 1.66±0.10 | 1.74 ±0.07 |
| 131 | | 2.40 ±0.24 | 2.24 ±0.22 | 2.27 ±0.07 | 2.45 ±0.18 | | 2.38 ±0.05 |
| 132 | | 3.03 ±0.90 | 3.56 ±0.72 | 3.48 ±0.35 | 2.38 ±0.34 | | 3.02 ±0.24 |
| 139 | | 5.95 ±0.68 | 4.75 ±0.41 | 4.72 ±0.18 | 4.63 ±0.22 | | 4.96 ±0.29 |
| 140 | 2.49±1.16 | 4.74 ±0.53 | 4.90 ±0.61 | 4.61 ±0.11 | 4.67 ±0.23 | 4.71±0.22 | 4.51 ±0.07 |
| 156 | | 0.055±0.026 | 0.037±0.018 | 0.029±0.004 | 0.024 ±0.002 | | 0.023 ±0.001 |
| $Pa^{233}$ | | | | | 1.31 (Max) | 38.8 ±1.8 | 31.1 ±1.7 |
| $Pa^{232}$ | 147 ±4 | 116 ±17 | 34.3 ±5.3 | 5.08 ±0.75 | 2.64 ±0.40 | 0.88±0.14 | 0.81 ±0.12 |

[a] Fission yields quoted are averages of three separate bombardments at this energy.

reaction. These rates may in turn be considered to be determined by the height of a potential "barrier" characteristic of that particular reaction. The rate and therefore the cross section for each reaction would then be given by the expression $\sigma_i = ce^{-E_i/E}$, where $\sigma_i$ is the cross section for a particular reaction (as for example fission into two nuclei of masses 115 and 116); $c$ is a constant which depends on the target nucleus, the bombarding particle, and the energy of the incident particles; $E_i$ is the height of the barrier for reaction $i$ and $E$ is the excitation energy. If we now take the ratio of cross sections for two particular reactions at a given energy, we get the expression $\ln(\sigma_1/\sigma_2) = (E_2 - E_1)/E$. Figure 11 shows a plot of $\log(\sigma_1/\sigma_2)$ *vs* $1/E$, where $\sigma_1$ is the cross section for production of $Cd^{115}$ and $\sigma_2$ is the cross section for production of $Sr^{89}$, with $E$ equal to the proton energy in the range of 6.7 to 21.1 Mev. It will be observed that the points fall on a straight line. The slope of this line gives for $E_2 - E_1$, i.e., the difference in height of the "barrier" for these two reactions, a value of 15 Mev. The plot becomes very insensitive to changes in energy on the high energy region, so it may or may not be significant that the value 0.5 for the ratio of these cross sections found by Newton[1] with 37.5-Mev helium ions also falls on the straight line within experimental error. The point obtained by Turkevich and Niday[3] for pile neutrons would appear to be rather far from the line if we use the value of 2.6 Mev for the effective neutron energy. However, a change to only 3.4 Mev for this effective energy brings this point to the line, and this value does not seem to be unreasonable since the authors estimated that half of the fissions were caused by neutrons of energy greater than 2.7 Mev. The compound nucleus is also different, of course, when helium ions or neutrons are the incident particles, so exact agreement could not be expected.

A second point of interest regarding the fission yield curves is the apparent presence of a secondary maximum in the yield curves at $A = 95$ and $A = 136$. This secondary maximum effect has been previously noted in the thermal neutron fission of $U^{235}$. Glendenin *et al.*[11] have conclusively shown by means of a mass spectrometric study that maxima exist at $A = 98$–$100$ and $A = 133$–$136$ in the fission yield curve. The maximum in the heavy fragment region was attributed by these workers to the stable 82-neutron configuration; the other maximum necessarily resulted from the nature of the fission process. Since the stabilizing effect of closed shells on fission yields would be expected to become of less importance as the excitation energy of the fissioning nucleus was increased, it is not surprising to note that the secondary maximum becomes less pronounced as as proton energies are increased.

The apparent flatness of the fission yield curves in the region of nearly symmetric fission is especially evident in those cases where high energy protons were used. It is probable, however, that this flatness would also be exhibited in the fission yield curves obtained with low energy particles, but the effect cannot be conclusively demonstrated since only one point was taken in the minimum yield region at each proton energy. The curve obtained by Turkevich and Niday[3] also shows this flat minimum. The effect has also been demonstrated with fast (pile) neutrons on $U^{235}$.[12] Apparently, only with slow neutron induced fission is there a sharp fission yield rise about a minimum symmetric point. These results are in agreement with the hypothesis that the energy barrier for symmetric or near symmetric fission is somewhat higher than that for asymmetric fission. This barrier is apparently quite uniform in height in the region where the fission

[11] Glendenin, Steinberg, Inghram, and Hess, Phys. Rev. **84**, 860 (1951).

[12] Engelkemeir, Seiler, Steinberg, and Winsberg, *Radiochemical Studies: The Fission Products* (McGraw-Hill Book Company, Inc., New York, 1951), Paper No. 218, National Nuclear Energy Series, Plutonium Project Record, Vol. 9, Div. IV.

fragments produced have mass numbers ranging from about 103 to 128. For the fission processes in which fragments with masses 85–95 and 136–146 are produced, the barrier height is lower (probably of the order of 7 Mev), and for those fissions producing fragments at the extreme ends of the fission yield curve the barrier height approaches infinity. It should be noted that these barrier heights do not include the Coulombic repulsion of the nucleus for the bombarding particle but are concerned only with the possible modes of decomposition of the compound nucleus.

We are grateful to Professor J. R. Richardson for his interest and cooperation and to Mr. S. Plunkett and the cyclotron operating staff for the numerous bombardments.

## APPENDIX

The chemical separation method and isotope identification for each element investigated are given briefly. In order to insure adequate purification of the elements, the individual samples were recycled at least twice through the chemical procedures outlined here. Those cases in which the amounts of activity dealt with were notably low will be indicated.

*Arsenic.*—Precipitated (as $As_2S_3$) from 6*f* HCl and dissolved in $NH_4OH$ solution; $GeCl_4$ removed by distillation from oxidizing medium; $AsCl_3$ subsequently distilled off under reducing conditions.

The 1.3-hour $As^{79}$ as well as the 40-hour $As^{77}$ were identified. By making two separations of the As fraction, the relative amounts of the $As^{77}$ being formed from the 59-second and 12-hour isomers of $Ge^{77}$, respectively, could be determined. In two separations, small amounts of a 12-day activity were observed; however, it was not possible to characterize this isotope. Due to the small amounts of total activity present in many of the arsenic fractions separated (especially in the ones where low energy protons were used in the bombardments), statistical counting errors were as high as 50 percent.

TABLE II. Fission yield curve trough depths.

| Proton energy (Mev) | Total yield of $Cd^{115}$ / Yield of $Sr^{89}$ |
|---|---|
| 6.7 | 0.078±0.017 |
| 8.0 | 0.116±0.009 |
| 9.3 | 0.117±0.011 |
| 13.3 | 0.232±0.010 |
| 17.8 | 0.329±0.020 |
| 19.5 | 0.331±0.017 |
| 21.1 | 0.344±0.016 |

*Bromine.*—Oxidized to $Br_2$, $Br_2$ (and $I_2$) extracted into $CCl_4$; reduced with $NaHSO_3$, $I^-$ oxidized to $I_2$ with $NaNO_2$, removed by $CCl_4$ extraction. $Br^-$ subsequently oxidized to $Br_2$ and extracted into $CCl_4$, reduced with $NaHSO_3$ to $I^-$ (aqueous solutions), precipitated as AgBr.

The 30-minute $Br^{84}$ and 2.4-hour $Br^{83}$ activities were detected in all bromine fractions; the 35-hour $Br^{80}$ (shielded isotope) was identified in two samples where the activity of this isotope was sufficiently high to allow for its characterization.

*Strontium.*—Precipitated as $Sr(NO_3)_2$ with fuming

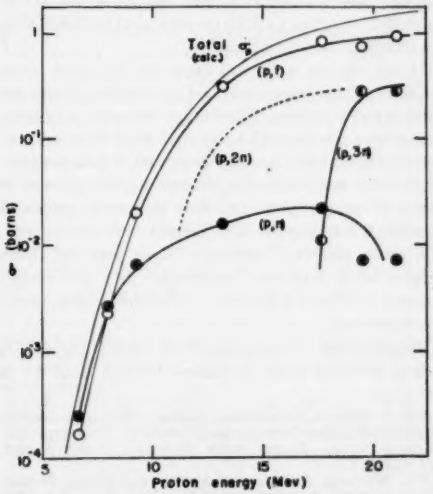


FIG. 9. Excitation functions for proton-induced reactions of $Th^{232}$.

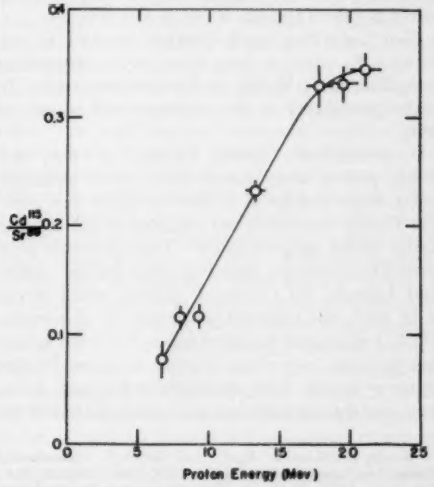


FIG. 10. Ratio of fission yield of $Cd^{115}$ to that of $Sr^{89}$ vs energy of incident protons.

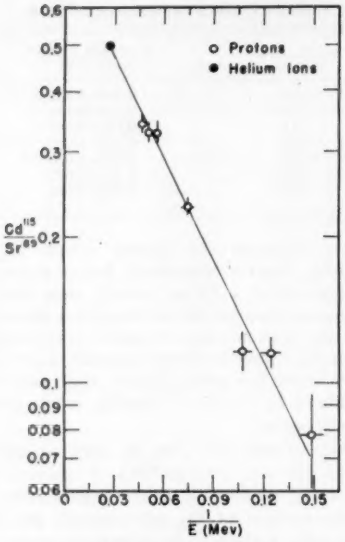


FIG. 11. Log of ratio of fission yields $Cd^{115}/Sr^{89}$ *vs* reciprocal of incident proton energy.

$HNO_3$; redissolved and Ba removed by precipitating $BaCrO_4$. Scavenged with $Fe(OH)_3$, Sr finally brought down as $SrC_2O_4$.

The 9.7-hour $Sr^{91}$ was identified in most samples. Also, a 50-day period was detected; this was assumed to be the isotope $Sr^{89}$, which has previously been reported to have a half-life of 53[13] or 55[14] days.

*Zirconium.*—Rare earth fraction removed as the fluorides, Ba added to bring down $BaZrF_6$. Precipitate redissolved using $H_2BO_3$, and concentrated acid; Zr finally precipitated as the cupferrate and ignited to $ZrO_2$.

Components of 17-hour, 1.$3_2$-day, 17.7-day, and 65-day periods were resolved after proton bombardments where energies of 18 Mev or higher were used. The 17-hour component was identified as $Zr^{97}$ and the 65-day period assigned to $Zr^{95}$. These activities were present in all samples, regardless of the proton energies used. Likewise, the 1.$3_2$-day $\beta^-$ activity, which proved to be $Pa^{232}$, was produced by protons of all energies. The 17.1-day period was identified as $Pa^{230}$; this isotope was produced only when protons of above 18-Mev energy were used. From the results of this work, it was concluded that protactinium was carried quantitatively by zirconium under the conditions used in making this separation. (See also section on Protactinium.)

*Cadmium.*—Precipitated as CdS from 0.2*f* HCl, redissolved, Fe, La, In scavengings made. CdS reprecipitated, redissolved, AgCl scavenging made. CdS again precipitated, redissolved, Pd and Sb separations run, CdS precipitated once more. Redissolved, final precipitation of $CdNH_4PO_4$.

The decay curves were separable into 2.19-day and 43-day activities, which were obviously identifiable with the two isomers of $Cd^{115}$. The 2.19-day half-life value was accurate to ~0.05 day, and differs slightly from that previously reported in the literature (2.33 days).[15]

*Iodine.*—Aliquot plus carrier oxidized with NaOCl to obtain all iodine in the same oxidation state. Reduced with $NH_2OH$, extracted into $CCl_4$. Reoxidized with $NaNO_2$, extracted with $CCl_4$. Reduced with $NaHSO_3$, AgI precipitated.

Both the 8.0-day $I^{131}$ and 2.4-hour $I^{132}$ (daughter of the 77-hour $Te^{132}$) were identified unambiguously.

*Barium.*—Precipitated as $Ba(NO_3)_2$ with fuming $HNO_3$. Redissolved, precipitated as $BaCrO_4$, dissolved in 6*f* HCl, precipitated as $BaCl_2$.

An 85-minute activity, identified as $Ba^{139}$, was found. The expected growth of the 40-hour $La^{140}$ into secular equilibrium with the 12.8-day $Ba^{140}$ was also observed.

*Europium.*—After removal of Th and Zr as the iodates, Ba and Sr hold-back carriers added, Ce and Eu precipitated with $NH_4OH$, Nb and Zr hold-back carriers added, $CeF_3$, $EuF_3$ precipitated. Redissolved in $H_3BO_3$—acid solution, Eu(III) reduced to Eu(II) in Jones reductor, and $Ce(OH)_3$ precipitated with $NH_4OH$. Eu finally obtained as $Eu_2(C_2O_4)_3$.

Decay curves with half-lives of 14.2 days were obtained; these were identified as resulting from the $Eu^{156}$ activity present. This isotope has previously been reported as having a 15.4-day half-life.[16] Also, an unidentifiable ~57-day activity was noted in some samples. Due to the small amounts of total activity present in many of the europium fractions separated, statistical counting errors as great as 50 percent were encountered. (In some samples, especially those prepared from targets which had been bombarded with low energy protons, activities of less than 1 *c/m* above background were detected.)

*Protactinium.*—Zirconium carrier added, 16*f* $HNO_3$ added, solution taken to fumes. Diluted until 4*f* in

[13] Novey, Engelkemeier, Brady, and Glendenin, *Radiochemical Studies: The Fission Products* (McGraw-Hill Book Company, Inc., New York, 1951), Paper 76, National Nuclear Energy Series, Plutonium Project Record, Vol. 9, Div. IV.

[14] D. W. Stewart, Phys. Rev. **56**, 629 (1939).

[15] R. P. Metcalf, *Radiochemical Studies: The Fission Products* (McGraw-Hill Book Company, Inc., New York, 1951), Paper 127, National Nuclear Energy Series, Plutonium Project Record, Vol. 9, Div. IV.

[16] L. Winsberg, *Radiochemical Studies: The Fission Products* (McGraw-Hill Book Company, Inc., New York, 1951), Paper 198, National Nuclear Energy Series, Plutonium Project Record, Vol. 9, Div. IV.

$HNO_3$. Solution scavanged with $I_2$ in benzene, then Zr, Nb, and Pa extracted into benzene, 0.4$f$ in TTA. Benzene phase ignited; resulting $ZrO_2$ solid mounted.

Same activities detected as in the zirconium fraction. As the ratios of the different activities detected were the same within experimental error as those found in the zirconium samples, it was concluded that protactinium was quantitatively carried in both procedures. The method of isolating Pa alone with Zr by two independent chemical procedures was adopted in order to determine the chemical yield without the necessity of adding $Pa^{231}$ tracer.

PHYSICAL REVIEW VOLUME 88, NUMBER 4 NOVEMBER 15, 1952

# Grain Boundary Barriers in Germanium*

W. E. TAYLOR,† N. H. ODELL,‡ AND H. Y. FAN
*Purdue University, Lafayette, Indiana*

(Received July 21, 1952)

High resistance at crystal grain boundaries in $n$-type germanium is investigated. The resistance is symmetrical with respect to the direction of the current and resembles the characteristics of a rectifier in the blocking direction. Such barriers are also photosensitive. The barrier is eliminated when the material is converted to $p$-type by nucleon bombardment or heat treatment. A theory is developed assuming the existence of surface states at the boundary. The ability of the barriers to withstand high voltages, around 100 volts, is explained by showing that the surface charge increases with increasing voltage. The dc conductance of the barrier, measured at different temperatures, agrees with theory in the dependence on temperature as well as in the order of magnitude. At sufficiently low temperatures the barriers show a capacitance independent of the frequency, whereas at higher temperatures the barrier admittance is strongly frequency dependent. These results are in agreement with the theory, showing that at low temperatures the current across the boundary is mainly carried by electrons, the hole current becoming increasingly important as the temperature is raised. The height of the potential barrier above the Fermi level is determined and found to be independent of temperature. A small difference in the measured breakdown voltage for the two directions of current is attributed to a difference in impurity concentration on the two sides of the boundary, which is confirmed by the ac measurements. The number of electrons on the boundary states is found to be of the order $10^{12}$ $cm^{-2}$ at the breakdown, which may be the saturation of the boundary states. However, the field at breakdown is only a few times lower than the critical value for the onset of the Zener current, and this mechanism cannot be definitely ruled out.

## INTRODUCTION

GRAIN boundaries in $n$-type germanium are often found to present a high resistance to current flow in either direction.[1–4] Curve A, Fig. 1, shows the potential variation as measured by a whisker probe along a germanium sample with a grain boundary. The potential is seen to make an abrupt jump at the boundary, corresponding to 95 percent of the total potential difference applied to the sample. This high boundary resistance is not due to an insulating layer of foreign material. Microphotographs do not reveal any second phase at such boundaries. Furthermore, when a sample with a high resistance grain boundary is changed into $p$-type, either by nucleon irradiation[5] (curve B, Fig. 1) or by heating to high temperatures and subsequent quenching,[2] the boundary resistance vanishes. It reappears when the sample is changed back to $n$-type by annealing.

The resistance of the boundary is nonohmic, increasing with increasing voltage, and is approximately symmetrical regarding the direction of current. Figure 2 shows a set of typical current-voltage curves. The curve for both directions of current flow resembles the ordinary rectifier characteristic in the blocking direction. Furthermore, the grain boundary is also photosensitive; the photovoltage generated by a sharp pencil of light reverse its sign as the light crosses the boundary, and the signs are such as to agree with the picture of two potential barriers of a $n$-type semiconductor existing at the boundary back to back.[6] Merritt[7] and Benzer[8] have shown that two wedge-shaped pieces of uniform $n$-type germanium brought to a point contact give a current-voltage characteristic similar to the curve in Fig. 2. The nonohmic contact resistance was interpreted as due to potential barriers at free surfaces of $n$-type

* Work supported by a Signal Corps contract. The dc measurements are part of a thesis submitted by W. E. Taylor and the ac measurements are part of a thesis submitted by N. H. Odell to the faculty of Purdue University in partial fulfillment of the requirements for the Ph.D. degree.

† Now at Motorola Research Laboratory, Phoenix, Arizona.

‡ Now at Bell Telephone Laboratories, Allentown, Pennsylvania.

[1] K. Lark-Horovitz, NDRC Report 14–585 (1945) (unpublished).

[2] G. Pearson, Phys. Rev. **76**, 459 (1949).

[3] W. E. Taylor and H. Y. Fan, Phys. Rev. **78**, 335 (1950).

[4] N. H. Odell and H. Y. Fan, Phys. Rev. **78**, 334 (1950).

[5] W. Taylor and K. Lark-Horovitz, Purdue Semiconductor Research Progress Report (October, 1948) (unpublished); reference 3.

[6] M. Becker and H. Y. Fan, Purdue Semiconductor Research Progress Report (June, 1949); see also reference 2.

[7] E. Merritt, Proc. Natl. Acad. Sci. **11**, 743 (1925).

[8] S. Benzer, Phys.Rev. **71**, 141 (1947).

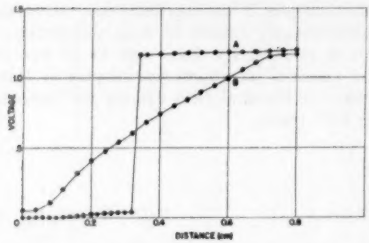


FIG. 1. Potential drop along a sample with a grain boundary. Curve A, original $n$-type sample. Curve B, sample converted to $p$-type by deuteron irradiation.

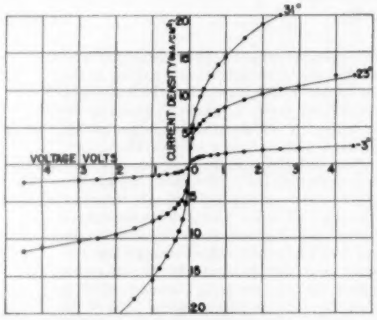


FIG. 2. Current-voltage characteristics of a grain boundary at different temperatures.

germanium due to surface states postulated by Bardeen.[9] Thus the similar behavior of grain boundaries can be due likewise to the existence of surface states at the boundary.

Surface states at the boundary may be produced either by the lattice misfits or by a segregation of acceptor impurities. The specimens studied were obtained from germanium melts, in which the resistivity indicates that the parts solidified last contain more $n$-type or less $p$-type impurities. The grain boundaries were formed as two separate crystals joined together in their growth. Although it does not provide a conclusive proof, this observation seems to be against the segregation of $p$-type impurities at the grain boundaries in these melts. In the following we shall first give a theoretical treatment of the problem on the basis of the existence of boundary states. Then the experimental results will be presented and discussed in the light of the theory. The theory is independent of the cause of the boundary states. However, if near the boundary there is an extensive region with excess acceptor impurities, then the problem could be treated by the same method used for $n$–$p$–$n$ junctions.[10] As we shall see, the experimental evidence is against such an interpretation.

[9] J. Bardeen, Phys. Rev. **71**, 717 (1947).
[10] Shockley, Sparks, and Teal, Phys. Rev. **83**, 151 (1950).

## THEORY

The electron energy level diagram according to our picture is shown in Fig. 3. Figure 3a corresponds to equilibrium condition, while Fig. 3b is drawn for the condition under an applied voltage $V_a$. Localized boundary states are assumed with energy levels in the forbidden gap. Under equilibrium some of these states, i.e., roughly those below the Fermi level, are occupied by electrons, giving rise to a negative surface charge $q$. A space charge region constituting a potential barrier results on either side of the boundary. The sum of the positive space charges is equal to $q$ in magnitude. When the specimen is converted to $p$-type, either by nucleon bombardment or by heat treatment, the Fermi level is shifted close to the bottom of the energy gap. Most of the boundary states will not be occupied by electrons, and there will no longer be appreciable potential barriers. The high resistance of the boundary is thereby eliminated.

Impurities in germanium usually have very small activation energies and are practically completely ionized even in the bulk material, except at very low temperatures. Thus the space charge density in the potential barriers is equal to the impurity concentration $N$, if the space charges of the carriers are neglected. These are easily seen to be small compared to the space charge of impurities, provided the top of the valence band does not come too close to the Fermi level at the boundary, in which case the hole concentration at the boundary may be too high for its space charge to be neglected. However, such a situation, if it exists, is limited to a small part of the barriers. We shall overlook this possible complication and deal with fixed space charge of impurity ions. Solution of the Poisson equation gives for the potential drop across such a barrier:

$$V=\kappa E^2/8\pi eN=2\pi eNl^2/\kappa. \tag{1}$$

The total space charge in the barrier is

$$Q=eNl=(\kappa eNV/2\pi)^{\frac{1}{2}}, \tag{2}$$

where $\kappa$ is the dielectric constant of the medium, $E$ is the electric field at the top of the barrier, and $l$ is the barrier thickness.

Referring to Fig. 3 we shall take the direction from left to right as positive. The potential difference across the boundary is

$$V_1-V_2=\frac{\kappa}{8\pi e}\left(\frac{E_1^2}{N_1}-\frac{E_2^2}{N_2}\right), \tag{3}$$

and the surface charge on the boundary states is

$$q=-(\kappa e/2\pi)^{\frac{1}{2}}[(N_1V_1)^{\frac{1}{2}}+(N_2V_2)^{\frac{1}{2}}]$$
$$=-(\kappa/4\pi)(E_1-E_2). \tag{4}$$

We shall see later that the experimental results show some dissymmetry between the two sides of the boundary, which is attributable to a small difference between $N_1$ and $N_2$. However, this difference is of no significant importance in some of the following discussions. For simplicity we shall assume $N_1=N_2=N$, except when we want to deal specifically with the unsymmetrical behavior. Thus, under equilibrium,

$$\phi_1=\phi_2=\phi; \quad V_{10}=V_{20}=\phi/e; \qquad E_{10}=-E_{20}=-2\pi q_0/\kappa. \tag{5}$$

Under an applied voltage across the barrier,

$$V_a=V_1-V_2, \tag{6}$$

we get from (3) and (4):

$$E_1=-2\pi q/\kappa-eNV_a/q, \quad E_2=2\pi q/\kappa-eNV_a/q. \tag{7}$$

Substituting in (1), we find

$$V_1=(\kappa/8\pi eN)(2\pi q/\kappa+eNV_a/q)^2, \qquad V_2=(\kappa/8\pi eN)(2\pi q/\kappa-eNV_a/q)^2. \tag{8}$$

$E_2$ and $V_2$ reduce to zero if $V_a$ reaches the critical value,

$$V_c=(2\pi/\kappa eN)q^2. \tag{9}$$

If $q$ remains equal to $q_0$ we find, in view of (5),

$$V_c=4\phi. \tag{10}$$

Thus the maximum voltage drop across the grain boundary is $4\phi$, where $\phi$ is only a fraction of 1 ev. Actually grain boundaries present a very high resistance for voltages up to 100 volts. This fact can be understood in the following way. We shall show shortly that, with increasing applied voltage, the electron concentration at the boundary surface increases whereas the hole concentration decreases. Consequently, the number of electrons on the boundary states will be increased due to the processes tending to establish equilibrium electron distribution among the boundary states, the conduction band, and the valence band. The increase of the negative charge on the boundary reduces the decrease of $V_2$ and shifts more of the applied voltage to the increase of $V_1$. Putting $V_2=V_{20}=\phi$ or $E_2=E_{20}$, we find by using (5),

$$2\pi q/\kappa-eNV_a/q=2\pi q_0/\kappa, \qquad q=(q_0/2)[1+(1+V_a/\phi)^{\frac{1}{2}}]. \tag{11}$$

Thus if $q$ could follow the increase of $V_a$ according to (11), then $V_2$ will remain constant and $V_1=V_{10}+V_a$. We shall not attempt to derive the actual relationship between $q$ and $V_a$, which requires detailed knowledge of electron transition processes between the various energy levels. The fact that the grain boundary stands voltages as high as 100 volts, while the change of $V_2$ must be less than $\phi$, shows that (11) is nearly fulfilled. There is a limit $q_m$ corresponding to the total number of the boundary states. Equation (9) then sets an upper limit for the voltage drop across the grain boundary. When this voltage is reached, the current will increase very steeply with little increase in $V_a$; the grain boundary barrier breaks down.

### Direct-Current Conductance

To derive the current-voltage relationship, we shall consider the barriers on the two sides of the boundary separately and join the solutions by the condition of current continuity. We assume that the electron-hole recombinations within the barriers and at the boundary surface do not contribute appreciably to the current. The electron and hole currents should then be constant separately throughout the composite barrier. According to Schottky's diffusion theory for barriers, the current density of either type of carriers is given approximately by

$$i=e\mu E[n_B-n_A\exp(\mp eV_{AB}/kT)]/[1-\exp(\mp eV_{AB}/kT)], \tag{12}$$

where $\mu$ is the carrier mobility, $E$ is the field at the top of the barrier, the subscript $A$ refers to the bottom of the barrier, and the subscript $B$ refers to the top of the barrier. The negative and the positive signs should be taken for electron current and hole current, respectively. For barriers in an $n$-type semiconductor we should have $eV_{AB}\gg kT$. Furthermore, the concentration of electrons at $A$ is equal to the bulk concentration $n_{e0}$. Thus we can write

$$i_e=e\mu_e E[n_{eB}-n_{e0}\exp(-eV_{AB}/kT)]. \tag{13}$$

For simplicity we shall assume that the bulk properties, and therefore $n_{e0}$, are the same on the two sides of the

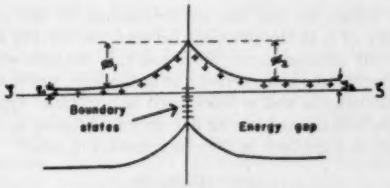


FIG. 3a. Energy level diagram for a grain boundary at equilibrium.

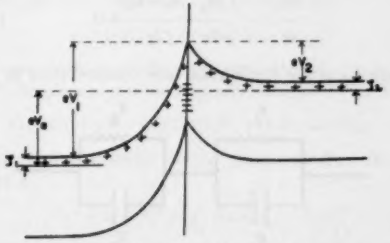

FIG. 3b. Energy level diagram for a grain boundary under applied voltage $V_a$.

boundary. Equating $i_e$ for the two sides, we get

$$n_{eB}(E_1-E_2)=n_{e0}[E_1\exp(-eV_1/kT) -E_2(-eV_2/kT)]. \quad (14)$$

Eliminating $n_B$ from (13) by (14), we get

$$i_e=-e\mu_e\frac{E_1E_2}{E_1-E_2}n_{e0}\exp(-eV_2/kT) \times[1-\exp(-eV_a/kT)] \quad (15)$$

for an applied voltage across the grain boundary $V_a=V_1-V_2$. It is to be remembered that $E_1>0$ and $E_2<0$ [see (5)]. The slope of $(i_e, V_a)$ curve at $V_a=0$, where $E_1=-E_2=E_0$, follows from (15):

$$G_{e0}=(e^2/2kT)\mu_eE_0n_{e0}\exp(-e\phi/kT) =(e^2/2kT)\mu_eE_0AT^{\frac{1}{2}}\exp[-(\phi+\zeta)/kT], \quad (16)$$

where $A=2(2\pi m_e k/h^2)^{\frac{1}{2}}$ and $\zeta$ is the Fermi energy.

The hole current can be treated in the same manner as the current through a $p$–$n$ junction. According to (12),

$$i_h=e\mu_hE[n_{hA}-n_{hB}\exp(-eV_{AB}/kT)], \quad (17)$$

in view of $eV_{AB}\gg kT$. The hole concentration at $A$ is, however, not equal to $n_{h0}$, the equilibrium concentration in the bulk. Equating $i_h$ for the two sides, we get

$$n_{h1}E_1-n_{h2}E_2 =n_{hB}[E_1\exp(-eV_1/kT)-E_2\exp(-eV_2/kT)], \quad (18)$$

$$i_h=e\mu_hE_1E_2\frac{n_{h2}\exp(-eV_1/kT)-n_{h1}\exp(-eV_2/kT)}{E_1\exp(-eV_1/kT)-E_2\exp(-eV_2/kT)}. \quad (19)$$

The values $n_{h1}$ and $n_{h2}$ are determined by the continuity of $i_h$ at the junctions between the barriers and the bulk semiconductor. Since $n_h\ll n_e$ in the bulk semiconductor, the hole current due to the field, which acts on electrons as well as holes, must be negligible. Appreciable hole current can be due only to diffusion as the result of a gradient in the concentration of holes:

$$i_h=-eD_h\,dn_h/dx. \quad (20)$$

For steady current,

$$\frac{\partial n_h}{\partial t}=-\frac{1}{e}\frac{\partial i_h}{\partial x}-\frac{n_h-n_{h0}}{\tau}=0, \quad (21)$$

where $n_{h0}$ is the equilibrium hole concentration in the semiconductor and $\tau$ is the lifetime of holes. The solution of these equations with the boundary condition $n_h=n_{h0}$ at $x=\infty$, gives for the current flowing into the semiconductor from its boundary with barrier, where $n_h=n_{hA}$,

$$i_h=e(D_h/\tau)^{\frac{1}{2}}(n_{hA}-n_{h0}). \quad (22)$$

Equating the hole current flowing into the grain boundary barrier from side 1 to that flowing out of it into side 2, we get

$$-(n_{h1}-n_{h0})=n_{h2}-n_{h0}; \quad n_{h1}+n_{h2}=2n_{h0}. \quad (23)$$

Equations (19) and (22) give

$$\frac{i_h}{e}\left\{\left[\frac{1}{\mu_hE_2}-\left(\frac{\tau}{D_h}\right)^{\frac{1}{2}}\right]\exp\left(-\frac{eV_1}{kT}\right) -\left[\frac{1}{\mu_hE_1}+\left(\frac{\tau}{D_h}\right)^{\frac{1}{2}}\right]\exp\left(-\frac{eV_2}{kT}\right)\right\} =n_{h0}\left[\exp\left(-\frac{eV_1}{kT}\right)-\exp\left(-\frac{eV_2}{kT}\right)\right].$$

For germanium at room temperature $\mu_h=2000$ cm$^2$/volt sec, $D_h=50$ cm$^2$/sec, and $\tau\gtrsim 10^{-6}$ sec. Usually $E$ is of the order $10^4$ volt/cm. Thus

$$\mu_hE\gg(D_h/\tau)^{\frac{1}{2}}, \quad (24)$$

$$i_h=e(D_h/\tau)^{\frac{1}{2}}n_{h0}[1-\exp(-eV_a/kT)]/ [1+\exp(-eV_a/kT)]. \quad (25)$$

Under equilibrium conditions, $V_1=V_2$, $E_1=-E_2=E_0$, and $n_{h1}=n_{h2}=n_{h0}$. It follows from (25) that the slope of $(i_h, V_a)$ curve at the origin is

$$G_{h0}=(e^2/2kT)(D_h/\tau)^{\frac{1}{2}}n_{h0}. \quad (26)$$

Having dealt with the current voltage relationship, we shall now show that the surface charge on the boundary actually increases with the applied voltage as stated at the end of the previous section. Consider first the electron concentration at the boundary $n_{eB}$. According to (14), for applied voltages $V_a\gg kT/e$,

$$n_{eB}(E_1-E_2)\approx-n_{e0}E_2\exp(-eV_2/kT).$$

In the convention adopted in the previous section, $E_1>0$ and $E_2<0$. According to (1), $|E_2|$ is proportional to $V_2^{\frac{1}{2}}$; and according to (4), $(E_1-E_2)$ is proportional to $-q$ or the number of electrons on the boundary states. If $q$ remains unchanged, then

$$\frac{dn_{eB}}{dV_a}\propto V_2^{\frac{1}{2}}(kT/2eV_2-1)\exp(-eV_2/kT)\frac{dV_2}{dV_a}.$$

According to (8), $(dV_2/dV_a)_q$ is negative. With $eV_2\gg kT$, the right-hand side is positive. Thus $n_{eB}$ will increase with the applied voltage. Consider now the hole concentration at the boundary. For $V_a\gg kT/e$ we get, from

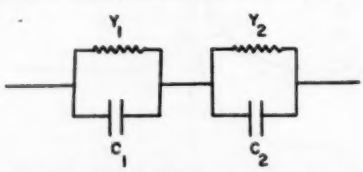


FIG. 4. Equivalent circuit for a grain boundary barrier.

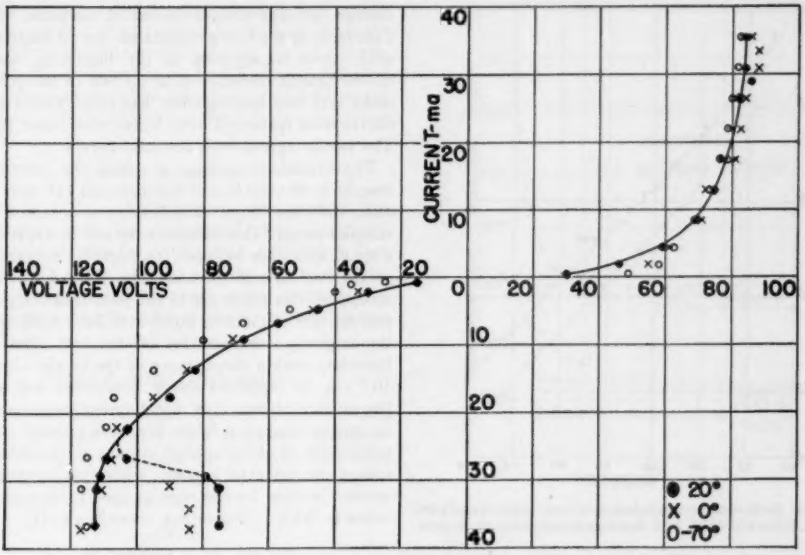


FIG. 5. Current-voltage relationship for a grain boundary at different temperatures, showing breakdown of the barrier.

(25),

$$i_h = e(D_h/\tau)^{\frac{1}{2}} n_{h0}[1-2\exp(-eV_a/kT)].$$

Comparing this expression with (22), we get for the hole concentration at the end of the grain boundary barrier on side 1:

$$n_{h1} = 2n_{h0}\exp(-eV_a/kT) \ll 2n_{h0}.$$

On the other hand we get, by combining (18) and (23),

$$n_{h1}E_1 - (2n_{h0}-n_{h1})E_2 \approx -n_{hB}E_2\exp(-eV_2/kT).$$

Neglecting the terms with $n_{h1}$ on the left-hand side, we get

$$n_{hB} = 2n_{h0}\exp(eV_2/kT).$$

Since $(dV_2/dV_a)_q$ is negative according to (8), $n_{hB}$ will decrease with increasing applied voltage. Thus, with a constant surface charge on the boundary, the electron concentration at the boundary increases while the hole concentration decreases with increasing applied voltage. The transition processes between the different energy levels will tend to increase the number of electrons on the boundary states.

### Alternating-Current Admittance

The grain boundary can be represented by the equivalent circuit, Fig. 4, where $Y_1$ and $Y_2$ are the admittances for the conduction current and the $C$'s are the capacitances of the barriers due to the variation of the space charge with the potential difference. We shall deal with $Y$'s and $C$'s per unit cross-section area of the specimen. These parameters are voltage dependent. We shall be interested in small ac voltages ($<kT/e$), when differential values can be used.

For zero dc bias, $Y_1=Y_2=Y_0$ and $C_1=C_2=C_0$ due to symmetry. Under this condition the conduction current as well as its separate components (electron and hole) are continuous throughout the grain boundary barrier. The electron current gives rise to a conductance given by (16). The hole current, however, gives as in the case of $p$–$n$ junction, a complex admittance owing to the fact that outside the barrier it depends on recombination. Equation (21) and therefore (26) for the differential conductance at zero bias apply only in the dc case. For ac applied voltage, $\partial n_h/\partial t$ in (21) cannot be equated to zero. We have to use the solution in the form $n_h(x)\exp(j\omega t)$. Instead of (22), we then get

$$i_h = e(D_h/\tau)^{\frac{1}{2}}(1+j\omega\tau)^{\frac{1}{2}}(n_{hA}-n_{h0}). \quad (27)$$

Consequently the differential conductance at zero bias (26) becomes now a complex admittance:

$$Y_{A0} = G_{A0} + jB_0 = (e^2/2kT)(D_h/\tau)^{\frac{1}{2}}(1+j\omega\tau)^{\frac{1}{2}}n_{h0}. \quad (28)$$

The total admittance of the grain boundary at zero bias is

$$Y_0 = G_0 + jB_0 = G_{\omega 0} + G_{h0} + j(B_{h0}+\omega C), \quad (29)$$

where $C$ is the capacitance of the grain boundary, being $C_1$ and $C_2$ in series. $B$ corresponds to an apparent capacitance $B/\omega$, which is frequency dependent on

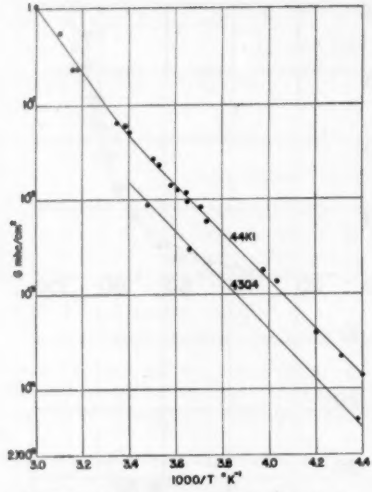


FIG. 6. Small-voltage conductance of two grain boundaries, samples 44K1 and 43Q4, as a function of reciprocal of temperature.

account of $B_h$. The hole concentration in the bulk material, $n_{h0}$, decreases rapidly with decreasing temperature. For sufficiently low temperatures, $\omega C \gg B_h$ and $B/\omega$ will be independent of frequency. It follows from (28) that $G_h > B_h$, the two approaching equality only at high frequencies. Therefore, if with decreasing temperature the conductance $G$ should become very small compared to $B$, then the condition $\omega C \gg B_h$ must be fulfilled. Thus

$B/\omega = C$, if $G \ll B$ and $B/\omega$ is independent of frequency. (30)

Since the barrier resistance increases with applied voltage [Fig. 1, Eqs. (15) and (25)] when the effect of the conduction currents becomes negligible at zero bias, it must do so under applied bias also. It is therefore possible to study the dependence of the space charge capacitance on the applied bias at low temperatures.

## EXPERIMENTAL RESULTS

### Breakdown Voltage

For measurements with large voltages, pulses have to be used to avoid heating. Figure 5 shows a typical current-voltage characteristic of a grain boundary, measured with constant current square-wave pulses of 1 millisecond duration and 2 pulse per second repetition rate. The ohmic voltage drop in the bulk material is calculated from the resistivity and subtracted from the measured voltage to give the voltage drop across the grain boundary. The voltage wave shape is square, except where a dotted branch is shown. There the voltage decreases toward the end of the pulse, showing a decrease in the barrier resistance due to heating. The solid curve corresponds to the beginning, and the dotted branch corresponds to the end of the pulse. To make sure that heating effect had been eliminated, the curves were measured with 5-$\mu$sec and 2-$\mu$sec pulses.[11] The results agreed with the solid curves.

The breakdown voltage at which the current rises steeply is 84 volts in one direction and 115 volts in the other direction. Some dissymmetry is observed for all samples tested. This dissymmetry can be explained by a small difference between the impurity concentration on the two sides of the boundary. Even when there is no appreciable difference in the bulk resistivity on the two sides, it will still be possible to have a difference in the impurity concentration on the two sides of the boundary within the distance of the barrier thickness, $10^{-3}$ cm. As explained above, breakdown will occur if the surface charge does not increase any more with increasing applied voltage. We have pointed out that practically all of the applied voltage $V_a$ is taken up by one of the potential barriers, while the potential drop across the other barrier remains close to its equilibrium value $\phi$. With $V_a \gg \phi$ we get, according to (4),

$$q = -(\kappa\epsilon/2\pi)^{\frac{1}{2}}(NV_a)^{\frac{1}{2}}. \quad (31)$$

For $V_a = (V_1 - V_2) > 0$ we should use $N = N_1$, and for $V_a = (V_2 - V_1) > 0$ we should use $N = N_2$. It is clear that, for a given maximum value of $q$, the limits of the applied voltage for the two directions have the relation

$$V_{1\max}/V_{2\max} = N_2/N_1. \quad (32)$$

The experimental values of $V_{1\max}$ and $V_{2\max}$ for three samples are given in Table I. For sample 43Q4, the values of $N_1$ and $N_2$ have been determined by capacitance measurements and are given in Table III. Comparing column 6, Table I with column 4, Table III we see that $V_{2\max}/V_{1\max}$ agrees well with $N_1/N_2$. The maximum number of electrons on the boundary surface states, $n_{s\max} = -q/e$, as calculated according to (31), is given in column 7. The values of impurity concentration $N$ used in this calculation is taken from Table III for sample 43Q4. For samples 44A2 and 44K1, the bulk impurity concentration given in column 3, Table I, and the average breakdown voltage for the two directions are used.

TABLE I. Breakdown measurements.

| Sample | $\rho$ ohm cm | $n_{s0}$ cm$^{-2}$ | $V_{1\max}$ volts | $V_{2\max}$ volts | $\frac{V_{2\max}}{V_{1\max}}$ | $n_{s\max}$ cm$^{-2}$ | $E_{\max}$ volt cm$^{-1}$ |
|---|---|---|---|---|---|---|---|
| 43Q4 | 3 | $7.0\times10^{11}$ | 84 | 115 | 1.37 | $1.08\times10^{12}$ | $1.2\times10^{5}$ |
| 44K1 | 4 | $5.2\times10^{11}$ | 108 | 145 | 1.34 | $1.08\times10^{12}$ | $1.2\times10^{5}$ |
| 44A2 | 15 | $1.5\times10^{11}$ | 133 | 158 | 1.18 | $0.62\times10^{12}$ | $0.7\times10^{5}$ |

[11] The authors are indebted to Dr. R. Bray for making these measurements.

McAfee, Ryder, Shockley, and Sparks[12] have shown that $p$–$n$ junctions in germanium break down when the electric field in the barrier reaches about $2\times10^5$ volt-cm. The steep rise of current at the breakdown is attributed to the Zener current. The highest electric field occurs in our case at the boundary and is related to $q$ according to (4):

$$q=-en_s\approx-\kappa E/4\pi.$$

The values of $E_{max}$ at breakdown, calculated in this way, are given in the last column of Table I. The values for the three samples are consistently smaller than that given by the above authors for the onset of Zener current. However, the difference is not more than a factor of three and is perhaps not big enough to rule out definitely such a possibility.

### Direct-Current Conductance

The conductance for small $V_a$ due to the electron current is given by (16). All the samples tested have bulk resistivity of a few ohm-cm or higher. For such materials the mobility is determined primarily by lattice scattering and may be written as

$$\mu=bT^{-\frac{3}{2}},$$

where $b$ is a constant. Equation (16) becomes

$$G_{s0}=K_sT^{-1}\exp[-(\phi+\zeta)/kT],$$

where (33)

$$K_s=(e^2/2k)E_0A_sb_e.$$

Within the exhaustion range, a temperature range over which all the effective impurities are ionized, the concentration of electrons remains constant and the value of $\zeta$ varies almost linearly with temperature, according to the relation given by statistics:

$$\zeta=(kT/e)\ln(A_sT^{\frac{3}{2}}/n_s).$$

The value of the $(\phi+\zeta)$, Fig. 3, gives the position of the Fermi level $\zeta$ in the energy gap at the boundary, and consequently it determines the occupation of the surface states by electrons. On the other hand, $\phi$ is related to the space charge on the two sides of the boundary. The neutrality condition, i.e., that the magnitude of the positive space charge should be equal to the magnitude of the negative surface charge, determines $\phi$. The space charge varies only slowly with $\phi$, being proportional to $\phi^{\frac{1}{2}}$. If the density of surface states per unit energy is high, then a small change in $(\phi+\zeta)$ will result in a large change in the surface charge. Under such conditions $(\phi+\zeta)$ will remain practically constant, and $\phi$ will vary with $\zeta$ as the temperature changes. The curve $\ln G_{s0}$ *versus* $1/T$ should then be an approximately straight line, the slope of which gives $(\phi+\zeta)$. The constancy of $(\phi+\zeta)$ is born out by ac measurements reported later.

TABLE II. Dc conductance measurements.

| Sample | $\phi$ ev | $\phi+\zeta$ ev | $K_s$ amp °K/volt cm² | $K_s$ calculated amp °K/volt cm² |
|---|---|---|---|---|
| 43Q4 | 0.515 | 0.535 | $0.7\times10^{11}$ | $3\times10^{11}$ |
| 44K1 | 0.495 | 0.517 | $1\times10^{11}$ | $\sim3\times10^{11}$ |

[12] McAfee, Ryder, Shockley, and Sparks, Phys. Rev. **83**, 650 (1951).

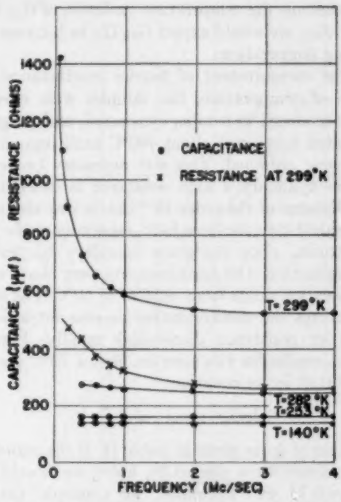


FIG. 3. Apparent capacitance and resistance of a grain boundary at different temperatures, as functions of frequency.

The conductance for small $V_a$ due to the hole current is given by (26). We have the statistical relationship

$$n_sn_h=4[2\pi(m_sm_h)^{\frac{1}{2}}k/h^2]^3T^3\exp(-E_G/kT),$$

where $E_G$ is the width of the forbidden energy gap. $E_G$ may vary with temperature, and if it has a term linearly dependent on temperature, this term will have the effect of modifying the constant coefficient on the right-hand side. Experimentally it is found for germanium[13] that

$$n_sn_h=\alpha T^3\exp(-E_{G0}/kT),$$

where (34)

$$\alpha=8.5\times10^{31}\ \text{cm}^{-6}\ °\text{K}^{-3};\quad E_{G0}=0.73\ \text{ev}.$$

Since $D_h=\mu_hkT/e$, it follows from (26) and (34) that

$$G_{h0}=K_hT^{7/4}\exp(-E_{G0}/kT),$$

where (35)

$$K_h=4.25\times10^{31}(e^3b_h/k\tau)^{\frac{1}{2}}n_{s0}^{-\frac{1}{2}}.$$

If $\tau$ does not vary very rapidly, the temperature dependence of $G_{h0}$ will be predominately determined by the exponential factor. Similarly, the exponential factor

[13] V. A. Johnson and H. Y. Fan, Phys. Rev. **79**, 899 (1950).

in (33) controls the temperature variation of $G_{e0}$. Since $(\phi+\zeta)<E_{G0}$, we would expect $G_{h0}/G_{e0}$ to increase with increasing temperature.

For the measurement of barrier conductance as a function of temperature, the samples were carefully cleaned, mounted in a tube, evacuated, and outgassed by repeated heating at about 400°C until reproducible results were obtained. This was necessary because at the grain boundary a high resistance is concentrated over a distance of the order $10^{-4}$ cm. It was also necessary to shield the tube from light, especially at the lower temperatures, since the grain boundary barriers are photoconductive. The measurements were made within the exhaustion range from −50°C to 60°C. For higher temperatures the semiconductor became intrinsic and the barrier resistance diminished rapidly. Figure 6 gives the results for two samples. Below 20°C the data can be fitted by an equation:

$$\ln G_0 = \text{const} - \psi/kT.$$

The values of $\psi$ are given in Table II. If the major part of the current were carried by holes, we should have $\psi \sim E_{G0} = 0.73$ ev. Therefore, we conclude that the current in this temperature range is carried mainly by electrons with $\psi \sim (\phi+\zeta)$. To determine $(\phi+\zeta)$ and $K_e$ of (33), the data were replotted with $\ln(G_0T)$ against $1/T$. The resulting curves have similar shapes to those shown in Fig. 6. The values of $(\phi+\zeta)$ and of $K_e$, obtained by straight line extrapolation to the axis $1/T=0$, are given in Table II for the two samples. For sample 44*K*1 the measurements were carried to 60°C, just before entering the intrinsic range. We see in Fig. 6, that above 20°C the slope of the curve becomes steeper, indicating that hole current begins to be appreciable. These result support the point of view underlying our treatment. If there is an extensive region of $p$-type conduction at the grain boundary, so that the problem can be treated as $p$–$n$–$p$ junctions, then the temperature dependence of both electron and hole currents will be determined essentially by[10] $\exp(-E_{G0}/kT)$, in contradiction with the experimental results.

A stringent test for the theory is the actual order of magnitude of the conductance. With a given value of $(\phi+\zeta)$, this means checking the value of the coefficient $K_e$. The last column in Table II gives the values calculated by using (33). The values of $E_0$ used are obtained from the barrier thickness $L$ and barrier height $\phi_0$ given in Table III. The calculated values of $K_e$ and the experimental values are of the same order of magnitude. This can be considered to be very satisfactory. Furthermore, we have explained in connection with the curve for 44*K*1, Fig. 6, that the larger slope at the high temperature end can be attributed to the hole current becoming appreciable. The bending begins at about $T=293$°K. According to the theoretical expression (35), for the hole current at this temperature to be 20 percent of the total measured current, $\tau$ should be around 200 $\mu$sec. This is a reasonable order of magnitude.

## Capacitance

The impedance of such barriers at zero bias was measured as a function of temperature and frequency. Figure 7 shows the result for one sample. The apparent capacitance $B/\omega$ at room temperature is seen to depend strongly on frequency. The resistance $1/G$ also varies with frequency. As shown in (28) and (29), this is what we would expect if there is appreciable hole current through the barrier. Below 282°K the capacitance becomes independent of frequency and the conductance becomes much smaller than the susceptance, $G \ll B$ (by a factor of over 20, depending on the temperature). According to (30), the susceptance should give the actual space charge capacitance of the grain boundary consisting of two barriers in series. We have, by using (2), the capacitance of each barrier:

$$C = dQ/dV = (\kappa\epsilon N/8\pi V)^{\frac{1}{2}}. \tag{36}$$

As discussed before, under an applied voltage

$$V_a = (V_1 - V_2) > 0,$$

we have $V_1 = V_a + \phi_1$, $V_2 = \phi_2$. Thus, with a dc bias $V_a$, we get for the grain boundary

$$1/C = (8\pi/\kappa\epsilon N_1)^{\frac{1}{2}}[(V_a+\phi_1)^{\frac{1}{2}} + (\phi_2 N_1/N_2)^{\frac{1}{2}}]. \tag{37}$$

The curves of Fig. 8 show $C$ plotted *versus* $1/[(V_a+\phi)^{\frac{1}{2}} + \phi^{\frac{1}{2}}]$, where the parameter $\phi$ is chosen to give the best fit of the data by straight lines through the origin. According to (37) two parameters should be used, i.e., $\phi_1$ and $\phi_2 N_1/N_2$ for one direction of the bias, and $\phi_2$ and $\phi_1 N_2/N_1$ for the other direction. However, the right-hand side of (37) is not very sensitive to the parameter which appears as an additive term to $V_a$. Since $N_2/N_1$ is not very different from unity and the difference between $\phi_1$ and $\phi_2$ is small, a single parameter was adequate to give the desired fit. The value of $\phi$ so obtained is largely determined by the second term on the right of (37). Two such curves as given in Fig. 8 were obtained at each temperature, one for each direction of bias. From the slopes of these curves the

TABLE III. Capacitance measurements (Sample 43*Q*4).

| $T$ °K | $N_1$ cm$^{-3}$ | $N_2$ cm$^{-3}$ | $N_1/N_2$ | $\phi'$ ev | $\phi''$ ev | $\phi_0$ ev | $\zeta$ ev | $\phi_0+\zeta$ ev | $C_0$ $\mu\mu$f | $C_0\phi_0^{\frac{1}{2}}$ $\mu\mu$f ev$^{\frac{1}{2}}$ | $L$ cm |
|---|---|---|---|---|---|---|---|---|---|---|---|
| 271 | $8.5\times10^{14}$ | $6\times10^{14}$ | 1.4 | 0.35 | 0.24 | 0.29 | 0.23 | 0.52 | 147 | 79 | $1.7\times10^{-4}$ |
| 201 | $7.5\times10^{14}$ | $5\times10^{14}$ | 1.5 | 0.43 | 0.30 | 0.36 | 0.16 | 0.52 | 125 | 75 | $2.0\times10^{-4}$ |
| 103 | $8\times10^{14}$ | $6\times10^{14}$ | 1.3 | 0.51 | 0.39 | 0.44 | 0.08 | 0.52 | 120 | 79 | $2.1\times10^{-4}$ |

impurity concentrations $N_1$ and $N_2$ on the two sides of the boundary were determined according to (37), and these are given in Table III. The values obtained at different temperatures agree within experimental accuracy. The ratio $N_2/N_1$ is in fair agreement with the value given in Table I for the ratio of breakdown voltages $V_{1max}/V_{2max}$ for this sample, as prescribed by (32).

The two values of $\phi$, $\phi'$ and $\phi''$, used for the two straight lines of Fig. 8, should be $\phi''=\phi_1 N_2/N_1$ and $\phi'=\phi_2 N_1/N_2$. These values are given in Table III. Values are also given for

$$\phi_0=(\phi'\phi'')^{\frac{1}{2}}=(\phi_1\phi_2)^{\frac{1}{2}}.$$

The condition for equilibrium gives

$$\phi_2-\phi_1=\zeta_1-\zeta_2=kT\ln(n_{e2}/n_{e1})=kT\ln(N_2/N_1).$$

The last expression follows from complete ionization of the impurities. Thus the difference between $\phi_1$ and $\phi_2$ is small compared to either one of them, which is of the order of a fraction of 1 ev. Hence

$$\phi_0\approx\phi_1\approx\phi_2. \tag{38}$$

Table III shows that $\phi_0$ varies with the temperature. The value of $\zeta$ calculated from the electron concentration in the bulk material is also given and it is seen that $(\phi+\zeta)$ remains constant for the various temperatures. This result confirms the discussions made in connection with the dc conductance measurements. The value of $(\phi_0+\zeta)$ agrees closely with the value in Table II for this sample.

The measured capacitance at zero bias $C_0$ is also given in Table III. According to (37) and (38), $C_0\phi_0^{\frac{1}{2}}$ should be a constant. The values for the three temperatures agree within the experimental accuracy. The total thickness of the grain boundary barrier $L$ is, according to (36),

$$1/C=1/C_1+1/C_2=4\pi(l_1+l_2)/\kappa=4\pi L/\kappa. \tag{39}$$

The values of $L$ at zero bias are given in the last column of Table III.

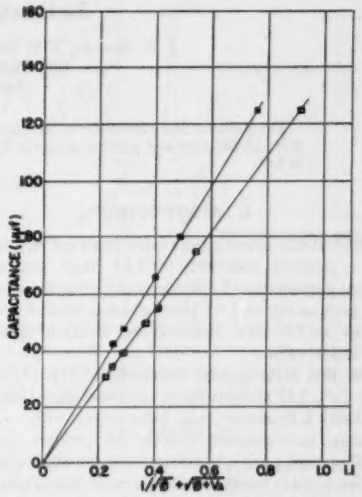


FIG. 8. Capacitance of a grain boundary for opposite polarities of applied bias $V_a$, at 201°K.

## SUMMARY

The dc conductance $G_{e0}$ of the grain boundary for sufficiently low temperatures agree with the theoretical expression (33) for the electron current. The capacitance measurements confirm the constancy of $(\phi+\zeta)$, the height of the barrier above the Fermi level. The values of $(\phi+\zeta)$ obtained from the capacitance measurements agree with the value estimated from the slope of the curve of $\ln(G_{e0}T)$ *versus* $1/T$. The increasing slope of this curve at the high temperature end and the large frequency dependence of the apparent capacitance at these temperatures are in agreement with the theory, and this indicates that the hole current should become more important with increasing temperature. Impurity concentrations on both sides of the grain boundary have been estimated from the measurements of capacitance as function of bias applied in both directions. A difference in the concentration is obtained; the ratio of the concentration agrees with the ratio of the breakdown voltages for the two directions. The maximum number of electrons on the boundary states, as calculated from the breakdown voltage, is of the order $10^{12}$ cm$^{-2}$. However, at the breakdown the electric field at the boundary approaches the field for the onset of Zener current, and it cannot be stated with certainty that the breakdown is caused by the saturation of the boundary states.

# Radioactivity of Scandium 43

J. R. Haskins, J. E. Duval, L. S. Cheng, and J. D. Kurbatov
*Ohio State University, Columbus, Ohio*

(Received August 1, 1952)

The positron and photoelectron spectra of radioactive $Sc^{43}$ have been investigated. A gamma-ray of 0.375±0.002 Mev and positron groups of 1.18±0.02 Mev and 0.77±0.04 Mev are assigned to the decay of $Sc^{43}$.

## I. INTRODUCTION

PREVIOUS investigators have reported $Sc^{43}$ to have a positron spectrum of 1.13 Mev[1] and a high energy gamma-ray.[1,2] Hibdon *et al.*[1] gives the energy of this gamma-ray as 1.65 Mev, whereas Walke[2] gives the energy as 1.0 Mev. Peacock and Deutsch[3] agree with this latter value.

For this investigation enriched $Ca^{43}CO_3$ (72.13 percent $Ca^{43}$, 5.17 percent $Ca^{44}$), obtained from Oak Ridge National Laboratory, was bombarded with ~7-Mev protons, and common $CaCO_3$ (97 percent $Ca^{40}$), of 99.97 percent purity, obtained from the Hach Chemical Company, was bombarded with ~20-Mev alpha particles in the Ohio State University cyclotron. Both the positron and photoelectron spectra have been investigated.

## II. POSITRON SPECTRUM

Carrier-free samples of scandium produced by both the proton and alpha-bombardments were prepared in the following manner:

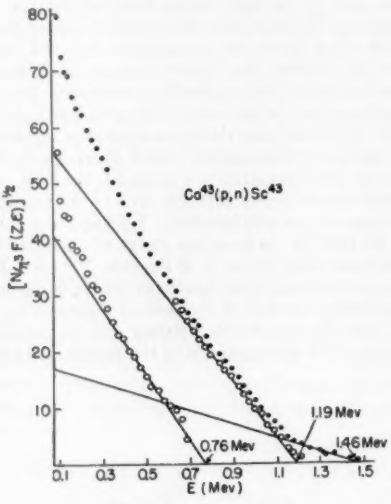


FIG. 1. Fermi plot of $Sc^{43}$.

The target material was covered with distilled water in a small beaker and was dissolved by the addition of a minimum amount of 3*N* hydrochloric acid. The solution was evaporated to dryness. This procedure was repeated twice more to insure the removal of radioactive fluorine. The residue was dissolved in 30 ml of 0.001*N* hydrochloric acid, titrated to pH 8.5 with 0.1*N* ammonium hydroxide, and filtered twice through Schleicher and Schuell Blue Ribbon filter papers. The filter papers, to which most of the scandium adhered, were washed thoroughly with a dilute solution of ammonium chloride, the pH of which was 8.5. The scandium was removed from the filter papers with boiling 3*N* hydrochloric acid, and the resulting solution was evaporated to a few drops. These were evaporated to dryness on a thin film of rubber hydrochloride, supported on an aluminum holder. The sample thickness was less than 0.7 mg/cm$^2$.

The positron spectrum of the active scandium produced by bombarding $Ca^{43}$ with protons was studied in a solenoidal spectrometer. The Fermi plot for this spectrum, the data having been corrected for 3.9-hr half-life, is shown in Fig. 1.

Three components, obtained when the Fermi plot was analyzed, are shown. The highest energy component, having an end point of 1.46 Mev and relative abundance of 11 percent, is identified as belonging to 4-hr $Sc^{44}$.[4] The main component has an end point of 1.19 Mev, in fair agreement with the value of Hibdon *et al.*,[1] and a relative abundance of 71.5 percent. A third component, with a relative abundance of about 16 percent, has an end point energy of 0.76 Mev.

The positron spectrum of the scandium produced by bombarding $Ca^{40}$ with alpha-particles was studied in a thick-lens spectrometer. The Fermi plot for this spectrum is shown in Fig. 2. The 1.46-Mev component is not observed in this case, showing that it does not belong to $Sc^{43}$. The first component has an end point of 1.18 Mev with a relative abundance of 76 percent, and the second component has an end point of 0.77 Mev with a relative abundance of 24 percent, in good agreement with the previous case.

In both cases the decay followed a 3.9-hr half-life in all regions of the spectrum for more than 20 hr after the start of measurements.

[1] Hibdon, Pool, and Kurbatov, Phys. Rev. **67**, 289 (1945).
[2] H. Walke, Phys. Rev. **57**, 163 (1940).
[3] W. C. Peacock and M. Deutsch, Phys. Rev. **69**, 306 (1946).
[4] J. A. Bruner and L. M. Langer, Phys. Rev. **79**, 606 (1950).

### III. PHOTOELECTRON SPECTRUM

For the investigation of the photoelectron spectrum, the $Ca^{43}$ was bombarded with ~7-Mev protons. The sample was removed from the cyclotron target holder and placed in an aluminum source holder with sufficient thickness to cut out all positrons.

Figure 3 shows the photoelectron spectrum obtained with a thin lens spectrometer. It has been corrected for

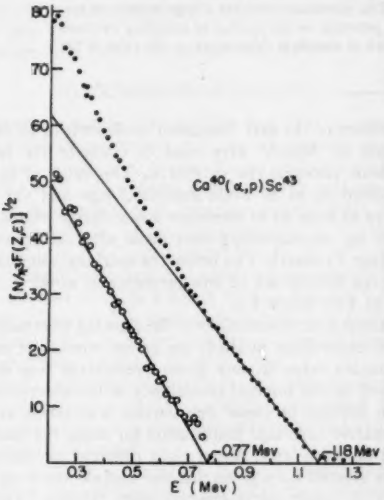


FIG. 2. Fermi plot of $Sc^{43}$.

3.9-hr half-life. A 21-mg/cm² uranium convertor was used for energies below 600 kev and a 40-mg/cm² uranium convertor was used for higher energies. In addition to the $K$ and $L$ annihilation peaks, a lower energy peak was observed, which decayed with a 3.9-hr half-life. This peak was also observed with a 17 mg/cm² lead convertor. From the positions of the peak with the lead and uranium convertors it is identified as the

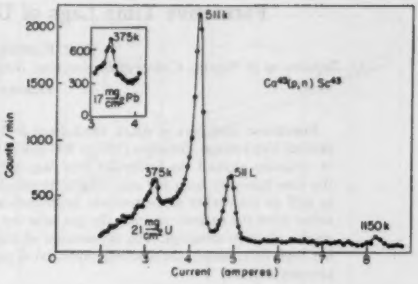


FIG. 3. Photoelectron spectrum of $Sc^{43}$.

$K$-peak for a 375-kev gamma-ray. The only high energy gamma-ray which was observed was one with energy of 1.15 Mev. It is probably the 1.16-Mev gamma-ray reported by Bruner and Langer,[4] for $Sc^{44}$.

### IV. SUMMARY

The positron spectrum of $Sc^{43}$ is complex with the main component having an end-point energy of 1.18 ±0.02 Mev and the second component having an end-point energy of 0.77±0.04 Mev. The branching ratio of the decay of $Sc^{43}$ is estimated, with the aid of the curves of Feenberg and Trigg[5] to correct for $K$-capture, to be 72 percent of the 1.18-Mev $\beta_1^+K$ branch and 28 percent of the 0.77-Mev $\beta_1^+K$ branch. The log($ft$) values of the two $\beta^+$ components are 5.1 and 4.8, respectively.

A gamma-ray of 0.375±0.002 Mev is ascribed to the decay of $Sc^{43}$. No higher energy gamma-ray was found for $Sc^{43}$, and it is believed that if such a ray were present, it would have less than 15 percent relative abundance.

The authors wish to express their thanks to The Ohio State University Development Fund for grants and to Mr. Weiler and the cyclotron group for bombardments. This research was supported in part from funds granted to The Ohio State University by the Research Foundation for aid in fundamental research.

[5] E. Feenberg and G. Trigg, Revs. Modern Phys. 22, 399 (1950).

# Formative Time Lags of Uniform Field Breakdown in $N_2$†

G. A. KACHICKAS* AND L. H. FISHER
*Department of Physics, College of Engineering, New York University, University Heights, New York, New York*
(Received July 3, 1952)

Formative time lags of spark breakdown in $N_2$ have been measured in uniform fields as a function of percent overvoltage, pressure (150 to 700 mm Hg) and electrode separation (0.3 to 1.4 cm). For the range of variables studied the formative time lags are almost identical with values previously observed in air; the time lags vary from 100 $\mu$sec close to threshold to 1 $\mu$sec at a few percent overvoltage. The present data as well as the earlier measurements in air indicate a secondary mechanism of photoemission of electrons either from the cathode or from the gas near the cathode. This mechanism requires a large number of successive electron crossings. The dependence of the sparking potential on the number of initiating electrons has been determined; the sparking potential of pure $N_2$ shows an enormous dependence on the value of the primary current.

## I. INTRODUCTION

THE present experiments are an extension of earlier work carried out in air.[1] The experiments of FB examined the nature of the threshold setting mechanism of the uniform field spark in air, and showed that formative time lags of breakdown in air near threshold are of the order of 100 $\mu$sec. FB state: "It is believed . . . that two processes acting together produce the observed long time lags at low overvoltages. These are (1) a suitable secondary mechanism (most probably photoemission at the cathode) . . . and (2) space charge distortion due to the large number of positive ions in the gap." Calculations show that space charge distortion alone cannot satisfactorily account for the observed time lag dependence on overvoltage in air.[2] It thus appears that a Townsend-like discharge sets the threshold for uniform field breakdown in air rather than a streamer-like process.[3] It seemed important to determine the generality of the results in air by investigating other gases.

## II. APPARATUS AND EXPERIMENTAL PROCEDURE

Unless otherwise noted, the apparatus and experimental procedure are as described by FB. The chamber was evacuated to a pressure ($p$) of about $10^{-5}$ mm,[4] and then filled with $N_2$ to a low pressure; a glow discharge was then maintained between the electrodes while the chamber was again evacuated. The process was repeated several times and fresh gas was then admitted.

Values of the first Townsend coefficient, $\alpha$, as determined by Masch[5] were used to evaluate the initial cathode photoelectric current $i_0$. The value of $i_0$ was adjusted so as to avoid statistical lags and yet was never so large as to introduce space charge effects. All time lag measurements were made with the approach voltage $V_0$ exactly 2 kv below the sparking potential $V_s$ (except for one set of measurements in which $V_0$ was set at 4 kv below $V_s$).

About four observations of the time lag were made at each overvoltage studied; the actual number of measurements taken at any given overvoltage was determined by the internal consistency of the observations. The average of these observations was taken as the formative time lag. Justification for using the average will be given later. About eight different overvoltages were studied for a given pressure and electrode separation ($\delta$); such measurements were taken at various values of $p$ and $\delta$. The dependence of the time lags on $i_0$ was also studied.

To determine the significance of the observed scatter in the time lag measurements, an extensive study of the time lag distribution was made for one particular overvoltage (with $\delta = 1$ cm and a pressure near atmospheric). A statistical distribution of time lags superimposed on a formative time lag $\tau$ is given by[6]

$$n = n_0 e^{-(t-\tau)/\sigma}, \qquad (1)$$

where $n$ is the number of lags out of $n_0$ observations which exceed $t$, and $\sigma$ is the mean statistical scatter time. If a straight line results when the data are plotted semilogarithmically according to Eq. (1), then the distribution is statistical; such a graph is referred to as a Laue plot.

The absolute values of all voltages are correct to within 0.5 percent since this is the accuracy of the voltage measuring resistors (all other errors are negligible compared to this). However, since the error in the resistors remains constant (except for small variations

† Supported by ONR and the Research Corporation. For preliminary reports of this work, see G. A. Kachickas and L. H. Fisher, Phys. Rev. 82, 318, 569 (1951). Also see L. B. Loeb, Phys. Rev. 81, 287 (1951).

* Now at North American Aviation, Downey, California.

[1] L. H. Fisher and B. Bederson, Phys. Rev. 81, 109 (1951). This paper will be referred to as FB.

[2] B. Bederson, Ph.D. thesis, New York University (1949) (unpublished).

[3] For a description of the streamer process, see J. M. Meek, Phys. Rev. 57, 722 (1940); L. B. Loeb and J. M. Meek, *The Mechanism of the Electric Spark* (Stanford University Press, Stanford, 1941); H. Raether, Arch. Elektrotech. 34, 49 (1940); Z. Physik 117, 375, 524 (1941); Ergeb. exakt. Naturwiss. 22, 73 (1949).

[4] All pressures are given in mm, meaning mm of Hg.

[5] K. Masch, Arch. Elektrotech. 26, 587 (1932).

[6] K. Zuber, Ann. Physik 76, 231 (1925); M. von Laue, Ann. Physik 76, 261 (1925); R. Strigel, *Elektrische Stossfestigkeit* (Julius Springer, Berlin, 1939), p. 67.

in temperature) relative voltages are correct to a much greater accuracy.

Voltage fluctuations usually prevent $V_0$ from being set closer than 3 v of the desired value at the instant the pulse voltage $V_1$ is applied. The value of $V_1$ may be set to within 0.5 v of the desired value, but the true pulse voltage is $V_1-V'$ where $V'$ is a correction due to the loss of part of $V_1$ in the circuit. It is estimated that $V_1-V'$ is known to within 2 v, and that the uncertainty in the total voltage applied to the electrodes is of the order of 5 v.

All pressures have been corrected to 22°C.

### III. EXPERIMENTAL RESULTS

Before presenting the time lag data, it is necessary to describe measurements of $V_s$ as this quantity must be known in order to obtain the percent overvoltage (percent o.v.). Since it was found that the presence of a very small amount of impurity greatly alters the sparking potential of $N_2$, measurements of $V_s$ were made in both "$N_2$" and "pure" $N_2$. By $N_2$ is meant Linde's high purity tank $N_2$[7] which was passed directly from the tank through a liquid $N_2$ trap into the "outgassed" chamber. The term pure $N_2$[8] refers to Linde's high purity tank $N_2$ which was passed over hot copper shot and then through a liquid $N_2$ trap.

The $V_s$ values for $N_2$ and pure $N_2$ with no ultraviolet illumination of the cathode have about the same values and are in close agreement with the values given by Ehrenkranz.[9]

The sparking potential of $N_2$ with and without ultraviolet light is definite at any given time to within 2 v for a $V_s$ of 30 kv. However, the actual value of $V_s$ in $N_2$ depends on the value of $i_0$ to a small extent. For example, at electrode separations of 1.0 and 1.4 cm and with pressures of 460 and 730 mm an $i_0$ of about 200 electrons/$\mu$sec ($\epsilon/\mu$ sec) lowers $V_s$ of $N_2$ by about one percent. For any given filling of $N_2$, the decrease of $V_s$ varies linearly with $i_0$ although the absolute variation changed somewhat from one filling to the next. Measurements of this decrease in $V_s$ could not be made at a product of $p\delta$ less than about 400 mm×cm because ultraviolet illumination under these conditions at high enough potentials initiates a partial breakdown giving rise to a glow on the anode; only when the potential is raised further does a spark occur. This partial breakdown (which was not observed in air) has associated with it only a small change in the potential across the electrodes; in this respect, as well as in the localization of the luminosity, there is strong similarity to the corona discharge. Further study of these partial breakdowns seems worthwhile.

[7] The Linde Company guarantees this $N_2$ to be 99.99 percent pure.

[8] A sample of pure $N_2$ was analyzed by mass spectrograph and found to contain by percentages $N_2$ 99.89, $CO_2$ 0.08, $O_2$ 0.03. We are indebted to Dr. J. A. Hornbeck of the Bell Telephone Laboratories for this analysis.

[9] F. Ehrenkranz, Phys. Rev. **55**, 219 (1939).

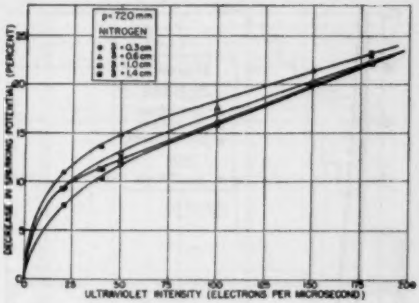


FIG. 1. Decrease in sparking potential *vs* primary current for pure $N_2$.

The sparking potential for pure $N_2$ without ultraviolet light varies at any given time within a range of 50 v in 30 kv, and the average value of about ten measurements was taken as the breakdown potential.[10] With ultraviolet illumination of the cathode, $V_s$ for pure $N_2$ is lowered enormously and its value varies over a wide range at a given illumination level (about 100 v for $V_s \sim 30$ kv). This decrease in $V_s$ is as great as 23 percent at atmospheric pressure with an $i_0$ of about 200 $\epsilon/\mu$sec.[11] The variation of this decrease in $V_s$ with $i_0$ for various electrode separations near atmospheric pressure is shown in Fig. 1. The only other measurements showing a large effect of $i_0$ on $V_s$ were made by White[12] who found a ten percent decrease in $V_s$ of air when $i_0$ was increased by a factor of a million. In fact, the variation of sparking potential with illumination in pure $N_2$ is so great that a spark can be induced to pass with an appropriate $V_0$ by shining the light from an ordinary flashlight through the quartz window of the chamber. This interesting effect merits further study.

Using the very definite sparking potentials obtained in $N_2$ (with no $i_0$) as $V_s$, formative time lags were measured with an $i_0$ of about 40 $\epsilon/\mu$sec. The results are shown in Fig. 2 for $\delta=1$ cm at three pressures along with the formative time lags for uniform field breakdown in air at atmospheric pressure as given by FB. As was the case in air, the time lags in $N_2$ are essentially independent of pressure over the range studied; this pressure independence allows the representation of the time lag data fairly well by a single curve at a given electrode separation. Figure 3 contains such a curve for the data of Fig. 2 with similar curve for $\delta=1.4$, 0.6 and 0.3 cm over the same range of pressures given in Fig. 2. The time lag *vs* percent o.v. curves in $N_2$ are almost identical with those for air, and as in air, the

[10] C. G. Miller and L. B. Loeb, J. Appl. Phys. **22**, 614 (1951) found that the exact breakdown potential in pure $N_2$ with negative wire coaxial geometry is difficult to determine.

[11] Ehrenkranz (reference 9) observed that for $N_2$ containing Hg and NO, $V_s$ is lowered by 7 to 13 percent below $V_s$ for pure $N_2$. Although Ehrenkranz employed an $i_0$, she gives no data for the variation of $V_s$ with $i_0$.

[12] H. J. White, Phys. Rev. **48**, 113 (1935).

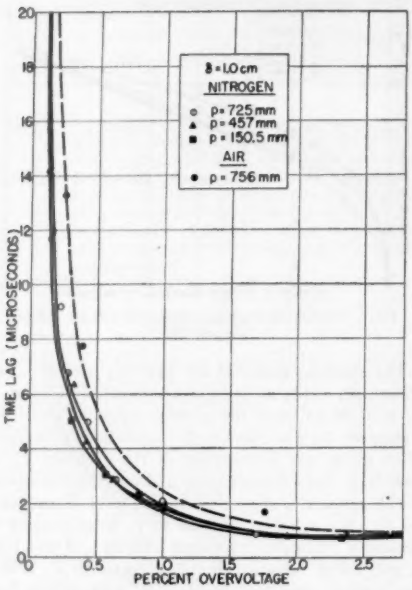


FIG. 2. Measured formative time lags *vs* percent overvoltage for $N_2$ and air at an electrode separation of one centimeter.

time lags at a given percent o.v. increase with increasing electrode separation.

Neither changing $i_0$ from 20 to 200 $\epsilon/\mu$sec nor changing $V_0$ from 2 to 4 kv below $V_s$ has any effect on the time lags in $N_2$. These statements are based on studies made primarily for an electrode separation of one centimeter at atmospheric pressure, although some measurements with varying $i_0$ and pulse voltage were made at other pressures and electrode separations.

To study the distribution of time lags for $N_2$, 50 observations were made at one overvoltage in the neighborhood of 0.2 percent for $\delta = 1$ cm and $p = 730$ mm. The results are shown as an ordinary distribution curve in Fig. 4 and as a Laue plot in Fig. 5. From the latter figure, it is seen that the time lag distribution is not statistical since the results plotted as described earlier do not form a straight line. Moreover, 80 percent of the time lag fluctuations may be accounted for by a voltage fluctuation of less than 5 v; the maximum fluctuation in the 50 observations may be ascribed to an error of about 10 v. Since an occasional error of 10 v out of 30 kv is not unreasonable, the entire distribution of time lags obtained in $N_2$ is attributed to voltage fluctuations. As was the case in air, the time lag distribution in $N_2$ at a given pressure and electrode separation broadens with decreasing percent o.v.; this broadening of the distribution with decreasing percent o.v. is associated with the steep slope of the time lag curves at low overvoltages. This discussion justifies the use of average values of the time lags in this gas as the significant values.

FB state that for air: "A part but not all of the fluctuations (in time lags) are due to the electronic errors. The other part of the fluctuation is probably inherent in the statistical nature of the spark." With the improved voltage regulation in the present experiment it was possible to investigate this conjecture. The distribution of time lags in air at $p = 757$ mm and $\delta = 1$ cm was studied by taking 100 observations at 0.285 percent o.v. The distribution obtained (shown in Figs. 4 and 5) is similar to that of $N_2$. Since the variation of time lags with percent o.v. is essentially the same for air and $N_2$, the time lag distribution in air may also be attributed to voltage fluctuations. Thus the conjecture of FB seems incorrect. Gänger[13] has observed statistical distributions of time lags of spark breakdown in air; however, the time lags measured were of the order of $5 \times 10^{-8}$ sec and the illumination was inadequate for the prevention of statistical lags.

Formative time lags in pure $N_2$ are troublesome to measure. Figure 1 shows that $V_s$ in pure $N_2$ with no $i_0$ is at least 12 percent higher than when $i_0$ is large enough to avoid statistical lags. In most cases it was found that in order to obtain time lags in pure $N_2$ that are shorter than 100 $\mu$sec (the maximum time measurable with the

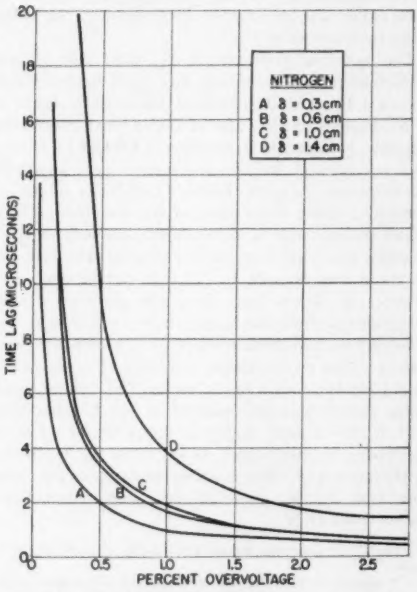


FIG. 3. Measured formative time lags *vs* percent overvoltage for $N_2$ at various electrode separations.

[13] B. Gänger, Arch. Elektrotech. **39**, 508 (1949).

equipment used), a total voltage must be applied across the gap which is greater than the sparking potential obtained with no cathode illumination. $V_0$ must therefore be set below the sparking potential obtained with $i_0$, and to avoid possible effects of space charge distortion, it should be possible to set $V_0$ at least 2 kv below the lower sparking potential. Therefore, in order to make a complete study of the formative time lags in pure $N_2$, a pulse of about 10 kv is required. Because of this difficulty and because the results obtained would be valid only for a specific ultraviolet intensity, no detailed study of the formative time lags in pure $N_2$ was undertaken. However, to obtain some information about the time lags, measurements were made at one pressure (730 mm) for three values of $\delta$, and the data are given in Fig. 6. The data to the right of the zero percent o.v. abscissa were taken with an $i_0$ of about 100 $e/\mu$sec; the data to the left of zero percent were taken with no ultraviolet illumination. The points shown are averages except those with arrows; arrows on points indicate that at least one reading was obtained at the time plotted, but that other sparks occurred at the same percent o.v. with lags longer than 100 $\mu$sec. However, at some plotted points (with arrows) to the left of zero percent failures also occurred. The curves obtained are similar to those for $N_2$ providing the sparking potential with no $i_0$ is used as the static breakdown value; it is also clear that further study of pure $N_2$ will be very rewarding.

## IV. DISCUSSION OF RESULTS

As was the case in air, the observed time lags in $N_2$ cannot be explained by secondary electron emission at the cathode by positive ion bombardment of the cathode. This mechanism leads to time lag *vs* percent o.v. curves lying way above the observed curves. The principal difficulty with fitting the data to such a mechanism is the low velocity of the positive ion. For example, the positive ion process requires time lags of microseconds at very high overvoltage whereas the experimental data yield time lags of the order of a microsecond at only a few percent o.v. As will be seen, the fit is no better for the data at overvoltages below a few percent.

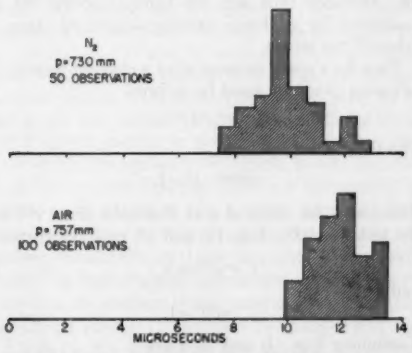


FIG. 4. Distribution of time lags at 0.2 percent overvoltage in $N_2$ and at 0.285 percent overvoltage in air.

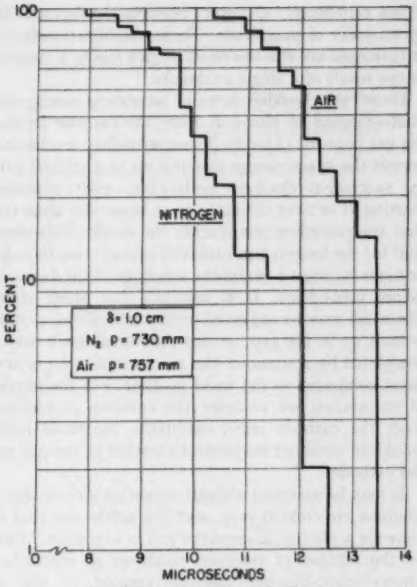


FIG. 5. Laue plots of data in Fig. 4.

The only remaining acceptable mechanisms for the production of secondary electrons are photoionization in the gas and photoemission of electrons from the cathode. The streamer theory considers that breakdown results from a single electron crossing either the entire gap or a fraction of the gap with photo-ionization in the gas close to the avalanche head as a secondary mechanism; the time required for a discharge to form on this basis is of the order of an electron transit time or less. Hence a streamer-like mechanism alone does not account for the long time lags observed at overvoltages below a few percent. Moreover, using either Masch's[5] or Posin's[14] values of $\alpha$ in $N_2$, the amplification factor $e^{\alpha d}$ was calculated at threshold as determined in this experiment; the average value of $e^{\alpha d}$ for all pressures and electrode separations studied is about 1000, a value much too low to give rise to a streamer as the result of a single avalanche. This small amplification factor at threshold indicates the unimportance of positive ion space charge distortion during all but the very latest phases of the build up.

In air, using FB's values of $V_s$ and values of $\alpha$ as given by Sanders,[15] the amplification factor is calculated to be about $6\times10^4$ at atmospheric pressure for a gap

[14] D. Q. Posin, Phys. Rev. **50**, 650 (1936).
[15] F. H. Sanders, Phys. Rev. **41**, 667 (1932).

of one centimeter; at lower pressures the factor is less by an order of magnitude. These amplification factors at threshold are still too small to give rise to a streamer as the result of a single avalanche.[16]

Hence we consider as valid secondary mechanisms photoemission of electrons from the cathode or from the gas near the cathode. These secondary mechanisms permit the space charge to build up to a critical value by successive electron avalanches, each avalanche starting at or near the cathode at about the same time that the preceding one reaches the anode. This means that for the longest lags observed perhaps one thousand or more successive avalanche crossings of the gap occur before breakdown. It is assumed that space charge distortion may be neglected until a critical space charge is built up in the gap; at this time breakdown may be completed by a streamer-like mechanism in an interval short compared to the build up time. For the purpose of calculation we consider the emission of electrons from the cathode only; essentially the same results would be obtained for photo-ionization in the gas near the cathode.

It may be assumed without appreciable error that all photons are created very near the anode and that the time for a photon to cross the gap is negligible.[17] Let $\gamma$ be the number of electrons produced at the cathode photoelectrically per electron created in the gas (assumed constant). Then a single electron starting at the cathode at time zero gives rise to $\gamma(e^{\alpha\delta}-1)$ photoelectrons from the cathode at time $t_e$, the electron transit time, $\gamma^2(e^{\alpha\delta}-1)^2$ photoelectrons at time $2t_e$, and $\gamma^n(e^{\alpha\delta}-1)^n$ photoelectrons at time $nt_e$ where $n$ is the number of electron crossings. Assume that a spark occurs when the number of electrons liberated from the cathode as the result of a single electron being emitted at an earlier time reaches the value $N$. The calculated time lags are not very sensitive to the value of $N$ chosen. It is to be expected that due to variations in diffusion, geometry and absorption of radiation the value of $N$ for breakdown will be somewhat different at various pressures and electrode separations. In the calculations to follow, electrons liberated from the cathode by an external source at times later than zero are not taken into account. Experimental results showing the independence of the time lags on $i_0$ indicate that the procedure adopted is justified. Even if these succeeding primary electrons are taken into account, the calculated time lags are hardly affected but are modulated by a slowly varying logarithmic term as Schade[17] has shown.

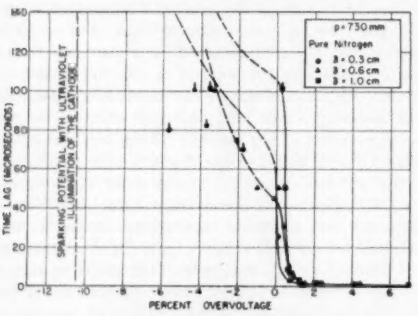


FIG. 6. Measured formative time lags *vs* percent overvoltage for pure $N_2$.

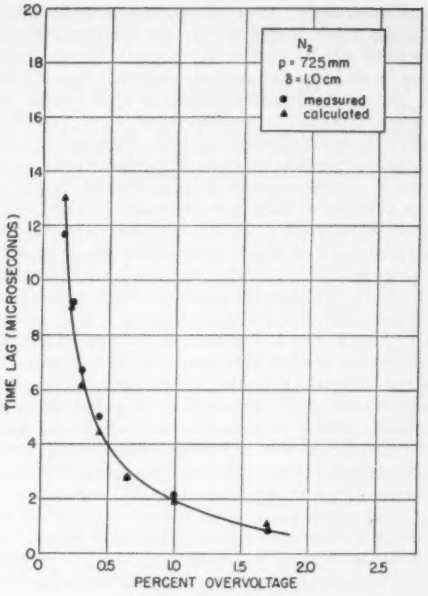


FIG. 7. Calculated and measured time lags *vs* percent overvoltage in $N_2$.

Then for a spark to occur after $n$ electron transits the following condition must be satisfied

$$\gamma^n(e^{\alpha\delta}-1)^n=N. \tag{2}$$

Threshold is set by

$$\gamma(e^{\alpha_s\delta}-1)=1, \tag{3}$$

where $\alpha_s$ is the value of $\alpha$ at threshold. Since $e^{\alpha_s\delta}$ is of the order of 1000, Eqs. (2) and (3) may be written as

$$\gamma^n e^{\alpha\delta n}=N, \tag{4}$$

and

$$\gamma e^{\alpha_s\delta}=1. \tag{5}$$

Combining Eqs. (4) and (5) gives

$$e^{n\delta\Delta\alpha}=N, \tag{6}$$

[16] See also the low values of the constant $K$ in Meek's equation obtained by L. H. Fisher, Phys. Rev. **72**, 423 (1947).

[17] R. Schade, Z. Physik **104**, 487 (1937) has calculated time lags assuming positive ion bombardment of the cathode neglecting electron transit times.

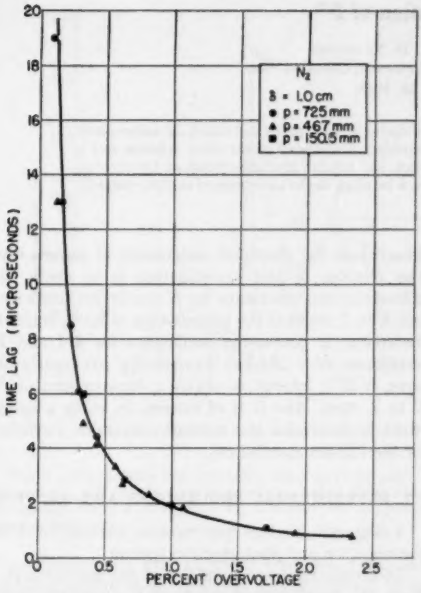


FIG. 8. Calculated time lags *vs* percent overvoltage showing pressure independence of time lags.

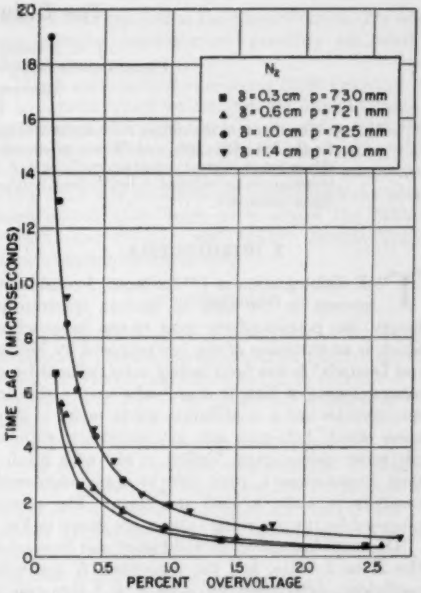


FIG. 9. Calculated time lags *vs* percentage overvoltage for various electrode separations near atmospheric pressure.

where $\Delta\alpha = \alpha - \alpha_s$. Since $n\delta = v\tau$, where $\tau$ is the time lag and $v$ is the electron velocity, Eq. (6) may be written

$$\tau = (\log N)/v\Delta\alpha. \tag{7}$$

Equation (7) was used to calculate formative time lags in $N_2$. Masch's[5] values of $\alpha$ were used and Nielsen's[18] measurements of electron mobility in $N_2$ were extrapolated. The value $N = 10^8$ was chosen to fit the observed time lag at one overvoltage at atmospheric pressure and at an electrode separation of one centimeter. The results are illustrated in Fig. 7. where measured and calculated time lag data are given for $\delta = 1$ cm and $p = 725$ mm. Of fourteen curves calculated (using $N = 10^8$) for comparison with the data at various pressures and electrode separations, seven gave fits as good as the one shown in Fig. 7; the remaining seven yielded curves parallel to the measured ones but displaced on the average some 70 percent. In addition, the calculations yielded time lags which are independent of pressure as illustrated in Fig. 8 where calculated time lags are plotted for three pressures for $\delta = 1$ cm. Figure 9 shows calculations of time lags near atmospheric pressure for four electrode separations. Using Posin's[14] values of $\alpha$, one does not obtain quite as good agreement especially as regards the pressure independence of the time lags. On the whole, the data must be considered well represented by Eq. (7). In view of the crudeness of the assumptions made, the agreement is even better than might be expected. It therefore seems reasonable to assume from these calculations that the secondary mechanism active in the spark breakdown of $N_2$ (and pure $N_2$) for the range of variables studied is photoemission at the cathode or photo-ionization in the gas near the cathode. The cathode photoelectric effect has some advantages over the gas ionization mechanism since the former requires photons only one-quarter as energetic as those required in the latter process.

Entirely analogous computations show that the results of FB in air are also described satisfactorily by Eq. (7). For these computations, electron velocity measurements of Nielsen and Bradbury[19] were extrapolated, and $N$ was again chosen to fit one measurement.

One notices from Eq. (7) that for positive ion bombardment of the cathode the time lags would be longer by the ratio of the electron to the positive ion velocity. Thus time lags calculated on the positive ion mechanism are some two hundred times greater than those observed.

We are indebted to Dr. M. Menes for a number of stimulating discussions; we also thank Professor L. B. Loeb of the University of California for continued interest and for the extended loan of the discharge chamber.

[18] R. A. Nielsen, Phys. Rev. **50**, 950 (1936).

[19] R. A. Nielsen and N. E. Bradbury, Phys. Rev. **51**, 69 (1937).

# The Disintegration of $I^{131}$

J. R. Haskins and J. D. Kurbatov
*Physics Department, Ohio State University, Columbus, Ohio*

(Received May 28, 1952)

The results of the authors for internal conversion coefficients, $K$ to $L$ ratios and multipole assignments for the 284-, 364-, 638-, and 723-kev gamma-rays are reported. A review of recent decay schemes and a tabulation of internal conversion coefficients, $K$ to $L$ ratios, and relative intensities obtained by previous investigators are included. A level scheme is proposed which involves the forbiddenness of certain magnetic dipole transitions.

## I. INTRODUCTION

THE disintegration of $I^{131}$ has been of considerable interest in the field of nuclear spectroscopy. Emery[1] has postulated the most recent decay scheme which is an extension of the one proposed by Metzger and Deutsch.[2] It has been largely substantiated by the measurements of Ketelle *et al.*,[3] who used a thin lens spectrometer and a scintillation spectrometer to determine which beta-rays are in coincidence with the particular gamma-rays. Verster *et al.*,[4] as a result of their measurements, were able to apply shell model concepts to make a level assignment. The schemes proposed by the preceding authors are shown in Fig. 1.

The empirical curves of Goldhaber and Sunyar[5] for the $K$ to $L$ ratio, and the theoretical $K$ conversion coefficients determined by Rose *et al.*,[6] give two approaches to the multipole assignment of gamma-rays. The purpose of this investigation is to check and extend the information on the $K$ conversion coefficients and $K$ to $L$ ratios of the gamma-rays of $Xe^{131}$. Since the theoretical $K$ conversion coefficients for $M1$ and $E2$ transitions of a 284-kev gamma ray are nearly the same, it is of interest to obtain a measurement of the $K$ to $L$ ratio. Also it is of interest to make a special effort to determine the internal conversion coefficient for the 723-kev gamma ray.

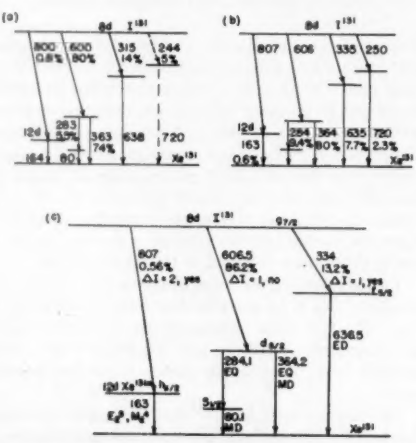


FIG. 1. Decay schemes for $I^{131}$. (a) Emery; Metzger and Deutsch. (b) Ketelle, Zeldes, Brosi, and Dandl. (c) Verster, Nijgh, Van Lieshaut, and Bakker.

## II. EXPERIMENTAL PROCEDURES AND RESULTS

A magnetic thin lens spectrometer was used to obtain the negatron and photoelectron spectra.

To obtain relative intensities of the gamma-rays of $Xe^{131}$, the photoelectron spectrum was measured using tin, lead, and uranium as convertors. The spectrum using a tin convertor is shown in Fig. 2. Intensities were determined by finding areas under peaks in a plot of $N/I$ *vs* $I$, after subtracting Compton background, and then correcting for photoelectric absorbtion coefficient. Photoelectric absorption coefficients were obtained with the aid of Gray's formula[7] and the theoretical calculations of Hulme *et al.*[8] The relative intensities are listed in Table I, where the 364-kev gamma-intensity is taken as 100.

The negatron spectrum was examined to obtain the relative intensities of the various groups of internal conversion electrons. Figure 3 shows this spectrum.

TABLE I. Experimental results.

| Energy of gamma kev | Rel. int. of gamma | Rel. int. of conv. el. and 606-kev cont. beta | | $K/L$ ratio | $K$ conv. coeff. |
|---|---|---|---|---|---|
| 284 | 6 | $K$ | 14.6 | 3.3 | 0.052 |
| | | $L$ | 4.7 | | |
| 364 | 100 | $K$ | 100 | 5.6 | 0.021 |
| | | $L$ | 16.7 | | |
| 638 | 10 | $K+L$ | 1.8 | | 0.0040 |
| 723 | 3 | $K+L$ | 0.5 | | 0.0034 |
| | | 606 beta | 5400 | | |

[1] E. W. Emery, Phys. Rev. **83**, 679 (1951).
[2] F. Metzger and M. Deutsch, Phys. Rev. **74**, 1640 (1948).
[3] Ketelle, Zeldes, Brosi, and Dandl, Phys. Rev. **84**, 585 (1951).
[4] Verster, Nijgh, Van Lieshout, and Bakker, Physica Deil **17**, No. 7, 637 (1951).
[5] M. Goldhaber and A. W. Sunyar, Phys. Rev. **83**, 906 (1951).
[6] Rose, Goertzel, and Perry, Oak Ridge National Laboratory Report ORNL 1023 (1951).
[7] L. H. Gray, Proc. Cambridge Phil. Soc. **27**, 103 (1931).
[8] Hulme, McDougall, Buckingham, and Fowler, Proc. Roy. Soc. (London) **149**, 131 (1935).

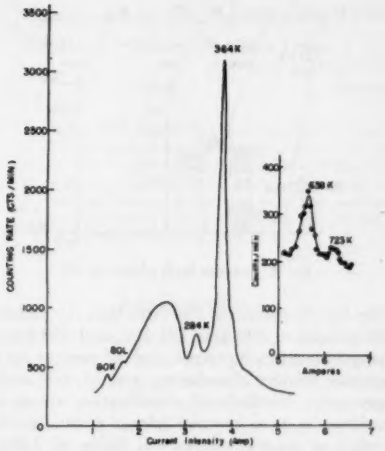


FIG. 2. $I^{131}$ photoelectron spectrum using a 12-mg/cm² tin convertor at 2.3 percent resolution setting. Inset: High energy photopeaks using a 30-mg/cm² tin convertor at 3.6 percent resolution setting.

The dashed lines are calculated from the Fermi plot with correction being made, at the end points of the 334-kev and the 606-kev continuous spectra, for resolution of the spectrometer. The relative intensities of the internal conversion groups and the 606-kev continuous spectrum are found in Table I, where the intensity of the 364-kev internal group is taken as 100.

In neither the photoelectric nor the internal conversion spectrum is an intensity estimate made for the 80-kev gamma-ray, since the Geiger tube window and scattering in the convertors distort results too much at this low energy.

The $K$-shell internal conversion coefficients were determined using as a standard the value 0.097 for the $K$ shell conversion coefficient of the 663-kev gamma-ray of $Cs^{137}$.[9] Sources of $Cs^{137}$ and $I^{131}$ were made, so that, in each case, the same sample could be used to measure both internal conversion and photoelectrons. The same sample holder, convertor, and geometry were used in the two cases.

The $K$ shell internal conversion coefficients and the $K$ to $L$ ratios which we obtained are listed in Table I. Some values of $K$ shell internal conversion coefficients obtained from Rose's tables[6] and $K$ to $L$ ratios taken from the curves of Goldhaber and Sunyar[5] are given in Table II. A comparison of our results with the values listed in this table, leads us to assign the 284-kev, 364-kev, and 638-kev, and 723-kev gamma-rays to electric quadrupole transitions.

TABLE II. Theoretical conversion coefficients (see reference 6) and empirical $K/L$ ratios (see reference 5).

| Energy of gamma, kev | Multipole | $K/L$ ratio | $K$ conv. coeff. |
|---|---|---|---|
| 284 | $E2$ | 4.6 | 0.042 |
| | $M1$ | 7.9 | 0.045 |
| 364 | $E2$ | 5.6 | 0.020 |
| | $M1$ | 8 | 0.024 |
| 638 | $E1$ | | 0.0015 |
| | $E2$ | | 0.0042 |
| | $M1$ | | 0.0060 |
| 723 | $E1$ | | 0.0011 |
| | $E2$ | | 0.0031 |
| | $M1$ | | 0.0044 |

[9] M. A. Waggoner, Phys. Rev. **82**, 906 (1951).

## III. DISCUSSION

In Table III is given a tabulation of the results obtained by previous investigators for relative intensities, $K$ conversion coefficients and $K$ to $L$ ratios of the gamma-rays of $Xe^{131}$. Our results are included in this table.

The 80-kev gamma-ray has been assigned as $M1$ by Verster *et al.*[4] The half-life measurements of Graham and Bell[10] support this assignment. On the basis of the results of Bergström,[11] Goldhaber and Sunyar[5] list the 163-kev gamma-ray as an $M4$ transition. This agrees with the scheme of Verster *et al.*,[4] where the transition goes from $h11/2$ to $d3/2$.

We find no alternative to Verster *et al.*'s assignment of $d5/2$ to the 364-kev level, even though we believe

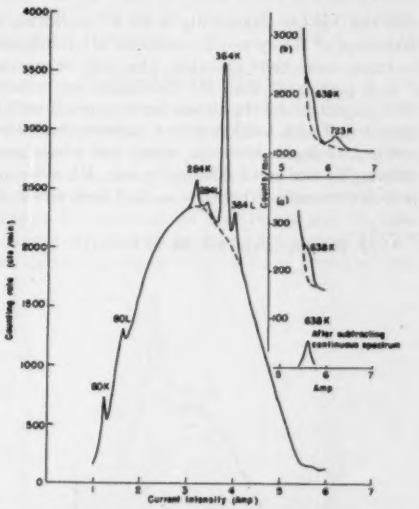


FIG. 3. $I^{131}$ negatron spectrum. Inset (a): Expanded scale to show conversion electrons of 638-kev gamma-ray. Inset (b): Conversion electrons of 638-kev and 723-kev gamma-rays using high activity source.

[10] R. L. Graham and R. E. Bell, Phys. Rev. **84**, 380 (1951).
[11] Ingmar Bergström, Phys. Rev. **80**, 114 (1951).

TABLE III. Gamma-rays of $Xe^{131}$.

| Energy (kev) | Author | Rel. int. | $K/L$ ratio | $K$ conv. coeff. | Other related measurements |
|---|---|---|---|---|---|
| 80 | Metzger[a] | 7.6 | 5.5 | 0.8 | |
| | Kern[b] | 21.8 | 8.4 | 0.17 | |
| | Verster[c] | 7.6 | 7.0 | 0.7 | |
| 163 | Verster | 0.56 | | | $N_K/(N_L+N_M)=1.67$ |
| | Bergström[d] | | 2.34 | | $N_L/N_M=3.4$ |
| | Brosi[e] | | | ~20 | |
| 284 | Metzger | 7.6 | >2 | 0.05 | |
| | Kern | 17.2 | | 0.079 | |
| | Verster | 7.6 | | 0.039 | |
| | Ketelle[f] | 11.8 | | | |
| | Lind[g] | 8.7 | | | |
| | Authors | 6 | 3.3 | 0.052 | |
| 364 | Metzger | 100 | 5.2 | 0.019 | |
| | Kern | 100 | 4.0 | 0.018 | |
| | Verster | 100 | 4.2 | 0.0185 | |
| | Ketelle | 100 | | | |
| | Lind | 100 | | | |
| | Authors | 100 | 5.6 | 0.021 | |
| 638 | Metzger | 19 | | <0.005 | |
| | Kern | 6.9 | | | |
| | Verster | 14.2 | | 0.0019 | |
| | Ketelle | 9.6 | | | |
| | Zeldes[h] | | | | $4\times10^{-4}$ conv. per 606$\beta^-$ |
| | Authors | 10 | | 0.0040 | |
| 723 | Verster | | | | $5\times10^{-5}$ conv. per disint. |
| | Ketelle | 2.9 | | | |
| | Thulin[i] | | | | 638$\gamma$ int./723$\gamma$ int. =7.8 |
| | Zeldes | | | | 723 conv./638 conv. =$\frac{1}{4}$ |
| | Authors | 3 | | 0.0034 | |

[a] See reference 2.
[b] Kern, Mitchell, and Zaffarano, Phys. Rev. **76**, 94 (1949).
[c] See reference 4.
[d] See reference 11.
[e] Brosi, DeWitt, and Zeldes, Phys. Rev. **75**, 1615 (1949).
[f] See reference 3.
[g] Lind, Brown, Klein, Miller, and Dumond, Phys. Rev. **75**, 1544 (1949).
[h] Zeldes, Brosi, and Ketelle, Phys. Rev. **83**, 642 (1951).
[i] Sigvard Thulin, Phys. Rev. **83**, 860 (1951).

that the 364-kev gamma-ray is an $E2$ transition and Weisskopf's[12] theory would predict an $M1$ transition to be many times more probable. This may be explained if it is postulated that $M1$ transitions are forbidden with respect to $E2$ transitions between levels with the same $L$ and with $I$ differing by 1 (between a $d5/2$ level and a $d3/2$ level). However, where two levels have $L$ differing by two and $I$ differing by one, $M1$ is the more probable transition (between an $s1/2$ level and a $d3/2$ level).

[12] V. F. Weisskopf, Phys. Rev. **83**, 1073 (1951).

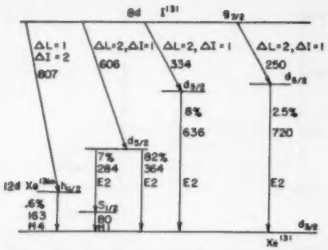


FIG. 4. Proposed level scheme for $I^{131}$.

The log($ft$) values for the three beta-ray transitions with energies of 606 kev, 334 kev, and 250 kev, and having 89 percent, 8 percent, and 2.5 percent for their respective relative abundances, are 6.7, 6.8, and 6.9, respectively. Nordheim's[13] classification allows these transitions to have selection rules of either $\Delta L=1$ and $\Delta I=0, 1$ or $\Delta L=2$ and $\Delta I=1$. Using $g7/2$ for the ground state of $I^{131}$ and $d3/2$ for the ground state of $Xe^{131}$, the selection rules $\Delta L=1$ and $\Delta I=1$ for a beta-transition would give an excited level $f5/2$ and an $E1$ transition to the ground state of $Xe^{131}$. The selection rules $\Delta L=2$ and $\Delta I=1$ would give an excited level $d5/2$ with an $M1$ or $E2$ transition to the ground state.

Since our measurements indicate that the 638-kev and the 723-kev transitions are both $E2$, we propose the level scheme in Fig. 4 with the 364-kev, 638-kev, and 723-kev levels all $d5/2$ and with the requirement that $M1$ transitions with selection rules $\Delta L=0$ and $\Delta I=0, 1$ are forbidden.

These results were obtained before the appearance of a recent publication on $I^{131}$ by Bell and Graham and support[14] their multipole assignments.

The authors wish to express their gratitude to the Ohio State University Development Fund for grants to carry on this research.

[13] L. W. Nordheim, Phys. Rev. **78**, 294 (1950).
[14] R. E. Bell and R. L. Graham, Phys. Rev. **86**, 212 (1952).

# Beta-Spectra of $Co^{56}$, $Co^{57}$, and $Co^{58}$

L. S. Cheng, J. L. Dick, and J. D. Kurbatov
*Department of Physics, Ohio State University, Columbus, Ohio*
(Received June 11, 1952)

For $Co^{58}$ the 472-kev positron spectrum has been confirmed and the $K$ conversion coefficient of the 805-kev gamma-ray has been found to be $(2.9\pm0.2)\times10^{-4}$. For $Co^{57}$ the positron spectrum has been found to have an end-point energy of $320\pm15$ kev. Conversion electrons of 119-kev and 133-kev gamma-rays and a very soft (<18-kev) gamma-ray emitted by $Fe^{57}$ have been observed. The $K/L$ ratios of the 119-kev and the 133-kev gamma-rays have been estimated to be about 6.3 and 5.2, respectively. For $Co^{56}$ two positron spectra have been observed, one having an end-point energy of $1.53\pm0.02$ Mev, the other having an end-point energy of $995\pm25$ kev.

## INTRODUCTION

PREVIOUS investigations have shown that (1) $Co^{58}$ has a 25-kev isomeric state[1] and disintegrates by emission of a 0.47-Mev positron (14.5 percent positron emission, 85.5 percent $K$ capture[2]) to an excited state of $Fe^{58}$ followed by an 805-kev gamma-ray,[3] the multipole order of which was found to be a mixture of magnetic dipole and electric quadrupole;[4] (2) $Co^{57}$ disintegrates by emission of a 0.26-Mev positron[4] to an excited state of $Fe^{57}$ which then makes transitions through two branches to the ground state. The $K/L$ ratios of the 119-kev and the 131-kev gamma-rays emitted in these two branches indicated that both gamma-rays are electric octopole radiations;[5,6] (3) $Co^{56}$ emits 1.50-Mev positron[6] to an excited state of $Fe^{56}$. There were six gamma-rays found due to transitions in $Fe^{56}$, ranging from 845 kev to 3.25 Mev.[6]

## APPARATUS AND PROCEDURE

For the present study two $Mn^{55}$ targets were bombarded in the cyclotron of the University of California, one with reduced and one with full beams of alpha-particles. The first target received 26.1 microampere hours of approximately 20-Mev alpha-particles, while the second target received 24 microampere hours of approximately 35.5-Mev alpha-particles.

About two months after receiving the radioactivity, a benzene extraction process was performed to separate the cobalt activity from the manganese residue. The sample of the target material was dissolved in 10$N$ hydrochloric acid. A fraction of the sample was diluted to 1$N$ hydrochloric acid, heated to 80°C and treated with 50 percent (by volume) acetic acid solution of alpha-nitroso beta-naphthol. After standing for 12 hours, the solution was extracted with benzene saturated with 1$N$ hydrochloric acid. The benzene extract was washed with distilled water, and the former was evaporated to dryness. The residue was then ignited in a platinum crucible almost to an invisible quantity. The activity was finally transferred from the crucible by heating with concentrated hydrochloric acid. The solution thus obtained was made 6$N$ and washed with ether to remove any iron that might be present. Following this the solution was reduced to almost dryness and taken up in 1$N$ hydrochloric acid and treated a second and third time as described above for purpose of repurification. Following the third repurification the sample was deposited on a rubber hydrochloride film and mounted in a solenoid type spectrometer for investigation of the beta-spectra of cobalt activity.

The spectrometer was equipped with a thin window Geiger-Müller tube which could pass electrons of energy down to 16 kev. The instrument was calibrated with $Cs^{137}$, $I^{131}$, $S^{35}$, $P^{32}$, and $Y^{90}$, giving undistorted spectra down to at least 50 kev for thin sources. The resolution setting was 1.5 percent.

## EXPERIMENTAL RESULTS

Figure 1 shows the momentum distribution curves for the radioactivity obtained from the low energy bombardment. Besides the continuous positron spectra, four conversion electron peaks have been observed. The two intense peaks are identified as being the conversion electron peaks of the 119-kev and the 133-kev gamma-rays emitted by the excited state of $Fe^{57}$.[5,6] In the high energy region a low intensity peak has been

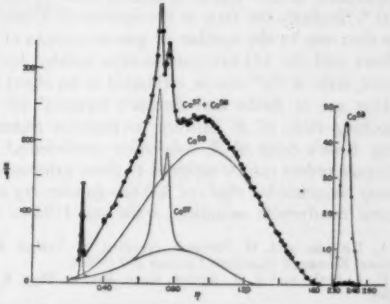


FIG. 1. Momentum distribution curves of $Co^{57}$ and $Co^{58}$.

[1] K. Strauch, Phys. Rev. **79**, 487 (1950).
[2] Good, Peaslee, and Deutsch, Phys. Rev. **69**, 313 (1946).
[3] M. Deutsch and L. G. Elliot, Phys. Rev. **65**, 211 (1944).
[4] J. J. Livingood and G. J. Seaborg, Phys. Rev. **60**, 913 (1941).
[5] E. H. Plesset, Phys. Rev. **62**, 181 (1942).
[6] L. G. Elliot and M. Deutsch, Phys. Rev. **64**, 321 (1943).

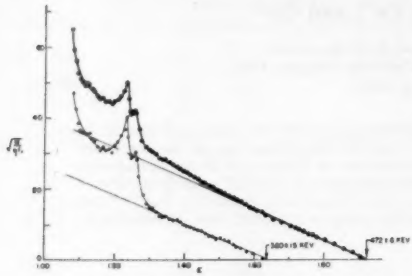

FIG. 2. Fermi plots of $Co^{57}$ and $Co^{58}$.

observed which is identified as being the conversion electron peak of the 805-kev gamma-ray emitted by the excited state of $Fe^{58}$.[1] A low energy conversion electron peak has been observed, which, after making the tube window absorption correction to the counting rate in the low energy region, shows relatively high intensity. The energy of these conversion electrons has been estimated to be less than 18 kev. They may be identified as being the $L$ conversion electrons going with the 14-kev gamma-ray emitted by the 0.11-$\mu$sec metastable state of $Fe^{57}$.[7]

Figure 2 shows the Fermi plots of $Co^{57}$ and $Co^{58}$. Two components can be seen in the figure. The high energy component shows a straight line and has an end-point energy of $472\pm6$ kev, which checks very well with the previously reported energy of the positron spectrum of $Co^{58}$.[1,3] The low energy component also shows a straight line and has an end-point energy of $320\pm15$ kev, which is somewhat higher than the previously reported energy of the positron spectrum of $Co^{57}$.[4] By extrapolating the straight lines in the Fermi plot back to low energy region, it is possible to construct the momentum distribution curves for the two individual components. They are shown in Fig. 1 under the experimental distribution curve. By this the $K$ conversion coefficient $\alpha_K$ of the 805-kev gamma-ray emitted following the 472-kev positron emission by the ground state of $Co^{58}$ can be estimated to be $(2.8\pm0.2)\times10^{-4}$. Similarly the ratio of the number of $K$ conversion electrons to the number of gamma-quanta of the 119-kev and the 133-kev gamma-rays emitted by the excited state of $Fe^{57}$ can be estimated to be about 0.7, making use of Bethe and Bacher's formula[8] for the branching ratio of $K$ capture to positron emission. Using Rose's table of $K$ conversion coefficients,[9] the multipole orders can be assigned to these gamma-rays. It may be concluded that the 805-kev gamma-ray is an electric quadrupole radiation, while the 119-kev and the 133-kev gamma-rays probably are a mixture of magnetic quadrupole and electric octopole radiations. In addition, the $K$ conversion coefficient of the 805-kev gamma-ray has also been estimated by comparing the number of its conversion electrons and the number of its photoelectrons ejected from a lead radiator. The $\alpha_K$ has been found to be $(3.0\pm0.25)\times10^{-4}$, which supports the assignment of electric quadrupole to the 805-kev gamma-ray.

Figure 3 shows the conversion electron spectrum of the 119-kev and the 133-kev gamma-rays emitted by the excited state of $Fe^{57}$. As pointed out by Kelly,[10] the monochromatic electron peak can be fitted on the low energy side by an exponential function and on the high energy side by a Gaussian distribution function. By this method it is possible to resolve approximately the $K$ and $L$ conversion electron peaks of each converted gamma-ray and thus to estimate $K/L$ ratios. The $K/L$ ratios of the 119-kev and the 133-kev gamma-rays have been estimated to be about 6.3 and 5.2, respectively.

Figure 4 shows the Fermi plot of the radioactivity obtained from the high energy bombardment. The highest energy component shows a straight line, having an end-point energy of $1.53\pm0.02$ Mev, which agrees with the previously reported value within the experimental error.[6] The next highest energy component, subtraction of Fermi plot having been made, shows a slightly curved line with an end-point energy of $995\pm25$ kev. Several runs have been made to check the shape of this component of the positron spectrum of $Co^{56}$. It appears that the curvature of the Fermi plot of this

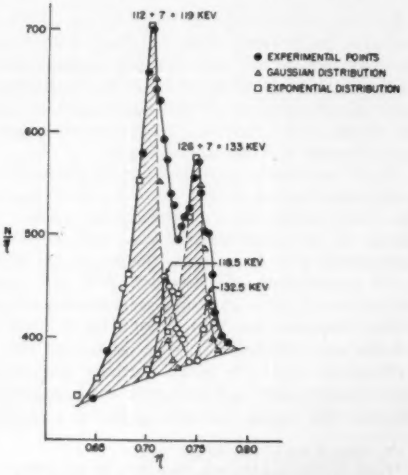


FIG. 3. Conversion electron peaks of 119-kev and 133-kev gamma-rays emitted by $Co^{57}$.

[7] A. Hedgran and M. Deutsch, reported in *Nuclear Data*, National Bureau of Standards Circular 499 (1950).

[8] H. A. Bethe and R. F. Bacher, Revs. Modern Phys. 8, 184 (1936).

[9] Rose, Goertzel and Perry, Oak Ridge National Laboratory Report ORNL-1023 (1951) (unpublished).

[10] W. C. Kelly, Phys. Rev. 85, 101 (1952).

component is not prominent enough to assure any definite shape for the spectrum. In the low energy region of Fig. 4, the 472-kev positron spectrum of $Co^{58}$ and the 320-kev positron spectrum of $Co^{57}$ are also shown. From the Fermi plot and making an estimation of the theoretical branching ratio of $K$ capture to positron emission,[8] it is possible to estimate the ratio of the number of disintegrations through 1.53-Mev positron emission (as well as the accompanying $K$ capture) to the number of disintegrations through 995-kev positron emission (as well as the $K$ capture). This ratio has been estimated to be 8:3.

## DISCUSSION

For $Co^{58}$ the log$ft$ value of the 472-kev positron emission is estimated to be 6.5, using Feenberg and Trigg's chart.[11] The beta-transition is thus expected to be first forbidden or $L$ forbidden. The assignment of electric quadrupole radiation to the 805-kev gamma-transition is supported by the nuclear shell theory which explains the rule that for even-even nuclei the first excited state usually has spin two and even parity.[12]

For $Co^{57}$ the log$ft$ value of the 320-kev positron emission is estimated to be 6.0 and expected to be first forbidden. The relative intensities, $K/L$ ratios, and the ratio of the number of $K$-conversion electrons to the number of gamma-quanta of the 119-kev and the 133-kev gamma-rays seem to support the assignment of a mixture of magnetic quadrupole and electric octopole to the former and an electric octopole to the latter. In this case the <18-kev gamma-ray is a magnetic dipole radiation.

For $Co^{56}$ the ratio between the numbers of disintegrations through the two positron emissions (as well as their respective accompanying $K$ captures) has been estimated to be 8:3, while the ratio of the 1.24-Mev to the 1.74-Mev gamma-rays emitted by the excited state of $Fe^{56}$ was found to be 5:2 by Elliot and Deutsch.[6] Thus it seems very likely that both the 1.53-Mev positron emission followed by a 1.24-Mev gamma-ray and the 995-kev positron emission followed by a 1.74-Mev gamma-ray lead to the first excited state of $Fe^{56}$. All other high energy gamma-rays[6] may be emitted due to transitions from still higher excited states of $Fe^{56}$, which can be reached by $K$ capture of $Co^{58}$. In this case the log$ft$ values of the 1.53-Mev positron emission and the 995-kev positron emission are estimated to be greater than 8 and 7.5, respectively. Both positron emissions are then expected to be first forbidden.

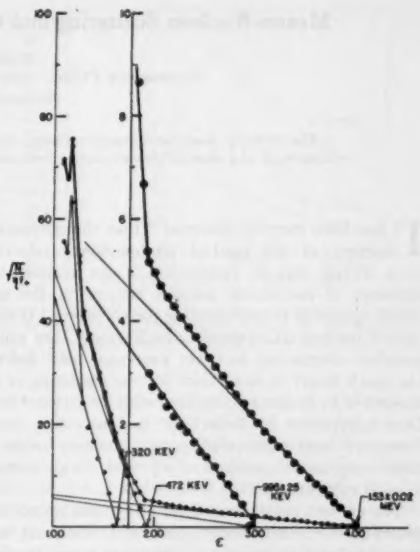


FIG. 4. Fermi plots of $Co^{55}$, $Co^{57}$, and $Co^{58}$.

This work was supported in part from funds granted to The Ohio State University by the Research Foundation for aid in fundamental research. The authors appreciate a grant from The Ohio State University Development Fund for purchase of instruments. We thank the cyclotron group in Crocker Laboratory of the University of California for the activation of manganese.

[11] E. Feenberg and G. Trigg, Revs. Modern Phys. 22, 399 (1950).
[12] M. Goldhaber and A. W. Sunyar, Phys. Rev. 83, 906 (1951).

# Meson-Nucleon Scattering and the Classical Strong-Coupling Theory*

DAVID FELDMAN
*Department of Physics, University of Rochester, Rochester, New York*
(Received August 4, 1952)

The ordinary elastic and charge-exchange scattering of mesons by nucleons is considered within the framework of a classical strong-coupling treatment of the charge-symmetric pseudoscalar field.

IT has been recently observed[1,2] that the qualitative features of the neutral photomeson production cross section can be understood if one assumes the existence of metastable nucleon isobars[3] of the sort which appear in strong-coupling meson theory.[4] If such excited nucleon states should actually occur, they would manifest themselves in other processes, and, indeed, the much larger cross sections for the scattering of $\pi^+$ mesons in hydrogen as compared with $\pi^-$ mesons[5] have been interpreted by Brueckner[6] in terms of a broad resonance level corresponding to a nucleon isobar of total angular momentum $J=\frac{3}{2}$ and total isotopic angular momentum $I=\frac{3}{2}$.

The current evidence in favor of metastable nucleon states is, of course, hardly conclusive. One must bear in mind that the presence of a resonant meson-nucleon interaction does not of itself necessarily imply the existence of isobars. There is also a good deal of uncertainty at the present time that meson-nucleon scattering does in fact take place predominantly in the $J=\frac{3}{2}$, $I=\frac{3}{2}$ state.[7] Nevertheless, much interest has been focused recently on the strong-coupling theory, and we therefore feel it worthwhile to indicate the qualitative features of meson-nucleon scattering which result from a classical treatment of the charge-symmetric pseudoscalar field.[8]

It must be emphasized from the very outset that, in addition to the usual approximations of strong-coupling theory,[8] the classical method treats the meson field as an unquantized field and the spin $\sigma$ and isotopic spin $\tau$ of the nucleon as classical unit vectors.[9] It is this last restriction particularly which has led to differences in the quantitative comparison of the results of the classical and quantum-mechanical methods, even in the extreme strong-coupling limit.[10] Actually, we are interested in moderately strong or intermediate coupling in which case the classical theory cannot be expected to serve other than as a qualitative guide.

In consequence of the classical treatment of $\sigma$ and $\tau$, it follows that one cannot separate the two processes of ordinary elastic scattering of a charged meson by a nucleon

$$\pi^+ + P \rightarrow \pi^+ + P, \tag{1}$$

$$\pi^+ + N \rightarrow \pi^+ + N, \tag{2}$$

from one another, but one is led, instead, to a classical average of the differential cross sections for (1) and (2) which we denote by $(d\sigma/d\Omega)_{\text{ord}}$. The exchange scattering of charged mesons by nucleons, corresponding to

$$\pi^+ + N \rightarrow \pi^0 + P, \tag{3}$$

is separable and leads to $(d\sigma/d\Omega)_{\text{exch}}$. Using natural units with $\hbar=c=1$, one finds for the differential scattering cross sections the following expressions:[11]

$$\left(\frac{d\sigma}{d\Omega}\right)_{\text{ord}} = \frac{4}{225}\left(\frac{f}{\mu}\right)^4 \frac{k^4}{\nu^2|1-R^2|^2}[(25-10\cos^2\theta) + |R|^2(11+52\cos^2\theta)], \tag{4}$$

$$\left(\frac{d\sigma}{d\Omega}\right)_{\text{exch}} = \frac{4}{225}\left(\frac{f}{\mu}\right)^4 \frac{k^4}{\nu^2|1-R^2|^2}[(10+5\cos^2\theta) + |R|^2(4+3\cos^2\theta)], \tag{5}$$

with

$$R=(\nu^2-a\mu^2)/\nu\nu_0+iak^3/\nu\nu_0. \tag{6}$$

Here, $k$, $\nu$, and $\mu$ are the momentum, energy, and mass of the meson, $f$ is the coupling parameter, and $\theta$ the angle of scattering. The quantity $a$ is a measure of the nucleon source size, and $\nu_0=3a\mu^2/2f^2$ is a measure of

* Assisted by the AEC.

[1] Y. Fujimoto and H. Miyazawa, Prog. Theoret. Phys. **5**, 1052 (1950).

[2] K. A. Brueckner and K. M. Case, Phys. Rev. **83**, 1141 (1951).

[3] R. E. Marshak, University of Rochester High Energy Physics Program, Final Report, July 1, 1949–August 31, 1950 (unpublished).

[4] The term strong-coupling theory is used throughout this note in its generic sense. We are actually concerned with moderately strong or intermediate coupling.

[5] Anderson, Fermi, Long, and Nagle, Phys. Rev. **85**, 936 (1952).

[6] K. A. Brueckner, Phys. Rev. **86**, 106 (1952).

[7] A phase shift analysis of the angular distributions of the scattering of 135-Mev mesons in hydrogen has been carried out by Anderson, Fermi, Nagle, and Yodh [Phys. Rev. **86**, 793 (1952)] under the assumption of charge independence. This has shown the $P_{\frac{1}{2}}$, $I=\frac{1}{2}$ interaction to be comparable to that in the $P_{\frac{3}{2}}$, $I=\frac{3}{2}$ state. More recently, R. E. Marshak (unpublished) and C. N. Yang [Report of the International Physics Conference, Copenhagen, June 3–17, 1952 (unpublished)] have pointed out that the analysis of the preceding authors is not at all unique and that one can equally well have the predominant interaction in the $P_{\frac{1}{2}}$, $I=\frac{1}{2}$ state. In all of these analyses, there is also a large interaction in the $S_{\frac{1}{2}}$, $I=\frac{1}{2}$ state.

[8] The quantum-mechanical problem is discussed by G. Wentzel, Phys. Rev. **86**, 437 (1952).

[9] J. R. Oppenheimer and J. Schwinger, Phys. Rev. **60**, 150 (1941).

[10] W. Pauli and S. M. Dancoff, Phys. Rev. **62**, 85 (1942).

[11] For details of the method of calculation, see W. Pauli, *Meson Theory of Nuclear Forces* (Interscience Publishers, Inc., New York, 1946).

the spacing between isobaric states. These formulas involve but two independent parameters which we can take to be $\nu_0$ and $a$.

If $a\mu \ll 1$ and $a\nu \ll 1$, one can write

$$|1-R^2|^2 \cong (1-(\nu/\nu_0)^2)^2 + 4(ak^3/\nu\nu_0)^2, \qquad (7)$$

whereupon the scattering cross sections will have a resonance at $\nu \sim \nu_0$ with a half-width $\Gamma \sim ak_0^3/\nu_0$. This is precisely the width found by Marshak[3] for the corresponding metastable nucleon state with precession frequency $\nu_0$ in the classical treatment of the neutral pseudoscalar field.

It is interesting to compare the predictions of the classical theory (near the resonance) with those of the quantum-mechanical strong- and weak-coupling approximations (with neglect of nucleon recoil). For the ratio of the integrated cross sections $\sigma_{\text{ord}}/\sigma_{\text{exch}}$, one finds 3, 2.5, and 1.5 for the three theories, respectively; for the angular distributions for ordinary scattering, one has $(1+1.2\cos^2\theta)$, $(1+3\cos^2\theta)$, constant; and, finally, for the angular distribution for exchange scattering, one has $(1+0.57\cos^2\theta)$, $(1+3\cos^2\theta)$, $\cos^2\theta$. We note the qualitative correspondence between the classical and quantum-mechanical strong-coupling theories.

Now, we recall that, in applying the classical strong-coupling theory to the neutral photomeson production process, Brueckner and Case[2] have shown that, for a resonance frequency of 250 Mev and a source radius of the order of the nucleon Compton wavelength, the excitation function is roughly in agreement with experiment. The angular distribution is $\sim(2+1.5\sin^2\theta)$ which is to be compared with the $(2+3\sin^2\theta)$ distribution observed by Silverman and Cocconi[12] for 290-Mev photons. In view of the crudity of the classical model, the general agreement is good.

In Fig. 1 we have plotted the integrated meson-nucleon scattering cross sections as predicted by the classical strong-coupling theory for $\nu_0 = 1.77\mu$ and $a = 1/4\mu$ (the corresponding resonance energy is 250 Mev with 63-Mev half-width); the choice of $\nu_0$ and $a$ corresponds closely to the parameters of Brueckner and Case.[13] If we assume that the charge-exchange scattering cross section of $\pi^-$ mesons in hydrogen is about twice that of the ordinary scattering of $\pi^-$ mesons,[14] we can make a rough comparison of $\sigma_{\text{ord}}$ and $\sigma_{\text{exch}}$ with the experimental data. While the energy variation of $\sigma_{\text{ord}}$ and $\sigma_{\text{exch}}$ is reasonably well given by the theory (except in the low energy region where the $S$-wave scattering is predominant), the absolute magnitudes of the cross sections are uniformly too small by a factor of 2. Although a detailed comparison of the theoretical angular distributions with experiment is difficult to make since our crude model includes no $S$-wave interaction, the general features of the predictions of the strong-coupling theory are far more encouraging than those of the weak-coupling approximation.

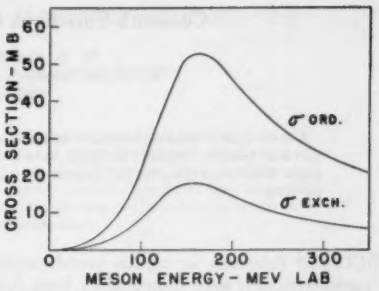


FIG. 1. The variation of the ordinary and exchange scattering cross sections with incident meson energy in the laboratory system. The resonance energy is 250 Mev and the nucleon source radius is $1/4\mu$.

In conclusion, we should like to re-emphasize that, while we have obtained some qualitative agreement with experiment in terms of the classical strong-coupling picture, the evidence for the existence of isobars is hardly definite at the present time, and it may ultimately turn out that the essential connection with reality of the model which we have been using is that it leads to a strong interaction in the $J=\frac{3}{2}$, $I=\frac{3}{2}$ meson-nucleon state.

I should like to thank Professor R. E. Marshak, who stimulated this investigation, for useful discussions.

[12] A. Silverman and G. Cocconi, Report of the International Physics Conference, Copenhagen, June 3–17, 1952 (unpublished).

[13] The strong-coupling condition can be expressed in the form $\nu_0 \ll \mu$; it is therefore clear that we are in fact dealing with an intermediate-coupling theory, as is also the case in the treatment of the photomeson process (see reference 2).

[14] Fermi, Anderson, Lundby, Nagle, and Yodh, Phys. Rev. **85**, 935 (1952); see also the more recent measurements at 135 Mev of Anderson, Fermi, Nagle, and Yodh, Phys. Rev. **86**, 793 (1952).

# Coulomb Functions for Heavy Nuclear Particles

W. D. Barfield and A. A. Broyles*
*Los Alamos Scientific Laboratory, Los Alamos, New Mexico*
(Received July 10, 1952)

Values of the regular and irregular solutions and the derivative of the regular solution of the wave equation for repulsive Coulomb potential have been computed by contour integrals at the classical turning point. Results are given for the range $\eta=10$ to $\eta=200$, corresponding to the Coulomb interaction of heavy particles.

COULOMB functions for certain useful ranges of parameters have been computed by Breit *et al.*[1,2] These do not extend above $\eta=30$. For large $\eta$'s, the steepest descent approximation is very useful[3] but breaks down near the classical turning point. The results of calculations by contour integrals for $\rho=2\eta$ are tabulated in Table I. The quantities $F_0$, $G_0$, and $F_0'$ were chosen because they allow quantities for higher $L$'s to be calculated with a minimum of cancellation from recursion formulas.[1] $G_0'$ can easily be obtained from the Wronskian relation, $F_L'G_L-G_L'F_L=1$. Recursion relation 11.5 of reference 1 and its derivative with respect to $\rho$ are useful to obtain values at higher $L$'s. Values of $F$, $G$, and $F'$ were also computed by contour integration for the values of $L$ up to $L=4$, and recursion formulas were used to check these values. None of these checks indicated an error greater than 0.1 percent, and many checked to better than 0.01 percent.

Table I. Coulomb functions calculated by contour integration for $\rho=2\eta$.

| $\eta$ | $F_0(2\eta)$ | $G_0(2\eta)$ | $F_0'(2\eta)$ |
|---|---|---|---|
| 10 | 1.034 | 1.797 | 0.2868 |
| 15 | 1.108 | 1.923 | 0.2668 |
| 20 | 1.163 | 2.016 | 0.2531 |
| 25 | 1.207 | 2.092 | 0.2431 |
| 30 | 1.244 | 2.157 | 0.2353 |
| 35 | 1.277 | 2.213 | 0.2290 |
| 40 | 1.306 | 2.262 | 0.2236 |
| 50 | 1.355 | 2.348 | 0.2150 |
| 60 | 1.397 | 2.420 | 0.2083 |
| 70 | 1.434 | 2.483 | 0.2028 |
| 80 | 1.466 | 2.539 | 0.1982 |
| 90 | 1.495 | 2.589 | 0.1942 |
| 100 | 1.522 | 2.635 | 0.1907 |
| 110 | 1.546 | 2.677 | 0.1876 |
| 120 | 1.569 | 2.716 | 0.1848 |
| 130 | 1.590 | 2.753 | 0.1823 |
| 140 | 1.609 | 2.787 | 0.1800 |
| 150 | 1.628 | 2.819 | 0.1779 |
| 160 | 1.646 | 2.849 | 0.1760 |
| 170 | 1.662 | 2.878 | 0.1742 |
| 180 | 1.678 | 2.906 | 0.1725 |
| 190 | 1.693 | 2.932 | 0.1709 |
| 200 | 1.708 | 2.957 | 0.1694 |

Table II. Number of terms, $N$, required in a series expansion around $\rho=2\eta$ to give a value of $G_0$ to within 1 percent accuracy at $2\eta-\rho=5$.

| $\eta$ | $N$ | Error in steepest descent formula |
|---|---|---|
| 20 | 6 | 8.1% |
| 100 | 4 | 8.4% |
| 200 | 3 | 6.2% |

Since the Coulomb functions and their first derivatives are given, an expansion around the point $\rho=2\eta$ can be made. Table II lists the number of terms in this expansion required to give a value of $G_0$ to within 1 percent of the correct value at $2\eta-\rho=5$. It also gives the error in the steepest descent approximation at this point. The steepest descent approximation should improve in accuracy for $\rho$ less than $2\eta-5$.[1] From the table we see that a combination of the steepest descent approximation and the expansion around $\rho=2\eta$ gives $G_0$ to better than 10 percent in this region of $\rho$ for $\eta$'s greater than 20.

The values listed in Table I may also be used to start a numerical integration to extend the range in $\rho$.

* On leave from the University of Florida, Gainesville, Florida.
[1] Bloch, Hull, Broyles, Bouricius, Freeman, and Breit, Phys. Rev. **80**, 553 (1950).
[2] Bloch, Hull, Broyles, Bouricius, Freeman, and Breit, Revs. Modern Phys. **23**, 147 (1951).
[3] A. A. Broyles and J. L. Powell, Phys. Rev. **72**, 155 (1947).

# Energy States of Overlapping Impurity Carriers in Semiconductors

CAVID ERGINSOY*
*High Voltage Laboratory, Queen Mary College, London, England*
(Received January 4, 1952)

An analytical solution of the Schrödinger equation for the spherically symmetrical wave function of an impurity carrier in a zero wave number state is given on the basis of the Wigner-Seitz cellular approximation. An approximate method is described for calculating the small deviations from the hydrogenic values. The variation of the lower band-edge energies with impurity concentration shows that the excited impurity bands may overlap each other strongly, but a continuous decrease of the activation energy from its hydrogenic value to zero cannot be accounted for by interaction alone.

## I. INTRODUCTION

THE object of this paper is to give an analytical solution of the Schrödinger equation for the spherically symmetrical wave function of an impurity carrier on the basis of the Wigner-Seitz cellular approximation. Although the solution is for the zero wave number states only, i.e., the lowest states in each impurity band, it reveals certain characteristics of the overlapping mechanism which were not foreseen either in our previous discussion[1] or in the approximate solution of Castellan and Seitz.[2]

## II. SOLUTION OF THE SCHRÖDINGER EQUATION

On the basis of the usual model of hydrogen analogy and the method of effective mass we assume that the impurity carriers satisfy the Schrödinger equation

$$\nabla^2\psi+(2m^*/\hbar)(E+e^2/\kappa r)\psi=0, \tag{1}$$

where $m^*$ is the effective mass of the carriers and $\kappa$ is the effective dielectric constant of the pure material. We are seeking a solution of Eq. (1) which satisfies the boundary condition that $d\psi/dr$ should vanish at the surface of a Wigner-Seitz sphere of radius $r_s$ given by

$$4\pi r_s^3/3=1/N, \tag{2}$$

where $N$ is the impurity concentration.

For a spherically symmetrical solution Eq. (1) reduces to the differential equation

$$d^2\psi/dr^2+(2/r)d\psi/dr+(2m^*/\hbar^2)(E+e^2/\kappa r)\psi=0. \tag{3}$$

We choose a dimensionless variable

$$x=2r/\kappa a_0 n, \tag{4}$$

and a dimensionless energy parameter

$$1/n^2=-E/(e^2/2\kappa a_0), \tag{5}$$

where $n$ is positive but not necessarily an integer and $a_0=\hbar^2/m^*e^2$ is the Bohr radius if $m^*$ is equal to the electronic rest mass.

Using Eqs. (4) and (5) we rewrite Eq. (3) in the form

$$d^2\psi/dx^2+(2/x)d\psi/dx+(n/x-\tfrac{1}{4})\psi=0 \tag{6}$$

for which we obtain in the usual way the solution

$$\psi=e^{-x/2}F(x), \tag{7}$$

where

$$F(x)=1+\sum_{\nu=1}^{\infty}\frac{(1-n)(2-n)\cdots(\nu-n)}{(\nu+1)!\nu!}x^\nu \tag{8}$$

is the confluent hypergeometric series[3] ${}_1F_1(1-n;2;x)$. Apart from an orthogonalizing constant $F(x)$ becomes the associated Laguerre polynomials $L_n^1(x)$ when $n=1, 2, 3, \cdots$, which is the well-known solution for the hydrogen-like isolated impurity.

We now introduce the Wigner-Seitz boundary condition

$$d\psi/dx=e^{-x_s/2}[(d/dx)F(x_s)-(1/2)F(x_s)]=0, \tag{9}$$

which gives for the finite values of $x_s$,

$$n+\sum_{\nu=1}^{\infty}\frac{(1-n)(2-n)\cdots(\nu-n)}{(\nu+2)!\nu!}(2n-\nu)x_s^\nu=0. \tag{10}$$

Equation (10) is of the form $f(n, x_s)=0$ and may be solved numerically or by the following simple approximation for small deviations of $n$ from the hydrogenic values.

## III. CALCULATION OF SMALL DEVIATIONS FROM HYDROGENIC STATES

For the depression of the ground state let

$$n=1-\epsilon, \tag{11}$$

so that Eq. (10) may be written in the form

$$1-\epsilon+2(1-\epsilon)\sum_{\nu=1}^{\infty}\frac{\epsilon(\epsilon+1)\cdots(\epsilon+\nu-1)}{(\nu+2)!\nu!}x_s^\nu - \sum_{\nu=1}^{\infty}\frac{\epsilon(\epsilon+1)\cdots(\epsilon+\nu-1)}{(\nu+2)!(\nu-1)!}x_s^\nu=0. \tag{12}$$

Neglecting the powers of $\epsilon$ above two, the series,

$$\sum_{\nu=1}^{\infty}\epsilon(\epsilon+1)\cdots(\epsilon+\nu-1)=\mathfrak{F}(\epsilon), \tag{13}$$

* Now with Sariyar Hydroelectric Project, Etibank, Turkey.

[1] C. Erginsoy, Phys. Rev. **80**, 1104 (1950).

[2] G. W. Castellan and F. Seitz, *Proceedings of the Reading Conference on Semiconducting Materials* (Butterworths Scientific Publications, London, 1951), p. 8.

[3] E. T. Whittaker and G. N. Watson, *Modern Analysis* (Cambridge University Press, Cambridge, 1950), fourth edition, p. 338.

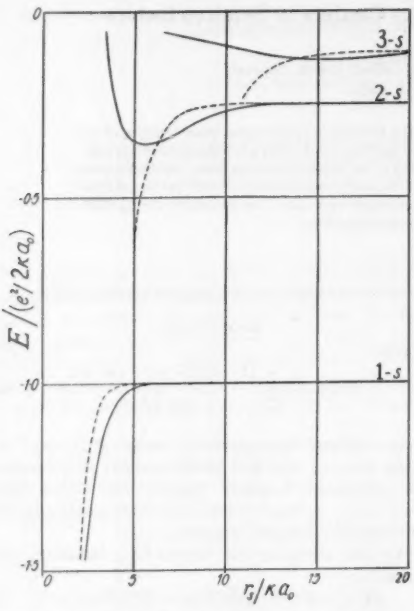


FIG. 1. The energy at the lower edge of the impurity bands formed by the splitting of $1-s$, $2-s$, and $3-s$ states, plotted as a function of the impurity concentration parameter $r_s/\kappa a_0$. The dotted curves belong to the approximate solution of Castellan and Seitz (reference 2).

may be approximated to

$$\mathfrak{F}(\epsilon)=\epsilon\sum_{\nu=1}^{\infty}(\nu-1)!+\epsilon^2\sum_{\nu=1}^{\infty}\left(1+\frac{1}{2}+\cdots+\frac{1}{\nu-1}\right)(\nu-1)!, \quad (14)$$

which reduces Eq. (12) to a quadratic in $\epsilon$,

$$[G_4-2(G_2-G_1)]\epsilon^2+[G_3+1-2G_1]\epsilon-1=0, \quad (15)$$

where $G_1$, $G_2$, $G_3$, and $G_4$ are convergent power series in $x_s$ alone.

$$G_1=\sum_{\nu=1}^{\infty}\frac{x_s^{\nu}}{\nu(\nu+2)!},$$
$$G_2=\sum_{\nu=1}^{\infty}\left(1+\frac{1}{2}+\cdots+\frac{1}{\nu-1}\right)\frac{x_s^{\nu}}{\nu(\nu+2)!},$$
$$G_3=\sum_{\nu=1}^{\infty}\frac{x_s^{\nu}}{(\nu+2)!}, \quad (16)$$
$$G_4=\sum_{\nu=1}^{\infty}\left(1+\frac{1}{2}+\cdots+\frac{1}{\nu-1}\right)\frac{x_s^{\nu}}{(\nu+2)!}.$$

The method consists in calculating the $G$'s for a given $x_s$ and solving Eq. (15) to obtain $\epsilon$. The results show good agreement with those of Wigner and Huntington[4] who obtained a numerical solution of a similar Schrödinger equation in connection with the hypothetical metallic modification of hydrogen.

The early stages of the depression of the excited $2-s$ and $3-s$ states may be calculated by similar approximations which are easy to set up. The cases where the approximation $\epsilon^2\approx 0$ is not justified must be calculated by solving Eq. (10) numerically.

## IV. CONCLUSIONS

Figure 1 shows the variation of the dimensionless energy parameter $1/n^2$ as a function of the dimensionless impurity concentration parameter $r_s/\kappa a_0$. The curves in dotted lines, plotted for comparison, belong to the approximate solution

$$1/n^2=1/s^2+(4/s^2)\exp[2(s^2-r_s/\kappa a_0)/s], \quad (s=1, 2, 3) \quad (17)$$

proposed by Castellan and Seitz.[2]

Our calculations give the energy of the lowest level in each impurity band form by the broadening of the hydrogenic $1-s$, $2-s$, and $3-s$ levels. The lowest levels correspond to a zero wave number and, of course, only two electrons can go into them. In order to find the other wave functions for which the wave number is not zero, it is necessary to solve the Schrödinger Eq. (1) with a further boundary condition expressing the symmetry of the "impurity lattice." We have not carried out this calculation and therefore we have no estimate of the energies at the top of each impurity band. However certain important characteristics of the overlapping mechanism may be derived from the lower band-edge energies:

(1) From the way in which the $2-s$ and $3-s$ bands deviate from the hydrogenic values, it may be predicted that the higher excited bands strongly overlap each other and the conduction band at moderate impurity concentrations ($r_s/\kappa a_0\approx 15$). An overlapping of the $2-s$ and the $3-s$ bands may also occur at a $r_s/\kappa a_0$ of about 5.

Apart from causing a depression of the effective conduction level, i.e., a decrease of the ionization energy, such a range of dense impurity levels adjoining the conduction band may trap a large number of carriers and affect the position of the Fermi level.

(2) The broadening of the $1-s$ level begins at a $r_s/\kappa a_0$ of about 5. Owing to the steep rise of the lower edge of the $2-s$ band, it is unlikely that these two bands overlap. The so-called "metallic" state, characterized by zero activation energy, cannot therefore be accounted for by interaction alone. It is possible that the screening of the impurity centers by the free carriers may affect considerably the potential energy of the bound carriers as the ionization becomes stronger. As Pincherle[5] has shown recently, a small change of the activation energy may be explained in this manner even without taking the interaction into account. The joint role of the two effects may be important.

[4] E. Wigner and H. B. Huntington, J. Chem. Phys. **3**, 764 (1935).
[5] L. Pincherle, Proc. Phys. Soc. (London) **A64**, 663 (1951).

# Electron Removal in Krypton Afterglows*

JOHN M. RICHARDSON†
*Department of Physics, Harvard University, Cambridge, Massachusetts*
(Received August 1, 1952)

The decay of the electrodeless microwave discharge in samples of Kr at 0.5- to 25-mm Hg was studied by the recently developed techniques of electron-concentration, optical spectrographic, and optical photometric measurements as a function of time after termination of the exciting fields out to a maximum of 15 msec. The Kr samples unavoidably contained traces of Xe estimated to be of the order of 0.01 to 0.1 mole percent, and such quantities of Xe were found to enter importantly into the afterglow processes of recombination and radiation in the pressure range 6 to 25 mm Hg. The observations are interpreted in terms of dissociative recombination of the molecular ions $Kr_2^+$ or $(MXe)^+$ (where M is an undertermined atom, either Kr or Xe) with subsequent atomic radiation by an excited dissociation product. For Kr, one quantum from various $2p$ to $1s$ transitions appears to be associated with each recombination event. Recombination coefficients of approximately $0.6\times10^{-6}$ and $2\times10^{-6}$ cm³/electron-sec are obtained for the Kr and Xe recombination process, respectively. These values do not appear to be pressure-dependent. Results of ambipolar diffusion measurements are also stated.

## I. INTRODUCTION

CONSIDERABLE experimental data dealing with electron removal from the afterglows of gas discharges have recently been obtained by microwave, spectrographic, and photometric means. Gases previously reported have been He,[1,2] $Ne$,[2-5] A,[3,6] Hg,[7] Cs,[8] $H_2$,[3,9,10] $N_2$,[3,11] and $O_2$.[3,11] The present article describes results obtained in Kr and certain inferences concerning Xe. These results are of dual interest because they both augment the list of gases studied and give information about Kr which has been the subject of virtually no previous investigation of this type.

Since the experimental portion of this work was completed, two significant advances in the subject have been reported. These are the identification of the recombination process as dissociative recombination of molecular ions proposed by Bates[12,13] and experimentally shown by Biondi,[14,15] and the analysis of ionic recombination including ion production during measurement by Kunkel.[16] It is thus possible to make use of these results in the interpretation of the present work, and to show that Kr behaves essentially like gases previously observed.

Of equal fundamental interest with the mechanism of recombination (the event by which a free electron passes to any bound state of either atom or molecule) are the mechanisms by which the recombined electron eventually passes to the ground state, and indeed these mechanisms may often give some clue as to the mechanism of recombination. The spectrography and photometry of the afterglow therefore, combined with electron loss measurements, give valuable additional information about these secondary processes.

## II. METHOD AND APPARATUS

The method and apparatus are substantially as previously described.[2,4,6,7] The experiment is arranged so that the electron concentration at the center of the sample, here designated by $n$, is proportional to the shift in resonant wavelength, $\Delta\lambda$, of an $S$-band cavity (2800 Mc). The sharpness of the resonance presentation in time is improved by sweeping the low-power search signal through resonance at a rate large (say 4 Mc per 60 $\mu$sec) compared to the rate of change of resonance due to $dn/dt$ instead of using the transient decay of the electron concentration to plot a resonance indication. This sweep is centered about any desired time in the afterglow. Figure 1 shows the circuits used. The breakdown pulse was of 10 $\mu$sec duration and a few hundred watts peak power. In the absence of cavity resonance, a signal of varying frequency but of substantially constant amplitude is delivered to the first detector, so that a plot of the $i$–$f$ response (4-Mc band width) is made on the indicator. If the occurrence of this pattern is adjusted either in frequency or time to embrace cavity resonance and if the probe is properly positioned, essentially the admittance curve of the cavity (~1 Mc band width) is superimposed on the indicator. In order to mark the position in time of a particular frequency differing a known amount from the indication of the frequency meter, a low-level marker signal in the $i$–$f$ band (11 Mc) accurately known to 0.01 Mc is injected into the $i$–$f$ amplifier. This signal produces a zero beat with the output of the first detector and is readily recognized on the indicator.

* Assisted by the ONR.
† Now at the National Bureau of Standards, Boulder, Colorado.
[1] M. A. Biondi and S. C. Brown, Phys. Rev. **75**, 1700 (1949).
[2] Johnson, McClure, and Holt, Phys. Rev. **80**, 376 (1950).
[3] M. A. Biondi and S. C. Brown, Phys. Rev. **76**, 1697 (1949).
[4] Holt, Richardson, Howland, and McClure, Phys. Rev. **77**, 239 (1950).
[5] M. A. Biondi, Phys. Rev. **79**, 733 (1950).
[6] A. Redfield and R. B. Holt, Phys. Rev. **82**, 874 (1951).
[7] P. Dandurand and R. B. Holt, Phys. Rev. **82**, 868 (1951).
[8] P. Dandurand and R. B. Holt, Phys. Rev. **82**, 278 (1951).
[9] John M. Richardson and R. B. Holt, Phys. Rev. **81**, 153 (1951).
[10] Lawrence J. Varnerin, Jr., Phys. Rev. **84**, 563 (1950).
[11] R. B. Bryan, Doctor's thesis, Harvard (1951) (unpublished).
[12] D. R. Bates, Phys. Rev. **77**, 718 (1950).
[13] D. R. Bates, Phys. Rev. **78**, 492 (1950).
[14] M. A. Biondi and T. Holstein, Phys. Rev. **82**, 962 (1951).
[15] M. A. Biondi, Phys. Rev. **83**, 1078 (1951).
[16] Wulf B. Kunkel, Phys. Rev. **84**, 218 (1951).

FIG. 1. Block diagram of electron-concentration apparatus, showing frequency-modulated search oscillator with sweep adjustable to occur at any desired afterglow time.

Measurements of $n$ are limited by the smallest accurately detectable frequency shift (here $\sim 0.1$ Mc) and by the largest permissible concentration of electrons consistent with the derivation of the applicable equation connecting $n$ and $\Delta\lambda$. In practice this means $2\times10^{7}$ $cm^{-3}<n<5\times10^{10}$ $cm^{-3}$. Times varied from 100 to 15,000 $\mu$sec.

Spectrograms of any 80-$\mu$sec interval of the afterglow period could be taken, intensity permitting, in the wavelength range 2000A to 8000A simultaneously with electron-concentration measurements.

The spectrographs could be replaced with a gated photomultiplier tube (1P28) for the purpose of making photometric measurements at any time in the afterglow of total light intensity within the 1P28 response band or within any smaller band defined by optical filters. A stepped attenuator (1000$\Omega$) was used before the amplifier-indicator chain to measure light levels. Advantages of the photomultiplier apparatus were that it supplied quick measurements, it enabled measurements very close (15 $\mu$sec) to the end of the main discharge to be made, and it was susceptible to an approximate calibration in absolute energy units if suitable corrections were made for system response and spectral characteristics of the source.

Samples of Kr in the pressure range 0.5 to 25.4 mm Hg were prepared from Air Reduction Company supply flasks. Spectrographic examination under continuous 2.5-Mc electrodeless discharge showed traces of the Cameron bands of CO, which, however, did not appear under microwave excitation nor in the afterglow. Xenon was present as an impurity in amounts estimated at 0.1 mole percent in some samples and in amounts of less than 0.02 mole percent (limit of detectability by mass spectrographic analysis) in other samples prepared from reagent grade Kr.

## III. RESULTS

### A. Spectra

The optical spectra proved of prime importance in interpreting the results. In all cases the continuous and main pulsed discharge exhibited only the spectrum Kr I, except that in a few samples the strongest lines of Xe I were observed faintly after long exposure.

At pressures of 2.7-mm Hg and below (where diffusion predominated) only Kr I was observed even to 4000 $\mu$sec in one sample. However, at higher pressures Xe I was always detected. In the three purest samples Kr I in the visible predominated until at least 500 $\mu$sec, after which Xe I predominated. In the two most impure samples Xe I predominated at times as short as 300 $\mu$sec and thereafter.

Figure 2 shows spectra obtained with one of the least pure samples. In the afterglow period centered at 90 $\mu$sec the enhancement of Xe I is well established. At 200 $\mu$sec, Xe I is greatly enhanced. At later times (600 to 1000 $\mu$sec), depending upon purity and pressure the only atomic lines which persisted were the strong lines of Xe I at 4624A and 4671A. (At still later times, using a wide spectrograph slit, a continuum was photographed, which is believed to be extraneous light possibly caused by the fluorescence of container walls. This view is substantiated by the character of the photometric curves at long times.) These spectral shifts are confirmed by other spectrograms in the red and in the near ultraviolet.

Examination of the entire set of spectrograms indicated that the process leading to Xe I is enhanced by increasing total pressure (relative concentrations being equal), and furthermore that the substitution of Xe I for Kr I occurs at later times in the red than in the violet. These results demand that interpretation of the electron removal and photometric data be made in terms of a process leading to xenon light at long times and in terms of a process leading to krypton light at short times, the transition time being that at which the complete spectral change occurs.

### B. Electron Removal

At low pressures (0.5- to 2.7-mm Hg) electron removal was found to be predominantly by diffusion, as shown

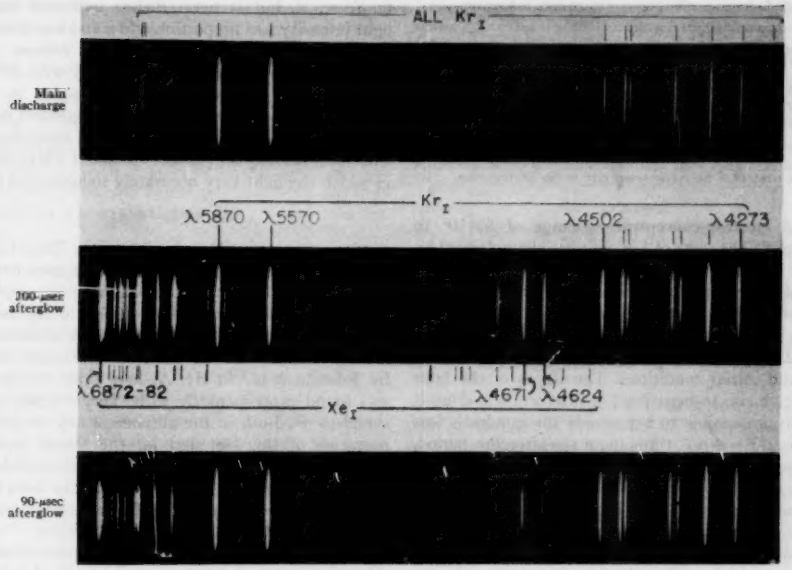


FIG. 2. Main discharge and afterglow spectra in one of the least pure samples, at 7.4 mm Hg. Eastman type 103a-F emulsion. Repetition rate ~240 pps; shutter speed 10, 80 and 80 μsec, respectively; exposure periods 90, 3180, and 715 sec, respectively.

by exponential or nearly exponential decay; and simultaneous spectrograms indicated that the xenon impurity had no effect on the process in that no lines of Xe I were observed. As the pressure was increased within this range, deviation from pure exponential decay occurred and the equation[17]

$$-\dot{n}=0.49\alpha n^2+n/\tau \qquad (1)$$

derived by Redfield and Holt[6] was assumed to apply, where $n$ is the electron concentration at the center of the cavity, and $\tau$ is the time constant of the decay due to diffusion. Figure 3 shows a typical run at 0.9 mm Hg with the experimental points obeying the integral of Eq. (1):

$$n/(1+0.49\alpha\tau n) = \{n(t_1)/[1+0.49\alpha\tau n(t_1)]\}\exp[-(t-t_1)/\tau]. \qquad (2)$$

The constants $\alpha$ and $\tau$ were fitted from two experimental points in addition to the point $[t_1, n(t_1)]$.

Results are summarized in Table I, from which it is noted firstly that the product $D_a p$ ($=\Lambda^2 p/\tau$, where $D_a$ is the ambipolar diffusion coefficient, $p$ is the pressure, $\Lambda$ is a characteristic diffusion length dependent on the geometry and particular solution of the diffusion equation employed) was not constant as found in He, Ne, and A. Secondly, $\alpha$ at low pressures was considerably below that observed at higher pressures (as was the case with argon); and within the limited range presented here, the values of $\alpha$ can be roughly fitted to a $p^2$ law.

At higher pressures (6.3- to 25.4-mm Hg) measurements were made over the time range of 200 to 5000

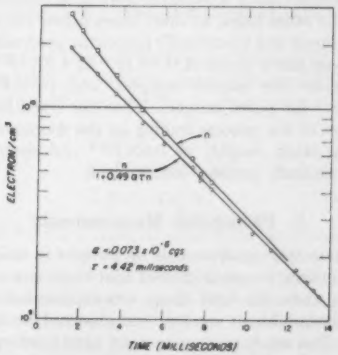


FIG. 3. Typical decay of electron concentration at low pressure (0.9 mm Hg) showing separation of $\alpha$ and $\tau$ according to Eq. (2).

[17] Redfield and Holt publish the constant in this equation as 0.54. After performing the integration which they indicate, the constant actually emerges as 0.49.

TABLE I. Average diffusion measurements in krypton.

| Pressure (mm Hg) | $10^8\alpha$ (cm³/electron-sec) | $\tau$ ($\mu$sec) | $D_0p$ (cm²−mm Hg/sec) |
|---|---|---|---|
| 0.5 | 0.0071 | 4150 | 50.8 |
| 0.9 | 0.0084 | 4540 | 82.6 |
| 2.7 | 0.14–0.19[a] | 2260 | 504 |

[a] Range of the average is the result of uncertainty of spatial distribution of electrons, whether of the cosine-bessel type or the uniform type.

$\mu$sec and electron-concentration range of $8\times10^7$ to $5\times10^9$ cm$^{-3}$. The plots of $1/n$ *vs* $t$ were characterized by a linear region at long times preceded by an initial region of either upward concavity or nearly constant slope distinct from that of the later region. An example is shown in Fig. 4. The time of transition was variously 500 to 2500 $\mu$sec, apparently influenced by pressure, purity and initial conditions. The slopes of the later regions give rise to negative $1/n$ intercepts, making it physically impossible to assign only the quadratic loss mechanism, $\dot{n}=-\alpha n^2$, throughout the afterglow period. Diffusion is excluded since here $\alpha\tau n\gg1$, so that some complex mechanism such as outlined in the discussion below must be invoked. For impure samples (7.4 to 19 mm Hg) at long times where the xenon processes were presumably well established, the slopes of the $1/n$ *vs* $t$ curves ranged from $1.4\times10^{-6}$ to $2.1\times10^{-6}$ cm³/electron-sec. The range is ascribed to slight variations in the predominance of the xenon recombination process. Surely no pressure variation as strong as the first power of pressure exists, and the coefficient may be taken as pressure-independent. For purer samples (6.3 to 25.4 mm Hg) at long times when the xenon processes predominated but were perhaps not so well-established as above, the apparent coefficient ranged from $1.2\times10^{-6}$ to $1.9\times10^{-6}$ cm³/electron-sec, again probably due to initial conditions and again pressure-independent. Thus the coefficient descriptive of the process leading to the spectrum Xe I may be taken roughly as $2\times10^{-6}$, and no greater accuracy is available from these experiments.

On the other hand, at short times before the transition of slopes and when the Kr I spectrum predominated, the slopes had a range of $0.7\times10^{-6}$ to $1.2\times10^{-3}$ cm³/electron-sec for impure samples, and $0.6\times10^{-6}$ to $1.0\times10^{-6}$ for purer samples. Thus the coefficient descriptive of the process leading to the spectrum Kr I may be taken roughly as $0.6\times10^{-6}$ cm³/electron-sec and is similarly pressure-independent.

### C. Photometric Measurements

Photometric measurements on samples in which diffusion mainly occurred showed that there was a region of time where the light decay was exponential and of time constant about one-half that observed for electron decay. This result was not in exact agreement over the entire observed range because of the existence of the aforementioned extraneous light ascribed to container fluorescence, but it nevertheless indicated that the light intensity was proportional to $n$ and was intimately connected with the small amount of volume recombination which proceeds simultaneously with diffusion.

Photometric measurements on samples in which recombination mainly occured were of greatest interest. As shown in Fig. 5, there was a region extending from extremely short times (15 $\mu$sec) to about 300 or 400 $\mu$sec in which the light very accurately followed the law

$$I^{-\frac{1}{2}}=I_0^{-\frac{1}{2}}+At \qquad (3)$$

over a range of 400:1 in intensity. This behavior suggests that the recombining positive ions were well established at the end of the exciting pulse, and there was not significant production of ions during the range of this measurement. For otherwise the observed light intensity would indicate the local maximum observed by Johnson *et al.*[2] in He. At long times the intensity was found experimentally to be very roughly proportional to $n^{\frac{1}{2}}$. Both in the absence of any simple interpretation of this fact and for the reason mentioned above under spectra, this intensity was considered to be extraneous and so great as to mask the more rapidly decaying intensity due to Xe I. Photometric measurements at long times were therefore ignored.

The fact that the law in Eq. (3) is maintained even though in some cases the light consisted of both Kr I and Xe I implies substantially similar rates of recombination for both types of ion, since the reasonable assumption may be made that substantially the same numbers and types of quanta in each case are emitted per recombination event. The law (3) establishes, avoiding the effect of extraneous light, that the light from the

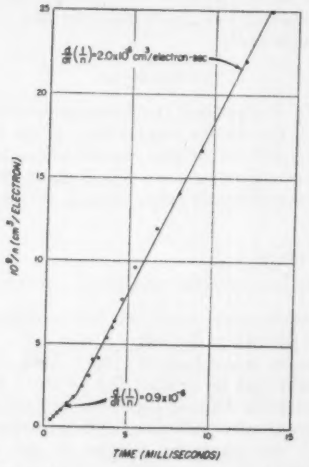


FIG. 4. Decay of electron concentration in sample emitting Kr I at short times and Xe I at long times. Pressure = 19 mm Hg. Two distinct line segments are apparent.

discharge tube from the very beginning is the result of a two-body process:

$$X^+ + Y^- \rightarrow XY + h\nu, \tag{4}$$

where $X^+$ and $Y^-$ are charged particles, each of concentration $N$. This follows if intensity is assumed proportional to $\dot{N}$, because $\dot{N}$ in the process (4) must be proportional to $N^2$. It is possible to establish that the negative particle in the above reaction is an electron by calculating $\alpha$ from the slope of the $I^{-\frac{1}{2}}$ plot from the relation:

$$\alpha = -\dot{n}/n^2 = d(1/n)/dt = (1/C)dI^{-\frac{1}{2}}/dt, \tag{5}$$

where $C^2 = n^2/I$ and is evaluated by a simultaneous measurement of $n$ and $I$ at any one time. The necessary proportionality between $I$ and $n^2$ was established experimentally over the range 200 to 600 $\mu$sec. Results of such calculations showed that the effective $\alpha$ in the short-time region inaccessible to direct observation of electron decay ($t < 200$ $\mu$sec) was very nearly the same as that obtained by the later observation of $n$ as a function of $t$.

Finally, when applied to short times and pure samples where the spectrum Kr I is the end product of the recombination process, the photometric measurements provided an estimate of how much radiant energy (within the band of the apparatus) appeared per disappearing electron, and this value may be compared with that expected from a consideration of the possible transitions from the ionized state to the ground state.

Using a photomultiplier tube whose sensitivity was calibrated in absolute units by means of a standard lamp, and making suitable corrections for viewing geometry, spectral distribution, and photosurface response, it was found that the radiant energy in the band 3300A to 6500A (3.72 ev to 1.90 ev) was of the order of 0.1 to 0.2 ev per disappearing electron, or one quantum of the average energy of 2.81 ev for every 14 to 28 disappearing electrons. Furthermore, the strong group of red lines, 7587A to 8928A, also contributed to the radiant energy per disappearing electron, but was not included in the above measurement since it lay outside the response band of the phototube. Therefore, the above estimate was extended to include the contribution of these red lines. Pairs of spectrograms of the two regions which applied to identical experimental conditions at 100 $\mu$sec in the afterglow where the krypton spectrum predominated were selected. Using previously published relative intensities within each group,[18,19] to define the relative power in the two groups of lines and correcting for different emulsion sensitivities, different observed densities of lines in each group of the same relative intensity, and different exposure

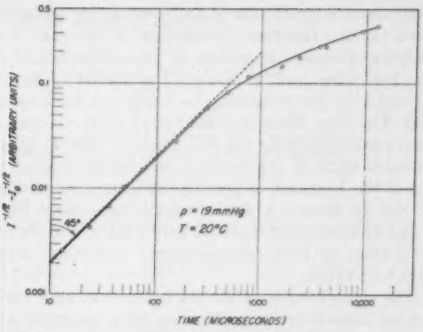


FIG. 5. Typical decay of visible intensity at high pressure (>6 mm Hg) showing region where $I \propto n^2$.

times, it was found that the radiant energy per disappearing electron in the band 7587A to 8928A (1.63 ev to 1.38 ev) was some 40 or 50 times that found in the shorter wavelength band with an uncertainty of perhaps a factor of 5. This result corresponds to one quantum of average energy of 1.5 ev for at most every 2 disappearing electrons, and strongly indicates that *every* recombination event is followed by the transition leading to one of these red lines. No such pronounced enhancement of the intensity of this red group relative to that of the shorter wavelengths was apparent in spectra of the main discharge.

## IV. DISCUSSION

From the foregoing experimental results it is evident that several processes occurred either in turn or simultaneously, depending on conditions of purity, pressure, initial ion concentrations, and time of observation. The task of quantitatively separating these processes on the basis of the limited data obtained here does not appear promising. Instead, a few qualitative and semiquantitative conclusions based mainly on the high pressure measurements and consistent with recent work will be drawn.

The excited states of Kr at short times in the afterglow are believed to arise by dissociative recombination of the molecular ion according to the scheme:

$$Kr^+ + Kr + M \rightarrow Kr_2^+ + M, \tag{6a}$$

$$Kr_2^+ + e \rightarrow Kr + Kr', \tag{6b}$$

$$Kr' \rightarrow Kr + h\nu, \tag{6c}$$

where M is a third body. Because of the aforementioned linearity of $I^{-\frac{1}{2}}$ from zero time, the ion $Kr_2^+$ probably is well-established in the main discharge. (Contrariwise, the pressure dependence of $\alpha$ at low pressures indicates that the molecular ion is there not so well-established, and that Eq. (6a) is operative.) The occurrence of two distinct slopes connected by a curved region in the $1/n$ plots is probably due to the xenon contamination

[18] Meggers, de Bruin, and Humphreys, J. Research Natl. Bur. Standards, **7**, 643 (1931).
[19] W. F. Meggers and C. J. Humphreys, J. Research Natl. Bur. Standards, **10** 427 (1933).

rather than to production of $Kr_2^+$ ions during measurement. It is, therefore, reasonable to assume that electrons disappear according to the quadratic law at the beginning and to assign the lowest observed $d(1/n)/dt$ as the recombination coefficient for process (6b). The large fraction (near unity) of $2p-1s$ transitions per disappearing electron indicates that the most probable state of the excited dissociation product is one of the $2p$ states, or possibly a higher state leading to the $2p$ states. A few afterglow transitions from initial $4p$ states were observed very weakly, and transitions from $3p$ levels were observed moderately from 4273A to 4502A.

The excited states of Xe are believed to arise from similar dissociative recombination of a molecular ion containing Xe, since the metastable states of Kr are not sufficiently energetic to raise Xe to the highest observed radiating levels. The same type of behavior as described above for Kr I was observed for Xe I when the latter spectrum appeared. The reaction might be either

$$Xe_2^+ + e \rightarrow Xe + Xe' \rightarrow 2Xe + h\nu \qquad (7a)$$

or

$$(KrXe)^+ + e \rightarrow Kr + Xe' \rightarrow Kr + Xe + h\nu. \qquad (7b)$$

The molecular ion in (7a) or (7b) must be produced during measurement, for the hypothesis that both the krypton and xenon ion are initially present in a given ratio cannot lead to the observed form of the electron decay curves. This production is believed to account for the curvature in the $1/n$ *vs* $t$ plots according to an analysis similar to that of Kunkel.[16] Once this ion predominates, the quadratic law again applies as shown by the new linearity of the $1/n$ plots at long times, with the observed $d(1/n)/dt$ at these times as the coefficient for process (7a) or (7b).

Recalling that initially there is no evidence for ionized xenon, a mechanism for producing the molecular ion in (7a) or (7b) must be postulated. It is possible that the $Xe_2^+$ ion might be formed in two steps by first a charge exchange between $Kr^+$ and Xe and subsequent collision between $Xe^+$ and Xe. The second step of this process is considered very improbable because of the low experimental concentration of Xe. The ion $(KrXe)^+$ might be formed (a) by a two-stage process involving collisions of $Xe^+$ (as formed above) with Kr, (b) by direct combination of $Kr^+$ and Xe or (c) by an exchange of Xe for Kr in the molecular ion $Kr_2^+$. There is as yet insufficient data to identify the recombining xenon ion or its origin, and all that can be said is that (c), above, is to be intuitively preferred. (See Note added in proof.)

## V. SUMMARY

At low pressures (0.5- to 2.7-mm Hg) characteristic ambipolar diffusion behavior was observed, and possible xenon contamination did not appear to influence the results. In this pressure region the effective recombination coefficient for krypton lies two orders of magnitude below its pressure-independent value for higher pressures, and apparently varies as $p^2$, lending support to the hypothesis of Eq. (6a). The product $D_a p$ was found to increase with pressure.

At higher pressures (6.3- to 25-mm Hg) recombination behavior was observed, but with the evident superposition of two recombination processes because of contamination of the samples with xenon. One of these is ascribed to $Kr_2^+$ and the other to an unknown molecular ion containing Xe. Coefficients for the two processes are respectively set at $(0.6\pm0.2)\times10^{-6}$ cm³/electron-sec and $(2\pm0.5)\times10^{-6}$ cm³/electron-sec, of the same general magnitude as recent similar observations in other gases. These figures were observed for the extremes represented, respectively, by the purest samples at shortest afterglow times emitting only Kr I, and the most impure samples at longest afterglow times emitting only Xe I. Better accuracy awaits the results of new work in which the contamination problem is avoided.

Photometric measurements in the early afterglow indicated light arising from a two-body process, the absolute decay of which, further, was consistent with the above coefficient as to order of magnitude. Coupled with rough spectrographic intensity estimates, these measurements strongly indicate that each recombination event gives rise to a transition from the $2p$ levels to the $1s$ levels with radiation in the band 7587A to 8928A, from which it is inferred that the most probable state of the excited dissociation product is a $2p$ state. Further spectroscopic studies of the afterglows of both Kr and Xe with improved apparatus in which relative intensities of afterglow and discharge spectra are emphasized should provide valuable information as to the radiation processes subsequent to recombination.

The author is indebted to Professor R. B. Holt for his guidance and to the AEC for fellowship aid granted during a portion of this research.

*Note added in proof.*—Professor O. Oldenberg has stressed to me that the existence of ions of the type $(KrXe)^+$ is questionable. The remaining alternative is that the positive carrier at long times is the atomic xenon ion, produced most likely by charge exchange. This ion would directly give the observed xenon spectrum and would disappear by ambipolar diffusion in Kr similarly to the behavior of $A^+$ in He as observed by Biondi. Although the present data favor the interpretation of Eq. (7b), it is recognized that a clear choice between the alternative processes was possibly prevented by the rather small time range of 5 msec. The conclusions regarding the recombination of xenon are correspondingly weakened.

# Deuteron Photodisintegration at High Energies*

W. S. GILBERT† AND J. W. ROSENGREN‡
*Radiation Laboratory, Department of Physics, University of California, Berkeley, California*
(Received July 7, 1952)

The reaction $\gamma+d\rightarrow p+n$ was investigated using the photon bremsstrahlung spectrum from the Berkeley 322-Mev electron synchrotron. Protons were detected by a scintillation counter telescope system consisting of three liquid scintillators, each viewed by two or three photomultiplier tubes. Two types of target system were used: high pressure, low temperature deuterium gas, and heavy water-with-water subtraction. Values for $(d\sigma/d\Omega)_\theta$ were determined at laboratory angles 30°–90° for $E_\gamma$ (center-of-mass) = 140±15 Mev and 200±15 Mev, and at laboratory angles of 30°–115° for $E_\gamma$ (center-of-mass) = 250±15 Mev. The following total cross sections were determined:

$$\sigma_{\text{total}}(140)=11.8\pm4.1\times10^{-29}\text{ cm}^2;\quad \sigma_{\text{total}}(200)=10.0\pm3.0;\quad \sigma_{\text{total}}(250)=15.9\pm6.4.$$

The uncertainties are standard deviations based on counting statistics only; there is an additional 40 percent absolute uncertainty.

These cross sections are far greater than the values predicted by theories which exclude the effects of meson interaction. However, a theoretical treatment which takes the specifically mesonic interaction into account does yield cross sections of a magnitude comparable with those observed.

## INTRODUCTION

THE deuteron, by virtue of being a two-body system, is of primary interest in nuclear theory since one might hope to determine its wave functions exactly. Ever since the theoretical papers of Bethe and Peierls[1] and Fermi,[2] relating to the photodisintegration of the deuteron and its inverse reaction, the $n$–$p$ capture process, numerous experimental studies have been carried out to test the theory and to determine specific parameters relating to the deuteron's binding energy, the shape, width, and depth of the nuclear potential well. The majority of these investigations have been carried out at energies of a few Mev using naturally radioactive $\gamma$-emitters. Recently, work has been carried to approximately 20 Mev.[3,4] The information obtained from photodisintegration of the deuteron is similar to that obtained from neutron-proton scattering data at corresponding energies. At low energies the photodisintegration data give information about the effective ranges of the neutron-proton interaction but do not yield any information on the shape of the potential. Theoretical calculations have been carried out for $\gamma$-energies up to 150 Mev,[5–7] using the best values for the parameters determined from other experiments such as $n$–$p$ scattering. These high energy calculations depend on the shape of the potential and the percentage of charge exchange and are affected by the use of tensor forces. They should give a reasonable picture of the cross sections due to the photoelectric dipole and quadrupole moments of the nucleons; however, no calculation was made of the contribution of meson effects due to interactions with the virtual meson field.

The Berkeley synchrotron yields photons of energies (relative to the center of mass of the deuteron-photon system) up to about 280 Mev, and it appeared desirable to investigate the photoeffect at these high energies. By comparison with the theoretical treatments described above, one could expect to discover the magnitude of the contributions made to the cross section by meson interactions.

## KINEMATIC CONSIDERATIONS

The reaction $\gamma+d\rightarrow p+n$ represents a two-body problem both before the photon interaction and afterwards. This being the case, it is possible to determine uniquely the energy of the initiating $\gamma$-ray by measuring the energy of the emergent proton and the angle of emission of this proton with respect to the incident $\gamma$-ray direction.

At high $\gamma$-energies it is possible for mesons to be produced along with two resultant nucleons, and the final products then form a three-body system. If one were to measure the energy and angle of only one of these emergent particles, he would not be able to determine uniquely the energy of the initiating $\gamma$-ray. However, because approximately 140 Mev of energy are required to create the meson and because of the kinematics of the conservation momentum between the meson and any recoil nucleons, the energy of any such recoil nucleons would be relatively low.

In the case of our determinations of $d\sigma/d\Omega$ for $E_\gamma=200$ Mev and $E_\gamma=250$ Mev, our counters defined various proton energy intervals depending upon the angle. In all cases any recoil protons associated with meson production by even the 322-Mev quanta would be of lower energy than the interval defined by our

* This work was carried out under the auspices of the AEC.
† Present address: North American Aviation, Inc., AER, Berkeley, California.
‡ Present address: Department of Physics, M.I.T., Cambridge, Massachusetts.
[1] H. A. Bethe and R. Peierls, Proc. Roy. Soc. (London) **A148**, 146 (1935).
[2] E. Fermi, Phys. Rev. **48**, 570 (1935).
[3] E. G. Fuller, Phys. Rev. **79**, 303 (1950).
[4] D. H. Wilkinson and J. H. Carver, Nature **167**, 154 (1951).
[5] J. F. Marshall and E. Guth, Phys. Rev. **76**, 1880 (1949).
[6] L. I. Schiff, Phys. Rev. **78**, 734 (1950).
[7] J. F. Marshall and E. Guth, Phys. Rev. **78**, 739 (1950).

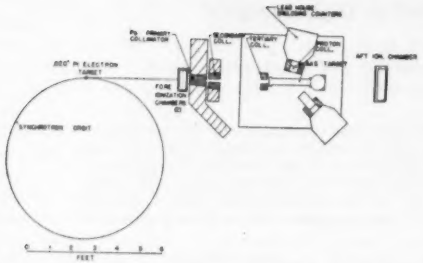

FIG. 1. Diagram of experimental arrangement using deuterium gas target (actually only one counter telescope was used).

counters. Therefore for these two energies it is energetically impossible for there to have been a contribution from any meson producing reaction. In the case of $E_\gamma = 140$ Mev, at a few of the larger angles, the maximum energy protons recoiling from produced mesons could enter the detection system. Since these protons are of a three-body system, one cannot determine how many of the recoil protons lie in the range of acceptance even though the meson production rate is known. However, since the known meson production rate is smaller than the observed proton rate and since presumably only a small fraction of the meson events would lead to maximum energy recoil protons, the contribution from this process is considered negligible.

## DESCRIPTION OF THE EXPERIMENT

The x-rays were produced in the Berkeley electron synchrotron by letting the internal electron beam strike a 0.020-inch platinum target placed on the inner side of the accelerating donut. The beam was spread out in time by modulating the rf accelerating voltage such that electrons spilled into the target over a period of some 3000 $\mu$sec. In the "spread out" beam, the electrons are of various energies corresponding to the magnetic field at the time they strike the internal synchrotron target. The relative beam intensity over the 3000-$\mu$sec period could be determined and the net bremsstrahlung distribution was found by combining the bremsstrahlung spectra corresponding to the various quantum limits (electron energies) weighted by the relative beam intensities at these electron energies.

In Fig. 1 is shown the deuterium gas target arrangement. At 55 inches from the platinum target the beam was collimated by a tapered hole in a lead block 9 inches thick. The collimating hole was a half-inch in diameter at the entrance end and was part of a cone whose apex lay at the platinum target. Directly behind the primary collimator was the 6-inch thick lead secondary collimator which had a 1-inch hole. Behind this and directly in front of the experimental target was a tertiary collimator of lead, 6 inches thick and with a 2-inch hole. The target and collimators were aligned by means of a transit. Photographs of the beam were then taken with a $\frac{1}{4}$-inch primary collimator and a final alignment of the target was made with respect to this small, well-defined beam. Then the larger primary collimator was replaced. At the end of a run the $\frac{1}{4}$-inch collimator was again inserted and photographs taken. The target proved to be still aligned at the end of each run.

The target (see Fig. 1) employed at $E_\gamma = 200$ Mev and 250 Mev was deuterium gas at a pressure of 2000 psi and at liquid nitrogen temperature (77°K) used in a line target assembly designed by White.[8] The walls of the gas target combined with the thickness of the first counter, however, represented so much absorber that protons initiated by 140-Mev $\gamma$-rays would not reach the second counter of the detection system. Therefore in order to investigate the cross section at 140 Mev, it was necessary to use a target whose self-absorption was small. Heavy and ordinary water targets, 0.20-inch thick, were used for this purpose. Energetically, Compton protons from hydrogen are of too low an energy to give a count in our detection system. Therefore it was concluded that the entire counting rate from regular water could be considered as being due to the oxygen present. Subtracting this number from the counting rate due to heavy water yields the deuterium contribution alone. The regular and heavy waters were interchanged between the two containers several times to eliminate the effect of any difference in thickness of the two target holders. The cross section for photoprotons from oxygen is several times larger than that from deuterium and the statistics of the subtraction are extremely unfavorable. Thus at higher energies where

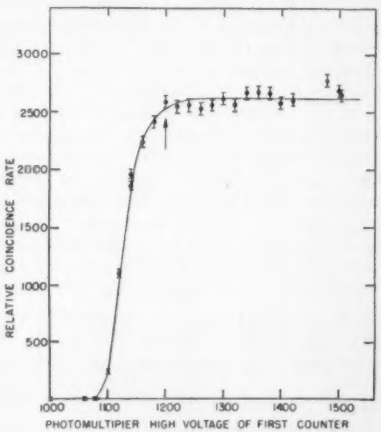


FIG. 2. Coincidence plateau for detection of protons produced by bombardment of paraffin with the cyclotron 90-Mev neutron beam. Standard deviation shown.

[8] White, Jakobson, and Schulz, Phys. Rev. 88, 836 (1952).

it was energetically possible to use the high pressure deuterium gas target, it was statistically advisable to do so.

The counter telescope was placed in a lead house with 4-inch thick walls in order to be shielded from the general background of electrons and x-rays which pervade the magnet room of the synchrotron. A hole in the front wall of the lead house served as one defining aperture in the proton collimator. In the case of the deuterium gas system, the source of protons was a line target and it was necessary to define the target volume by a collimator system preceding the counter telescope. The value of effective target volume combined with the effective counter solid angle was obtained by a graphical integration for each proton angle. The angular resolution of the collimation system was such that the bulk of the protons accepted from the gas target were in the angular range $\theta \pm 4°$. However, a few protons were accepted from between 4°–6° from $\theta$. Therefore the over-all angular resolution was $\pm 6°$ from the gas target. From the water targets the over-all angular resolution was $\pm 4°$. At each proton angle at which the counter telescope was placed a copper absorber was inserted before the counter with thickness appropriate to the proton angle and the desired photon energy.

To monitor the beam, three ionization chambers, two in front and one in back of the target, were used simultaneously. Their ratios were observed to remain constant throughout the experiment. The absolute calibration of the beam was due to Blocker and Kenney.[9,10] The uncertainty in the absolute calibration at the time of this experiment was estimated to be 30 percent.

## PROTON DETECTION AND IDENTIFICATION

The protons were identified essentially by their range and $dE/dx$. A counter telescope consisting of three counters in line was employed. A particle's range was specified by demanding that it pass through the first counter and stop in the second. All three counters were connected in a coincidence circuit and the first two counters were connected in a separate double coincidence circuit. A subtraction of the two coincidence rates gave the rate of particles stopping in the second counter. The protons were then distinguished from other particles by the pulse height in the first counter.

The counters were liquid scintillators of terphenyl dissolved in toluene. The first counter, in which the particle's $dE/dx$ was determined was three inches in diameter, 1.6 g/cm² of toluene in thickness, and was viewed from the side by three 1P21 photomultiplier tubes with outputs connected in parallel. Counter 2, which consisted of 0.86 g/cm² of liquid, and counter 3, which was 1.1 g/cm² thick, were both four inches in diameter and were each viewed by two 1P21 photomultiplier tubes. A 2.6 g/cm² copper absorber was permanently placed between counters 1 and 2 to improve the discrimination of the telescope. The pulses from the phototubes were fed to a pulse-height discriminator and gate former. The gate length, the recovery time, and the resolution time were all about 0.4 μsec.

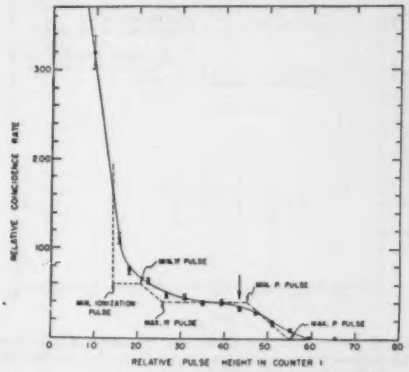


FIG. 3. Integral bias curve for detection at 60° of protons produced by bombardment of carbon with 322-Mev bremsstrahlung. Standard deviation shown. Scale in discriminator volts.

For particles of different masses and identical residual ranges, it can be shown that the ratio of the $(dE/dx)$'s in traversing matter is approximately $(m_1/m_2)^{0.44}$. In the case of protons and mesons, this ratio equals 2.30. This means that a proton would give up 2.30 times as much energy in counter 1 as would a meson, and if the scintillators were perfectly proportional, the proton pulse would be 2.30 times as large as the meson pulse. This ratio, call it the merit ratio, is a limiting maximum since it holds only for identical residual ranges or, to put it another way, for a second counter of zero thickness. In practice, counter 2 was of finite thickness and the ratio of the smallest proton pulse to the largest meson pulse was calculated to be 1.83. For protons the band of energies accepted was 62.5–71.0 Mev, with the corresponding energies given up in the first counter being 20.5–17.0 Mev, respectively. For mesons the band was 28.0–32.0 Mev, and the energy lost in the first counter was 9.3–8.0 Mev, respectively. To examine higher energy particles, a copper absorber was inserted between the target and the counter telescope.

To ascertain the conditions under which one would be counting protons with full efficiency, a run was made using the 90-Mev neutron beam of the Berkeley 184-inch synchrocyclotron. This neutron beam is obtained by deuteron stripping and has a wide spread in energy (a total width at half-maximum of about 30 Mev). This beam was used to bombard a paraffin target, and since the energy is below the threshold for meson production, the particles observed will be almost entirely protons with a small fraction of heavier particles.

[9] Blocker, Kenney, and Panofsky, Phys. Rev. 79, 419 (1950).
[10] McMillan, Blocker, and Kenney, Phys. Rev. 81, 455 (1951).

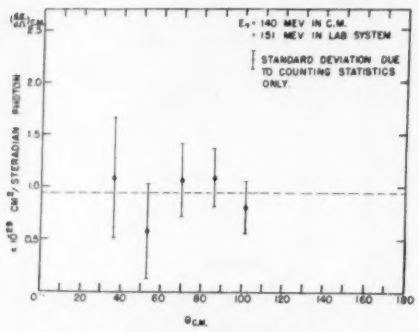


FIG. 4. Differential cross sections in the center-of-mass frame for photodissociation (without meson production) of the deuteron, $E_\gamma = 140$ Mev (center of mass).

The curve giving counting rate per unit beam *vs* photomultiplier high voltage on counter 1 is shown in Fig. 2. The arrow indicates a standard point on the curve. The operating conditions of the first counter at this point were made reproducible by determining the singles counting rate of this counter with a beta-source in a standard geometry. To be able to count the betas a standard 20-db attenuator, present in the output of the first counter during proton detection, was removed.

In Fig. 3 is shown the integral bias curve of coincidence counting rate *vs* discriminator bias of the first counter obtained at 60° from a carbon target in the 322-Mev x-ray beam of the synchrotron. The arrow indicates the calibration point obtained using the 90-Mev neutron beam. The dotted curve indicates an ideal integral bias curve when there are only protons and $\pi$-mesons. The maximum proton pulse is arbitrarily taken as shown and the other points are calculated from range energy relations. The absolute values taken for the proton and meson production are based on the experimental data of Keck[11] and of Peterson, Gilbert, and White,[12] respectively.

The observed curve from carbon is affected by electrons at the low bias end and perhaps by deuterons at the large bias points.

An operating point was selected at a bias five volts lower than the calibration point from the cyclotron run. From comparison of the ideal curve and the observed curve, we believe that only protons were counted at the operating point and that the protons were counted with full efficiency. A more detailed investigation in the low bias region (considerably beyond the operating point for proton counting) indicated a meson plateau. It was possible to measure a meson yield as a function of meson energy which was in fair agreement with previous experimental data.[12]

Counting rate *versus* bias plateaus were obtained for counters 2 and 3.

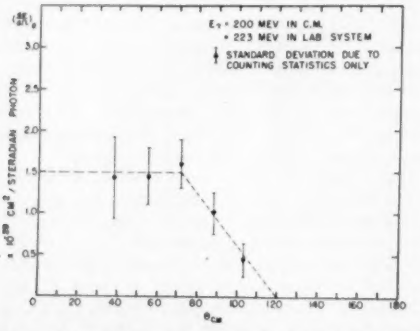


FIG. 5. Differential cross sections in the center-of-mass frame for photodissociation (without meson production) of the deuteron, $E_\gamma = 200$ Mev (center of mass).

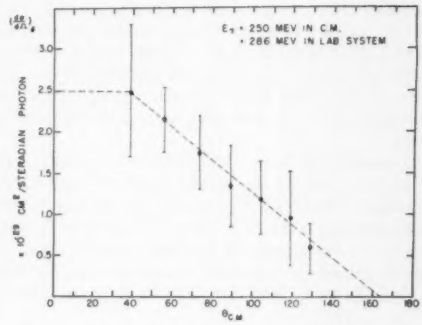


FIG. 6. Differential cross sections in the center-of-mass frame for photodissociation (without meson production) of the deuteron, $E_\gamma = 250$ Mev (center of mass).

## RESULTS

The experimental values for the differential cross section are plotted in Figs. 4, 5, and 6 as a function of proton angle in the center-of-mass system. These values have been corrected for attenuation of the protons by nuclear interaction in the copper absorbers used to fix the proton energy. The cross section for this was taken to be equal to the geometrical nuclear area taking the nuclear radius to be $1.4\times10^{-13}\,A^{\frac{1}{3}}$ cm. These data have also been corrected for loss of protons to the detection system due to small angle multiple Coulomb scattering in the absorbers. The effect of penetration of the protons through the edges of the collimator system was calculated to be negligible.

It is to be noted that the uncertainty in the photon energy due to the angular and energy intervals presented by the counter telescope is different for each

[11] J. C. Keck, Phys. Rev. **85**, 410 (1952).
[12] Peterson, Gilbert, and White, Phys. Rev. **81**, 1003 (1951).

angle; however, an average over-all uncertainty of 15 Mev has been assigned.

The uncertainties shown are standard deviations based on counting statistics only, including the subtraction of background taken with the empty target assembly, and should be indicative of the relative values. With respect to the absolute cross sections, however, there is an additional uncertainty of some 40 percent. Chief among the uncertainties leading to this value is the beam calibration with smaller uncertainties in the effective thickness of the second counter, scattering corrections, etc. In addition it should be noted that the 140-Mev data were taken at a considerably later date with a different geometry, and so the absolute value of this point relative to the 200- and 250-Mev points is suspect.

The total cross sections were obtained by integrating under the arbitrarily assumed curves shown drawn through the differential cross section data in Figs. 4, 5, and 6. The results are given in Table I. The uncertainties are standard deviations based on counting statistics only. It should be recalled that all these cross sections are for photodissociation of the deuteron where a meson is not produced.

There is an uncertainty due to the extrapolation over angles for which the differential cross sections were not obtained. Since the solid angle and apparently also the differential cross sections are small at most of the angles not investigated, the error due to this extrapolation should be small.

The values of the total cross section given in Table I are plotted in Fig. 7 along with the theoretical curves of Marshall and Guth,[7] calculated for an exponential shape potential and for a Hulthèn potential, their results being essentially the same as those of Schiff.[8] Their calculations take only the nucleon electric dipole and quadrupole transitions into account and ignore the transitions which involve meson effects. It is seen that the experimental cross sections are much higher than such theoretical predictions, indicating a sizeable contribution from mesonic processes. These high experimental values are in fair agreement with the results obtained by Kikuchi,[13] who investigated the photodissociation of the deuteron at high energies using nuclear emulsions. The data obtained at 140 Mev do not agree too well with that obtained by Benedict and

TABLE I. Total cross section for photodissociation of the deuteron without meson production.

| Photon energy, Mev (center of mass) | Total cross section $cm^2$ |
|---|---|
| 140 | $(11.8\pm4.1)\times10^{-29}$ |
| 200 | $(10.0\pm3.0)\times10^{-29}$ |
| 250 | $(15.9\pm6.4)\times10^{-29}$ |

[13] S. Kikuchi, Phys. Rev. **85**, 1062 (1952).

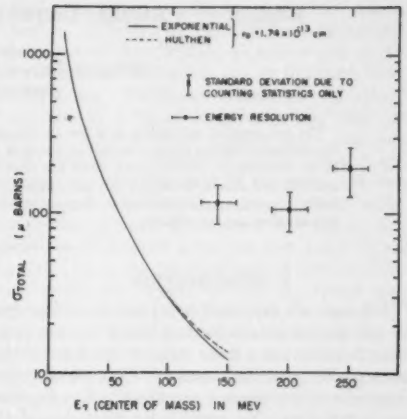


FIG. 7. Total cross sections for photodissociation (without meson production) of the deuteron.

Woodward,[14] who measured $d\sigma/d\Omega$ for deuteron dissociation at 60°, 90°, and 120° in the laboratory frame up to about 160 Mev. Our values at 60° and 90° are about a factor of three higher at 140 Mev.

*Note added in proof*: R. M. Littauer—private communication: Keck and Littauer have measured these cross sections in the same energy region and generally find them to be about half those reported here.

Preliminary calculations by Huddlestone and Lepore[15] using a pseudoscalar theory show that the meson exchange contributions to the disintegration process can be large enough to explain these experimental data. Recently Austern[16] has made some preliminary calculations of deuteron photodissociation using a nucleon isobar model, and his results are in rough agreement with our values for total cross section.

One can conclude that the cross section for deuteron photodisintegration at high energies (140 Mev and above) is much larger than predicted by theories ignoring mesonic interactions. These data combined with those of Kikuchi[13] strongly indicate that above the threshold for meson production the cross section actually increases with energy.

The authors are indebted to Professor A. C. Helmholz for his continued guidance and encouragement throughout this investigation. They wish to thank Mr. George McFarland and the crew of the Berkeley synchrotron for their cooperation in making the bombardments. Thanks are due Dr. R. S. White for the use of the high pressure deuterium gas target system and Mr. John Barale for invaluable assistance with the electronics employed.

[14] T. S. Benedict and W. M. Woodward, Phys. Rev. **85**, 924 (1952).
[15] R. Huddlestone and J. Lepore, Phys. Rev. **87**, 207 (1952).
[16] N. Austern, Phys. Rev. **87**, 208 (1952).

# Explicit $\gamma-\gamma$ Angular Correlations. II. Polarization Correlations

STUART P. LLOYD*
*Institute for Advanced Study, Princeton, New Jersey*
(Received July 30, 1952)

The $\gamma$-$\gamma$ angular correlation function for the case where one or both of the $\gamma$-ray detectors is able to discriminate between plane polarization states of a $\gamma$-ray is given in terms of the corresponding $\gamma$-$\gamma$ directional correlation. The formulas given are directly applicable to one-three type correlations in a triple cascade, and also to direction-plane polarization correlations in which the unpolarized particle is not necessarily a $\gamma$-ray, e.g., $\beta$-polarized $\gamma$. Correlations for the case where the detectors are sensitive to circular polarizations are not treated.

## 1. INTRODUCTION

THE methods explained in a previous article[1] give the angular correlation function of two successive nuclear radiations as a finite series in the three-dimensional rotation group functions $d^{(\lambda)}(\theta)_{\mu'\mu}$, which reduce to Legendre polynomials $P_\lambda(\cos\theta)=d^{(\lambda)}(\theta)_{0,0}$ in directional correlations. One possible interpretation of the correlation formula so obtained is to say that one is using two different coordinate systems with which to describe the detectors of the successive radiations and that each detector lies on its own $z$-axis (the source is at the common origin of the two coordinate systems); the $d^{(\lambda)}(\theta)_{\mu'\mu}$ appear then in the correlation formula when one makes use of the linear relations that hold between sets of nuclear states quantized with respect to the two different coordinate systems. In addition to the simplicity gained by needing only matrix elements for emission of the radiations along the quantization axis, one finds other deep simplicities in the structure of the coefficients of the $d^{(\lambda)}(\theta)_{\mu'\mu}$ in such an expansion of the correlation. One of these, the breaking up of the coefficients into independent factors for the separate transitions of the cascade, has already been brought out in (Ia). In the following another property of the coefficients is made use of: the coefficients break up into a nuclear factor (involving spins and multipole amplitudes) and a polarization factor depending only on the multipole orders and parities of the $\gamma$-rays.[2,3] The situation is probably best made clear by offering for inspection Eq. (2), below, for plane polarization-plane polarization $\gamma$-$\gamma$ correlations.

It does not seem that circular-circular $\gamma$-$\gamma$ polarization correlations† can be obtained from considerations as easy as those of Sec. II, and we postpone detailed examination of the circular-circular case until a practical "quarter-wave plate for $\gamma$-rays," or some such device, has been developed.

## 2. POLARIZATION CORRELATIONS

### (a) $\gamma$-Ray Detectors

We suppose that a $\gamma$-ray detector, besides establishing the direction from source to detector as the direction of the $\gamma$-ray, establishes also a detector reference plane, or, for short, a *detector plane*, containing the direction of the $\gamma$-ray, which has the property that the number of counts per plane polarized $\gamma$-ray traversing the detector is $\epsilon+\rho\cos2\chi$, where $\chi$ is the angle the electric vector of the $\gamma$-ray makes with the "detector plane." Clearly, $\epsilon$, $(\geq0)$, is the efficiency of the detector averaged over plane polarizations and $|\rho/\epsilon|$, $(\leq1)$, is a measure of the ability of the detector to sense the direction of polarization in a plane polarized beam.[4] These efficiencies are functions of the $\gamma$-ray energy.

The response of the detector to a beam of $\gamma$-rays for which the vector potential is, say, $\mathbf{A}=\mathbf{a}\exp(-ikz+ikct)+$c.c. will in general have the form: (counting rate) $\doteq\mathbf{a}^*\cdot R\cdot\mathbf{a}$ where $R=R_s^*$ is a plane hermitian dyadic. A canonical form (with respect to real rotations in the $x$, $y$-plane) for such an $R$ is:

$$R=\epsilon(\mathbf{ii}+\mathbf{jj})+\rho(\mathbf{ii}-\mathbf{jj})+i\sigma(\mathbf{ij}-\mathbf{ji}).$$

Here, $\mathbf{i}$ and $\mathbf{j}$ are unit vectors along the $x$ and $y$ axes, respectively, and $\epsilon$, $\rho$, and $\sigma$ are all real. The $\sigma$-term in this expression for $\mathbf{R}$ is invariant under real rotations in the $x$, $y$-plane, and, just as $|\rho/\epsilon|$ measures the sensitivity of the detector to plane polarizations, the independent coefficient $|\sigma/\epsilon|$, $(\leq1)$, measures the sensitivity of the detector to circular polarizations. It is assumed in the following that $\sigma=0$. If $\sigma\neq0$ were the case one would have to go back and calculate the angular correlation with the quantum field quantized according to "normal modes" of the detector; i.e., setting $\rho=\tau\cos2\upsilon$, $\sigma=\tau\sin2\upsilon$, one would use the two elliptical polarization states: $\mathbf{e}_1=\mathbf{i}\cos\upsilon+i\mathbf{j}\sin\upsilon$, $\mathbf{e}_2=i\mathbf{i}\sin\upsilon+\mathbf{j}\cos\upsilon$, $(\mathbf{e}_1^*\cdot\mathbf{e}_1=\mathbf{e}_2^*\cdot\mathbf{e}_2=1$, $\mathbf{e}_1^*\cdot\mathbf{e}_2=0)$, as the (complex) independent polarization states of a $z$-axis quantum. (There is a different set of $\mathbf{e}$'s for each detector, of course.) In terms of these the response dyadic $R$ of the detector is again diagonal: $R=\epsilon(\mathbf{e}_1^*\mathbf{e}_1+\mathbf{e}_2^*\mathbf{e}_2)+\tau(\mathbf{e}_1^*\mathbf{e}_1-\mathbf{e}_2^*\mathbf{e}_2)$, so that one needs only probabilities (and not amplitudes) for emission into the independent states $\mathbf{e}_1$ and $\mathbf{e}_2$.

In the angular correlation, allowing $\sigma\neq0$ would bring in terms

* Now at Bell Telephone Laboratories, Murray Hill, New Jersey.

[1] S. P. Lloyd, Phys. Rev. **85**, 904 (1952), referred to hereafter as (Ia). The notation of the present article is mostly that of (Ia).

[2] See G. Racah, Phys. Rev. **84**, 910 (1951).

[3] This is not quite true for $\beta$-decay, where one can have several distinct interfering "multipoles" of the same angular momentum and parity in a given transition. The notation and results of (Ia) can be modified easily to cover the $\beta$-ray case. The formulas for correlations measured with $\beta$-polarimeters will be rather more complicated than the ones given in the following for $\gamma$-polarimeters. The author has not investigated the point in detail. See D. L. Falkoff and G. E. Uhlenbeck, Phys. Rev. **79**, 334 (1950) for detailed discussion of $\beta$-ray directional correlations; also, M. Fuchs, thesis, University of Michigan, 1951 (unpublished).

† There are no direction—circular or plane—circular correlations.

[4] See M. Deutsch and F. Metzger, Phys. Rev. **74**, 1542 (1948), Fig. 1. If the detector plane is taken to be the plane through crystals $A$ and $B$ of the polarimeter, the parameter $\rho$ is negative, i.e., $\rho/\epsilon=-(D-1)/(D+1)$ in terms of the parameter $D$ of Deutsch and Metzger. For their $D=2.1$, $\rho/\epsilon=-0.35$.

involving the $d^{(\lambda)}(\theta)_{\mu'\mu}$ for which the index $\lambda$ is odd[3]; in particular, odd Legendre polynomials in circular—circular polarization correlations. In the plane polarization correlations of the present article, the pure multipole $\lambda$=odd terms vanish identically, and the multipole mixture $\lambda$=odd terms vanish as a result of the reality property of the multipole scalar amplitudes.

### (b) Polarization-polarization Correlations

Let the directional correlation between the $\gamma$-rays emitted in the nuclear cascade $J_1(\gamma)J(\gamma)J_2$ be written as

$$W(\theta)=1+\sum_{L_1\le L_1'}\sum_{L_2\le L_2'}\times\sum_\lambda A_\lambda(L_1L_1';L_2L_2')P_\lambda(\cos\theta). \quad (1)$$

The coefficients $A_\lambda(L_1L_1';L_2L_2')$, where $L_1$ and $L_1'$ are the orders of the interfering multipoles in the $J_1(\gamma)J$ transition and $L_2$ and $L_2'$ those for $J(\gamma)J_2$, have been given in some detail in (Ia),‡ and tabulations of the lowest multipole coefficients are to be found in (I).[5] The coefficients $A_\lambda(L_1L_1';L_2L_2')$ of Eq. (1) depend also on nuclear angular momenta, and contain as factors the appropriate scalar relative amplitudes $(J_f\|L_1\|J_i)$ for $2^L$-pole multipole emission, which are defined in (Ia).

When the plane polarization-dependent correlation is worked out from Eqs. (8), (13), and (29) of (Ia) the advantages of the $d^{(\lambda)}(\theta)_{\mu'\mu}$ expansion are apparent: the polarization correlation can be obtained from the corresponding directional correlation by replacing $P_\lambda(\mathbf{\Omega}_1\cdot\mathbf{\Omega}_2)$ by a function $f_\lambda(L_1L_1',L_2L_2';\mathbf{\Omega}_1\mathbf{e}_1,\mathbf{\Omega}_2\mathbf{e}_2)$ which is independent of nuclear spins and nuclear matrix elements. Instead of giving these functions explicitly, we give the result of combining the correlation function $W(\mathbf{\Omega}_1,\mathbf{e}_1;\mathbf{\Omega}_2,\mathbf{e}_2)$ so obtained with the appropriate detector efficiencies. Let $\epsilon_{a1}$, $\rho_{a1}$ be the efficiencies of detector $a$ for the first $\gamma$-ray $J_1(\gamma)J$ of $J_1(\gamma)J(\gamma)J_2$, $\epsilon_{b1}$, $\rho_{b1}$ the efficiencies of detector $b$ for the same $\gamma$-ray, etc. Angles $\varphi_a$ and $\varphi_b$, which are the inclinations of the respective detector planes to the ($a$, $b$, source) plane, are both positive when measured counterclockwise, looking toward the source. The function $N(\theta;\varphi_a,\varphi_b)$, the theoretical mean coincidence rate in counters $a$ and $b$ due to correlations between successive $\gamma$-rays, works out after straightforward calculation to be, apart from normalization factors:

$$N(\theta;\varphi_a,\varphi_b)=1+\sum_{L_1\le L_1'}\sum_{L_2\le L_2'}\sum_\lambda A_\lambda(L_1L_1';L_2L_2')\Big\{P_\lambda(\mu)+\frac{(\lambda-2)!}{(\lambda+2)!}[\epsilon^{-1}(\rho_{a1}\epsilon_{b2}K_\lambda(L_1L_1')$$
$$+\rho_{a2}\epsilon_{b1}K_\lambda(L_2L_2'))P_\lambda^2(\mu)\cos2\varphi_a+\epsilon^{-1}(\rho_{b1}\epsilon_{a2}K_\lambda(L_1L_1')+\rho_{b2}\epsilon_{a1}K_\lambda(L_2L_2'))P_\lambda^2(\mu)\cos2\varphi_b$$
$$+\epsilon^{-1}(\rho_{a1}\rho_{b2}+\rho_{a2}K_\lambda\rho_{b1})(L_1L_1')K_\lambda(L_2L_2')\{\tfrac{1}{2}d_\lambda(-\mu)\cos2(\varphi_a-\varphi_b)+\tfrac{1}{2}d_\lambda(\mu)\cos2(\varphi_a+\varphi_b)\}]\Big\}, \quad (2)$$

where $\epsilon=\epsilon_{a1}\epsilon_{b2}+\epsilon_{b1}\epsilon_{a2}$. Also, $P_\lambda^2(\mu)$ are unnormalized associated Legendre functions (with $\mu=\cos\theta$):

$$P_\lambda^2(\mu)=(1-\mu^2)\frac{d^2}{d\mu^2}P_\lambda(\mu)=\left[\frac{(\lambda+2)!}{(\lambda-2)!}\right]^{\frac{1}{2}}d^{(\lambda)}(\theta)_{2,0}, \quad (\lambda\ge2), \quad (3)$$

and $d_\lambda(\mu)$ is an abbreviation for

$$d_\lambda(\mu)=d^{(\lambda)}(\theta)_{2,-2}=d^{(\lambda)}(\pi-\theta)_{2,2}$$
$$=\sum_{\kappa=0}^{\lambda-2}\frac{(-1)^\kappa(1-\mu)^{\kappa+2}(1+\mu)^{\lambda-\kappa-2}}{\kappa!(\kappa+4)!((\lambda-2-\kappa)!)^2}\cdot\frac{(\lambda-2)!(\lambda+2)!}{2^\lambda}. \quad (4)$$

The coefficients $K_\lambda(LL')$ are explicitly:

$$K_\lambda(LL')=s(LL')k_\lambda(LL'),$$

with

$$s(LL')=1 \quad \text{for} \quad \text{el } L, \text{ el or mag } L',$$
$$s(LL')=-1 \quad \text{for mag } L, \text{ el or mag } L', \quad (5)$$

and (with $\lambda$=even)

$$k_\lambda(LL')=-\left[\frac{(\lambda+2)!}{(\lambda-2)!}\right]^{\frac{1}{2}}\frac{(LL'11|LL'\lambda2)}{(LL'-11|LL'\lambda0)}$$
$$=L'(L'+1)-L(L+1) \quad \text{when} \quad L+L'=\text{odd},$$
$$=\frac{\lambda(\lambda+1)[L(L+1)+L'(L'+1)]-[L'(L'+1)-L(L+1)]^2}{L(L+1)+L'(L'+1)-\lambda(\lambda+1)} \quad \text{when} \quad L+L'=\text{even}. \quad (6)$$

The original $W(\mathbf{\Omega}_1\mathbf{e}_1,\mathbf{\Omega}_2\mathbf{e}_2)$ from which Eq. (2) was obtained can be recovered by setting $\epsilon_{a1}=\epsilon_{b2}=\rho_{a1}=\rho_{b1}=1$, $\epsilon_{a2}=\epsilon_{b1}=\rho_{a2}=\rho_{b1}=0$, and then putting $\varphi_a=\varphi_1$, $\varphi_b=\varphi_2$. One has then $N(\theta;\varphi_1,\varphi_2)=W(\mathbf{\Omega}_1\mathbf{e}_1,\mathbf{\Omega}_2\mathbf{e}_2)$, where $\varphi_1$ and $\varphi_2$ are the angles the electric vectors $\mathbf{e}_1$ and $\mathbf{e}_2$ of the successive quanta make with the plane containing directions $\mathbf{\Omega}_1$ and $\mathbf{\Omega}_2$ of the quanta, and where $\mu=\cos\theta=\mathbf{\Omega}_1\cdot\mathbf{\Omega}_2$.

### (c) Direction-Polarization Correlations

Evidently, direction-polarization correlations can be obtained from Eq. (2) by setting the appropriate detector efficiencies equal to zero. For example, if detector $b$ is not a polarimeter one puts $\rho_{b1}=\rho_{b2}=0$, leaving only the polarization terms involving $\cos2\varphi_a$.

‡ There is an obvious misprint (due to ms error) in the expression for $a_\lambda(LL')$, Eq. (23) of (Ia): the first factorial in the denominator which now reads $(\frac{1}{2}(\lambda+L+L'))!$ should read $(\frac{1}{2}(\lambda+L-L'))!$.

[5] S. P. Lloyd, Phys. Rev. **83**, 716 (1952). The coefficients in the multipole mixture terms should have signs opposite to those given in (I), as explained in footnote (22) of (Ia).

TABLE I. $P_\lambda^2(\mu)$. The $P_\lambda^2(\mu)$ are even in $\mu$: $P_\lambda^2(-\mu)=P_\lambda^2(\mu)$.

| $\mu$ | $P_2^2(\mu)$ | $P_4^2(\mu)$ | $P_6^2(\mu)$ |
|---|---|---|---|
| 0.0 | 3.00 | −7.500 | 13.125 |
| 0.1 | 2.97 | −6.905 | 10.698 |
| 0.2 | 2.88 | −5.184 | + 4.193 |
| 0.3 | 2.73 | −2.525 | − 4.213 |
| 0.4 | 2.52 | +0.756 | −11.413 |
| 0.5 | 2.25 | 4.219 | −14.150 |
| 0.6 | 1.92 | 7.296 | −10.107 |
| 0.7 | 1.53 | 9.295 | + 0.691 |
| 0.8 | 1.08 | 9.396 | 14.160 |
| 0.9 | 0.57 | 6.655 | 20.128 |
| 1.0 | 0 | 0 | 0 |

Furthermore one sees from the derivation that Eq. (2) gives direction-polarization correlations whatever the unpolarized radiation. Thus the $\beta$-(plane polarized $\gamma$) correlation for $J_1(\beta)J(\gamma)J_2$ is obtained from Eq. (2) as follows: (1) For the coefficients $A_\lambda(L_1L_1';\ L_2L_2')$ in Eq. (2) use the coefficients of the $J_1(\beta)J(\gamma)J_2$ directional correlation, which are assumed to be known; (2) if detector $a$ is the $\beta$-counter, put $\rho_{a1}=\rho_{a2}=0$, corresponding to the fact that the $\beta$-counter is not sensitive to polarizations in either the $\beta$-ray or the $\gamma$-ray beam; (3) put $\rho_{b1}=0$, since the $\gamma$-polarimeter is not supposed to measure polarization in the $\beta$-ray beam.§ If the $\gamma$-counter is shielded against $\beta$-rays, so that also $\epsilon_{b1}=0$, the efficiency $\epsilon_{a1}$ of the $\beta$-counter drops out of the correlation, leaving $\rho_{b2}/\epsilon_{b2}$ as the only parameter needed for $\gamma$-polarimeter $b$.

One can also use Eq. (2) as it stands for one-three polarization correlations in triple cascades;[6] one requires only that the coefficient of $P_\lambda(\mu)$ in the corresponding directional correlation be broken up into a sum of contributions from each interfering multipole pair $L$, $L'$ in each transition. Specialized forms of Eq. (2) have been given by Falkoff,[7] Hamilton,[8] and Zinnes.[9]

TABLE II. $d_\lambda(\mu)=d^{(\lambda)}(\cos^{-1}\mu)_{2,-2}$.

| $\mu$ | $d_2(\mu)$ | $d_4(\mu)$ | $d_6(\mu)$ |
|---|---|---|---|
| −1.0 | 1.0000 | 1.0000 | +1.0000 |
| −0.9 | 0.9025 | +0.3339 | −0.1845 |
| −0.8 | 0.8100 | −0.0972 | −0.4135 |
| −0.7 | 0.7225 | −0.3396 | −0.2188 |
| −0.6 | 0.6400 | −0.4352 | +0.0717 |
| −0.5 | 0.5625 | −0.4219 | 0.2791 |
| −0.4 | 0.4900 | −0.3332 | 0.3379 |
| −0.3 | 0.4225 | −0.1986 | 0.2559 |
| −0.2 | 0.3600 | −0.0432 | +0.0835 |
| −0.1 | 0.3025 | +0.1119 | −0.1117 |
| 0.0 | 0.2500 | 0.2500 | −0.2656 |
| +0.1 | 0.2025 | 0.3584 | −0.3315 |
| 0.2 | 0.1600 | 0.4288 | −0.2893 |
| 0.3 | 0.1225 | 0.4569 | −0.1491 |
| 0.4 | 0.0900 | 0.4428 | +0.0513 |
| 0.5 | 0.0625 | 0.3906 | 0.2537 |
| 0.6 | 0.0400 | 0.3088 | 0.3933 |
| 0.7 | 0.0225 | 0.2099 | 0.4173 |
| 0.8 | 0.0100 | 0.1108 | 0.3093 |
| 0.9 | 0.0025 | 0.0324 | 0.1195 |
| 1.0 | 0 | 0 | 0 |

§ Correlations involving electron polarimeters would bring in $\cos\varphi$ instead of $\cos2\varphi$, anyway.

[6] Biedenharn, Arfken, and Rose, Phys. Rev. **83**, 586 (1951).

## 3. TABLES

### (a) Power Series and Legendre Series

If

$$A_0+A_2P_2(\cos\theta)+A_4P_4(\cos\theta)+A_6P_6(\cos\theta)+A_8P_8(\cos\theta)$$
$$=Q+R\cos^2\theta+S\cos^4\theta+T\cos^6\theta+U\cos^8\theta,$$

then

$$A_0=Q+(1/3)R+(1/5)S+(1/7)T+(1/9)U$$
$$A_2=(2/3)R+(4/7)S+(10/21)T+(40/99)U$$
$$A_4=(8/35)S+(24/77)T+(48/143)U$$
$$A_6=(16/231)T+(64/495)U$$
$$A_8=(128/6435)U$$

and

$$Q=A_0-(1/2)A_2+(3/8)A_4-(5/16)A_6+(35/128)A_8$$
$$R=(3/2)A_2-(30/8)A_4+(105/16)A_6-(1260/128)A_8$$
$$S=(35/8)A_4-(315/16)A_6+(6930/128)A_8$$
$$T=(231/16)A_6-(12012/128)A_8$$
$$U=(6435/128)A_8.$$

TABLE III. The $k_\lambda(LL)$.

| $\lambda$ \ $L$ | 1 | 2 | 3 | 4 | 5 |
|---|---|---|---|---|---|
| 2 | −12 | 12 | 8 | 120/17 | 30/3 |
| 4 | — | −30 | 120 | 40 | 30 |
| 6 | — | — | −56 | −840 | 140 |

### (b) The Angular Functions

The first few of the functions of Eqs. (3) and (4) are given in Tables I and II. They are explicitly:

$$P_2^2(\mu)=3(1-\mu^2)$$
$$P_4^2(\mu)=(15/2)(1-\mu^2)(7\mu^2-1)$$
$$P_6^2(\mu)=(105/8)(1-\mu^2)(33\mu^4-18\mu^2+1)$$

and

$$d_2(\mu)=(1/4)(1-\mu)^2$$
$$d_4(\mu)=(1/4)(1-\mu)^2(7\mu^2+7\mu+1)$$
$$d_6(\mu)=(1/64)(1-\mu)^2(495\mu^4+660\mu^3+90\mu^2-108\mu-17).$$

### (c) The Coefficients $k_\lambda(LL')$

The multipole mixture coefficients for the usual case $L'=L+1$ are $k_\lambda(L\,L+1)=2(L+1)$; the pure multipole coefficients for correlation up to $P_6(\cos\theta)$ and $L'=L\leq5$ are given in Table III.

The author would like to express his gratitude to The Institute for Advanced Study for a grant-in-aid, and to its director, Professor Robert Oppenheimer, for hospitality extended to him during his stay at The Institute.

[7] D. L. Falkoff, Phys. Rev. **73**, 518 (1948).

[8] D. R. Hamilton, Phys. Rev. **74**, 782 (1948).

[9] I. Zinnes, Phys. Rev. **80**, 386 (1950).

# Ferromagnetism at Very High Frequencies. IV. Temperature Dependence of the Magnetic Spectrum of a Ferrite*

G. T. Rado, R. W. Wright, W. H. Emerson, and A. Terris
*Naval Research Laboratory, Washington, D. C.*

(Received July 16, 1952)

The magnetic spectrum of a sintered ferrite, previously studied by the authors at room temperature and found to contain an rf resonance, attributed to domain wall displacements, and a microwave resonance, attributed to domain rotations, has now been observed at 77°K, 195°K, and 411°K. By using single-domain particles of this material embedded in wax, the rotational resonance was observed separately. The principal aspect of the experimental results is the fact that with increasing temperature the resonance frequencies decrease, the fractional change being about the same in all three cases and exceeding that of the saturation magnetization. A semiquantitative theoretical interpretation of this fact is given. Auxiliary experiments, performed as an aid in interpreting the magnetic spectrum, include measurements of the spectroscopic splitting factor $g$ at various temperatures. The deviation of the apparent $g$ factor values from $g=2$, as well as their temperature dependence, was found to decrease with increasing resonance field, i.e., increasing resonance frequency.

## 1. INTRODUCTION

IN a previous paper[1] of this series it was shown that the magnetic spectrum[2] of a certain ferrite contains two resonances at room temperature. The corresponding dispersion mechanisms were identified by comparing, in the region between zero and 10,000 Mc/sec, the magnetic spectrum of solid samples with that of single-domain particles made from the same sintered material. It was concluded that one of the resonances is due to the Larmor precession of domains in the internal magnetic field, a mechanism previously invoked by Snoek[3] and others[4] in interpreting[5] the single resonance (or relaxation) found by them in various substances at rf or microwave frequencies. The other resonance, however, had not been observed previously. We showed it to be due to oscillations of domain walls and thus obtained experimental support for the concept of domain wall inertia. This inertia had been calculated by Döring,[6] and a generalized treatment was given by Rado.[7]

In the present paper we report on an extension of our work to temperatures other than room temperature. We begin with the measurements of the temperature dependence of the magnetic spectrum in solid samples and single-domain particles (Sec. 2A) and then describe some auxiliary experiments on the temperature dependence of the $g$ factor (Sec. 2B) and the saturation magnetization and coercive force (Sec. 2C). These auxiliary experiments are limited in scope since they were designed primarily to aid in the interpretation of the magnetic spectrum. Nevertheless, the $g$ factor work is of independent interest because it casts doubt on the validity of some previous measurements made on polycrystalline materials. In Sec. 3 we attempt a theoretical interpretation of the magnetic spectrum. While the polycrystalline nature of our samples makes it extremely difficult to give a quantitative treatment of the problem, it will be shown that the principal aspects of the temperature dependence can be explained in a semiquantitative manner.

The same magnetic samples were used in the present work as in paper III. They consist of a commercial ferrite, "ferramic $A$," which is composed of several oxides but is primarily magnesium ferrite. The precise chemical composition of the samples is not important for our purposes because our conclusions are based on comparisons of various magnetic properties measured on the same material. It should be noted, furthermore, that the two resonances which we observed at room temperature are not a unique property of ferramic $A$. We have found similar effects in pure magnesium ferrite, lithium ferrite $[(Li_{0.5}Fe_{0.5})Fe_2O_4]$, and nickel ferrite prepared at this laboratory. The investigations on these and other materials will be reported at a later date.

## 2. EXPERIMENTAL METHODS AND RESULTS

### A. Magnetic Spectrum

The methods described in paper III have been adapted to measure the complex permeability, $\mu=\mu_1-i\mu_2$, as a function of frequency as well as temperature. As in the room temperature experiments, no static magnetic field was used, and precautions were taken to ensure that (1) the alternating field was sufficiently

* A preliminary account was given at the New York meeting of the American Physical Society, January 31, 1952 [Phys. Rev. **86**, 599 (1952)].

[1] Rado, Wright, and Emerson, Phys. Rev. **80**, 273 (1950), referred to as III.

[2] The term "magnetic spectrum" is used throughout the present paper to denote the frequency dependence of the complex *initial* permeability.

[3] J. L. Snoek, Physica **14**, 207 (1948); Nature **160**, 90 (1947); H. G. Beljers and J. L. Snoek, Philips Tech. Rev. **11**, 313 (1949).

[4] J. B. Birks, Proc. Phys. Soc. (London) **B63**, 65 (1950); Brockman, Dowling, and Steneck, Phys. Rev. **77**, 85 (1950); Welch, Nicks, Fairweather, and Roberts, Phys. Rev. **77**, 403 (1950).

[5] A discussion of the interpretations proposed in references 3 and 4 is given in references 1 and 10.

[6] W. Döring, Z. Naturforsch. **3a**, 374 (1948). For a simplified calculation, see R. Becker, J. phys. et radium **12**, 332 (1951); C. Kittel, Phys. Rev. **80**, 918 (1950).

[7] G. T. Rado, Phys. Rev. **83**, 821 (1951).

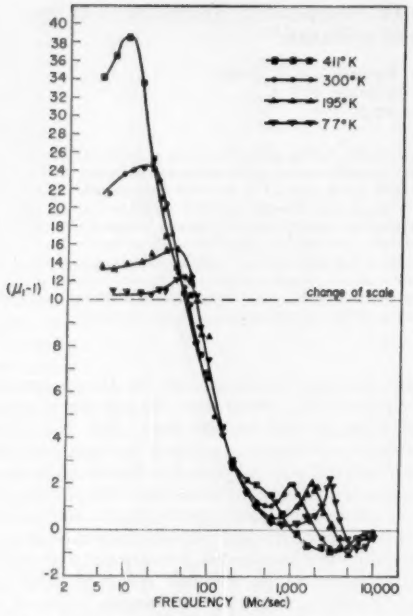


FIG. 1. $\mu_1-1$ *versus* frequency for solid ferramic $A$ at various temperatures.

small to justify referring to $\mu$ as the *initial* permeability,[8] (2) dimensional effects were excluded (thin sample method), and (3) the effect of wave-guide types of modes (i.e., other than TEM) was negligible. The measured permeabilities represent, of course, average values of a position-dependent permeability, so that from this point of view there is no essential distinction between the high frequency case and the static case, as long as the variations in local properties caused by the domain structure of the (macroscopically isotropic) samples are on a scale which is small compared to $\lambda$, the wavelength in the material. This requirement is clearly fulfilled in our case because the thickness of each sample is small compared to $\lambda$.

The apparatus was modified for the low temperature measurements by surrounding the end of the coaxial line containing the sample with a cylindrical jacket and filling the latter with liquid air or a mixture of solid $CO_2$ and alcohol. Measurements with a thermocouple attached to either side of the sample showed that the temperature did not exceed that of the fixed points by more than 3°C. During the actual rf measurements, however, the thermocouple was attached only to the side of the sample that was backed by a short. To avoid dielectric effects due to water droplets, we inserted a very thin Teflon window into the line at some distance from the sample and forced helium through this section of line. Tests showed that reflections from the window and other disturbances were negligible. The high temperature data were taken by inserting the end of the line into a furnace.

As noted in paper III, the formulas that were used for evaluating $\mu_1$ and $\mu_2$ are based on the assumption that the ohmic losses in the line are negligible. However, under the "thin-sample conditions" previously stated, the line losses may be taken into account by replacing Eq. (III-2) by

$$\mu_2=\left(\frac{1}{\xi}-\frac{1}{\xi'}\right)\frac{1}{k_0L}. \tag{1}$$

In deriving this equation we assumed that the measurements are confined to the first few standing wave minima near the sample, a requirement that ensures that the line losses may be regarded as a small perturbation. As before, $L$ is the sample thickness, $k_0$ the wave number in free space, and $\xi$ the voltage standing wave ratio (VSWR). The quantity $\xi'$ is the VSWR of the empty line and represents the effect of line losses. This correction has been applied to all our results, including those of paper III. It can be shown that the expression for $\mu_1$ [Eq. (III-1)] is not affected by small

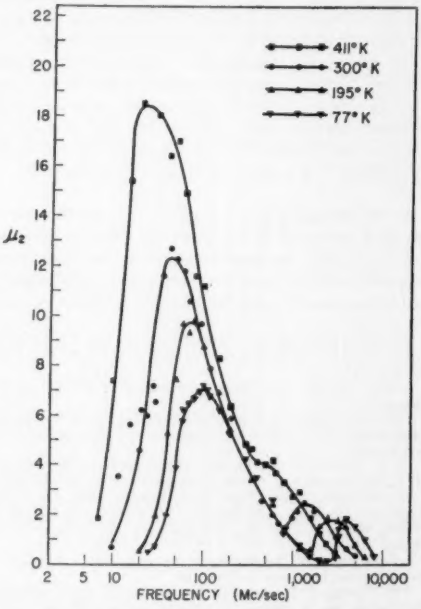


FIG. 2. $\mu_2$ *versus* frequency for solid ferramic $A$ at various temperatures.

[8] For nonlinear effects in a ferrite, see J. J. Went and H. P. J. Wijn, Phys. Rev. **82**, 269 (1951); Physica **17**, 976 (1951). See also the comments in reference 19.

line losses because the shift of the standing wave minimum is measured relative to an empty line characterized by the same ohmic losses as the line containing the sample.

The measured magnetic spectrum of the solid samples is shown in Figs. 1 and 2 for various temperatures, the two sets of curves representing $\mu_1-1$ and $\mu_2$, respectively, as a function of frequency. It is seen that two resonances were observed at each of the four temperatures (77°K, 195°K, 300°K, 411°K) used in the experiments and that at the highest temperature the two resonances begin to merge.[9] As stated in paper III, we attribute the rf resonance (occurring at 43 Mc/sec at 300°K) to domain walls and the microwave resonance (occurring at 1400 Mc/sec at 300°K) to domain rotations. The corresponding mean resonance frequencies, which we take to be the positions of the peaks of the $\mu_2$ curve, will again be denoted by $\omega_0''$ and $\omega_0'$, respectively. Both of these frequencies are seen to decrease by a factor of about five as the temperature is increased in the range stated. This fact appears to be one of the principal aspects of the experimental results, and the appropriate numerical data will be given later (Sec. 3) in tabulated form. Another interesting aspect of the results is that the total static initial permeability (which is primarily due to domain walls) varies much more with temperature than the contribution of the rotations. It may also be noted that $\mu$ is almost independent of temperature (in the range stated) at frequencies around 200 Mc/sec, a fact which may be of some practical interest.

Finally, we note that Figs. 1 and 2 do not contain any data for frequencies less than about 5 Mc/sec, even though some measurements (in addition to those

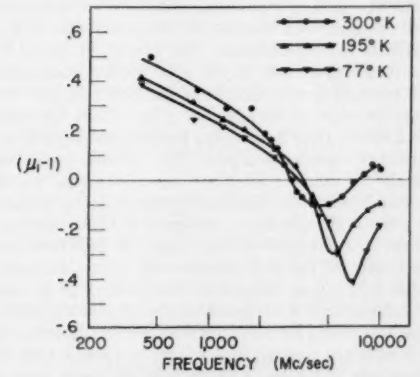


FIG. 3. $\mu_1-1$ *versus* frequency for 70 percent (by weight) mixture of ferramic *A* powder and wax at various temperatures.

[9] It will be shown in a later publication that this effect may be related to the apparent coalescence, at room temperature, of the two resonances in ferrites containing zinc. See G. T. Rado, Revs. Modern Phys. (scheduled for January, 1953, issue).

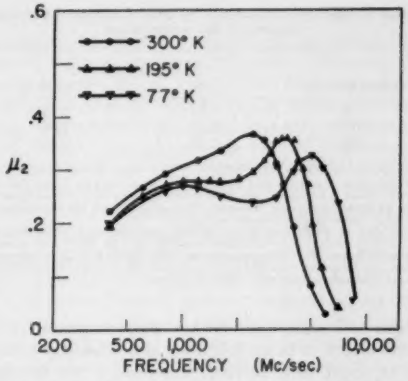


FIG. 4. $\mu_2$ *versus* frequency for 70 percent (by weight) mixture of ferramic *A* powder and wax at various temperatures.

reported in paper III) were made in this range. This omission is due to the fact that in this range of relatively low frequencies the permeability appears to depend on the thermal history of the material in an unexpected manner. Thus, the value of $\mu_1-1$ at 1000 cps, which is essentially the static value, was measured to be 18.6, 12.6, and 9.8 at temperatures of 300°K, 195°K, and 77°K, respectively; these values agree satisfactorily with those obtained by extrapolating the curves of Fig. 1 to very low frequencies. However, after the material was allowed to reach room temperature again, the remeasured values of $\mu_1$ at 300°K and 77°K were found to be about 40 percent higher than the original values, and only small changes were observed when the temperature was recycled. It appears that this effect is caused in some way by the exposure of the material to very low temperatures, because in an interval of 18 months we did not detect any changes in the 1000-cps permeability of samples that had been kept at room temperature. Although a more detailed investigation of this effect might prove interesting, it can be stated that we did not find evidence of this effect at the frequencies ($\gtrsim$5 Mc/sec) included in the graphs of Figs. 1 and 2.

The measured magnetic spectrum of the samples containing a mixture of small particles of ferramic *A* (70 percent by weight) and wax is shown in Figs. 3 and 4 for various temperatures, the two sets of curves representing $\mu_1-1$ and $\mu_2$, respectively, as a function of frequency. The particles are essentially single domains, as shown in paper III. Data are given for frequencies above 200 Mc/sec only, and the single resonance observed at each temperature is attributed to domain rotations. The absence of the rf resonance in these samples, as demonstrated by the room temperature studies, has been the main reason for our conclusion that the rf resonance observed in the solid samples

TABLE I. Apparent $g$ factors for ferramic $A$ measured at variosu frequencies[a] and temperatures.

| Temperature (°K) | Frequency (Mc/sec) 9200 | 24,000 |
|---|---|---|
| 77 | 2.67 | 2.14 |
| 195 | 2.48 | 2.06 |
| 300 | 2.26 | 2.01[b] |

[a] Okamura, Torizuka, and Kojima, Sci. Rep. Tohoku Univ. **A2**, 663 (1950), found that the $g$ factor of Ni-ferrite at room temperature increases with increasing frequency. However, their samples were not saturated and the sphere sizes may have been too large.

[b] It may be noted that Yager, Merritt, and Guillaud, Phys. Rev. **81**, 477 (1951), obtained $g=2.03$ and $g=2.06$ for two Mg-ferrite samples having different $M_s$. Their measurements were performed at room temperature, the frequency was 24,164 Mc/sec, and the $g$ values represent estimated extrapolations to zero diameter spheres.

is due to domain walls. At low temperatures, however, there is seen to be an indication of a subsidiary peak in $\mu_2$ at about 1000 Mc/sec; this peak is not spurious, and it may be due to rudimentary walls, impurities, or some unknown causes, but the effect is relatively small and will not be considered further at this time. Returning to the main effect, the mean resonance frequency, to be denoted by $\Omega_0'$, is seen to decrease as the temperature is increased, this behavior being similar to that of $\omega_0''$ and $\omega_0'$. The static value (measured at 1000 cps) of $\mu_1-1$ was measured to be 0.65 at room temperature.

### B. Spectroscopic Splitting Factor

Numerous measurements of the spectroscopic splitting factor $g$ have been reported in the literature, and they have resulted in repeated confirmations of Kittel's formulas for the frequency of ferromagnetic resonance absorption in the presence of a strong magnetic field.[10,11] However, only Healy[12] appears to have studied the dependence of $g$ on temperature in ferrites, and his experiments were limited to a single frequency ($\sim$10,000 Mc/sec). In the present work, we used less elaborate apparatus but measured the temperature dependence of $g$ at three frequencies. Since the techniques involved in resonance experiments are well known, we shall describe but briefly our particular procedure.

The samples were small spheres[13] of ferramic $A$. Four to eight spheres, appropriately separated from each other, were attached to one end plate of a transmission-type, half-wave, rectangular cavity which operated at about 3000, 10,000, or 24,000 Mc/sec and was surrounded by a suitable cooling jacket. The cavity was supplied with microwave energy and situated between the polefaces of an electromagnet (see Sec. 2C) in such a way that the static field was perpendicular to the microwave field as well as to the direction of microwave propagation. A microwave spectrum analyzer was used as the detector at each of the frequencies mentioned. The experiment consisted of measuring the static field at which the cavity transmission was a minimum. For observations involving fields on either side of resonance, small adjustments of the frequency were made in order to prevent the small, but detectable, detuning of the cavity caused by the real part of the effective permeability. The $g$ factor was obtained from Kittel's[14] relation for a sphere, $\omega=\gamma H$, where $\omega$ and $H$ are the values, at resonance, of the circular frequency and static field, respectively, and $\gamma$ is given by $ge/2mc$; the numerical value of $\gamma/2\pi$ is approximately 2.80 Mc/(sec oersted) for $g=2$. It is well known that Kittel's formula applies only in the limiting case where the wavelength in the sample is very large compared to the sphere diameter. Since the relevant electromagnetic problem has never been solved, even to a first approximation,[15] for the case of a reasonably small sphere having an anisotropic permeability and since the samples are, furthermore, inhomogeneous (on account of cavities, etc.), we shall regard the measured $g$ values as *apparent* $g$ factors. To test the importance of the size effect, we measured the apparent $g$ factor at 77°K and 300°K on spheres having various sizes. At 9200 Mc/sec and 300°K, $g$ varied by 2 to 3 percent when the sphere diameter was reduced from 0.080 to 0.010 inches.

The final results, assembled in Table I, were obtained at 77°K, 195°K, and 300°K, using 0.010-inch diameter spheres at frequencies of 9200 and 24,000 Mc/sec. Additional measurements were made at 3000 Mc/sec, but the data could not be interpreted because the material is definitely not saturated at the low resonance field required, and because the frequency falls into a region of natural resonance (see Fig. 2). It should be mentioned that even in the 9200-Mc/sec experiment the material is not completely saturated, so that the large deviation of the apparent $g$ factor from the value $g=2$, as well as its pronounced temperature dependence, cannot be regarded as a basic effect. (Similarly, caution should be used in all other cases involving porous materials before ascribing undue theoretical significance to $g$ factor measurements performed at 10,000 Mc/sec.) There is, in fact, no assurance that our 24,000-Mc/sec data refer to the true $g$ factor, and higher resonance fields (i.e., higher frequencies) might have to be used to achieve a more complete saturation and thus elucidate this point. For our purposes (see Sec. 3), however, it is sufficient to state, on the basis of Table I, that the deviations of the *true* $g$ factor from the value $g=2$, as well as the temperature dependence of $g$, are very small or nonexistent.

[10] For a review of this subject, see C. Kittel, J. phys. et radium **12**, 332 (1951).

[11] This type of resonance is sometimes referred to as "induced" esonance to distinguish it from the "natural" resonances observedr (e.g., in Sec. 2A) in the absence of a static field.

[12] D. W. Healy, Tech. Rept. No. 135 (August 15, 1951), Cruft Laboratory, Harvard University. See also Phys. Rev. **86**, 1009 (1952).

[13] The spheres were made by the method of W. L. Bond, Rev. Sci. Instr. **22**, 344 (1951).

[14] C. Kittel, Phys. Rev. **73**, 155 (1948).

[15] See the remarks of H. B. G. Casimir at the end of Kittel's paper, reference 10.

### C. Saturation Magnetization and Coercive Force

An oscillation magnetometer, similar to that described by Griffiths and MacDonald,[16] was used to measure the saturation magnetization $M_s$ of ferramic $A$ at 77°K, 195°K, and 300°K. The sample is a flat circular cylinder (cut from the material used for making the rings for the rf experiments), having a diameter of 0.917 inch and a thickness of 0.051 inch, and is mounted on a polished glass rod whose moment of inertia is such that the period of oscillation in the fields used (~2000 to 5500 oersteds) ranged from $\frac{1}{4}$ to $\frac{1}{2}$ second. At the low temperatures, the glass rod is arranged to oscillate in a bath of liquid air or a mixture of solid $CO_2$ and ether. Tests in a water bath at room temperature showed that friction effects are negligible in liquids of these viscosities. The period of oscillation is measured by reflecting a light beam from a mirror attached to the glass rod and using a photocell which is connected to a Sanborn low frequency amplifier and recorder. The electromagnet, used also in the $g$ factor work, has a sufficiently uniform field throughout the extent of the large pole pieces (90 square inches in area). A motor-generator set supplies the current, a stability of ±0.05 percent being assured by a Fluke regulator. By using a calibrated flip coil with a ballistic galvanometer, the field *versus* current relation was found to be linear in the range of interest. The reproducibility of the final results is better than ±2 percent, while the absolute error, estimated by measuring $M_s$ for very thin nickel disks, is less than 5 percent and seems to be partially due to the error in measuring the volume of porous samples. It therefore appears that the accuracy of the instrument is comparable to that of Griffiths and MacDonald, the disadvantage of using a liquid bath and porous samples with a relatively small axial ratio (~18) being compensated by the advantage of using the recorder and other improvements. The experimental results, shown in Table II, represent $M_s$ referred to a unit volume of sample, rather than solid material.

Finally, the coercive force $H_c$ of the samples containing a mixture of single-domain particles and wax was measured at 77°K and 300°K by means of a ballistic method. The ratio $(H_c)_{77}/(H_c)_{300}$ was found to be equal to $(M_s)_{77}/(M_s)_{300}$. This indicates that the coercive force of the particles is primarily due to shape anisotropy, an interesting (and somewhat surprising) fact in view of the conclusion (Sec. 3) that the microwave resonance frequency is determined by both crystalline and shape anisotropy in this case.

### 3. THEORETICAL INTERPRETATION

The resonances observed in the magnetic spectrum of the solid samples are undoubtedly composed of many individual resonances whose frequencies might be represented by some kind of distribution function. A calculation of this function appears to be prohibitively complicated and would require considerable information about the size, shape, and position of the crystallites and inclusions in the sample. Similar difficulties (treatment of magnetic interactions, geometry of the particles) would exist in the case of the single-domain particles. It is not yet possible, therefore, to predict the widths and shapes of the absorption "lines," or even the exact magnitude of the mean resonance frequencies, from a (supposed) knowledge of the saturation magnetization, crystalline anisotropy, damping constant, and other basic properties of the material.

As shown in Table II, however, there are two remarkably simple experimental facts concerning the temperature dependence of the mean resonance frequencies in this material. (a) In the range[17] between 77°K and 300°K, the three frequencies $\omega_0''$, $\omega_0'$, and $\Omega_0'$ depend on temperature in approximately the same way. (b) This common temperature dependence is qualitatively similar to, but quantitatively more pronounced than, that of the saturation magnetization. In the interpretation attempted below, we shall consider these two facts only.

We begin by discussing the nature of the internal fields. It is well known[1,2] that

$$H_i = \omega_0'/\gamma, \tag{2}$$

where $H_i$ is the internal field responsible for the rotational resonance. Since $\omega_0'/2\pi \sim 10^3$ Mc/sec, Eq. (2) yields $H_i \sim 300$ oersteds. To account for this field in terms of internal stresses, we must assume that they are of the order of $|M_s H_i/\lambda_s|$, where $\lambda_s$ is the saturation magnetostriction. Using the value $\lambda_s \approx -2 \cdot 10^{-6}$ measured on ferramic $A$, we obtain about $10^{10}$ dynes/cm² (≈$10^3$ kg/mm²) for the required stresses. In view of the brittleness of ferramic $A$, and the fact that the x-ray diffraction lines at room temperature are quite sharp,[1] it is very unlikely that stresses of this magnitude exist in our material at room temperature. While this argument does not apply to $\omega_0''$, and may not[18] apply to $\Omega_0'$, the temperature dependence of these frequencies was found to be approximately the same as that of $\omega_0'$, so that the role of the stresses is probably unimportant in all three cases. It seems reasonable, therefore, to simplify the problem by completely neglecting the effect of internal stresses. The contributions to $H_i$ of crystalline anisotropy and internal demagnetizing fields, on the other hand, must both be taken into account. This necessity was indicated in paper III in a qualitative way and will now be formulated quantitatively on the basis of room temperature data. If only anisotropy

[16] J. H. Griffiths and J. R. MacDonald, J. Sci. Instr. **28**, 56 (1951).

[17] We do not discuss the data taken at 411°K because at temperatures approaching the Curie point (≈550°K in ferramic $A$) the distinction between domains and domain walls becomes meaningless.

[18] The diffraction lines in the case of the single-domain particles are not very sharp (see reference 1), a fact which may be due to the small size of the particles or the presence of stresses.

TABLE II. Mean resonance frequencies and saturation magnetization for ferramic *A*.

| Temperature °K | $\omega_0''/2\pi$ Mc/sec | % | $\omega_0'/2\pi$ Mc/sec | % | $\Omega_0'/2\pi$ Mc/sec | % | $M_s$ cgsm | % |
|---|---|---|---|---|---|---|---|---|
| 77 | 100 | 100 | 3900 | 100 | 5000 | 100 | 140 | 100 |
| 195 | 71 | 71 | 2700 | 69 | 3600 | 72 | 123 | 88 |
| 300 | 43 | 43 | 1400[a] | 36[a] | 2300 | 46 | 105 | 75 |

[a] This low value is probably due to the relatively pronounced overlap of the two resonances at this temperature; at 411°K the overlap is even more pronounced.

fields were important, we would expect $\Omega_0'=\omega_0'$, rather than the observed $\Omega_0'>\omega_0'$; and if only demagnetizing fields were important, we would expect $\Omega_0'/2\pi \leq 2\pi M_s(\gamma/2\pi)\approx 1800$ Mc/sec, the limiting value appropriate for infinitely separated, long, thin, cylindrical particles of single-domain size, whereas experimentally $\Omega_0'/2\pi=2300$ Mc/sec, as measured on particles that have been ground so that their shape should be roughly spherical rather than cylindrical. Finally, we allow for the possibility that torques due to exchange fields, which are known to be important inside domain walls, may affect the rotation of the spins within any domain that contains sufficiently small regions of inhomogeneous magnetization.

On the basis of the above statements we can describe rotations by writing Eq. (2) in the form

$$\omega_0'=\gamma f(K, M_s, E_J), \tag{3}$$

with a similar equation for $\Omega_0'$. Here $f$ is some unknown function whose temperature dependence is determined by $K$, $M_s$, and $E_J$ (and whose form may be different if $\omega_0'$ is replaced by $\Omega_0'$), $K$ is the first-order anisotropy constant, and $E_J$ is the exchange energy density. While $M_s$ can be measured on polycrystalline samples (see Sec. 2C), an unambiguous and reasonably accurate determination of $K$ requires a single crystal; owing to the effect of magnetic interactions, only the order of magnitude of $K$ can be measured[19] on a polycrystal. Since ferramic *A* is not available in the form of single crystals, $K$ must be treated as an unknown parameter. The quantity $E_J$ cannot be measured directly, and an indirect measurement is not now possible because of insufficiencies in the statistical aspects of the theory of ferromagnetism at all but very low temperatures. However, the molecular field approximation leads to the proportionality[20]

$$E_J \propto M_s^2 \tag{4}$$

for the temperature dependence of $E_J$. This relation[21] follows directly from the Néel[22] theory of the ferrites because in magnesium ferrite ($MgOFe_2O_3$) all the magnetic ions are of the same kind ($Fe^{+++}$); the relatively small net magnetization is ascribed to the presence of an excess number of $Fe^{+++}$ ions on the "octahedral" lattice sites of the incompletely inverted spinel structure. Using the relation (4) and noting that $f$ must have the dimensions of a magnetic field, we can equate $f$ to the product of $M_s$ (or $K^{\frac{1}{2}}$, or $K/M_s$) and some function whose temperature dependence is determined by the dimensionless ratio $K/M_s^2$. Without loss of generality, we may therefore replace Eq. (3) by

$$\omega_0' \propto gM_sF(K/M_s^2), \tag{5}$$

where $F$ is some unknown function. The value of $F$ can be derived in a few special cases. If, for example, magnetic interactions are entirely neglected, $H_i$ is known to be given by $2K/M_s$ for a substance in which $K$ is positive, so that in this case

$$F \propto K/M_s^2, \tag{6a}$$

a relation that applies equally well to the case of a uniformly magnetized, single-domain particle which is free of imperfections and spherical in shape. If, on the other hand, the effect of demagnetizing fields outweighs that of anisotropy, we expect $H_i \propto M_s$, so that in this case

$$F=\text{constant}, \tag{6b}$$

with respect to temperature. In the general case, however, we cannot progress beyond Eq. (5) unless we make some assumption about the form of $F$ or the temperature dependence of $K/M_s^2$.

To describe wall displacements,[23] we use the equation[1, 6]

$$\omega_0''=(\alpha/m_w)^{\frac{1}{2}}, \tag{7}$$

where $\alpha$ is the stiffness constant[24] of a domain wall and $m_w$ is its inertia (or apparent mass per unit wall area). In principle, $\alpha$ can be obtained from the static initial susceptibility due to wall displacements, $\chi_0''$, by using the formula[1]

$$\alpha=M_s^2/\chi_0''d. \tag{8}$$

In practice, however, this determination is not possible because in a polycrystal there is no way of accurately separating $\chi_0''$ from the measured $(\chi_0)_{\text{total}}$ and because the average domain size $d$ is difficult to ascertain. It is therefore necessary to obtain $\alpha$ from theoretical considerations. Before doing this, we recall that the mechanism responsible for impeding wall motion in a given substance determines not only $\alpha$ but also the

[19] G. T. Rado and A. Terris, Phys. Rev. **83**, 177 (1951).

[20] The proportional sign ($\propto$) is used throughout the present paper to indicate proportionality of two quantities in the course of temperature changes.

[21] Several papers which do not explicitly consider temperature effects, e.g., the review of static domain theory by C. Kittel, Revs. Modern Phys. **21**, 541 (1949), give the impression that $E_J$ is independent of temperature. This may be a fair approximation near room temperature for materials having a high Curie point (e.g., silicon iron), but in most cases the relation (4) is probably a better approximation.

[22] L. Néel, Ann. phys. **3**, 137 (1948).

[23] It should be pointed out that the possibility of the existence of domain walls in ferrites, which are ferrimagnetic (see reference 22), was proved beyond doubt by the observations of J. K. Galt, Phys. Rev. **85**, 664 (1952) on a single crystal of magnetite. As noted by Néel (reference 22), the theory of ferrimagnetic walls is expected to be quite similar to that of ferromagnetic walls.

[24] See Eq. (11) of reference 1; the restoring force acting on a unit wall area during a small displacement, $X$, is given by $\alpha X$.

coercive force. In ferramic $A$ there are air-filled cavities, and probably other nonmagnetic inclusions, so that the coercive force (and thus $\alpha$) may well be due to Néel's[25] disperse fields or to Kersten's surface tension effect,[26] depending on whether the size of the inclusions is comparable to, or much smaller than, the wall thickness. It is also possible that the size and irregularity of sufficiently small crystallites plays a role, as discussed qualitatively by Döring.[27] In view of the many detailed models which may have to be treated, the complications of the problem, and the unavailability of a precise description of the structure of our material, it is clearly necessary to keep the discussion as general as possible. Remembering that the effect of internal stresses is probably small, we therefore express each of the quantities $\alpha$ and $g^2m_w$ by some function whose temperature dependence is determined by $K$, $M_s$, and $E_J$. On the basis of Eqs. (7) and (4) and a dimensional argument similar to that used in connection with Eq. (5), we obtain

$$\omega_0'' \propto gM_s\Phi(K/M_s^2), \tag{9}$$

where $\Phi$ is some unknown function. It is instructive to calculate $\Phi$ for a special case. If the size of the inclusions is very much smaller than the wall thickness, a straightforward expansion of the restoring force obtained from Néel's[28] model leads to $\alpha \propto K/\delta^3$, where $\delta$ is the wall thickness parameter. In deriving this expression we have neglected, for simplicity, the contribution of magnetic energy in comparison with that of exchange and anisotropy energy, a step justified by the supposed smallness of the inclusions. Using the same model, we find that $m_w$ depends on the position of the wall. However, it can be shown by means of rough calculations and the properties of ferramic $A$ that this effect may be neglected because it depends primarily on the small change of magnetic energy in a moving wall as it passes through an inclusion. Consequently we use the usual expression for $m_w$ and write it in the form[7] $m_w \propto 1/g^2\delta$ for any given type of wall. On the basis of Eqs. (4) and (7) and the relation $\delta \propto (E_J/K)^{\frac{1}{2}}$, we therefore obtain in this case

$$\Phi \propto (K/M_s^2)^{\frac{1}{2}}. \tag{10}$$

In the general case, however, we cannot progress beyond Eq. (9) unless we make additional assumptions, as stated in connection with Eq. (5).

It has been assumed implicitly that there is neither a change of phase (or atomic order) nor a change in the sign of $K$ in the temperature range under consideration. We now assume, in addition, that $K/M_s^2$ is independent of temperature between 77°K and 300°K. This assumption represents merely a rough first approximation, as discussed later, and its usefulness arises from the fact that no other reasonable assumption leads to a definite prediction on the basis of Eqs. (5) and (9). (In view of the difficulties outlined above, the situation would not be markedly improved if the temperature dependence of $K/M_s^2$ were known.) Our assumption leads to the simple result

$$\omega_0'' \propto \omega_0' \propto \Omega_0' \propto gM_s, \tag{11}$$

which is seen to agree quantitatively with "fact (a)" mentioned near the beginning of this section. However, the agreement between the relation (11) and "fact (b)" is only qualitative because the results of Sec. 2B show that the temperature dependence of $g$, if it exists at all, is too small to account for the observation that the temperature dependence of the resonance frequencies is more pronounced than that of $M_s$.

The most probable explanation of the residual discrepancy is that $K$ decreases with increasing temperature somewhat faster than $M_s^2$. Such a behavior is to be expected if the known thermal characteristics of nickel ferrite[12] provide a guide to those of ferramic $A$. In an attempt to decide this question experimentally, we measured the static initial permeability of the single-domain particles and found it to decrease by at most one percent (which is about equal to the experimental error) between 77°K and 300°K. Since we are concerned here with rotations, one is tempted to conclude from this measurement that $K/M_s^2$ is independent of temperature in the range specified. However, the experimental data refer to an apparent permeability because of the (large) demagnetizing field of the particles, so that the observed temperature dependence of the permeability is necessarily less pronounced than the true dependence.[29] It is therefore possible that $K/M_s^2$ does, in fact, decrease somewhat as the temperature is increased. If this is the correct explanation of "fact (b)," however, then it is by no means clear why the functions $F$ and $\Phi$ should have the same temperature dependence, a required behavior if we are to explain "fact (a)" without assuming that $K/M_s^2$ is constant. The best we can do at present is to surmise that $F$ and $\Phi$ do have nearly the same temperature dependence in the limited range under discussion because in some special cases both of these functions vary less rapidly than $K/M_s^2$; this can be seen by comparing Eqs. (6a) and (6b), which represent the limiting cases for $F$, with Eq. (10), which represents one particular case for $\Phi$. Finally, we summarize the discussion by noting that our interpretation, based on the relation (11) supplemented by the above remarks, appears to account semiquantitatively for the measured temperature dependence of the resonance frequencies.

We wish to thank M. Maloof for assistance in solving problems connected with the apparatus.

[25] L. Néel, Annales Univ. Grenoble **22**, 299 (1946); Physica **15**, 225 (1949).

[26] For an improved calculation, see L. Néel, Cahiers phys. **25**, 21 (1944). This paper also contains the prediction of "Néel spikes" for the case where the inclusions are much larger than the wall thickness.

[27] W. Döring, Z. Naturforsch. **4a**, 605 (1949).

[28] Reference 26, pp. 16–18.

[29] This is similar to the air-gap effect in magnetic circuits.

# Neutron Capture $\gamma$-Ray Spectra from the Elements $Z=17$–30 and $Z=45$–57

BERNARD HAMERMESH AND VIRGINIA HUMMEL
*Argonne National Laboratory, Chicago 80, Illinois*

(Received July 9, 1952)

A NaI(Tl) scintillation counter and a 5819 photomultiplier have been used in conjunction with a very accurate and flexible twenty-channel pulse-height discriminator to study thermal neutron capture gamma-ray spectra. The energy range 20 kev–10 Mev was studied for the elements of atomic numbers 17–30 and 45–57 excluding the noble gases. In the case of chlorine, four lines are found below 2.1 Mev. These probably correspond to the first four excited states of $Cl^{38}$. A neutron binding energy of $8.57\pm0.03$ Mev is found for $Cl^{38}$ by combining these lines with pair spectrometer data on the high energy lines. The method yields information on only the most prominent transitions in the capture gamma-decay schemes. No systematic distribution of these prominent lines is evident from the limited number of lines that can be resolved by this technique.

## I. INTRODUCTION

RECENTLY a small measure of progress has been made in the study of the instantaneous gamma-rays that are emitted following thermal neutron capture. One new method that has been used is the nuclear emulsion technique.[1] The emulsions are loaded with deuterium in some form and capture gamma-rays are detected by observing photoproton tracks in the emulsion. This method is useful only above 3 Mev and has very poor energy resolution.

A much more fruitful technique has been the use of a pair spectrometer[2] by Kinsey and his colleagues at Chalk River. Although the method has a low energy cutoff between 2.5 and 3.5 Mev, it has about a 1.5–2 percent energy resolution in the 6–10 Mev range. Many interesting and surprising results ($Pb^{208}$) have been found by this technique.

The development of scintillation counters with high gamma-ray detection efficiencies has made it possible to study capture gamma-ray spectra[3,4] below the low energy cutoff of the methods mentioned above. In fact, we have now made measurements down to 20 kev by this technique.

We have begun a systematic study of thermal neutron capture gamma-ray spectra by using a scintillation counter gamma-ray spectrometer. The program is intended to study groups of elements in the low, intermediate and high atomic number regions of the periodic table. Whenever possible, a series of elements of adjacent atomic numbers is studied. It is hoped that in this way some systematic features of the spectra will be made evident. The present paper deals with the two groups of elements $Z=17$–30 and $Z=45$–57 excluding the noble gases, argon and xenon. The results[3] on chlorine, manganese, and iron which were previously reported have been extended to lower energies with higher resolution and greater accuracy.

## II. APPARATUS

The detecting apparatus consists of a probe made of a NaI(Tl) crystal, a 5819 photomultiplier, and a 2-stage preamplifier. The crystal is $\frac{3}{4}$-inch high and $1\frac{1}{2}$ inches in diameter. It is packaged according to the method of Swank and Moenich.[5] This packaging technique is very successful and the crystals seem to last indefinitely. A $\frac{1}{2}$-inch Lucite light pipe is used between the crystal package and the photomultiplier.

The pulses from the probe are fed into a window amplifier and then in turn into a twenty-channel pulse-height discriminator and a twenty-channel recording console. Each recording channel has a decade scaler which can be cascaded into the adjacent channel. Channel No. 20 acts as an integrating channel and records the integrated counting rate of all gamma-rays above the region of the spectrum that is being searched.

The window amplifier chassis contains an accurate auxiliary pulse generator whose output may be taken in one or two volt steps for setting the twenty channels to be as nearly equal to each other as possible. The window amplifier has a gain of 5 when set for 1-volt intervals and a gain of 2.5 when set for 2-volt intervals; i.e., its output pulses are always 5-volt pulses.

The window amplier contains appropriate attenuators so that any energy range may be studied. For example, there are five gain settings, $A$–$E$. The attenuation of pulse height that is controlled by each gain setting allows the use of the following convenient scheme.

By choosing the correct photomultiplier voltage, the gain settings $A$–$E$ can be made to correspond to 5, 10, 12.5, 25 and 50-kev/volt pulse height. By raising the voltage properly, gain $A$ can be used to give 2.5 kev/volt and by lowering the voltage, gain $E$ can be set to give 100 kev/volt. On all gain settings, a voltage range of 0–100-volts pulse height is available and since the 20 channels can be made to correspond to 1 or 2 volt intervals, a 20 or 40-volt interval can be studied. The

[1] B. Hamermesh, Phys. Rev. **76**, 182 (1949); **80**, 415 (1950); **81**, 487 (1951).
[2] Kinsey, Bartholomew, and Walker, Phys. Rev. **77**, 723 (1950); **78**, 77 (1950); **79**, 218 (1950); **81**, 150 (1951); **82**, 380 (1951); **83**, 519 (1951).
[3] B. Hamermesh and V. Hummel, Phys. Rev. **83**, 663 (1951).
[4] Thornton, der Mateosian, Motz, and Goldhaber, Phys. Rev. **86**, 604 (1952).
[5] R. Swank and J. Moenich, Rev. Sci. Instr. **23**, 502 (1952).

20 or 40-volt interval may be located anywhere along the 0–100-volt interval. In this manner a very flexible searching scheme is available.

The spectrometer is calibrated by use of gamma-ray sources having simple decay schemes. The instrument is usually calibrated with gamma-rays from $Au^{198}$ (0.411 Mev), $Cs^{137}$ (0.669 Mev) and $Na^{24}$ (1.38 and 2.76 Mev). The first two sources provide sharp peaks due to the photoelectric effect in NaI. The $Na^{24}$ provides a total of five peaks, three of which are sharp. These three are the photoelectric peaks from each of the two gamma-rays and the pair production peak (with escape of both annihilation quanta) from the 2.76-Mev line. The $Na^{24}$ gives three good calibration values in a single counting sequence.

Various other sources have been used for calibration and resolution determinations. It has been found that the resolution[6] is given by the relation

$$\Delta E/E=(a/\sqrt{E})+b,$$

where $\Delta E$ is the full width of a line at half-maximum, $E$ is the energy of the line, and $a$ and $b$ are constants. For the work described here, with $E$ in kev, $a$ was 1.64 and 2.05 and $b$ was 0.05 and 0.036, respectively, for the two probes used.

## III. METHOD

Figure 1 shows the experimental arrangement used in these experiments. A narrow beam of neutrons from the Argonne heavy water moderated pile is allowed to impinge on the capturing material. The capture gamma-rays generated are emitted in all directions and a narrow beam passes through the slit onto the NaI crystal.

The crystal and photomultiplier are inside of a heavy bismuth shield. There are 8 inches of bismuth on the side of the shield facing the pile and 4 inches on all other sides. The block of bismuth containing the 1½-inch circular aperture is 2 inches thick. The sides of the aperture are lined with ¼ inch of steel. This is needed to attenuate the annihilation quanta that arise from capture gamma-rays and scattered pile gamma-rays that strike the bismuth sides of the aperture. The whole shield is wrapped in 30-mil cadmium. The aperture is free of cadmium but ¼ inch of LiF inside a thin cardboard container is placed over the aperture to absorb scattered thermal neutrons from the capturing samples. The crystal is in line with the capturing samples and the aperture. Back of the crystal (in a downward direction) is a gap of two feet to the floor of the pile room.

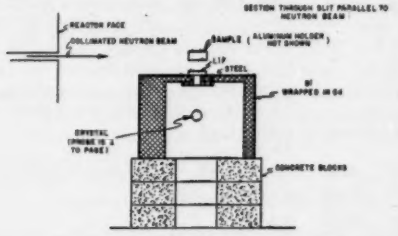


FIG. 1. Schematic arrangement of apparatus.

[6] V. Hummel and B. Hamermesh, A.E.C.U. 2020.

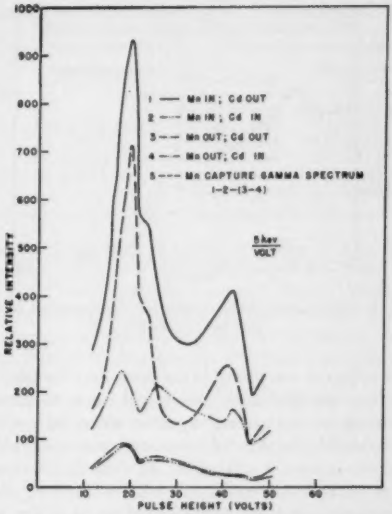
1 —— Mn IN ; Cd OUT
2 —— Mn IN ; Cd IN
3 —— Mn OUT; Cd OUT
4 —— Mn OUT; Cd IN
5 —— Mn CAPTURE GAMMA SPECTRUM
1–2–(3–4)
5 kev/VOLT
RELATIVE INTENSITY
PULSE HEIGHT (VOLTS)

FIG. 2. Pulse-height distribution from low energy capture gamma-rays from manganese.

The samples used were in the shape of disks ¾ inch in diameter where the solid element was available. If powders were used, they were placed inside of ¾-inch diameter lusteroid test tubes. The thickness of a sample (in the direction of the neutron beam) was made as large as possible, consistent with conservative counting rates (except for Sc where only 5 grams of the oxide was available). The criteria used were not to allow any mechanical recorder to count faster than 250 clicks per minute and, in addition, not to allow the last channel (the integrating channel), to count more than 25,000 counts per minute. These limits were found to be very safe.

The neutron flux on the target was monitored with a $BF_3$ pulse chamber placed in a hole in the reactor near the beam hole used in these experiments. It was found that equal monitor intervals usually occurred in equal time intervals.

## IV. RESULTS

In order to make a measurement at a given region of a spectrum, a cycle of four measurements was required. These measurements are:

1. Source in—no cadmium in the beam.
2. Source in—cadmium in the beam.
3. Source out—no cadmium in the beam.
4. Source out—cadmium in the beam.

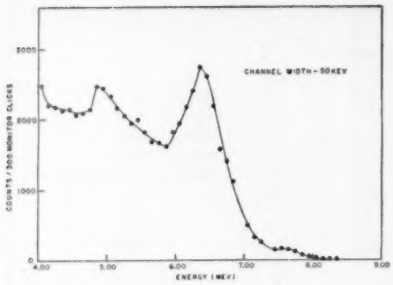


FIG. 3. High energy pulse distribution from neutron capture gamma-rays of iron.

The cadmium was placed in the beam near the pile, i.e., far from the photomultiplier shield, so as to prevent cadmium capture gamma-rays from seeing the aperture in the shield. The effect of the capture gamma-rays from a given sample is related to the four measurements given above by the relation 1–2–(3–4). Figure 2 shows a curve for manganese in the low energy region on gain $A$ (5 kev/volt) set for 2-volt intervals. The curves 3 and 4 are so nearly the same (as they should be if the beam is well collimated) that steps 3 and 4 may be omitted, and the effect can be found by taking data with and without cadmium in the beam with the capturing sample in place. The data of Fig. 2 show two very intense lines, one at 90 kev and the other at 190 kev,

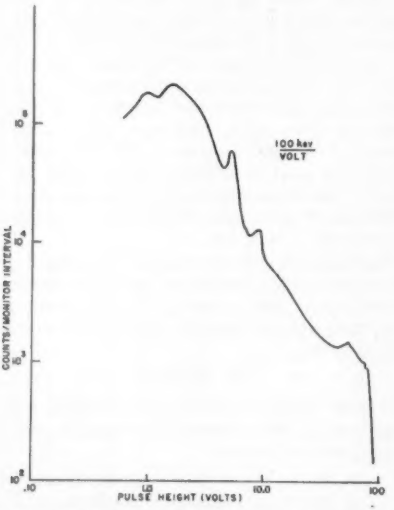


FIG. 4. Pulse-height distribution from capture gamma-rays from chromium.

emitted by the rapidly decaying[7] $Mn^{56}$ compound nucleus formed on neutron capture.

Figure 3 shows a typical high energy portion of a spectrum from an iron sample. There are three peaks present. They arise from pair production in NaI caused by gamma-rays at 6.0, 7.4, and 8.5 Mev. The 6.0- and 7.4-Mev lines are most likely from $Fe^{57}$, whereas the 8.5-Mev line, which is much weaker, is probably from a ground-state transition in $Fe^{55}$. The very poor high energy resolution (5–6 percent) makes it difficult to observe very much of the structure of the high energy parts of the spectra such as is seen by a pair spectrometer.

In the lower energy portions of the spectra a very serious difficulty arises due to Compton scattering of the high energy lines in the NaI. Consider a low energy

TABLE I. Prominent thermal neutron capture gamma-rays from the elements $Z=17-30$.

| Element | Sample | Gamma-ray energy (Mev) | Remarks |
|---|---|---|---|
| Cl | $C_2Cl_6$ | 0.784±0.010<br>1.15 ±0.010<br>1.59 ±0.013<br>2.00 ±0.025<br>6.2±0.2, 7.7±0.2 | |
| K | Fluoride | 6.0, 8.2 | |
| Ca | Metal | 6.8, 8.2 | |
| Sc | Oxide | 0.152, 0.220, 7–9 | 0.152 line is from the 20-sec isomer of $Sc^{46}$. This has been measured as 0.142 ±0.005 in a separate experiment.<br>No crossover of 0.152 and 0.220 lines is observed. Not enough material was available to study high energy region. Curves show possible lines in 7–9-Mev region. |
| Ti | Oxide | 1.0, 1.38, 5.0, 6.5–7.0 | The 1.0 line is probably a Compton peak from the 1.38-Mev line.<br>There are two lines between 6.5 and 7.0 Mev. |
| V | Metal | 5.3, 5.7, 6.8, 7.4 | A line at 1.4 Mev from $V^{52}$ beta-decay is observed. |
| Cr | Metal | 0.880, 5–6, 8.0–8.5, 8.5–9 | Spectrum is very complex at high energies. |
| Mn | Metal | 0.090, 0.190, 5.0, 7.2 | No crossover of the 90- and 190-kev lines is observed. A 900-kev line from the 2.6-hour $Mn^{56}$ activity is observed. |
| Fe | Metal | 0.425, 6.0, 7.4, 8.5 | No line at 1.4 Mev is observed. (See reference 3.) |
| Co | Oxide | 0.220, 1.1, 1.5, 5.8, 7.0 | |
| Ni | Metal | 6.5–7.5, 8.5–9 | Very complex spectrum. |
| Cu | Metal | 0.150, 6.5–7, 7–8 | |
| Zn | Metal | 1.0, 7.5 | |

[7] The nucleus emitting the capture spectrum will be the one usually listed unless otherwise stated.

TABLE II. Prominent thermal neutron capture gamma-rays from the elements $Z=45-57$.

| Element | Sample | Gamma-ray energy (Mev) | Remarks |
|---|---|---|---|
| Rh | Metal | 0.080, 0.160 | Gamma-rays probably from $Rh^{104}$ 4.34-min and $Rh^{104}$ 44-sec activities. |
| Pd | Metal | Unresolved | |
| Ag | Metal | 0.187 | |
| Cd | Metal | 0.558, 8.5 | See reference 4. |
| In | Metal | 0.160, 0.256 | No crossover observed. |
| Sn | Metal | 7.5–8.0 | |
| Sb | Metal | Unresolved | |
| Te | Metal | 0.609 | |
| I | $CHI_3$ | Unresolved | |
| Cs | Nitrate | Unresolved | |
| Ba | Metal | Unresolved | |
| La | Metal | 4.5 | |

portion of a capture spectrum. Then all of the higher energy lines feed their Compton electrons (formed in NaI) into lower energy parts of the spectrum. Therefore, the lower energy lines sit on top of a rapidly rising background. Figure 4 shows the complete normalized counting rate *vs* energy curve for the capture gamma-rays from chromium. The rapid rise toward low energies means that only the most prominent lines of the capture spectra can be observed.

Tables I and II contain those lines that stand out above the rapidly rising background that is present with all elements as one goes toward low energies. Gamma-rays following beta-decay are also observed. In all cases listed the spectra were explored from the region of 20 kev up to the point where no counts were detectable above background. All lines below 700 kev were measured to $\pm 10$ kev. In the case of chlorine, the lines were measured with the accuracy indicated in Table I.

The results given in the tables show no systematic structure of the spectra. In the case of chlorine, however, interesting conclusions can be drawn since the spectrum has recently been studied with the pair spectrometer by Kinsey, Bartholemew, and Walker.[8] The decay scheme of $Cl^{36}$ that is presented in Fig. 10 of their paper proposes that the first four excited states have the energies $0.79\pm0.04$, $1.14\pm0.04$, $1.58\pm0.04$, and $1.94\pm0.07$ Mev, respectively. These energies are obtained by subtracting from the neutron binding energy of $Cl^{36}$ the energies of the lines which Kinsey *et al.*, label *B–E*. The neutron binding energy has been reported as 8.54 Mev by Shrader and Pollard[9] and 8.49 Mev by Ennis.[10] Kinsey *et al.*,[8] find that the most energetic gamma-ray from $Cl^{36}$ has an energy of 8.56 $\pm 0.03$ Mev. This line probably arises from a ground-state transition from the initial state of $Cl^{36}$ that is formed upon neutron capture.

The lines that we find at 0.784, 1.15, 1.59, and 2.00 Mev correspond to the transitions to the ground state from the levels reached by Kinsey's line *B–E* in $Cl^{36}$. The line at 6.2 Mev is probably Kinsey's line *F* and the line at 7.7 Mev is probably his line *B*. The 7.7-Mev line and the 0.784-Mev line are in cascade. The error in our measurement of the 7.7-Mev line does not permit us to make a good binding energy determination from our data alone.

TABLE III. Neutron binding energy of $Cl^{36}$ from combined scintillation spectrometer and pair spectrometer data.

| Line | Scintillation spectrometer | Pair spectrometer | Binding energy of $Cl^{36}$ |
|---|---|---|---|
| *A* | ... | 8.56±0.03 Mev | 8.56±0.03 Mev |
| *B* | 0.784±0.010 Mev | 7.77±0.03 Mev | 8.55±0.03 Mev |
| C | 1.15 ±0.010 Mev | 7.42±0.03 Mev | 8.57±0.03 Mev |
| *D* | 1.59 ±0.013 Mev | 6.98±0.03 Mev | 8.57±0.03 Mev |
| *E* | 2.00 ±0.025 Mev | 6.62±0.06 Mev | 8.62±0.06 Mev |
| | | Weighted average | 8.57±0.03 Mev |

If we label our four lowest lines *B–E* and combine each of them with Kinsey's line of the corresponding letter, then we find the values for the neutron binding energy of $Cl^{36}$ shown in Table III.

The results in Table III indicate that these four branches of the capture gamma-decay scheme of $Cl^{36}$ involve only two steps. Of course, the order of emission of the two lines in a branch is not definitely known. However, on the basis of our present knowledge (dependence of intensity on energy difference), it seems more likely that the more energetic transition in a given branch will occur first. This would mean that the four lowest lines that we observe arise from the first four excited states of $Cl^{36}$.

## V. CONCLUSIONS

The use of a NaI gamma-ray spectrometer for the study of the capture gamma-ray spectra of the elements $Z=17-30$ and $Z=45-57$ yields data on only the most prominent lines in these spectra. The poor high energy resolution plus the rapidly rising background at lower energies makes it difficult to observe more than the most prominent lines. The low energy lines that are observed probably arise from states very near the ground state. In the case of chlorine, it is very likely that the line at 784 kev is emitted from the first excited state of $Cl^{36}$ and that the lines at 1.15, 1.59, and 2.00 Mev arise from the next three excited states. No apparent systematics of the spectra are evident.

It is with great pleasure that we extend our thanks to our colleagues from various divisions at the Argonne National Laboratory who have helped make this work possible. We are especially grateful to Robert Swank of our Instrument Research Division and Robert Schumann of our Electronics Section. Mr. Swank provided the excellently packaged, high resolution crystals and the selected photomultipliers and a very stable single-channel analyzer which was used in the very early stages of our investigation. Mr. Schumann designed and built the 20-channel analyzer.

[8] Kinsey, Bartholomew, and Walker, Phys. Rev. **85**, 1012 (1952).
[9] E. F. Shrader and E. Pollard, Phys. Rev. **59**, 277 (1941).
[10] W. W. Ennis, Phys. Rev. **82**, 304 (1951).

# Acceptors Produced in Germanium by Quenching from High Temperatures

COLMAN GOLDBERG
*Westinghouse Research Laboratories, East Pittsburgh, Pennsylvania*
(Received June 2, 1952)

Acceptors were produced in germanium single crystals by heating at high temperatures and then quenching very rapidly. Fuller *et al.* have measured the diffusion coefficient for these thermally produced acceptors and on the basis of their measurements the assumption is made here that the acceptor levels are due to Schottky defects. An expression is derived for the equilibrium density of ionized Schottky defects and on the basis of this theoretical expression and the experiments performed it is found that (1.49±0.12) ev must be supplied to the crystal to form a Schottky defect. An estimate of (2.0±0.1) ev is made for the "activation energy" of self-diffusion in germanium if diffusion occurs by a vacancy mechanism.

## I. INTRODUCTION

IT has been found[1,2] that if germanium is cooled rapidly from temperatures greater than 500°C perceptible numbers of acceptors are added. These acceptors can be removed by annealing at temperatures of 500°C or less. Lark-Horovitz and his co-workers[3] have found a similar effect in nucleon bombarded samples of germanium. As with rapidly cooled samples, the acceptors added by nucleon bombardment can be removed by low temperature annealing. DeSorbo and Dunlap's low temperature resistivity measurements[4] indicate that the added acceptor levels are 0.03 ev above the valence band.

Lark-Horovitz[3] has proposed that the thermally produced $p$-type carriers may be the result of acceptor levels introduced by lattice defects produced by physical displacement of the germanium atoms from their normal lattice sites. This theory has been generally accepted as correct.

## II. LATTICE DEFECTS

Frenkel defects occur when an atom leaves its normal lattice position and moves to an interstitial position. Schottky defects occur when atoms move from their normal lattice sites and go to the surface of the crystal. Actually Schottky defects are created by a diffusion of vacant lattice sites from the surface to the interior of the crystal.

There is a deficiency of electrons around a vacant lattice site and, hence, there should be localized acceptor levels at these positions. Thus Schottky defects should introduce $p$-type carriers. Lark-Horovitz[3] has postulated that interstitial atoms produce localized donor levels, but if these levels lie far below the conduction band they will not introduce many $n$-type carriers and the net effect of a Frenkel defect will be acceptor levels around the vacant lattice sites.

In Sec. III we discuss the work of Fuller, Theuerer, and van Roosbroeck and conclude from their work that the acceptors created by rapid cooling from high temperatures are due to ionized Schottky defects. For this reason we will concentrate on Schottky defects in this section.

The equilibrium density of Schottky defects, $n_s$, in a polar crystal is[5]

$$n_s = N_L \exp(\Delta s/k) \exp(-\Delta h/kT), \tag{1}$$

where $N_L$ is the density of lattice sites, $\Delta s$ is the change in entropy of the atoms about a vacant lattice site due to the increase of the amplitude of vibration, and $\Delta h$ is the energy necessary to create a Schottky defect. However, Eq. (1) does not hold for Schottky defects in germanium. In germanium we must take into consideration the fact that these defects are ionized and, hence, when a defect is created we change the density of electrons in the conduction band and holes in the valence band and the electron energy changes accompanying these changes of density must be considered.

The Gibbs free energy should be invariant to small arbitrary changes in $n_s$, $p_v$, and $n_c$, where $n_s$ is the number of Schottky defects and is equal to the number of electrons trapped in these defects if we assume that each defect produces one acceptor level and all these acceptor levels are ionized (see Sec. VI). $p_v$ is the number of holes in the valence band and $n_c$ is the number of electrons in the conduction band. The only restriction on the small arbitrary change is

$$\delta n_c + \delta n_s = \delta p_v. \tag{2}$$

For thermal equilibrium the total change of the Gibbs free energy is

$$\delta G = \delta G_v + \delta G_c + \delta G_s = 0, \tag{3}$$

where $G_v$, $G_c$, and $G_s$ are the free energies of the $p_v$ holes in the valence band, $n_c$ electrons in the conduction band, and the $n_s$ Schottky defects respectively.

$$G_s = n_s \Delta h - kT \ln \frac{N_L!}{n_s!(N_L - n_s)!} - T n_s \Delta s, \tag{4}$$

where $\Delta h$, $\Delta s$, and $N_L$ are the same as in Eq. (1).

[1] H. C. Torrey and C. A. Whitmer, *Crystal Rectifiers* (McGraw-Hill Book Company, Inc., New York, 1948), p. 365.
[2] H. C. Theuerer and J. H. Scaff, Trans. Am. Inst. Mining Met. Engrs. **189**, 59 (1951).
[3] K. Lark-Horovitz in *Semi-Conducting Materials*, H. K. Henisch, Editor (Butterworths Scientific Publications, London, 1951).
[4] W. DeSorbo and W. C. Dunlap, Jr., Phys. Rev. **83**, 869, 879 (1951).
[5] N. F. Mott and R. W. Gurney, *Electronic Processes in Ionic Crystals* (Clarendon Press, Oxford, 1948), Chap. 2.

We let $(\delta n_s, \delta n_c, \delta p_v) = (1, -\frac{1}{2}, \frac{1}{2})$ which is the same as saying we ionize a vacancy by taking one-half an electron from the valence band and one-half an electron from the conduction band.[6] With this variation, we have

$$\delta G_v = \tfrac{1}{2}(E_s - E_v) + \text{entropy term}, \quad (5)$$

$$\delta G_c = \tfrac{1}{2}(E_s - E_c) + \text{entropy term}, \quad (6)$$

where $E_s$ is the energy of an electron trapped at a defect, and $E_c$ and $E_v$ are the energies of electrons at the bottom of the conduction band and at the top of the valence band respectively. With the variation used here it can be shown that the entropy terms in (5) and (6) are equal in magnitude but of opposite sign.

From (4) we find

$$\delta G_s = \Delta h - T\Delta s - kT \ln[(N_L - n_s)/n_s], \quad (7)$$

and substituting (5), (6), and (7) into (3) we obtain the relation

$$E_s - E_F + \Delta h - T\Delta s - kT \ln[(N_L - n_s)/n_s] = 0, \quad (8)$$

where $E_F = \frac{1}{2}(E_c + E_v)$ is the Fermi level in an intrinsic semiconductor. (Germanium is in the intrinsic range at all temperatures used to produce thermal acceptors.)

Rewriting (8) and using the approximation $n_s \ll N_L$ we get

$$n_s = N_L \exp(\Delta s/k) \exp(-\Delta H/kT), \quad (9)$$

where $\Delta H = \Delta h - (E_F - E_s)$. DeSorbo and Dunlap's[4] low temperature resistivity measurements show that $E_s$ is 0.03 ev above the top of the valence band. Then if we assume that the energy gap in germanium is 0.72 ev, $E_F$ is 0.36 ev above the top of the valence band and $\Delta H = \Delta h - 0.33$ ev. Hence in creating a vacancy at high temperatures an energy $\Delta h$ is needed, 0.33 ev of which comes from the electrons in the crystal and $\Delta H$ comes from the heat reservoir surrounding the crystal.

The assumptions used in the derivation of Eq. (9) limit its use to temperatures where germanium is an intrinsic semiconductor. This is true, however, at all temperatures where a perceptible number of defects are formed.[7]

Mott and Gurney[5] show that $\Delta s/k = \ln(\nu/\nu')^x$, where $x$ is the number of nearest neighbors, $\nu$ is the normal frequency of vibration and $\nu'$ is the frequency of vibration along a line between an atom and an adjacent vacant site. For germanium $x=4$, and if we assume that $(\nu/\nu') = \sqrt{2}$ then $\exp(\Delta s/k) = 4$. It should be emphasized that this prediction for $\exp(\Delta s/k)$ is only a rough approximation to give the order of magnitude and depends on the magnitude of $(\nu/\nu')$.

[6] Although the Gibbs free energy should be invariant for any arbitrary variation $(\delta n_s, \delta n_c, \delta p_v)$ it is shown in the appendix to this paper that when $\delta n_s = 1$, then $\delta p_v = -\delta n_s = \frac{1}{2}$.

[7] The equilibrium density of ionized Frenkel defects can also be derived by the method used in this paper. The result is

$$n_f = N_L \exp(\Delta s/2k) \exp(-\Delta H/2kT),$$

where $\Delta H$ is the same as in Eq. (9) and $\Delta s = \Delta s_i + \Delta s_v$, with $\Delta s_i$ and $\Delta s_v$ being the entropy changes of the atoms surrounding an interstitial atom and a vacancy, respectively.

## III. PREVIOUS STUDIES OF THERMALLY PRODUCED ACCEPTORS

In studies of thermally produced acceptors it has always been assumed that the equilibrium number of defects is reached in a reasonable time at high temperatures and that these defects are "frozen in" when the crystal is rapidly cooled to lower temperatures. At room temperature the approach to equilibrium is extremely slow and the number of defects present is dependent upon the temperature from which the sample was rapidly cooled.

Fuller, Theuerer, and van Roosbroeck[8] have observed the diffusion of these acceptors from the surface to the interior of the crystal and they measured the diffusion coefficients at several temperatures. The values they obtained for diffusion coefficients fit the relation

$$D = D_0 \exp(-E/kT), \quad (10)$$

where $D_0 = 0.02$ cm²/sec and $E = 0.5$ ev. The diffusion coefficients they measured ranged from $3.2 \times 10^{-6}$ cm²/sec at 670°C to $9.5 \times 10^{-5}$ cm²/sec at 850°C. The observed value of $E$ is small compared to most energies found in diffusion measurements and should be equal to the height of the potential barrier that an atom must go through or pass over when moving to an adjacent lattice site that is vacant (if we assume we are observing the diffusion of Schottky defects).

If there is an equilibrium density of defects at the surface, then there will be an appreciable fraction of the equilibrium density at a distance $x$ from the surface after a time $t = x^2/4D$. At 560°C Eq. (10) gives $D = 1.8 \times 10^{-5}$ cm²/sec, and we would expect equilibrium in a sample 1 mm thick in less than one minute. This is in contradiction to the experimental evidence. Theuerer and Scaff[2] indicate that it is a matter of hours before equilibrium is reached at this temperature, so Eq. (10) does not give the proper values for $D$ at low temperatures.

Although there may be some doubt about the accuracy of Eq. (10), the diffusion experiments do have one important conclusion which can be reached from the qualitative results. These experiments show that the thermally produced acceptors are produced at the surface and diffuse into the bulk of the crystal from the surface. From the discussion in Sec. II we can see that if these acceptors are due to lattice defects, these defects must be Schottky and not Frenkel defects because there would be no diffusion from the surface in the case of Frenkel defects. (The diffusion experiment does not give us any information about the type of defect produced by nucleon bombardment and it seems quite likely that bombardment may produce Frenkel defects.) If we assume that each Schottky defect produces one acceptor and that all these acceptors are ionized at room temperature (these assumptions are discussed in Sec. VI) $\Delta n$, the increase in the number

[8] Fuller, Theuerer, and van Roosbroeck, Phys. Rev. 85, 678 (1952).

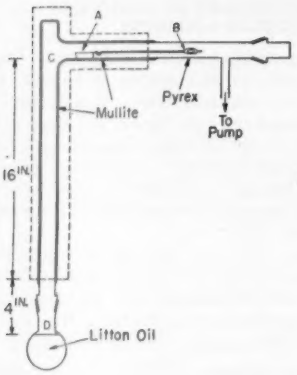


FIG. 1. Rapid quenching apparatus.

of carriers at room temperature created by quenching from temperature $T$, should be [see Eq. (9)]

$$\Delta n = N_L \exp(\Delta s/k) \exp(-\Delta H/kT), \qquad (11)$$

with $\exp(\Delta s/k) \simeq 4$.

Fuller, Theuerer, and van Roosbroeck also measured the equilibrium density of acceptors added as a function of the temperature at which the samples were heat treated before quenching. Their data fit Eq. (11) with $\exp(\Delta s/k) = 0.053$ and $\Delta H = 1.2$ ev. They used resistivity measurements to determine the number of acceptors introduced, using the relation $1/\rho = ne\mu$, where $\rho$ is the resistivity, $n$ the density of carriers, $e$ is the electronic charge, and $\mu$ the mobility.

Taylor[9] has studied the number of acceptors introduced by quenching from different temperatures. (He assumed that the acceptor levels were due to Frenkel defects.) He treated his samples in a vacuum of $10^{-2}$ mm. After approximately one hour of heating, air was admitted to the system, the sample was quickly removed and quenched in ethyl alcohol that was at room temperature. (Renzema[10] feels that the air admitted when the system is opened so that the sample may be removed may be the mechanism of the rapid cooling. However, from simple calorimetric considerations this does not seem very probable. The air would not cool the sample more than a few degrees.)

Taylor determined the number of acceptors introduced by making resistivity measurements before and after quenching. He had previously[11] prepared a graph giving the number of carriers as a function of resistivity. This graph was prepared from a study of the correlation between Hall constant and resistivity. A straight line was drawn through a log log plot of resistivity and Hall constant. Inspection of this plot leaves considerable doubt as to the accuracy of carrier concentration that could be obtained from resistivity measurements using the straight line approximation.

Taylor's quenching experiments show that $\Delta n$ fits Eq. (11) with $\Delta H = 1.8$ ev and $\exp(\Delta s/k) = 330$.

## IV. EXPERIMENTAL APPARATUS

The apparatus used for rapid quenching is shown in Fig. 1. A vacuum of better than $10^{-5}$ mm was attainable. The "$T$" shaped Mullite tube was made to our specifications by the McDanel Refractory Porcelain Company, Beaver Falls, Pennsylvania. The parts of the system within the dashed line are inside a furnace. The germanium sample was placed in a porcelain boat and the boat was moved to the position $A$. A slug of iron was enclosed at $B$ in the frame connected by a hook to the boat containing the germanium. To cool the sample rapidly a magnet was used to move the iron slug at $B$ to the left, the germanium dropping into the Litton oil quenching bath when the boat got to position $C$. Due to the fact that the germanium was heated during the early part of its fall, it was moving rapidly when it left the furnace. Simple calculations show that the sample took only 0.034 second to fall the last 4 inches. The total time of fall is only 0.323 second. If the entire furnace is at the same temperature then the sample goes from the temperature at which is was heat treated to the quenching bath in 0.034 second. In actual practice the temperature at the lower part of the furnace was less than at the top. If the top of the furnace was at 900°C, the lower part of the furnace was at about 670°C. We have not made quantitative calculations concerning the effect this would have on the temperature of the sample as it left the furnace, but we feel it is safe to say that the sample reached the quenching bath in a time considerably less than 0.3

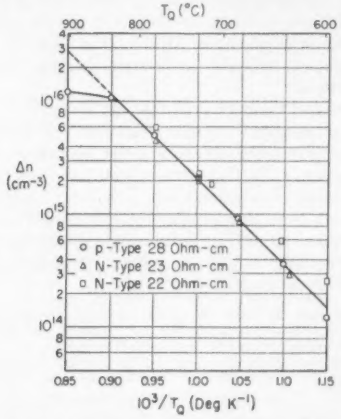


FIG. 2. Change in carrier density produced by quenching from temperature $T_Q$.

[9] W. E. Taylor, Purdue Sixth Quarterly Report (1950) p. 1; Phys. Rev. 86, 642 (1952).
[10] T. S. Renzema, Purdue Twelfth Quarterly Report (1951) p. 16 (unpublished).
[11] W. E. Taylor, Purdue Sixth Quarterly Report (1950) p. 3 (unpublished).

second, which is a marked improvement over other systems described in the literature.

## V. RESULTS AND ANALYSIS OF THE MEASUREMENTS

Single crystals of germanium of both $n$- and $p$-type were used. Sample thickness was between 0.3 and 0.8 mm. After low temperature annealing to insure that there were very few lattice defects present, Hall measurements were made. The density of carriers present was determined from the well-known approximation

$$n = 7.37 \times 10^{18}/R \text{ cm}^{-3},$$

where $R$ is the Hall constant. Hall measurements were again made after quenching and $n$ was determined by the above relation. The increase in carriers was then determined by algebraic subtraction of the two values:

$\Delta n$ = Carriers after quenching minus carriers in annealed sample.

With the apparatus used in our early experiments, it took at least 6 seconds for the sample to move from the furnace to the quenching bath. These experiments indicated that the density of carriers added by quenching from 904°C was not much greater than the density added by quenching from 727°C. We felt that this might be due to the fact that in six seconds that elapsed from the time the sample was removed from the furnace to the time that it was dropped into the quenching bath the sample may have cooled appreciably by radiation. If equilibrium is reached very quickly at these high temperatures, the number of defects frozen in would correspond to a lower temperature than that of the furnace.

As mentioned in Sec. IV, the system shown in Fig. 1 was constructed so that the sample would be transported from the furnace to the quenching bath in minimum time. The results obtained with this furnace are shown in Fig. 2 and fit Eq. (11) with $\Delta H = (1.49 \pm 0.12)$ ev, $\exp(\Delta s/k) = 1.5$. This value for $\exp(\Delta s/k)$ compares favorably with our estimated value of 4 when we consider the possible error involved in the extrapolation to $1/T = 0$ when there is an uncertainty in $\Delta H$. From the discussion following Eq. (9) we see that a value of $\Delta H = (1.49 \pm 0.12)$ ev means that the energy necessary to form a Schottky defect is $(1.82 \pm 0.12)$ ev, 0.33 ev being supplied by electrons and $(1.49 \pm 0.12)$ ev being supplied by the surroundings of the crystal.

The values of $\Delta n$ were reproducible for different samples as long as the sample was not quenched from temperatures greater than 850°C. If the samples were quenched from temperatures greater than 850°C and later quenched from lower temperatures, the value of $\Delta n$ at these lower temperatures would be about 20 percent higher than values obtained before the high temperature quenching. One sample was heated to 900°C and then cooled to 727°C before quenching. This treatment did not cause the effect described above so the effect must be due to the quenching from high temperatures and not to the high temperature heat treatment. We have not been able to explain this phenomenon.

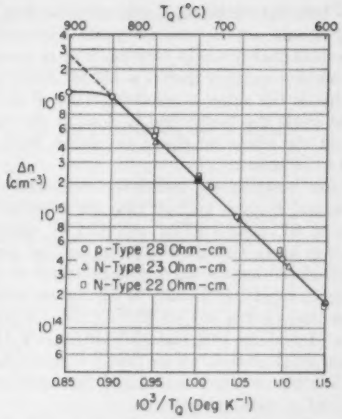


FIG. 3. Corrected data from Fig. 2 (see text).

Our data are scattered more at the lower temperatures than at the higher temperatures. This is to be expected since an error in measuring the Hall constant before quenching would have a greater effect on the low temperature results than on the high temperature results. We have found that if we make a small correction to the number of carriers in each sample before quenching, the data will almost all fall on a straight line (Fig. 3) and at temperatures below 840°C this straight line will fit Eq. (11) with $\exp(\Delta s/k) = 0.96$ and $\Delta H = (1.45 \pm 0.05)$ ev.

The leveling off at the higher temperatures is probably due to the fact that at high temperatures equilibrium is reached in a time which is short compared to the time that the sample takes to cool to low temperatures in the quenching bath. This seems reasonable because other workers whose systems did not quench as rapidly as ours found the leveling off at lower temperatures.

Our values of $\Delta n$ are roughly equal to those of Fuller, Theuerer, and van Roosbroeck[8] (see Sec. III). However, our data gives a better value for $\exp(\Delta s/k)$ and a higher value for $\Delta H$.

## VI. MISCELLANY

As pointed out in Sec. II, there is a deficiency of electrons around a vacant lattice site and the vacant site can act as an acceptor of electrons. We have assumed that each vacancy accepts but one electron, whereas a vacant site may be able to accept a maxi-

mum of four electrons and, if this were the case, each vacancy should act as four acceptors. However, we would expect that it would take much more energy to doubly ionize a vacancy than it would for single ionization. This is the same as assuming that of the four acceptor levels the lowest one is close to the valence band and the others lie above any donor levels that happen to be present.

The low temperature resistivity measurements of DeSorbo and Dunlap[4] indicate that the acceptor levels introduced by rapid cooling are 0.03 ev above the conduction band. Calculations based on the work of Longini[12] show that for acceptor levels 0.03 ev above the valence band the fraction of un-ionized acceptors at room temperature will be $10^{-3}$ for $(N_a-N_d)=10^{16}$; $10^{-4}$ for $(N_a-N_d)=10^{15}$; and $10^{-5}$ for $(N_a-N_d)=10^{14}$. From these calculations we see that it is safe to assume that all acceptor levels introduced by rapid cooling are ionized at room temperature.

If the diffusion process for chemical impurities in germanium is a vacancy mechanism, we can make an estimate as to the temperature dependence of the diffusion coefficient. The diffusion coefficient can be represented as $D=D_0\exp(-W/kT)$. For a vacancy mechanism of diffusion $W=E'+E''$, where $E'=\Delta H$, the energy that has to be supplied to form a Schottky defect, and $E''$ is the height of the potential barrier that a diffusing atom must pass through or over in moving from a normal lattice site to an adjacent vacant lattice site. From our data $E'=1.49$ ev and the measurements of Fuller, Theuerer, and van Roosbroeck (see Sec. III) indicate that $E''=0.5$ ev for self-diffusion in germanium. Hence the "activation energy" for self-diffusion in germanium should be about $(2.0\pm0.1)$ ev. The activation energy for diffusion of impurities in germanium would depend on the value of $E''$ for these impurities. It is reasonable to assume that for those impurities that fit into the normal lattice sites of germanium (the Group III and V elements) $E''$ would not be too much different from the value for self diffusion. Dunlap[13] reports a value of $W=2.5$ ev for the diffusion of antimony in germanium compared with our estimated value of $(2.0\pm0.1)$ ev for self-diffusion. Our, comments in Sec. III indicate that if the experiments of Fuller, Theuerer, and van Roosbroeck are in error, the correct value should be higher than the 0.5 ev they report. If this is true our estimate of the activation energy for self-diffusion will be raised closer to the value that Dunlap reports for the diffusion of antimony in germanium.[14]

The early part of this work was carried out in collaboration with Mr. R. E. Brown and we wish to thank him for the many valuable suggestions he made at that time. Thanks are also due to Drs. R. L. Longini and C. Zener who contributed many useful ideas.

## APPENDIX

### Effect of Adding an Ionized Vacancy on the Number of Conduction Band Electrons and Valence Band Holes

If there are $n_e$ electrons in the conduction band and $p_v$ holes in the valence band then

$$n_e p_v = A(T), \tag{1}$$

where $A(T)$ depends only on temperature. If we add $n_s$ ionized vacancies to a crystal then

$$n_s + n_e = p_v. \tag{2}$$

Substituting (2) in (1) we find

$$p_v^2 - n_s p_v - A(T) = 0, \tag{3}$$

and solving this by the quadratic formula

$$p_v = \frac{n_s}{2} + \tfrac{1}{2}[n_s^2 + 4A(T)]^{\frac{1}{2}},$$

$$\delta p_v = \delta n_s/2, \tag{4}$$

since $n_s^2 \ll A(T)$. Using (4), (2) gives us

$$\delta n_e = -\delta n_s/2.$$

*Note added in proof:*—Recently Fuller and Struthers (Phys. Rev. **87**, 526 (1952)) have published evidence that thermal acceptors in germanium may be due to the presence of copper as an impurity.

[12] R. L. Longini, Westinghouse Research Report R-94416-3-D (1951) (unpublished).

[13] W. C. Dunlap, Jr., Phys. Rev. **86**, 615 (1952).

[14] C. Fuller has recently [Phys. Rev. **86**, 1936 (1952)] published the results of measurements on the diffusion coefficients of arsenic and antimony in germanium. He finds an "activation energy" of 2.2 ev which is to be compared with our estimated value of $(2.0\pm0.1)$ ev. If "probable errors" were given for Fuller's measurement of the activation energy for diffusion of impurities in germanium and for Fuller, Theurer, and van Roosbroeck's measurement (reference 8) of the activation energy for diffusion of vacancies in germanium, our estimate of the activation energy for self diffusion in germanium would undoubtedly agree within the probable errors with Fuller's measurement of the activation energy for impurity diffusion in germanium. This is a strong indication that the mechanism of diffusion in germanium is a vacancy mechanism.

# Anelastic Measurements of Atomic Mobility in Substitutional Solid Solutions*

A. S. Nowick†
*Institute for the Study of Metals, University of Chicago, Chicago, Illinois*

(Received July 29, 1952)

A recently developed method for obtaining atomic mobility in solid solutions from the rate of anelastic relaxation makes possible the measurement of mobilities at temperatures far below those at which conventional diffusion experiments can be carried out. It is shown that the anelastic effects obtained in substitutional solid solutions are due to a phenomenon of stress-induced ordering and that the relaxation rate is determined primarily by the rate of movement of the slower atomic species. This method is applied to a series of silver-zinc solid solutions (silver rich) and the relaxation time measured as a function of temperature and concentration. The results show a slight deviation from an Arrhenius law, but a mean heat of activation may be obtained for each alloy concentration. Values for the heat of activation as a function of zinc concentration range from 36.1 kcal/mole at 15.8 atom percent zinc to 32.5 kcal/mole at 30.2 atom percent zinc. The entropy of activation, in each case, is positive and in reasonable agreement with Zener's "strain theory." A correlation of the magnitude of the anelastic effects for various specimens of the same composition with the rigidity modulus of these specimens, shows that the contribution to the torsional anelasticity from grains with ⟨111⟩ direction close to the specimen axis is much larger than from grains aligned in the ⟨100⟩ direction.

## I. INTRODUCTION

THE only widely-used method for the determination of atomic mobility in metals and alloys is the diffusion experiment, which measures the manner in which a concentration gradient changes with time. It is therefore not surprising that the study of atomic mobility in metals is most often classified under the heading of "diffusion." In substitutional solid solutions, the rate of interdiffusion of two different atomic species is expressed in terms of the diffusion coefficient, $D$, measured in an experiment in which there is an initial chemical concentration gradient. Aside from a thermodynamic correction,[1] this diffusion coefficient is related to an appropriate atomic jump rate, $\Gamma$, by the equation

$$D=\beta a^2\Gamma, \tag{1}$$

where $a$ is the lattice parameter and $\beta$ is a numerical coefficient determined by the geometry of the lattice. (For diffusion in f.c.c. solid solutions[2] the value of $\beta$ is 1/12.) The well-known experiments of Kirkendall,[3] and of da Silva and Mehl[4] show that the rate of movement of the two atomic species, say $A$ and $B$, during an interdiffusion experiment are not the same, at least for several f.c.c. alloys. The "appropriate" interdiffusion jump rate, $\Gamma$, that appears in Eq. (1) may be related under suitable assumptions, to the mean frequency of jump of $A$ atoms and of $B$ atoms ($\Gamma_A$ and $\Gamma_B$, respectively) by the relation[5]

$$\Gamma=f_B\Gamma_A+f_A\Gamma_B, \tag{2}$$

where $f_A$ and $f_B$ are the mole fractions of $A$ and $B$, respectively. When neither of the mole fractions is much less than unity, the quantity $\Gamma$ is determined, essentially, by the rate of movement of the faster diffusing component.

From statistical-mechanical considerations, it may be shown[6] that, regardless of the mechanism of the elementary atomic jump, the quantities $\Gamma_A$ and $\Gamma_B$ may be expressed in the form[7]

$$\Gamma_i=z\nu_i e^{-\Delta G_i/RT}, \tag{3}$$

($i=A$ or $B$), where $z$ is the coordination number of the lattice (the number of nearest neighbor sites), $\nu_i$ the appropriate atom vibration frequency, $R$ the gas constant, $T$ the absolute temperature and $\Delta G_i$ the isothermal work required to carry the elementary diffusion process (for the appropriate type of atom) into the saddle configuration. The quantity $\Delta G_i$ is, therefore, a thermodynamic potential and may be separated into enthalpy and entropy terms according to

$$\Delta G_i=\Delta H_i-T\Delta S_i. \tag{4}$$

When Eq. (4) is substituted into (3), the quantity $\Gamma_i$ assumes the form of an Arrhenius equation:

$$\Gamma_i=\Gamma_{i0}e^{-\Delta H_i/RT};\quad(\Gamma_{i0}=z\nu_i e^{\Delta S_i/R}). \tag{5}$$

If we write an analogous equation for the quantity $\Gamma$ of Eq. (1), a corresponding Arrhenius equation for $D$ is obtained:

$$D=D_0e^{-H/RT};\quad(D_0=\beta a^2 z\nu e^{\Delta S/R}). \tag{6}$$

The quantities $H$ and $\Delta S$ that appear in this equation are termed, respectively, the "heat and entropy of activation for diffusion." In view of Eq. (2) and the fact that $\Gamma_A$ and $\Gamma_B$ obey Eq. (5) with (in general)

* This research has been supported in part by the ONR.

† Now at Hammond Laboratory, Yale University, New Haven, Connecticut.

[1] A. D. Le Claire, *Progress in Metal Physics. I* (Interscience Publishers, Inc., New York, 1949), Chapter VII (B. Chalmers, Editor).

[2] A. D. Le Claire, Phil. Mag. **42**, 673 (1951).

[3] A. D. Smigelskas and E. O. Kirkendall, Trans. Am. Inst. Mining Met. Engrs. **171**, 130 (1947).

[4] L. C. C. da Silva and R. F. Mehl, Trans. Am. Inst. Mining Met. Engrs. **191**, 155 (1951).

[5] L. S. Darken, Trans. Am. Inst. Mining Met. Engrs. **175**, 184 (1948).

[6] C. Zener, J. Appl. Phys. **22**, 372 (1951).

[7] The symbol $\Gamma$ is used by Zener to represent the probability per second for an atom to jump into a specific nearest neighbor site. It, therefore, differs from the present definition by the factor $z$.

$\Delta H_A \neq \Delta H_B$, it is clear that Eq. (6) is only an approximation to the temperature dependence of the interdiffusion coefficient. Zener has shown[6] that it is quite reasonable to expect that the quantity $\Delta S$, appearing in Eq. (6), will be positive. Furthermore, he shows that, if we associate a major part of the isothermal work to produce activation with elastic straining of the surrounding lattice, then

$$\Delta S \approx -(H/\mu_0)d\mu/dT, \tag{7}$$

where $\mu$ is the shear modulus ($\mu_0$ at $T=0$).

In order to check this "strain theory" of $\Delta S$ and to obtain reliable values of $H$ with which to compare theoretical predictions, precise measurements of $D$ as a function of temperature are required, and over as wide a temperature range as possible. Actually, many of the values of $D_0$ reported in the literature are probably too low[8] by factors of $10^2$ to $10^4$ and the corresponding reported values of $H$ are greatly in error. Much of the difficulty in obtaining precise values of $H$ and $D_0$ is due to the limited range of temperature in which diffusion methods may be used for the study of atomic mobility. The limitations of diffusion experiments may be explained as follows. Since atom movement is a random walk problem, the mean distance that an atom travels from its starting point is proportional to the square root of the number of atomic jumps. Thus, in order that diffusion take place, even over distances of the order of 0.1 mm, the mean number of atomic jumps required is about $10^{11}$. If such a large number of jumps is to take place within a reasonable time limit, the jump frequency must be very great; an experiment conducted under conditions where the mean time of stay of atoms is greater than $10^{-4}$ sec is a practical impossibility. Diffusion experiments are therefore limited to a narrow range of temperatures close to the melting point. The corresponding available range of values of $D$ is usually only two to three powers of ten.

In addition to the difficulty in obtaining precise values of $D_0$ and $H$, the restriction of conventional diffusion experiments to high temperatures places important limits on the type of information that may be obtained by such methods. The following are some illustrations: (1) Diffusion in metals is generally described in terms of a vacancy mechanism.[9] If this mechanism is correct, there is much to be learned from a study of atomic movement under conditions where a nonequilibrium excess of vacancies is trapped by rapid quenching from a high temperature. If measurements are limited to high temperatures, such a vacancy excess cannot be maintained. (2) In order to study the effect of dislocations (cold work) on atomic mobility, it is necessary to carry out experiments below the recrystallization temperature. Such a temperature is too low for conventional diffusion experiments. (3) In the study of precipitation it is often desirable to measure the rate of atomic movements directly in the supersaturated solid solution. Such information cannot be obtained by diffusion experiments.

These limitations of conventional diffusion experiments can be overcome by a method that permits the measurement of atomic mobilities in a time of the order of that required for a single atomic jump, rather than for $10^{11}$ atomic jumps. Such a method is available through the measurement of anelastic effects resulting from stress-induced ordering in an initially disordered solid solution. The principle of the method is discussed in Sec. II, and is, briefly, as follows: The application of stress to a random solid solution will, in general, change the equilibrium configuration to a nonrandom one. Atomic redistribution must, therefore, follow the application of stress: this redistribution is accompanied by typical anelastic effects[10] such as an internal friction peak and an elastic after-effect. The relaxation time, $\tau$, for this redistribution, obtained from the measurements, is related to an appropriate atom jump frequency, $\Gamma_r$, by

$$1/\tau = \alpha\Gamma_r. \tag{8}$$

The dimensionless proportionality constant, $\alpha$, is of the order of unity, since the atomic redistribution, required in order that equilibrium be maintained, can be accomplished by a small number of atom jumps. By analogy to Eq. (5), $\Gamma_r$ may be assumed to obey an equation of the form

$$\Gamma_r = z\nu e^{\Delta S_r/R} e^{-H_r/RT}, \tag{9}$$

so that the relaxation time obeys the Arrhenius equation

$$\tau = \tau_0 e^{H_r/RT}. \tag{10}$$

The appropriate jump rate, $\Gamma_r$, is, in general, not the same as the quantity $\Gamma$ that appears in Eq. (1). Its relation to the individual jump rates, $\Gamma_A$ and $\Gamma_B$, will be discussed in Sec. II.

This method for obtaining atomic mobility by the measurement of anelastic relaxation has been used extensively in the study of the mobility of interstitial solutes in b.c.c. lattices.[11] In the latter case, the application of stress results in the preferential occupation of certain interstitial sites at the expense of others, a form of stress-induced ordering. The details of the process are sufficiently straightforward to permit an exact calculation of the quantity $\alpha$ of Eq. (8); the result[12,13] is $\alpha = 3/2$. The quantity $\Gamma_r$ in this case is simply the mean number of jumps, per unit time, of an interstitial atom; the mobility of the solvent atoms does not, of course, enter into consideration. The combination of the results of relaxation measurements

[8] A. S. Nowick, J. Appl. Phys. **22**, 1182 (1951).
[9] H. B. Huntington, *Atom Movements* (American Society for Metals, Cleveland, 1951), p. 69.
[10] C. Zener, *Elasticity and Anelasticity of Metals* (The University of Chicago Press, Chicago, 1948).
[11] C. Wert and C. Zener, Phys. Rev. **76**, 1169 (1949); C. Wert, Phys. Rev. **79**, 601 (1950); J. Appl. Phys. **21**, 1196 (1950).
[12] D. Polder, Philips Research Repts. **1**, 1 (1945).
[13] A. S. Nowick, chapter on "Internal friction in metals" to be published in *Progress in Metal Physics IV*.

at relatively low temperatures, with those of conventional diffusion experiments, at relatively high temperatures, makes possible very precise determination of the quantities $H$ and $D_0$, of Eq. (6), for these interstitial systems. Detectable anelastic effects are obtained even for solute concentrations well below 0.01 percent.

The existence of analogous anelastic effects in substitutional solid solutions offers the possibility for a very much enlarged applicability of anelastic measurements to the study of atomic mobility. Such anelastic effects were first observed by Zener,[14] as an internal friction peak in a single crystal of alpha-brass (30 percent zinc). These measurements were only at one frequency (about 600 cps) and for only the one composition, and the origin of the effect was not explained at the time. Later Kê[15] verified the existence of such an internal friction peak in 70–30 brass at lower frequencies, and obtained a heat of activation for the relaxation process in reasonable agreement with the heat of activation for diffusion of zinc in brass. A possible mechanism for the observed anelastic effects in brass was suggested by Zener.[16] This is the mechanism of pair reorientation, which will be discussed in the next section; it will be shown that this mechanism is an oversimplification. On the basis of the concept of pair reorientation, Le Claire[5] calculates the quantity $\alpha$ [Eq. (8)] and interprets $\Gamma$, as the jump frequency of zinc atoms in brass. He then correlates the anelastic measurements with conventional diffusion measurements for the case of 70–30 brass.

Inasmuch as the only previous anelastic measurements of atomic mobility in substitutional alloys are for one alloy composition, and even these measurements cover only a limited range of relaxation times, the present work is undertaken in order to obtain relaxation data over a wide range and for a series of compositions. In this way it is hoped to utilize anelastic measurements to obtain precise knowledge of the concentration and temperature dependence of atomic mobility, and to learn more about the mechanism of the relaxation process. The alpha-silver-zinc solid solutions are used, for this study, in preference to the alpha-brasses. The reason for this choice lies in the fact that the difference in atomic radii of silver and zinc is about twice the difference in the radii of copper and zinc, yet the solubility of zinc in copper and in silver is very nearly the same (in atom percent). Inasmuch as the magnitude of the anelastic effects, for a given concentration of solute, is anticipated to depend strongly on the difference in atomic radii of solute and solvent,[10,16] the effects in silver-zinc may be several times larger than in brass of the same composition. This increased magnitude is particularly desirable in dealing with relatively low concentrations of solute, when the anelastic effects tend to become very small.

The use of anelastic methods for the study of atomic mobility in substitutional solid solutions makes possible measurements at temperatures considerably below those at which conventional diffusion measurements could be carried out. As a result, the limitations of diffusion measurements, discussed earlier, can be overcome. For example, it is possible, by the relaxation method, to detect the presence of a nonequilibrium number of vacancies produced by quenching. A preliminary report of this work has appeared[17] and further details will be given in a subsequent paper. In addition to the fact that the relaxation method makes possible measurements at low temperatures, it also has the advantage that it uses an alloy of constant concentration; the interpretation of the measurements is, therefore, not complicated by the existence of a variable chemical concentration, as in interdiffusion experiments. (In this sense, the relaxation measurements are like radioactive-tracer diffusion experiments.)

The relaxation method has limitations of its own and, therefore, is not suggested as a method to replace diffusion studies, but simply to provide additional information that cannot be obtained from diffusion experiments. Among its disadvantages is the fact that it cannot be applied to pure metals and to alloys in which the two components have the same atomic radii. Even when the atomic size difference of the two components is sufficiently large, the method, as applied to substitutional solid solutions, is limited to relatively high solute concentrations, of the order of 10 percent.

## II. THEORY OF STRESS-INDUCED ORDERING

A discussion of *order* concerns itself with the distribution of different atomic species in a solid solution on various lattice sites. If there is any deviation from a completely random distribution in the manner in which lattice sites are occupied, the alloy is said to show a degree of order. The well-known[18] concepts of long-range and short-range order are special cases of this definition. The application of stress to a system may result in a change in the state of order, if one already exists, or it may produce a state of order in an initially disordered solid solution. In the present case we will consider that the solution is random for zero stress. From thermodynamic reciprocity,[19] it follows that the application of stress will produce a degree of order if, and only if, the production of order is accompanied by strain. Thus, for an applied stress, $\sigma$, the instantaneous value of the appropriate strain, $\epsilon$, is not only dependent on $\sigma$, but also on a parameter, $p$, which is a measure of the degree of order. The strain, at any instant, is, then, made up of two parts:

$$\epsilon = \epsilon' + \epsilon''. \tag{11}$$

[14] C. Zener, Trans. Am. Inst. Mining Met. Engrs. **152**, 122 (1943).
[15] T. S. Kê, J. Appl. Phys. **19**, 285 (1948).
[16] C. Zener, Phys. Rev. **71**, 34 (1947).
[17] A. S. Nowick, Phys. Rev. **82**, 551 (1951).
[18] H. Lipson, *Progress in Metal Physics. II* (Interscience Publishers, Inc., New York, 1950), Chapter I (B. Chalmers, Editor).
[19] See reference 10, p. 113, or reference 13.

The quantity $\epsilon'$ is the perfectly elastic strain which obeys Hooke's law

$$\epsilon' = \sigma/M, \tag{12}$$

where $M$ is called[10] the appropriate *unrelaxed modulus*. The *anelastic strain*, $\epsilon''$, may be assumed proportional to $p$, for small values of $p$, or

$$\epsilon'' = \lambda p, \tag{13}$$

where $\lambda$ is the constant of proportionality. For any value of $\sigma$, the quantity $p$ assumes an equilibrium value, $\bar{p}$, if sufficient time is allowed. The quantity $\bar{p}$ may be taken to be proportional to $\sigma$, at low stress levels. Correspondingly, the equilibrium anelastic strain, $\bar{\epsilon}''$, is proportional to $\sigma$. We may write

$$\bar{\epsilon}'' = \Delta_M \sigma/M, \tag{14}$$

where $\Delta_M$ is a dimensionless constant called the *relaxation strength*, which measures the magnitude of the anelastic effect. It is reasonable to assume that, at constant stress, the quantity $p$ approaches its equilibrium value, $\bar{p}$, according to a relaxation equation,

$$\dot{p} = -(p-\bar{p})/\tau, \tag{15}$$

where $\tau$ is the time of relaxation. The anelastic strain, therefore, also obeys the relaxation equation

$$\dot{\epsilon}'' = -(\epsilon'' - \Delta_M \sigma/M)/\tau. \tag{16}$$

When a harmonic solution is substituted into Eqs. (12) and (16), and the assumption $\Delta_M \ll 1$ introduced, the phase angle, $\phi$, by which strain lags behind the stress is found to be

$$\phi = \Delta_M \omega\tau/(1+\omega^2\tau^2), \tag{17}$$

where $\omega$ is the angular frequency with which the stress and strain vary. The quantity $\phi$ is a convenient measure of the internal friction;[10, 12] it is equal to the logarithmic decrement divided by $\pi$, and is also often represented by the symbol $Q^{-1}$, by analogy to electrical circuits. Equation (17) represents the well-known internal friction peak with maximum value at $\omega\tau = 1$. Rather than obtain the peak by variation of the frequency at constant $\tau$, it is more convenient experimentally to observe $\phi$ as a function of temperature, i.e., to vary $\tau$ [see Eq. (10)] and keep $\omega$ constant. If $T_m$ is the temperature of maximum damping, we then have

$$\tau(T_m) = 1/\omega \tag{18}$$

as the basis for the determination of $\tau$ at one particular temperature, $T_m$, from an internal friction peak. Although Eq. (17) is derived under the assumption $\Delta_M \ll 1$, and must be slightly modified[10] if this assumption is not valid, it may be applied without significant error up to $\Delta_M \cong 0.2$.

In order to obtain the relaxation time at different temperatures, internal friction measurements at various frequencies may be used conveniently, so long as the order of magnitude of $\tau$ is less than one second. To measure relaxation times somewhat greater than one second, static rather than oscillatory methods are best. One convenient static method is the elastic aftereffect, in which the specimen is subjected to stress and sufficient time allowed for the attainment of equilibrium. When the specimen is released the anelastic strain decays to zero exponentially, i.e., setting $\sigma = 0$ for $t > 0$ in Eq. (16), it follows that

$$\epsilon'' = \epsilon_0'' e^{-t/\tau}. \tag{19}$$

By observation of this exponential decay, $\tau$ may be obtained.

The simple relaxation Eq. (15) would be expected to hold when there is no fluctuation in the rate of atomic movement from one position to another in the crystal lattice. Actually, fluctuations in concentration result in a distribution of relaxation times, so that the internal friction peak does not strictly obey Eq. (17), but is equal to a weighted sum or integral of such terms over a narrow range of values of $\tau$. The peak width is then greater than that predicted by Eq. (17). Similarly the elastic after-effect is no longer the simple exponential decay of Eq. (19), but a sum of such terms.

In order to relate the measured relaxation time to the atomic mobility in substitutional solid solutions in which the jump rates of the two components, $\Gamma_A$ and $\Gamma_B$, are not the same, it is necessary to calculate the quantity $\alpha$ and to interpret the quantity $\Gamma_\tau$ of Eq. (8). To achieve this end, it is desirable to know what is the nature of the ordering induced by stress in such a solid solution. The only suggestion, thus far, is Zener's concept of pair reorientation,[16] which may be summarized as follows: In a lattice of cubic symmetry, the elastic distortion produced by a single solute atom, which differs in size from the solvent atoms, must have cubic symmetry. On the other hand, a *pair* of solute atoms in nearest neighbor positions produces tetragonal distortion about the direction of the pair axis. Zener therefore proposes that pairs of solute atoms, which have their axes randomly distributed over permissible crystallographic directions under zero stress, will tend to be aligned preferentially when a shear or tensile stress is applied to the lattice. The total number of pairs is assumed fixed. The attempt of the lattice to maintain equilibrium when the stress is varied, results in the observed anelastic effects. This stress-induced preferential orientation of pairs of atoms is a form of stress-induced ordering. The type of order involved does not fall into the category of either long-range or short-range order, for it is assumed that the pairs themselves are formed by random fluctuation; the preference of pair axes for special directions is, nevertheless, a deviation from randomness and therefore a form of ordering. The emphasis on pairs of solute atoms also shows why large concentrations of solute are required to produce observable anelastic effects in substitutional solutions as compared to b.c.c. interstitial

solid solutions. In the latter case, individual solute atoms produce tetragonal distortion.

The description of the relaxation phenomena in substitutional solutions in terms of the reorientation of solute atom pairs cannot be taken too seriously for several reasons. The "pair" concept is probably most nearly satisfactory at low solute concentrations, where most solute atoms are far apart and the number of pairs is quite small. Even in such a dilute solution, where the anelastic effects are probably too small to be observed, it may not be correct to think in terms of a fixed number of pairs of solute atoms, since a tendency toward preferential creation or dissolution of nearest neighbor pairs may occur under stress; also, the effect of next-nearest neighbors in producing relaxation effects must be considered. In actual measurements, solutions containing as high as $\frac{1}{3}$ solute atoms are used; here clusters of solute atoms considerably more complex than pairs occur with great frequency. The behavior of such clusters under stress cannot properly be taken into account in terms of a theory of reorientation of solute pairs. Finally, the theory of reorientation of "solute" atom pairs under stress focuses attention on the movement of solute atoms as the rate controlling process. Thus, Le Claire,[3] using the pair reorientation concept, considers that relaxation is controlled by the mobility of the solute (zinc) atoms in 70–30 brass. It will be seen, from the subsequent discussion, that this belief may be incorrect.

The concept of pair reorientation, therefore, seems to be an oversimplification. Even without suggesting an alternate mechanism for the observed anelasticity in substitutional solutions, we can be reasonably certain that the phenomenon is one of stress-induced ordering, controlled by atomic movements within the crystal lattice. In the first place these effects are observed in well-annealed single crystals, and the results are not structure sensitive. The possibility that the observed phenomena are related to the presence of internal surfaces or of dislocations is therefore discounted. The fact that the width of the internal friction peak corresponds closely to a single time of relaxation, also indicates that we are dealing with a volume (or bulk lattice) property. Secondly, these anelastic effects are only observed in alloys, and are, apparently, larger the greater the atomic size difference of solute and solvent atoms. Finally, the heat of activation for the process is of the same magnitude as that for volume diffusion. In view of this evidence, it seems fairly certain that the relaxation is controlled by atomic movements in the lattice, which act to produce an ordered condition of the alloy under an applied stress.

In order to evaluate theoretically the constant $\alpha$ of Eq. (8), and to calculate the relation between the rate determining frequency for relaxation, $\Gamma_r$, and the individual jump rates $\Gamma_A$ and $\Gamma_B$, it is necessary to know more precisely the nature of the ordering induced by stress. In the absence of a detailed picture of stress-induced ordering, it is still possible to show which of the individual jump rates is rate determining under limiting conditions, and to obtain an approximate relation of more general validity. Let us assume that atomic movement occurs primarily by means of vacancies. It is reasonable to expect that the normal vacancy concentration is far too small for any relaxation effects to be observable as a consequence of a preferential distribution of the vacancies themselves. Vacancies will therefore contribute to the relaxation process only through their ability to produce a redistribution of $A$ and $B$ atoms. The relative probabilities for an $A$ atom and a $B$ atom to move into a given vacant lattice site are $f_A\Gamma_A$ and $f_B\Gamma_B$, respectively. Consider the limiting condition where one of these probabilities is much greater than the other, say, $f_B\Gamma_B \gg f_A\Gamma_A$. Then in most cases, when a $B$ atom moves into a neighboring vacancy, the vacancy which then appears in the original site of the $B$ atom will subsequently be filled by another $B$ atom. In this way no contribution is made to the redistribution of atoms, necessary for the relaxation process. Only on those relatively rare occasions when an $A$ atom makes a jump, does a redistribution in the occupation of lattice sites occur. Thus if $f_B\Gamma_B \gg f_A\Gamma_A$, the movement of $A$ atoms is rate determining for the relaxation process. This means that the rate of relaxation is determined either by the component present in the much smaller amount, or if, as in these experiments, $f_A$ and $f_B$ are of the same order of magnitude, by the slower moving component. When the relative probabilities $f_A\Gamma_A$ and $f_B\Gamma_B$ are of the same order of magnitude, an approximate formula for the rate-determining factor may be obtained as follows. We define a *replacement* as the movement of a $B$ atom into a vacant lattice site formerly occupied by an $A$ atom, or of an $A$ atom into a former $B$ site. It seems reasonable to regard the replacement as the unit process that leads to atomic redistribution. It is readily shown that the probability per second, $\Gamma_{rep}$, for the occurrence of a replacement at any given lattice site is given by

$$\frac{2}{\Gamma_{rep}} = \frac{1}{f_A\Gamma_A} + \frac{1}{f_B\Gamma_B}. \tag{20}$$

In deriving this equation, the possibility that the next jump after a replacement might be the reverse of the previous jump is neglected. The correction for such a possibility is small, of the order of the reciprocal of the coordination number. From Eq. (20) the rate of replacement reduces essentially to the rate of movement of the slower component when the two atomic jump rates differ in order of magnitude, in agreement with the previous discussion. (It should be noted that the rate determining component need not be the solute.) If we assume that the rate of a replacement is essentially the relaxation rate, then Eq. (20) parallels Eq. (2). The main difference between the two cases is that the faster

moving component controls the diffusion rate, while the slower component controls the relaxation rate. This fact must be considered when one attempts to relate relaxation and diffusion measurements for the same alloy.

In view of the dependence of the quantity $\Gamma_r$, in general, on both $\Gamma_A$ and $\Gamma_B$, the Arrhenius equations (9) and (10) are [in the same way as Eq. (6)] only approximately valid.

## III. PREPARATION OF SPECIMENS

The silver-zinc specimens used in this investigation were prepared by melting electrolytic silver and high purity zinc in graphite crucibles under charcoal. Each casting was given a homogenizing anneal, after which it was reduced in diameter by rolling and swaging. Specimens in the form of rods $\frac{1}{4}$ and $\frac{1}{8}$ inch in diameter were saved for high frequency measurements and the remainder drawn down to wire 0.032 inch in diameter, for use in the torsion pendulum. In order to grow coarse-grained specimens a special annealing procedure was used for both the wire and rod specimens: the specimens were sealed in vacuum and heated from 220°C to 700°C over a period of two days, then left at 700°C for five days. To obtain a final grain size larger than the specimen diameter, it was necessary to start with vacuum remelted silver, so as to remove traces of oxygen.

The percent of silver in the various specimens was determined by conventional gravimetric analysis.

## IV. EXPERIMENTAL METHODS

The "high frequency" internal friction measurements are obtained using equipment similar to that described by Kê,[20] but modified in details. This method uses a magnetic drive and pickup; an audio-oscillator supplies the driving power and a tuned amplifier serves as a detector. Soft iron pole pieces are attached to flattened ends of the specimens, facing downward, so that flexural vibrations are produced. The fundamental frequency of the $\frac{1}{4}$-inch specimens (about 4 inches long) is about 1300 cps, while that of the $\frac{1}{8}$-inch specimens (about 6 inches long) is about 300 cps. Specimens are supported horizontally at the nodes of vibration. Internal friction is obtained from the half-width of the amplitude resonance curve for forced vibration. All measurements are made in air, at temperatures below 450°C. The fact that the measurements did not change with time indicates that no appreciable zinc loss took place during the experiments and that the surface oxidation that occurred did not affect the measurements. This latter result is not surprising in view of the fact that the internal friction is interpreted as arising from volume atomic mobility.

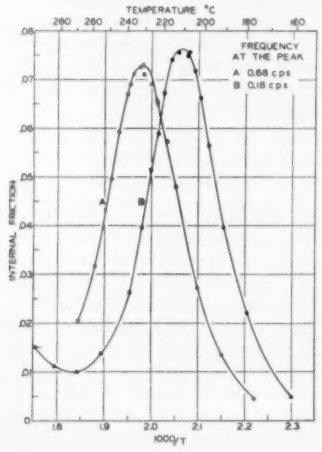


FIG. 1. Internal friction as a function of temperature, at two different frequencies, for a 70–30 silver-zinc solid solution.

The "low frequency" internal friction measurements are obtained in a torsion pendulum, in which the wire specimens serve as the suspension, by the free decay method. This apparatus is well known.[21] The frequency range of 0.2 to 2.0 cps is conveniently obtained by varying the inertia number.

Elastic after-effect measurements are made in the same apparatus as the low frequency internal friction, so modified that in place of the inertia member there is an arrangement that permits the twisting of the wire through a few degrees and its release at any desired time. The measurements consist in the determination of the residual strain after the wire is released, as a function of time. If the anelastic behavior were describable in terms of a single time of relaxation [Eq. (16)], the elastic after-effect would obey Eq. (19). One could then obtain $\tau$ in several ways—as the time for the anelastic strain to fall to $1/e$ of its initial value, from the slope of a plot of log strain against time, or from the inflection point in a plot of linear strain *versus* log time. The last method is particularly convenient because it does not require a knowledge of the initial deflection of the wire and of the final position after relaxation is complete. (The latter is especially hard to determine when grain-boundary relaxation occurs in addition to the stress-induced ordering phenomenon.) Actually, the anelastic behavior cannot be described in terms of a single time of relaxation, but shows a distribution of relaxation times, as discussed in Sec. II. Under these circumstances, it is readily shown that the time at the point of inflection, in a plot of strain against log time, is equal to a properly weighted average of the distribution of relaxation times. Thus, the average $\tau$ is best obtained by this method. Similarly, in the internal friction measurements, the time of relaxation, as

[20] T. S. Kê, J. Appl. Phys. **20**, 1226 (1949).
[21] T. S. Kê, Phys. Rev. **71**, 533 (1947).

obtained from Eq. (18), represents the same weighted average of the distribution of relaxation times.

The measurement of temperature in both the high frequency and torsion apparatus is by means of a calibrated chromel-alumel thermocouple placed close to the center of the specimen. The variation of temperature over the length of the wire in the torsion equipment is about 2°C at 300°C. The temperature is controlled within $\pm\frac{1}{2}$°C by means of an electronic proportioning temperature controller.

Measurements of the rigidity modulus are obtained from the frequency of torsional vibration of wires at various temperatures. The modulus is proportional to the square of the vibration frequency, except for a small correction for thermal expansion of the wires as the temperature is varied. The rigidity modulus is always measured at temperatures below those at which the internal friction becomes appreciable, to avoid the contribution attributable to relaxation.[10]

In all measurements of internal friction and rigidity modulus the maximum shear strain is less than $10^{-6}$. Under such conditions, internal friction and vibration frequency are found to be independent of the amplitude of vibration.

## V. EXPERIMENTAL RESULTS

### A. Relaxation Measurements

The anticipated large relaxation effects in silver-zinc alloys are readily demonstrated by low frequency internal friction measurements. Figure 1 shows the results of measurements in a torsion pendulum at two different frequencies, on a specimen containing 30 atomic percent zinc. The height of these internal friction peaks is about seven times the height of peaks observed[15] in 70–30 brass at similar frequencies. From the frequency and temperature at the maximum, the corresponding relaxation time is obtained from Eq. (18). A series of peaks are obtained at essentially the same frequency for different silver-zinc solid solutions; these data are shown in Fig. 2. The result of decreasing the concentration of zinc is a rapid decrease in the peak height, and a shift of the peak to higher temperatures. The latter effect means that, at a given temperature, the relaxation time is lower the higher the concentration of zinc. The change in the height of the peak with concentration is to be expected because the degree of ordering induced by stress should fall off rapidly as the concentration of zinc decreases, regardless of the mechanism of the ordering. From Fig. 2 it appears as if the peak height, and therefore the relaxation strength, $\Delta_M$, varies approximately as the square of the concentration of zinc. It should be noted that when the height of the peak is sufficiently small (curve *D* of Fig. 2) grain-boundary relaxation[31, 10] contributes to the internal friction at high temperatures and distorts the "mobility" peak. Such grain boundary effects are at a minimum in Fig. 2 because the specimens from which

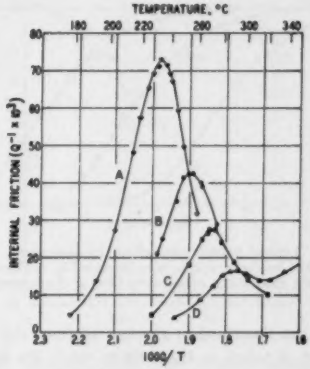


FIG. 2. Internal friction measurements, at a frequency of about 0.7 cps, for a series of silver-zinc solid solutions. The atomic percent zinc in the four alloys is 30.2, 24.2, 19.3, and 15.8, corresponding to the curves *A* to *D*, respectively.

these data are obtained are prepared in such a way (described in Sec. III) as to produce grains larger than the specimen diameter. In such specimens the grain boundary internal friction occurs at higher temperatures and is smaller in magnitude than the corresponding effects in finer grained specimens.

Measurements were also obtained for finer grained specimens, obtained when the silver used in preparation of the alloys was not vacuum remelted, and also when lower final annealing temperatures were used. In addition to the fact that the grain boundary internal friction in these specimens is more pronounced, so that the curves even for the 70-30 composition assume a shape somewhat like that of curve *D* of Fig. 2, the height of the mobility peak is also observed to be lower in these finer grained specimens. For example, for 70-30 silver-zinc, peak heights ranging from 0.04 to 0.073 are observed, the highest peaks being obtained from the coarsest grained specimens. On the other hand, the location of the internal friction peak at a given frequency, which determines the relaxation time, is found to be the same for all specimens of the same composition within experimental error. Apparently, the relaxation strength may depend on factors other than the composition, but the relaxation time is completely insensitive to structural differences which arise from the method of preparation.

The range of values of relaxation time that may be obtained by internal friction measurements in the torsion pendulum are very limited. In order to measure much shorter relaxation times (at higher temperatures) the high frequency measurements are employed; to measure much larger values of $\tau$, the elastic after-effect method is used. Typical measurements of the elastic after-effect, for the same specimen as used for Fig. 1, are presented in Fig. 3. The method of plotting the

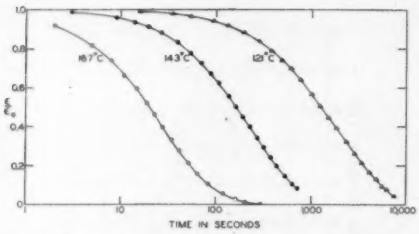


FIG. 3. Typical elastic after-effect measurements, at three temperatures, on the same specimen used for Fig. 1. The relaxation time, in each case, is the value of the time at the inflection point.

data is that described in the last section; the time of relaxation is taken as the time to reach the inflection point.

By the use of low and high frequency internal friction and elastic after-effect measurements, it is possible to cover a range of relaxation times from $10^{-4}$ to about 2000 seconds, i.e., more than seven logarithmic cycles. The combined data for relaxation time as a function of the reciprocal of the absolute temperature is given in Fig. 4, for solid solutions of four different compositions. The dependence on concentration is very striking; a ten percent increase in the atomic percent zinc increases the relaxation time at a given temperature by about a factor of ten. A straight line is drawn for each composition, but it is clear that there is a regular deviation from a simple Arrhenius law. This deviation means that the effective heat of activation is a function of temperature. It has been customary to assume that $H$ is a constant in diffusion studies (except when grain boundary diffusion plays a significant role), but this assumption is only used because the precision and range of conventional diffusion data does not permit one to detect such deviations. The slopes of the straight lines shown in Fig. 4 give a mean value for the heat of activation over the temperature range of these experiments. These mean values, $H_r$, and the corresponding mean intercepts, $\tau_0$ [see Eq. (10)], are given in Table I, for the various compositions. Examination of the values of the intercepts shows that the four straight lines when extrapolated to $T^{-1}=0$, meet almost at a point, within one-tenth of a logarithmic cycle. Consequently, the variation of relaxation time (and, therefore, of atomic mobility) with concentration is attributable almost entirely to the quantity $H_r$, and practically not at all to the quantity $\tau_0$ of Eq. (10). The values $H_r$ are plotted as a function of concentration, in Fig. 5. Within the precision of the measurements a straight line may be drawn through these four points. It is interesting to note that this line extrapolates to 40.2 kcal/mole at zero concentration, and not to 46 kcal/mole, the value obtained from self-diffusion of pure silver.

Knowing the values of the heat of activation, we may compare the widths of the observed internal friction peaks with the theoretical width at half-maximum,

$$\delta(1/T)=2.62R/H,$$

which may be obtained from Eqs. (17) and (10). In this way we have a measure of the extent of deviation from a single time of relaxation. It is found that the observed peaks are 15 to 20 percent wider than the theoretical value. This is about the same magnitude as the deviation from a single time of relaxation in the study of the mobility of interstitial solutes.[23]

### B. Measurements of Rigidity Modulus

Relative values of the rigidity modulus at room temperature are obtained for the various wire specimens used in the relaxation experiments already described. These include those specimens of the same composition that had been given different treatments in preparation, resulting in differences both in grain size and in the heights of the observed internal friction peaks. A correlation is found to exist between the rigidity modulus and the height of the internal friction peak, the highest values of the modulus being observed for the specimens that show the lowest peaks. The range of variation of the rigidity modulus, observed for

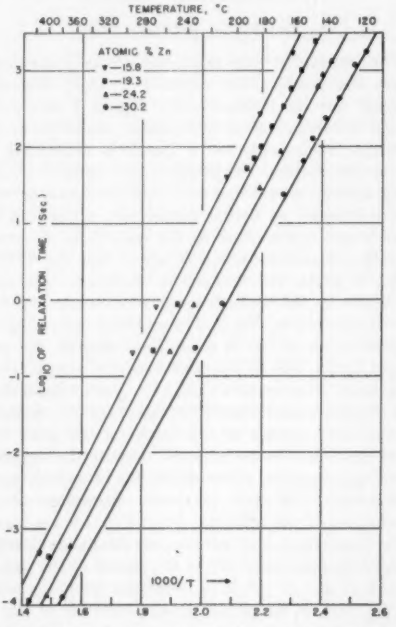


FIG. 4. The variation of the time of relaxation for stress-induced ordering with temperature, for a series of silver-zinc solid solutions.

[23] See C. Wert and C. Zener, reference 11.

different specimens of the same concentration, is 16 percent. Such large variations in the modulus cannot be accounted for by differences in such factors as dislocation density or by the presence of impurities, but is undoubtedly a consequence of differences in the degree of preferred orientation of the grains that compose the specimen.

Inasmuch as Eq. (7) for the entropy of activation, $\Delta S$, involves the quantity $\mu_0^{-1}(d\mu/dT)$, this quantity is obtained experimentally for the various alloys, by measurement of the temperature dependence of the frequency of torsional vibration between room temperature and 200°C. Above 200°C relaxation effects produce deviations from the linearity of the curve of rigidity modulus *versus* temperature. The values of $\mu_0^{-1}(d\mu/dT)$ are practically the same for all specimens of a given composition, i.e., not dependent on the degree of preferred orientation. These values are listed in Table I; the value obtained from measurements on a wire of high purity silver are also included for comparison. Within the error of the measurements, the tabulated values may be regarded as independent of the concentration of zinc.

## VI. DISCUSSION

The measurements of relaxation time as a function of temperature and composition show that the atomic mobility in silver-zinc solid solutions is strongly concentration dependent. The only previous data for concentration dependence of atomic mobility are obtained by Matano analysis of the results of an intermetallic diffusion experiment.[32] Such data are never precise enough to make possible a reliable determination of the heat of activation as a function of concentration. The present experiments trace the strong concentration dependence of the relaxation time to the variation of the mean heat of activation with zinc concentration, and indicate that the quantity $\tau_0$, Eq. (10), is practically independent of concentration.

In view of the concentration dependence of the mean activation energy, it is not surprising that the curves of Fig. 4 are not straight lines, and also that the anelastic effects are not describable in terms of a single time of relaxation. Both of these facts may be explained in terms of statistical fluctuations in concentration

TABLE I. Results obtained from relaxation and rigidity measurements on silver-zinc alloys.

| Atomic percent Zn | $H_\tau$ kcal/mole | $-\log_{10}\tau_0$ ($\tau_0$ in sec) | $\mu_0^{-1}(d\mu/dT)$ (°K$^{-1}\times 10^6$) | $\alpha$ |
|---|---|---|---|---|
| 0 | — | — | 4.4 | — |
| 15.8 | 36.1 | 14.75 | 4.3 | 0.26 |
| 19.3 | 35.2 | 14.84 | 4.3 | 0.34 |
| 24.2 | 33.8 | 14.76 | 4.4 | 0.34 |
| 30.2 | 32.5 | 14.78 | 4.6 | 0.42 |

[32] See, for example, F. N. Rhines and R. F. Mehl, Trans. Am. Inst. Mining Met. Engrs. **128**, 185 (1938).

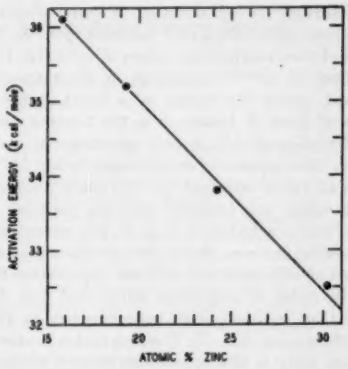


FIG. 5. The dependence of the mean activation energy, for the relaxation process in silver-zinc alloys, on concentration.

throughout the solid solution, leading to a statistical distribution in the values of the activation energy and, correspondingly, in the relaxation times. Another factor that may contribute to the deviation of the curves of Fig. 4 from straight lines has already been discussed in Sec. II, i.e., the fact that the relaxation frequency depends on both $\Gamma_A$ and $\Gamma_B$ (Eq. (5)), while $\Delta H_A$ and $\Delta H_B$ are, in general, not equal.

The present experiments have obtained $H_\tau$ and $\tau_0$ for different compositions of silver-zinc alloys. It is therefore important that some attention be given to the interpretation of these measured quantities. The relaxation time is related, by means of Eq. (8), to an appropriate jump frequency, $\Gamma_\tau$. In view of the discussion of Sec. II, it appears that we may regard $\Gamma_\tau$ essentially as the jump frequency of the slower component of the solid solution, provided that one component moves considerably slower than the other. $H_\tau$ is then very nearly equal to the larger of the two quantities $\Delta H_A$ and $\Delta H_B$. To give a complete interpretation to the quantity $\tau_0$ requires a knowledge of the numerical constant $\alpha$ of Eq. (8). In the absence of a theoretical calculation for $\alpha$, an attempt will be made to estimate its value empirically. Combining Eqs. (8), (9), and (10) we obtain

$$1/\tau_0 = 12\alpha\nu e^{\Delta S_\tau/R}, \tag{21}$$

where the coordination number, $z$, is set equal to 12, for f.c.c. alloys. A reasonable value for $\nu$ may be obtained from the Debye frequency, while $\Delta S_\tau$ may be estimated from Eq. (7). In calculating $\Delta S_\tau$, we make use of our experimental result that, within the precision of measurement the quantity $\mu_0^{-1}(d\mu/dT)$ is independent of concentration for these silver-zinc alloys. Equation (7) may then be reduced to

$$\Delta S_\tau/\Delta S_{Ag} \cong H_\tau/H_{Ag},$$

where $\Delta S_{Ag}$ and $H_{Ag}$ are the values obtained from

measurements[24] of self-diffusion in pure silver: $H_{Ag} = 45.9$ kcal/mole, $\Delta S_{Ag} = 9.5$ cal/mole per °K. Comparison of the experimental values of $\tau_0$ (Table I) with the values of $\nu e^{\Delta S_r/R}$ calculated in the manner just described, yields the values of $\alpha$ listed in the final column of Table I. Inasmuch as the formula used for the calculation of $\Delta S_r$ is only approximate, and the quantity $\Delta S_r$ appears in an exponent in Eq. (21), the numerical values obtained by this calculation should not be taken too seriously and are probably only correct within a factor of 2 or 3. The importance of these results, however, lies in the fact that they may be regarded as self-consistent with the expectation that $\alpha$ is of the order of magnitude unity, and that $\Delta S_r$ is greater than zero and given approximately by Zener's strain theory, i.e., Eq. (7). The fact that $\alpha$ is somewhat less than unity is also reasonable, since it means that the relaxation frequency is somewhat less than the rate-controlling jump frequency. These results, therefore, are further indication that the interpretation of the relaxation phenomena in terms of stress-induced ordering is correct.

There is another method by which the constant $\alpha$ may be estimated empirically: by direct comparison of relaxation data with high temperature diffusion measurements. The obstacles to such a comparison are first, the lack of suitable diffusion data, and second, the difficulty in correcting for the appropriate jump frequency. The only diffusion data for silver-zinc alloys[25] are obtained by the evaporation method (in the temperature range 650°C to 850°C); the fact that data obtained by the same authors for copper-zinc alloys are in poor agreement with the results of more conventional diffusion experiments, indicates that the silver-zinc diffusion data is probably not reliable.[26] As for the corrections required, the earlier discussion has shown that the effective frequency in intermetallic diffusion [the quantity $\Gamma$ of Eqs. (1) and (2)] is not generally the same as the effective frequency in relaxation (the quantity $\Gamma_r$); in fact, whereas $\Gamma$ is essentially the mobility of the faster diffusing component, $\Gamma_r$ is that of the slower component. It is, therefore, difficult to make a reliable comparison between intermetallic diffusion and relaxation data. Le Claire[2] has made such a comparison for 70–30 brass and found that the value of $\alpha$ is close to unity; in correcting for the effective frequency, however, he assumed that the movement of zinc atoms (the faster component) controlled the rate of relaxation. Much more reliable information could be obtained by comparison of the relaxation results with data from diffusion experiments in which radioactive tracers of each component are diffused, in turn, through binary solid solutions of constant chemical concentration. Such tracer experiments, when carried out for a series of solid solutions will give $\Gamma_A$ and $\Gamma_B$ separately as functions of temperature and concentration. Unfortunately, such data are not yet available.

The measurements of rigidity modulus of various wire specimens have enabled us to trace differences in the heights of internal friction peaks of specimens of the same composition to differences in the degree of preferred orientation of the grains. There are no data available for the elastic moduli of single crystals of silver-zinc alloys, but examination of such data for copper, silver, and gold shows that in all cases the shear modulus for the ⟨100⟩ direction is considerably larger than that for the ⟨111⟩ direction. It seems reasonable to expect that this same condition applies to the silver-zinc alloys. Then, the fact that the larger moduli are observed for specimens that show the lower peaks leads to the conclusion that grains for which the ⟨111⟩ direction lies close to the wire axis show much greater anelastic effects in a torsion experiment than those aligned in the ⟨100⟩ direction. Single crystal measurements are contemplated to verify this conclusion and to determine the ratio of the relaxation strengths for the ⟨100⟩ and ⟨111⟩ directions. Such information will aid in determining the nature of the stress-induced ordering.

The fact that the degree of preferred orientation, and therefore the relaxation strength, is so sensitive to the prior heat treatment of the specimen means that the apparent dependence of peak height on the square of the concentration, as indicated by Fig. 2, should not be taken too seriously. In fact, rough considerations, based on a comparison of the data for elastic modulus as measured by Köster and Rauscher[27] with the rigidity data obtained in these experiments indicate that the peak height for a given orientation may vary more nearly linearly with the concentration of zinc.

In conclusion, the author wishes to express his gratitude to Mr. A. Vernon and Mr. R. Sladek for assisting with the measurements, to Dr. N. Nachtrieb for the chemical analyses, and particularly to Dr. W. Bergmann for the preparation of the specimens and for the numerous experiments that he conducted to obtain sufficiently coarse-grained specimens.

[24] W. A. Johnson, Trans. Am. Inst. Mining Met. Engrs. **143**, 107 (1941).
[25] W. Bugakow and B. Ssirotkin, J. Tech. Phys. (U.S.S.R.) **7**, 1577 (1937).
[26] O. Kubaschewski, Trans. Faraday Soc. **46**, 713 (1950).
[27] W. Köster and W. Rauscher, Z. Metallkunde **39**, 111 (1948).

# Evidence for Nonadditivity of Nucleon Moments in Heavy Nuclei*

MARC ROSS†
*Department of Physics, University of Wisconsin, Madison, Wisconsin*
(Received July 25, 1952)

This paper is an attempt to evaluate additional evidence for the nonadditivity of nucleon moments and to correlate it with the evidence provided by the existence of the anomaly in the $H^3$, $He^3$ moments. Attention is first given to the deviations of the static moments of heavy nuclei from the Schmidt lines. This is shown to be an unreliable and ambiguous source of information because the moments are so sensitive to deviations from pure shell model wave functions. Furthermore, the observed differences from the Schmidt lines are opposite in sign and much larger in magnitude than would be expected on the basis of $H^3$ and $He^3$, so they could only be ascribed to a nonadditivity effect if that were a many-body effect. Much more reliable information is shown to be provided by the lifetimes of certain "forbidden" magnetic dipole transitions in heavy nuclei. These are the radiative processes which seem to involve one-particle transitions with $\Delta l=2$; hence they are forbidden on the basis of the ordinary additive moment. Here the influence of reasonable deviations from shell model functions is quite small, so the existence of the transitions is good evidence for a nonadditive contribution to the moment operator. Furthermore, the magnitude of the effect is quite compatible with what would be expected on the basis of the $H^3$, $He^3$ moment anomaly.

## I. INTRODUCTION

STUDY of the interaction between nuclei and the electromagnetic field has long been an important tool in the investigation of nuclear structure. However, it seems likely that such study concerns not only nuclear structure, but also the mechanism of nuclear forces. Aside from the portion of the interaction with the electromagnetic field associated with the charges and intrinsic magnetic moments of the nucleons, an important term may arise in connection with the nucleon-nucleon interaction as suggested by the belief that nuclear forces are produced by a field bearing charged mesons. The term "interaction" effects will be used here to refer to this influence of the specifically nuclear interaction on the coupling with the electromagnetic field.

In recent years a number of authors have drawn some evidence from nuclear data, particularly data on magnetic moments, for the existence of interaction effects. In no case has the evidence been completely unambiguous, and in some cases the ambiguities have been so marked that little weight can be given to the arguments involved. The total picture, however, certainly seems to indicate the existence of such effects. The present work is an attempt to investigate systematically the available information concerning this matter, to distinguish the relatively clear-cut arguments from the very ambiguous ones, and to thereby obtain an estimate of the magnitude of those effects which seem to be established with some certainty.

For our purpose, the phenomenological approach is adopted, i.e., the empirical evidence is expressed directly in terms of the simplest operators involving the nucleon coordinates. The results will of course be valid only to the extent that the effects can be expressed in terms of operators involving just the nucleon coordinates.[1] It is known that while magnetic multipole moment operators are directly connected with meson currents and the details of the nuclear interaction, the electric multipole operators depend, in the long wavelength approximation ($h\nu \ll 50$ Mev), only on the positions of the charges (protons), and hence are independent of the nuclear interaction.[2] This result, known as the Siegert theorem, means that just the magnetic multipole data need be examined in terms of interaction effects. In fact, because of their simpler nature and the much greater abundance of data, it is practical to limit the investigation to magnetic dipole moments and magnetic dipole transition probabilities.

The most striking evidence of an interaction effect is found in the magnetic moments of the three-body systems.[3] Under assumptions that $H^3$, and $He^3$ are accurately described as mirror nuclei, and that the ground state is primarily $^2S$, it is found that there are moment anomalies of about $\pm\frac{1}{4}$ nuclear magneton for $H^3$ or $He^3$, respectively, which require an interaction moment for their explanation. The interaction moment operator capable of yielding this effect is almost uniquely determined under the conditions that the moment is a two-body, momentum independent, operator which yields equal and opposite contributions to mirror nuclei.[4] The operators capable of contributing the three-body anomaly will be called spin interaction moments since they must involve the nucleon spin operators.[5] All the spin moments have essentially the

* This work supported by the AEC.
† Now at Laboratory of Nuclear Studies, Cornell University, Ithaca, New York.

[1] F. Villars, Phys. Rev. **86**, 476 (1952).
[2] R. G. Sachs and N. Austern, Phys. Rev. **81**, 705 (1951).
[3] R. G. Sachs, Phys. Rev. **72**, 312 (1947); R. Avery and R. G. Sachs, Phys. Rev. **74**, 1321 (1948).
[4] N. Austern, thesis, University of Wisconsin (1951) (unpublished). M. Ross, thesis, University of Wisconsin (1952) (unpublished).
[5] Villars, employing a meson theoretical approach, arrived essentially at a spin interaction moment explaining the anomaly [F. Villars, Phys. Rev. **72**, 257 (1947); Helv. Phys. Acta **20**, 476 (1947)]. Sachs considered an interaction moment, known as the exchange moment, which arises in connection with a nucleon potential containing space exchange. The contribution of the

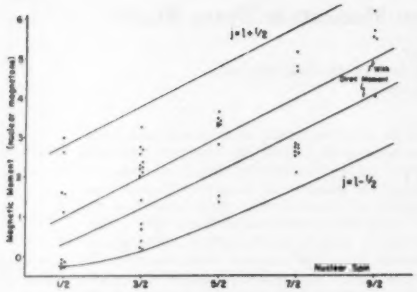


FIG. 1. Schmidt diagram for odd proton nuclei.

same form in the symmetric $^2S$ portion of the ground state of the three-body system, but for further applications it is necessary to note the detailed differences. Any spin interaction moment can be expressed as a linear combination of

$$\mu(1): \left(\frac{e\hbar}{2mc}\right)\tfrac{1}{2}\sum_{\alpha,\beta}(\sigma_\alpha-\sigma_\beta)(\tau_\alpha-\tau_\beta)\Phi(|\varrho_{\alpha\beta}|);$$

$$\mu(2): \left(\frac{e\hbar}{2mc}\right)\tfrac{1}{2}\sum_{\alpha,\beta}(\sigma_\alpha-\sigma_\beta\cdot\varrho_{\alpha\beta})\varrho_{\alpha\beta}(\tau_\alpha-\tau_\beta)\Phi(|\varrho_{\alpha\beta}|);$$

$$\mu(3): \left(\frac{e\hbar}{2mc}\right)\tfrac{1}{2}\sum_{\alpha,\beta}(\sigma_\alpha-\sigma_\beta)(\tau_\alpha-\tau_\beta)\Phi(|\varrho_{\alpha\beta}|)P^r{}_{\alpha\beta};$$

$$\mu(4): \left(\frac{e\hbar}{2mc}\right)\tfrac{1}{2}\sum_{\alpha,\beta}(\sigma_\alpha-\sigma_\beta\cdot\varrho_{\alpha\beta})\varrho_{\alpha\beta}(\tau_\alpha-\tau_\beta)\Phi(|\varrho_{\alpha\beta}|)P^r{}_{\alpha\beta};$$

where $\varrho_{\alpha\beta}$ is the separation vector of a pair of nucleons, $\tau$ is the third component of the single particle isotopic spin operator (with eigenvalues $\pm1$ for neutrons and protons, respectively), and $\Phi$ determines the intensity as a function of distance with which these interaction effects take place. The quantity $\Phi$ is expected to be intimately associated with the range and shape of the nuclear potential.

A very simple physical interpretation can be given for these moments: They are of a form of modifications of the free intrinsic moment of the nucleon due to the proximity of other nucleons. The contribution of the nucleons' free intrinsic moments, $\sum_\alpha \mu_\alpha\sigma_\alpha$, is proportional to the nucleons' spin vector. Similarly, the interaction moments are made up of terms proportional to the spin vectors of each nucleon, but now, the magnitude of the coefficient of $\sigma_\alpha$ depends on the positions of the other nucleons, and only those that are within the range of interaction have an appreciable effect. The modifications of the nucleons' intrinsic moments by these spin interaction moments are equal and opposite for neutrons and protons.

## II. STATIC MOMENTS OF HEAVY NUCLEI

### A. Deviation of the Moments from the Schmidt Lines

Recently the static moments of odd-even heavy nuclei have been the subject of considerable study and speculation.[6] In some of this work particular attention has been paid to the role played by interaction moments, while in other work possibilities of modifying the wave function have been considered. In no case has there been a simultaneous examination of both phases of this rather complex mass of information.

Much evidence, including the qualitative features of the magnetic moment data, supports the assumption that the nuclear wave functions are largely characterized by the odd particle model, that model in which the total angular momentum of the nucleus is vested in a single odd nucleon.[7] The magnetic moments predicted by the odd particle model are known as the Schmidt lines[8] (Figs. 1 and 2). These magnetic moments are of course calculated from the ordinary additive moment operator:

$$(\hbar/2mc)[\textstyle\sum_\alpha e_\alpha \mathbf{L}_\alpha + e\sum_\alpha \mu_\alpha\sigma_\alpha],$$

without any reference to interaction effects. The Schmidt values agree qualitatively with the experimental moments; in fact, one generally speaks in terms of deviations of the moments from the Schmidt lines. In spite of this manner of speaking, the deviations are often large, of the order of 50 percent of the moment. Examination of the Schmidt diagrams shows several obvious systematic features of the deviations; the most important of them is that all moments (except $H^3$ and $He^3$) lie between the Schmidt lines.

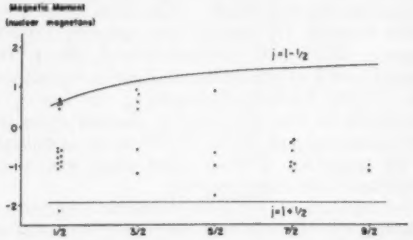


FIG. 2. Schmidt diagram for odd neutron nuclei.

exchange moment to the three-body moment is very small (see reference 16). Interaction moments arising in connection with the spin-orbit coupling suggested by the shell model have been considered too. These moments were also found to be small in $H^3$ and $He^3$. Blanchard, Avery, and Sachs, Phys. Rev. **78**, 292 (1950); J. G. Brennan, thesis, University of Wisconsin (1952) (unpublished).

[6] H. Margenau and E. P. Wigner, Phys. Rev. **58**, 103 (1940); A. Bohr, Phys. Rev. **81**, 134 (1951); H. Miyazawa, Prog. Theoret. Phys. **6**, 263 (1951); A. De Shalit, Helv. Phys. Acta **24**, 296 (1951); F. Bloch, Phys. Rev. **83**, 839 (1951); J. Davidson, Phys. Rev. **85**, 432 (1951).

[7] M. G. Mayer, Phys. Rev. **78**, 16, 22 (1950).

[8] T. Schmidt, Z. Physik **106**, 358 (1937).

One feature noted by some authors is the apparent trend of the moment deviations with respect to the proximity of the odd nucleon number to a magic number or closed shell. However, this trend is actually only the result of a correlation of the nuclear spins with the magic numbers and is not directly a property of magnetic moments. A feature of the shell structure is that there are many $j=l-\frac{1}{2}$ nuclei with small spin in the near neighborhood of the magic numbers, and it is a general feature of nuclear moments that they are near the Schmidt lines for small $j$ and $j=l-\frac{1}{2}$. Thus a plot of all moments together against odd $N$ or $Z$ appears to show an influence of the magic numbers, particularly the values 20 and 50. For a more precise picture the moment deviations are plotted in Fig. 3 against the difference between the number of odd nucleons and the closest magic number for given nuclear spin. The plots are extended over all measured moments of odd-even nuclei of mass greater than 35, except those located so far away from the magic numbers 28, 50, 32, 126 that a reasonable identification could not be made. Clearly there are no definite trends.

### B. Deviations of Nuclear Wave Functions from the Shell Model

It is generally accepted that the wave functions of *light* nuclei deviate markedly from the simple odd particle functions. This is evidenced by large fluctuations in the magnetic moments and in other properties of the nuclei. On the other hand, the behavior of heavier nuclei ($A>50$) shows comparative regularity and seems to support the view that the odd particle model gives a good description of the predominant term in the wave function. In particular, the deviations from the Schmidt lines for the heavy nuclei are *comparatively* regular. Regularity is a property that would be expected if the deviations were entirely due to interaction effects, since the interaction effects involve many nucleons. Thus we limit attention to the heavy nuclei in searching for interaction effects. We will come to the conclusion that even here the fluctuations are sufficiently irregular

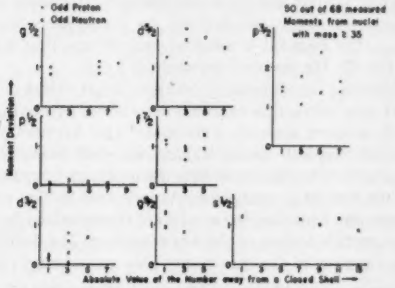
Odd Proton
Odd Neutron
50 out of 68 measured Moments from nuclei with mass ≥ 35
Moment Deviation
Absolute Value of the Number away from a Closed Shell

FIG. 3. Moment deviation *vs* proximity of odd $N$ or $Z$ to closed shells 20, 28, 50, 82, 126.

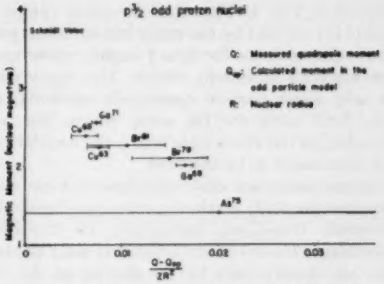


FIG. 4. Correlation of magnetic dipole and electric quadrupole moments.

for the deviations to be ascribed to admixtures in the wave function, although it is by no means clear what fraction of the deviations can be assigned to each of the two causes.

In evaluating the importance of modifications of the wave functions, one fact to keep in mind is that the expectation value of the moment may be linear in the amplitude of small admixtures to the wave function. Thus if a wave function is of the form $(1-|a|^2)^{\frac{1}{2}}\Psi^0+a\Psi'$, where $\Psi^0$ is the shell model function and $\Psi^0$ and $\Psi'$ differ by at most one single-particle state, then the expectation value of the moment,

$$(1-|a|^2)(\Psi^0,\mu\Psi^0)+[a(1-|a|^2)^{\frac{1}{2}}(\Psi^0,\mu\Psi') +\text{complex conj.}]+|a|^2(\Psi',\mu\Psi'),$$

contains a nonvanishing cross term; a very substantial modification of the moment can be associated with a very small modification of the wave function. Admixtures to the odd particle wave function are expected to fluctuate considerably from nucleus to nucleus; contributions to the moments due to admixture should show comparable fluctuations. Thus the non-uniformity of the moment deviations may be taken to be a strong indication of impure wave functions. However, it is important to search for evidence for modification of the wave function other than that provided by the magnetic moments, since it is easy to find a mixed wave function parameterized in such a way that agreement with the moments can be obtained without reference to interaction effects. There are several independent indications of admixture.

First, the electric quadrupole moment data, and particularly the several very large quadrupole moments, necessitate modification of the odd particle model.[9] The core, or some core nucleons, must share the total angular momentum of the nucleus. A correlation of quadrupole moments with magnetic moments is suggested by this evidence. The data, where available, are consistent with the suggested strong correlation, as is

[9] J. Rainwater, Phys. Rev. **79**, 432 (1950); E. Feenberg and K. C. Hammack, Phys. Rev. **81**, 285 (1951); A. Bohr, Phys. Rev. **81**, 134 (1951).

illustrated in Fig. 4. That the correlation cannot be complete is indicated by the many important magnetic moment discrepancies for spin $\frac{1}{2}$ nuclei, whose quadrupole moments necessarily vanish. Also, many nuclei have only single particle quadrupole moments; evidently their cores are for some reason not very polarizable, so the effect upon which the correlation is based is too small to be observed.

A second indication that wave functions are mixed comes from the study of selection rules and classification of isomeric transitions, particularly $E3$ transitions. This evidence has led to the belief that some low-lying levels are characterized by the sharing of the total nuclear spin $J$ by, say, three of the odd type nucleons (all in the same $n$, $l$, $j$ shell with $j>J$) instead of only by a single nucleon. If this were assumed to be a general property to a greater or lesser extent of all nuclei, it would provide a simple understanding of the major part of the deviations from the Schmidt lines. The magnetic moment associated with such a level is $\mathfrak{M}_j J/j$ where $\mathfrak{M}_j$ is the Schmidt value associated with the state $l$, $j$. Hence the moment associated with this state is as indicated in Table I. The feature that these moments are all inside the Schmidt lines (as are the experimental values) seems characteristic of almost any reasonable attempt to modify the single odd particle wave functions. Although it may occasionally be found that agreement becomes slightly poorer for $j=l-\frac{1}{2}$ nuclei, the over-all agreement is improved in this way. The particular modification just discussed, and the pure odd particle model, could be combined linearly for each nucleus to yield good agreement with the experimental moments. Such a theory does not seem justified in the absence of other evidence for it.

A third clear indication of admixture to the odd particle wave function is given by the relatively short lifetimes for electric multipole transitions in the odd neutron nuclei. Since the neutron carries no charge, such transitions would be expected to occur in a pure shell model only as a result of recoil of the core, whence the transition probability would be of the order of $Z^2/A^{2l}$ times the corresponding probabilities for odd proton nuclei. But there are many examples of $E3$ transitions for which the lifetime, although larger than that for the odd proton nuclei, is much smaller than this. Since, according to the Siegert theorem, no electric multipole interaction effects are to be expected at these energies, the most plausible explanation of the intensity of the transitions is that the odd particle function is not pure. This interpretation tends to be confirmed by the fact that the lifetimes show large fluctuations, as would be expected on the basis of fluctuations in the amount of admixture.

TABLE I. Magnetic moments associated with the configuration $j^n$ with total angular momentum $J$.

| | $j=l+\frac{1}{2}$ | $j=l-\frac{1}{2}$ |
|---|---|---|
| Odd proton | $J+2.29J/j$ | $J-2.29J/(j+1)$ |
| Odd neutron | $-1.91J/j$ | $1.91J/(j+1)$ |

### C. Interaction Effects

We are now prepared to evaluate the deviations of the moments of heavy nuclei from the predictions of the odd particle model as evidence for interaction effects. This evidence is, as we have seen, bound to be quite ambiguous. Our program is confined to (a) determining the implications in heavy nuclei of the interaction moment suggested by the three-body anomaly, and (b) discussing in very general terms the possibility and nature of an interaction effect which would account for the major portion of the moment deviations.

In order to make any statement about the implications of the three-body anomaly on observations in heavy nuclei, it is necessary to make the powerful assumption that the forms and strengths of the interaction moment operators remain unchanged as the number of nucleons in the nucleus changes. It is true that we have already assumed a two-body operator, but the use of a two-body operator as such in a specific situation corresponds to the comparatively mild assumption that the effect of the neighboring nucleons on the interaction of any pair has a smoothed out, average influence; the effect need not be small. On the other hand, the assumption that the operator remains the same as we pass from $A=3$ to $A\gtrsim 100$ is valid only if the effect of neighboring nucleons on the interaction of a pair is extremely small.

Qualitatively, the contribution of an interaction moment based on the three-body moments to the moments of heavy nuclei is readily found. Consider an odd-even heavy nucleus in the odd particle model. Because the moment is an operator between unlike nucleons, the contribution depends on the interaction between the single odd nucleon which accounts for the nuclear spin and the core of oppositely charged nucleons (which we define to be the "even type" nucleons). Since the interaction moment is a short range operator, the dependence of the moment contribution on the mass number $A$ is approximately $AV_I/V_N$, where $V_N$ is the nuclear volume and $V_I$ is the effective interaction volume of the single odd nucleon. As $V_N$ is proportional to $A$, the moment is roughly constant and thus equal to the $H^3$, $He^3$ moment anomaly of $\frac{1}{4}$ nm.

Detailed calculations of the expectation values of the four spin interaction moments determined by the three-body moment anomaly were made[19] (see Appendix) for several "typical" heavy nuclei with shell model wave functions. The results confirm the qualitative argument of the foregoing paragraph. As indicated in this argument, one finds that the results are characterized by the odd particle feature of the wave function. The details of the coupling in the core do not play an important role.

[19] A. Russek and L. Spruch [Phys. Rev. 87, 1111 (1952)], have carried through similar calculations with moment operators of the same form.

Any attempt to predict detailed results for every nucleus is doomed by lack of knowledge concerning the intensity function $\Phi(|\rho_{\alpha\beta}|)$ in the moment operator and lack of acknowledge concerning the radial wave functions. Arbitrariness in these radial functions even precludes a conclusive statement about the dependence of the moment contributions on the odd particle orbital angular momentum $l$. Because the spin interaction moments can be interpreted simply as modifications of the nucleons' intrinsic moments, it is assumed that the results are actually independent of details and are best represented, in heavy nuclei, as an average modification of the nucleon intrinsic moment. The results are presented in this way in Table II. The total spin interaction moment contribution can, of course, be expressed as

$$\langle\mu\rangle = a\langle\mu(1)\rangle + b\langle\mu(2)\rangle + c\langle\mu(3)\rangle + d\langle\mu(4)\rangle,$$

where $a+b+c+d=1$.

Table II shows that the moment contributions are not very large unless a range considerably greater than the usual range of forces ($1.18\times10^{-13}$ cm) is used. Much more important is the fact that the sign of each of these moment contributions is the same as in the three-body nuclei; hence, opposite to all observed deviations from the Schmidt lines.

Three reasonable conclusions are possible:

(1) The deviations of the moments are explained by admixtures of other states to the odd particle wave function and the spin interaction effects are correctly estimated on the basis of the three-body anomaly. Although the small ($\lesssim\frac{1}{2}$ nm) contribution of the spin moment is in the wrong direction, it and any other small interaction effects are presumed to be obscured by the effect of admixed wave functions.

(2) As in (1) we again assume that our extension to heavy nuclei of the effect giving rise to the three-body anomaly is valid; but we assume that the deviations of the moments are explained in large part by some other two-body interaction moment which happens not to contribute to the three-body system.

(3) The assumption of a two-body form of the operator is not valid. In particular, the operator changes rather markedly in passing from light to heavy nuclei. Then an interaction moment in the three-body system or, in fact, any interaction effect based on the two- or three-body systems, has no direct implications in heavy nuclei.

We shall now consider further the conclusion (2), in order to show it is untenable. Let us assume that there is a two-body momentum independent interaction moment operator that will yield the major portion of the deviations, admixture of other states to the odd particle wave function accounting for a relatively small portion. Then the data impose the following conditions on the interaction moment: (a) Its contribution to any nucleus is approximately equal but of opposite sign to the contribution in the mirror nucleus. (b) Its contribution is of the same order in an $S$ state of the odd particle model as in other orbital angular momentum states.

TABLE II(a). Contribution of the spin interaction moments determined by the three-body anomaly, to the moments of heavy nuclei. Range, $\alpha^{-1}=1.18\times10^{-13}$ cm.

| Moment | Well strength (Mev) | Moment contribution[a] (nm) |
|---|---|---|
| $\mu(1)$ | −13.0 | 0.4 |
| $\mu(2)$ | −30.8 | 0.7 |
| $\mu(3)$ | −13.0 | 0.4 |
| $\mu(4)$ | −30.8 | 0.7 |

TABLE II(b). Dependence of the contribution of $\mu(1)$ on the range of the intensity function $\Phi$.

| Range $\alpha^{-1}$ | 1.18 | 2.0 | 3.0 | 4.0 |
|---|---|---|---|---|
| Well strength (Mev) | −13.0 | −1.9 | −0.40 | −0.20 |
| Moment contribution[a] (nm) | 0.4 | 0.6 | 0.8 | 1.0 |

[a] The moment contributions are calculated increases in the magnitude of the odd nucleon intrinsic moment. The intensity function of the moment operator is taken to be $\Phi=C\exp(-\alpha|\rho_1-\rho_2|)/\alpha|\rho_1-\rho_2|$ (see Appendix). The well strength is $(\hbar^2\alpha^2/m)(2C)$ Mev. Errors of a factor of two are likely even if the odd particle model is a good characterization of the wave function.

It is found that there are just four static two-body moment operators which can meet both these conditions, and these are the four operators $\mu(1)$, $\mu(2)$, $\mu(3)$, $\mu(4)$ which have been discussed above.[11] Hence it is not possible to avoid an unacceptable contribution to the three-body moments.[12]

We are left with conclusion (3), that the interaction moment is a many-body phenomenon, as the only possibility for ascribing the major portion of the deviations from the Schmidt lines to an interaction effect. Yet it is certainly expected that a many-body effect, even to

[11] These are in effect the moment operators considered by H. Miyazawa, Prog. Theoret. Phys. 6, 263 (1951); A. DeShalit, Helv. Phys. Acta. 24, 296 (1951); F. Bloch, Phys. Rev. 83, 839 (1951). They do not consider any other empirical evidence in connection with this effect. Bloch erroneously states that the nonuniformity that one observes in the deviations is further evidence for an interaction effect.

Other types of interaction moments, such as the space exchange moment (reference 16), have also been considered relative to heavy nuclei. It is not surprising that a moment such as the exchange moment will not fit the deviations. Actually its contribution is approximately $\mp0.1\,l$ nm for odd neutron and odd proton nuclei, respectively, a contribution which would generally be small enough to be obscured by other effects. See reference to Miyazawa above and reference 10. The interaction moments associated with the spin orbit coupling suggested by the shell model also yield small contributions to the static moments of heavy nuclei; Blanchard, Avery, and Sachs, Phys. Rev. 78, 292 (1950); C. H. Blanchard, thesis, University of Wisconsin (1950) (unpublished); J. H. D. Jensen and M. G. Mayer, Phys. Rev. 85, 1040 (1952).

[12] One extreme possibility has been disregarded. It is seen from Table I that the three-body anomaly and the qualitative trend of the deviations of the moments of heavy nuclei could be accounted for if the intensity function $\Phi(\rho)$ in the moment were a combination of a strong short-range well and a very long-range well of opposite sign and less strength.

a greater extent than a two-body effect, will vary smoothly from one nucleus to another, while the observed moments show large fluctuations.[13] Another feature of the observations that is difficult to understand on the basis of any interaction moment is the small size of some of the deviations from the $j=l-\frac{1}{2}$ Schmidt line.[14] Both of these facts speak for an interpretation of the deviations based, in large part at least, on the mixing of wave functions. Therefore we conclude that the deviations from the Schmidt lines provide no direct evidence for or against the existence of a nonadditive contribution to the nucleon moments.

## III. "FORBIDDEN" MAGNETIC DIPOLE TRANSITIONS

An opportunity to avoid the confusion between the effects of interaction moments and the effects of impure wave functions is offered by the occurrence of certain magnetic dipole isomeric transitions in heavy nuclei.[15] These radiative transitions seem to involve one particle transitions with $\Delta l=2$, which are forbidden on ordinary grounds. The scanty information as yet available concerning lifetimes indicates that the transitions proceed almost as rapidly as ordinary $M1$ transitions (see Fig. 5). In view of the success of the shell model in describing nuclear levels in the neighborhood of those in question, it is strongly indicated that some interaction moment provides the transition since the interaction moment because of its space dependence is not subject to the selection rule forbidding $\Delta l=2$.

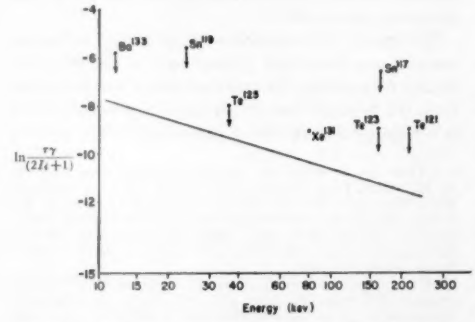


FIG. 5. $\gamma$-lifetime *vs* energy for certain $M1$ transitions. The vertical arrows indicate upper bounds only. The curve indicates the extreme lifetime for *ordinary* $M1$ transitions with special wave functions at variance with the odd particle model (see text).

[13] The observed non-uniformity might be associated with details of the radial wave functions which alter the contributions of the interaction moment. This possibility cannot be ruled out, but it does not seem too likely. The simple physical interpretation of the moment indicates that uniformity is a fundamental property of the effect. In this case the fluctuations must be explained on the basis of admixtures to the odd particle wave function.

[14] This difficulty was pointed out by J. P. Davidson, Phys. Rev. **85**, 432 (1952); but it may not be too important since only a fraction of the nucleon intrinsic moment is effective in these particular cases, so the absolute deviations are small, say $\lesssim\frac{1}{4}$ nm.

[15] R. G. Sachs and M. Ross, Phys. Rev. **84**, 379 (1951).

Table III contains all the relevant information on seven more or less well-investigated isomers of the type under discussion. All but one of the seven are assigned the decay scheme $h_{11/2}\rightarrow d_{\frac{3}{2}}\rightarrow s_{\frac{1}{2}}$, an $M4$ transition followed by the $M1$ transition of interest. These assignments were made with the aid of the sequence of one particle levels predicted by the shell model. Of particular importance are the facts that the $M1$ transitions occur in cascade with $M4$ transitions whose characteristics are generally very well established and that most of the $M1$ transitions end in final states of measured spin.

We must, of course, examine the possibility that the transitions proceed by ordinary means because of the deviation of the wave function from the odd particle model. The magnetic dipole radiative transition probability is

$$w_\gamma=\frac{1}{(2I_i+1)}\left(\frac{e^2}{\hbar c}\right)E^3\left(\frac{m}{M}\right)^2\sum_{i,f}|\langle\mathbf{n}\cdot\boldsymbol{\mu}\rangle_{if}|^2\left(\frac{mc^2}{\hbar}\right),$$

where $E$ is the photon energy in units of $mc^2$, $m$ and $M$ are now the masses of the electron and nucleon, respectively, $\mathbf{n}$ is an arbitrary unit vector (the sum over direction of polarization and propagation vectors having been taken under the assumption that the initial nuclear state $i$ is unpolarized). Let $|\mu|^2\equiv\sum_{i,f}|\langle\mathbf{n}\cdot\boldsymbol{\mu}\rangle_{if}|^2$ be the square of the matrix element summed over final and initial sublevels. We then have

$$w_\gamma=\frac{1}{(2I_i+1)}1.68\times10^{12}E^3|\mu|^2\ \text{sec}^{-1},$$

or

$$\tau_\gamma/(2I_i+1)=4.13\times10^{-13}/|\mu|^2E^3\ \text{sec},$$

where $\tau_\gamma$ is the lifetime for photon emission. The absolute lifetime has been obtained only for $Xe^{131}$, in which case the value is $4.8\pm2.0\times10^{-10}$ sec. From $w_\gamma(1+\beta)=(\ln2)/(4.8\times10^{-10})$, where $\beta$ is the total conversion coefficient, we obtain the corresponding matrix element $|\mu|^2\approx0.15$ (nm)$^2$.

If we assume that this matrix element is due to the ordinary magnetic moment operator, it must be produced by an admixture of functions other than those characteristic of the odd particle model. It turns out that a lower limit on the amount of admixture can be established on the basis of the above lifetime and that the amount is unreasonably large.

Let $\Psi_i^0$, $\Psi_f^0$ be the principal portions of the initial and final states, with total angular momentum $\frac{3}{2}$, $\frac{1}{2}$, respectively. The shell model is taken literally in forming these states. We then write the wave functions as $\Psi_i=(1-|a_i|^2)^{\frac{1}{2}}\Psi_i^0+a_i\Psi_i'$ and $\Psi_f=(1-|a_f|^2)^{\frac{1}{2}}\Psi_f^0+a_f\Psi_f'$. If the transition is *not* due to interaction effects, the transition probability is proportional to the square of the matrix element of the ordinary moment $\mu$. This matrix element is

$$(\Psi_i,\mathbf{n}\cdot\boldsymbol{\mu}\Psi_f)=a_i^*(1-|a_f|^2)^{\frac{1}{2}}(\Psi_i',\mathbf{n}\cdot\boldsymbol{\mu}\Psi_f^0)+a_f(1-|a_i|^2)^{\frac{1}{2}}\times(\Psi_i^0,\mathbf{n}\cdot\boldsymbol{\mu}\Psi_f')+a_i^*a_f(\Psi_i',\mathbf{n}\cdot\boldsymbol{\mu}\Psi_f'),$$

TABLE III. Data on "forbidden" $M1$ isomeric transitions.

| | Ground state spin | $E$(kev) | Total half-life (sec) | $K$ conv. coeff. | $K/L$ ratio | Total conversion | Log of $\gamma$ lifetime | Theor. $K$ conv. | Scheme | Refer-ences |
|---|---|---|---|---|---|---|---|---|---|---|
| $Sn^{117}$ | $\frac{1}{2}$ | 162 | $<10^{-6}$ | 0.10±0.03 | not meas. | not meas. | 6.0 | 0.14 | $d_{\frac{3}{2}}\rightarrow s_{\frac{1}{2}}$ | a |
| $Sn^{119}$ | $\frac{1}{2}$ | 24 | $<10^{-6}$ | zero | zero | 7.3±1.7 | 5.0 | zero | $d_{\frac{3}{2}}\rightarrow s_{\frac{1}{2}}$ | b–d |
| $Te^{121}$ | assumed $\frac{1}{2}$ | 213 | $<4\times10^{-9}$ | 0.085±0.035 | 7.3±0.3 | 0.10±0.04 | 9.6 | 0.08 | $d_{\frac{3}{2}}\rightarrow s_{\frac{1}{2}}$ | e–g |
| $Te^{123}$ | $\frac{1}{2}$ | 159 | $<4\times10^{-9}$ | 0.18±0.08 | 8.9±0.8 | 0.20±0.08 | 9.6 | 0.19 | $d_{\frac{3}{2}}\rightarrow s_{\frac{1}{2}}$ | e–g |
| $Te^{125}$ | $\frac{1}{2}$ | 35.4 | $<4\times10^{-9}$ | 11.4±3 | 7.3±2 | 13.3±4 | 8.6 | ··· | $d_{\frac{3}{2}}\rightarrow s_{\frac{1}{2}}$ | g–k |
| $Xe^{131}$ | $\frac{3}{2}$ | 80 | $<4.8\pm2.0$ $\times10^{-10}$ | 1.73±0.4 | 7. ±2 | 2.0±0.4 | ~9.15 | ~1.6 | $s_{\frac{1}{2}}\rightarrow d_{\frac{3}{2}}$ | l–o |
| $Ba^{139}$ | assumed $\frac{1}{2}$ | 11.7 | $<5\times10^{-7}$ | zero | not meas. | ~130 | 6.8 | zero | $d_{\frac{3}{2}}\rightarrow s_{\frac{1}{2}}$ | p |

[a] J. W. Mihelich and R. D. Hill, Phys. Rev. **79**, 781 (1950).
[b] Scharff-Goldhaber, der Mateosian, Goldhaber, Johnson, and McKeown, Phys. Rev. **83**, 480 (1951).
[c] J. C. Bowe and P. Axel, Phys. Rev. **84**, 939 (1951).
[d] R. D. Hill, Phys. Rev. **83**, 865 (1951).
[e] R. D. Hill, Phys. Rev. **76**, 333 (1949).
[f] Katz, Hill, and Goldhaber, Phys. Rev. **78**, 9 (1950).
[g] M. Deutsch and W. E. Wright, Phys. Rev. **77**, 139 (1950).
[h] F. K. McGowen, Phys. Rev. **77**, 138 (1950).
[i] Hill, Scharff-Goldhaber, and Friedlander, Phys. Rev. **75**, 324 (1949).
[j] Friedlander, Perlman, and Scharff-Goldhaber, Phys. Rev. **80**, 1103 (1950).
[k] P. Axel and J. C. Bowe, Phys. Rev. **85**, 734 (1952).
[l] F. R. Metzger and M. Deutsch, Phys. Rev. **74**, 1640 (1948).
[m] Kern, Mitchell, and Zaffarano, Phys. Rev. **76**, 94 (1949).
[n] R. L. Graham and R. E. Bell, Phys. Rev. **84**, 380 (1951).
[o] R. E. Bell and R. L. Graham, Phys. Rev. **85**, 212 (1952).
[p] Hill, Scharff-Goldhaber, and McKeown, Phys. Rev. **84**, 382 (1951).

if cognizance is taken of the selection rule forbidding the $\Psi_i^0\rightarrow\Psi_f^0$ transition. As a result of the selection rule, the transition probability is therefore at least quadratic in the amplitude of the admixture $a_i$ or $a_f$.

In considering the terms in the matrix element of the form $(\Psi', \mathbf{n}\cdot\boldsymbol{\mu}\Psi^0)$, it seems most reasonable to assume that the states $\Psi'$ will contain the same filled $n$, $l$, $j$ shells (of the odd type nucleons) which appear in the cores of $\Psi_i^0$ and $\Psi_f^0$. In other words, $\Psi'$ is formed by distributing the nuclear spin in any manner among the half-dozen or so nucleons not in filled shells. A direct calculation then shows that any matrix element of the type $(\Psi', \mathbf{n}\cdot\boldsymbol{\mu}\Psi^0)$ vanishes.

If we lift the restrictive assumption that $\Psi'$ contains the same filled shells as appear in the shell model functions, it is found for the particular group of nuclei under consideration that only one matrix element of the type $(\Psi', \mathbf{n}\cdot\boldsymbol{\mu}\Psi^0)$ has a significant magnitude, namely, that for a $\Psi_f'$ formed by replacing a $2d_{\frac{3}{2}}$ state by a $2d_{\frac{5}{2}}$ state in $\Psi_f^0$. The states $\Psi_i^0$, $\Psi_f^0$, and $\Psi_f'$ in question, have configurations:

$$\Psi_i^0\sim(\text{core})(d_{\frac{5}{2}})^6(s_{\frac{1}{2}})^2d_{\frac{3}{2}},$$
$$\Psi_f^0\sim(\text{core})(d_{\frac{5}{2}})^6(d_{\frac{3}{2}})^2s_{\frac{1}{2}},$$
$$\Psi_f'\sim(\text{core})(d_{\frac{5}{2}})_{J=0}{}^4(s_{\frac{1}{2}})^2[d_{\frac{3}{2}}(d_{\frac{3}{2}})^2{}_{J=2}]_{J=\frac{1}{2}}.$$

For these states, the transition matrix element of $\mu$ is such that $|\mu|^2=0.65|a_f|^2$ ($a_i$ is assumed to be zero). The lifetime of $Xe^{131}$ corresponds to $|\mu|^2\approx0.15$ so the probability $|a_f|^2$ of admixture, would have to be at least 23 percent. This seems to be a very unnatural modification of the shell model since the introduction of the $d_{\frac{3}{2}}$ state in place of a $d_{\frac{5}{2}}$ is in direct contradiction of the basic principle of the model; hence it will not be considered further.

The transition matrix element then has only the one nonvanishing term $a_i^*a_f(\Psi_i', \mathbf{n}\cdot\boldsymbol{\mu}\Psi_f')$, so the transition probability depends on the fourth power of the amplitude of admixture. Thus it is indeed much less sensitive to the structure of the wave function than the static moment. To obtain a conservative estimate of the amplitude required to give the transition we set $|a_i|^2=|a_f|^2=|a|^2$. If $\Psi_i'$ and $\Psi_f'$ differ by at most one single particle state, and if no other selection rule intervenes, the transition probability is proportional to $a^4$. Hence, if the odd particle wave function is a good characterization of the states, the transition is extremely forbidden by ordinary means. Furthermore, modification of both final and initial wave functions with just the right states is necessary if the transition is to proceed via the ordinary magnetic dipole interaction.

We can estimate the smallest amplitude $a$ with which reasonable and simple states $\Psi'$ must be admixed to both final and initial wave functions to yield the transition via the ordinary moment. If wave functions having the total nuclear spin distributed among $h_{11/2}$, $d_{\frac{3}{2}}$, and $s_{\frac{1}{2}}$ single particle states are considered, the most rapid transition occurs between the pair of configurations

$$\Psi_{\frac{1}{2}}'\sim(\text{core})\{[(h_{11/2})^2{}_n]_{J=5}d_{\frac{3}{2}}\}_{J=\frac{1}{2}}.$$

The transition matrix element of $\mu$ is such that $|\mu|^2=2.47a^4$, so these states would have to be admixed with probabilities of 25 percent to produce the transition. We will assume that such strong admixtures of just the right states to the odd particle wave function do not occur; but it must be realized that while such admixtures are very unlikely, they are certainly possible.

To see whether interaction moments provide a more reasonable explanation of the transitions, their matrix elements between pure shell model states must be determined. The spin moments $\mu(1)$ and $\mu(3)$ and the space exchange moment[16] lead to very small or zero transition probabilities. It appears that only moments such as $\mu(2)$ and $\mu(4)$ whose angular dependence has the form of a $D$ function can contribute significantly. If we require that the moment yield exactly the experimental transition probability for $Xe^{131}$ (with a Yukawa intensity function in the moment operator, of range $1.18\times10^{-13}$ cm), then the strength of $\mu(2)$ or $\mu(4)$ will

[16] R. G. Sachs, Phys. Rev. **74**, 433 (1948).

lie between 8 and 35 Mev. The spread is due to the uncertainty in the radial integrals. The three-body anomaly falls well within this range (see Table I).

It is seen that the forbidden $M1$ transitions place fairly strong upper and lower limits on the strength of interaction moments which contain $D$ functions in the coordinates of each of the particles. If $a\mu(1)+b\mu(2)+c\mu(3)+d\mu(4)$ is the interaction moment and if each $\mu(i)$ is normalized to yield the three-body anomaly so that $a+b+c+d=1$, then $0.3\lesssim|b+d|\lesssim 1.2$. The best value for $|b+d|$ is 0.6.

## IV. CONCLUSION

It seems unlikely that the static moments of heavy nuclei can provide any evidence for the nonadditivity of nucleon moments until much more detailed information concerning nuclear structure is available. On the other hand, the lifetimes for magnetic dipole transitions are so much less sensitive to nuclear structure that they seem to provide direct evidence for the existence of the effect. Adequate lifetime data are sparse but those available suggest an interaction moment for heavy nuclei of the same general form and magnitude as that which accounts for the anomaly in the $H^3$, $He^3$ magnetic moments.

Further data on the lifetimes of the "forbidden" $M1$ transitions are required to test the validity of the qualitative conclusions. Other data of interest would be static moments of mirror pairs other than $H^3$ and $He^3$; for example, the pair $Li^7$, $Be^7$. It would, of course, be most interesting to have the static moment in the excited state which undergoes the forbidden $M1$ transition.

This investigation was suggested by Professor R. G. Sachs, who contributed valuable advice during the course of the work.

## APPENDIX

The evaluation of matrix elements of the spin interaction moments $\mu(1)$, $\mu(2)$, $\mu(3)$, $\mu(4)$ with respect to shell model wave functions is divided into two parts: spin and angle integration, and purely radial integration. The spin and angle integration can be carried through directly without approximation. The results are characterized by the odd particle feature of the wave function and are in all essentials independent of the details of the coupling in the core. The radial integrals are, in general, more difficult to perform. In particular, the integrands concerned are not very well specified by the physics of the problem. These integrals were carried through with reasonable functions and without approximation only for the simple spin moment $\mu(1)$. In this direct calculation the functions

$$f_l(\rho)=c_l\rho^l e^{-b\rho},$$
$$\Phi(|\varrho_1-\varrho_2|)=C\exp(-\alpha|\varrho_1-\varrho_2|)/\alpha|\varrho_1-\varrho_2|$$

were employed, where $f_l(\rho)$ is the single particle radial function for single particle orbital angular momentum $l$, and $\Phi(|\varrho_1-\varrho_2|)$ is the intensity function in the moment operator. In the purely radial integrals one deals with the terms $\Phi_L(\rho_1,\rho_2)$ occurring in the expansion

$$\Phi(|\varrho_1-\varrho_2|)=\sum_{L,M}\Phi_L(\rho_1,\rho_2)Y_L{}^M(\theta_1,\phi_1)Y_L{}^{M*}(\theta_2,\phi_2).$$

The "well strength" $J$ associated with the moment is given by $J=(\hbar^2\alpha^2/m)(2C)$ Mev.

The radial integrals were also performed for all the $\mu(j)$ with a certain short-range approximation. The functions used for this calculation were

$$f_2(\rho)=\begin{cases}c_l\rho^l & \text{for } \rho\leq R\\ 0 & \text{for } \rho>R\end{cases},$$

$$\Phi(|\varrho_1-\varrho_2|)=C\exp[-\beta^2(\varrho_1-\varrho_2)^2],$$

with the approximation that the Gaussian

$$\exp[-\beta^2(\rho_1-\rho_2)^2]$$

is replaced by an appropriately normalized $\delta$-function in heavy nuclei. $R$ is taken to be the nuclear radius. This short-range approximation should be valid for a range of interaction $\beta^{-1}\ll R$. By means of the comparison with the more accurate and reasonable calculation of the radial integrals for $\mu(1)$, an attempt was made to estimate reasonable values of the radial integrals involved in the matrix elements of the other interaction moments. The results stated for $\mu(2)$, $\mu(3)$, and $\mu(4)$ are based upon such estimates of the radial integrals in regions where the short-range approximation was already fairly reliable.

# Internal Conversion of Neutron Capture $\gamma$-Rays

C. T. HIBDON AND C. O. MUEHLHAUSE*
*Argonne National Laboratory, Chicago, Illinois*
(Received July 25, 1952)

Prompt internal conversion electron lines resulting from neutron capture in $_{48}Cd^{113}$, $_{62}Sm^{149}$, $_{64}Gd^{odd}$, $_{66}Dy^{164}$, and $_{80}Hg^{199}$ have been observed. Their energies were measured in a 180° focusing, constant magnetic field, film recording $\beta$-ray spectrograph. The spectrograph was placed in a neutron beam from the Argonne heavy water reactor in such a way that the source underwent bombardment during recording. In some cases $K$, $L$, and $M$ lines were observed. Each element except mercury exhibited two strongly converting capture $\gamma$-ray states from a single isotope.

## INTRODUCTION

SLOW neutron capture usually results in the emission of cascade $\gamma$-rays of average energy $\sim 2$ Mev and lifetime per state $\sim 10^{-14}$ sec. In addition, however, a longer-lived ($\sim 10^{-10}$ sec) low energy state with a high internal conversion coefficient may be formed close to ground. The phenomenon of internal conversion of neutron capture $\gamma$-rays was first observed in cadmium by Hoffman and Bacher[1] and in gadolinium by Amaldi and Rasetti.[2] The latter found, for example, that in the case of thermal neutron absorption in gadolinium a prompt soft electron radiation having a half-value thickness of 2.3 mg Al/cm$^2$ was emitted. Since (1) this observation was only possible with the isotopes having the strongest absorption (odd $A$) and (2) these isotopes on capture simply form the next heavier isotopes, the radiation clearly must have been due to one or more very short-lived isomeric states in the cascade.

Goldhaber[3] and co-workers attempted to measure the lifetime of the low energy capture $\gamma$-rays from gadolinium using Geiger counters and a trigger sweep scope. They were able to show that the lifetime was $<10^{-7}$ sec.

Goldhaber and Muehlhause[4] made a limited survey of the strongly absorbing nuclei (Cd, Sm, Eu, Gd, Dy, Hg) in an attempt to establish the generality of the phenomenon of internal conversion accompanying neutron absorption. Thin films of the absorbing materials ($\sim 1$ mg/cm$^2$) were placed next to a photographic plate and bombarded in the thermal column of the Argonne heavy water reactor. A dense blackening of the plates resulted which could be removed by interposing thin absorbers of either Be, Al, or Pb between the capturing material and the photographic plate. Internal conversion was indicated for all the materials examined, the electron energies ranging from $\sim 50$ to $\sim 500$ kev.

By an entirely different technique Wexler and Davies,[5] and Davies and Yosim[6] showed that internal conversion is associated with neutron capture in Br, In, and Au. In the experiments on indium, positive $In^{116}$ ions were found to be "emitted" from an indium surface during neutron bombardment. Since neutralization would occur if the positive ions were formed only in the surface, the conclusion of Davies and Yosim was that positive ions were formed as a result of internal conversion $\sim 10^3$A away from the surface after the $In^{116}$ nuclei recoiled from the emission of energetic capture $\gamma$-rays. This was an entirely logical observation since one would expect the short-lived isomeric state(s) responsible for conversion to be near the ground state, i.e., to be not competing with the more rapidly decaying cascade $\gamma$-ray states. This conclusion has been verified for dysprosium in the present work.

Recently the authors decided to make accurate energy measurements of a few internal conversion lines emitted promptly on neutron capture. $Cd^{113}$, $Sm^{149}$, $Gd^{odd}$, $Dy^{164}$, and $Hg^{199}$ were measured by the techniques of $\beta$-ray spectroscopy.

## APPARATUS

Neutrons from the Argonne heavy water reactor were collimated by boron to make a beam of rectangular cross section $\sim 3$ mm wide and $\sim 20$ mm high. This passed along the axis of an evacuated tube into a constant magnetic field $\beta$-ray spectrograph. There the beam bombarded a thin film of absorbing material ($\sim 1$–3

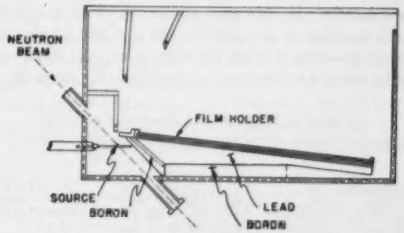


FIG. 1. Spectrograph camera.

* Now at Brookhaven National Laboratory, Upton, New York.
[1] J. G. Hoffman and R. F. Bacher, Phys. Rev. **54**, 664 (1938).
[2] E. Amaldi and F. Rasetti, Ricerca sci. **10**, 115 (1939).
[3] Sala, Axel, and Goldhaber, Phys. Rev. **74**, 1249 (1948).
[4] C. O. Muehlhause, Phys. Rev. **83**, 235 (1951); C. T. Hibdon and C. O. Muehlhause, Phys. Rev. **83**, 235 (1951).
[5] S. Wexler and T. H. Davies, Brookhaven National Laboratory Report C-7 (AECU-50) (1948).
[6] S. Yosim and T. H. Davies, J. Phys. and Colloid Chem. (to be published).

TABLE I. Line energies, work functions, and γ-ray energies.

| Compound nucleus | $E_\beta$ | $K$ | $L_2$ | $L_3$ | $M$ | $E_\gamma$ |
|---|---|---|---|---|---|---|
| $_{48}Cd^{114}$ | 70.1 | 26.8 | | | | 96.9 |
| | 92.8 | | | 3.5 | | 96.3 |
| | 535.1 | 26.8 | | | | 561.9 |
| $_{62}Sm^{150}$ | 290.3 | 46.9 | | | | 337.2 |
| | 329.5 | | | 6.7 | | 336.2 |
| | 393.5 | 46.9 | | | | 440.4 |
| | 433.3 | | | 6.7 | | 440.0 |
| $_{64}Gd^{even}$ | 28.9 | 50.1 | | | | 79.0 |
| | 38.4 | 50.1 | | | | 88.5 |
| | 70.7 | | 8.0 | | | 78.7 |
| | 71.3 | | | 7.3 | | 78.6 |
| | 77.0 | | | | 1.2 | 78.2 |
| | 80.4 | | | 7.3 | | 87.7 |
| | 130.4 | 50.1 | | | | 180.5 |
| $_{66}Dy^{165}$ | 73.9 | | 8.6 | | | 82.5 |
| | 74.6 | | | 7.8 | | 82.4 |
| | ~79 | | | | ~2 | ~81 |
| | 96.9 | | 9.1 $L_1$? | | | 106.0 |
| | 135.0 | 53.8 | | | | 188.8 |
| $_{80}Hg^{200}$ | ~270 | | ~14 | | | ~284 |
| | ~282 | | | | ~2 | ~284 |

percent neutron absorption) located at the normal source position of the spectrograph (see Fig. 1). The transmitted beam left the instrument through another evacuated tube and was eventually absorbed in a boron block. Internal conversion electrons resulting from neutron capture in the source moved in a 180° arc to be focused as lines on no-screen x-ray film, $K$, $L$, and $M$ lines were readily observed. Several field strengths were employed ranging from 100 to 250 gauss.

The sources studied were: enriched $Cd^{113}$ metal plated on thin aluminum (0.235 mg/cm²), enriched $Sm_2{}^{149}O_3$ made to adhere to aluminum, Gd metal evaporated on aluminum, $Dy_2O_3$ made to adhere to aluminum, and enriched $Hg^{199}$ metal amalgamated with ~1 mil gold. The metal films were $\sim 5\times 10^3$A thick. These resulted in ~1–2 percent electron absorption.

## RESULTS

Table I lists line energies, work functions, and γ-ray energies for the isotopes measured. The relevant $L$ work function is not certain, the one given being that which agrees best with the total energy as inferred by other lines. In the case of gadolinium, however, the rough $K/L$ ratio observed is in agreement with the observation of $L_2$ and $L_3$ conversion lines for an $E2$ transition.[7] It will be noted that in every element except mercury it is certain that two states are to be associated with a single isotope. To make this statement true for dysprosium one must include the 1.2-min metastable state.[8] Only in the case of dysprosium was the cross-over observed.

TABLE II. Predicted and observed $K/L$ ratios.

| Compound nucleus | $E_\gamma$ | $Z^3/E$ | $K/L$ ratio $M1$ Predicted | $K/L$ ratio $E2$ Predicted | $K/L$ ratio Observed | $L/M$ ratio Observed |
|---|---|---|---|---|---|---|
| $_{62}Sm^{150}$ | 336.7 | 11.4 | 7.9 | 4.2 | 4.4 | |
| | 440.2 | 8.73 | 8.0 | 5.4 | ~3 | |
| $_{64}Gd^{even}$ | 78.6 | 52.1 | 7.6 | 0.30 | ~0.3 | 2.5 |
| | 88.1 | 46.5 | 7.7 | 0.35 | | |

Table II relists a few of the state energies along with predicted[9] and observed $K/L$ ratios. It should be pointed out, however, that the observed ratios are only approximate. In the cases of samarium and gadolinium enough supplementary experiments on film density *vs* intensity were carried out to support the assignment of $E2$ (electric quadrupole).

## CONCLUSION

The technique employed is limited to materials having very large thermal absorption cross sections (≳500 b). Furthermore, the present work does not directly demonstrate that the lifetimes are less than minutes. Indirectly, however, the approximate $K/L$ ratios and the energies favor magnetic dipole or electric quadrupole transitions which would range in lifetime from $10^{-12}$–$10^{-9}$ sec.[9–11]

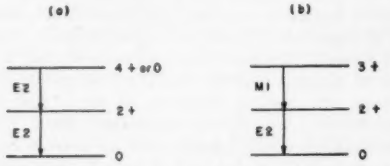


FIG. 2. Possible level schemes for the first excited states of even-even nuclei.

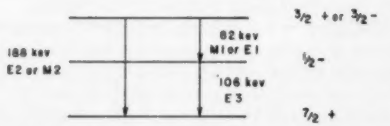


FIG. 3. Possible level scheme for the first excited states of the even-odd nucleus $_{66}Dy^{165}$.

The "prompt" charged radiation observed has been shown to be monoenergetic electrons (i.e., lines) and to require work functions characteristic of the absorbing element. Two possible level schemes for the compound even-even nuclei are given in Fig. 2: (a) most probable, (b) possible. Figure 3 gives the level scheme near ground of the even-odd nucleus, $_{66}Dy^{165}$.

[7] J. W. Mihelich and E. L. Church, Phys. Rev. **85**, 733 (1952).
[8] R. L. Caldwell, Phys. Rev. **78**, 407 (1950).
[9] M. Goldhaber and A. W. Sunyar, Phys. Rev. **83**, 906 (1951).
[10] M. Goldhaber, Phys. Rev. **82**, 323 (1951); A. W. Sunyar and M. Goldhaber, Phys. Rev. **83**, 216 (1951).
[11] S. A. Moszkowski, Phys. Rev. **83**, 240 (1951).

# The Theory of Hydrogen Three*†

ROBERT L. PEASE‡ AND HERMAN FESHBACH
*Department of Physics and Laboratory for Nuclear Science and Engineering, Massachusetts Institute of Technology, Cambridge, Massachusetts*

(Received July 29, 1952)

The binding energy of the triton has been calculated by the variational method. The forces between the particles are assumed to be charge independent and to be composed of central and tensor parts, the radial dependence of each being given by Yukawa wells. The binding energy calculation is employed to determine the range of the tensor component; the other constants are fixed by the low energy two-body data. The effective triplet range, the percentage $D$ state in the triton, and the Coulomb energy of $He^3$ are then predicted. The first two of these are in satisfactory agreement with experiment; the third is in error by twenty-five percent. The final "best" potential contains only four constants, the ranges and depths of the central and tensor potentials. The triplet and singlet central forces are equal.

## I. INTRODUCTION

IT is now well known that the low energy two-body data are not sensitive to the shape of the two-body nuclear potential. For this information it is more profitable to turn to high energy two-body scattering experiments and to the nuclear three-body system upon which our attention is focused here. This sensitivity of the three-body problem was recently discussed by Svartholm,[1] who employed several different central force potentials. We interpret his results as follows: If the range and depth of the internucleon potential are adjusted to the low energy two-body data, the calculated binding energy of $H^3$ will be greater for those wells which are deeper at small interparticle distances. Thus the Yukawa potential involving a $(1/r)$ singularity yields a larger binding energy than the Gaussian. This is in agreement with the calculation of Thomas,[2] who showed that the calculated binding energy of $H^3$ is infinite for a zero-range potential.

Svartholm also found that the calculated binding energy considerably exceeded the experimental value. We may take this as indirect evidence for the existence of noncentral forces (evidence of course not so cogent as is the existence of the quadrupole moment of the deuteron); for, as Inglis[3] pointed out, such a force reduces the ratio of the theoretical $H^3$ binding energy to the binding energy of the deuteron.

In the present paper a variational calculation of the binding energy of $H^3$ and $He^3$ is made. The internucleon potential $V_{12}$ between particles 1 and 2 is taken to be

$$V_{12}=-V_0\{[1-\tfrac{1}{2}g+\tfrac{1}{2}g\boldsymbol{\sigma}_1\cdot\boldsymbol{\sigma}_2]f(r/r_0)+\gamma S_{12}f(r/r_t)\}, \quad (1)$$

where

$$S_{12}=r_{12}^{-2}[3(\boldsymbol{\sigma}_1\cdot\mathbf{r}_{12})(\boldsymbol{\sigma}_2\cdot\mathbf{r}_{12})]-\boldsymbol{\sigma}_1\cdot\boldsymbol{\sigma}_2,$$

$$f(x)=e^{-x}/x, \quad \mathbf{r}_{12}=\mathbf{r}_2-\mathbf{r}_1,$$

and $V_0$, $\gamma$, $g$, $r_0$, and $r_t$ are constants. We assume charge independence of nuclear forces—which is consistent[4] with the use of the Yukawa potential as far as low energy two-body data are concerned. Ideally the constants in potential (1) are fixed by the deuteron binding energy $\epsilon$, the deuteron quadrupole moment $Q$, the singlet scattering length, the singlet effective range, and the triplet effective range $\rho_1$. The singlet effective range is taken from $p-p$ scattering data. The relation between these experimental results and the constants in our potential has been considered for the triplet state by Feshbach and Schwinger.[5] The calculations of Hoisington, Share, and Breit[6] and of Jackson and Blatt[7] were employed in the determination of $r_0$ and $V_0(1-2g)$, the only constants in the singlet potential; the numerical values are $r_0=1.184\times10^{-13}$ cm, $V_0(1-2g)=46.48$ Mev. At the time that these calculations were performed, the triplet effective range was not a very useful parameter. For a given tensor range $r_t$, $\epsilon$ and $Q$ determine $V_0$ and $\gamma$ quite closely. However, $r_t$ itself is insensitive to $\rho_1$, so that $\rho_1$ must be known very accurately before $r_t$ is determined. As we shall see, the theoretical binding energy of $H^3$ is much more sensitive to $r_t$; therefore, we employed it to determine $r_t$ and then predicted $\rho_1$. We obtain a rather close agreement with the most recent experimental values; hence we may conclude that potential (1) provides a good description of the nuclear two-body potential in the low energy domain.

Our results have a certain irreducible inaccuracy arising from, first, the possible existence of three-body forces[8] and, second, the inaccuracy of potential (1) in the high energy domain.[9] No corrections were made for these effects. If at some future time the two-body force is completely understood, the theory of $H^3$ will then be useful in the investigation of three-body forces.

We have also neglected exchange effects; however,

* Supported in part by the joint program of the ONR and AEC.
† A preliminary report was published as a Letter to the Editor, Phys. Rev. 81, 142 (1951).
‡ Now at the RAND Corporation, Santa Monica, California.
[1] N. Svartholm, thesis, Lund (H. Ohlssons Boktryckeri, 1945).
[2] L. H. Thomas, Phys. Rev. 47, 903 (1935).
[3] D. R. Inglis, Phys. Rev. 55, 988 (1939).
[4] J. Schwinger, Phys. Rev. 78, 135 (1950).
[5] H. Feshbach and J. Schwinger, Phys. Rev. 84, 194 (1951).
[6] Hoisington, Share, and Breit, Phys. Rev. 56, 884 (1939).
[7] J. D. Jackson and J. M. Blatt, Revs. Modern Phys. 22, 77 (1950).
[8] H. Primakoff and T. Holstein, Phys. Rev. 55, 1218 (1939).
[9] R. S. Christian and E. W. Hart, Phys. Rev. 77, 441 (1950); R. S. Christian and H. P. Noyes, Phys. Rev. 79, 85 (1950).

both Svartholm[1] and Hu and Hsu[10] have found that these have very little effect.

Other calculations which have been made with tensor forces include those of Gerjuoy and Schwinger,[11] Feshbach and Rarita,[12] and Clapp.[13] These authors employed the Rarita-Schwinger potential,[14] which is, however, no longer in agreement with experiment. Hu and Hsu[10] have made calculations employing a potential of form (1), but primarily with $r_c=r_t$, the values of $r_c$ chosen precluding any charge independence. A preliminary calculation in which $r_c\neq r_t$ was made by Avery and Adams.[15]

## II. VARIATIONAL PROCEDURE

The major portion of the investigation consisted in constructing a nuclear Hamiltonian with potentials given by (1), choosing suitable trial wave functions, and determining an upper bound to the ground-state energy by means of the Ritz variation method.

Choice of the relative coordinate system of Fig. 1 permitted the expression of the $D$ state wave functions in terms of operations upon the $S$ state wave functions by operators of the form $S_{ij}$. In such a system, the kinetic energy

$$T=-\frac{\hbar^2}{M}(\nabla_1^2+\nabla_1\cdot\nabla_2+\nabla_2^2), \tag{2}$$

where $M$ is the nucleon mass.

The trial functions were chosen to be combinations of the spin-antisymmetric $^3S_1$ state and the three independent $^4D_1$ states, designated, respectively, $D$, $D'$, and $D''$. The other possible $^2S_1$ state, symmetric in the neutron spins and thus antisymmetric in the neutron space coordinates, was not used because it vanished for $r_1=r_2$; Feshbach and Rarita[12] found that it added only 0.4 percent to their computed binding energy. Since the $S-P$ coupling was of higher order than the $S-D$ coupling and the percentage $D$ state was less than 4 percent, no $P$ states were included. The four spin-angular wave functions were

$$\begin{aligned}
\chi_S&=(2)^{-\frac{1}{2}}[\alpha(1)\beta(2)-\beta(1)\alpha(2)]\alpha(3),\\
\chi_D&=[r_1^2S_{13}+r_2^2S_{23}]\chi_S,\\
\chi_{D'}&=[r_1^2S_{13}-r_2^2S_{23}]\chi_S,\\
\chi_{D''}&=[3(\boldsymbol{\sigma}_1\cdot\mathbf{r}_1\times\mathbf{r}_2)(\boldsymbol{\sigma}_2\cdot\mathbf{r}_1\times\mathbf{r}_2)\\
&\qquad-(\boldsymbol{\sigma}_1\cdot\boldsymbol{\sigma}_2)(\mathbf{r}_1\times\mathbf{r}_2)\cdot(\mathbf{r}_1\times\mathbf{r}_2)]\chi_S.
\end{aligned} \tag{3}$$

If the trial wave function is $\sum|i\rangle A_i$, then the Ritz variation method automatically chooses optimum values of $A_i$ through solution of the secular determinant

$$|\langle i|H-E|j\rangle|=0, \tag{4}$$

where $|i\rangle$ and $|j\rangle$ represent typical terms. For convenience in computation, the matrix elements were broken up into a sum of terms:

$$\begin{aligned}
\langle i|H-E|j\rangle=&\frac{\hbar^2}{M}\langle i|KE|j\rangle+\langle i|V|j\rangle_{NT}\\
&+2\langle i|T_{13}|j\rangle+\langle i|T_{12}|j\rangle-E\langle i|j\rangle.
\end{aligned} \tag{5}$$

The sign of the "$KE$" matrix element was changed for convenience. The "$NT$" (nontensor) elements arise from the central-force potential terms and are grouped together because of similarity. The three matrix elements of the tensor-force part of the potential, involving $S_{13}$, $S_{23}$, and $S_{12}$, respectively, were designated as $\langle i|T_{13}|j\rangle$, $\langle i|T_{23}|j\rangle$, and $\langle i|T_{12}|j\rangle$, the first two of which are equal. After summation over spins, spatial integration was carried out by the techniques of Hylleraas[16] and of Coolidge and James.[16,17]

The variational calculation began with a four-term trial function and proceeded to a more complex trial function in a series of stages:

*Step 1.* A four-term trial function was used, with one term for each spin state, of the form

$$\begin{aligned}
\psi^{(1)}&=A_S\psi_S+A_D\psi_D+A_{D'}\psi_{D'}+A_{D''}\psi_{D''},\\
\psi_S&=\chi_S\exp-\tfrac{1}{2}\lambda(r_1+r_2+\rho),\\
\psi_D&=\chi_D\exp-\tfrac{1}{2}\mu(r_1+r_2+\rho),\\
\psi_{D'}&=\chi_{D'}(r_1-r_2)\exp-\tfrac{1}{2}\nu(r_1+r_2+\rho),\\
\psi_{D''}&=\chi_{D''}(r_1-r_2)\exp-\tfrac{1}{2}\omega(r_1+r_2+\rho).
\end{aligned} \tag{6}$$

Reasonable values for $\lambda$, $\mu$, and $\nu$ were determined by applying the Ritz method to the first three terms. Then

TABLE I. Comparison of results. The entries in columns labeled Step 1, Step 2, and Step 5 are the respective calculated binding energies in Mev for the four-term wave function (Step 1), the five-term wave function (Step 2), and the nine-term wave function (Step 5). The units of $r_t$ are $10^{-13}$ cm.

| $r_t$ | $r_t/r_c$ | Step 1 | Step 2 | Step 5 |
|---|---|---|---|---|
| 2.122 | 1.792 | −9.10 | −9.46 | −10.05 |
| 1.827 | 1.543 | −7.86 | −8.21 | −9.06 |
| 1.533 | 1.294 | −5.72 | −6.06 | −7.50 |

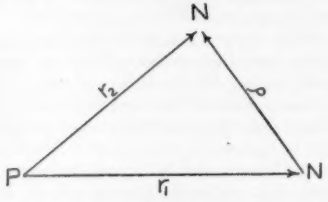


FIG. 1. Coordinate system for $H^3$.

[10] T.-M. Hu and K.-N. Hsu, Phys. Rev. **78**, 633 (1950).
[11] E. Gerjuoy and J. Schwinger, Phys. Rev. **61**, 138 (1942).
[12] H. Feshbach and W. Rarita, Phys. Rev. **75**, 1384 (1949).
[13] R. E. Clapp, Phys. Rev. **76**, 873 (1949).
[14] W. Rarita and J. Schwinger, Phys. Rev. **59**, 436 (1941).
[15] R. Avery and E. N. Adams, Phys. Rev. **75**, 1106 (1949).
[16] E. A. Hylleraas, Z. Physik **54**, 347 (1929); A. S. Coolidge and H. M. James, Phys. Rev. **51**, 855 (1937).
[17] See Appendix A.

TABLE II. Physical results.[a]

| $r_1$ | $r_1/r_e$ | $E$ | $\gamma$ | $V_3$ | $\delta$ | $P_D$ | $E_{coul}$ | $\rho_1$ |
|---|---|---|---|---|---|---|---|---|
| 2.122 | 1.792 | −10.05 | 0.2259 | 55.054 | 0.0779 | 2.2 | 1.088 | 1.79 |
| 1.827 | 1.543 | −9.06 | 0.3799 | 50.123 | 0.0364 | 2.8 | 1.059 | 1.76 |
| 1.70 | 1.44 | −8.48[b] | 0.5085 | 46.96 | 0.005 | 3.1 | 1.041 | 1.74 |
| 1.56 | 1.32 | −7.63[c] | 0.7365 | 42.00 | −0.053 | 3.5 | 1.014 | 1.72 |
| 1.533 | 1.294 | −7.50 | 0.7894 | 40.918 | −0.0679 | 3.6 | 1.008$_5$ | 1.71 |

[a] Unit of length $10^{-13}$ cm; unit of energy 1 Mev.
[b] Experimental value of binding energy.
[c] 90 percent of experimental value of binding energy.

the fourth term was added and $E$ was minimized for $\omega$; it was found that the inclusion of the $D'$ term contributed about 5 percent to the computed energy. Next, the 4×4 determinant was minimized in $E$ simultaneously for $\lambda$, $\mu$, and $\nu$, using the value of $\omega$ previously determined. Finally, $\omega$ was varied slightly. Incidentally, we would like to note that $\psi_S$ is an exceedingly good trial function for the pure central force case. When employed with the exponential or Yukawa wells it gives well over 90 percent of the binding energy obtained by Rarita and Present[18] and Svartholm,[1] respectively.

*Step 2.* A five-term trial function was formed by increasing the number of $S$ terms to two. The $S$ part of the wave function had the form

$$As_1\psi_{S1}+As_2\psi_{S2},$$
$$\psi_{Si}=\chi_S \exp[-\tfrac{1}{2}\lambda_i(r_1+r_2+\rho)]. \quad (7)$$

The energy was minimized for variation of the five parameters $\lambda_1$, $\lambda_2$, $\mu$, $\nu$, and $\omega$.

*Step 3.* A seven-term trial function ($S_1$, $S_2$, $D_1$, $D_2$, $D_1'$, $D_2'$, $D''$) was formed from the function of Step 2 by splitting the $D$ and $D'$ states, just as was done in Step 2 to the $S$ states. The parameters $\lambda_1$, $\lambda_2$, and $\omega$ were retained from Step 2, and the energy was minimized for variations of the four parameters $\mu_1$, $\mu_2$, $\nu_1$, and $\nu_2$.

*Step 4.* The wave function of Step 2 was enlarged by multiplying the $S$ terms by series in $(r_1-r_2)^2$, in $\rho$, and in $(r_1+r_2)$; i.e., such that the $S$ parts of the wave function assumed such forms as

$$[As_1+As_1^{\alpha}(r_1-r_2)^2]\exp[-\tfrac{1}{2}\lambda_1(r_1+r_2+\rho)]+(S_1\rightleftarrows S_2),$$
$$[As_1+As_1^{\alpha}\rho]\exp[-\tfrac{1}{2}\lambda_1(r_1+r_2+\rho)]+(S_1\rightleftarrows S_2),$$
$$[As_1+As_1^{\alpha}(r_1+r_2)]\exp[-\tfrac{1}{2}\lambda_1(r_1+r_2+\rho)]+(S_1\rightleftarrows S_2),$$

where the symbol $(S_1\rightleftarrows S_2)$ denotes a similar expression involving the $S_2$ term. The five parameters $\lambda_1$, $\lambda_2$, $\mu$, $\nu$, and $\omega$ were retained from Step 2.

*Step 5.* A procedure similar to that of Step 4 was applied to the $D$ and $D'$ states. A series involving $\rho$, a series involving $(r_1+r_2)$, and then a series involving both were used.

Steps 3 and 4 did not produce a sufficient decrease in computed energy to justify the correspondingly increased complexity of the wave function, and hence were dropped. However, Step 5 was retained; the final wave function was

$$\psi=As_1\psi_{S1}+As_2\psi_{S2}+[A_D+\rho A_{D^{\alpha}}+(r_1+r_2)A_{D^{\beta}}]\psi_D +[A_{D'}+\rho A_{D'^{\alpha}}+(r_1+r_2)A_{D'^{\beta}}]\psi_{D'}+A_{D''}\psi_{D''}. \quad (8)$$

The behavior of the calculated binding energy as the wave function was improved is shown in Table I. For tensor ranges $r_t=2.122\times10^{-13}$ cm and $1.827\times10^{-13}$ cm (corresponding, respectively, to $r_t/r_e=1.792$ and 1.543), convergence seems to have been obtained. The results for $r_t=1.533\times10^{-13}$ cm ($r_t/r_e=1.294$) are somewhat more uncertain, but we estimate the computed binding energy to be no more than a few percent above the correct value.

## III. RESULTS

Matrix elements obtained after removal of spin dependence are tabulated in Appendix B.[19]

Table II shows the constants of the assumed internuclear potential (1), both for the three values of $r_t$ for which the calculations were carried through and (by interpolation) for cases corresponding to variationally computed energies of 7.63 and 8.48 Mev, which represent, respectively, 90 percent and 100 percent of the experimental value.[20] Calculated percent $D$ state, Coulomb energy, and effective triplet scattering ranges for the above cases are also shown. Wave function parameters are shown in Table III.

## IV. DISCUSSION

Inspection of Table II reveals the sensitivity of the computed triton binding energy to variations in the range of the tensor force; the computation of triton binding energy thus allows a sharply defined tensor range to be set. One can see that the triplet effective range is not nearly so sensitive to variations in tensor range as the binding energy is.

However, the above does not necessarily indicate that a large effect upon the properties of the system is

TABLE III. Wave function parameters.

| $r_t/r_e$ | $\lambda/r_e$ | $\lambda'/r_e$ | $\mu/r_e$ | $\nu/r_e$ | $\omega/r_e$ | $A_{S_1}$ | $A_{S_2}$ | $A_D$ | $A_{D'}$ | $A_{D''}$ | $A_{D^{\alpha}}$ | $A_{D'^{\alpha}}$ | $A_{D^{\beta}}$ | $A_{D'}$ |
|---|---|---|---|---|---|---|---|---|---|---|---|---|---|---|
| 1.792 | 1.0 | 2.0 | 2.2 | 2.5 | 2.8 | 1.464 | 4.672 | 1.0 | −1.204 | 0.693 | 0.426 | −0.1085 | −0.248 | 0.168 |
| 1.543 | 1.0 | 1.9 | 2.2 | 2.5 | 2.8 | 1.369 | 3.537 | 1.0 | −1.178 | 0.902 | 0.493 | −0.1945 | −0.269 | 0.180 |
| 1.44 | 0.9$_5$ | 1.8 | 2.2 | 2.5 | 2.8 | 1.08 | 3.01 | 1.0 | −1.29 | 0.91 | 0.45 | −0.136 | −0.27 | 0.20 |
| 1.32 | 0.8 | 1.5$_5$ | 2.2 | 2.5 | 2.8 | 0.44 | 2.36 | 1.0 | −1.59 | 0.80 | 0.30 | 0.058 | −0.25 | 0.25 |
| 1.294 | 0.8 | 1.5 | 2.2 | 2.5 | 2.8 | 0.272 | 2.241 | 1.0 | −1.666 | 0.758 | 0.254 | 0.1129 | −0.241 | 0.263 |

[18] W. Rarita and R. D. Present, Phys. Rev. **51**, 788 (1937).
[19] Integrated matrix elements are not shown because of space limitations, but are available in hectographed form.
[20] Li, Whaling, Fowler, and Lauritsen, Phys. Rev. **83**, 512 (1951).

produced by variations of $r_t$ alone, for the requirement that two-body data be satisfied necessitates a change in $\gamma$, $V_0$, and $g$ when $r_t$ is changed, and $r_t$ occurs in the expression for tensor well depth as well.

From Table II, we see that the appropriate value of $r_t$ is $1.70\times10^{-13}$ cm. The corresponding value of $\rho_1$ is $1.74\times10^{-13}$ cm. This agrees very well with the experimental value[21] of $1.71\times10^{-13}$ cm. The corresponding value of the percent $D$ state is 3.1 percent, which is to be compared with the value 3.7$_5$ percent obtained by the theory of Sachs and Schwinger[22] from the sum of the magnetic moments of $H^3$ and $He^3$. This agreement seems satisfactory, in view of the uncertainties arising from relativistic effects in the Sachs and Schwinger calculation. We finally turn to the Coulomb energy, the expectation value of $e^2/\rho$, equal to the difference in $H^3$ and $He^3$ binding energies. The predicted Coulomb energy is higher than the experimental value of 0.77 Mev.[23] This discrepancy may be in part due to the unsuitability for this calculation of our wave function, determined as it has been by a variational expression for the energy. Further explanations of the discrepancy include the following possibilities: (1) effects of the magnetic interaction; (2) inequality of $n-n$ and $p-p$ forces; (3) requirement that the potential be less singular at zero interparticle distances than is the Yukawa potential. The first of these has been investigated.[24] It is found that the magnetic effects increase the binding energy difference between $H^3$ and $He^3$; thus the discrepancy is increased. Suggestion (2) can hardly be investigated at the present time. Meson field theory does, however, indicate that higher order effects of this kind do exist. Suggestion (3) is buttressed to some extent by the fact[9] that the exponential well does give a better value for the total $n-p$ cross section at high energy than the Yukawa well. On the other hand, the latter yields a better angular distribution.

In conclusion, potential (1) with the constants given in Table II for $E=-8.48$ Mev summarizes all the low energy two-body data and gives the correct binding energy and percent $D$ state for $H^3$. A discrepancy of twenty-five percent in the Coulomb energy remains.

Note that by only a slight reduction of the range of the tensor forces one may place $g$ equal to zero, for which the singlet and triplet central potentials are equal. This four-parameter potential is consistent with the experimental data and is more satisfying in that these four constants predict six experimental numbers, the singlet and triplet scattering lengths and effective ranges, the deuteron quadrupole moment, and the binding energy of $H^3$.[25]

[21] Hughes, Burgy, and Ringo, Phys. Rev. **77**, 291 (1950).
[22] R. G. Sachs and J. Schwinger, Phys. Rev. **70**, 41 (1946).
[23] Tollestrup, Jenkins, Fowler, and Lauritsen, Phys. Rev. **75**, 1947 (1949).
[24] George Stuart (private communication).
[25] *Note added in proof:* Recent calculations by Irving [Phys. Rev. **87**, 519 (1952)] indicate that this potential will also predict the binding energy of $He^4$ with fair accuracy.

We are greatly indebted to Dr. Jane S. Pease for verifying some of our calculations. Most of the numerical work was ably and patiently performed by Miss Hannah Paul of the Joint Computing Group at the Massachusetts Institute of Technology.

## APPENDIX

### A. Methods of Integration

Since the Hamiltonian is independent of the location or orientation of the system, the only noncyclic coordinates are $r_1$, $r_2$, and $\rho$ or a system derived from them. The general volume element may be shown rigorously by direct computation of the Jacobian to be

$$(8/3)\pi^2 r_1 r_2 \rho dr_1 dr_2 d\rho;$$

we can, however, drop the numerical factor for simplicity.

The integration limits on the above set of variables involve, for the first variable integrated, the sum and (absolute value of) the difference of the other two variables. As this is rather unwieldy where exponentials are involved, we shall use two other schemes in actual computations.

Integration of the matrix elements involving exponentially only $(r_1+r_2)$ and $\rho$ is carried out most simply by the Hylleraas method as used by Rarita and Present.[18] If one chooses as variables the quantities $s\equiv r_1+r_2$, $t\equiv r_1-r_2$, and $\rho$, the integration scheme becomes

$$\int f(s,t,\rho)d\tau=\int_0^\infty ds\int_0^s d\rho\int_0^\rho dt\rho(s^2-t^2)f(s,t,\rho), \quad \text{(A1)}$$

for which recursion formulas were developed.[18]

However, this scheme proved overly difficult where the exponentials involved $r_1$ and $r_2$ unsymmetrically. Instead of permuting the variables, we used the scheme of Coolidge and James,[16] which has the advantage of compartmenting the integrations. Making the substitutions

$$\begin{aligned}\xi&\equiv r_1+r_2-\rho,\\ \eta&\equiv r_1-r_2+\rho,\\ \zeta&\equiv -r_1+r_2+\rho,\end{aligned} \quad \text{(A2)}$$

and inserting a numerical factor chosen simply to give the same result as the Hylleraas method for the same integrand, one obtains

$$\int f(\xi,\eta,\zeta)d\tau=(1/8)\int_0^\infty d\xi\int_0^\infty d\eta\int_0^\infty d\zeta \times(\xi+\eta)(\xi+\zeta)(\eta+\zeta)f(\xi,\eta,\zeta). \quad \text{(A3)}$$

When $(\xi+\eta)^3$ appears in the denominator of $f(\xi,\eta,\zeta)$, the integration cannot be carried out independently over $\xi$ and $\eta$, but the integrals may easily be evaluated

by the further substitutions

$$\xi=y-x, \qquad \eta=y+x, \tag{A4}$$

or the substitutions

$$\xi=r\cos^2\phi, \qquad \eta=r\sin^2\phi. \tag{A5}$$

### B. Matrix Elements, Not Integrated

Let typical $S$, $D$, $D'$, and $D''$ components of the trial wave function be, respectively, $b(r_1,r_2,\rho)\chi_S$, $g(r_1,r_2,\rho)\chi_D$, $h(r_1,r_2,\rho)\chi_{D'}$, and $p(r_1,r_2,\rho)\chi_{D''}$. Then the matrix elements, expressed as integrals over spatial coordinates, are as follows:

*1. Normalization Elements*

$$(S|S)=\int b^2 d\tau$$

$$(S|D)=0$$

$$(S|D')=0$$

$$(S|D'')=0$$

$$(D|D)=\int g^2 d\tau 6[r_1^4+r_2^4+r_1^2r_2^2(1-3\cos^2\theta)]$$

$$(D|D')=\int ghd\tau 6[r_1^4-r_2^4]$$

$$(D|D'')=\int gpd\tau(-3)(r_1^2-r_2^2)r_1^2r_2^2(1-\cos^2\theta)$$

$$(D'|D')=\int h^2 d\tau 6[r_1^4+r_2^4-r_1^2r_2^2(1-3\cos^2\theta)]$$

$$(D'|D'')=\int hpd\tau(-3)(r_1^2+r_2^2)r_1^2r_2^2(1-\cos^2\theta)$$

$$(D''|D'')=\int p^2 d\tau 6[r_1^2r_2^2(1-\cos^2\theta)]^2$$

$$\cos\theta=(r_1^2+r_2^2-\rho^2)/2r_1r_2.$$

*2. Kinetic Energy Elements*

Let

$$P(u,v)\equiv\frac{u}{r_1^2}\frac{\partial}{\partial r_1}\left(r_1^2\frac{\partial v}{\partial r_1}\right)+\frac{u}{r_2^2}\frac{\partial}{\partial r_2}\left(r_2^2\frac{\partial v}{\partial r_2}\right)+\frac{u}{\rho^2}\frac{\partial}{\partial\rho}\left(\rho^2\frac{\partial v}{\partial\rho}\right)+\frac{\mathbf{r}_1\cdot\mathbf{r}_2}{r_1r_2}u\frac{\partial^2 v}{\partial r_1\partial r_2}-\frac{\mathbf{r}_1\cdot\boldsymbol{\rho}}{r_1\rho}u\frac{\partial^2 v}{\partial r_1\partial\rho}+\frac{\mathbf{r}_2\cdot\boldsymbol{\rho}}{r_2\rho}u\frac{\partial^2 v}{\partial r_2\partial\rho}.$$

Then

$$(S|KE|S)=-\int d\tau P(b,b)$$

$$(S|KE|D)=0$$

$$(S|KE|D')=0$$

$$(S|KE|D'')=0$$

$$(D|KE|D)=-\int d\tau\left\{\left[P(g,g)+\frac{2g}{\rho}\frac{\partial g}{\partial\rho}\right]\times 6[r_1^4+r_2^4+r_1^2r_2^2(1-3\cos^2\theta)]+\frac{4g}{r_1}\frac{\partial g}{\partial r_1}\times[6r_1^4+3r_1^2r_2^2(1-3\cos^2\theta)-3(r_1^2-r_2^2)r_1r_2\cos\theta]+\frac{4g}{r_2}\frac{\partial g}{\partial r_2}[6r_2^4+3r_1^2r_2^2(1-3\cos^2\theta)+3(r_1^2-r_2^2)r_1r_2\cos\theta]\right\}$$

$$(D|KE|D')=-\int d\tau\left\{[P(g,h)6(r_1^4-r_2^4)]+\frac{4g}{r_1}\frac{\partial h}{\partial r_1}\times[6r_1^4+3r_1^2r_2^2(1-3\cos^2\theta)+3(r_1^2-r_2^2)r_1r_2\cos\theta]+\frac{4g}{r_2}\frac{\partial h}{\partial r_2}[-6r_2^4-3r_1^2r_2^2(1-3\cos^2\theta)+3(r_1^2-r_2^2)r_1r_2\cos\theta]+\frac{4g}{\rho}\frac{\partial h}{\partial\rho}[3(r_1^4-r_2^4)-6(r_1^2-r_2^2)r_1r_2\cos\theta]\right\}$$

$$(D|KE|D'')=-\int d\tau\left\{\left[P(g,p)+\frac{4g}{r_1}\frac{\partial p}{\partial r_1}+\frac{4g}{r_2}\frac{\partial p}{\partial r_2}+\frac{4g}{\rho}\frac{\partial p}{\partial\rho}\right](-3)(r_1^2-r_2^2)r_1^2r_2^2(1-\cos^2\theta)+gp[-12(r_1^4-r_2^4)+12(r_1^2-r_2^2)r_1r_2\cos\theta]\right\}$$

$$(D'|KE|D')=-\int d\tau\left\{[P(h,h)]\times 6[r_1^4+r_2^4-r_1^2r_2^2(1-3\cos^2\theta)]+\frac{4h}{r_1}\frac{\partial h}{\partial r_1}\times[6r_1^4-3r_1^2r_2^2(1-3\cos^2\theta)+3(r_1^2+r_2^2)r_1r_2\cos\theta]+\frac{4h}{r_2}\frac{\partial h}{\partial r_2}[6r_2^4-3r_1^2r_2^2(1-3\cos^2\theta)+3(r_1^2+r_2^2)r_1r_2\cos\theta]+\frac{4h}{\rho}\frac{\partial h}{\partial\rho}[3(r_1^4+r_2^4)-3r_1^2r_2^2(1-3\cos^2\theta)-6(r_1^2+r_2^2)r_1r_2\cos\theta]\right\}$$

$$(D'|KE|D'')=-\int d\tau\Big\{\Big[P(h,p)+\frac{4h}{r_1}\frac{\partial p}{\partial r_1}+\frac{4h}{r_2}\frac{\partial p}{\partial r_2}+\frac{4h}{\rho}\frac{\partial p}{\partial \rho}\Big](-3)(r_1^2+r_2^2)r_1^2r_2^2(1-\cos^2\theta)+hp[-12(r_1^4+r_2^4)-12r_1^2r_2^2(1-3\cos^2\theta)+12(r_1^2+r_2^2)r_1r_2\cos\theta]\Big\}$$

$$(D''|KE|D'')=-\int d\tau\Big\{\Big[P(p,p)+\frac{4p}{r_1}\frac{\partial p}{\partial r_1}+\frac{4p}{r_2}\frac{\partial p}{\partial r_2}+\frac{4p}{\rho}\frac{\partial p}{\partial \rho}\Big]6[r_1^2r_2^2(1-\cos^2\theta)]^2+p^2[6(r_1^2+r_2^2-r_1r_2\cos\theta)r_1^2r_2^2(1-\cos^2\theta)]\Big\}.$$

### 3. Nontensor Potential Elements

$$(S|V|S)_{NT}=-V_0\int b^2d\tau\times\{(1-\tfrac{1}{2}g)[f(r_1/r_c)+f(r_2/r_c)]+(1-2g)f(\rho/r_c)\}.$$

With the exception of the $S-S$ element, the nontensor potential elements are the same as the corresponding normalization elements, premultiplied by $(-V_0)$, and with a factor of

$$[f(r_1/r_c)+f(r_2/r_c)+f(\rho/r_c)]$$

inserted into the integrand. As a typical example,

$$(D|V|D')_{NT}=-V_0\int ghd\tau 6(r_1^4-r_2^4)\times[f(r_1/r_c)+f(r_2/r_c)+f(\rho/r_c)].$$

### 4. $T_{13}$ Potential Elements

$$(S|T_{13}|S)=0$$

$$(S|T_{13}|D)=-\gamma V_0\int bgd\tau f(r_1/r_t)\times[6r_1^2+(3-9\cos^2\theta)r_2^2]$$

$$(S|T_{13}|D')=-\gamma V_0\int bhd\tau f(r_1/r_t)\times[6r_1^2-(3-9\cos^2\theta)r_2^2]$$

$$(S|T_{13}|D'')=+\gamma V_0\int bpd\tau f(r_1/r_t)[3r_1^2r_2^2(1-\cos^2\theta)]$$

$$(D|T_{13}|D)=-\gamma V_0\int g^2d\tau f(r_1/r_t)\times[-12r_1^4+6(r_2^4-2r_1^2r_2^2)(1-3\cos^2\theta)]$$

$$(D|T_{13}|D')=-\gamma V_0\int ghd\tau f(r_1/r_t)\times[-12r_1^4-6r_2^4(1-3\cos^2\theta)]$$

$$(D|T_{13}|D'')=-\gamma V_0\int gpd\tau f(r_1/r_t)[6r_1^4r_2^2(1-\cos^2\theta)+3r_1^2r_2^4(4-10\cos^2\theta+6\cos^4\theta)]$$

$$(D'|T_{13}|D')=-\gamma V_0\int h^2d\tau f(r_1/r_t)[-12r_1^4+6r_2^4(1-3\cos^2\theta)+12r_1^2r_2^2(1-3\cos^2\theta)]$$

$$(D'|T_{13}|D'')=-\gamma V_0\int hpd\tau f(r_1/r_t)[6r_1^4r_2^2(1-\cos^2\theta)-3r_1^2r_2^4(4-10\cos^2\theta+6\cos^4\theta)]$$

$$(D''|T_{13}|D'')=-\gamma V_0\int p^2d\tau f(r_1/r_t)6[r_1^2r_2^2(1-\cos^2\theta)]^2.$$

### 5. $T_{12}$ Potential Elements

$$(S|T_{12}|S)=0$$

$$(S|T_{12}|D)=0$$

$$(S|T_{12}|D')=0$$

$$(S|T_{12}|D'')=0$$

$$(D|T_{12}|D)=-\gamma V_0\int g^2d\tau f(\rho/r_t)\times\Big\{12[r_1^4+r_2^4+\tfrac{1}{2}r_1^2r_2^2(3\cos^2\theta-1)]-\frac{12}{\rho^2}[2r_1^6+2r_2^6+r_1^2r_2^2(r_1^2+r_2^2)+(2r_1^2r_2^2-4r_1^4-4r_2^4)r_1r_2\cos\theta]\Big\}$$

$$(D|T_{12}|D')=-\gamma V_0\int ghd\tau f(\rho/r_t)\Big\{12(r_1^4-r_2^4)-\frac{12}{\rho^2}[2r_1^6-2r_2^6+\tfrac{1}{2}r_1^2r_2^2(r_1^2-r_2^2)-4(r_1^4-r_2^4)r_1r_2\cos\theta+\tfrac{3}{2}(r_1^2-r_2^2)r_1^2r_2^2\cos^2\theta]\Big\}$$

$$(D|T_{12}|D'')=-\gamma V_0\int gpd\tau f(\rho/r_t)\times6(r_1^2-r_2^2)r_1^2r_2^2(1-\cos^2\theta)$$

$$(D'|T_{12}|D')=-\gamma V_0\int h^2d\tau f(\rho/r_t)\Big\{12[r_1^4+r_2^4+\tfrac{1}{2}r_1^2r_2^2(1-3\cos^2\theta)]-\frac{12}{\rho^2}[2r_1^6+2r_2^6-2(2r_1^4+r_1^2r_2^2+2r_2^4)r_1r_2\cos\theta+3(r_1^2+r_2^2)r_1^2r_2^2\cos^2\theta]\Big\}$$

$$(D'|T_{12}|D'')=-\gamma V_0\int hpd\tau f(\rho/r_t)\times\Big\{6(r_1^2+r_2^2)r_1^2r_2^2(1-\cos^2\theta)-\frac{36}{\rho^2}[r_1^2r_2^2(1-\cos^2\theta)]^2\Big\}$$

$$(D''|T_{12}|D'')=-\gamma V_0\int p^2d\tau f(\rho/r_t)6[r_1^2r_2^2(1-\cos^2\theta)]^2.$$

# Letters to the Editor

*PUBLICATION of brief reports of important discoveries in physics may be secured by addressing them to this department. The closing date for this department is five weeks prior to the date of issue. No proof will be sent to the authors. The Board of Editors does not hold itself responsible for the opinions expressed by the correspondents. Communications should not exceed 600 words in length and should be submitted in duplicate.*

## Microwave Spin Resonance Absorption by Conduction Electrons in Metallic Sodium

T. W. GRISWOLD, A. F. KIP, AND C. KITTEL
*Department of Physics, University of California, Berkeley, California*
(Received September 25, 1952)

WE have observed conduction electron spin resonance absorption in fine particles of metallic sodium, suspended in paraffin wax, at a frequency of 9240 Mc/sec at room temperature and at 77°K. This is the first occasion, as far as we know, that conduction electron resonance has been reported.[1] The spectroscopic splitting factor $g$ is provisionally bracketed between 1.998 and 2.004, with a probable error of $\pm 0.003$ on these limits. The width of the resonance at half-maximum power is 78 oersteds. We believe, for reasons given below, that it will be possible in subsequent work to sharpen the resonance line considerably.

The particles were produced by a supersonic technique. The particle diameter ranged from under $10^{-4}$ cm to about $10^{-3}$ cm. A sample containing of the order of $10^{19}$ sodium atoms was placed in a 3-cm wavelength microwave cavity. Only a small fraction of these sodium atoms were in the microwave magnetic field, since the skin depth in sodium at the frequency used is about $10^{-4}$ cm. We cannot estimate closely the actual number of atoms within the skin depth in our sample since we do not know the distribution of particle size. It seems likely, however, that not more than 1 percent of the atoms were in the microwave field.

The resonance absorption is shown in Fig. 1, which is from a photograph of the CRO pattern. The horizontal scale is linear with the external magnetic field and shows the region in the neighborhood of the absorption peak. The microwave absorption puts a modulation on the vertical signal in such a way that the amplitude of the vertical signal is proportional to the resonance absorption; thus, the top of the pattern is a trace of the absorption curve of the sample. The upper signal on the trace has to do with the proton resonance equipment used to measure the external magnetic field. The small dot, approximately above the absorption maximum, is the proton resonance signal.

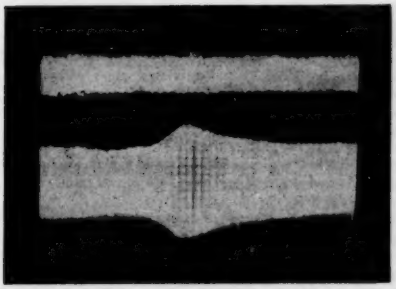

FIG. 1. Resonance absorption curve of conduction electrons in metallic sodium. Vertical scale gives absorption, horizontal scale gives applied magnetic field. At a frequency of 9240 Mc/sec, peak absorption occurs at 3304 oersteds.

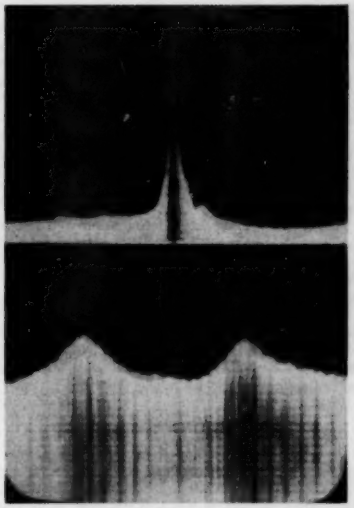

FIG. 2. Copper sulfate resonance compared to metallic sodium resonance at two temperatures. Lower curve: at room temperature; signal on left is from copper sulfate; signal on right is from metallic sodium. Upper curve: 77°K, same samples; large signal is from copper sulfate. Small signal to the right of this is from sodium. Horizontal scale is different in the two pictures.

At room temperature at 9240 Mc/sec the absorption maximum occurs at $3304 \pm 5$ oersteds. A small correction to the value of the field for maximum absorption must be applied because of the variation of eddy current losses with applied field.[2] Because the distribution of particle size is unknown, it is not possible to correct properly for this shift. We can, however, establish limits between which the $g$ factor must lie by calculating the corrections for spheres with diameters small and large compared to the skin depth. Taking the particles as small, $g = 1.998 \pm 0.003$; taking the particles as large, $g = 2.004 \pm 0.003$. The theoretical free electron $g$ is 2.0023, while Yafet[3] has calculated for the conduction electrons of sodium $g \approx 2.0019$, considering spin-orbit effects.

The close proximity of the observed $g$ to the free electron $g$ suggests that we are observing either the conduction electron resonance or resonance in an organic free radical or certain transition element ions. The problem of making certain that the observed resonance is in fact caused by conduction electrons and not by a paramagnetic impurity is made simple by the fact that the susceptibility of conduction electrons is temperature independent in contrast to the approximate $1/T$ dependence of ordinary paramagnetism. A comparison of relative intensities of our sodium sample compared to a small crystal of $CuSO_4 \cdot 5H_2O$ was made at room temperature and at 77°K. An amount of $CuSO_4 \cdot 5H_2O$ was put in the cavity next to the sodium sample such that the amplitudes of the two absorption peaks were approximately the same at room temperature. (Since the $g$ factor for $CuSO_4 \cdot 5H_2O$ is different from 2.0 the two peaks are separated from each other, so that comparison is easily made.) Figure 2 shows the results of this test of absorption *vs* temperature. In the lower photograph, taken at room temperature, the left-hand peak is due to copper sulfate and the right-hand peak is due to the sodium sample. In the upper photograph, at 77°K, the large peak is from the same sample of copper sulfate, and the small peak to the right of this is the sodium resonance. The horizontal scales at the two temperatures are not the same. At 77°K the copper

sulfate signal was approximately 20 times the height of the sodium signal. On the basis of a $1/T$ dependence of the susceptibility of the copper sulfate, the signal from it should increase by about a factor of 4 in going from 300°K to 77°K. This means that the signal from the sodium decreased by about a factor of 5 in going to the lower temperature. A major fraction of this decrease is perhaps to be attributed to the decrease in skin depth at the lower temperature, owing to the lower resistance of Na. The remainder of the change may be due to changes in the width of the absorption curves. It seems clear from these results that the observed line is not caused by a paramagnetic impurity in the specimen.

We believe that the dominant mechanism of line broadening in the specimen may be the random phase and frequency modulation of the microwave field as seen by an observer on a conduction electron diffusing around in the eddy current field of the metal. Spin-spin and spin-lattice relaxation times for conduction electrons in sodium have been calculated in detail by Overhauser.[4] His shortest relaxation time gives a line width less than one oersted. Yafet's calculated variation of $g$ with the direction of the electronic wave vector gives a width of about one oersted. A rough estimate of the width arising from the diffusion mechanism[5] gives

$$\Delta H/H \approx N r_0 \Lambda^2, \tag{1}$$

where $N$ is the concentration of conduction electrons, $r_0$ the classical radius of the electron, and $\Lambda$ the electronic mean free path. This relation applies when $\Lambda$ is much smaller than the skin depth and when the particle size is of the order of the skin depth or larger. The observed width is compatible with $\Lambda$ of the order of 200A, whereas $\Lambda$ from the conductivity of bulk sodium is about 3 times larger. The discrepancy may be caused by (a) the influence of very fine particles; (b) the rough approximations made in deriving Eq. (1); or (c) major structural distortions of the sodium lattice in the fine particles resulting from their production by supersonic fragmentation. One would expect to be able to sharpen the line by going to particle diameters (or film thicknesses) less the mean free path.

We wish to express our thanks to Mr. Frank Abell, who provided us with the finely divided sodium sample used in this experiment. This work was supported in part by the ONR.

[1] An account of this work was given by A. F. Kip at the ONR Conference on Magnetism, College Park, Maryland, Sept. 2–6, 1952, unpublished.
[2] W. A. Yager, Phys. Rev. **75**, 316 (1949).
[3] Y. Yafet, Phys. Rev. **85**, 478 (1952); Thesis, University of California, Berkeley, 1952, unpublished.
[4] A. W. Overhauser, Thesis, University of California, Berkeley, 1951, unpublished; Phys. Rev. (to be published).
[5] Detailed calculations are presently being carried out by Dr. Elihu Abrahams.

## Interpretation of the Electron-Inertia Experiment for Metals with Positive Hall Coefficients

NORMAN ROSTOKER
*Department of Physics, Carnegie Institute of Technology, Pittsburgh, Pennsylvania*
(Received September 15, 1952)

IN a recent paper Brown and Barnett[1] described measurements of $e/m$ for the conduction electrons of metals such as Mo and Zn which are known to have positive Hall effects. While their experimental results appear to be correct, I find it impossible to accept their conclusion that positive Hall effects cannot be explained by hole conduction in a nearly filled Brillouin zone as originally proposed by Peierls.[2] If this conclusion is correct, then a substantial part of the modern theory of solids would appear to need revision. It should also be pointed out that the Hall effect in nickel is negative[3] and not positive as stated by Brown and Barnett in reference 1.

The value of $e/m$ obtained for conduction electrons in metals in an "electron-inertia" experiment should always be very nearly equal to the value for free electrons in slow motion, even if the conductor has a positive Hall effect. Darwin[4] has explained why the electron-inertia experiments do not reveal the energy levels in metals and lead to the ordinary value of $e/m$. Brown and Barnett imply that this contradicts the usual explanation of positive Hall effect based on hole conduction. In the opinion of the author of this letter, this is not the case.

Let us consider a specific representation of a metal, namely, a simple cubic lattice which, from the approximation of tight binding, has the following energy levels in the first Brillouin zone:[5]

$$E = E_0 - \alpha - 2\gamma\,(\cos k_x a + \cos k_y a + \cos k_z a), \tag{1}$$

where $E$ is the electron energy, $\mathbf{k}$ is the electron wave vector; $-\pi/a \leq k_x \leq \pi/a$, etc., in the first zone. $E_0$, $\alpha$, and $\gamma$ are constants and $a$ is the lattice parameter. In the neighborhood of the zone boundary ($k_x \cong \pm\pi/a$, etc.), the energy levels are to a good approximation given by

$$\epsilon = \epsilon_{\max} - (\hbar^2/2m^*)\,|\mathbf{l}|^2, \tag{2}$$

where $\epsilon = E - E_{\min}$, $E_{\min} = E_0 - \alpha - 6\gamma$, $\epsilon_{\max} = 12\gamma$, and $\hbar^2/2m^* = \gamma a^2$. $\mathbf{l}$ is a new wave vector which is related to $\mathbf{k}$ by the equations, $l_x = \pm\pi/a - k_x$, etc. Consider the case of a nearly filled zone with $N_h$ unoccupied states or "holes," where the energy levels in the neighborhood of the Fermi level are given by Eq. (2). It is well known that the calculated Hall effect for this representation of a metal is positive with a Hall coefficient $R = 1/N_h ec$.[6]

Electric current density $j_x$ is defined by the equation[6]

$$j_x = -e\Sigma_o v_x = +e\Sigma_u v_x, \tag{3}$$

where the summation index "$o$" indicates that the sum is to be taken over all occupied states and the index "$u$" indicates that the sum is to be taken over all unoccupied states. $v_x$ is the average value of the velocity operator $(\hbar/im)(\partial/\partial x)$ which for electron wave functions of the Bloch type has the value[6]

$$v_x = (1/\hbar)(\partial\epsilon/\partial k_x). \tag{4}$$

There are two alternate expressions for the current by virtue of the fact that the sum over all states,

$$\Sigma_o v_x + \Sigma_u v_x = 0, \tag{5}$$

because there can be no current in a filled zone. When a simple expression such as Eq. (2) is available for the unoccupied energy levels near the zone boundary, it is convenient to carry out the summation over the unoccupied states and attribute the current to holes with a positive charge. However, it is not difficult to arrive at incorrect results by taking this interpretation too literally.

The momentum operator is $p_x = (\hbar/i)(\partial/\partial x)$, so that the total $x$ component of momentum of the conduction electrons is simply

$$P_x = m\Sigma_o v_x = -(m/e) j_x, \tag{6}$$

making use of Eq. (3). Equation (6) is perfectly general and applies to either hole or electron conduction. The momentum of the conduction electrons is always in the opposite direction to the current. To be sure, the results of Brown and Barnett "discriminate against theories for which current and momentum can have the same direction," if the momentum is interpreted as that of the conduction electrons. They are in agreement with a common direction of the current and the momentum of holes. [The momentum of the holes is $\Sigma_u v_x = +(m/e) j_x$, making use of Eqs. (5) and (6).

The ordinary value of $e/m$ appears in Eq. (6) so that any experiment such as the experiment in question, which is based on the relation between current and momentum, will measure the ordinary value of $e/m$.

It is possible that Brown and Barnett have used, instead of the momentum $p_x = mv_x$, what Shockley[7] calls the crystal momentum, $p_x' = \hbar k_x$, which is introduced so that the equation of motion for electron wave packets $(dp_x'/dt) = F_x$ (where $F_x$ is the force due to the applied field) will resemble Newton's law. For this purpose $p_x' = -\hbar l_x$ is an equally convenient definition of the crystal momentum. The total crystal momentum is

$$P_x' = -\hbar\Sigma_o l_x = \hbar\Sigma_o k_x. \tag{7}$$

It is more convenient to carry out the summation over the unoccupied states for which Eq. (2) is applicable. According to Eqs. (2) and (4), $v_x=(\hbar/m^*)l_x$, so that

$$P_x'=m^*\Sigma_n v_x.$$

Replacing $\Sigma_n v_x$ by means of Eq. (3), one obtains

$$P_x'=-(m_{eff}/e)j_x, \tag{8}$$

where $m_{eff}=-m^*$ is the effective mass of electrons for which the energy levels are given by Eq. (2). Equation (8) for $P_x'$ resembles Eq. (6) for $P_x$ except that the electron mass is replaced by the effective mass, and since $m_{eff}$ is negative $P_x'$ is in the same direction as $j_x$.[8] The use of the crystal momentum $P_x'$ instead of the actual momentum $P_x$ in the conservation conditions for the coil employed by Brown and Barnett would seem to account for the remarks in their paper that the writer considers misleading.

Electron-inertia experiments do not reveal the energy levels in metals. This is consistent with the modern theory of solids and in particular with the accepted explanation for positive Hall coefficients.

[1] Sheldon Brown and S. J. Barnett, Phys. Rev. **87**, 601 (1952).
[2] R. Peierls, Z. Physik **53**, 255 (1929).
[3] See, for example, *International Critical Tables* **6**, 416 (1929); I. K. Kikoin, Physik. Z. Sowjetunion **9**, 1 (1936); Pugh, Rostoker, and Schindler, Phys. Rev. **80**, 688 (1950); J. P. Jan and H. M. Gijsman, Physica **5**, 277 (1952).
[4] C. G. Darwin, Proc. Roy. Soc. (London) **A154**, 61 (1936).
[5] N. F. Mott and H. Jones, *The Theory of the Properties of Metals and Alloys* (Clarendon Press, Oxford, 1936).
[6] The symbol "e" as employed in this note represents the magnitude of the electronic charge.
[7] W. Shockley, *Electrons and Holes in Semiconductors* (D. Van Nostrand Company, New York, 1950).
[8] See, for example, N. Rostoker, Am. J. Phys. **20**, 100 (1952), where this point is discussed in detail. (The term "momentum" in that paper should be replaced by "crystal momentum" in order to be consistent with present terminology.)

## Interpretation of $e/m$ Values for Electrons in Crystals

W. SHOCKLEY
*Bell Telephone Laboratories, Murray Hill, New Jersey*
(Received October 6, 1952)

A RECENT investigation[1] by Brown and Barnett of $e/m$ for electrons in molybdenum and zinc by an inertial method has shown that the charge to mass ratio is that of an electron. It is the purpose of this letter to point out that this is the result expected from the theory of electronic conductivity; the new and precise experimental results are in excellent agreement with the theory and do not require any modification of the interpretation of the anomalous or positive Hall effect.

The paradox that $e/m$ is negative in the Brown-Barnett experiment and positive in the Hall effect experiment is due to the fact that two different meanings $m_B$ and $m_H$ should be associated with the symbol $m$.

The fact that $m_B$ should be taken as the electron mass follows at once from the theory of both holes and electrons in semiconductors and for electronic conduction in general.[2] In fact, the current due to "positive carriers" or "holes" is simply a shorthand way of dealing with the combined actions of many electrons. Hence, the ratio of current density to momentum density is simply $-e/m$, where $e=|e|$ is the electronic charge and $m$ the electronic mass.[3]

On the other hand, if one could view the behavior of an isolated hole in a semiconductor under the influence of electric and magnetic fields, one would conclude that its behavior was that of a particle of charge $+e$ and a positive mass.[4] The behavior of small groups of holes introduced by light or injection in germanium has, furthermore, put these theoretical conclusions on a sound operational footing.[5]

Certain other consequences of the theoretical model show, however, that the hole should not be considered to have positive mass. For example, one readily concludes that if the mass of a natural and perfect germanium crystal is $M$, then adding one electron gives it a mass $M+m$ and adding one hole $M-m$. The weights and momenta of the crystal will be consistent with these masses. Evidently, a gravitational field exerted on a stationary crystal will cause electrons to be drawn downwards and holes upwards.

An electron (respectively, hole) wave packet moving in a stationary crystal with group velocity $v_g$ imparts a momentum $mv_g$ (respectively, $-mv_g$) to the system. Thus, upon collision with phonons, a hole transfers momentum to the rest of the system as if it had a negative mass.

The consequences discussed above arise simply from the fact that conduction by both "excess electrons" and "holes" is really produced by electrons. The magnitude of the effective mass to use in conductivity theory depends on more complicated aspects of the interaction of the electron waves and the crystal. It is highly probable, for example, that the "effective masses" for electrons and holes in germanium cannot be described by one number each but must be regarded from a much more sophisticated viewpoint.[6]

[1] Sheldon Brown and S. J. Barnett, Phys. Rev. **87**, 601 (1952).
[2] This general conclusion has been expressed by C. G. Darwin, Proc. Roy. Soc. (London) **A154**, 61 (1936).
[3] For the case of one hole, this follows directly from Eqs. (2) and (3) on page 179 of W. Shockley, *Electrons and Holes in Semiconductors* (D. Van Nostrand Company, Inc., New York, 1950).
[4] Negative charge and negative mass do not lead to sensible results as is shown in reference 3, p. 181.
[5] See reference 3 for references to the literature and also W. Shockley, Phys. Today **3**, 16 (1950).
[6] See, for example, reference 3, p. 341.

## Optical Properties of Crystalline Thoria

O. A. WEINREICH AND W. E. DANFORTH
*Bartol Research Foundation, Franklin Institute, Swarthmore, Pennsylvania*
(Received July 30, 1952; Revised copy received October 1, 1952)

THE optical properties of fused transparent crystalline thoria have been investigated. Spectroscopic analysis of the crystals showed that their purity is comparable to that of mantle grade thorium nitrate and standard thorium metal. The purity is estimated to be in the vicinity of 99.9 percent. Rather complex changes of the absorption spectrum could be observed when the specimen was heated in vacuum, oxygen, or hydrogen. Figure 1 shows the absorption spectrum (uncorrected for reflection) of a thoria crystal, which has been taken through the following cycle: (a) heating to 1800°C in vacuum, (b) heating to 1000°C in air, (c) heating to 1000°C in vacuum, (d) reheating in vacuum at 1800°C.

Heating in oxygen or air reddens the crystal and following heating in vacuum or hydrogen at 1000°C results in bleaching. The ultraviolet cutoff for these states is at 3700A. This fundamental absorption may be associated with the gap between the filled band and conduction band. The change of the absorption

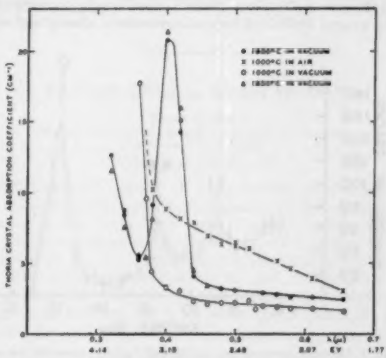


FIG. 1. Optical absorption of crystalline thoria.

curve following the heating to 1000°C in vacuum (curves *a* or *d* in Fig. 1) is characterized by: (1) a shift in the ultraviolet cutoff from about 3700A to 3200A, and (2) the appearance of a sharp absorption peak at about 4000A.

Tentatively, we relate this absorption peak to the presence of excess thorium (oxygen deficiency) of the specimen. Consistent with this hypothesis are weight changes, which are found when alternating the 1000°C oxygen and 1800°C vacuum treatment. The weight changes account for intake or release of approximately $10^{16}$ oxygen atoms per cc. The weight changes have been checked by gas analysis. No measurable weight changes, however, could be found, when the 1000°C oxygen and 1000°C vacuum treatment were alternated. We refer to these crystals as oxygen-rich. Oxygen-rich crystals bleached in vacuum or hydrogen turn red when exposed to light in the region just beyond the cutoff. The trapping centers for the radiation-produced reddening are shallow; bleaching occurs at 200°C in vacuum.

Another variety of color is obtained by rapid quenching which results in a deep black color. These crystals are opaque in the measured spectral range from 0.2 to $2\mu$.

No photoconductivity has been observed for any of the described crystals at light intensities, where that of diamond is easily detected.

Measurements pertinent to the mechanism of electrical conductivity of oxygen-poor thoria specimens have been recently published.[1] In this case part of the current is electrolytic, causing rapid decomposition of the crystal. Measurements of electrical conductivity with oxygen-rich crystals were made at 1100°C in oxygen of atmospheric pressure. In contrast to the oxygen-poor specimen, no electrolytic decomposition is detected.

It is a pleasure to acknowledge the services of Harry Bleecher, who developed the necessary polishing techniques and prepared the specimens.

[1] W. E. Danforth, Phys. Rev. **86**, 416 (1952).

## Evidence for a New Level in $Be^7$

D. M. THOMSON
*Palmer Physical Laboratory, Princeton University, Princeton, New Jersey*
(Received October 2, 1952)

THE study of the energy levels of mirror nuclei is one of the most effective ways of testing the hypothesis that proton-proton and neutron-neutron forces are equal in the low energy region. In several cases it has been possible to demonstrate very close similarities between the level spectra of mirror nuclei and also to account fairly well for the apparent differences in excitation of corresponding levels.[1-4]

In the case of the mirror nuclei $Li^7$ and $Be^7$ the correspondence of the ground states and first excited states is already well established,[5] and there is some evidence that there are levels in $Li^7$ corresponding to levels at about 6.4 and 7.3 Mev in $Be^7$.[6] Franzen and Likely[7] were probably not able to observe the 7.54-Mev level in $Li^7$ by the inelastic scattering of protons on Li, since the protons coming from a $(p, pn)$ reaction produced too much background at that energy. Recently a new level has been found[8,9] in $Li^7$ at 4.62 Mev. The corresponding region of excitation in $Be^7$ has not previously been adequately explored, and it was therefore of some interest to discover whether or not there is a mirror level.

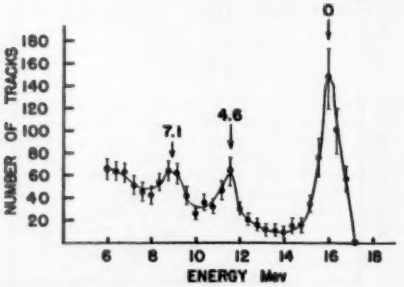


FIG. 1. Neutron spectrum from $Li^7(p, n)Be^7$ at 16°, corrected for escape and for the variation of $n-p$ cross section (about 1000 tracks; bombarding energy = 18.2 Mev).

In the present work 18.3-Mev protons from the external beam of the Princeton cyclotron bombarded natural metallic lithium targets 0.006 in. in thickness. Neutrons produced by the reaction $Li^7(p, n)Be^7$ were detected at 16° and 60° to the incident beam by the proton recoils they produced in Eastman Kodak NTB emulsions of 200-microns thickness. Tracks were accepted up to angles of 15° in the neutron direction in the plane of the emulsion and up to about 11° in dip. About 1000 tracks were counted at each angle. The neutron spectrum at 16°, suitably corrected for the escape of long tracks and for the energy dependence of the neutron-proton scattering cross section, is shown in Fig. 1. Besides the ground-state group which also includes the transitions to the first excited state at 0.43 Mev which could not be resolved and a continuous background probably due mainly to three-body breakup of the compound nucleus, the spectrum shows evidence for excited states in $Be^7$ at 4.6 Mev and 7.1 Mev. The spectrum obtained at 60° showed the same groups with energies consistent with their arising from the $Li^7(p, n)Be^7$ process. The 7.1-Mev level can be identified with that found from proton scattering on $Li^6$,[4] and the 4.6-Mev level as the mirror of the 4.62-Mev level in $Li^7$.

The energy of the new level in $Be^7$ cannot be determined very accurately from the data. The range energy relation in nuclear emulsions depends somewhat on the humidity of the atmosphere in which they are exposed, and in this work the energy of the ground state group at 16° was calculated and used to determine one fixed point on the range-energy relation; the rest of the curve being assumed to have the same shape as that used by Richards *et al.*[10] Since the ground-state group is composite and the relative strength of the two components is not known, it is possible that an error of up to 200 kev may be introduced into the estimate of the energy of the excited level. The best estimate that can be given for the excitation energy is therefore $4.6 \pm 0.2$ Mev. Within the somewhat large experimental error, this is the same as the excitation of the corresponding level in $Li^7$. No useful comparison of the energies of the two levels can be made until the energy of the $Be^7$ level is known with greater precision.

I am greatly indebted to Professor P. C. Gugelot for his advice on this problem and to Mrs. L. Anderson for reading the plates. This work was supported by the AEC and the Higgins Scientific Trust Fund.

[1] R. A. Laubenstein and M. J. W. Laubenstein, Phys. Rev. **84**, 18 (1951).
[2] V. R. Johnson, Phys. Rev. **86**, 302 (1952).
[3] R. G. Thomas, Phys. Rev. **81**, 148 (1951).
[4] R. G. Thomas, Phys. Rev. (to be published).
[5] Brown, Snyder, Fowler, and Lauritsen, Phys. Rev. **82**, 159 (1951).
[6] S. Bashkin and H. T. Richards, Phys. Rev. **84**, 1124 (1951).
[7] W. Franzen and J. G. Likely, Phys. Rev. **87**, 667 (1952).
[8] H. E. Gove and J. A. Harvey, Phys. Rev. **82**, 658 (1951).
[9] Gelinas, Class, and Hanna, Phys. Rev. **83**, 1260 (1951).
[10] Richards, Johnson, Ajzenberg, and Laubenstein, Phys. Rev. **83**, 994 (1951).

## *T*-Tracks in Nuclear Emulsions*

M. BLAU AND E. O. SALANT
*Brookhaven National Laboratory, Upton, New York*
(Received September 30, 1952)

IN emulsions exposed[1] for about 5 hours at 15 g/cm[2] and geomagnetic latitude 41°N, we have observed examples of novel but puzzling events which we call *T*-tracks. A *T*-track appears as a black track with its last grain crossed by a straight thin track, the last grain being at the end of the dense track corresponding to the end of travel of the heavily ionizing particle, which we call

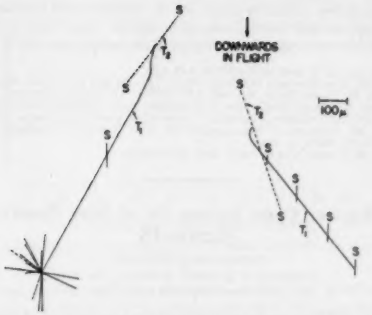


FIG. 1. Two examples of $T$-events. $T_1$=black $T$-track; $T_2$=minimum $T$-track; $S$=emulsion surface.

the $T$-particle. The $T$-particle's direction of travel is seen from small-angle scattering of the black track as well as, in some cases, by its observed origin in a star. Figure 1 is a drawing, in projection, of two $T$-events.

The emulsions were Eastman NTB3 pellicles, 200$\mu$ thick, density of minimum tracks about 25 grains per 100$\mu$. There seemed nothing peculiar about these emulsions, the numbers and distribution of shower particles, stars, mesons, $\pi-\mu-e$ decays, etc., being as expected from previous flights at other latitudes.

Each coincidence of a minimum track with the last grain of a dense track was verified by at least 6 observers, and a tilting stage was used for observing coincidence in depth. No break (to within 0.5°) was seen at the crossing. The small-angle scattering of the dense track was also checked by at least 6 observers. 1000× magnification was used. For following tracks through successive emulsions, the latter were aligned by $G$ rays.

In an area of about 46 cm$^2$, in examining the ends of 2583 black tracks, 11 $T$-tracks were found.

Accidental crossing of last grains of black tracks by the many thin tracks traversing the emulsion was estimated in three ways. First, it was noted that in no accepted $T$-event was the line of the crossing thin track observed as far as 0.25$\mu$ from the center of the end grain of the black track. Letting $L$ be the average length of thin track, in $\mu$, per $\mu^2$ of emulsion, the probability $P$ of coincidence between a single grain and a random thin track was calculated by $P=\pi(0.5)^2L$. By measuring directions and lengths (totalling 7.9 cm) of thin track, a value $L=(4.3\pm0.4)\times10^{-4}$ was obtained, giving $P=3.4\times10^{-4}$. Chance alone would account for $2583P$, or 0.9 crossing of the last grains of 2583 tracks, in contrast to the 11 observed.

Another method involved a count of random tracks passing close to ends of black tracks. The number of random minimum tracks passing within a distance of 0.3$\mu$ from the centers of end grains should be a fraction $(0.3/5)^2=1/250$ of all those passing within a distance of 5$\mu$. In a distance of 5$\mu$ from 1638 ends, 82 were counted, so that 0.33 should pass by chance within 0.3$\mu$ of the centers of the end grains, whereas, in fact 10 tracks out of the 82 were observed within that distance. (The tracks within 3$\mu$ and within 5$\mu$ distances were consistent with the ratio 9/25.)

Finally, grains in the central sections of black tracks were observed for chance crossings by thin tracks. For 88,400 such grains examined, 16 crossings were found, the quotient being $(1.81\pm0.45)\times10^{-4}$. Taking into account straggling at the end of black tracks and the possibility of mistaking a grain of the thin track for the last grain of the black track would at most double this number as a measure of chance crossings of the ends. The result is in adequate agreement with the estimated $P$.

TABLE I. Stars with $T$-tracks.

| Event No. | | 1 | 5 | 6 | 8 | 9 | 11 |
|---|---|---|---|---|---|---|---|
| Range of black $T$-track, $\mu$ | | 600 | 860 | 300 | 180 | 1450 | 140 |
| Incoming particle of star | | $p$ | $\pi$ | $p$ | $\pi$ or $\alpha$ | $\pi$ or $\alpha$ | $\pi$ or |
| No. of other star tracks | min | 0 | 3 | 10 | 0 | 0 | 1 |
| | gray | 1 | 0 | 0 | 1 or 0 | 2 or 1 | 1 or 0 |
| | black | 4 | 11 | 6 | 1 | 0 | 7 |

If these tests are valid estimates of the chance coincidences, it would seem justified to regard the occurrence of $T$-tracks as a physical event. The physical event is, presumably, the break-up of the heavy, slow $T$-particle at (or near) the end of its range into two fast, singly-charged particles, the break-up occurring either by decay of the $T$-particle or by its annihilation with one of the charged particles of the emulsion.

Of the 11 $T$-tracks, the origins of 5 black tracks (lengths 0.4, 0.7, 1.7, 4, and 8 mm, respectively) were at some emulsion surface. Table I records the more obvious features of the six remaining $T$-tracks which were traced to stars. Events 8, 9, and 11 are usually considered low energy stars.

Distortion and shortness of usable track made the information from scattering of the crossing minimum tracks disappointingly meager. In all cases, electrons of energy less than 10 Mev (in most cases less than 20 Mev) were excluded as possible fast particles. One track gave $p\beta\geq400$ Mev/$c$; if the break-up is by decay, the $T$-particle has a mass $\geq0.85$ proton mass.

In event No. 1 only, the thin track shows a break (of 2° in depth) at the crossing point and is gray, 1.5 minimum grain density, $\beta=0.7$. Its scattering gave $p\beta\geq130$ Mev/$c$, so that each fast particle is at least as heavy as a $\pi$-meson. Apparently, this event represents a different break-up than the other 10 events.

Three more events, called $T_0$-tracks, in other respects like the other $T$-tracks, have their origins in the center of the emulsion, with no other track detectable at the origin. By contrast, in 5 stars classified as (1$p$1) stars, scattering showed the heavy particles move away from the thin crossing track which, moreover, shows a break at the crossing point.

Not merely $T_0$-tracks, but the low energy of the other $T$-particles and their origins in low energy stars, make it difficult to account for the particles reasonably. Seeking a fallacy in the estimates of random coincidences, we have, so far, been unable to find any reasons for enlarging adequately the region allowed to chance crossings of ends, nor can we understand how some peculiar property of these pellicles could give so many spurious $T$-tracks. Accordingly, scattering and ionization of black $T$-tracks have been measured; the limits these set to mass and charge of the heavy $T$-particles will be presented later.

We are indebted to Dr. Hartland S. Snyder for critical discussions and to the emulsion-scanning staff for their indefatigable work.

* Research carried out at the Brookhaven National Laboratory under the auspices of the AEC.
† Balloon flights by courtesy and arrangement of ONR.

## The Hall Effect in Nickel Ferrite*

SIMON FONER
*Physics Department, Carnegie Institute of Technology, Pittsburgh, Pennsylvania*
(Received September 26, 1952)

PRELIMINARY results of measurements on a sample of nickel ferrite show that its Hall effect is like that of the ferromagnetic metals. As in these metals the effect can be divided into two parts;[1] the extraordinary effect which is proportional to magnetization $M$ and is predominant at low fields, and the ordinary effect which is proportional to the field $H$. The latter can be separated[1] from the former by making accurate measurements at high fields. As in the case of the ferromagnetic metals, the Hall potential $E_H$ can be expressed by the relation[1]

$$E_H=R_0(H+4\pi\alpha M)I/t, \quad (1)$$

where $I$ is the current through the sample, $t$ is the thickness of

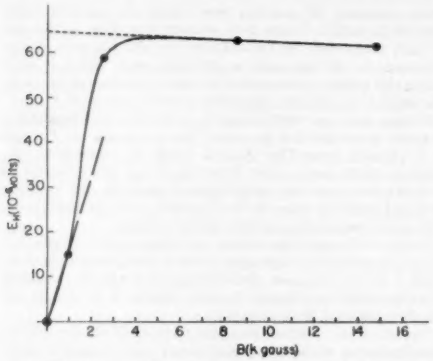


FIG. 1. Hall potential *versus* magnetic induction in nickel ferrite.

the sample, and $\alpha$ is a parameter which is characteristic of the sample.

The particular sample, having a slight excess of iron, was selected because it allowed using a moderately sensitive ac null detection method for the measurements at room temperature. The sample characteristics were as follows: length 1.9 cm, width 1.0 cm, thickness 0.223 cm, resistivity 0.55 ohm-cm, density 5.41 g/cc. The ends of the sample were copper plated and current leads soldered to them so that the primary current (100 ma at 45 cycles/sec) was along the 1.9-cm length. Two phosphor bronze spring contacts across the width and equally spaced from the ends were connected to the Hall potential measuring leads.

With the relatively flat sample used here, the magnetic field measured is the $B(=H+4\pi M)$ within the sample. Equation (1) can be written

$$E_H=\{B+4\pi(\alpha-1)M\}R_0I/t. \tag{2}$$

A plot of the Hall potential $E_H$ *versus* magnetic induction $B$ is shown by the solid line in Fig. 1, where the points for $E_H$ represent the average of 5 to 10 readings for reversal of $B$. The slope of this curve at any point is

$$dE_H/dB=\{\alpha+(1-\alpha)/\mu\}R_0I/t, \tag{3}$$

where $\mu$ is the incremental permeability. At high fields $\mu\cong1$ and the slope is $R_0I/t$, from which $R_0$ is calculated to be $(-5.0\times10^{-10}$ volt-cm/amp-oersted). At low fields, if $\mu\gg1$, the slope is $\alpha R_0I/t$. The ratio between the low and the high field slopes would then be $\alpha$. However, the maximum initial permeability of nickel ferrite[2] is of the order of 10 and this introduces a correction. The corrected value of $\alpha$ from the ratio of slopes is $-64$. Provided Eq. (1) applies to this material, an independent determination of $\alpha$ can be obtained by extrapolating the high field straight line back to the axis $B=0$. From Eq. (2) this intercept is $4\pi(\alpha-1)M_sR_0I/t$, from which $\alpha$ can be determined if $M_s$ is known. $M_s$ was not measured, but it may be approximated using the measured density and assuming a pure $NiFe_2O_4$ sample with a saturation moment of 2.3 Bohr magnetons per molecule.[3] The value of $4\pi M_s$ so calculated is 3.5 kgauss and from this $\alpha=-80$. Considering the approximations required, these two values of $\alpha$ are in good agreement.

The results, therefore, show that the Hall effect in this nickel ferrite sample is well described by Eq. (1), which has been shown to express the Hall effect in ferromagnetic metals. The room temperature values of the constants for this nickel ferrite are $R_0=-5.0\times10^{-10}$ volt-cm/amp-oersted and $\alpha$ between $-60$ and $-80$. Thus Eq. (1), which applies to ferromagnetic metals, also applies here.

A more detailed investigation of ferrites is now in progress and will be reported at a later date.

The author wishes to thank Dr. N. Rostoker and Professor E. M. Pugh for their helpful comments, and Dr. G. C. Clark of Linde Air Products Company for supplying the sample material.

* Supported in part by the ONR and AEC.

[1] Pugh, Rostoker, and Schindler, Phys. Rev. **80**, 688 (1950); N. Rostoker and E. M. Pugh, Phys. Rev. **82**, 125 (1951); Technical reports on ONR contract No. Nonr-206(00) by A. Schindler, June, 1951 and Simon Foner, June, 1952, unpublished. The gist of these reports will be published soon.

[2] R. M. Bozorth, *Ferromagnetism* (D. Van Nostrand Company, Inc., New York, 1951), p. 246.

[3] E. W. Gorter, Comp. rend. **230**, 192 (1950).

## Nuclear Cross Section for 37-Mev Positive Pions in Pb*

KENNETH J. BUTTON†
*University of Rochester, Rochester, New York*
(Received September 22, 1952)

RECENT measurements of nuclear cross sections of negative pions in Pb at 85 Mev,[1] 109 Mev, and 133 Mev[2] have indicated geometric values and no dependence on energy. These measurements were made by observing the attenuation of negative pion beams in Pb.

The attenuation in Pb of the 50-Mev positive pion beam of the University of Rochester 130-inch cyclotron is reported here. The attenuation method and apparatus of Barnes, Clark, Perry, and Angell,[3] designed for their determination of the total cross sections of positive pions in hydrogen, have been used.

This method employed three 1 in.×1 in.×0.2 in. *trans*-stilbene crystals in a scintillation counter telescope to define the beam. A Pb attenuator plate, 5.248 g/cm$^2$ thick, was placed between the third crystal and a fourth crystal. The fourth crystal was 2 in. in diameter and $\frac{1}{2}$ in. thick.

In order to stop some of the fast proton star prongs, without reducing the efficiency for counting pions of this low energy, a copper sheet, 710 mg per cm$^2$ thick, was placed over the face of the fourth crystal.

As shown in Fig. 1, there was a distance of $1\frac{1}{4}$ in. between the facing surfaces of the third and fourth crystals and $\frac{3}{16}$ in. between the facing surfaces of the Pb attenuator and the fourth crystal. The efficiency for recording scattering interactions as a function of pion scattering angle is shown in Fig. 2.

A multiple scattering computation was performed using the method described by Williams.[4] Correction for the finite size of the Pb nucleus was included in the computation. The results assured that the effects of multiple scattering and large angle single Coulomb scattering are avoided in the geometry described above.

The attenuation observed in this geometry yields a cross section of 1.30±0.07 barns at a pion interaction energy of 37±5 Mev.

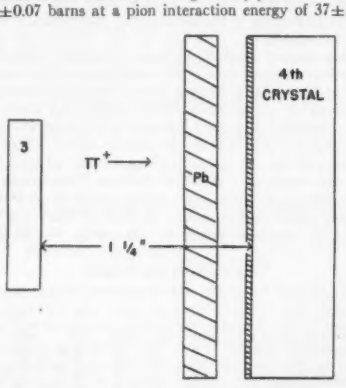


FIG. 1. Scale drawing of the region of interaction.

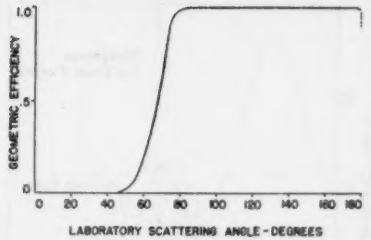


FIG. 2. The efficiency for recording pions scattered from Pb as a function of the laboratory scattering angle.

The cross section has been corrected for positive muon contamination (4 percent) and for counting losses in the pulse height discriminator (6 percent). The error consists of statistical error and uncertainty in the determination of counting losses, muon contamination and geometrical dimensions.

The cross section has not been corrected for fast proton star prongs that may have counted in the fourth crystal. On the basis of findings reported by Bernardini and Levy[5] for the absorption and scattering of positive pions of this energy in photographic emulsions, this correction may result in the increase of the quoted cross section by as much as 15 percent.

The author is grateful to Professor S. W. Barnes for his interest and guidance. Appreciation is expressed to Dr. D. L. Clark, J. P. Perry, and C. E. Angell for the use of their apparatus and for their helpful discussions. Theoretical assistance was effectively rendered by Dr. J. B. French and Dr. J. H. Tinlot.

* This work was performed under the auspices of the AEC.
† This material is part of a thesis submitted to the University of Rochester for the M.S. degree.

[1] Chedester, Isaacs, Sachs, and Steinberger, Phys. Rev. **82**, 958 (1951).
[2] Martin, Anderson, and Vodh, Phys. Rev. **85**, 486 (1952).
[3] Barnes, Clark, Perry, and Angell, Phys. Rev. **87**, 669 (1952).
[4] E. J. Williams, Proc. Roy. Soc. (London) **A169**, 531 (1939).
[5] G. Bernardini and F. Levy, Phys. Rev. **84**, 610 (1951).

## Induced Infrared Absorption in Hydrogen and Hydrogen Foreign Gas Mixtures at Pressures up to 1500 Atmospheres

D. A. CHISHOLM,* J. C. F. MACDONALD,† M. F. CRAWFORD, AND H. L. WELSH
*McLennan Laboratory, University of Toronto, Toronto, Canada*
(Received September 19, 1952)

IN previous communications[1,2] the characteristics of the normally forbidden fundamental infrared absorption in $H_2$ as induced by molecular collisions have been delineated for the pure gas and for $H_2-He$, $H_2-A$, and $H_2-N_2$ mixtures at pressures up to 150 atmos. The range of experimental conditions has now been extended to pressures of 1500 atmos at temperatures from 90°K to 376°K. The results obtained in the region of high densities, approaching and sometimes exceeding those of the corresponding liquids at their normal boiling points, have revealed new properties of induced absorption.

A reflection cell,[3] adjusted for a path length of 2.1 cm and fitted with a Dewar-type vacuum jacket for temperature control, was used for the experiments. When fitted with a quartz window 18 mm thick, the cell withstood pressures up to 1500 atmos at all experimental temperatures.

The contours in Fig. 1 show the enhancement of the absorption in a given base density (168 amagat) of $H_2$ due to various densities of He at 298°K; the enhancement was obtained by subtracting the absorption of the $H_2$ alone from the absorption of the mixture. The dotted curve is inserted for comparison; it is the absorption contour calculated for 168 Agt of $H_2$ and 796 Agt of He using the specific absorption contour obtained for the lower pressure range.[3] The outstanding feature of the high density contours is the splitting of the $Q$ branch into two well-resolved components. The higher frequency component, referred to as $Q_R$, corresponds to the main maximum at low densities; the lower frequency component $Q_P$ corresponds to the weak imperfectly resolved component, which was a puzzling feature of the low density results.[3] The frequency of the minimum between $Q_R$ and $Q_P$ is at all densities equal to $\nu_0$, the frequency of the fundamental vibrational transition in the free $H_2$ molecule. Similar splittings of the $Q$ branch were observed at high densities with pure $H_2$ and with $H_2-A$ and $H_2-N_2$ mixtures; in these cases, especially for $H_2-N_2$, the $Q_R$ and $Q_P$ components are not as well resolved as for $H_2-He$. Also from these three cases, where the $S(0)$ and $S(1)$ lines are relatively much more pronounced than in $H_2-He$, it was established that there is no splitting in the $S$ lines.

The separation and relative intensities of the $Q_R$ and $Q_P$ components are strongly dependent on density and temperature. The observations may be summarized as follows: (a) The separation of the maxima increases linearly with density from a limiting value at low densities. The limiting value is least for $H_2-A$ and greatest for $H_2-He$. The rate of increase of the separation with density is greatest for $H_2-A$ and least for $H_2-He$. (b) For a given density the separation of the maxima increases with the temperature. (c) The relative intensity of the $Q_P$ component decreases rapidly as the temperature is lowered. (d) The contours of the components show a simple intensity relationship. If $I_P(\nu-\nu_0)$ is the intensity in the $Q_P$ component at the point $\nu-\nu_0$

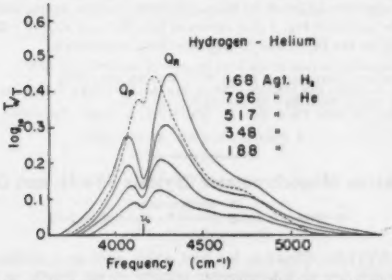


FIG. 1. Contours of the infrared absorption of hydrogen induced by various densities of helium.

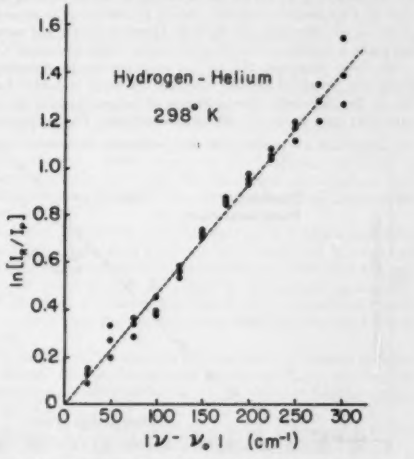


FIG. 2. An empirical relationship between $I_P(\nu-\nu_0)$ and $I_R(\nu-\nu_0)$, the intensities in the $Q_P$ and $Q_R$ components.

from the origin (4160 cm$^{-1}$) and $I_R(\nu-\nu_0)$ is the corresponding quantity for the $Q_R$ component, the plot of $\ln[I_R(\nu-\nu_0)/I_P(\nu-\nu_0)]$ against $|\nu-\nu_0|$ is a straight line whose reciprocal slope is very nearly $kT$. Figure 2 shows the graph for three densities of $H_2$ and He at room temperature. The reciprocal slope of the line, drawn by least squares, is 212 cm$^{-1}$; the value of $kT$ at 298°K is 208 cm$^{-1}$.

The observations indicate that the splitting of the $Q$ branch is a kinetic phenomenon. The splitting at low densities is a property of the colliding pair alone and is probably caused by a change of the relative kinetic energy of the pair during the absorption. The increase in the splitting with increasing density suggests that the kinetic energy of one or more near neighbors can also be involved; the third molecule need not be in close collision with the absorbing pair.

In the region of high density the integrated absorption coefficient increases more rapidly than the product of the densities of the absorbing and perturbing gases; this effect, which is especially marked for $H_2-N_2$ and $H_2-A$ mixtures, is related to the reduction of the free volume in a gas at high densities. The absorption coefficient also shows a marked increase with increasing temperature. These results will be published in detail.

The authors are indebted to the National Research Council of Canada for generous financial assistance.

* Holder of the E. F. Burton Fellowship in Physics, School of Graduate Studies, University of Toronto, 1950–1952.
† Present address: The Ontario Cancer Treatment and Research Foundation, Toronto, Canada.
[1] Welsh, Crawford, and Locke, Phys. Rev. **76**, 580 (1949).
[2] Crawford, Welsh, MacDonald, and Locke, Phys. Rev. **80**, 469 (1950).
[3] Welsh, Pashler, and Dunn, J. Chem. Phys. **19**, 340 (1951).

## $(\gamma, pn)$ Reaction in Phosphorus*

J. HALPERN, A. K. MANN, AND R. NATHANS
*University of Pennsylvania, Philadelphia, Pennsylvania*
(Received September 24, 1952)

MEASUREMENT of particle emission from nuclei under photon bombardment leads to values for the probability of photon capture provided one can measure the relative importance of emission of the various nuclear particles. For heavy elements, where charged particle emission is strongly inhibited by the Coulomb barrier, the $(\gamma, n)$ reaction is dominant. The $(\gamma, 2n)$ reaction can, however, contribute significantly to the total cross section.[1] For light elements, where barrier effects are small and the threshold energy for proton emission can be appreciably lower than that for neutron emission, the $(\gamma, p)$ reaction is as important as the $(\gamma, n)$.[2] Similarly, for the light elements the $(\gamma, pn)$ reaction can make a significant contribution to the total cross section.[3]

We have measured the $(\gamma, pn)$ contribution in phosphorus, where the threshold for this reaction (18 Mev) is 5 Mev below the $(\gamma, 2n)$ threshold. The technique of measurement is identical with that used in the $(\gamma, 2n)$ determinations.[1] The radioactivity yields from the $(\gamma, n)$ reaction is measured as a function of the maximum energy of the bremsstrahlung produced by the University of Pennsylvania betatron. This yield curve is compared with the yield curve of neutrons directly detected by a method of delayed counting.[1] Figure 1 shows the neutron yield from a 2.3-g/cm$^2$ target of phosphorus compared with the radioactivity yield from targets of 1.2-g/cm$^2$ thickness. The two curves are normalized at 18 Mev.

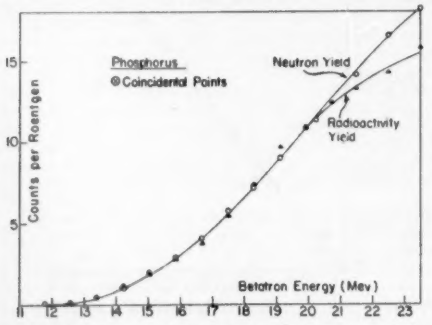


FIG. 1. Yields from the $(\gamma, n)$ reaction in phosphorus as measured by neutron detection and by radioactivity.

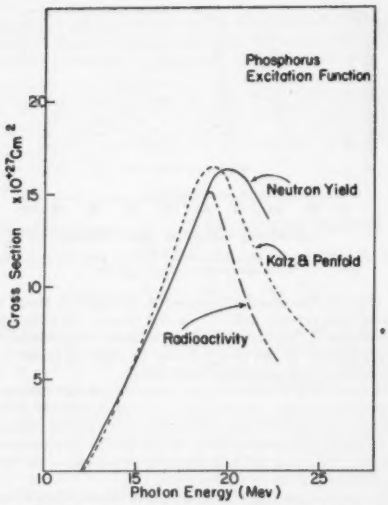


FIG. 2. Excitation functions computed from the curves of Fig. 1.

The divergence of the two curves at the upper energies is attributed to the onset of the $(\gamma, pn)$ reaction. The identity of the two curves below 18 Mev indicates that the efficiency of the neutron detection apparatus does not depend on neutron energy, because from threshold to 18 Mev the photoneutron energy distribution has changed from thermal to one with a mean of approximately one Mev. Above 18 Mev the neutron energy spectrum remains essentially unchanged.

Figure 2 shows the excitation functions constructed from the yield curves of Fig. 1, using the calculated bremsstrahlung spectra at the various betatron energies. Absolute values for the cross section are obtained by a measurement of the efficiency of the neutron detection apparatus using a Ra–Be source of known strength. The excitation function of Katz and Penfold[4] obtained from radioactivity data is also shown for comparison. Although the measurements do not extend to sufficiently high energies for a precise calculation of the integrated cross sections, extrapolation of the curves of Fig. 2 give values of $99\times10^{-3}$ and $47\times10^{-3}$ Mev barns for the $(\gamma, n)$ and $(\gamma, pn)$ reactions, respectively.

* Supported in part by the joint program of the ONR and AEC.
[1] Halpern, Nathans, and Mann, Phys. Rev. **88**, 000 (1952).
[2] A. K. Mann and J. Halpern, Phys. Rev. **82**, 733 (1951); J. Halpern and A. K. Mann, Phys. Rev. **83**, 370 (1951).
[3] Karl Strauch, Phys. Rev. **81**, 973 (1951); L. Eyges, Phys. Rev. **86**, 325 (1952).
[4] L. Katz and A. S. Penfold, Phys. Rev. **81**, 815 (1951).

## Neutron Monochromator Crystals—$Fe_3O_4$ and Ge†

A. W. MCREYNOLDS
*Brookhaven National Laboratory, Upton, New York*
(Received July 25, 1952)

CRYSTAL diffraction has been widely used as a method of selection of monoenergetic neutron beams, mostly in the range of wavelengths 1–2 angstroms. In some cases, it has also

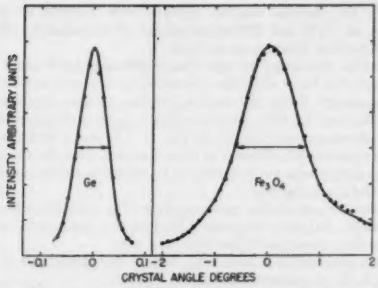


FIG. 1. Angular spread of diffracted neutron beams from crystals of Ge and $Fe_3O_4$. Curve for Ge was determined by single crystal rocking curve, and $Fe_3O_4$ by double crystal.

been used in the range 4–5.5 angstroms,[1] but use at intermediate or longer wavelengths has been precluded by several factors: (1) All of the commonly used crystals such as NaCl, LiF, $CaCO_3$, Pb, Cu, and Be have lattice spacings such that the cut-off wavelengths beyond which no diffraction occurs are around 5 angstroms. (2) The crystal imperfections are of the order of a few minutes angular spread, corresponding to a relatively narrow range of wavelengths in the diffracted beam. Since the incident flux decreases as $1/\lambda^4$, the intensity becomes very low at long wavelengths. (3) Since short wavelengths are much more abundant, second and higher order reflections become comparable to or greater than the first order for $\lambda > 1.5$–2 angstroms.

Thus desirable characteristics for monochromator crystals for longer wavelengths are a large lattice spacing, large angular spread of the crystal mosaic or lineage structure, and absence of higher order reflections. Two crystals partly satisfying these conditions have been tested, a Ge crystal supplied by Dr. G. Pearson of Bell Laboratories and natural magnetite crystals $Fe_3O_4$ of which large geological specimens are available. Ge has a diamond cubic structure with lattice constant 5.647 angstroms, corresponding to a cutoff $\lambda = 6.51$ from the (111) planes. The second-order (222) reflection is forbidden. [It has been confirmed, using the spectrometer of J. Hastings and L. Corliss, that the (222) reflection is present, but less than one percent of the (111).] Magnetite has a lattice constant of 8.37 angstroms corresponding to a cutoff $\lambda = 9.66$ from the (111) planes, and a weak (222) reflection.

Angular spread of the $Fe_3O_4$ crystals was measured by both single and double crystal rocking curves, using a neutron beam of 15 minutes half-width from the reactor. Figure 1 shows that it is large (about 1.3 degrees), and the single crystal curve was found to be smooth, indicating that spread results from either mosaic or small scale lineage structure. The single crystal curve for Ge, on the other hand, shows a very small spread. Actually a half-width of 10–30 minutes for Ge would be much more desirable to obtain greater intensity. Figure 2 shows the diffracted intensity from the (111) planes of the two crystals as a function of wavelength as determined by the crystal angle. The curve for Ge represents the reactor spectrum. Ge is particularly applicable to the range 1–3.6 angstroms where incident intensity is adequate, but high resolution is required where there are crystal diffraction effects in transmission measurements, and where second-order reflections cannot be eliminated by filters. The beam incident on the $Fe_3O_4$ crystal was first filtered through BeO and Pb to remove second-order reflections, BeO having a relatively sharp cutoff at 4.7 angstroms and Pb having, because of its large grain structure, a cross section decreasing fairly smoothly with wavelength from 1–5 angstroms. Be with cutoffs at 3.6 and 3.9 angstroms was also used. Intensity from magnetite is high enough to extend the useful range of crystals through the region 3.6–9 angstroms, and for both Ge and $Fe_3O_4$ the intensity could be increased tenfold by wider collimation without sacrifice of resolution. Thus, the single crystal spectrometer, using these two crystals combined with appropriate filters, covers the range 0.7 to 9 angstroms with high resolution and intensity greater than available from time-of-flight velocity selectors. It should be added that Ge may be useful in diffraction spectrometers to eliminate second-order reflections, and that Shull[2] has demonstrated the polarization of long wavelength neutrons with magnetite. The author is indebted to R. J. Weiss for discussions and collaboration.

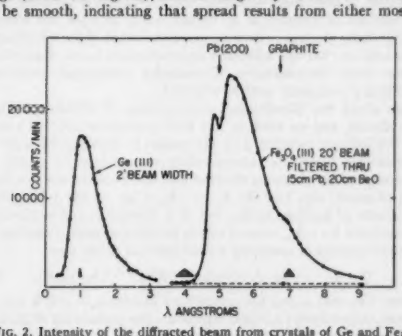


FIG. 2. Intensity of the diffracted beam from crystals of Ge and $Fe_3O_4$. Curve for Ge represents the pile spectrum and for $Fe_3O_4$ that part of the pile spectrum transmitted through a BeO filter.

† Work done under the auspices of the AEC.

[1] Weiss, Clark, Hastings, and Corliss, Phys. Rev. **86**, 656 (1952).
[2] C. G. Shull, Phys. Rev. **81**, 626 (1950).

## Fission-to-Capture Cross-Section Ratio

JOHN R. HUIZENGA
*Argonne National Laboratory, Chicago, Illinois*
AND
ROBERT B. DUFFIELD
*Physics Department, University of Illinois, Urbana, Illinois*

(Received September 19, 1952)

THE energies $E_f$, required to produce a critical deformation of heavy nuclei leading to fission have been calculated by Bohr and Wheeler.[1] Frankel and Metropolis[2] have extended these calculations. Several attempts to correlate existing experimental data with the above theoretical expectations have been unfruitful. For example, Frankel and Metropolis predict an $E_f$ value of 7.7 Mev[2] for $Th^{230}$. The binding energy of a neutron to $Th^{229}$ is 6.6 Mev.[3] Therefore, $Th^{229}$ would be predicted to be stable to thermal neutron fission by ~1 Mev. However, experimentally the thermal neutron fission cross section of $Th^{229}$ is ~45 barns.[4]

An empirical relationship between spontaneous fission half-life and a function of $Z$ and $A$ has been shown by Seaborg.[5] The existing theory[1,2] would predict a much greater variation in spontaneous fission rates than that experimentally observed. The theory also does not predict the slower spontaneous fission rates of odd nuclei.

Measured photofission thresholds[6] are quite constant and differ a good deal from values predicted by Frankel and Metropolis.[2] This, plus such evidence as the fissionability of $Th^{229}$ with thermal neutrons, indicates that $E_f$ values do not depend as strongly on $Z$ and $A$ as the theory predicts. From the above discussion, it is evident that the present fission theory leaves much to be desired.

The purpose of this paper is to point out a correlation between the thermal neutron fission cross section of $(Z, A)$, the thermal neutron capture cross section of $(Z, A)$, and the binding energy of a neutron to $(Z, A)$.

The ratio of the thermal neutron fission cross section to the thermal neutron capture cross section can be expressed as

$$\sigma_f/\sigma_c = \Gamma_f/\Gamma_c,$$

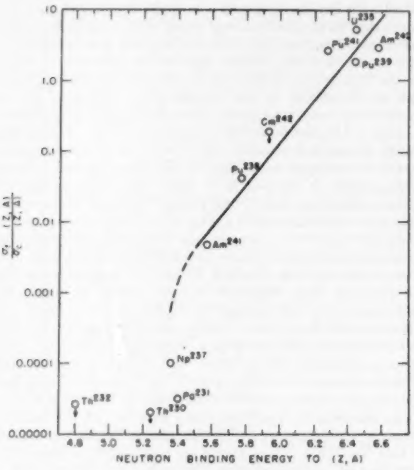


FIG. 1. $\text{Log}[\sigma_f(Z,A)/\sigma_c(Z,A)]$ *vs* the binding energy of a neutron to $(Z, A)$.

where $\Gamma_f$ is the probability per unit time that the compound nucleus lose its excitation by fission, and $\Gamma_c$ is the probability per unit time that the compound nucleus lose its excitation by gamma-ray emission. If $\Gamma_c$ is a very slowly changing function of the nuclear excitation energy in the region under consideration (4.8 to 6.6 Mev), and if $\Gamma_f$ is a highly dependent function of nuclear excitation energy in the above energy range, one would expect a correlation of the ratio $\sigma_f/\sigma_c$ with neutron binding energies. Implicit in the above reasoning is that the critical deformation energies $E_f$ are roughly constant for the nuclides considered. The difference between the neutron binding energy and $E_f$ would be a better quantity to plot on the abscissa.

The plot of $\log\sigma_f(Z,A)/\sigma_c(Z,A)$ *vs* the binding energy of a neutron to $(Z, A)$ for several nuclides is shown in Fig. 1. In Table I are listed the cross-section and binding energy data.

From Fig. 1, it is readily seen that the logarithm of the ratio $\sigma_f/\sigma_c$ decreases sharply with decreasing neutron binding energy. With two of the three variables ($\sigma_f$, $\sigma_c$, neutron binding energy) known, the third can be predicted. Using our calculated neutron binding energies,[3] several interesting $\sigma_f/\sigma_c$ ratios can be predicted. For example, $\sigma_f/\sigma_c$ should be about 0.1 or less for $U^{239}$. The measured thermal neutron capture cross section of $U^{239}$ is 22 barns.[4] Therefore, the predicted thermal neutron fission cross section of $U^{239}$ is $\leqslant 2$ barns. Likewise, it would be of interest to measure the thermal neutron capture cross sections of such nuclides as $Th^{229}$ and $U^{233}$ since values[4] are reported for their thermal neutron fission cross sections.

TABLE I. Binding energy of a neutron to $(Z, A)$ and the thermal neutron capture and fission cross-sections of several nuclides.

| Nuclide $(Z, A)$ | $\sigma_f(Z,A)$[a] barns | $\sigma_c(Z,A)$[a] barns | $\dfrac{\sigma_f(Z,A)}{\sigma_c(Z,A)}$ | Neutron binding energy to $(Z, A)$[b] Mev |
|---|---|---|---|---|
| $Th^{230}$ | <0.001 | 45 | $<2.2\times10^{-5}$ | 5.25 |
| $Th^{232}$ | <0.0002 | 7 | $<2.8\times10^{-5}$ | 4.80 |
| $Pa^{231}$ | 0.01 | 290 | $3.4\times10^{-5}$ | 5.41 |
| $U^{233}$ | 545 | 100 | 5.45 | 6.43 |
| $Np^{237}$ | 0.019 | 170 | $1.1\times10^{-4}$ | 5.36 |
| $Pu^{238}$ | 20 | 455 | $4.4\times10^{-2}$ | 5.77 |
| $Pu^{239}$ | 664 | 361 | 1.84 | 6.43 |
| $Pu^{241}$ | 1060 | 400 | 2.65 | 6.27 |
| $Am^{241}$ | 1 | 884 | $\sim5\times10^{-2}$ | 5.57 |
| $Am^{242}$ | ~6000 | ~2000 | 3 | 6.58 |
| $Cm^{242}$ | <5 | ~25 | $<2\times10^{-1}$ | 5.93 |

[a] See reference 4.
[b] See reference 3.

It is also interesting to note that $Cm^{243}$ and $Am^{243}$ show no irregularity[5] in Fig. 1 when the variable $\sigma_f/\sigma_c$ is plotted *vs* neutron binding energy. When the neutron binding energies decrease to values of about 5.4 Mev, the plot of $\log(\sigma_f/\sigma_c)$ *vs* neutron binding energy shows an irregularity (see Fig. 1). The fission mechanism may be considerably different at these energies, since the neutron binding energy may not be sufficient to bring the excited nucleus above the fission barrier.

Refinements, of course, can be made in Fig. 1 for the different type nuclei. However, the present data do not justify separating the odd compound nuclei from the even type.

It is a pleasure to acknowledge helpful discussion with P. R. Fields, L. B. Magnusson, and M. H. Studier.

[1] N. Bohr and J. A. Wheeler, Phys. Rev. **56**, 426 (1939).
[2] S. Frankel and N. Metropolis, Phys. Rev. **72**, 914 (1947).
[3] J. R. Huizenga and L. B. Magnusson (unpublished results).
[4] See the compilation of cross sections by Manning, Ghiorso, and Seaborg, *The Transuranium Elements: Research Papers* (McGraw-Hill Book Company, Inc., New York, 1949), Chapter 20, National Nuclear Energy Series, Plutonium Project Record, Vol. 14B, Div. IV.
[5] G. T. Seaborg, Phys. Rev. **85**, 157 (1952).
[6] Koch, McElhinney, and Gasteiger, Phys. Rev. **77**, 329 (1950).

## The Motion of Slow Electrons in Polar Crystals

TSUNG-DAO LEE[6] AND DAVID PINES
*Department of Physics, University of Illinois, Urbana, Illinois*
(Received September 17, 1952)

WE have investigated the low-lying energy levels of a conduction electron in a polar crystal, using the "intermediate coupling" variational technique introduced by Tomonaga.[1] This problem is of considerable interest because of the strong interaction between the electron and the ionic polarization it produces in its motion through the crystal. The electron may be pictured as accompanied by a cloud of phonons (i.e., the associated waves of ionic polarization), and the combined system (electron plus associated phonon cloud) is known as a polaron. The strength of the electron-lattice interaction furnishes a measure of the average number of phonons in the cloud around the electron, and hence of the effective mass of the polaron.

The reduction in the electron energy as a consequence of its interaction with the lattice was first computed semi-classically by Pekar,[2] and by Markham and Seitz,[3] using an adiabatic approximation. Fröhlich, Pelzer, and Zienau[4] calculated this energy and the effective mass of the polaron in a quantum-mechanical treatment which is appropriate provided the electron-lattice interaction is sufficiently weak. Pekar[5] has also given a quantum treatment of these aspects, using the adiabatic approximation. However, in most cases of interest the interaction is so strong that the method of Fröhlich *et al.* breaks down, and yet the kinetic energy of the electron is only comparable to that of the vibrational quantum, so that the adiabatic approximation is not applicable. Under these circumstances, Tomonaga's variational technique furnishes a promising method of attack.

We adopt the Hamiltonian and notation of Fröhlich, Pelzer, and Zienau, and we work in the Fock representation,[6] in which the Schrödinger function $\psi$ of our system is described by a set of Schrödinger functions corresponding respectively to states of electron and no phonons, electron and one phonon, electron and two phonons, etc. Let $\langle \mathbf{k}_1, \mathbf{k}_2, \cdots, \mathbf{k}_n, \mathbf{r}_e/\psi\rangle$ be the probability amplitude of finding the electron at a position $\mathbf{r}_e$ and $n$ phonons of momenta $\mathbf{k}_1 \cdots \mathbf{k}_n$, respectively in the phonon field. Tomonaga's method consists of assuming a trial function of the form

$$\langle \mathbf{k}_1, \mathbf{k}_2, \cdots, \mathbf{k}_n, \mathbf{r}_e/\psi\rangle = c_n f(\mathbf{k}_1) f(\mathbf{k}_2) \cdots f(\mathbf{k}_n) \chi_n(\mathbf{r}_e), \qquad (1)$$

where $f(\mathbf{k})$ and $\chi_n(\mathbf{r}_e)$ are normalized functions in the $\mathbf{k}$ and $\mathbf{r}_e$ spaces, respectively; $c_n^2$ thus represents the probability of finding $n$ phonons and one electron in the system. If we further require that $\psi$ be an eigenfunction of the total momentum of the system

$\mathbf{P}$, the form of $\chi_n$ is automatically fixed. It is

$$\chi_n(\mathbf{r}_n)=\frac{1}{\sqrt{V}}\exp\left\{\frac{i}{\hbar}\left(\mathbf{P}-\sum_{i=1}^{n}\hbar\mathbf{k}_i\right)\cdot\mathbf{r}_n\right\}. \quad (2)$$

On varying the energy with respect to $f(\mathbf{k})$ and $\epsilon_n$, the best form of $f(\mathbf{k})$ and a difference equation for $\epsilon_n$ can be obtained.[7] Our choice (1) of $(\mathbf{k}_1, \mathbf{k}_2, \cdots, \mathbf{k}_n, \mathbf{r}_n/\psi)$ reflects our assumption of no correlation between the emission of successive phonons, so that the form of $f$ is the same for all the phonons. Yet, as in any application of Ritz's variational principle, the value of $E$ thus determined will be better than the form of $\psi$ chosen.

We confine our attention here to the low-lying energy levels of the system, such that the total *system* momentum $P$ satisfies $(P^2/2m)<\hbar\omega$, where $m$ is the effective mass of the electron (as a consequence of its interaction with the *periodic* lattice field), and $\omega$ the frequency of the optical vibrational mode of the lattice oscillation. Under these circumstances, the difference equation can be solved analytically, and the best form of $f(\mathbf{k})$ turns out to be

$$f(\mathbf{k})=N\{k(k^2+2m\omega/\hbar)-[12kP\cos\vartheta/(\alpha+6)\hbar]\}^{-1}, \quad (3)$$

where $N$ is a normalization constant, $\vartheta$ is the angle between $\mathbf{k}$ and $P$, and $\alpha$ is the coupling constant of the lattice-electron interaction.

$$\alpha=\left(\frac{e^2}{\hbar c}\right)\left(\frac{mc^2}{2\hbar\omega}\right)^{\frac{1}{2}}\left(\frac{1}{n^2}-\frac{1}{\epsilon}\right),$$

where $n$ is the index of refraction and $\epsilon$ the dielectric constant of the crystal. The average number of phonons in the cloud around the electron turns out to be approximately $\alpha/2$. The corresponding energy of the ground state of the system with a total momentum $\mathbf{P}$ is

$$E=-\alpha\hbar\omega+(P^2/2m)(1+\alpha/6)^{-1}+\cdots+O(P^2/2m\hbar\omega)^2+\cdots, \quad (4)$$

relative to the energy of a free electron at the bottom of the crystal conduction band.

Thus, for the slow electrons we here considered, the interaction introduces two effects: (1) all electronic energy levels are reduced by $\alpha\hbar\omega$; and (2) the motion of the polaron is that of a free particle with an effective mass $m_{\text{eff}}=m(1+\alpha/6)$. In the limit of weak coupling $\alpha\ll 1$, our result reduces to that of Fröhlich *et al.*, and for larger values of $\alpha$, our result always corresponds to a lower energy. For a typical polar crystal, NaCl, ($\alpha=5.2$, $\omega=4.8\times10^{13}$ sec$^{-1}$), we find $E_0=-\alpha\hbar\omega\cong-0.16$ ev, and $m_{\text{eff}}=1.9$ m. In this case Fröhlich *et al.*, and also Pekar, obtain $E_0\cong-0.09$ ev. Thus, the Tomonaga scheme provides a better determination of the lowest energy of the system. For NaCl, Pekar[6] and Landau and Pekar[8] found $m_{\text{eff}}=432$. However, as might be inferred from Pekar's much higher value of $E_0$, this high effective mass is due to the lack of applicability of the adiabatic approximation. A detailed calculation confirms this point.

The interaction of a fast electron with both the acoustic and polarization waves is now under investigation. A detailed account of the above work will be submitted for publication soon.

We thank Professor John Bardeen for many stimulating discussions. One of us (D.P.) would like to acknowledge the support of the Office of Ordnance Research during this work.

* Now at the Institute for Advanced Study, Princeton, New Jersey.
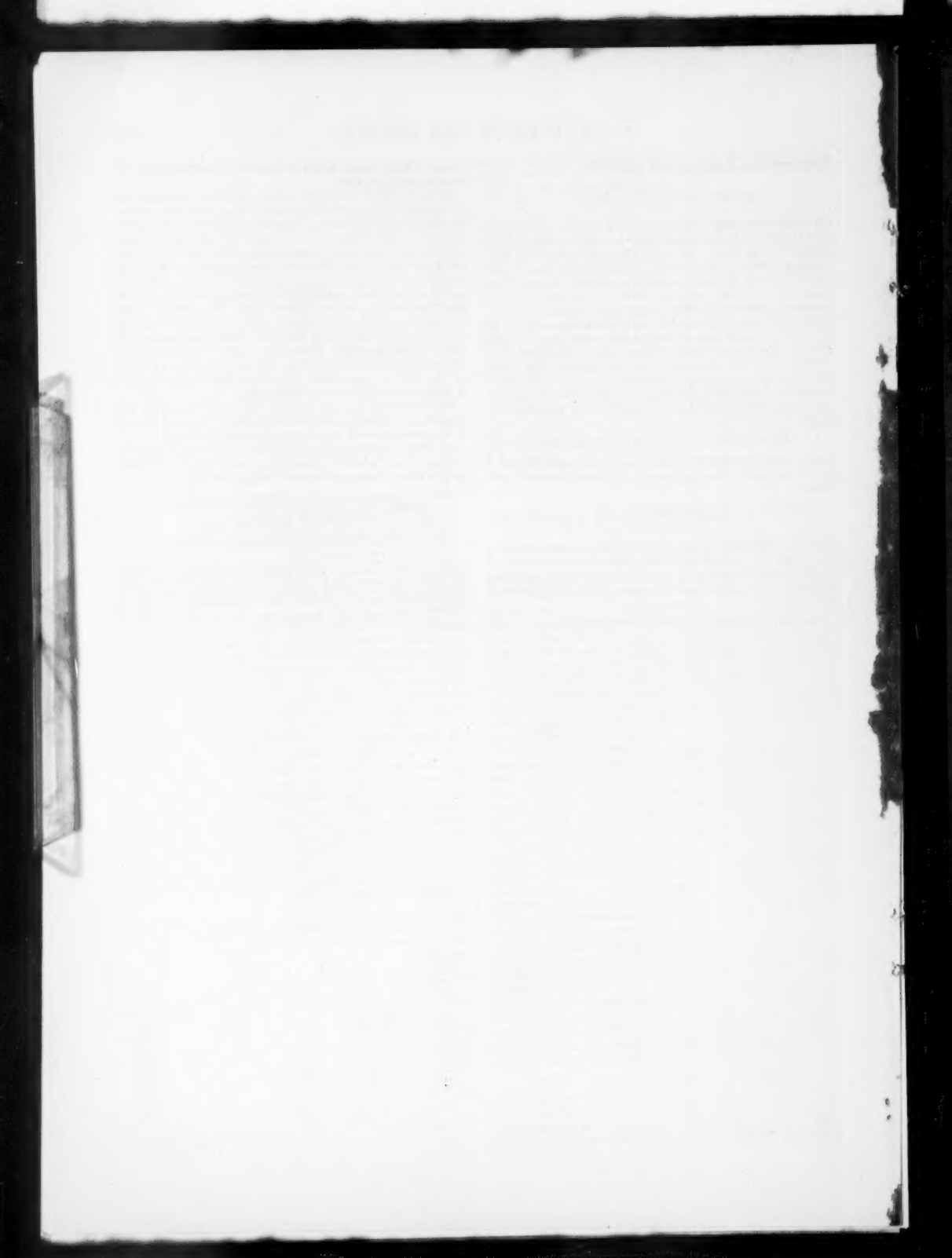
[1] S. Tomonaga, Prog. Theor. Phys. **2**, 6 (1947).
[2] S. Pekar, J. Phys. (U.S.S.R.) **10**, 341 (1946).
[3] J. Markham and F. Seitz, Phys. Rev. **74**, 1014 (1948).
[4] Fröhlich, Pelzer, and Zienau, Phil. Mag. **41**, 221 (1950).
[5] S. Pekar, J. Exptl. Theor. Phys. (U.S.S.R.) **19**, 796 (1949).
[6] V. Fock, Z. Physik **75**, 622 (1932).
[7] Our approach differs from Tomanaga's in two respects. First, we have determined the best form of $f$ by a variation calculation, rather than assuming a definite form for $f$. (Actually, in the case considered by him, Tomonaga's assumed form for $f$ is also the best one.) Second, we have extended his technique to include the case of a moving particle (here, the electron).
[8] L. Landau and S. Pekar, J. Exptl. Theor. Phys. (U.S.S.R.) **18**, 419 (1948).